

**Seismic Performance Evaluations and Analyses for Composite Moment
Frames with Smart SMA PR-CFT Connections**

A Dissertation

Presented to

The Academic Faculty

By

Jong Wan Hu

In Partial Fulfillment

of the Requirement for the Degree

Doctor of Philosophy in the

School of Civil and Environmental Engineering

Georgia Institute of Technology

April 2008

**Seismic Performance Evaluations and Analyses for Composite Moment
Frames with Smart SMA PR-CFT Connections**

Approved by:

Dr. Roberto T. Leon, Advisor
School of Civil and Environmental
Engineering
Georgia Institute of Technology

Dr. Barry J. Goodno
School of Civil and Environmental
Engineering
Georgia Institute of Technology

Dr. Don White
School of Civil and Environmental
Engineering
Georgia Institute of Technology

Dr. W. Steven Johnson
School of Materials Science and
Engineering
Georgia Institute of Technology

Dr. Reginald DesRoches
School of Civil and Environmental
Engineering
Georgia Institute of Technology

Date Approved: March 26, 2008

Acknowledgements

There is one motto I always have believed and followed in my life: *A man of genius cannot exceed a hard worker and a hard worker cannot exceed a person who enjoys his work.* I never have been a man of genius; however, I have been a hard worker and enjoyed my research since I decided to work in this field. I have spent four and half years for my Ph.D. course. It was tough time but it was very precious time of my life.

At this time, I would like to express my sincere appreciation to my thesis advisor, Dr. Roberto T. Leon, for his thoughtful guidance, encouragement, patient, and constructive criticism thought the course of this study. I would also like to acknowledge the invaluable comments provided by Dr. Don White, Dr. Reginald DesRoches, Dr. Barry J. Goodno, and Dr. W. Steven Johnson who participated in his dissertation exam committee.

This research project was funded by NEESR/NSF project. The financial and technical support of this research association is greatly acknowledgement. I would also like to thank Korean Science Foundation and Korean Ministry of Science & Technology for abroad study scholarship.

I would certainly like to extend my gratitude to my pervious advisor for M.S. study and professors in Inha University: Dr. Won Sup Hwang, Dr. Min-Seoi Koo, Dr. Myung Pil Shim, and Dr. Jae Sung So.

Grateful appreciation is extended to my senior alumni and colleagues, Dr. Uksun Kim, Dr. Do-Hwan Kim, Dr. Chuang-Sheng Yang, Tiziano Perea, Matthew Speicher, Masahiro Kurata, and Naiyu Wang. Also, many thanks go to the Korean students in the School of Civil Environmental Engineering at Georgia Tech who shared my ups and downs throughout my study.

My deepest thank and love go to my father, my mother, my brother, my sister-in-law, my sister, and my nephew for their understanding and warm support.

Table of Contents

Acknowledgement	iii
List of Tables	vii
List of Figures	xi
Notations	xxiv
Abbreviations	xxxii
Summary	xxxiv
Chapter 1 Introduction	1
1.1 Research Background	1
1.2 Research Objective	7
1.3 Research Methodology	8
1.4 Outline	9
Chapter 2 Literature Review	12
2.1 Related Research	12
2.2 Unique Characteristics of Proposed Research	20
Chapter 3 Design Procedure for Prototype Connections	22
3.1 Design Requirement Strength	22
3.2 Preliminary Design Procedure for Connection Components	57
3.3 Design Discussion	73
Chapter 4 Smart PR-CFT Connections	74
4.1 Design Principles	74
4.2 Specimen Details	77
4.3 Failure Modes	86

4.4	Instrumentations	89
4.5	Summary and Discussion	98
Chapter 5	3D Finite Element Modeling	99
5.1	3D Solid Modeling Method	99
5.2	FE Test Results	122
5.3	Observations of Monotonic Behavior	137
5.4	Observations of Failure Modes	150
5.5	Summary and Discussion	157
Chapter 6	Connection Modeling under Cyclic Loads	158
6.1	Joint Model	158
6.2	Joint Elements	175
6.3	Cyclic Behavior	179
6.4	Observations of Model Tests	186
6.5	Summary and Discussion	197
Chapter 7	Design of Composite Moment Frames with Smart SMA PR-CFT Connections	198
7.1	Characteristics of Composite Moment Frames	198
7.2	Building Configurations	203
7.3	Seismic Design Method	210
7.4	Design of Composite Moment Frame Specimens	215
7.5	Modeling Attributes for the Numerical Frame Models	227
7.6	Summary and Discussion	231
Chapter 8	Nonlinear Analyses for the Composite Moment Frames	
8.1	Introduction for Nonlinear Analyses	232

8.2	Nonlinear Pushover Analyses	236
8.3	Nonlinear Dynamic Analyses	260
8.4	Summary and Discussion	284
Chapter 9	Seismic Performance and Damage Evaluation	285
9.1	Introduction	285
9.2	Seismic Performance and Damage Evaluation	292
9.3	Comparisons for the Damage Evaluation	308
9.4	Summary and Discussion	317
Chapter 10	Conclusion	318
10.1	Summary	318
10.2	Conclusions	321
10.3	Recommendations for the Future Work	327
	The List of Appendix	330
	Appendix A: Detailed Design Examples for CFT Columns	331
	Appendix B: Design Examples and Failure Modes	354
	Appendix C: Instrumentation	414
	Appendix D: The Equivalent Lateral Force Procedures	423
	Appendix E: Detail Design Examples for Panel Zones	439
	Appendix F: Earthquake Ground Motion	466
	References	477
	Vita	489

List of Tables

Table 1.1:	Summary of frame analyses	9
Table 2.1:	Available experimental moment-rotational data for several connection types (<u>Summarized by Chan and Chui, 2000</u>)	13
Table 3.1:	Equations for the specific 5 points in the P-M interaction diagram	29
Table 3.2:	Current LRFD design resistant factors	32
Table 3.3:	Pre-qualification limitations for geometric parameters (ANSI 385-05, Unit: inches)	63
Table 3.4:	Summary and comparison of design procedures for T-stub and clip angle connections	73
Table 4.1:	Detailed specifications of the smart PR-CFT connections	75
Table 5.1:	ABAQUS Input values for A572-Gr.50 Steel	105
Table 5.2:	ABAQUS Input values for A490 bolts	106
Table 5.3:	Summary of material constitutive models for confined concrete	108
Table 5.4:	ABAQUS input values for concrete properties	109
Table 5.5:	ABAQUS input values for concrete properties	110
Table 5.6:	FE model cases for full PR connections	122
Table 5.7:	Comparisons between foundation models vs. concrete models	122
Table 5.8:	Comparisons between external moment and internal moment including prying response (End-plate connection)	142
Table 5.9:	Comparisons between external moment and internal moment including prying response (T-stub connection)	147
Table 5.10:	Comparisons between external moment and internal moment including prying response (Clip Angle Connection)	150
Table 6.1:	Comparisons between results of the simplified model and those of 3D FE model test	163
Table 7.1:	General classes of composite moment frame (C-MF)	199
Table 7.2:	Location, loads, and structural classifications common to all frames	203
Table 7.3:	Design response spectra for CMF in LA area	211
Table 7.4:	Design loads for all composite moment frames	212

Table 7.5:	Design results for composite frame buildings	217
Table 7.6:	Design checks for deflection and drift ratio	223
Table 7.7:	Properties of panel zones for all frame model connections	229
Table 8.1:	Overall frame analyses and data measurements	233
Table 8.2:	Earthquake ground motions with 2% probability of exceedance in 50 years	260
Table 8.3:	Peak response of the 6END-C1 case under various EQ motions	269
Table 8.4:	Peak inter-story drift ratio of the 6END-C1 case under various EQ motions	269
Table 8.5:	Peak response of the 6END-C2 case under various EQ motions	270
Table 8.6:	Peak inter-story drift ratio of the 6END-C2 case under various EQ motions	270
Table 8.7:	Peak response of the 6END-C7 case under various EQ motions	271
Table 8.8:	Peak inter-story drift ratio of the 6END-C7 case under various EQ motions	271
Table 8.9:	Peak response of the 6TSU-C1 case under various EQ motions	272
Table 8.10:	Peak inter-story drift ratio of the 6TSU-C1 case under various EQ motions	272
Table 8.11:	Peak response of the 4END-C1 case under various EQ motions	273
Table 8.12:	Peak inter-story drift ratio of the 4END-C1 case under various EQ motions	273
Table 8.13:	Peak response of the 4END-C2 case under various EQ motions	274
Table 8.14:	Peak inter-story drift ratio of the 4END-C2 case under various EQ motions	274
Table 8.15:	Peak response of the 4END-C7 case under various EQ motions	

		275
Table 8.16:	Peak inter-story drift ratio of the 4END-C7 case under various EQ motions	275
Table 8.17:	Peak response of the 6END case under the LA21 motion with relatively strong PGA	279
Table 8.18:	Peak response of the 6END case under the LA23 motion with relatively weak PGA	279
Table 8.19:	Peak response of the 4END case under the LA21 motion with relatively strong PGA	279
Table 8.20:	Peak response of the 4END case under the LA23 motion with relatively weak PGA	279
Table 9.1:	Available information on damage evaluations for the composite columns	290
Table 9.2:	Damage evaluations for RCFT columns (HSS 16X16X500) for the 6END-C1 model case	298
Table 9.3:	Damage evaluations for CCFT columns (HSS 18X500) for the 6END-C2 model case	299
Table 9.4:	Damage evaluations for RCFT columns (HSS 16X16X500) for the 6END-C7 model case	300
Table 9.5:	Damage evaluations for CCFT columns (HSS 18X500) for the 6END-C8 model case	301
Table A.1:	Summary of the CFT columns	331
Table A.2:	Equations for the specific 5 points in the P-M interaction diagram (RCFT columns)	332
Table A.3:	Equations for the specific 5 points in the P-M interaction diagram (CCFT columns)	333
Table A.4:	Calculation results for five points in P-M interaction diagram	347
Table B.1:	Prequalification dimension limits	355
Table B.2:	Material properties for the end-plate connection (Case 1)	374
Table B.3:	Material properties for the end-plate connection (Case 2)	382
Table B.4:	Material properties for the end-plate connection (Case 3)	390

Table B.5:	Material properties for the end-plate connection (Case 5)	402
Table E.1:	Summary of the geometric dimensions for panel zone models	440
Table E.2:	Theoretical results for the panel zone strength	465
Table F.1:	Earthquake ground motions with 2% probability of exceedence in 50 year	466

List of Figures

Figure 1.1:	3 story by 3 bay CFT composite frame with buckling restrained braces (Tasi, K.C et al., 2003)	2
Figure 1.2:	Details of connections to CFT columns	3
Figure 1.3:	Typical moment-rotation curve	4
Figure 1.4:	Stress-strain-temperature relationships for a SMA (DesRoches et al.,2004)	5
Figure 1.5:	Super-elastic Nitinol tendon connection (Penar, 2005)	6
Figure 1.6:	Summary of the research approach	11
Figure 2.1:	T-Stub and Seat Angle connection configurations	14
Figure 2.2:	Extended End-Plate connection configurations	14
Figure 2.3:	Typical welded connections to composite columns (Alostaz and Schneider, 1997)	16
Figure 2.4:	Isolator system for buildings	18
Figure 2.5:	Test specimen of beam to column connection using martensite Nitinol tendons (Ocel et. al. 2002)	19
Figure 2.6:	Retrofit application using Nitinol devices - The bell tower of the S. Giorgio Church in Trignano (Indirli et al. 2001)	20
Figure 3.1:	Types of cross sections for composite column system	23
Figure 3.2:	Full plastic stress distributions for RCFT and CCFT at point A, E, C, D, and E.	27
Figure 3.3:	P-M interaction diagrams for composite beam-columns	28
Figure 3.4:	Behavior of PR moment connections used in this study	30
Figure 3.5:	Typical connection types with friction slippage (SAC Project)	31
Figure 3.6:	View of a connection with a bolts in tension and shear	33
Figure 3.7:	Components before tension bolt fracture (SAC Project)	36
Figure 3.8:	Typical flange prying action	37
Figure 3.9:	Three possible failure modes	37
Figure 3.10:	Bolt bearing strength	41
Figure 3.11:	Stress distribution and net section fracture in T-stub members	42

Figure 3.12:	Block shear failure mechanism (Swanson, 1999)	43
Figure 3.13:	The detail of end-plate connection (4E, Four-bolt unstiffened type)	44
Figure 3.14:	Parameters for four bolt extended unstiffened end-plate (4E) yield line Mechanism	48
Figure 3.15:	Parameters for four bolt extended stiffened end-plate (4ES) yield line Mechanism	49
Figure 3.16:	Parameters for eight bolt extended stiffened end-plate (8ES) yield line Mechanism	49
Figure 3.17:	Schematic figures for deformation of steel tube in the panel zone region	52
Figure 3.18:	Average tensile strength for a bar	64
Figure 4.1:	Typical connection configurations	78
Figure 4.2:	Schematic drawing of RCFT end-plate connection details	80
Figure 4.3:	Schematic drawing of CCFT end-plate connection details	81
Figure 4.4:	Schematic drawing of RCFT T-stub connection details	82
Figure 4.5:	Schematic drawing of CCFT T-stub connection details	83
Figure 4.6:	Schematic drawing of RCFT clip angle connection details	84
Figure 4.7:	Schematic drawing of CCFT clip angle connection details	85
Figure 4.8:	3D configurations of SMA PR-CFT connection details	86
Figure 4.9:	Failure modes for SMA PR-CFT connections	89
Figure 4.10:	Measurement points for the end plate connection (Side and top view)	91
Figure 4.11:	Measurement points for the T-stub connection (Side and top view)	92
Figure 4.12:	Measurement points for the angle connection (Side and top view)	93
Figure 4.13:	Response mechanism for each connection model at ultimate	94
Figure 4.14:	Measurement points for the stress and strain for the end plate connection (Side and top view)	95
Figure 4.15:	Measurement points for the stress and strain for the T-stub connection (Side and top view)	96
Figure 4.16:	Measurement points for the stress and strain for the clip angle connection (Side and top view)	97
Figure 5.1:	Partitioned 3D solid models for the SMA PR-CFT connection	

	(RCFT case)	102
Figure 5.2:	Partitioned 3D solid models for the SMA PR-CFT connection (CCFT case)	102
Figure 5.3:	3D solid elements for the PR-CFT connections	103
Figure 5.4:	3D solid elements for the connection	103
Figure 5.5:	3D solid elements for the component members	104
Figure 5.6:	Tensile stress-strain curves for A572-Gr. 50 Steel	105
Figure 5.7:	Tensile stress-strain curves for A490 bolts	107
Figure 5.8:	Decomposition of the total strain into elastic and plastic strain	108
Figure 5.9:	Equivalent stress-strain curve for concrete (Hu et al. 2005 and Torres et al.2004)	108
Figure 5.10:	Stress-strain curve for confined concrete (RCFT)	109
Figure 5.11:	Stress strain curve for confined concrete (CCFT)	110
Figure 5.12:	Tensile stress-strain curve for super-elastic SMA bar (DesRoches et. al. 2004)	111
Figure 5.13:	Surface interactions with friction coefficient	113
Figure 5.14:	Contact interactions between steel and concrete	114
Figure 5.15:	Modeling method for concrete cracks (Left)	115
Figure 5.16:	Multi-linear constraint equation points (Right)	115
Figure 5.17:	Symmetry boundary conditions for half model (Left)	117
Figure 5.18:	Initial pretension force in bars and bolts (Right)	117
Figure 5.19:	Application of the load (end displacement)	117
Figure 5.20:	Basic step manager	118
Figure 5.21:	Load manager for bolt pretensions incorporated with time steps	118
Figure 5.22:	Solution and control for the computation associated with step manager	119
Figure 5.23:	Comparison models to investigate the effect of concrete filling	120
Figure 5.24:	Comparison models to investigate the effect of clearance distance	120
Figure 5.25:	Elastic foundation model for the CFT column model	121
Figure 5.26:	Load-deflection curve for confined concrete under compression	121
Figure 5.27:	Non-linear behavior of end-plate connections	125

Figure 5.28:	Non-linear behavior of the T-stub connections	127
Figure 5.29:	Non-linear behavior of the clip angle connection	127
Figure 5.30:	Comparisons of behavior for all connection models with the CFT column	128
Figure 5.31:	Force and deformation in the tension bars (End-plate connections)	129
Figure 5.32:	Force and deformation in the tension bars (T-stub connections)	130
Figure 5.33:	Force and deformation in the tension bars (Clip angle connections)	130
Figure 5.34:	Stress contour levels for each material	131
Figure 5.35:	Stress distributions for the end-plate connections at ultimate	132
Figure 5.36:	Stress distributions for the T-stub connections at ultimate	132
Figure 5.37:	Stress distributions for the clip angle connections at ultimate	133
Figure 5.38:	Stress distributions for tension bars of end-plate connections at ultimate	134
Figure 5.39:	Stress distributions for tension bars of T-stub connections at ultimate	134
Figure 5.40:	Stress distributions for tension bars of clip angle connections at ultimate	135
Figure 5.41:	Stress distributions for inside concrete at ultimate	136
Figure 5.42:	Reaction force and deformation for end-plate connections subjected to the maximum force (T) at the tip of beam	137
Figure 5.43:	Panel zone behavior of the end-plate connections	138
Figure 5.44:	Measurement of end-plate uplift displacement at location of tension bars	139
Figure 5.45:	Reaction force of tension bars in the end-plate connections	141
Figure 5.46:	Bar prying response for end-plate connections	141
Figure 5.47:	Reaction force and deformation for T-stub connections subjected to the maximum force (T) at the tip of beam	143
Figure 5.48:	Bar alignment position and bar uplift displacement	144
Figure 5.49:	Force and deformation of T-stub connection components	145
Figure 5.50:	Reaction force in tension bars of the T-stub connections	146
Figure 5.51:	Bar prying response for the end-plate connections	147

Figure 5.52:	Reaction force and deformation for clip angle connections subjected to the maximum force (T) at the tip of beam	148
Figure 5.53:	Force and deformation of clip angle connection components	149
Figure 5.54:	Bar prying response of the clip angle connection	149
Figure 5.55:	Plastic moment and rotation curves for the connections	152
Figure 5.56:	Investigation of local buckling from deformation measurements	152
Figure 5.57:	Failure modes for end-plate connections based on the stresses	154
Figure 5.58:	Failure modes for T-stub connections based on the stresses	155
Figure 5.59:	Failure modes for clip angle connections based on the stresses	156
Figure 6.1:	Load distribution and deformed configuration of the frame building	159
Figure 6.2:	Idealized joint model of the end-plate connection	160
Figure 6.3:	External and internal forces at the joint for the end-plate connection	161
Figure 6.4:	Response mechanism of the joint element under bending deformation	161
Figure 6.5:	Assemblage procedure for spring elements	162
Figure 6.6:	Properties of the individual component	162
Figure 6.7:	Algorithm for the formulation of an equivalent spring element	163
Figure 6.8:	Measuring points and comparisons of results between two tests (Cyclic Test vs. Monotonic Test)	164
Figure 6.9:	External and internal forces in the joint model for the T-stub connection	165
Figure 6.10:	Response mechanism of the joint element under bending deformation	165
Figure 6.11:	Component model for the 3D FE T-stub and its deformed configuration under axial force	166
Figure 6.12:	Specimen details of T-stub component model	166
Figure 6.13:	Force vs. deformation of T-stub component model	167
Figure 6.14:	Properties of the individual component model	168
Figure 6.15:	Comparisons between results of T-stub experiments and those of element tests	169

Figure 6.16:	External and internal forces for the joint model of the clip angle connection	170
Figure 6.17:	Response mechanism of the joint element under bending deformation	171
Figure 6.18:	Specimen details for the clip angle component model	171
Figure 6.19:	Force vs. deformation of clip angle component model	172
Figure 6.20:	Properties of the individual components	173
Figure 6.21:	Comparisons between results of clip angle experiments and those of element tests	174
Figure 6.22:	Typical joint element for a joint model (Cruciform Connection)	175
Figure 6.23:	Internal and external displacements and forces	176
Figure 6.24:	Typical joint element for a joint model (One Beam-to-Column Connection)	177
Figure 6.25:	Nonlinear beam-column element and 2D fiber sections	177
Figure 6.26:	Material properties for the analyses	178
Figure 6.27:	Test setup for a full scale connection (Swanson, 2000)	179
Figure 6.28:	Comparisons between monotonic loading of a 3D FE model and cyclic loading of the joint element	181
Figure 6.29:	Comparisons between the cyclic loading test of the SAC experiment model and the cyclic loading test	182
Figure 6.30:	Comparisons between the monotonic loading test of a 3D FE model and the cyclic loading test (Monotonic Test vs. Cyclic Test)	182
Figure 6.31:	Generation of the behavioral properties of components through observations of 3D FE test (Monotonic Test vs. Cyclic Test)	183
Figure 6.32:	Comparisons between the cyclic loading test of SAC experiment model and the cyclic loading test (SAC Experimental Test vs. Cyclic Test)	184
Figure 6.33:	Comparisons between the monotonic loading test of 3D FE model and the cyclic loading test (Monotonic Test vs. Cyclic Test)	184
Figure 6.34:	Generation of the behavioral properties of component models through observations of 3D FE test (Monotonic Test vs. Cyclic Test)	185
Figure 6.35:	Displacement loading history for the models	187

Figure 6.36:	Results of tests for end-plate connections with different combinations of tension bars	189
Figure 6.37:	Analytical predictions for the behavior of the component models	190
Figure 6.38:	Displacement loading history for the models	191
Figure 6.39:	Results of model tests for T-stubs connections with different combinations of tension bars	192
Figure 6.40:	Analytical predictions for the behavior of the component models	193
Figure 6.41:	Displacement loading history for the models	194
Figure 6.42:	Results of model tests for clip-angle connections with different combination of tension bars	195
Figure 6.43:	Analytical predictions for the behavior of the component models	196
Figure 7.1:	Typical composite partially restrained moment connection (AISC 2005 Seismic Provisions)	200
Figure 7.2:	Bidirectional bolted connections between CFT columns and H-beams (Wu et al., 2007)	201
Figure 7.3:	Typical composite special moment connection (AISC 2005 Seismic Provisions)	203
Figure 7.4:	Building elevation and plan view for the 4 story building	205
Figure 7.5:	Cruciform connection details for moment frames (4 story building)	206
Figure 7.6:	Building elevation and plan view for the 6 story building	208
Figure 7.7:	The cruciform connection details for moment frames (6 story building)	209
Figure 7.8:	Design response spectra for CMF in LA area	211
Figure 7.9:	Plan views of the 3D building and perimeter composite moment frames (C-MF)	219
Figure 7.10:	Moment interaction ratio for beam members under load combination 5	222
Figure 7.11:	Model trees for all composite moment frame specimens	226
Figure 7.12:	Numerical frame model composed of joint and nonlinear elements (C-PRMF case)	228
Figure 7.13:	Structural details of a joint element (Left)	229

Figure 7.14:	Tri-linear model of the panel zone (Right)	229
Figure 7.15:	Numerical frame model composed of nonlinear beam-column elements (C-SMF case)	230
Figure 7.16:	Numerical modeling of a panel zone for the welding connection	230
Figure 8.1:	Detail information for frame analysis and measurement cases	233
Figure 8.2:	Ground motions used in nonlinear dynamic analysis	234
Figure 8.3:	Schematic view of data collected	235
Figure 8.4:	Nonlinear monotonic pushover curves for C-MF with end-plate and welded connections (6END)	239
Figure 8.5:	The nonlinear monotonic pushover curves for C-MF with T-stub and welded connections (6TSU)	239
Figure 8.6:	The nonlinear monotonic pushover curves for C-MF with end-plate and welded connections (4END)	240
Figure 8.7:	Nonlinear monotonic pushover curves for C-MF with clip angle and welded connections (4CLI)	240
Figure 8.8:	Displacement history for the nonlinear cyclic pushover analysis	241
Figure 8.9:	Nonlinear cyclic pushover curves for C-MF with end-plate and welded connections (6END)	243
Figure 8.10:	The nonlinear cyclic pushover curves for C-MF with T-stub and welded connections (6TSU)	244
Figure 8.11:	The nonlinear cyclic pushover curves for C-MF with end-plate and welded connections (4END)	245
Figure 8.12:	The nonlinear cyclic pushover curves for C-MF with end-plate and welded connections (4CLI)	246
Figure 8.13:	Measurement points for the performance levels	247
Figure 8.14:	Allowable story drift check and inter story drift ratio at the measurement points (6END)	249
Figure 8.15:	Allowable story drift check and inter story drift ratio at the measurement points (6TSU)	250
Figure 8.16:	Interstory drift ratio at the measurement points (4END)	251
Figure 8.17:	Interstory drift ratio at the measurement points (4CLI)	251

Figure 8.18:	Story panel zone rotation angle at the measurement points (6END)	252
Figure 8.19:	Story panel zone rotation angle at the measurement points (6TSU)	253
Figure 8.20:	Determination of the failure mechanism using the failure hinge	254
Figure 8.21:	Failure hinge formation during the nonlinear monotonic pushover analysis (6END-C1)	256
Figure 8.22:	Failure hinge formation during the nonlinear monotonic pushover analysis (6END-C7)	257
Figure 8.23:	Failure hinge formation during the nonlinear monotonic pushover analysis (6END-C3)	258
Figure 8.24:	Failure hinge formation during the nonlinear monotonic pushover analysis (6END-C8)	259
Figure 8.25:	Displacement at the roof level under ground motions (6END)	263
Figure 8.26:	Displacement at the roof level under ground motions s (6TSU)	265
Figure 8.27:	Displacement at the roof level under ground motions (4END)	267
Figure 8.28:	Peak ISDR for the 6END-C1 case	276
Figure 8.29:	The peak ISDR for the 6END-C2 case	276
Figure 8.30:	Peak ISDR for the 6END-C7 case	276
Figure 8.31:	Peak ISDR for the 6TSU-C1 case	276
Figure 8.32:	Peak ISDR for the 4END-C1 case	277
Figure 8.33:	Peak ISDR for the 4END-C2 case	277
Figure 8.34:	Peak ISDR for the 4END-C7 case	277
Figure 8.35:	Peak ISDR under the LA21 motion	280
Figure 8.36:	Peak ISDR under the LA23 motion	280
Figure 8.37:	Peak ISDR under the LA21 motion	280
Figure 8.38:	Peak ISDR under the LA23 motion	280
Figure 8.39:	Hinges for 6END-C1 at RCFT columns under LA21 Motion (t=10.04sec)	281
Figure 8.40:	Hinges for 6END-C7 at RCFT columns under LA21 Motion (t=10.22sec)	282
Figure 8.41:	Hinges for 6END-C2 at CCFT columns under LA21 Motion (t=9.96sec)	

	282
Figure 8.42: Hinges for 6END-C1 at RCFT columns under LA26 Motion (t=3.10sec)	283
Figure 8.43: Hinges for 6END-C2 at CCFT columns under LA26 Motion (t=3.10sec)	283
Figure 9.1: Basic concept for the elastic strength ratio (ESR)	288
Figure 9.2: Basic concept for the inelastic curvature ductility ratio (ICDR)	289
Figure 9.3: Identification for nodes and elements on the composite moment frames	291
Figure 9.4: Specific examples for ESR calculations (6END-C1 Model)	294
Figure 9.5: Relationship between ESR values at the basement of interior column lines and hinge formation	295
Figure 9.6: Specific examples for ICDR calculations (6END-C1 Model)	297
Figure 9.7: Damage evaluations of the 6END-C1 model	303
Figure 9.8: Damage evaluations of the 6END-C2 model	304
Figure 9.9: Damage evaluations of the 6END-C7 model	305
Figure 9.10: Damage evaluations of the 6END-C8 model	306
Figure 9.11: Relationship between ESR and hinges during the pushover analyses	307
Figure 9.12: Performance levels on the pushover curves	309
Figure 9.13: Comparisons of ESR under pushover loads (6END-C1 vs. 6END-C7)	311
Figure 9.14: Comparisons of ESR under pushover loads (6END-C2 vs. 6END-C8)	311
Figure 9.15: Comparisons of ESR under pushover loads (6TSU-C1 vs. 6TSU-C7)	312
Figure 9.16: Comparisons of ESR under pushover loads (6TSU-C2 vs. 6TSU-C8)	312
Figure 9.17: Comparisons of ESR under pushover loads (4END-C1 vs. 4END-C7)	313
Figure 9.18: Comparisons of ESR under pushover loads (4END-C2 vs. 4END-C8)	313

	313
Figure 9.19: Comparisons of ESR under pushover loads (4CLI-C1 vs. 4CLI-C7)	314
Figure 9.20: Comparisons of ESR under pushover loads (4CLI-C2 vs. 4CLI-C8)	314
Figure 9.21: ESR under various ground motions (6END-C1 & 6END-C2)	315
Figure 9.22: ESR under various ground motions (6TSU-C1 & 6TSU-C2)	316
Figure 9.23: ESR under various ground motions (4END-C1 & 4END-C2)	316
Figure 10.1: Summary of the overall procedures in the dissertation	319
Figure 10.2: Original contributions for this research	328
Figure A.1: Numerical models and test setup for the fiber analyses	349
Figure A.2: Fiber analyses results and P-M interaction diagrams (RCFT 16X16X500)	350
Figure A.3: Fiber analyses results and P-M interaction diagrams (CCFT 18X500)	350
Figure A.4: Fiber analyses results and P-M interaction diagrams (RCFT 12X12X500)	351
Figure A.5: Fiber analyses results and P-M interaction diagrams (CCFT 14X500)	351
Figure A.6: Fiber analyses results and P-M interaction diagrams (RCFT 16X16X375)	352
Figure A.7: Fiber analyses results and P-M interaction diagrams (CCFT 18X375)	352
Figure A.8: Fiber analyses results and P-M interaction diagrams (RCFT 14X14X500)	353
Figure A.9: Fiber analyses results and P-M interaction diagrams (CCFT 16X500)	353

Figure B.1:	8 bolt stiffened extended end-plate connection geometry (8ES)	355
Figure B.2:	The limit check for the geometric parameters	356
Figure B.3:	Geometry summary and yield line failure mechanism (4 Bolt Unstiffened, 4E)	359
Figure B.4:	Geometry summary and yield line failure mechanism (4 Bolt Stiffened, 4ES)	359
Figure B.5:	Geometry summary and yield line failure mechanism (8 Bolt Stiffened, 8ES)	360
Figure B.6:	The arrangement of the shear bolts on the T-stub	363
Figure B.7:	The arrangement of the tension on the T-stub flange	364
Figure B.8:	The connection details (T-stub connection)	367
Figure B.9:	The arrangement of the shear bolts on the clip angle	369
Figure B.10:	The arrangement of the tension on the T-stub flange	370
Figure B.11:	The connection details (Clip angle connection)	373
Figure B.12:	Structural failure types based on the stress measurement (End-plate connection with RCFT Columns)	381
Figure B.13:	Structural failure types based on the stress measurement (End-plate connection with CCFT Columns)	389
Figure B.14:	Structural failure types based on the stress measurement (T-stub connection with RCFT Column)	398
Figure B.15:	Structural failure types based on the stress measurement (T-stub connection with CCFT Column)	401
Figure B.16:	Structural failure types based on the stress measurement (Clip angle connection with RCFT Columns)	410
Figure B.17:	Structural failure types based on the stress measurement (Clip angle connection with CCFT Columns)	413
Figure C.1:	The measurement points for displacements and reaction forces in the end-plate connection (without slippage)	415
Figure C.2:	The measurement points for displacements and reaction forces in the T-stub connection (with slippage)	415

Figure C.3:	The measurement points for strains and stresses in the end-plate connection	416
Figure C.4:	The measurement points for strains and stresses in the T-stub connection	416
Figure C.5:	The definition of the set points	417
Figure C.6:	The output request manager	418
Figure C.7:	The definition of the output request	418
Figure C.8:	The creation of the results for the output requests	419
Figure C.9:	The stress measurement at the T-stem	419
Figure D.1:	Design Response Spectrum	425
Figure D.2:	Design Response Spectrum (4END Case)	432
Figure D.3:	Design Response Spectrum (6END Case)	436
Figure D.4:	Dominant load combination (LC5) and load application in the 4END frame model	438
Figure D.5:	Dominant load combination (LC5) and load application in the 6END frame model	438
Figure E.1:	The geometric dimensions of the panel zone	439
Figure E.2:	The behavioral models for composite panel zones	465
Figure F.1:	Earthquake ground motions in 1995 Kobe	467
Figure F.2:	Earthquake ground motions in 1989 Loma Prieta	468
Figure F.3:	Earthquake ground motions in 1994 Northridge	469
Figure F.4:	Earthquake ground motions in 1994 Northridge	470
Figure F.5:	Earthquake ground motions in 1974 Tabas	471
Figure F.6:	Earthquake ground motions in 1992 Mendocino	472
Figure F.7:	Earthquake ground motions in 1992 Erzincan	473
Figure F.8:	Earthquake ground motions in 1949 Olympia	474
Figure F.9:	Earthquake ground motions in 1965 Seattle	475
Figure F.10:	Earthquake ground motions in 1985 Valpariso	476

Notation

α	The slenderness ratio for the composite column members
β	The ratio of shear demand to shear capacity for the story between story levels
γ_{wy}	The yield strain at the panel zone
δ_{xe}	The deflections determined by an elastic analysis for C-SMF system
Δ	The design story drift occurring simultaneously with V_x
ε	The strain
θ	An arc angle
σ	The stress
τ_{cu}	The ultimate shear stress of the concrete
τ_{sy}	The yield shear stress of steel
ϕ	The design reduction factor
ϕ_b	The design reduction factors for plastic yielding
ϕ_c	The design reduction factor for the axially loaded column
ϕ_{conn}	The concentrated rotational angle
$\phi_{elastic}$	The elastic rotational angle
ϕ_f	The design reduction factors for fracture failure
$\phi_{plastic}$	The plastic rotational angle
a	The distance from the centerline of the tension bolt to the edge of the flange

A_b	The nominal area of a bolt shank
A_{be}	The effective tensile area of the bolt's threaded portion
A_c	The cross section area of concrete core
A_{gt}	The gross section area under tension force
A_{gv}	The gross section area under shear force
A_n	Net area of the end-plate when standard holes are used
$A_{net,stem}$	The stem net section area
A_{nt}	The net section area under tension force
A_{nv}	The net section area under shear force
A_s	The cross section area of steel tube
A_{sr}	The area of continuous reinforcing bars
b	The distance from the centerline of the tension bolt to the surface of the clip leg/T-stem
b_{bf}	The width of the beam flange
b_c	The width of the column
b_p	The end-plate width
B	The force acting on the bars and bolts
B_n	The resistance strength for the bar and bolt members
$B_{n, shear}$	The resistance strength for the bolts subjected to the shear force
$B_{n, tension}$	The resistance strength for the bolts subjected to the tensile force

C_d	The deflection amplification factor
C_{pr}	Factor to account for the peak connection strength including strain hardening, local restraint, additional reinforcement, and other connection conditions.
d	Depth of the beam
d_b	The diameter of bars/bolts
$d_{b, req}$	The required bar/bolt diameter
d_c	The depth of the column
D	The dead load
E	The elastic modulus of the steel
E_c	Elastic modulus of concrete
E_s	Elastic modulus of steel
E	The earthquake load
EI_{eff}	Effective stiffness of the composite section
f'_c	Specific compressive strength of concrete
F_{tu}	Specified minimum tensile strength of the end-plate
F_{nt}	Nominal tensile stress of bolt
F_t	The effective ultimate tensile strength
F_u	The specified minimum tensile strength of the connected material
F_v	The effective shear strength of the shear bolts
F_y	Specified minimum yield stress of the type of steel

F_{yb}	Specified minimum yield stress of beam material
F_{yp}	Specified minimum yield stress of the end-plate material
F_{yr}	Specific minimum yield stress of reinforcing bars
F_{ys}	Specified minimum yield stress of stiffener material, ksi
g_t	The gauge length
G_s	The shear modulus of steel
h_i	Distance from the centerline of the beam compression flange to the centerline of the i^{th} tension bolt holes.
h_n	The equivalent height
h_{st}	The height of the stiffener
h_{xe}	The story height at each story level x
I_c	Moment of the inertia of the concrete section
I_E	The occupancy importance factor ($I_E=1.0$ for an ordinary occupancy)
I_f	Moment of inertia of the column flange
I_s	Moment of the inertia of the steel section
I_{sr}	Moment of the inertia of the reinforcing bars
K	The effective length factor determined in the boundary conditions
K_f	The shear stiffness for the column flange at the panel zone
K_w	The shear stiffness in the two column webs
L	Laterally unbraced length of the members

L	The live load
L'	The distance between plastic hinges
L_c	The clear distance
L_{st}	The width of the stiffener
M	The moment capacity of the flange
M	The moment in the connection
M_{design}	The design strength determined by the full plastic strength of the beam
M_p	The plastic moment based on the full plastic strength of the beam
$M_{plastic}$	The plastic moment in the connection
M_r	Required flexural strength
n_{sb}	The number of shear bolts along the effective width
n_{tb}	The number of tension bolts connecting the component member
n_{th}	The number of threads per inch of the bolt
N_b	The number of bolts
N_i	The number of inner bolts (2 for 4E and 4ES, and 4 for 8ES connections)
N_o	The number of outer bolts (2 for 4E and 4ES, and 4 for 8ES connections)
p	The effective width per tension bolt
P	The axial compression loaded on CFT
P_e	The flexural buckling load at the column
P_n	The nominal capacity for the axially loaded members
P_o	The nominal capacity for the axially loaded composite column
P_r	Required axial strength

P_u	The factored axial force
P_x	Total un-factored vertical design load at and above story level x
Q	The prying force per bolt
Q	The prying force
r_m	Effective radius of the CFT section
R_n	The resistance strength for the component members except for bar and bolts
$R_{n,block}$	The resistance strength for the block shear failure
$R_{n,net}$	The resistance strength for the net section of the component member
$R_{n,slip}$	The slip resistance strength
R_{ni}	The bearing strength at the inner bolts
R_{no}	The bearing strength at the outer bolts
R_y	Material over strength factor
s	The bolt spacing
S	The snow load
t	The thickness of the connected material
t_a	The thickness of T-stem
t_{bf}	The thickness of the beam flange
t_{bw}	The thickness of the beam web
t_f	The thickness of the flange
t_f	The thickness of the column flange

t_p	The thickness for the end-plate
$t_{p, req}$	The required thickness for the end-plate
$t_{s, min}$	Thickness of the end-plate stiffener
t_w	The thickness of the column web
T	The sum of the forces of the pre-stressed bolts
T	The applied tension force equivalent to one tension bolt
T	The axial force applied to the members
T_m	Specified minimum bolt pretension
T_u	The required strength in tension
u	The mean slip coefficient
V_{base}	The base shear force at the bottom of the composite frame
V_{design}	The base shear force equivalent to the summation of the equivalent lateral loads
V_{su}	The ultimate shear strength caused by the steel tube to the panel zone
V_{sy}	The yield shear strength caused by the steel tube to the panel zone
V_u	The ultimate shear strength at the panel zone
V_{wy}	The resulting shear yield strength
V_x	The seismic lateral force between story level x and story level $x-1$
V_y	The yield shear strength at the panel zone
w_c	Weight of concrete per unit volume

W	The wind load
W_{clip}	The width of the clip angle normal to the section area
W_{eff}	The effective width
$W_{\text{T-stub}}$	The width of the T-stub at the flange
x	Subscript referring to symbol related to strong axis bending
y	Subscript referring to symbol related to weak axis bending
Y_p	The yield line mechanism for the end-plate
Z_c	Plastic section modulus of concrete shape
Z_e	The effective plastic section modulus
Z_s	Plastic section modulus of steel shape
Z_x	Plastic section modulus of the beam

Abbreviation

AISC	American Institute of Steel and Construction
ASCE	American Society of Civil Engineers
ASTM	American Society of Testing and Materials
CCFT	Circular Concrete Filled Tube
CFT	Concrete Filled Tube
CLI	Clip Angle Connection
CMF	Composite Moment Frames
C-PRMF	Composite PR Moment Frames
C-SMF	Composite Special Moment Frames
DOF	Degree of Freedom
END	End-Plate Connection
ESR	Elastic Strength Ratios
FE	Finite Element
FEMA	Federal Emergency Management Agency
FR	Fully Restraint
FS	Full Strength
HSS	Hollow Steel Section
IBC	International Building Code
ICDR	Inelastic Curvature Ductility Ratio
ISDR	Inter Story Drift Ratios
LC	Load Combination
LRFD	Load and Resistance Factor Design
NEHRP	National Earthquake Hazard Reduction Program
PGA	Peak Ground Acceleration
PR	Partially Restraint
PS	Partial Strength
PZ	Panel Zone
PZRA	Panel Zone Rotation Angle
RCFT	Rectangular Concrete Filled Tube

RF	Reaction Force
SAC	Three Joint Venture Partners –SEAOC, ATC, and CUREE
SDC	Seismic Design Category
SE-SMA	Super-Elastic SMA
SMA	Shape Alloy Memory
TSU	T-Stub Connection
U	Displacement
UBC	Universal Building Code
USGS	US Geographical Survey

Summary

This thesis investigates the performance of composite frame structures with smart partially-restrained (PR) concrete filled tube (CFT) column connections through simplified 2D and advanced 3D computational simulations. It also provides a design methodology for new types of innovative connections based on achieving a beam hinging mechanism. These types of connections intend to utilize the recentering properties of super-elastic SMA tension bars, the energy dissipation capacity of low-carbon steel bars, and the robustness of CFT columns.

In the first part of this study, three different PR-CFT connection prototypes were designed based on a hierarchy of strength models for each connection component. Numerical simulations with refined three dimensional (3D) solid elements were conducted on full scale PR-CFT connection models in order to verify the strength models and evaluate the system performance under static loading. Based on system information obtained from these analyses, simplified connection models were formulated by replacing the individual connection components with spring elements and condensing their contributions. Connection behavior under cyclic loads was extrapolated and then compared with the monotonic behavior.

In the second part of this study, the application of these connections to low-rise composite frames was illustrated by designing both 2D and 3D, 4 and 6 story buildings for the Los Angeles region. A total of 36 frames were studied. Pushover curves plotted as the normalized shear force versus inter story drift ratio (ISDR) showed significant transition points: elastic range or proportional limit, full yielding of the cross-section, strength hardening, ultimate strength, and strength degradation or stability limit. Based on the transition points in the monotonic pushover curves, three performance levels were defined: Design Point, Yield Point, and Ultimate Point. All frames were stable up to the yield point level. For all frames, after reaching the ultimate point, plastic rotation increased significantly and concentrated on the lower levels. These observations were quantified through the use of elastic strength ratios and inelastic curvature ductility ratios. The composite frames showed superior performance over traditional welded ones in terms of ductility and stability, and validated the premises of this research.

Chapter 1

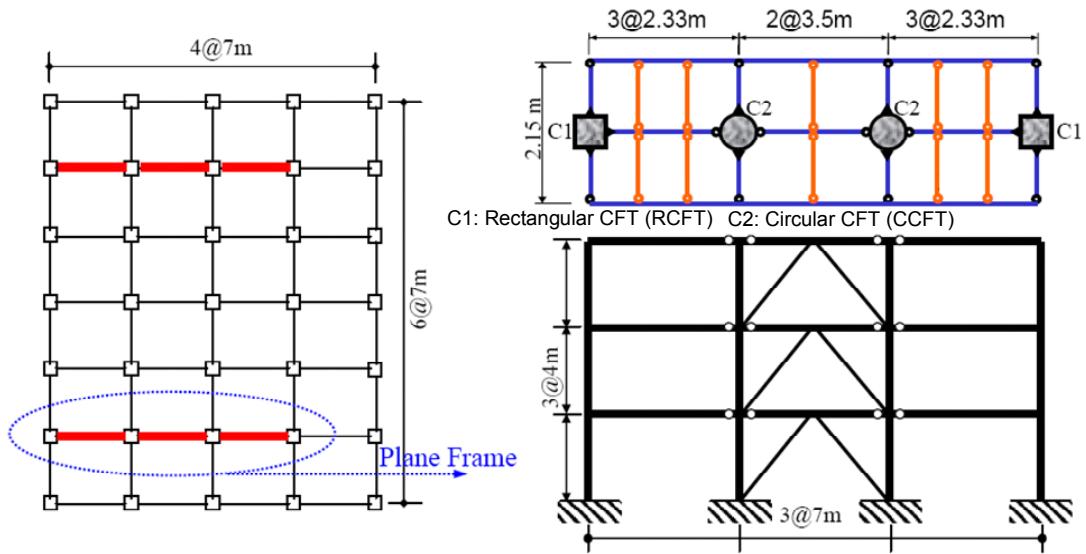
Introduction

1.1 Research Background

In this research, three structural design concepts are integrated: the use of composite concrete-filled tube columns, the use of partially restrained connections, and the introduction of innovative materials (shape memory alloys) in the connection area. To understand the integration of these concepts and the scope of this dissertation, a brief description of each of these three topics will be given first.

In recent years, concrete filled steel tube (CFT) columns have become widely accepted and used in multistory buildings as well as bridges. These elements provide the synergetic advantages of ductility and toughness associated with steel structures and high compressive strength associated with confined concrete components. The advantages of CFT columns over other so-called mixed or hybrid systems (fully encased or partially encased systems) include the fact that the concrete prevents local buckling of the steel tube wall and the confinement action of the steel tube extends the usable strain of the concrete. In other words, the advantages of two materials (steel and concrete) can be utilized while their disadvantages can be compensated or offset. In addition, a CFT column has improved fire resistance (if properly reinforced) and significant cost reductions in comparison with traditional steel construction. Moreover, the steel tubes can be utilized as the formwork for casting concrete, giving CFT structures improved constructability over conventional reinforced concrete structures.

Composite CFT columns are especially efficient as the vertical elements in moment resisting frames in high seismic areas because they have a high strength to weight ratio, provide excellent monotonic and dynamic resistance under biaxial bending plus axial force, and improve damping behavior (Tsai et al. 2004). A typical composite frame consisting of steel I shape girder and either circular or rectangular CFT (CCFT or RCFT) columns tested by Tsai et al (Tsai et al. 2004) is illustrated in Figure 1.1.



(a) The prototype 3 story building (6 bay by 4 bay in plane) (b) The CFT composite frame with moment connections

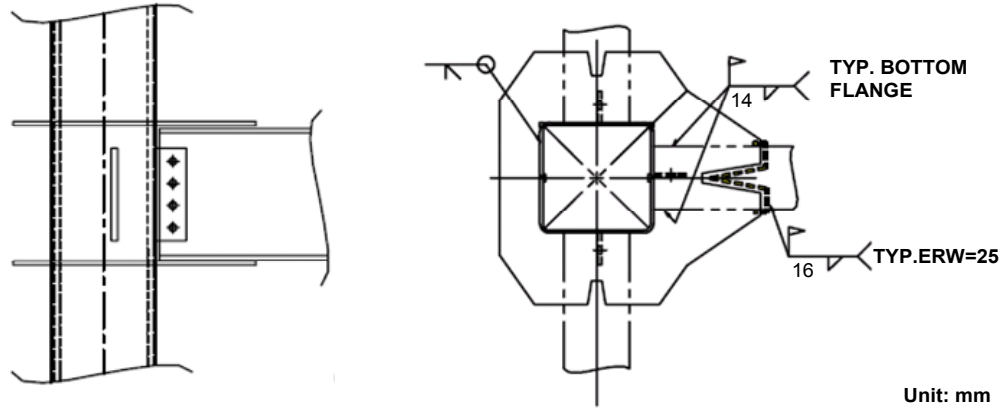


(c) Overview of the test frame

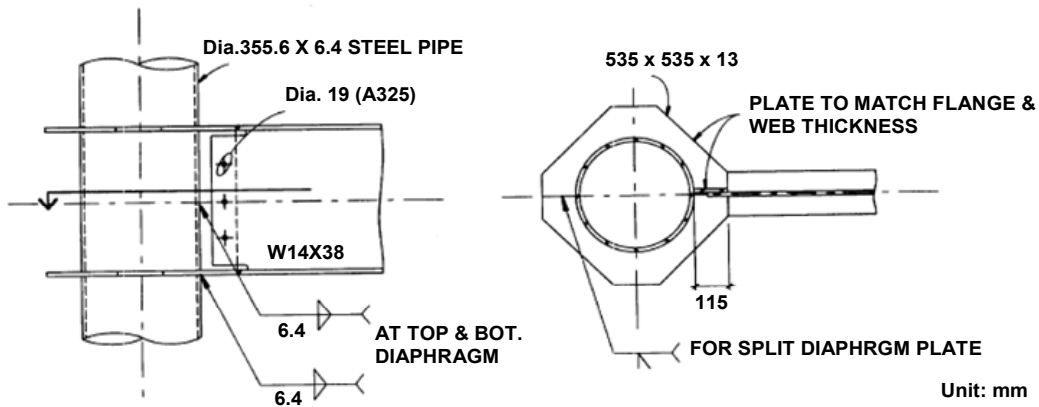
Figure 1.1 3 story by 3 bay CFT composite frame with buckling restrained braces
(Tasi, K.C et al. 2003)

Typical details of moment connections to RCFT or CCFT columns for this type of structure as constructed in the Far East and the USA are shown in Figure 1.2. The

external diaphragm plates are intended to alleviate the severe distortions of the steel tube skin during fabrication and provide a simple location for making a welded or bolted connection in the field.



(a) Moment connection details with diaphragm plates (RCFT, Tasi, K.C et al., 2003)



(b) Moment connection details with diaphragm plates (CCFT, Schneider, S. P. and Alostaz, Y.M.,1997)

Figure 1.2 Details of connections to CFT columns

To evaluate the performance of a moment frame subjected to lateral-loads, the flexural effects on the rotational deformation at the connections are the critical issue. Therefore, connection behavior can be generally represented by a moment-rotation curve as shown in Figure 1.3. Connections are classified by three main parameters: stiffness, strength, and ductility (Leon 1997). For stiffness, connections are classified as fully restrained (FR), partially restrained (PR) or simple pinned connections. An ideal pinned connection only transmits shear force from the beam to columns. For strength, connections are classified as either full strength (FS) or partial strength (PS) depending on whether they can transmit the full plastic moment (M_p) of the beam. Finally,

connections are classified as brittle or ductile connections based on their ability to achieve a certain plastic rotational demand. The rotational demands at the connections vary according to whether they are in use in ordinary, intermediate, or special moment frames. For example, in the aftermath of Northridge earthquake, the capacity to undergo an elastic rotation of 0.01 radian and a plastic rotation of 0.03 radians under cyclic loading has been accepted as the rotational limit between ductile and brittle connections for special moment resisting frames. This limit accepts up to a 20% decrease from peak bending resistance at the rotational limit.

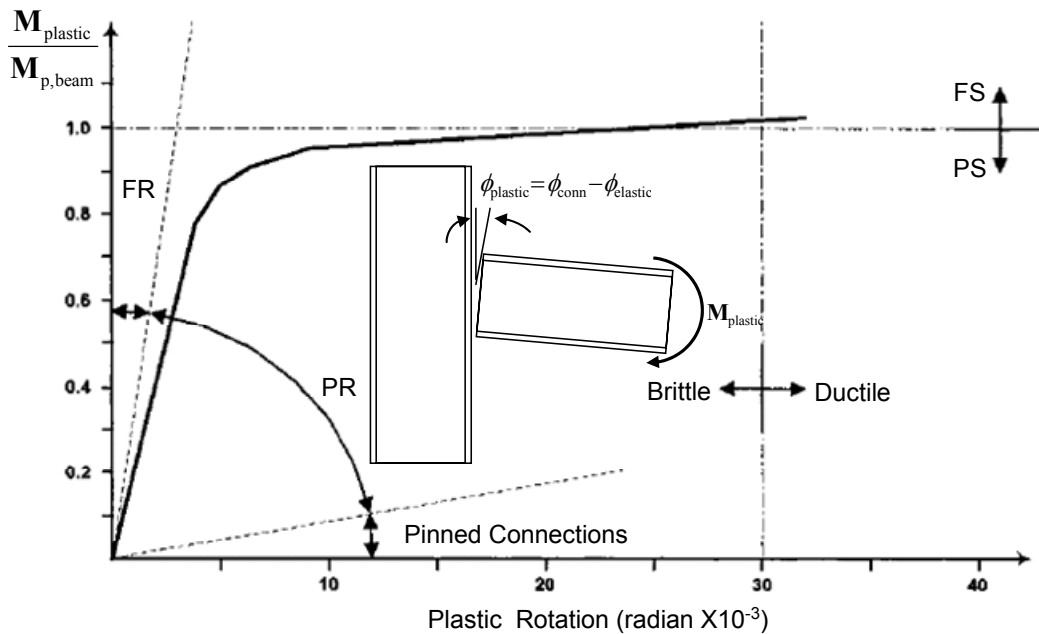


Figure 1.3 Typical moment-rotation curve

Major failures of fully welded moment connections during the 1994 Northridge and 1995 Kobe earthquakes have led to the conclusion that the traditional fully welded moment connections (FR/FS) have several structural disadvantages and that bolted connections or combinations of field bolted-shop welded connections (PR/FS or PR/PS) pose an attractive solution to this brittle failure dilemma (Swanson and Leon 2000). It also has been demonstrated that well-detailed PR structures can provide similar or superior seismic behavior to their FR counterparts (Rassati et al. 2004). The improved performance is derived from the combination of both (a) the decrease in seismic forces stemming from the additional flexibility of the component members owing to the PR

nature of the connections and (b) the increase in the structural strength reserve capacity owing to the lack of brittle connection failure modes.

More recently, work at GT on shape memory alloys (SMAs) has explored the applications of this material to the design of connections in steel structures subjected to large cyclic loads. SMA undergo large deformations with little permanent residual strain through either the shape memory effect or the super-elastic effect due to changes in either temperature or stress. Super-elastic Nitinol (NiTi) is a type of SMA with the unique ability to sustain large strains (e.g. 6 to 8 percents) that are crystallographically reversible, thereby maintaining the material without residual deformation as illustrated in Figure 1.4 (DesRoches et al. 2004).

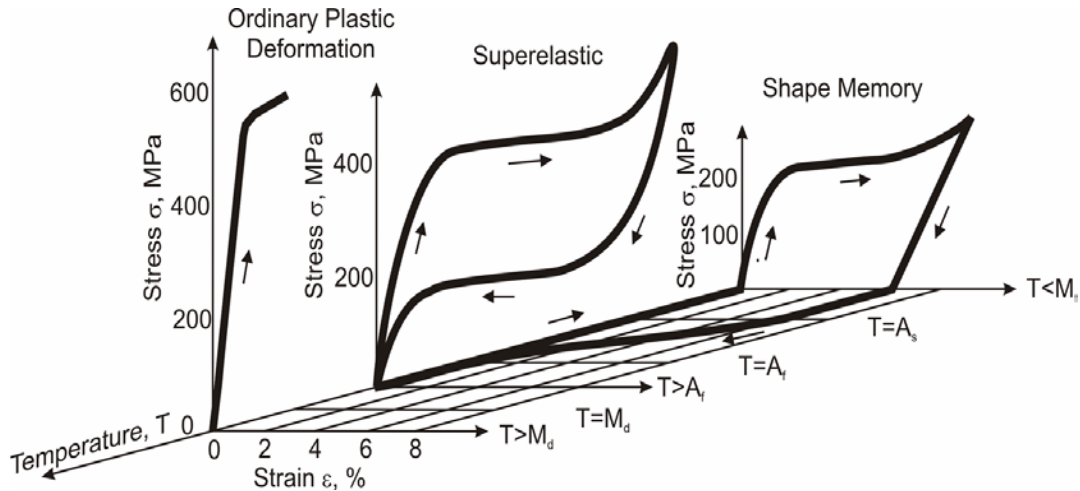
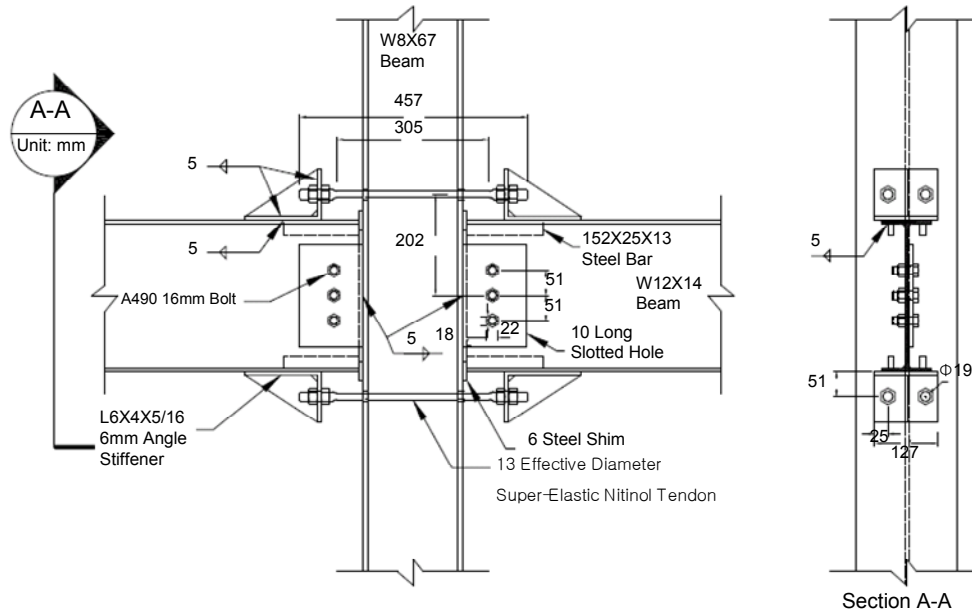


Figure 1.4 Stress-strain-temperature relationships in SMA (DesRoches et al. 2004)

Utilizing super-elastic Nitinol tendons as the moment transfer elements in a steel beam-column connection will create smart structures that automatically adjust to seismic activity (Ocel et al. 2004 and Penar 2005). This type of connection (See Figure 1.5) not only contains all the advantages of bolted PR connections mentioned above, but also provides a recentering capacity because of the lack of permanent residual deformation in the tendons due to the SMA material characteristics.

The ultimate purpose of this research is to develop suitable new design criteria for incorporating composite CFT structures into a partially restrained, partially strength connections. In addition, this research intends to explore a mixture of steel bars and

super-elastic Nitinol bars as connecting elements to CFT columns. It is hypothesized that such combinations of CFT columns and SMA connections will achieve excellent ductility, high strength, and recentering capability.



(a) Auto-CAD detail of the Super-elastic Nitinol tendon connection



(b) Picture of Nitinol tendon connection

Figure 1.5 Super-elastic Nitinol tendon connection (Pinar, 2005)

The initial studies will use refined 3 dimensional finite element (FE) analyses (ABAQUS, Hibbit 2006) of individual connections subjected to static loading. These FE experimental works will then be augmented by simpler analytical models of connection behavior under cyclic loading using the nonlinear analysis program OPENSEES (Berkeley 2006). Finally, parametric studies on large 2D frames will be carried out to assess system behavior.

1.2 Research Objectives

This research intends to synthesize the results of both (a) advanced computational full-scale simulations of connection models and frame structures under both static and dynamic loading, and (b) simplified connection models for connections using steel and super-elastic SMA bars as tension fasteners in smart SMA PR-CFT beam-column connections. In addition, it intends to develop (c) practical design recommendations for composite frames suitable for incorporation into design codes. The overall objectives are:

- To develop innovative PR connections that provide superior performance in terms of seismic behavior, ductility, and energy dissipation to those of conventional welded frames.
- To investigate the basic failure modes in these connections and how their basic yielding and failure mechanisms can be combined into simple models suitable for the analyses and design of large frames.
- Separate connection behavior into ductile and brittle categories and investigate methods of ameliorating behavior by delaying brittle modes of failure and promoting semi-ductile ones such as slippage of shear bolts and bearing yielding around bolt holes.
- To generate a simple nonlinear cyclic behavior model of PR-CFT connections for the OPENSEES program through detailed analytical studies on nonlinear monotonic behavior of connection components.
- To develop new knowledge on building performance and building damage on a

composite frame structures including realistic PR joint behavior under earthquake motions.

- To propose design recommendations and performance requirements for these composite structures for dependable seismic design.
- To examine the practicality of using smart SMA PR-CFT connection structures.

1.3 Research Methodology

The following steps will be performed to achieve the objectives of this research:

Step 1: Through a completely literature review, previous studies done in this research area will be examined in order to assess the most beneficial research directions.

Step 2: Select applicable design specifications and design several complete smart SMA PR-CFT connections, including all connection components such as regular steel tension fasteners mixed with SMA bars, shear tabs, CFT columns, and shear/web bolts.

Step 3: Investigate the main failure modes for the different connection models. Generally, failure modes are divided into ductile and brittle failure modes in seismic design of steel components. These modes should occur in order of desirability, the most ductile and desirable failure modes to the most brittle and undesirable failure modes. Moment capacities and design requirements for each failure mode are discussed in this research.

Step 4: Implement three dimensional FE models for PR-CFT connections using a nonlinear analysis program (ABAQUS) and perform nonlinear static analysis under pushover loading. Deformation of components, slippage distance, prying forces, and moment-rotation behavior at the connection should be measured to determine an envelope for monotonic connection behavior.

Step 5: Based on the failure modes and envelope of monotonic behavior, develop simple analytical models consisting of spring elements in order to simulate the behavior of connection components under any load path, either static or dynamic.

Step 6: Assemble the one dimensional component springs obtained from the 3D analytical models into a user joint element for OPENSEES.

Step 7: Design and model in 2D several building prototypes, including four- and six-story frames with a variety of connections and column configurations.

Step 8: Perform the frame analyses as summarized in Table 1.1.

Step 9: Conclude with some discussion of (a) areas where the specification needs improvement, (b) step by step procedures to compute the elastic interactive strength ratios/inelastic ductility curvature ratios of the individual CFT beam-columns, and (c) member vs. system performance measures.

Step 10: Develop a worksheet-based design procedure, examine seismic design criteria on the basis of the current code provisions, and calculate the moment capacity for each of failure mode for the smart PR-CFT connection models.

Step 11: Estimate the damage characteristics and distributions for composite frame structures with smart SMA PR-CFT connections subjected to large seismic loads.

Table 1.1 Summary of frame analyses

(a) Linear Frame Analysis
Equivalent Static Analysis
Dynamic Analysis (Ground Motion)
(b) Second Order Inelastic Analysis
Equivalent Static Pushover Analysis
Dynamic Analysis (Ground Motion)

1.4 Outline

This thesis is composed of ten main chapters and six appendices, and its organization is summarized in Figure 1.6.

The first two chapters are composed of introduction and literature review. Chapter 1 represents the research background and objectives. Chapter 2 contains a brief literature review on topics related to PR connections, CFT columns, and SMA applications.

The study of local connection models is summarized in Chapters 3 through 6. Chapter 3 covers detailed design procedures for connection components such as tension bars,

shear bolts, web bolts, plate members, connection angle so on. Detailed design examples for CFT columns are provided in Appendix A. Chapter 4 describes the individual smart SMA PR-CFT connections designed as part of this research. This chapter includes general configurations, design principles, failure modes, and data collection. Basic background information for the design examples and failure modes is presented in Appendix B. Chapter 5 presents 3D finite element work for the PR-CFT connections. It focuses on the monotonic behavior of each connection type. Appendix C describes the data collected by the history output function in ABAQUS FE that was used to obtain connection characteristics such as component deformation and connection rotation. Chapter 6 extends the model to include the cyclic behavior of both components and connection models.

Based on the study of local connection models, the analyses and performance evaluation of full frames is conducted in Chapters 7 to 9. Chapter 7 describes the prototype building configurations and the design results. The detailed calculation procedures for design loads and panel zone models are given in Appendix D and Appendix E respectively. Chapter 8 deals with the frame analyses under static and dynamic loading. The results of frame analyses, such as interstory drift, member forces and rotational curvature are described in this chapter in order to assess the behavior of frame structure and the deformation of its components. The information on the ground motions used for these studies is described in Appendix F. Based on the results of frame analyses, Chapter 9 evaluates the seismic performance of the PR-CFT connections in accordance with both elastic and inelastic evaluation factors.

Finally, Chapter 10 presents conclusions at the basis of the major research results and suggests research recommendations to perform in future. The Reference part provides a list of references related to a research topic.

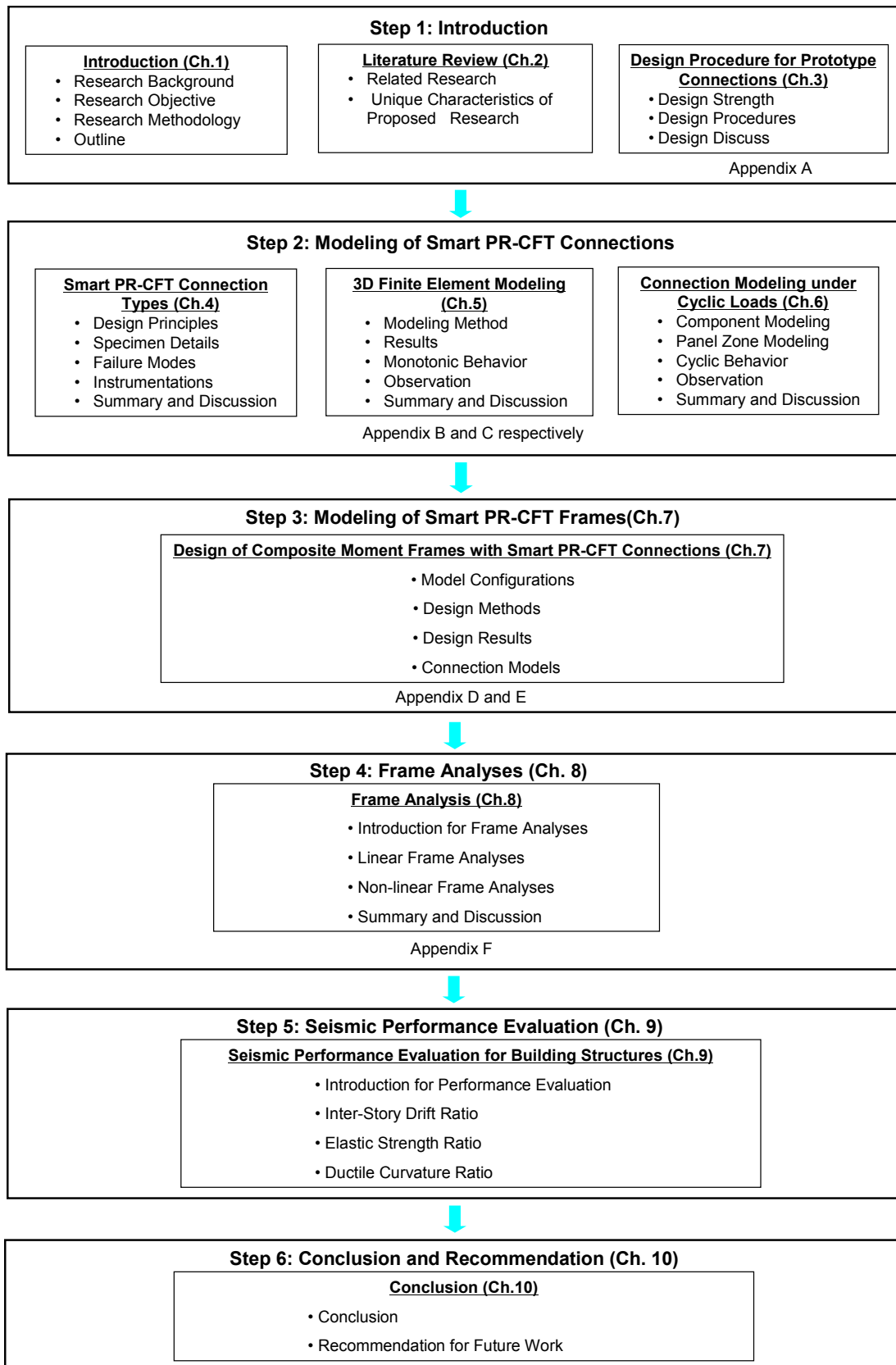


Figure 1.6 Summary of the research approach

Chapter 2

Literature Review

2.1 Related Research

This research is intended to take advantage of the synergetic characteristics of steel and SMA tendon bars to develop a flexible (PR) moment resisting connection with recentering capabilities. This chapter briefly describes some past experimental and analytical research on traditional PR/CFT connections relevant to the innovative types of connection models to be developed in this thesis. This chapter does not intend to provide a complete and systematic literature search on that topic but rather just present some examples of how connections have been investigated in the past. In addition, previous research on recentering connections as well as prior practical uses of shape memory alloys for seismic applications will be reviewed.

2.1.1 Brief Literature Survey on PR Connection

Numerous investigations on a wide range of bolted connection types has been performed since the early 1900s both to understand behavior of various PR connection types and to model the connection behavior in the analysis of entire frames. Table 2.1 summarizes some of the data available for each type of PR connection. This review of the literature will describe the behavior and modeling of typical PR connections in steel moment frame construction (Figure 2.1 and Figure 2.2) as the goal of present work is to apply PR connections to composite structures.

Since the earliest tests aimed at determining the rotational stiffness of PR connections by Wilson and Moore (1917), hundreds of tests have been performed to establish the relationship between moments and relative rotations in beam-to-column connections. Before 1950s, tests of riveted connections were performed by Young and Jackson (1934) and Rathbun (1936). PR connections with high strength bolts as structural fasteners were first tested by Bell et al. (1958). Thereafter, behavior of header plate (or end plate) connections was investigated in twenty tests by Sommer (1969).

Table 2.1 Available experimental moment-rotational data for several connection types
(Summarized by Chan and Chui, 2000)

Connection Type	Reference	Fastener	Column Axis Restrained	Number of Test
Single Web Cleat	Lipson (1977)	Bolts	Major	43
	Lipson and Antonio (1980)	Bolts	Major	33
Double Web Cleat	Lathbun (1936)	Rivets	Minor	7
	Tompson et al. (1970)	Bolts	Major	24
	Bjorhovde (1984)	Bolts	Major	10
Header Plate	Sommer (1969)	Bolts	Major	16
	Kennedy and Hafez (1986)	Bolts	Major	19
Top and Seat Angle	Hechtman and Johnston (1947)	Rivets	14 Major 5 Minor	19
	Azizinamini et al. (1985)	Rivets	Major	20
	Zoetemeijer and Kolstein (1975)	Bolts	Major	12
Flush End Plate	Ostrander (1970)	Bolts	Major	24
	Sherbourne (1961)	Bolts	Major	4
Extended End Plate	Bailey (1970)	Bolts	Major	13

Extended end-plate and flush end-plate connections have been extensively accepted since the late 1960s. Flush end-plate and extended end-plate connections with performance close to that of rigid connections were tested by Ostrander (1970) and Johnstone and Walpole (1981), respectively. A series of tests on a variety of beam-to-column connections containing the web-cleat, flange cleat, seating cleat and web cleat, flush end-plate and extended end-plate connections were performed by Davison et al. (1987).

The earliest relevant T-stub connection research available was conducted by Batho and Rowan (1934). Eighteen beam-to-column tests were performed by Rathburn (1936). The work included the result of web angle, clip angle and T-stub connection tests. Following this work, forty seven nominally pinned connections were tested by Hechtman and Johnston (1947), who concluded that the connection slip contributes greatly to the overall rotation of a bolted or riveted connection. Dulty and McGuire (1964, 1965) carried out twenty seven component tests of wide flange and built up T-stubs in addition to fifteen splice plate tests intended to replicate the interaction between the T-stem and beam flange. Azizinamini (1982, 1985) performed an extensive and detailed experimental study for top and bottom seat angle connections with double web angles along with pull

tests. Recently, Swanson and Leon (2000) performed tests on forty eight T-stub specimens in order to provide insight into failure modes, deformations, and ductility of these components. Smallidge (1999) and Schrauben (2000) also conducted tests on ten full scale T-stub and thick clip angle connection specimens and compared the results to the component tests performed by the SAC project (Swanson 1999).

The available data on cyclic behavior of PR connections was reviewed by Leon (1997). Similar surveys for monotonic load cases have been given by Bjorhovde (1984), Nethercot (1986), Chen and Lui (1991), and Chan and Chui (2000), among others. The reader is referred to those sources for more detailed descriptions.

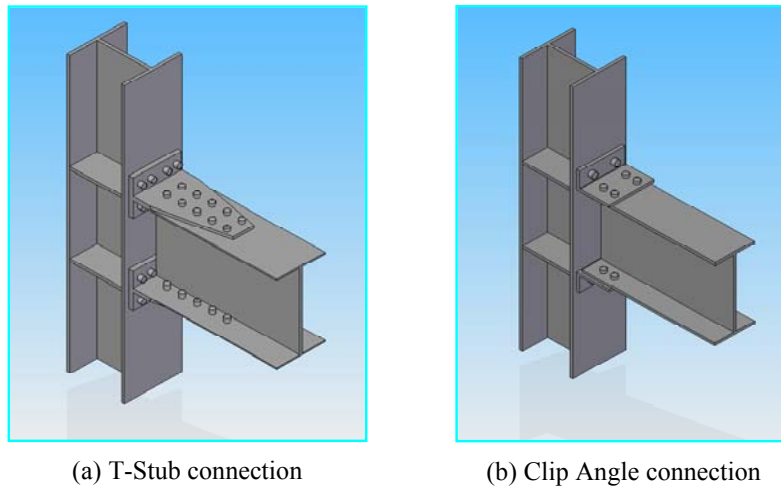
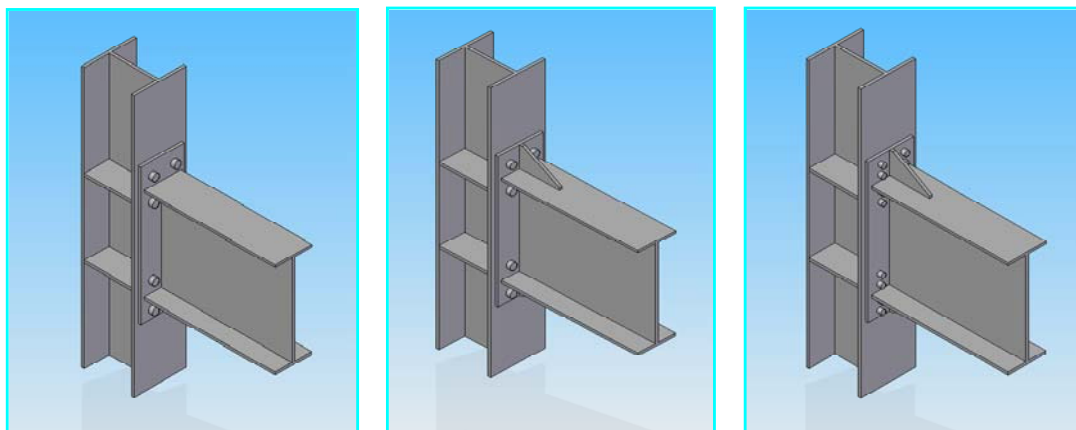


Figure 2.1 T-Stub and Seat Angle connection configurations



(a) Four bolt unstiffened, 4E (b) Four bolt stiffened, 4ES (c) Eight bolt stiffened, 8ES

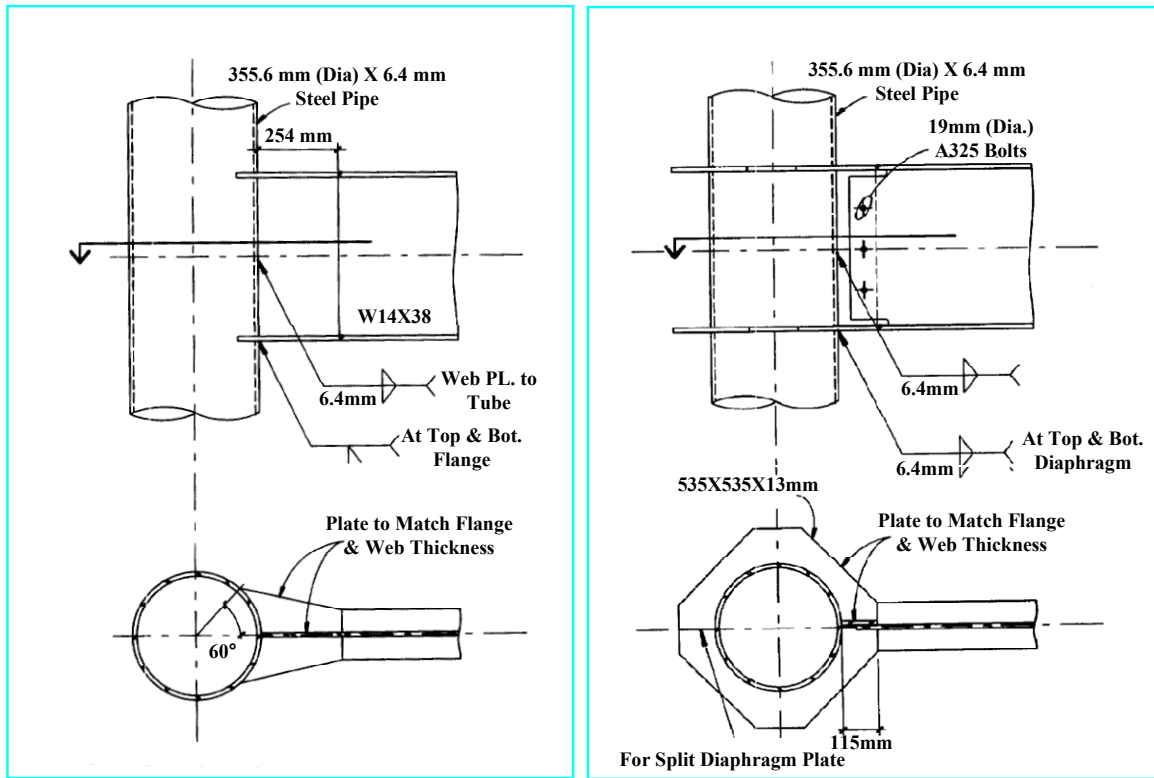
Figure 2.2 Extended End-Plate connection configurations

2.1.2 Literature Review on Steel Beam to CFT Column Connection

Experimental research on CFT connection details has been conducted on a wide variety of configurations depending on the tube shape and the desired connection performance. The beam-to-column connections used with CFT columns can be classified broadly into two categories. In the first connection category, the most convenient connection method is to weld the steel beam directly to the skin of the steel tube (Figure 2.3 (a)) or through the diaphragm (Figure 2.3 (b)). For this type of connection, the very large stresses and strains due to welding will lead to severe distortions of the tube wall. Shakir-Khalil (1992) tested structural steel girders connected to CFT columns using shear tabs which were fillet welded to the wall of circular steel tube columns. Many configurations for continuity diaphragms were tested by this research group in order to reduce severe distortions on the tube skin. Morino et al. (1992) used diaphragm plates continuous through square CFT columns at each girder flange location. The steel tube column was spliced and rewelded above and below each diaphragm.

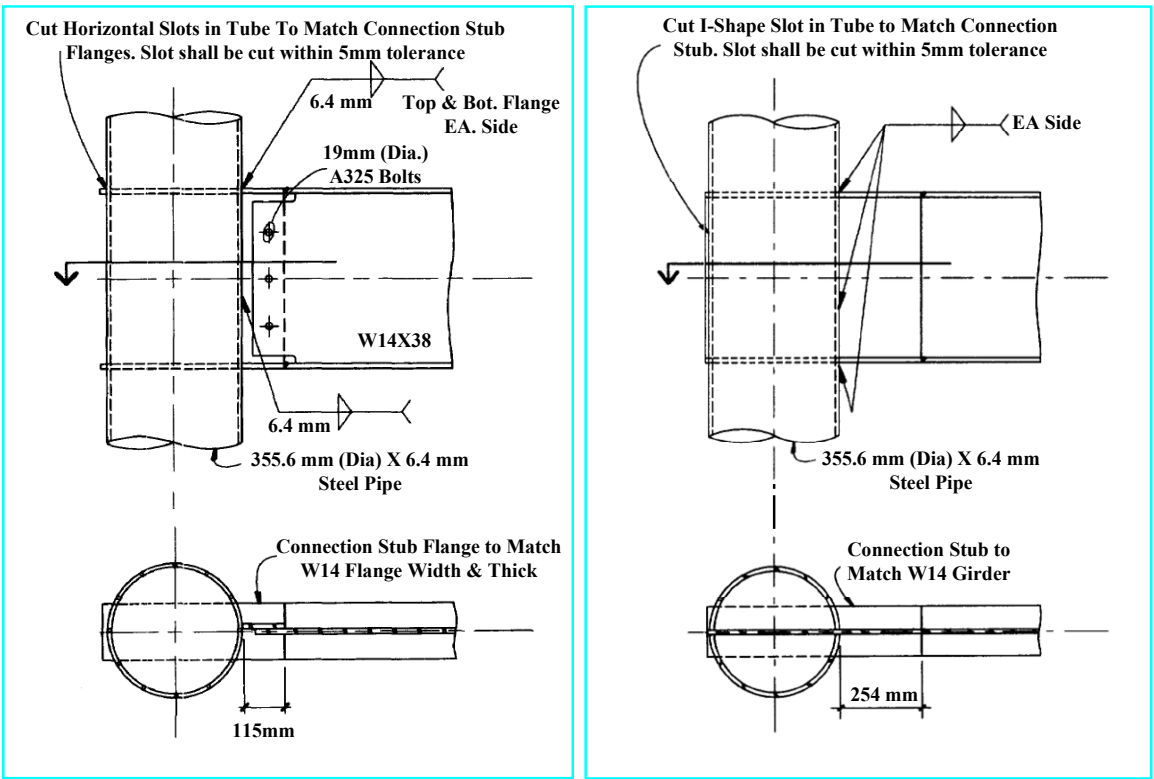
In the second connection method, the beam flange, fastener, web or entire cross section goes through the steel tube (See Figure 2.3 (c)) or the girder end-plate is welded with embedded elements in the CFT column (See Figure 2.3 (d)). Embedding connection components into the concrete core reduces the high shear demand on the tube skin. Several tests were conducted by Kanatani et al. (1987) and Prion and McLellan (1992) on penetrated bolted connections to square tube columns. Kanatani used T-stub connection element by bolting the stem of the T-stub to the girder flanges and attaching the T-stub flanges to the column with bolts continuous through the CFT. Prion tested similar bolted connections but using end-plates fully welded to the girder. Azizinamini and Prakesh (1993) examined behavior of a beam-to-column connection in which the steel beam extended continuously through the CFT.

Alostaz and Scheider (1996, 1997) investigated six types of connection details with circular CFTs. These details were arranged in approximate order of increased fabrication difficulty. Alostaz and Scheider suggested four kinds of fabrication methods. The first one was embedding weldable deformed bars. It was shown through experimental and analytical results that the deformed bars could transfer the beam flange force to the concrete core. In the second method, headed studs were welded to the inside wall at the



(a) Simple Connection

(b) Diaphragm Plate Connection



(c) Continuous Flange Connection

(d) Continuous Cross Section Connection

Figure 2.3 Typical welded connections to composite columns (Alostaz and Schneider, 1997)

beam flange to alleviate severe distortion of the steel tube wall. In the third method, a configuration extending the web plate into the concrete core with attached headed studs was investigated. In the fourth method, continuing the beam through the depth of the CFT column was considered to be the most rigid connection type. The last connection type had the best seismic resistance behavior, but the fabrication difficulties are the main disadvantage of this connection type.

2.1.3 Literature Review on Application of SMA in Structures

Smart structures for civil engineering are described as systems that can automatically adjust structural characteristics in response to external disturbances and unexpected severe loading. The idea is that the structure can be coaxed towards performance that results in improved structural safety, serviceability and extension of structural life (Otani, 2000). The focus in seismic design and retrofit has been towards performance-based design, often leading to structural solutions that make use of passive energy dissipation devices in order to mitigate inter-story drift and structural damage. One key avenue to achieve these goals is the development and implementation of smart materials. These materials exhibit synergetic functions such as sensing, actuating, self recovery and healing. One example of smart material is a class of metals known as shape memory alloys (SMAs). When SMA are integrated within structures, SMA can act as passive, semi-active or active components to reduce damage under strong ground motions. SMA exhibit high power density, solid state actuation, high damping capacity, durability, and fatigue resistance.

The widest use of SMA for seismic applications is for passive structural control and self recentering applications in order to reduce the response to external disturbances and the resulting residual deformation. Saadat et al. (2002) suggested that SMA could be effectively used as the devices for passive structural control through two systems: a ground isolation system and an energy dissipation system.

With regard to a ground isolation system, SMA for isolators which connect a superstructure to the ground foundation can screen the seismic energy transferred from the ground acceleration to the superstructure. These systems have the ability to reduce the damage to the superstructure. Wilde et al. (2000) applied a base isolation system using

super-elastic SMA bars to elevated highway bridges. Choi et al. (2005) proposed an isolation device in which SMA wires were incorporated in an elastomeric bearing to improve conventional lead-rubber bearings, which have problems related to instability and residual deformation under a strong ground motion. As the part of MANSIDE (Memory Alloys for New Seismic Isolation and Energy Dissipation Devices) project to study the feasible use of Nitinol wire for vibration isolation, Dolce et al. (2001) proposed and tested the three types of Nitinol wire based devices: supplemental recentering devices (SRCD), non recentering devices (NRD), and recentering devices (RCD). Uses of SRDC and SMA isolation systems in buildings are illustrated in Figure 2.4. Khan and Lagoudas (2002) analytically studied SMA springs to isolate a single degree of freedom (SDOF) system from a ground excitation simulated by a shake table, while Corbi (2003) proposed SMA tendon to isolate a multi-story shear frame from the ground excitation.

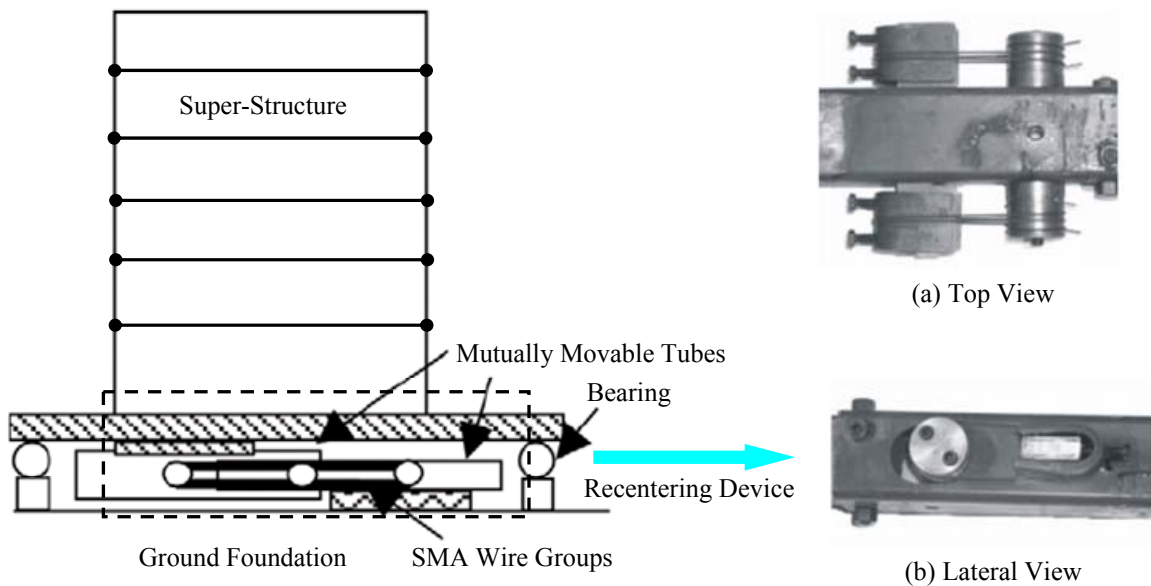


Figure 2.4 Isolator system for buildings

With regard to an energy dissipation system, martensite or super-elastic SMA materials integrated into structures absorb vibration energy through hysteretic behavior. Some SMA energy dissipation devices that have been used include: braces for framed structures, dampers for simply supported bridges, and tendons for connection elements and retrofitting devices for historical building.

Casciati et al. (1998) studied the application of the large martensite Nitinol bar in seismic protection devices for bridges. They used a finite element model to analyze the device under both static and dynamic response. Dolce et al. (2000, 2001) proposed Nitinol wire recentering braces and tested several different scale prototypes of the devices. Tamai and Kitagawa (2002) proposed a combined steel-SMA type brace as their seismic resistance device. DesRoches and Delemont (2002) performed testing on a full scale super-elastic SMA bar and applied it to seismic retrofit of simply supported bridges. They also performed analytical simulations on a multi-span simply supported bridge with the SMA restrainer. Leon et al. (2002) applied martensite SMA tendons to the primary bending elements in a steel beam-column connections as shown in Figure 2.5. Tami and Kitagawa (2002) suggested an exposed type column base with a SMA anchorage made of Nitinol SMA bars in order to resist seismic loading.

SMA's have been used to retrofit damaged structures. Super-elastic SMA bars were used by Indirli et al. (2001) so that they rehabilitated the S. Giorgio Church Bell Tower seriously damaged by the earthquake of Oct. 15th 1996 as shown in Figure 2.6.

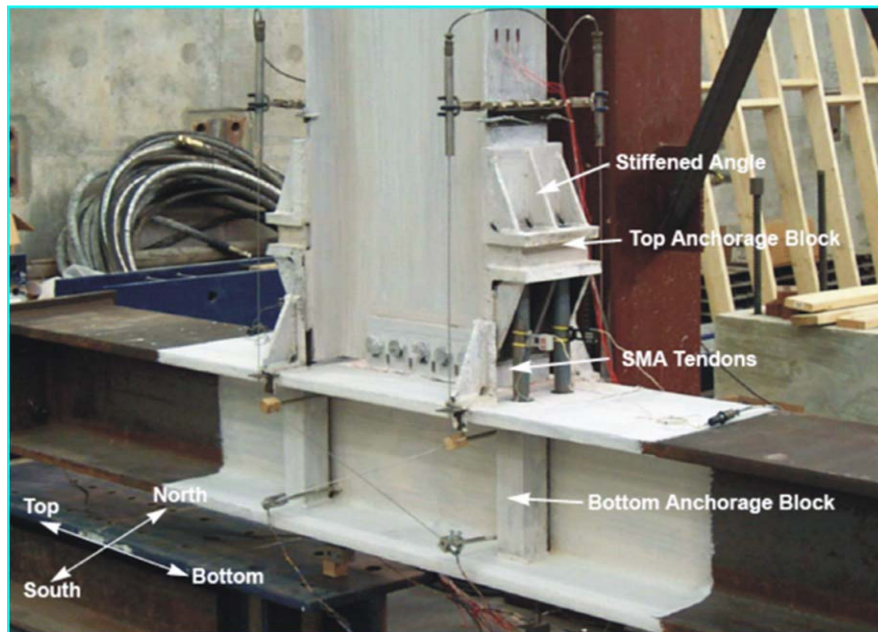


Figure 2.5 Test specimen of beam to column connection using martensite Nitinol tendons (Ocel et. al. 2002)

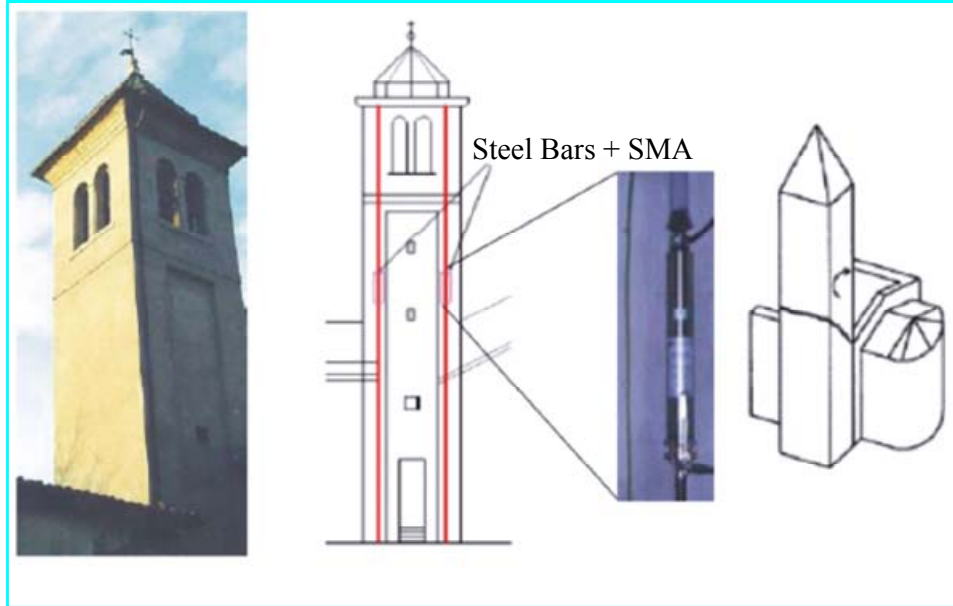


Figure 2.6. Retrofit application using Nitinol devices - The bell tower of the S. Giorgio Church in Trignano (Indirli et al. 2001)

2.2 Unique Characteristics of Proposed Research

Several new types of connection details are proposed in this research. Contrasting these proposed configurations with those described briefly in this chapter, it can be said that the characteristics of this research that set it apart from previous studies are:

- **Complete Design Details for Several Innovative PR-CFT Connections:** Several types of CFT connections with fasteners penetrating through the steel tube or the beam end are designed based on step by step procedures consistent with current code provisions. Strength models for connection components such as shear bolts, shear tab, web bolts, component angles, and plates are investigated in this research. The strength of each connection component obtained from the design strength model should exceed the demand strength based on the full plastic capacity of the beam element in order to induce the ideal yielding/failure modes.
- **Smart Structure Systems:** The combined use of steel and SMA through bars in assemblies that connect beams to columns is examined. Super-elastic SMA bars have a strong recentering force to reconstitute the structure to its original position

with little residual strain. Steel bars are used to help dissipate more energy and increase damping capacity.

- Refined FE Analysis Using Three-Dimensional (3-D) Elements: Nonlinear 3-D FE studies on a variety of details for smart SMA PR-CFT connections are presented in this thesis. Different types of 3-D elements include material inelastic and geometric nonlinear behavior. In order to formulate FE models very close to real connections in buildings, advanced modeling tools such as surface interactions, interface elements and initial pretensions are introduced into the FE models.
- Connection Behavior under Static and Cyclic Response: Behavior of connection components has a significant influence on that of full connections. First, behavior models for bolted components under either uniaxial static or uniaxial cyclic deformations are developed. These models intend to consider interactions between angles and bolts such as prying action, slip distance, bearing effects and various other possible failure modes. For the computational simulations, the behavior of the entire connections can be formulated based on superposition of the behavior models of individual components.
- Frame Analyses and Performance Evaluations: Two-dimensional (2-D) and 3-D composite frame structures will be designed and their performance assessed using typical PR moment-rotation behavior. Both building performance and new findings to estimate the building damage are developed from frame analyses consisting of both linear elastic analyses and second order inelastic analyses (Refer to Table 1.1).

Chapter 3

Design Procedures for Prototype Connections

Several PR moment connections were designed including detailed designs of the panel zone, angle, web shear plate, stiffener, shear bolts, and tension fasteners. These connections are meant to be pre-qualified to meet the strength and ductility requirements in applicable design codes. The pre-qualification will be accomplished through the advanced analyses to be discussed in later chapters of this dissertation. The term “pre-qualified” implies that the connections will not be subject to the stringent physical testing requirements that connections used in steel and composite structures must currently undergo (2005 AISC Seismic Provisions).

The design of these connections is divided into two parts. In Section 3.1 of this chapter, the calculation of the resistance of the connection components and the composite column are described. In Section 3.2 a series of step-by-step seismic design procedures are proposed for PR-CFT connection systems. Appendix A (Interaction Strength for CFT Columns) and Appendix B (Design Examples for PR Connections) are associated with this section. In Appendix A, it is shown that the *2005 AISC Specification* accurately evaluates the capacity of composite CFT columns when comparing its results with those obtained from numerical experiments. The US unit systems (kip and inch) will be used throughout this research because this is the current construction practice in US.

3.1 Design Requirement Strength

This section describes the prequalification design limits and required strength for PR-CFT connections. The scope of this section includes overall models, geometric

configurations, and rational formulas to estimate the capacity of these connections. These are shown, when possible, as step-by-step procedures.

3.1.1 Composite Column Strength

In steel-concrete composite structures, the advantages of two materials can be added while their disadvantages can be compensated by the composite effect. Two systems are widely utilized in the vertical members of composite construction: steel reinforced concrete (SRC), where a steel section is encased in concrete, and concrete filled tube (CFT) columns. Typical cross sections for the composite columns are illustrated in Figure 3.1.

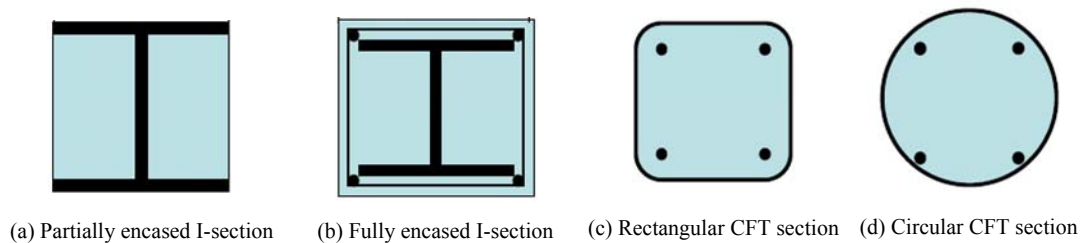


Figure 3.1 Types of cross sections for composite column system

The connection developed in this research are intended to connect CFT columns to steel I-shape beams so only CFT column systems will be considered. The current applicable design code, the *2005 AISC Specification* (AISC 2005 Specification), includes design guidelines for composite columns consisting of rolled or built-up structural steel shapes, pipe or hollow steel section (HSS) and structural concrete acting together as a composite member. To qualify as a composite CFT column, the following limits listed in the *2005 AISC Specification* should be satisfied:

- The cross sectional area of HSS shall be at least 1 percent of the total composite cross section.

- The maximum width-thickness ratio for a rectangular HSS shall be equal or less than $2.26\sqrt{E/F_y}$.
- The maximum diameter-thickness ratio for a circular HSS filled with concrete shall be less than or equal to $0.15E/F_y$. Higher ratios are accepted when their use is verified by testing or analysis.

The design compressive strength, $\phi_c P_n$, for an axially loaded composite CFT columns should be determined for the limit state of flexural buckling based on the column slenderness ratio as shown below:

$$\phi_c = 0.75 \text{ (LRFD resistance factor for axially loaded columns)}$$

(a) If $P_e \geq 0.44P_o$,

$$P_n = P_o [0.658]^{(P_o/P_e)} \quad (\text{EQ 3.1})$$

otherwise,

$$P_n = 0.877 P_e \quad (\text{EQ3.2})$$

where,

$$P_o = A_s F_y + A_{sr} F_{yr} + C_2 A_c f'_c \quad (\text{EQ 3.3})$$

$C_2 = 0.85$ for rectangular CFT sections and $C_2 = 0.95$ for circular CFT sections

$$P_e = \pi^2 (EI_{eff}) / (KL)^2 \quad (\text{EQ 3.4})$$

where,

$$EI_{eff} = E_s I_s + 0.5 E_s I_{sr} + C_1 E_c I_c \quad (\text{EQ 3.5})$$

$$C_1 = 0.6 + 2 \left(\frac{A_s}{A_c + A_s} \right) \leq 0.9 \quad (\text{EQ 3.6})$$

EI_{eff} = effective stiffness of the composite section

A_s = area of the steel section

A_c = area of the concrete section

A_{sr} = area of continuous reinforcing bars

E_c = elastic modulus of concrete = $w_c^{1.5} \sqrt{f'_c}$ ksi

E_s = elastic modulus of steel = 29000 ksi

f'_c = specific compressive strength of concrete

F_y = specific minimum yield stress of steel

F_{yr} = specific minimum yield stress of reinforcing bars

I_c = moment of the inertia of the concrete section

I_s = moment of the inertia of the steel section

I_{sr} = moment of the inertia of the reinforcing bars

K = effective length factor determined in the boundary conditions

L = laterally untraced length of the members

w_c = weight of concrete per unit volume

The design tensile strength, $\phi_t P_n$, for filled composite columns should be determined for the limit state of yielding, neglecting the tensile strength of concrete, as shown below:

$$\phi_t = 0.90 \text{ (LRFD resistance factor for columns under tension)}$$

$$P_o = A_s F_y + A_{sr} F_{yr} \quad (\text{EQ 3.7})$$

In addition to the available axial strength, the flexural strength also needs to be calculated. The *2005 AISC Specification* adopts a full plastic stress distribution based on the assumption of linear strain across the section and perfect elasto-plastic material behavior. With these simple assumptions, the nominal strength can be estimated by assuming that the steel has reached its yield stress under either tension or compression and that the concrete has reached the crushing strength under compression (Figure 3.2).

The P-M interaction diagram illustrated in Figure 3.3 for a composite section is based on a full plastic stress distribution and can be approximated by a conservative linear interpolation between five points (Galambos 1998). Points (A) and (B) correspond to the crushing axial strength and the flexural strength of the section, respectively. Point (C) is anchored to the same plastic neutral axis (PNA) position from corresponding to that of Point (B) but on the other side of the centerline, so it contains the same flexural capacity as Point (B) and the same magnitude of axial resistance from the concrete alone. For Point (D), the PNA is located at the centerline. As a result, this point corresponds to the maximum flexural strength and one half of axial strength of that determined for Point (C). Point (E) is an additionally arbitrary point to better describe the curvature of the interaction diagram at high axial loads. The five points can be easily calculated as shown in Table 3.1. For design, a simplified bilinear interpolation may be used between Point (A), (C), and (B) as shown in Figure 3.3. The simplified interaction equations shown as EQ 3.8 and EQ 3.9 can be used to check the design of composite beam-columns. They are reasonably accurate and conservative. Exact expressions will be too cumbersome to use in everyday design practice.

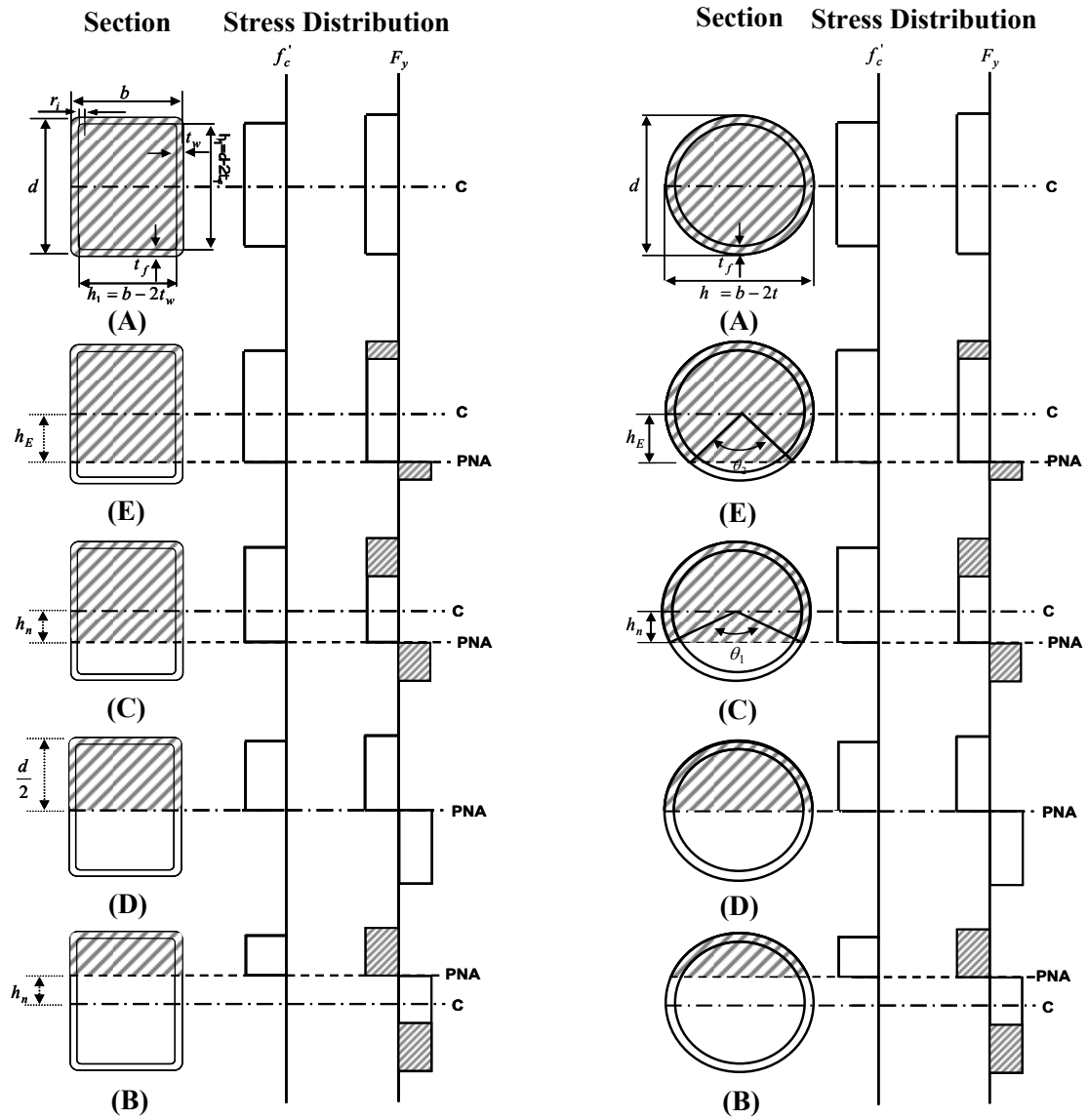


Figure 3.2 Full plastic stress distributions for RCFT and CCFT at point A,E,C,D, and E.

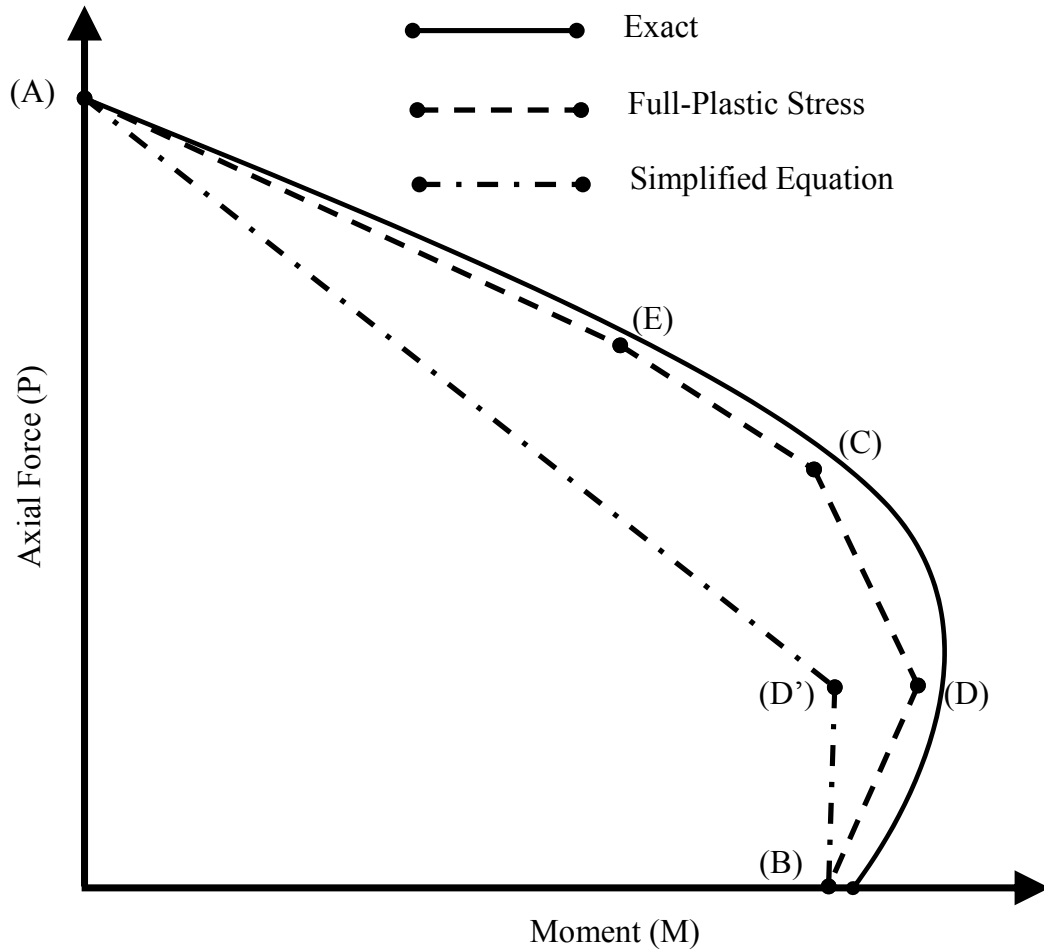


Figure 3.3 P-M interaction diagrams for composite beam-columns

If $P_r \leq P_D$

$$\frac{M_{rx}}{M_{Bx}} + \frac{M_{ry}}{M_{By}} \leq 1.0 \quad (\text{EQ 3.8})$$

otherwise

$$\frac{P_r - P_D}{P_A - P_D} + \frac{M_{rx}}{M_{Bx}} + \frac{M_{ry}}{M_{By}} \leq 1.0 \quad (\text{EQ 3.9})$$

where,

$M_A = \dots = M_E =$ allowable flexural strength (Capital subscript indicates the observed

point)

M_r = required flexural strength

$P_A = \dots = P_E$ = allowable axial force (Capital subscript indicates the observed point)

P_r = required axial strength

x = subscript referring to symbol related to strong axis bending

y = subscript referring to symbol related to weak axis bending

Table 3.1 Equations for the specific 5 points in the P-M interaction diagram

Point	Equations for RCFT	Equations for CCFT
(A)	$P_A = A_s F_y + A_c (0.85 f_c')$ $M_A = 0$ $A_s = \text{area of steel shape}$ $A_c = h_1 h_2 - 0.858 r_i^2$	$P_A = A_s F_y + 0.95 f_c' A_c \quad r_m = \frac{d-t}{2}$ $M_A = 0 \quad A_c = \frac{\pi h^2}{4}$ $A_s = \pi r_m^2$
(E)	$P_E = \frac{1}{2} (0.85 f_c') A_c + 0.85 f_c' h_1 h_E + 4 F_y t_w h_E$ $M_E = M_{\max} - \Delta M_E$ $Z_{sE} = b h_E^2 - Z_{cE} \quad Z_{cE} = h_1 h_E^2$ $\Delta M_E = Z_{sE} F_y + \frac{1}{2} Z_{cE} (0.85 f_c')$ $h_E = \frac{h_n + d}{2} + \frac{d}{4}$	$P_E = (0.95 f_c' A_c + F_y A_s) - \frac{1}{2} [F_y (d^2 - h^2) + \frac{1}{2} (0.95 f_c') h^2] \left[\frac{\theta_2}{2} - \sin \frac{\theta_2}{2} \right]$ $M_E = Z_{sE} F_y + \frac{1}{2} Z_{cE} (0.95 f_c') \quad h_E = \frac{h_n + d}{2} + \frac{d}{4}$ $Z_{sE} = \frac{d^3 \sin^3(\theta_2/2)}{6} - Z_{cE} \quad Z_{cE} = \frac{h^3 \sin^3(\theta_2/2)}{6}$ $\theta_2 = \pi - 2 \arcsin\left(\frac{2h_E}{h}\right)$
(C)	$P_C = A_c (0.85 f_c')$ $M_C = M_B$	$P_C = 0.95 f_c' A_c$ $M_C = M_B$
(D)	$P_D = \frac{0.85 f_c' A_c}{2}$ $M_D = Z_s F_y + \frac{1}{2} Z_c (0.85 f_c')$ $Z_s = \text{full y-axis plastic section modulus of steel shape}$ $Z_c = \frac{h_1 h_2^2}{4} - 0.192 r_i^3$	$P_D = \frac{0.95 f_c' A_c}{2}$ $M_D = Z_s F_y + \frac{1}{2} Z_c (0.95 f_c')$ $Z_s = \text{plastic section modulus of steel shape} = \frac{d^3}{6} - Z_c$ $Z_c = \frac{h^3}{6}$
(B)	$P_B = 0$ $M_B = M_D - Z_{sn} F_y - \frac{1}{2} Z_{cn} (0.85 f_c')$ $Z_{sn} = 2 t_w h_n^2$ $Z_{cn} = h_1 h_n^2$ $h_n = \frac{0.85 f_c' A_c}{2 [0.85 f_c' h_1 + 4 t_w F_y]} \leq \frac{h_2}{2}$	$P_B = 0$ $M_B = Z_{sB} F_y + \frac{1}{2} Z_{cB} (0.95 f_c')$ $Z_{sB} = \frac{d^3 \sin^3(\theta/2)}{6} - Z_{cB} \quad K_c = f_c' h^2$ $Z_{cB} = \frac{h^3 \sin^3(\theta/2)}{6} \quad K_s = F_y r_m t \quad (\text{"thin" HS})$ $h_n = \frac{h}{2} \sin\left(\frac{\pi - \theta}{2}\right) \leq \frac{h}{2}$ $\theta_1 = \frac{0.0260 K_c - 2 K_s + \sqrt{(0.0260 K_c + 2 K_s)^2 + 0.857 K_c K_s}}{0.0848 K_c}$

3.1.2 Component Member Strength

This section presents the determination of the strength for the components which connect the I-shape or wide flange beam to the column. Force transfer components include tension bolts/bars, shear bolts, shear tabs, web bolts, plates, and angles. The prediction of the ultimate strength for connections is a quite complex process because the yielding and failure modes of the components interact with one another and are tied to uncertainties in material properties and fabrication/construction tolerances. Typical T-stub, clip angle and end-plate connections, respectively, were shown in the previous chapter (See Figures 2.1 and Figure 2.2).

A complicating factor for both T-stub connection and clip angle connections (See Figure 2.1) is the need to include slip in the moment-rotational behavior due to the shear force acting on the faying surface between the beam flange and the corresponding T-stub stem/clip angle leg. On the other hand, end-plate connections (See Figure 2.2), which are fabricated by directly welding the beam to the moment plate, do not produce slip for lack of the faying surface. Figure 3.4 shows schematically the influence of slip on the monotonic and cyclic behavior of bolted connections. Component member strength will be classified according to the existence of slip.

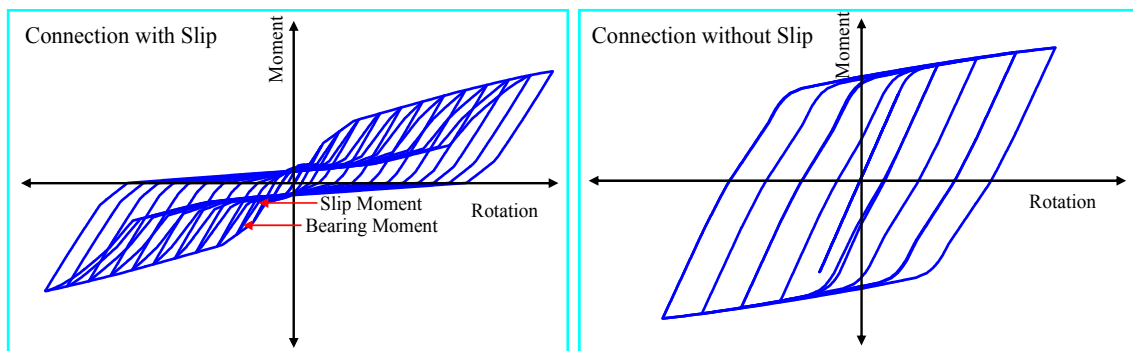


Figure 3.4 Behavior of PR moment connections used in this study

3.1.2.1 Components with Slip

Slip between surfaces of bolted components occurs as the shear force on the slip plane exceeds that provided by the clamping force from the pretensioned bolts. Slip occurs because construction tolerances require that bolt holes be at least 1/16" larger than the nominal bolt diameter. Once this tolerance is exceeded, the bolt begins to bear on the plates and the stiffness and strength increase again (Figure 3.4). The amount of rotation that will result from a 1/16" slip on a 24 inch deep connection is about 0.005 radian, a non-trivial value if one assumes that typical connections are assumed to reach their yield strength at about 0.01 radian.

Slip gives rise to temporary loss of stiffness that acts as a fuse during reversed cyclic loading (Astaneh-Asl 1995). Slip limits the force which is transmitted through the bolts at a given deformation and produces significant energy dissipation and damping. Figure 3.5 shows typical T-stub and clip angle connections that will exhibit slip. This section discusses the existing strength models for components which are cut from standard rolled shapes.

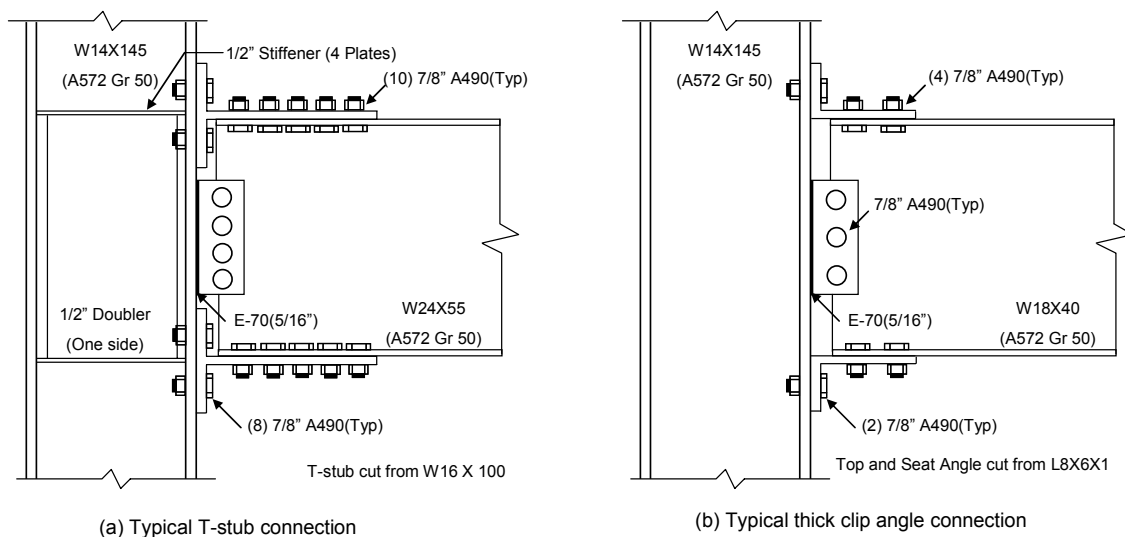


Figure 3.5 Typical connection types with friction slippage (SAC Project)

(A) Design Resistance Factor

The design strength must equal or exceed the required strength (P_r , M_r , and V_r). The design strength is computed as the product of the resistance factor (ϕ) and the nominal strength (P_n , M_n , and V_n) per the current AISC LRFD provisions (AISC 2001). In general, the resistant factor is less than unity. The value usually depends on the accuracy of the models used to estimate nominal capacities, the desirability of specific failure modes and the scatter on material properties. Representative resistance factors for connection design are shown in Table 3.2.

Table 3.2 Current LRFD design resistance factors

Failure Modes	The Value of Design Resistance Factor
Member yielding	0.9
Bending and plastic moment	0.9
Compression buckling	0.85
Bolt fracture	0.75
Net section and block shear failure	0.75
Bolt bearing failure	0.75
Member rupture	0.75

(B) Slip Resistance

Slip is produced by the shear force parallel acting to the faying surface as shown in Figure 3.6. Expressions for the nominal resistance to slip are based on simple friction models calibrated to numerous tests on bolted splices. The design slip resistance ($\phi R_{n,slip}$) is given in Section 16.4 - 34 of the LRFD (AISC 2005) as follows:

$$\phi_f = 1.0 \text{ for the slip}$$

$$R_{n,slip} = 1.13u h_{sc} T_b N_s \left(1 - \frac{T_u}{1.13 T_b N_b} \right) \quad (\text{EQ 3.10})$$

where,

$h_{sc} = 1.00$ for standard holes

$h_{sc} = 0.85$ for oversized and short-slotted holes

$h_{sc} = 0.70$ for long-slotted holes transverse to the direction of the load

where,

N_b = the number of bolts

N_s = the number of shear plane

T_b = specified minimum bolt pretension (i.e. A490 bolt with $d_b = 1"$ has 64 kips)

T_u = the required strength in tension

and where,

u = the mean slip coefficient

$u = 0.33$ for Class A faying surfaces

$u = 0.50$ for Class B surfaces

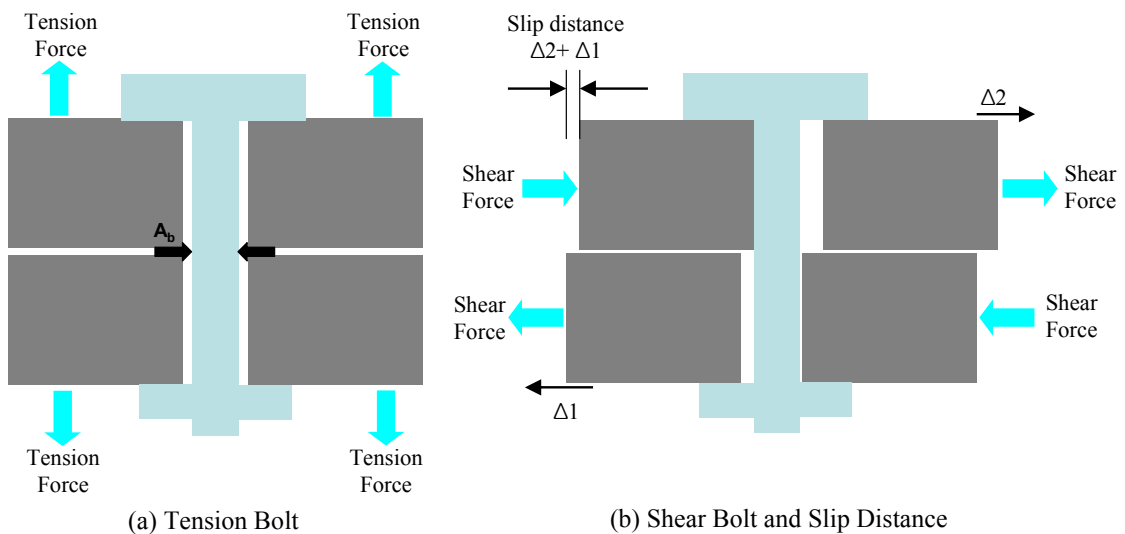


Figure 3.6 View of a connection with a bolts in tension and shear

(C) Tensile Strength of Bolts

The design tensile strength of a bolt ($\phi_f B_{n,tension}$) can be taken as (AISC 2001):

$$B_{n,tension} = A_b F_t \quad (\text{EQ 3.11})$$

where,

$\phi_f = 0.75$ for the bolt fracture

A_b = nominal area of a bolt shank

and where,

$F_t = 90$ ksi for A325 bolts

$F_t = 113$ ksi for A490 bolts

Alternatively, the strength of a bolt may be determined by another procedure (Swanson 1999):

$$B_{n,tension} = A_{be} F_u \quad (\text{EQ 3.12})$$

$$A_{be} = \frac{\pi}{4} \left(d_b - \frac{0.9743}{n_{th}} \right)^2 \quad (\text{EQ 3.13})$$

where,

A_{be} = effective tensile area of the bolt's threaded portion

d_b = diameter of the bolt's shank

n_{th} = number of threads per inch for the bolt (Table 8.7 in LRFD)

F_u = ultimate strength of the bolt

$F_u = 105$ ksi for A325 bolts larger than 1" in diameter

$F_u = 120$ ksi for A325 bolts up to 1" in diameter

$F_u = 150$ ksi for A490 bolts

(D) Shear Strength of Bolts

The design shear strength of a bolt ($\phi B_{v, \text{shear}}$) is given by (AISC 2001) as:

$$B_{v, \text{shear}} = A_b F_v \quad (\text{EQ 3.14})$$

where,

$\phi_f = 0.75$ for the bolt fracture

A_b = nominal area of a bolt shank

F_v = ultimate shear strength

$F_v = 48$ ksi for A325 bolts with threads included from the shear plane

$F_v = 60$ ksi for A325 bolts with threads excluded from the shear plane

$F_v = 60$ ksi for A490 bolts with threads included from the shear plane

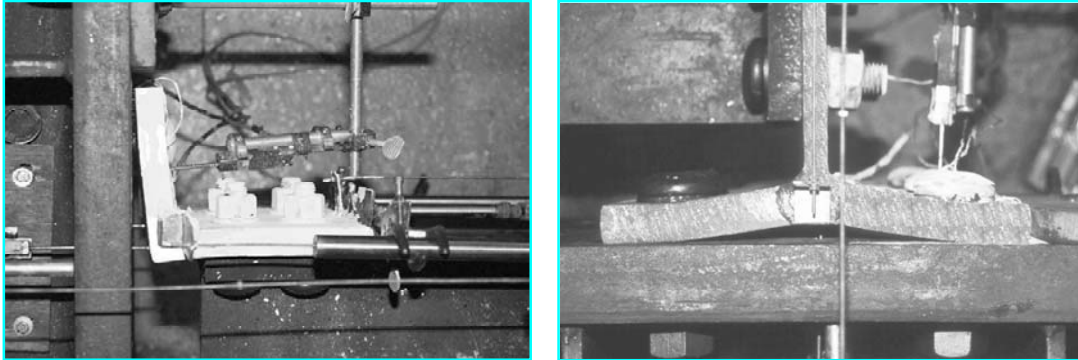
$F_v = 75$ ksi for A490 bolts with threads excluded from the shear plane

(E) Prying Action Mechanism

Figure 3.7 shows the flange of components prior to the tension bolt failure. Prying action refers to the additional forces due to the reactions at the tip of the uplifting plate shown in these photographs; these additional forces increase the tension in the bolts and can lead to premature failure.

The basic prying mechanism and the fundamental equilibrium equation ($B = T + Q$) are shown in Figure 3.8 (a). In general, the prying force (Q) acting on the tip of the flange can be minimized by either increasing the member thickness or

reducing the tension bolt gauge length.



(a) Flange prying of clip angle component

(B) Flange prying of T-stub component

Figure 3.7 Components before tension bolt fracture (SAC Project)

The prying model used in the LRFD (AISC 2001) is based upon one of the most widely used models developed by Kulak, Fisher, and Struik (1987). In this model, the bolt force is assumed to act at the inside edge of the bolt shank instead of acting at the centerline of the bolt shank. For this model, the moment is shown in Figure 3.8 (b) and the geometry in Figure 3.8 (c).

The ultimate capacity of the component members is computed based upon considering three possible failure modes (Figure 3.9). These three failure modes can be expressed by EQ 3.15 to EQ 3.17. They correspond to formation of a plastic mechanism on the flange, bolt prying mixed with flange yielding (Thornton 1985), and tension bolt fracture without the prying force, respectively.

Plastic mechanism formation:

$\phi_y = 0.9$ for the plastic flange

$$T = \frac{(1 + \delta) p F_y t_f^2}{4b'} \quad (\text{EQ 3.15})$$

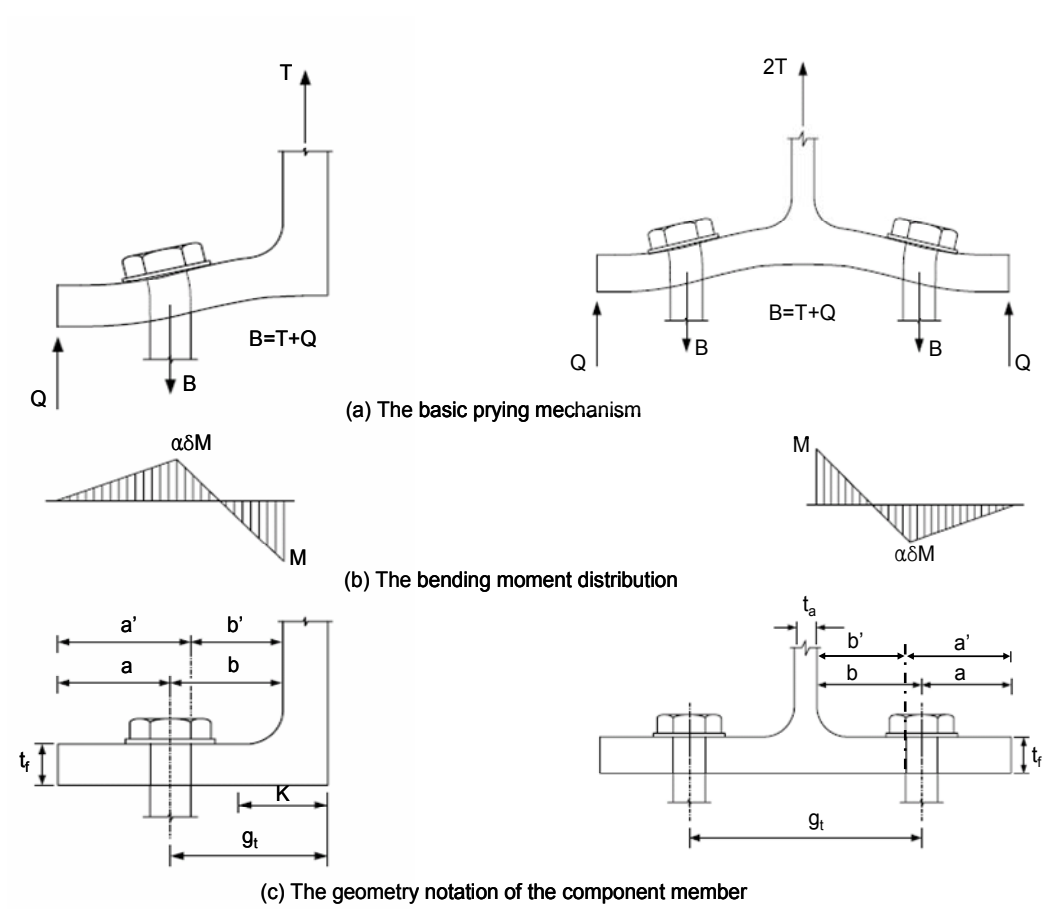


Figure 3.8 Typical flange prying action

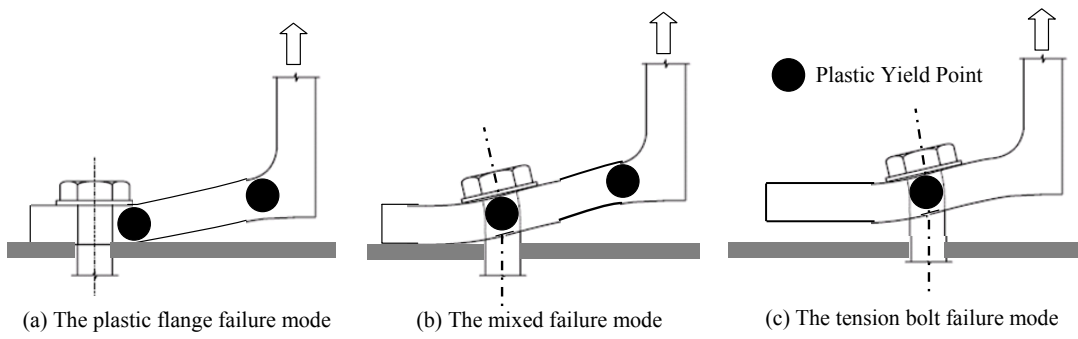


Figure 3.9 Three possible failure modes

Bolt prying mixed with the flange yielding:

$\phi_f = 0.75$ for the bolt fracture and $\phi_y = 0.9$ for the plastic flange

$$T = \frac{B_{n, \text{tension}} a'}{a' + b'} + \frac{p F_y t_f^2}{4b'} \quad (\text{EQ 3.16})$$

Tension bolt fracture without the prying force:

$\phi_f = 0.75$ for the bolt fracture

$$T = B_{n, \text{tension}} \quad (\text{EQ 3.17})$$

where,

$$p = \frac{2W_{T\text{-stub}}}{n_{tb}} = \frac{W_{\text{Clip}}}{n_{tb}} \quad (\text{EQ 3.18})$$

n_{tb} = number of tension bolts connecting the component member

p = effective width per tension bolt

$W_{T\text{-stub}}$ = width of the T-stub at the flange

W_{Clip} = width of the clip angle normal to the section area

a = distance from the centerline of the tension bolt to the edge of the flange

b = distance from the centerline of the tension bolt to the surface of the clip leg/T-stem

B = bolt reaction force

M = moment capacity of the flange

t_a = thickness of T-stem

t_f = thickness of the flange

g_t = gauge length

T = applied tension force equivalent to one tension bolt

Q = prying force per bolt

and where,

$$\delta = 1 - \frac{d_h}{p} \quad (\text{EQ 3.19})$$

$$a' = a + \frac{d_b}{2} \quad (\text{EQ 3.20})$$

$$b' = b - \frac{d_b}{2} \quad (\text{EQ 3.21})$$

$$\alpha = \frac{1}{\delta} \left(\frac{Tb'}{M} - 1 \right) \quad (\text{EQ 3.22})$$

δ = ratio of the net section area to the gross flange area

d_h = diameter of the bolt hole

α = parameter for the level of prying present

The parameter (α) is an indicator of the level of prying present (Kulak et al. 1987). When α excess unity ($\alpha \geq 1.0$), the thickness of the flange is sufficient to cause the plastic flange mechanism to form as if the flange were a fixed-fixed beam (Figure 3.9(a)). When $\alpha \leq 0$, the flange can separate from the contact surface and the combination of bolt fracture due to tension and flange yielding are dominant (Figure 3.9(b)).

(F) Bearing Strength at Bolt Holes

The bearing strength can be determined by the sum of the strengths of the connected material at the individual bolt holes (AISC 2001, Section J3). The design resistance ($\phi R_{n,bearing}$) due to bearing in a standard bolt hole, oversized bolt hole, or short-slotted bolt hole is taken as either:

$$R_{n,bearing} = 1.2L_c t F_u \leq 2.4d_b t F_u \quad (\text{EQ 3.23})$$

if deformation of the bolt hole under the service load is a design consideration, or

$$R_{n,bearing} = 1.5L_c t F_u \leq 3.0d_b t F_u \quad (\text{EQ 3.24})$$

if deformation of the bolt hole under the service load is not a design consideration. For

both cases, $\phi_f = 0.75$

The design resistance ($\phi_f R_{n,bearing}$) due to bearing in a long-slotted bolt hole is taken as:

$$R_{n,bearing} = L_c t F_u \leq 2.0d_b t F_u \quad (\text{EQ 3.25})$$

with $\phi_f = 0.75$ for the resistant factor for the bearing failure.

In EQS (3.23) thru (3.25),

F_u = specified minimum tensile strength of the connected material

L_c = clear distance (Figure 3.10)

s = bolt spacing

t = thickness of the connected material

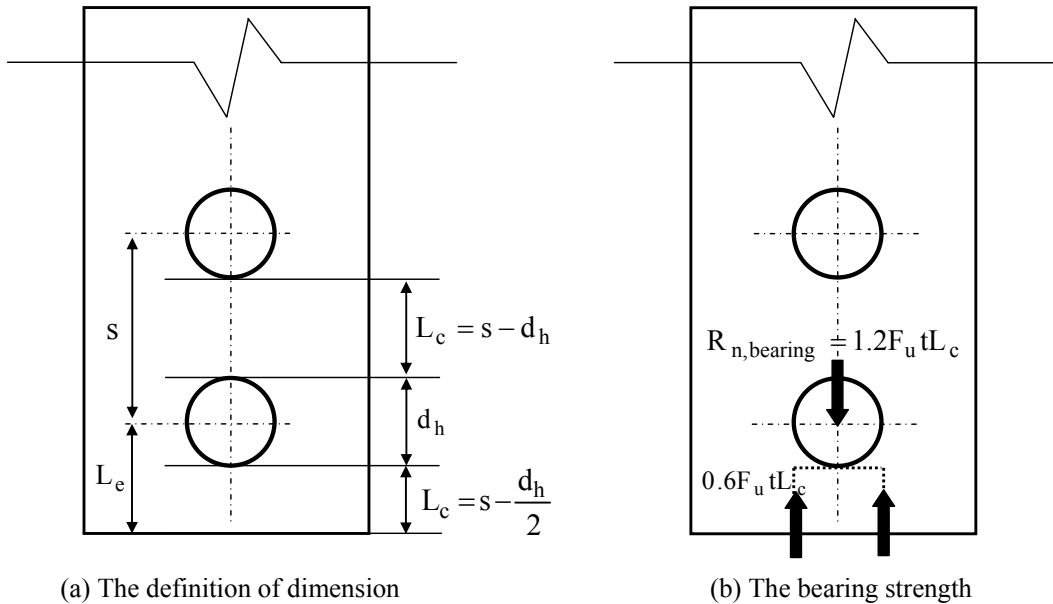


Figure 3.10 Bolt bearing strength

(G) Net Section Strength

In general, the net section is defined as the cross sectional area excluding any area lost to drilling or punching of the bolt holes. A stress concentration occurs around the edges of bolt holes as shown in Figure 3.11 (a). Yielding is concentrated along the lines connected by the shear bolt holes and the tapered edge in the stem. The yielding will lead to a fracture of the T-stem along the lines shown in Figure 3.11 (b). The resistance of the stem against the net section fracture ($\phi_t R_{n,net}$) can be taken as follows (AISC 2001):

$$R_{n,net} = \phi_u A_{net,stem} \quad (\text{EQ 3.26})$$

where,

$$A_{net,stem} = (W_{eff} - n_{sb} d_h) t \quad (\text{EQ 3.27})$$

$A_{net,stem}$ = stem net section area

n_{sb} = number of shear bolts along the effective width

W_{eff} = effective width

ϕ_t = for the resistant factor for fracture on the net section.

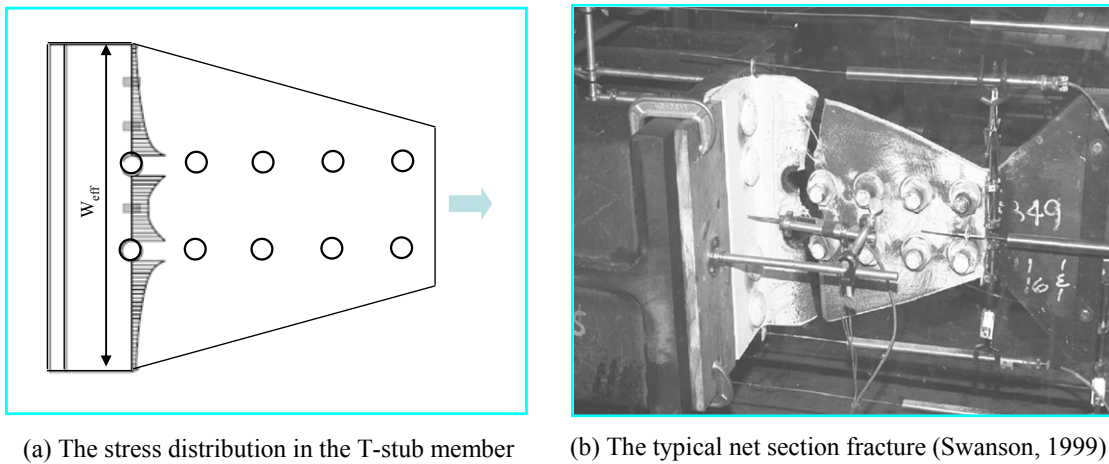


Figure 3.11 Stress distribution and net section fracture in T-stub members

(H) Block Shear Failure

Block shear failure is a combined failure, with one surface fracturing as the other one yields. It consists of either shear yielding plus tensile fracture as shown in EQ 3.28 or shear fracture plus tensile yielding as shown in EQ 3.29. Components that have failed by block shear are illustrated in Figure 3.12. The design resistance against the block shear failure ($\phi_f R_{n,block}$) is determined in accordance with the model suggested by the

LRFD (AISC 2001):

$\phi_f = 0.75$ for the resistant factor for the fracture

If $F_u A_{nt} \geq 0.6F_u A_{nv}$

$$R_{n,block} = 0.6F_y A_{gv} + F_u A_{nt} \quad (\text{EQ 3.28})$$

otherwise

$$R_{n,block} = 0.6F_u A_{nv} + F_y A_{gt} \quad (\text{EQ 3.29})$$

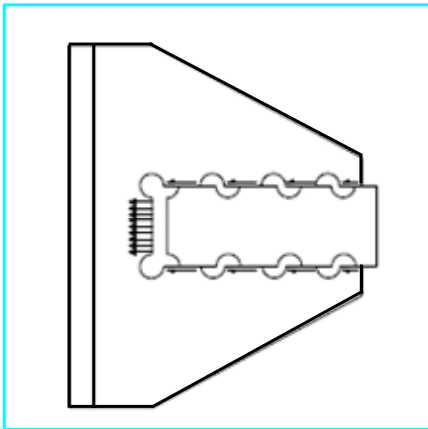
where,

A_{gv} = gross section area under shear force

A_{gt} = gross section area under tension force

A_{nv} = net section area under shear force

A_{nt} = net section area under tension force



(a) The force distribution in T-stub member (b) The typical block shear failure of T-stub member

Figure 3.12 Block shear failure mechanism (Swanson, 1999)

3.1.2.2 Components without Slip

The end-plate connection is composed of a plate shop welded to the tip of the beam and tension bolted to the member. End-plate moment connections such as that shown in Figure 3.13 are generally referred to as four tension bolt type without slip. Reliable welding can be achieved with end plate connections because they are generally fillet welds executed in the shop as compared to complete joint penetration welds executed in the field for traditional full moment welded ones (Adey et al. 2000). End-plate connections also have advantages such as easy fabrication and fast erection when compared to welded connections. Moreover, end-plate connections provide enhanced ductility they share some of the deformation modes of typical semi-rigid connection.

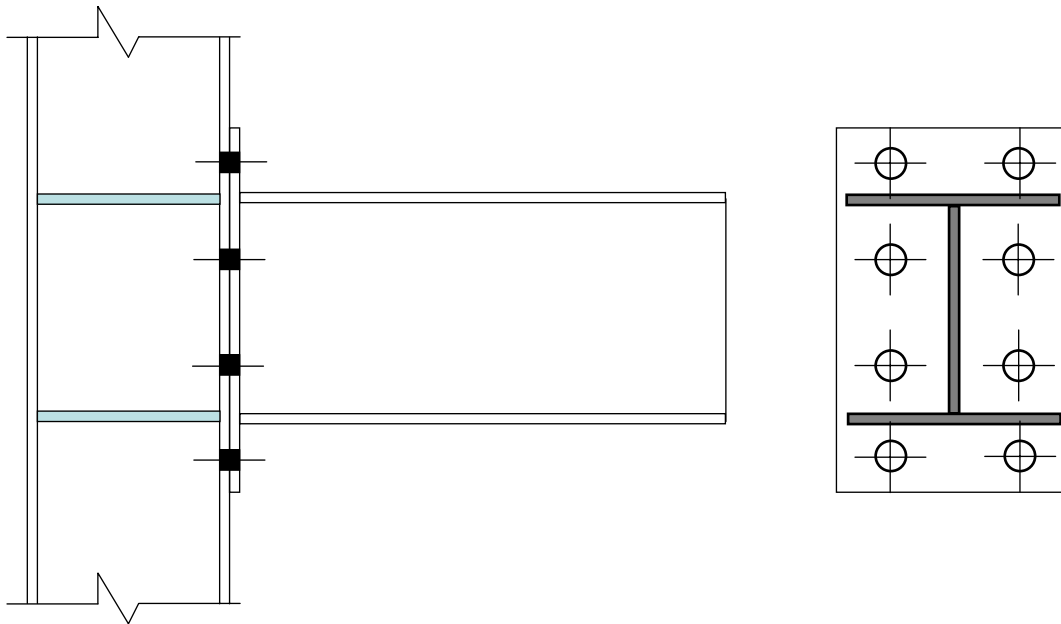


Figure 3.13 The detail of end-plate connection (4E, Four-bolt unstiffened type)

As a result of the absence of faying surfaces, end-plate connections exhibit moment-rotational behavior without slippage and a different main failure mechanism (either a

ductile yielding of the connected beam. Formation of a plate yield mechanism in the plate or an undesirable tension fracture of the connecting bolts). The design, detailing, fabrication and quality criteria for end-plate connections in this research shall conform to the requirement of the *2005 AISC Seismic Provisions* (2005 AISC Seismic Provisions). The design procedures for finding the adequate size of end-plate and tension fastener are as follows:

(A) Required bolt diameter

The *2005 AISC Seismic Provisions* require that the tension fasteners at the end-plate connection should be strong enough to resist the maximum probable moment (M_{pr}). The maximum probable moment intends to account for both the material over-strength and the fact that the material will likely begin to strain harden before failure occurs. The bolt force and bending moment mechanism according are shown in Figure 3.14(a) to Figure 3.16(a) for three types of end plate connections (4E, 4ES, and 8ES). To determine the required bolt diameter ($d_{b, req}$), the following equations are used:

$\phi = 0.90$ for the non-ductile limit state (2005 AISC Seismic Provisions)

$$\text{4E and 4ES Connection: } d_{b, req} = \sqrt{\frac{2M_{pr}}{\pi \phi F_{nt} (h_1 + h_2)}} \quad (\text{EQ 3.30})$$

$$\text{8ES Connection: } d_{b, req} = \sqrt{\frac{2M_{pr}}{\pi \phi F_{nt} (h_1 + h_2 + h_3 + h_4)}} \quad (\text{EQ 3.31})$$

where,

$$M_{pr} = C_{pr} R_y F_y Z_e \quad (\text{EQ 3.32})$$

$$C_{pr} = \frac{F_y + F_u}{2F_y} \leq 1.20 \quad (\text{EQ 3.33})$$

C_{pr} = factor to account for the peak connection strength including strain hardening, local restraint, additional reinforcement, and other connection conditions.

F_{nt} = nominal tensile stress of bolt (90 ksi for A325 bolts and 120 ksi for A 490 bolts)

F_u = specified minimum tensile stress of the type of steel, ksi

F_y = specified minimum yield stress of the type of steel, ksi

h_i = distance from the centerline of the beam compression flange to the centerline of the i^{th} tension bolt holes.

R_y = material over strength factor (2005 AISC Seismic Provisions)

$R_y = 1.5$ for A36 steel

$R_y = 1.3$ for A572-42 steel

$R_y = 1.1$ for other types of rolled shapes and bars

Z_e = effective plastic section modulus

(B) Required end-plate thickness

The behavior of this type of connection is controlled by the thickness of the end plate. Typically end plate connections in seismic areas are designed such that beam hinging will occur before a plastic mechanism (yield lines) forms in the plate. The

controlling yield line mechanisms for end-plates (Y_p) are illustrated in Figures 3.14(b) to Figure 3.16(b). The required end-plate thickness ($t_{p, req}$) is:

$\phi = 1.0$ for the ductile limit state (2005 AISC Seismic Provisions)

$$t_{p, req} = \sqrt{\frac{1.11M_{pr}}{\phi F_{yp} Y_p}} \quad (\text{EQ 3.34})$$

where,

F_{yp} = specified minimum yield stress of the end-plate material, ksi

Y_p = end-plate yield line mechanism parameter from EQ 3.36 to EQ 3.40

The basic spacing parameter (s) is given by:

$$s = \frac{1}{2} \sqrt{b_p g} \quad (\text{If } pf_2 \geq s, \text{ use } pf_2 = s) \quad (\text{EQ 3.35})$$

For four-bolt unstiffened end-plate connections (See Figure 3.14):

$$Y_p = \frac{b_p}{2} \left[h_2 \left(\frac{1}{pf_2} + \frac{1}{s} \right) + h_1 \left(\frac{1}{pf_1} + \frac{1}{s} \right) - \frac{1}{2} \right] + \frac{2}{g} [h_2 (pf_2 + s)] \quad (\text{EQ 3.36})$$

For four-bolt stiffened end-plate connections (See Figure 3.15):

Case 1 ($d_e \leq s$)

$$Y_p = \frac{b_p}{2} \left[h_2 \left(\frac{1}{pf_2} + \frac{1}{s} \right) + h_1 \left(\frac{1}{pf_1} + \frac{1}{s} \right) - \frac{1}{2} \right] + \frac{2}{g} [h_2 (pf_2 + s) + h_1 (pf_1 + d_e)] \quad (\text{EQ 3.37})$$

Case 2 ($d_e > s$)

$$Y_p = \frac{b_p}{2} \left[h_2 \left(\frac{1}{pf_2} + \frac{1}{s} \right) + h_1 \left(\frac{1}{pf_1} + \frac{1}{s} \right) - \frac{1}{2} \right] + \frac{2}{g} [h_2 (pf_2 + s) + h_1 (pf_1 + s)] \quad (\text{EQ 3.38})$$

For eight-bolt stiffened end-plate connection (See Figure 3.16)

Case 1($d_e \leq s$)

$$Y_P = \frac{b_p}{2} \left[h_1 \left(\frac{1}{2d_e} \right) + h_2 \left(\frac{1}{pf_1} \right) + h_3 \left(\frac{1}{pf_2} \right) + h_4 \left(\frac{1}{s} \right) \right] + \frac{2}{g} \left[h_1 \left(d_e + \frac{p_b}{4} \right) + h_2 \left(pf_1 + \frac{3p_b}{4} \right) + h_3 \left(pf_2 + \frac{p_b}{4} \right) + h_4 \left(s + \frac{3p_b}{4} \right) + p_b^2 \right] + g \quad (\text{EQ 3.39})$$

Case 2($d_e > s$)

$$Y_P = \frac{b_p}{2} \left[h_1 \left(\frac{1}{2d_e} \right) + h_2 \left(\frac{1}{pf_1} \right) + h_3 \left(\frac{1}{pf_2} \right) + h_4 \left(\frac{1}{s} \right) \right] + \frac{2}{g} \left[h_1 \left(s + \frac{p_b}{4} \right) + h_2 \left(pf_1 + \frac{3p_b}{4} \right) + h_3 \left(pf_2 + \frac{p_b}{4} \right) + h_4 \left(s + \frac{3p_b}{4} \right) + p_b^2 \right] + g \quad (\text{EQ 3.40})$$

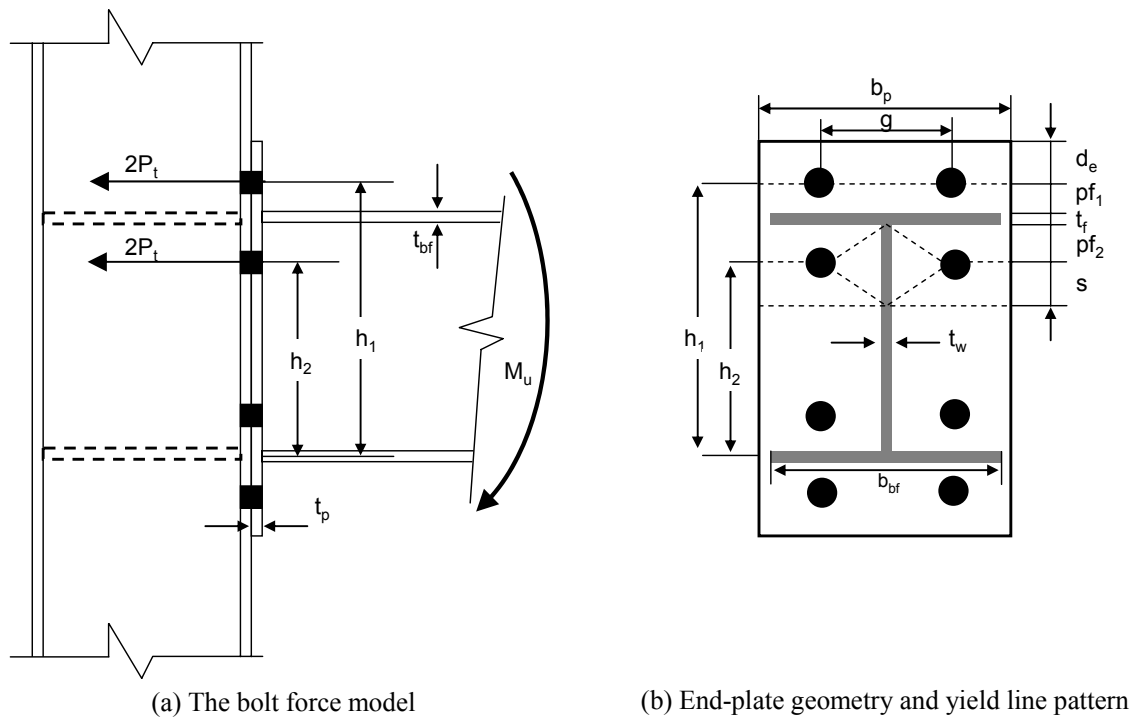


Figure 3.14 Parameters for four bolt extended unstiffened end-plate (4E) yield line mechanism

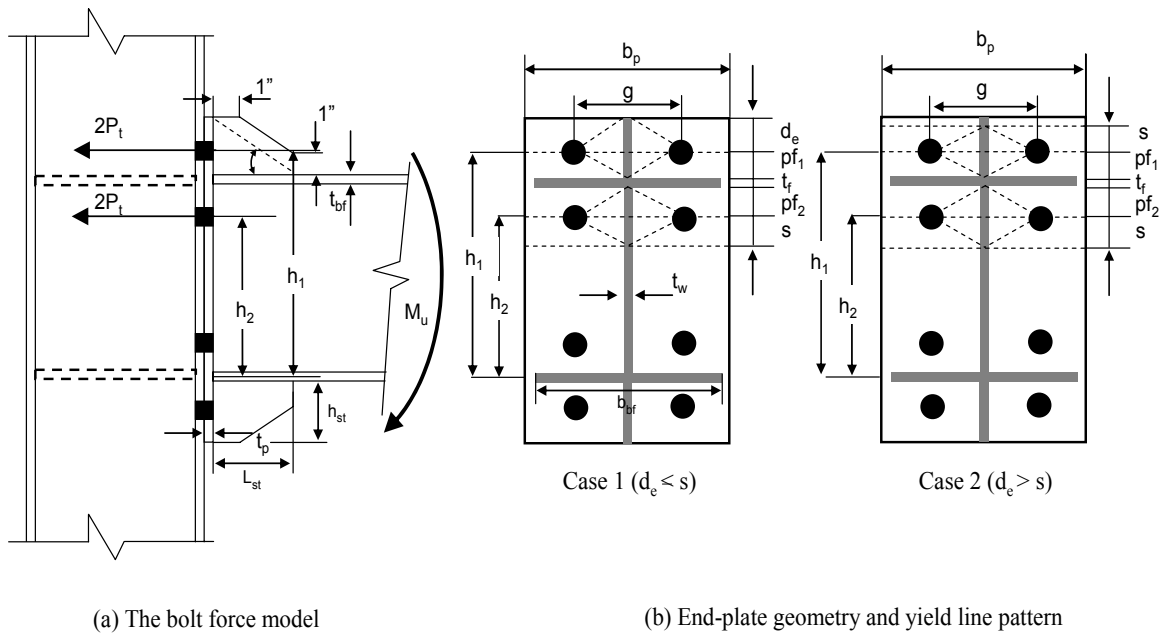


Figure 3.15 Parameters for four bolt extended stiffened end-plate (4ES) yield line mechanism

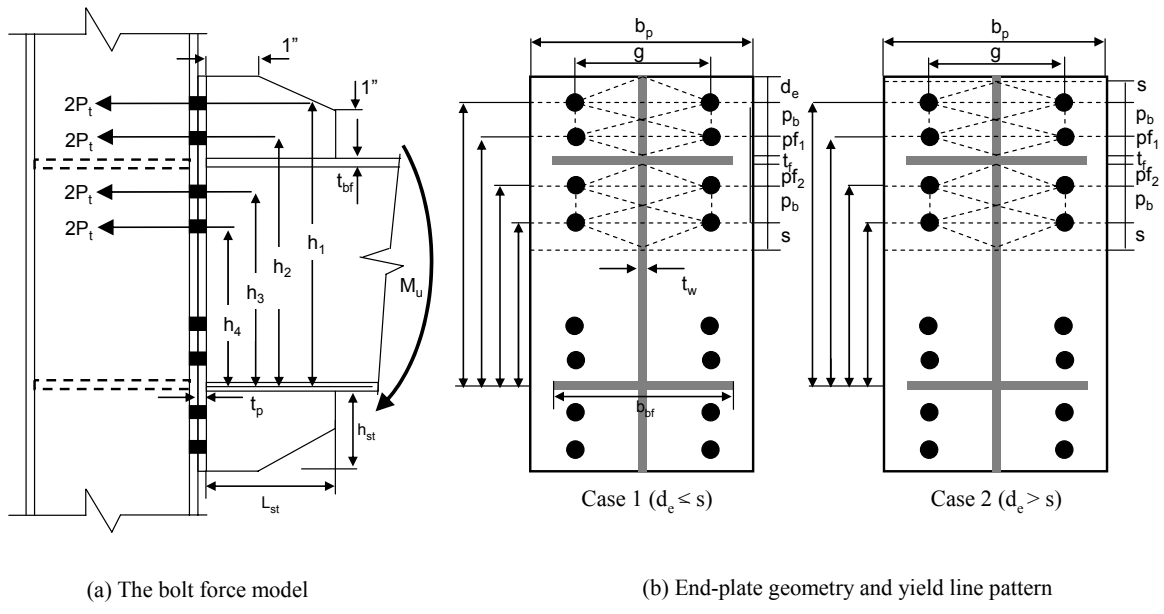


Figure 3.16 Parameters for eight bolt extended stiffened end-plate (8ES) yield line mechanism

Yield line analysis has proven to be a useful instrument in calculating the ultimate capacity of end-plates. This analysis focus on the plastic deformation caused by the

formation of the plastic hinges or yield lines and neglects the elastic deformation. The yield lines are selected from any valid pattern that results in a mechanism. The yield lines are assumed as straight and the moment along each line is constant and equal to the plastic moment capacity of the plate. The beam web and stiffeners are considered as rigid sections that provide boundaries to the yield lines along the end-plate width (b_p).

(C) Welds

Welding procedures in this research are assumed to satisfy the requirements of section 7.3 and Appendix W of the *2005 AISC Seismic Provisions*. Welding of the beam to the end-plate shall be in accordance with the following limitations:

- Welding near to the holes shall not be used.
- The beam web to end-plate connection shall be fabricated using either fillet welds or complete joint penetration (CJP) groove welds.
- The beam flange to end-plate connection shall be fabricated using a CJP groove weld without backing. The CJP groove weld shall be fabricated in that the root of the weld lies on the beam web side of the flange.
- All end-plate stiffener connections shall be fabricated using CJP groove welds.

3.1.3 Composite Panel Zone Strength

The composite panel zone treated in this research is composed of the steel tube and concrete core. In general, the shear strength of the composite panel zone can be calculated as the superposition of the shear strengths of the steel and concrete components. A mechanical model proposed by Wu et al. (2005 and 2007) is used in this research in order to compute the stiffness, the yielding shear strength, and the ultimate

shear strength of the composite panel zone. The theoretical equations for this mechanical model are driven by using the shear stiffness contributions of both materials.

(A) Steel Tube

The contribution of the rectangular steel tube to the shear resistance is composed of two parts: (a) the column flanges deforming in a flexural mode and (b) the webs deforming in a shear mode (Figure 3.17). Therefore, the shear strength and stiffness of the panel zone are affected by both deformation mechanisms.

The two column flanges subjected to shear force can be modeled as columns with fixed supports resisting flexural deformations. The shear stiffness of the two column flanges (K_f) is:

$$K_f = 2 \frac{12E_s I_f}{(d_b - t_{bf})^2} \quad (\text{EQ 3.41})$$

where,

$$I_f = \frac{b_c t_f^3}{12} \quad (\text{EQ 3.42})$$

and where,

b_c = width of the column

d_b = depth of the beam

K_f = shear stiffness for the column flange at the panel zone

I_f = moment of inertia of the column flange

t_{bf} = thickness of the beam flange

t_f = thickness of the column flange

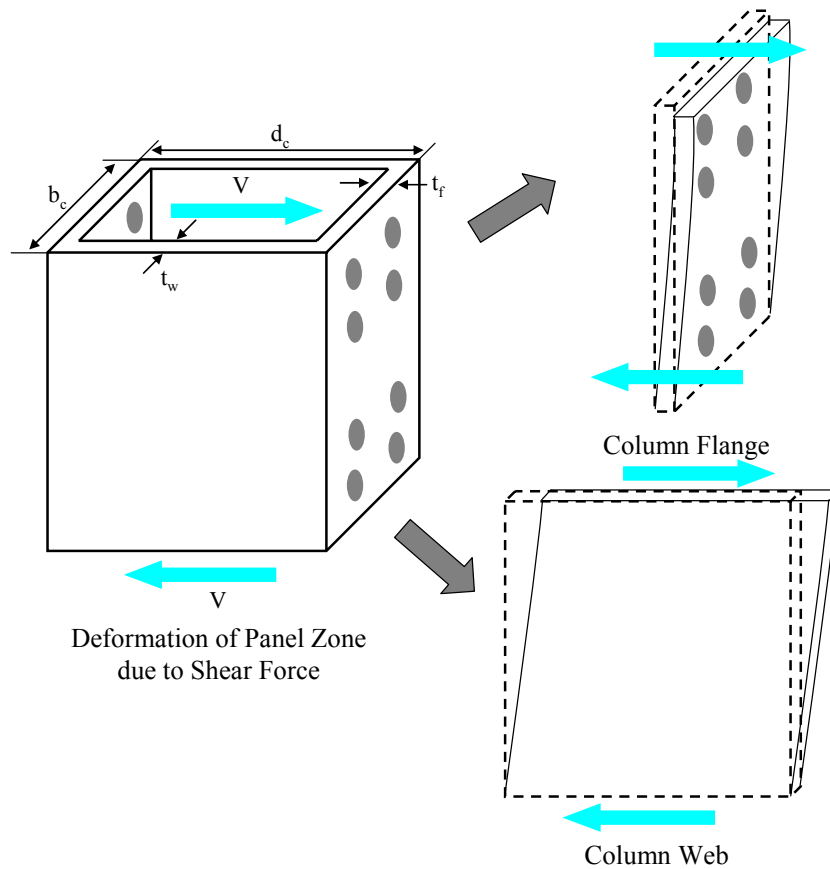


Figure 3.17 Schematic figures for deformation of steel tube in the panel zone region

The existence of bolt holes can reduce the shear strength of the tube.. As a result, the steel tube column is divided into two regions which are a column web without bolt holes and a column flange without bolt holes. The original mechanical model by Wu et al. (2005 and 2007) considers this effect. However, only column webs without bolt holes will be treated in this study because the specimens shown in the next chapters do not contain any bolt holes in the column webs. The shear stiffness of the two column webs (K_w) is as follows:

$$K_w = 2(d_c - 2t_f)t_w G_s \quad (\text{EQ 3.43})$$

where,

d_c = depth of the column

G_s = shear modulus of steel

K_w = shear stiffness in the two column webs

t_w = thickness of the column web

The shear stiffness (K_{s1}) of the rectangular steel tube at the panel zone is the superposition of the shear stiffness of the column webs (K_w) and the shear stiffness of the column flanges (K_f).

$$K_{s1} = K_f + K_w \quad (\text{EQ 3.44})$$

The resulting shear yield strength (V_{wy}) and yield strain (γ_{wy}) at the column web are as follows:

$$V_{wy} = 2(d_c - 2t_f)t_w \tau_{sy} \quad (\text{EQ 3.45})$$

$$\gamma_{wy} = \frac{V_{wy}}{K_w} \quad (\text{EQ 3.46})$$

where,

$$\tau_{sy} = \frac{F_y}{\sqrt{3}} \quad (\text{EQ 3.47})$$

τ_{sy} = yield shear stress of steel

When the shear strain in the panel zone reaches the yield shear strain (γ_{wy}) of the column web, the yield shear strength (V_{sy}) is the superposition of the shear strengths of the column webs and that of the column flanges.

$$V_{sy} = K_{s1}\gamma_{wy} \quad (\text{EQ 3.48})$$

As the external loads increase, the column webs will yield and the stiffness of the column webs vanishes. After this yielding occurs, the shear stiffness (K_{s2}) is the shear stiffness of the column flange (K_f) alone:

$$K_{s2} = K_f \quad (\text{EQ 3.48})$$

The stress in the column flanges subsequently arrives at the yielding point as the external load increases. The resulting shear yield strength (V_{fy}) and yield strain (γ_{fy}) at the column web are as follows:

$$V_{fy} = \frac{4M_{fy}}{(d_b - t_{bf})} \quad (\text{EQ 3.49})$$

$$\gamma_{fy} = \frac{V_{fy}}{K_f} \quad (\text{EQ 3.50})$$

where,

$$M_{fy} = \frac{b_c t_f^2 F_y}{6} \quad (\text{EQ 3.51})$$

M_{fy} = yielding flexural strength of the column flanges

The ultimate shear strength (V_{su}) of the panel zone is the summation of the shear strengths of the column webs and column flanges when the shear strain of the panel zone arrives at the yield strain (γ_{fy}) for the column flange.

$$V_{su} = V_{wy} + V_{fy} \quad (\text{EQ 3.52})$$

(B) Confined Concrete Core

A Mohr-Coulomb failure criterion is adopted to estimate the ultimate shear strength of the concrete. The ultimate shear stress (τ_{cu}) of the concrete in the panel zone can be obtained as:

$$\tau_{cu} = \sqrt{\left[\frac{f_c'}{11} + \frac{9(f_{cp} + f_{ct})}{22} \right]^2 - \left(\frac{f_{cp} - f_{ct}}{2} \right)^2} \quad (\text{EQ 3.53})$$

where,

$$f_{cp} = \frac{PE_c}{E_s A_s + E_c A_c} \quad (\text{EQ 3.54})$$

$$f_{ct} = \frac{-T}{b_c d_b} \quad (\text{EQ 3.55})$$

A_c = cross section area of concrete core

A_s = cross section area of steel tube

P = axial compression loaded on CFT

T = sum of the forces of the pre-stressed bolts

The shear stiffness (K_c) and the ultimate shear strength (V_{cu}) of the concrete core in the panel zone are as follows:

$$K_c = G_c A_c \quad (\text{EQ 3.56})$$

$$V_{cu} = \tau_{cu} A_c \quad (\text{EQ 3.57})$$

The corresponding ultimate shear strain of the concrete in the panel zone is:

$$\gamma_{cu} = \frac{\tau_{cu}}{G_c} \quad (\text{EQ 3.58})$$

(C) Combined Steel Tube and Concrete Core

The steel tube at the panel zone is divided structurally into webs and flanges. The strain and strength at which the steel webs yield is defined as the yielding shear strain and strength of the panel zone, while the strain and strength at which the steel flanges

yield is defined as the ultimate shear strain and strength of the panel zone. For the composite panel zone, the shear stiffness (K), the yielding shear strength (V_y), and the ultimate shear strength (V_u) is the summation of those of the steel tube and the concrete core respectively, as follows:

$$K = K_{sl} + K_c \quad (\text{EQ 3.59})$$

$$V_y = V_{sy} + V_{cu} \quad (\text{EQ 3.60})$$

$$V_u = V_{wy} + V_{fy} + V_{cu} \quad (\text{EQ 3.61})$$

3.2 Preliminary Design Procedure for Connection Components

Practical methods for ductile design of components will be presented in this section. The ductility and strength of the moment connections should be greater than the demand due to the external response in order to satisfy the general requirements of seismic design. Strength requirements can be met by satisfying the strength equations discussed in the previous sections and this is a relatively straight forward process based on well-established limit theories. On the other hand, satisfying ductility (or drift) requirements is a difficult task and one not amenable to simplification. As shown by the calculations for the shear capacity of the panel zones, strength and deformation capacity need to be carefully considered for each component. When several components are merged to make a connection, these relationships become complex and simple equations can generally not be used to insure that available ductility exceeds demand. In this dissertation an approach that emphasizes strength design will be used for the

preliminary design, with the deformation checks carried out with the aid of advanced analyses.

In the seismic design of steel components, limit states can be classified as either ductile (yielding) or brittle (fractures) modes. The dominant failure modes for steel or composite components should be ductile failure modes such as slip, yielding of steel and minor local buckling in order to avoid the entire collapse and ensure the survival of the structure (Astaneh-Asl 1995). An approach to fulfill this requirement is to require that the minimum capacity of all brittle failure modes be greater than that of the strongest yielding modes. In this way, several ductile mechanisms will be activated before any brittle one can occur. Suitable use of capacity reduction factors and reliability approaches will lead to connection designs with a suitable low probability of not achieving the desired ductility. Seismic design procedures considering this approach for the design of composite PR-CFT connection frames are discussed in the next sections.

3.2.1 Composite Column Design

The *2005 AISC Specification* contains revised rules for the design of composite columns. As the design of columns is governed by stability effects, the first step is to determine the factored design demand including the dead and the live load on the floor systems. In the real composite frame structures, the composite column systems behave as members subjected simultaneously to axial load and bending moment (So called beam-columns). Beam-column behavior as related to the composite frame performance will be treated in the following chapters. The second step is to determine the slenderness effects. Finally, the design capacity can be determined by applying the design resistance

factor to the nominal strength. A detail step-by-step design procedure for the composite columns under the axially compressive load is as follows:

Step 1) Compute the design demand

The first step for the design is to determine the required design strength for the composite columns. The initial design will be based on the highest compressive axial load, which is given by the load combination:

$$P_u = P_r = 1.2P_D + 1.6P_L \quad (\text{EQ 3.62})$$

Step 2) Select the cross section area

To qualify as a composite filled column, all column elements shall be within the limitations as mentioned Section 3.1.1. Note that this step includes a check for local buckling that ensures that the plastic capacity of the section can be achieved.

Step 3) Compute effective moment of inertia for the composite section

Once the cross section selected has been shown to exceed the required design strength (P_r), the modified stiffness (EI_{eff}) is calculated for the CFT:

$$EI_{eff} = E_s I_s + 0.5E_s I_{sr} + C_1 E_c I_c \quad (\text{EQ 3.5})$$

$$C_1 = 0.6 + 2 \left(\frac{A_s}{A_c + A_s} \right) \leq 0.9 \quad (\text{EQ 3.6})$$

Step 4) Compute the slenderness ratio

The limit state global buckling (P_o) is based upon the slenderness ratio (α) as shown below:

$$\alpha = \sqrt{\frac{P_o}{P_e}} \quad (\text{EQ 3.63})$$

$$P_o = A_s F_y + A_{sr} F_{yr} + C_2 A_c f_c' \quad (\text{EQ 3.64})$$

$$P_e = \pi^2 (EI_{eff}) / (KL)^2 \quad (\text{EQ 3.65})$$

Step 5) Compute the factored design capacity

To fulfill the general axiom of design, the factored design strength should be equal or greater than the design demand as shown below.

$$\phi_c P_n \geq P_u \quad (\text{EQ 3.66})$$

The nominal compressive strength should be determined based on the slenderness ratio.

When $\alpha \leq 1.5$,

$$\phi_c P_n = P_o (0.658^{\alpha^2}) \quad (\text{EQ 3.67})$$

When $\alpha > 1.5$,

$$\phi_c P_n = P_o \frac{0.877}{\alpha^2} \quad (\text{EQ 3.68})$$

Extensive numerical examples of composite column design are given in Appendix A. In that Appendix, comparisons between the simplified AISC procedure used here and more “exact” fiber models are also given.

3.2.2 End Plate Connection

The ANSI standard (ANSI 358-05) specifies design, detailing, fabrication, limitation, and quality criteria for end-plate connections that satisfy the *2005 AISC Seismic Provisions* (2005 AISC Seismic Provisions) for use with composite moment frame structures. The behavior of this type of connections is generally controlled by a number of different limit states closely related to the ductile modes such as local buckling of the beam flanges, flexural yielding of the beam section, flexural yielding of the end-plate, and yielding of the column panel zone. The resistance to brittle failure modes such as tension failure of the end-plate bolts, shear failure of the end-plate bolts or tearing of various welded connections should be greater than those computed for the ductile modes. Example 1 in Appendix B is a complete example of the application of the procedure described in the next subsections.

Step 1) Compute the design strength

The first step is to determine the design strength for the end-plate connection. In case of a full strength connection, i.e., one where all the plastic deformations will be confined to the framing beam, the required design strength shall be determined by the plastic moment specified in the *2005 AISC Seismic Provisions*.

$$M_{\text{design}} = C_{\text{pr}} F_{\text{ye}} Z_x \quad (\text{EQ 3.69})$$

where,

$$C_{pr} = \frac{F_y + F_u}{2F_y} \leq 1.2 \quad (\text{EQ 3.33})$$

$$F_{ye} = R_y F_y \quad (\text{EQ 3.70})$$

C_{pr} = factor to consider the peak connection strength, typically taken as 1.1

F_{ye} = factored yield stress at the beam

R_y = material over strength factor (See EQ 3.32)

Z_x = plastic section modulus of the beam

On the other hand, for a partial strength connection requires the advanced analysis including second order effect and overall frame stability in order to find the design strength.

Step 2) Select the geometric parameters for connection components

One of the three end-plate moment connection configurations, preliminary value for the connection geometric parameters and bolt grades should be selected in this step. All connection components shall satisfy the following limitations as shown in Table 3.3 associated with Figures 3.14 to Figure 3.16 in order to avoid the stress concentrations and possible brittle fractures.

Step 3) Determine the tension bar/bolt diameter

For an end plate connection, the dominant brittle failure modes that needed to be

avoided are the tension/shear fracture of the welds or tension fracture of the bolts. For any kind of full strength bolted connections, the connection must insure that the ductile limit state given by beam yielding occurs well before tension bolts or welds fail. The required bolt diameter ($d_{b,req}$) can be determined by using EQ 3.30 or EQ 3.31. The tension bars designed in this structure consist of the super-elastic SMA tension bars and the A490 type tension bars. The nominal strength of the individual tension bar should reflect the difference in material properties between steel and SMA as well as the different strain demands based on the placement of the bars relative to the centerline of the bottom beam flange. The procedure about the averaged strength according to the different connection types is illustrated in Figure 3.18.

Table 3.3 Prequalification limitations for geometric parameters (ANSI 385-05)

Parameter	4E		4ES		8ES	
	Max.	Min.	Max.	Min.	Max.	Min.
t_p	2.25	0.5	1.5	0.5	2.5	0.75
b_p	10.75	7	10.75	10.75	15	9
g	6	4	6	3.25	6	5
P_{f1}, P_{f2}	4.5	1.5	5.5	1.75	2	1.75
P_b	-	-	-	-	3.75	3.5
d	55	25	24	13.75	36	18.5
T_{bf}	0.75	0.375	0.75	0.375	1	0.593
b_{bf}	9.25	6	9	6	12.25	7.75

Unit: inch

Step 4) Determine the required end-plate thickness

After the size of the bolt diameter has been determined, the geometric parameters for the end-plate should be established. The most significant parameter is the end-plate thickness (t_p). It is necessary to understand the effect of the end-plate geometry on the

response of the connection as the behavior can be highly nonlinear and counterintuitive. Based on these considerations, the end plate thickness can be computed from EQ 3.34 to EQ 3.40. The plate deformations should be consistent with the selected yield line mechanism as shown in Figure 3.16 to Figure 3.18.

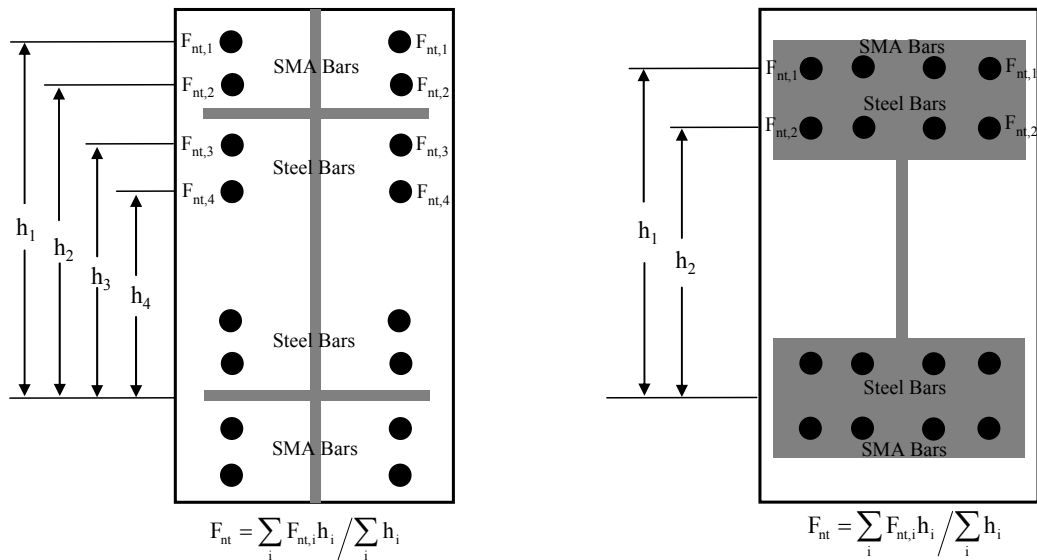


Figure 3.18 Average tensile strength for a bar

Step 5) Check the shear resistance of the end-plate

For a full strength connection, the design axial force (F_{fu}) at the beam flange can be backcalculated by a simple model from the factored plastic moment of the beam as mentioned in the *2005 AISC Seismic Provisions*. After finding of the factored design axial force for the beam flange, that the designer must insure that the shear yielding resistance and shear rupture resistance at the end-plate should be equal or larger than this design force (See EQ 3.72 to EQ 3.73).

$\phi = 0.90$ for the non-ductile limit state (2005 AISC Seismic Provisions)

$$F_{fu} = \frac{M_{design}}{d - t_{bf}} \quad (EQ 3.71)$$

$$\frac{F_{fu}}{2} \leq \phi R_{n, shear} = 0.6\phi F_{yp} b_p t_p \quad (EQ 3.72)$$

$$\frac{F_{fu}}{2} \leq \phi R_{n, shear} = 0.6\phi F_{up} A_n \quad (EQ 3.73)$$

where,

$$A_n = \left[b_p - 2 \left(d_b + \frac{1}{16} \right) \right] t_p \quad (EQ 3.74)$$

A_n = net area of the end-plate when standard holes are used

b_p = width of the end-plate

d = depth of the beam

d_b = diameter of bolts

F_{fu} = specified minimum tensile strength of the end-plate

If either EQ 3.72 or EQ 3.73 is not satisfied, the thickness of the end-plate must be increased until these relationships are satisfied.

Step 6) Select the thickness of the end-plate stiffener

In case of either the four bolt extended stiffened end-plate (4ES) or eight bolt extended stiffened end-plate (8ES) connection, the end-plate stiffener needs to be designed. After the thickness of the end-plate stiffener ($t_{s, min}$) is determined, the

stiffener to beam-flange and the stiffener to end-plate welds are modeled.

$$t_{s,\min} = t_{\text{bw}} \left(\frac{F_{\text{yb}}}{F_{\text{ys}}} \right) \quad (\text{EQ 3.75})$$

where,

t_{bw} = thickness the beam web

$t_{s,\min}$ = thickness of the end-plate stiffener

F_{yb} = specified minimum yield stress of beam material, ksi

F_{ys} = specified minimum yield stress of stiffener material, ksi

The following width to thickness criterion should be satisfied in order to prevent local buckling of the stiffener plate:

$$L_{\text{st}} = \frac{h_{\text{st}}}{\tan 30^\circ} \quad (\text{EQ 3.76})$$

$$\frac{h_{\text{st}}}{t_s} \geq 0.56 \sqrt{\frac{E}{F_{\text{ys}}}} \quad (\text{EQ 3.77})$$

where,

h_{st} = height of the stiffener

L_{st} = width of the stiffener

Step 7) Check the rupture and bearing failure of bolts

The design shear capacity ought to exceed the design shear strength as follows:

$\phi = 0.90$ for the non-ductile limit state (2005 AISC Seismic Provisions)

$$V_u \leq \phi B_{n, \text{shear}} = \phi N_b F_v A_b \quad (\text{EQ 3.78})$$

where,

$$V_u = \frac{2M_{\text{design}}}{L'} \quad (\text{EQ 3.79})$$

A_b = nominal gross area of the bolts

F_v = effective ultimate shear strength (See EQ 3.14)

L' = distance between plastic hinges

The tear-out failure at the end-plate and column flange due to bolt bearing is required to be checked next. The geometric parameters are shown in Figure 3.10.

$\phi = 0.90$ for the non-ductile limit state (2005 AISC Seismic Provisions)

$$V_u \leq \phi R_{n, \text{bearing}} = \phi(N_i)R_{ni} + \phi(N_o)R_{no} \quad (\text{EQ 3.80})$$

where,

$$R_{ni} = 1.2L_c t F_u \leq 2.4d_b t F_u \quad (\text{EQ 3.23})$$

$$R_{no} = 1.2L_c t F_u \leq 2.4d_b t F_u \quad (\text{EQ 3.24})$$

and where,

N_i = number of inner bolts (2 for 4E and 4ES, and 4 for 8ES connections)

N_o = number of outer bolts (2 for 4E and 4ES, and 4 for 8ES connections)

R_{ni} = bearing strength at the inner bolts

R_{no} = bearing strength at the outer bolts

3.2.3 T-stub Connections

A practical design procedure for T-stub connections is presented in this section. The LRFD manual (AISC 2001) provides more information on the design and detailing of T-stub connections. Similar to the design procedure for end-plate connections, the governing mode should be ductile failure modes and the required design strength should exceed that given by the plastic moment of the beam flange. Some design steps for T-stubs are duplicate of those discussed in the design procedures for end-plate connection (See Section 3.2.2). Only new design steps pertinent only to T-stub connections will be discussed in detail in this section. Example 2 in Appendix B is a complete example of the application of the procedure described in the next subsections.

Step 1) Determine the design force

The design strength should be more than the factored plastic moment of the beam as shown in EQ 3.69 to EQ 3.70.

Step 2) Select bolt type and size

Components for the connecting elements in T-stub connections will be limited to high strength structural bars and super-elastic shape memory alloy (SMA) bars. A490 tension bars have a specific ultimate tensile strength for 150 ksi and will be used exclusively in a 1 inch diameter size. They are fabricated from alloy steel and used in parallel with super-elastic SMA bars to transfer bending from beam to column panel zone. The SMA tension bars are also available in a 1 inch diameter and will be used in that size to maintain the geometric consistency. Bars above 1 inch diameter are difficult to pretension and bars smaller than 1 inch cannot provide the required force in a

sufficiently small number of bars to make the connection economical.

As noted earlier, steel and SMA bars are used in parallel as the former provide energy dissipation and high strength and stiffness, while the later provide recentering capabilities.

Construction practice dictates that the tension bolts should share the same size and grade with the shear bolts. One of the most significant characteristics for the usage of shear bolts leads to the slip deformation. Slip is the preferred mode for increasing energy dissipation capacity and avoiding catastrophic failure. Therefore, the slip resistance should stay in the ductile region between the service load and the ultimate load. On the basis of this axiom, it is necessary for tension bars to satisfy the required diameter using the Step 3 procedure in the end-plate connection design. The general failure of bolts due to shear and tension needs to be checked. The failure modes will be illustrated with more details in the next chapter.

Step 3) Determine the configuration of the bolts

After Step 2, a preliminary configuration of the T-stub, including the spacing, gage length and arrangement for bolt holes can be determined. These design parameters have a significant influence on the effective width and strength of the T-stub members as shown by EQS. 3.15 through 3.22. The shear bolt arrangements should guarantee an adequate edge distance for the beam flange so as to avoid stress concentrations in the stem.

Step 4) Determine the required stem thickness

The conventional net section failure calculation adopted in this T-stub component

design (See EQ 3.26 and EQ 3.27) can estimate the ultimate strength of the component element as the product of the material ultimate strength of the material used and the net cross section area defined as the gross section area minus punching area of the bolt holes. The required stem thickness can be determined after the configuration of bolts and the width of T-stub member are established as shown in below:

$\phi_f = 0.75$ for the resistant factor for the fracture

$$t_{\text{stemmin}} = \frac{M_{\text{design}}}{\phi_f F_u (W_{\text{eff}} - n_{\text{sb}} d_h) d} \quad (\text{EQ 3.81})$$

The effective width (W_{eff}) as shown in Figure 3.11 is not valid for the all stem tapering configuration and drives the simple approximate estimation.

Step 5) Determine the T-stub flange width and thickness

The ultimate strength for a T-stub flange subject to prying was described in Section 3.1.2.1. On the basis of this prying action phenomenon, an adequate T-stub width and thickness can be computed. The capacity of the existing T-stub can be determined by the failure modes based on the EQ 3.15 to EQ 3.17 which correspond to a pure flange mechanism, combined failure mode, and bolt fracture respectively. The balanced load (T_o) and critical thickness (t_c) for a T-stub flange can be derived by using a balanced failure approach in which the ultimate strength of the T-stub flange is reached at the same time as the bolt force including the prying action becomes critical (Astaneh, 1985). The balanced load and critical thickness for T-stub flange can be obtained by:

$\phi_f = 0.75$ for the bolt fracture

$$T_o = \frac{\phi_f B_{n,tension}}{1 + \left(\frac{\delta}{1 + \delta}\right)\left(\frac{b'}{a'}\right)} \quad (\text{EQ 3.82})$$

$$t_c = \sqrt{\frac{4B_{n,tension} b'}{pF_y}} \quad (\text{EQ 3.83})$$

If the balanced load is equal to the design load (T_{design}), the value of a' is equal to $2d_b$, and assuming that the tension bolt gage (g_t) will be relatively large compared to the flange width (B_f), the required value of b' and flange width are (Swanson, 2001):

$$b' = \left(\frac{\phi B_{n,tension} - T_{design}}{T_{design}}\right)\left(\frac{1 + \delta}{\delta}\right)a' \quad (\text{EQ 3.84})$$

$$B_{f,design} = 2b' + 4d_b + 2t_{s,min} \quad (\text{EQ 3.85})$$

Step 6) Check the T-stub section

After T-stub section has been selected, the capacity of the T-stub section should be checked by comparing the available failure modes which occur in either the flange or the stem. In order to ensure a ductile failure with significant deformation, the yielding capacity of the stem net section should be nearly equal to the ultimate capacity of the flange due to the prying mechanism.

$\phi_y = 0.90$ for the resistance factor against yielding

$$\phi_y F_y A_{net, stem} \leq \phi n_{tb} T \quad (\text{EQ 3.86})$$

Step 7) Check the yield and fracture for the component members

Block shear failure is a combined yield fracture type of failure where the boundary of a block of tensile yielding in some area and tensile fracture in the remaining areas. (EQ 3.28 and EQ 3.29). Block shear needs to be checked but it will only be critical if the bolt spacing and gages fall below the recommended value of $3d_b$.

Step 8) Design the shear connection

Finally, the shear connection should be designed. Failure modes for the shear connections and reliable design procedures are available in the current LRFD code (AISC 2001). In case of the partial strength moment connections, the usage of the short slotted holes on the shear tab connections in the loading direction can avoid a complete connection failure and reduce the torsion into the connection and beam (Swanson, 2001). Failure of the shear connection as the fracture of the net area, web bolts or welds can induce the catastrophic collapse of the connection and miss the opportunity to resist the gravity loads after the flange failure. Therefore, the shear connection has to endure large rotation before the yield failure.

3.2.4 Clip Angle Connection

A practical design procedure for the clip angle connections with heavy angles t ($t = 1''$) will be presented in this section. The design procedures are very similar to that for T-stub connections described in the previous section and for simplicity the procedure is summarized in Table 3.4. Example 3 in Appendix B is a complete example of the application of the procedure described in the next subsections.

Table 3.4 Summary and comparison of design procedures for T-stub and clip angle connection

Design Step	T-stub Connection Type	Thick Clip Angle Connection Type
1	$M_{design} = C_{pr} F_{yc} Z_x$	<p>Determine the design force</p> $C_{pr} = \frac{F_y + F_u}{2F_y} \leq 1.2$ $F_{yc} = R_y F_y$
2	<p>Determine the adequate bar diameter Two rows of tension bar arrangement</p> $F_{nt} = \frac{\sum_i F_{nt,i} h_i}{\sum_i h_i} \quad d_{b,req} = \sqrt{\frac{4M_{pr}}{2\pi\phi F_{nt}(h_1 + h_2)}}$	<p>Determine the adequate bar diameter One row of tension bar arrangement</p> $F_{nt} = \frac{\sum_i F_{nt,i} h_i}{\sum_i h_i} \quad d_{b,req} = \sqrt{\frac{4M_{pr}}{3\pi\phi F_{nt}(h_1)}}$
3	<p>Determine the configuration of the bolts In general, four or five rows of the shear bolt arrangement Check the gage and bolt spacing (Typ. S=3")</p>	<p>Determine the configuration of the bolts In general, two rows of the shear bolt arrangement Check the gage and bolt spacing (Typ. S=3")</p>
4	<p>Determine the stem thickness</p> $R_{n,net} = F_u A_{net,stem} \quad A_{net,stem} = (W_{eff} - n_{sb} d_h) t$	<p>Determine the clip angle thickness</p> $R_{n,net} = F_u A_{net,angle} \quad A_{net,angle} = (W_{eff} - n_{sb} d_h) t$
5	<p>Determine the T-stub flange width and thickness Consider T-shape to find the effective width per bolt</p> $p = \frac{2W_{T-stub}}{n_b}$	<p>Determine the clip angle flange width and thickness Consider L-shape to find the effective width per bolt</p> $p = \frac{W_{Clip}}{n_b}$
6	<p>Check the T-stub section</p> $\phi_y F_y A_{net,stem} \leq \phi n_b T \quad \phi_y = 0.90$	<p>Check the clip angle section</p> $\phi_y F_y A_{net,angle} \leq \phi n_b T \quad \phi_y = 0.90$
7	<p>Check the yield-fracture failure (Block shear failure modes)</p> <p>If $F_u A_{nt} \geq 0.6 F_u A_{nv}$ $R_{n,block} = 0.6 F_y A_{gv} + F_u A_{nt}$ Otherwise $R_{n,block} = 0.6 F_u A_{nv} + F_y A_{gt}$</p>	
8	<p>Design the shear connection</p> <p>Use shear tab or double web angle connection with short slotted bolt holes</p>	

3.3 Design Discussion

The main purpose of this chapter is to provide reliable preliminary design procedures for the proposed connections on the basis of strength models. The strength models presented here were based upon the current design codes. Design examples are presented in Appendix A and Appendix B. The resistance factors for bending, bearing, yielding, and fracture can produce overly conservative design strengths. The behavior of all types of connections can be generally controlled by a number of different limit states closely related to the ductile modes in order to avoid a complete collapse due to the brittle modes. Therefore, the required design strength shall be determined by the plastic moment of the steel beam. The design principles and specific detailed configurations for PR-CFT connections will be illustrated in the next chapter.

Chapter 4

Smart PR-CFT Connections

This chapter describes the specimen design for the smart PR-CFT connections, with emphasis on connection materials, geometry, and constructability. Three connection models utilizing the components described in Chapter 3 are developed: an end-plate, a T-stub, and a thick clip angle connection. Descriptions of the connections are given in Table 4.1. Detailed design examples for these connections, using Math-Cad worksheets, are provided in Appendix B.

This chapter will be organized as follows. First, the basic design principles are presented and the advantages of using these connections discussed (Section 4.1). Second, a description of the connection details, including the material properties, schematic drawings, and bolt/bar specifications, are presented (Section 4.2). Third, the governing failure modes for each connection are introduced, followed by the discussion of the structural characteristics of each component (Section 4.3). Fourth, the processing of the analytical data related to computing axial deformations and relative rotations is described (Section 4.4 and Appendix C). Finally, summary and conclusion are presented (Section 4.5).

4.1 Design Principles

All connections were designed as full strength (FS) connections, meaning that they can transfer the full plastic beam moment ($M_{p,beam}$) from the beam to the column. They fulfill the requirements for connection design given in both the AISC LRFD Standard (AISC 2001) and the AISC Seismic Provisions (*2005 AISC Seismic Provisions*). However, the connections transfer the $M_{p,beam}$ at relatively large rotations and after significant yielding of the connection components. Because of results from the flexibility of the components, the connections will be considered as partial restraint (PR) ones. The primary purpose of this chapter is to develop design methods for the PR composite connections that will result in ductile connection behavior. Since some shear yielding and

local buckling have been observed in the panel zone of connections to hollow steel columns before reaching $M_{p,beam}$, the columns' (and thus the panel zones') capacity was increased by filling the column with concrete. Thus all columns used were concrete-filled tubes or CFT columns.

The design approach used in this research explicitly considered the feasibility of integrating shape memory alloys (SMA) and regular steel bars into steel-concrete composite connections. Super-elastic Nitinol bars used as tension fasteners and subjected to large deformations can provide re-centering capabilities because their permanent strains remain small. When combined with A490 steel bars, they will result in connections with better energy dissipation and permanent deformation performance as compared with connections using either all super-elastic Nitinol bars or all conventional steel ones.

Finally, components such as shear/web bolts, shear tab plates, and clip angles or T-stubs were designed with the intent to avoid catastrophic losses of stiffness and strength due to brittle failure modes. All design strengths were checked against the demand from both code-based forces and those given by non-linear analyses. Details of those analyses are given in later chapters. The designs were based on weak beam-strong column conditions.

Table 4.1 Detailed specifications of the smart PR-CFT connections

Unit: kip, inch	End-Plate Connection with RCFT	End-Plate Connection with CCFT
Beam	W24X103	W24X103
Column	HSS16X16X500	HSS18X500
SMA Bar Material	Super-Elastic Nitinol	Super-Elastic Nitinol
Steel Bar Material	Corresponding to A490 Bolts	Corresponding to A490 Bolts
Bar Gauge Length	16"	18"
Bar Diameter	1"	1"
Bar Slenderness Ratio	51.88	58.36
Bolt Material	A 490 Bolts	A 490 Bolts
Shear Bolt Size	No Shear Bots	No Shear Bolts
Web Bolt Size	No Web Bolts	No Web Bolts
Nut Type	A 563 Nuts Corresponding to 1" Dia. Bolts	A 563 Nuts Corresponding to 1" Dia. Bolts
Component Members	End-Plate 15X38.5X1 (8ES Type)	End-Plate 15X38.5X1 (8ES Type)
Shear Tab	No Shear Tab	No Sear Tab
Panel Zone Shape & Size	Rectangular 16X16X24.5	Rectangular 18X18X24.5
Inside Concrete Material	Rec. Confined Concrete ($F/F_u=0.2$, $f_c'=4$ ksi)	Cir. Confined Concrete ($F/F_u=0.2$, $f_c'=4$ ksi)

(a) A detailed specification of the smart PR-CFT connection with an end-plate component member

Unit: kip, inch	End-Plate Connection with RCFT	End-Plate Connection with CCFT
Beam	W24X55	W24X55
Column	HSS16X16X500	HSS18X500
SMA Bar Material	Super-Elastic Nitinol	Super-Elastic Nitinol
Steel Bar Material	Corresponding to A490 Bolts	Corresponding to A490 Bolts
Bar Gauge Length	16"	18"
Bar Diameter	1"	1"
Bar Slenderness Ratio	51.88	58.36
Bolt Material	A 490 Bolts	A 490 Bolts
Shear Bolt Size	1X4 (One Washer)	1X4 (One Washer)
Web Bolt Size	1X4 (One Washer)	1X4 (One Washer)
Nut Type	A 563 Nuts Corresponding to 1" Dia. Bolts	A 563 Nuts Corresponding to 1" Dia. Bolts
Component Members	Cut from W16X100 (T-stub)	Cut from W16X100 (T-stub)
Shear Tab	Plate 4.5X9X0.56 (Fillet Welding 5/16")	Plate 4.5X9X0.56 (Fillet Welding 5/16")
Panel Zone Shape & Size	Rectangular 16X16X23.6	Rectangular 18X18X23.6
Inside Concrete Material	Rec. Confined Concrete (F/Fu=0.2, fc'=4 ksi)	Cir. Confined Concrete (F/Fu=0.2, fc'=4 ksi)

(b) A detailed specification of the smart PR-CFT connection with a T-stub component member

Unit: kip, inch	End-Plate Connection with RCFT	End-Plate Connection with CCFT
Beam	W18X50	W18X50
Column	HSS12X12X500	HSS14X500
SMA Bar Material	Super-Elastic Nitinol	Super-Elastic Nitinol
Steel Bar Material	Corresponding to A490 Bolts	Corresponding to A490 Bolts
Bar Gauge Length	12"	14"
Bar Diameter	Steel Bar: 1" , SMA Bar: 17/16"	Steel Bar: 1" , SMA Bar: 17/16"
Bar Slenderness Ratio	Steel Bar:38.90, SMA Bar: 32.43	Steel Bar: 45.39, SMA Bar: 37.84
Bolt Material	A 490 Bolts	A 490 Bolts
Shear Bolt Size	1X4 (One Washer)	1X4 (One Washer)
Web Bolt Size	1X4 (One Washer)	1X4 (One Washer)
Nut Type	A 563 Nuts Corresponding to 1" Dia. Bolts	A 563 Nuts Corresponding to 1" Dia. Bolts
Component Members	L6X8X1 (Thick Clip Angle)	L6X8X1 (Thick Clip Angle)
Shear Tab	Plate 4.5X9X0.56 (Fillet Welding 5/16")	Plate 4.5X9X0.56 (Fillet Welding 5/16")
Panel Zone Shape & Size	Rectangular 12X12X18.1	Rectangular 14X14X18.1
Inside Concrete Material	Confined Concrete (F/Fu=0.2, fc'=4 ksi)	Confined Concrete (F/Fu=0.2, fc'=4 ksi)

(c) A detailed specification of the smart PR-CFT connection with a clip angle component member

4.2 Specimen Details

Three types of smart PR-CFT connections were designed and detailed as shown in Appendix B: an end-plate, a T-stub, and a clip angle one. Each connection type was designed to connect to both a rectangular concrete filled tube column (RCFT) and a circular concrete filled tube column (CCFT) to a wide flange shape. Conventional A490 bolts were used to connect the flanges, and web bolts and a shear tab were used for the T-stub and clip angle connections.

4.2.1 Typical Configurations

Typical connection sub-assembly configurations are shown in Figure 4.1. The column and beam lengths were selected for a building with 12.5 ft. floor heights and 29 ft. bays, and the models developed with the assumption of hinges forming at the mid-height and mid-span of the columns and beams, respectively, for an exterior bay. Based on a simplified model of a story subjected to lateral loads, column was taken as 12.5 ft. in height and the beams as 14.5 ft. long for all the sub-assemblies. These models were used to study the behavior of the connection components and the adjacent areas of the beam and column.

The end-plate connection consisted of a concrete filled tube using either a HSS 16X16X500 (RCFT = rectangular CFT) or a HSS 18X500 (CCFT = circular CFT), and a W25x103 beam. Similar columns sections and lengths were used for the T-stub connections, but with a smaller beam (W24X55) size and a T-stub cut from a W16X100 section. The clip angle connection, which provided the smallest design capacity among the three types of connections, consisted of a either HSS12X12X500 (RCFT) or HSS 14X500 (CCFT), W18X50 beams and a clip angle member. The column sections were chosen such that the CCFT and RCFT columns had a similar equivalent area and capacity.

Monotonic and cyclic displacements were applied to the tip of beam. These analyses were used to investigate the deformation and strength performance of the different

connections. These analyses or numerical simulations will be discussed exhaustively in the next two chapters.

4.2.2 Connection Details

Detailed calculations for all three connection types are shown in Appendix B. The resulting configurations for typical interior joints are given in Figures 4.2 to 4.7. The specimen identifications for the smart PR-CFT connections are composed of the shape of the column (i.e. CCFT or RCFT) and the connection type (i.e. End-plate, T-stub or Clip Angle).

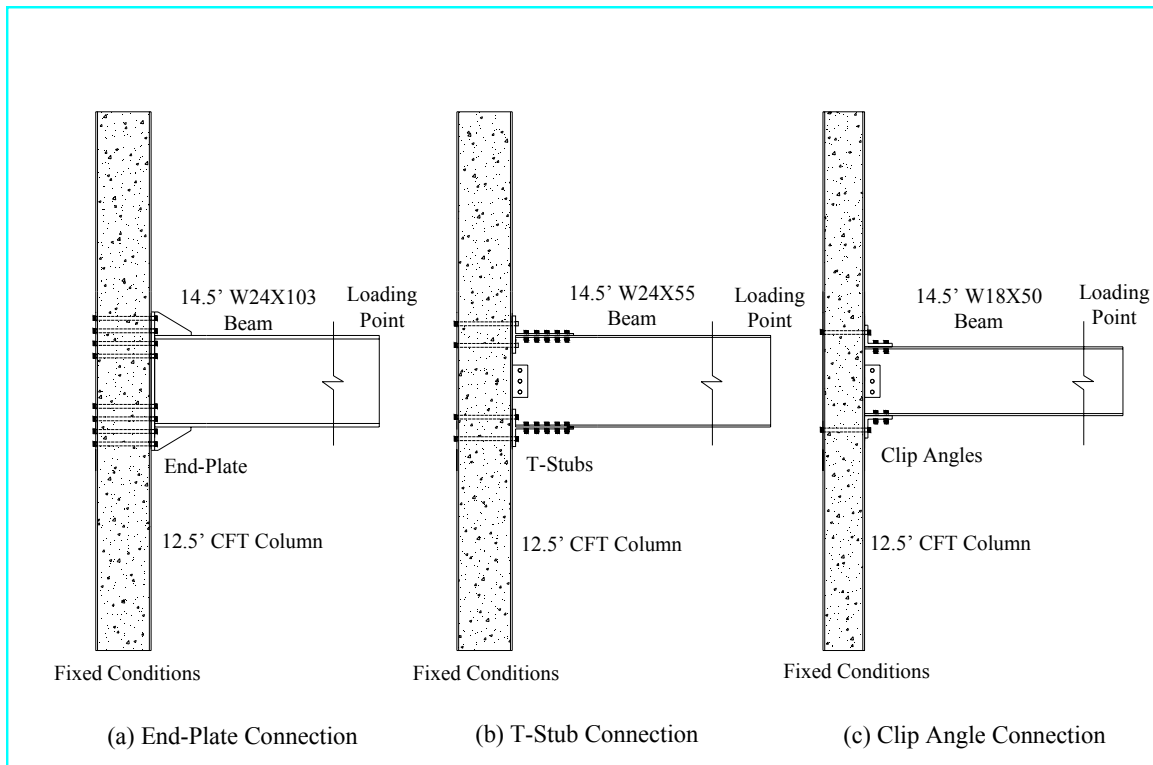


Figure 4.1 Typical connection configurations

A572 Grade 50 steel was used for all members and joint components. A490 high strength bolt material was used for all bolts, with corresponding washers and nuts. Materials with equivalent properties to A490 bolts were used for the steel tension bars, while the material properties for the super-elastic Nitinol (Shape Memory Alloy, SMA)

were taken from work of other researchers (Davide 2003). SMA tension bars were placed at the farthest practical locations from the centroid of the connection in order to take advantage of the re-centering effect during unloading (refer to Figures 4.2 through 4.7 below).

The end-plate connection (Figures 4.2 and 4.3), was composed of a 38-1/2"x 15"x1" plate welded to the beam by with a 5/16" fillet weld. The design required the use of extended stiffener plates welded between the beam flange and the end-plate. They were terminated at the beam flange and at the end of the end-plate with landings about 1" long. The plate stiffeners had the same material strength (A572-Gr. 50l) as the beam and their thickness was equal to the beam web thickness. The tension fasteners that ran through the CFT column were sixteen 1" diameter, either 20" long (RCFT column) or 22" long bars (CCFT column) with washers at either end.

The T-stub connection (Figures 4.4 and 4.5) had tension fasteners that also ran through the CFT column. These were eight 1" diameter, either 20" long (RCFT column) or 22" long bars (CCFT column). Twelve 1" diameter, 4" long A490 bolts were used to fasten each T-stub stem to the beam flange and three 1" diameter, 4" long A490 bolts were used as web bolts.

The clip angle connection (Figures 4.6 and 4.7), was composed of thick clip angles cut from a L6X8X1 and a 9"X4.5"X9/16" shear tab. The tension fasteners through the CFT column were two 1" diameter (SMA bar) and one 1-1/16" diameter (steel bar), either 16" long (RCFT column) or 18" long bars (CCFT column). Four 1" diameter, 4" long A490 bolts were used to fasten each clip angle leg to the beam flange and three 1" diameter, 4" long A490 bolts were used as web bolts. 3D configurations of all three smart PR-CFT connections are shown in Figure 4.8.

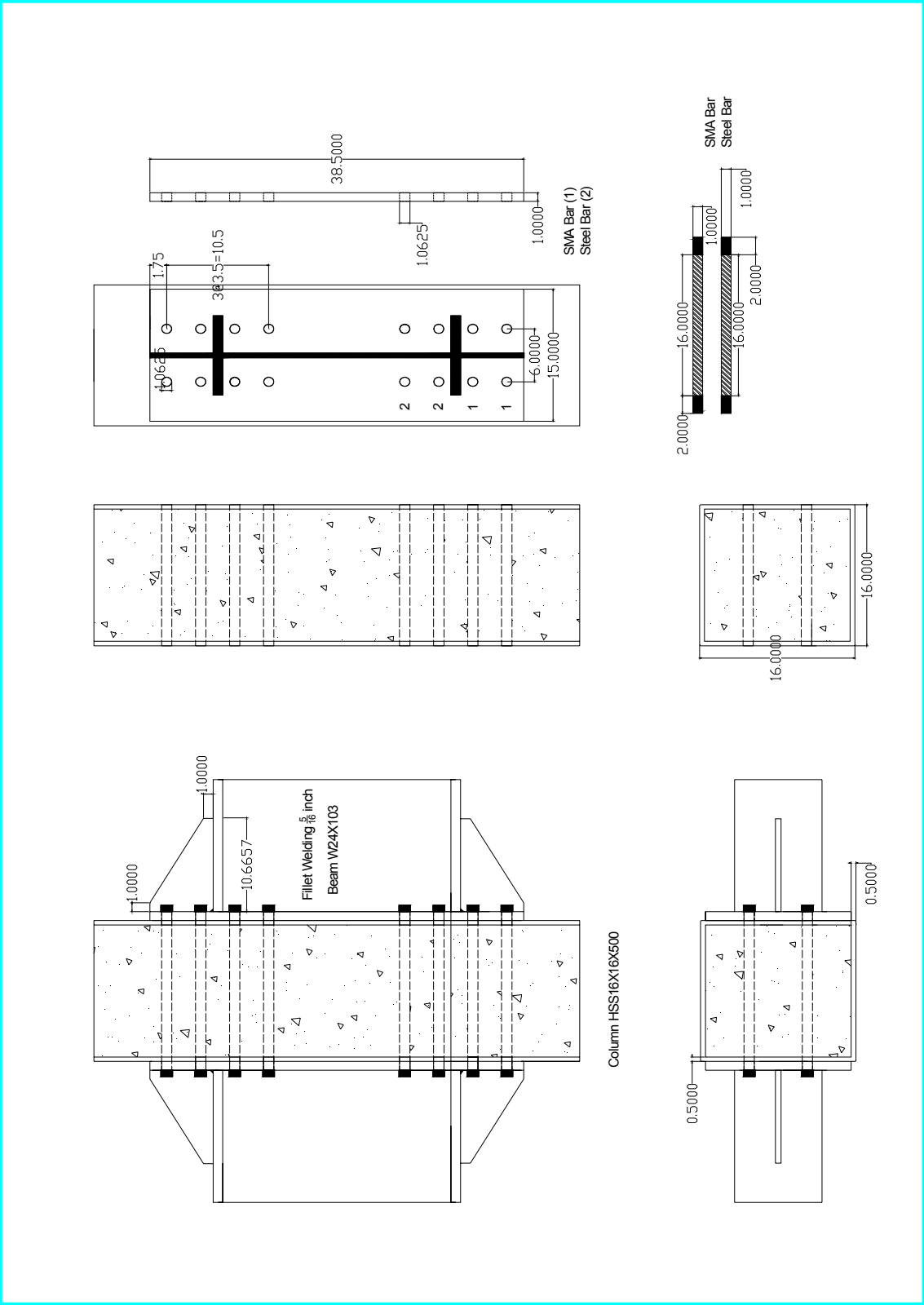


Figure 4.2 Schematic drawing of RCFT end-plate connection details

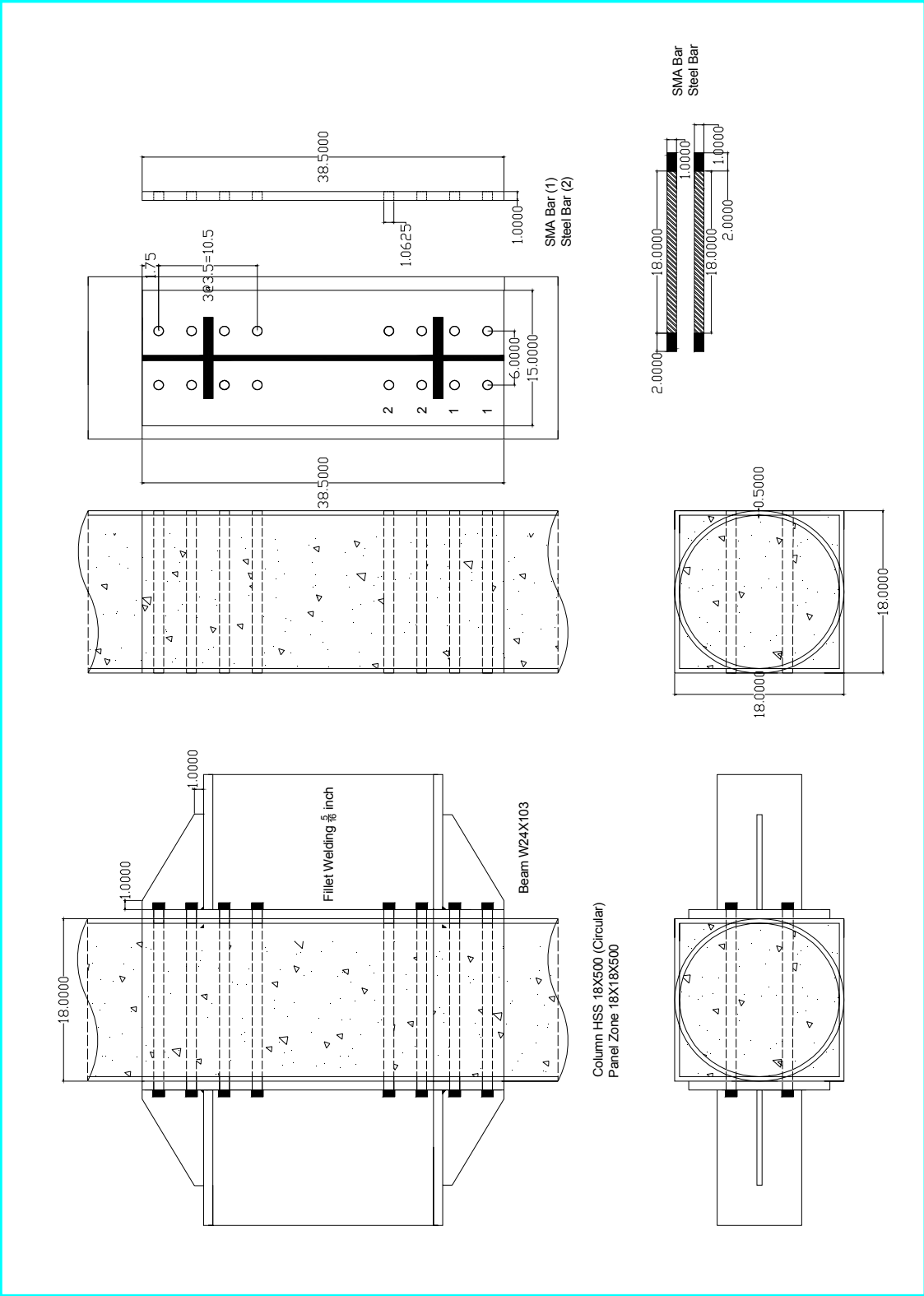


Figure 4.3 Schematic drawing of CCFT end-plate connection details

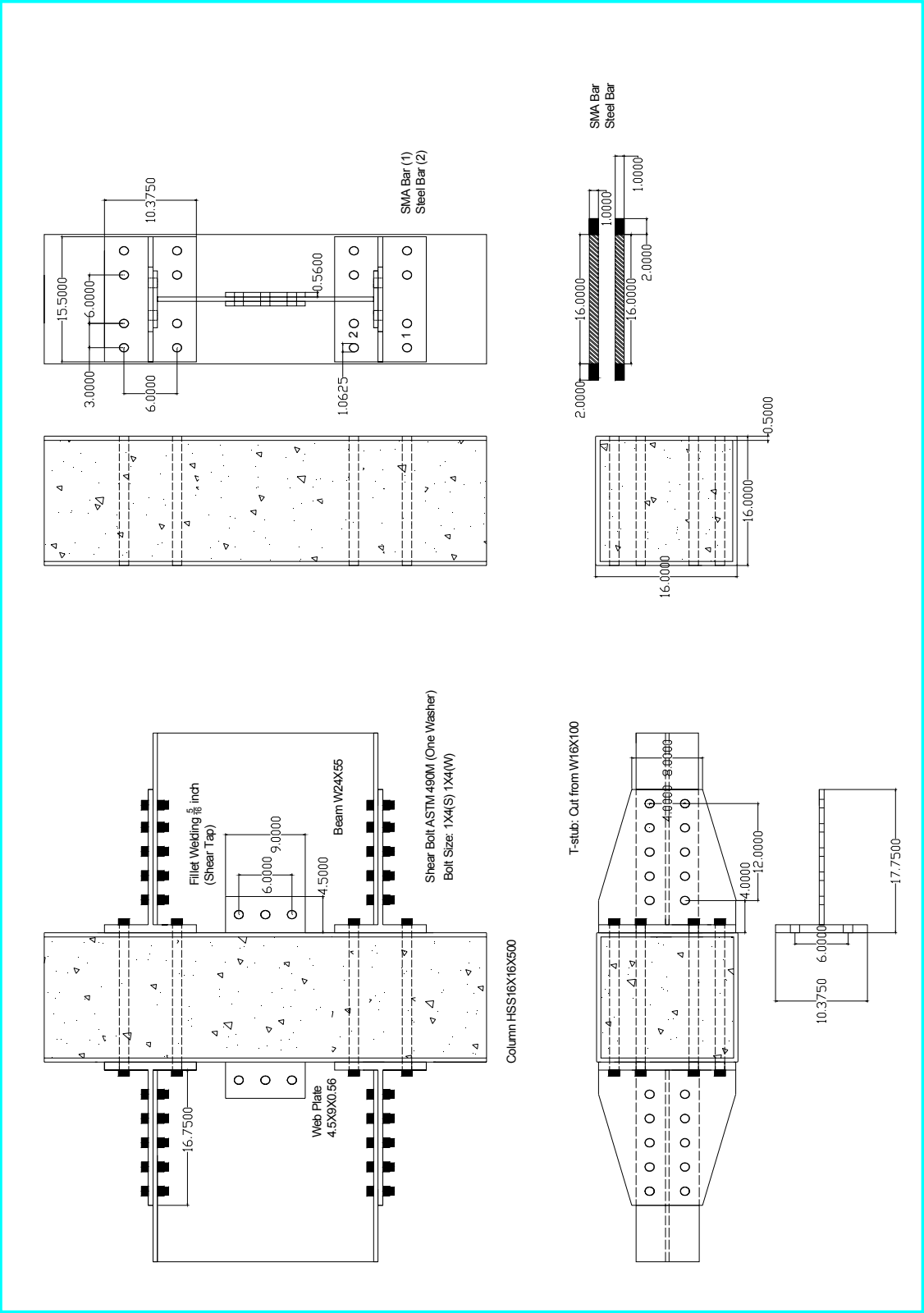


Figure 4.4 Schematic drawing of RCFT T-stub connection details

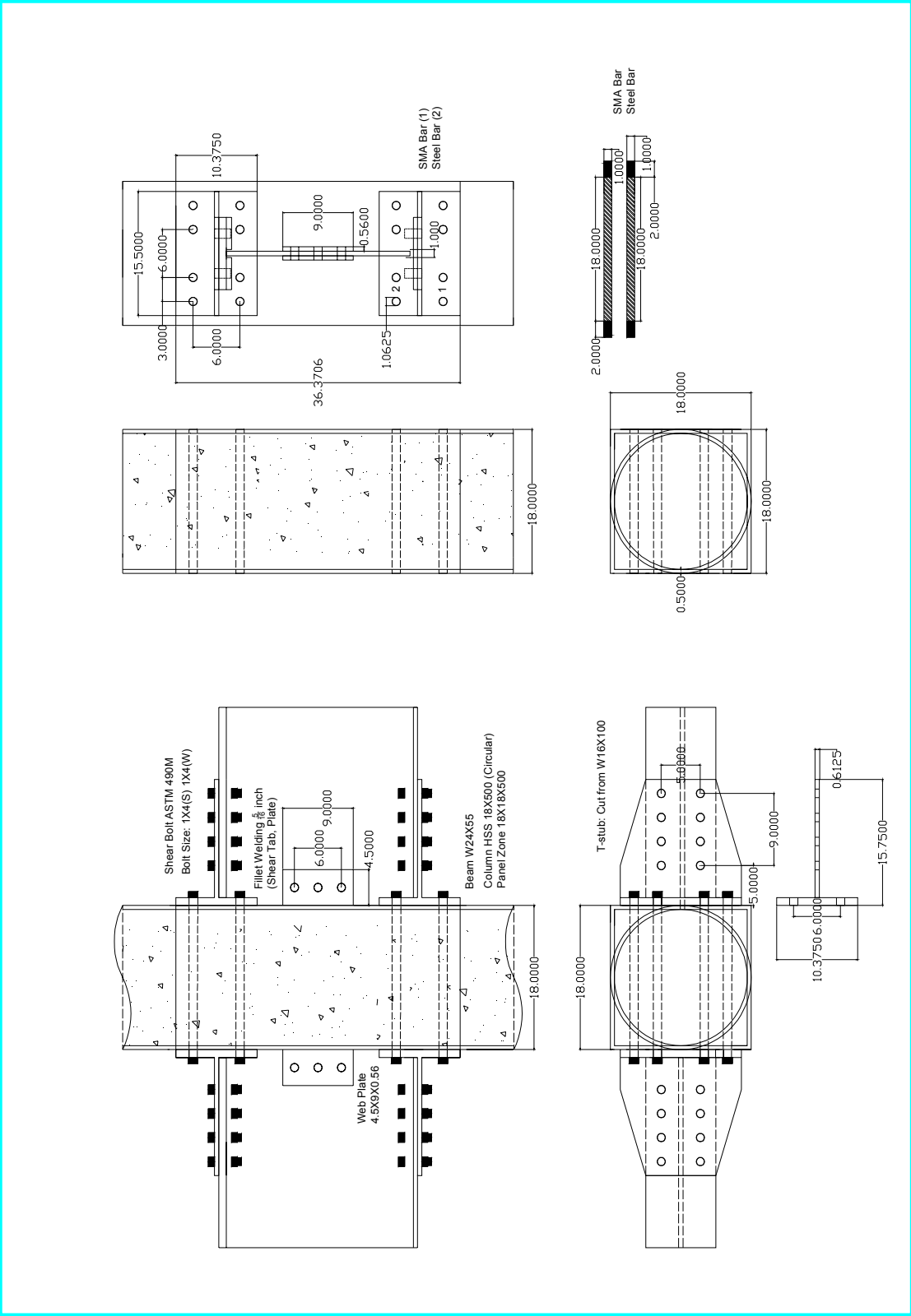


Figure 4.5 Schematic drawing of CCFT T-stub connection details

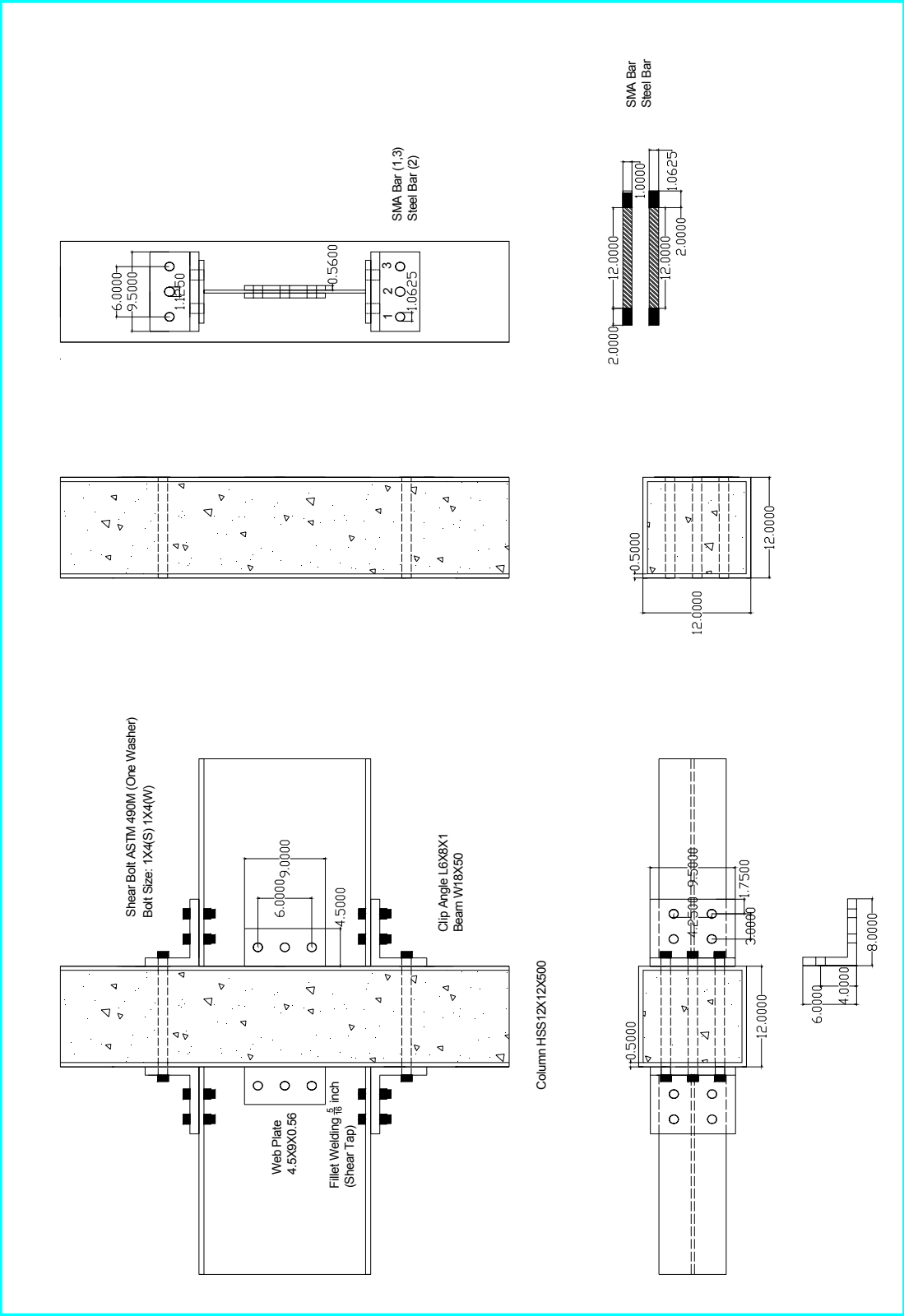


Figure 4.6 Schematic drawing of RCFT clip angle connection details

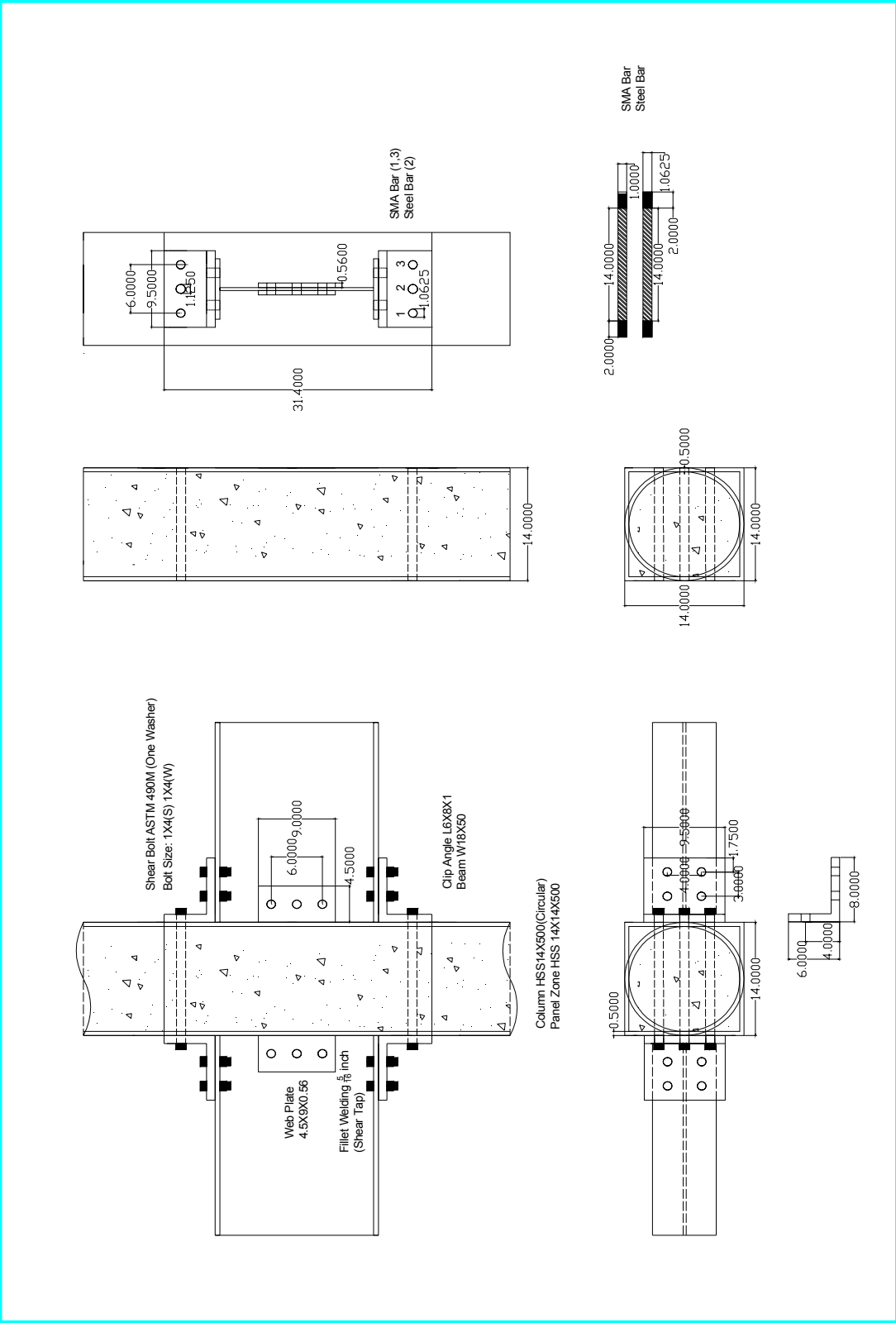


Figure 4.7 Schematic drawing of CCFT clip angle connection details

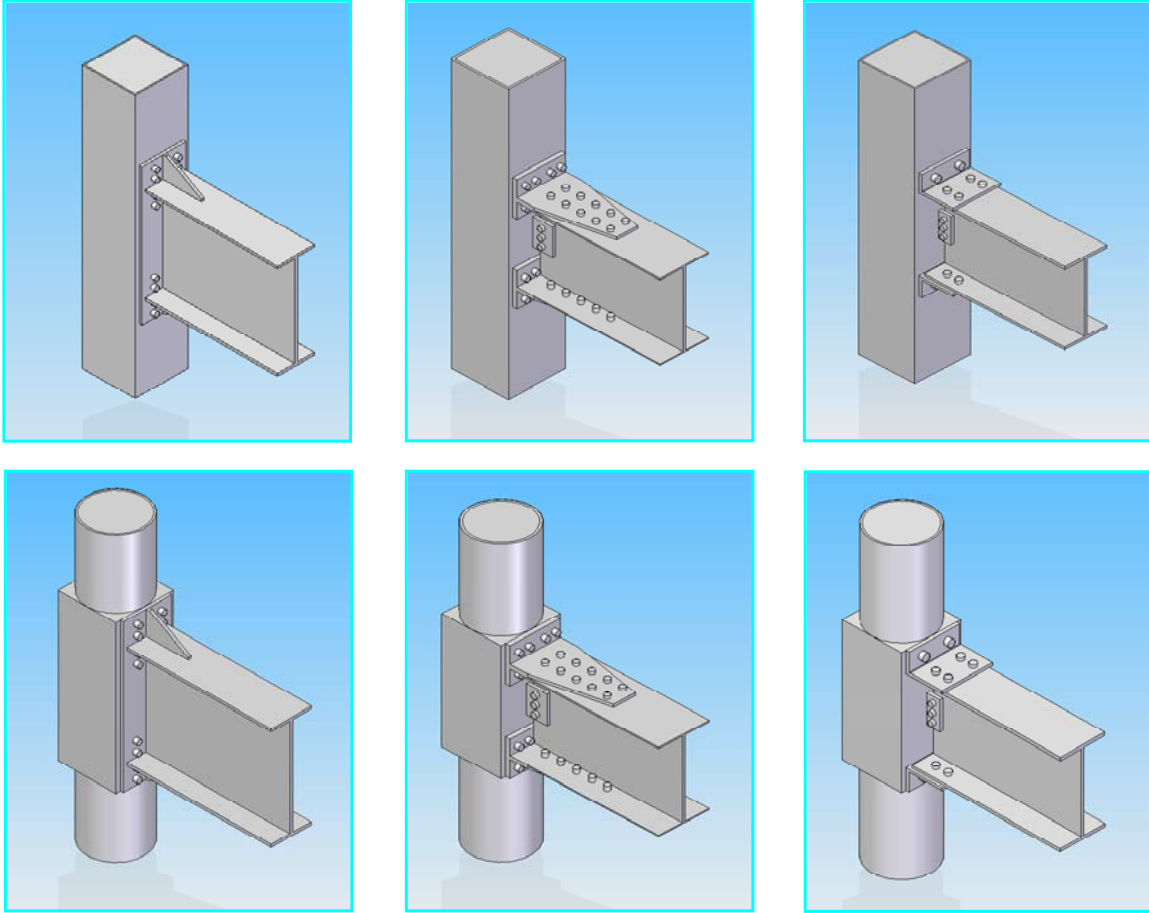


Figure 4.8 3D configurations of SMA PR-CFT connection details

4.3 Failure Modes

All smart PR-CFT connection models were designed to reach yielding on the connection components when the beam produced its probable maximum moment at the plastic hinge (ANSI/AISC 358-05, FEMA 2000). This criterion satisfies a weak beam-strong column design and increases the ductility of the connection. Therefore, no fractures should occur even under the most severe ground motion and yielding of the components should be the dominating behavior mode. The possible yielding and failure modes for smart PR-CFT connections are given in Figure 4.9 and can be categorized as follows:

Ductile Failure Modes:

- Slippage on the shear surface (T-stub and clip angle connections)

- Yielding of the gross area of component members
- Bearing yielding at the around bolt holes
- Plastic yielding of the gross area of the beam

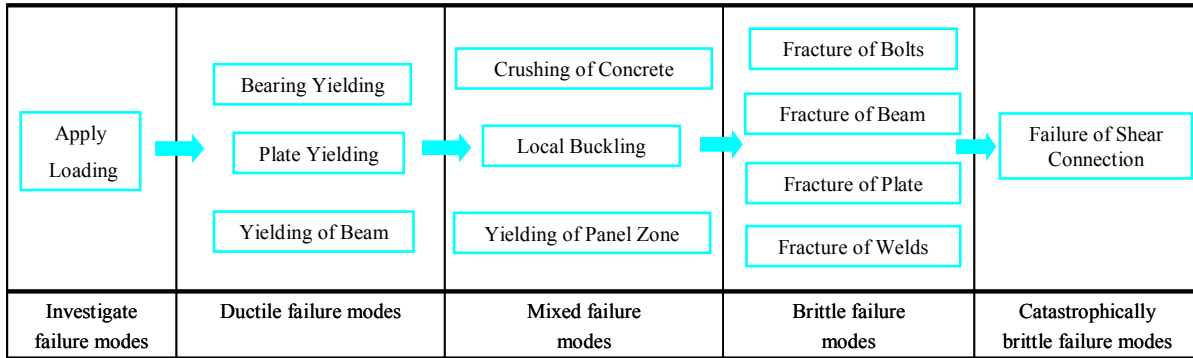
Failure Modes with Limited Ductility:

- Local buckling of component members
- Local buckling of the beam flange
- Shearing yielding of the composite panel zone
- Local buckling of CFT columns including crushing at the inside concrete

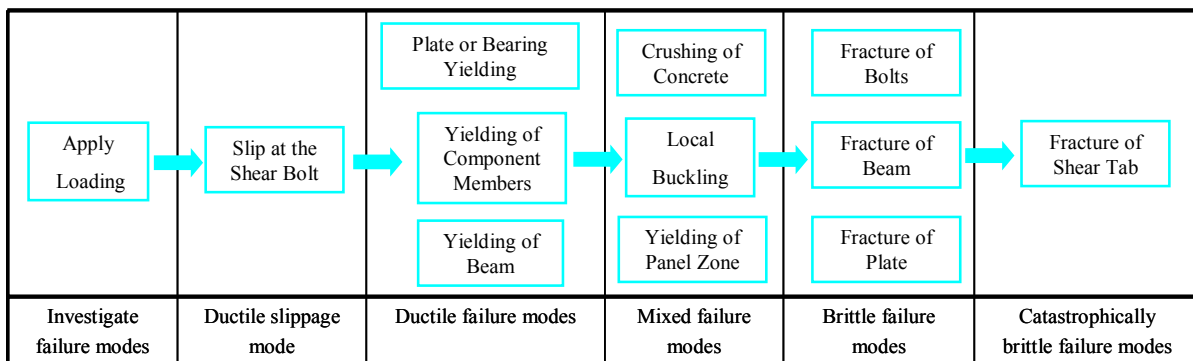
Brittle Failure Modes:

- Fracture of the edge distance or bolt spacing
- Block shear failure of T-stub/clip angle under direct shear force
- Fracture of the net section area of component members
- Block shear failure of the beam flange
- Shear fracture of the shear bolts
- Tension fracture of bars connecting the component member to the CFT column
- Fracture of the welds at the end-plate and plate stiffeners
- Shear fracture of web bolts and a shear tap

Slippage of the shear bolts is the most desirable failure mode while shear fracture of a shear connection is the least desirable failure mode. The smart PR-CFT connection with end-plates does not show slippage because of the lack of the shear surface. The feasible yielding and failure modes for smart PR-CFT connections are listed below in the order of desirability, as suggested by Astaneh-Asl (1995 and 1997). Figure 4.9 (c) shows photos of many failure modes achieved in previous experimental work at GT aimed at establishing the capacity of the different connection components. The state of stress based on Von-Mises failure theory under static loads will be used to determine whether a particular yielding or failure mode has been reached. The results of the numerical studies on these connections are shown in the next chapter.

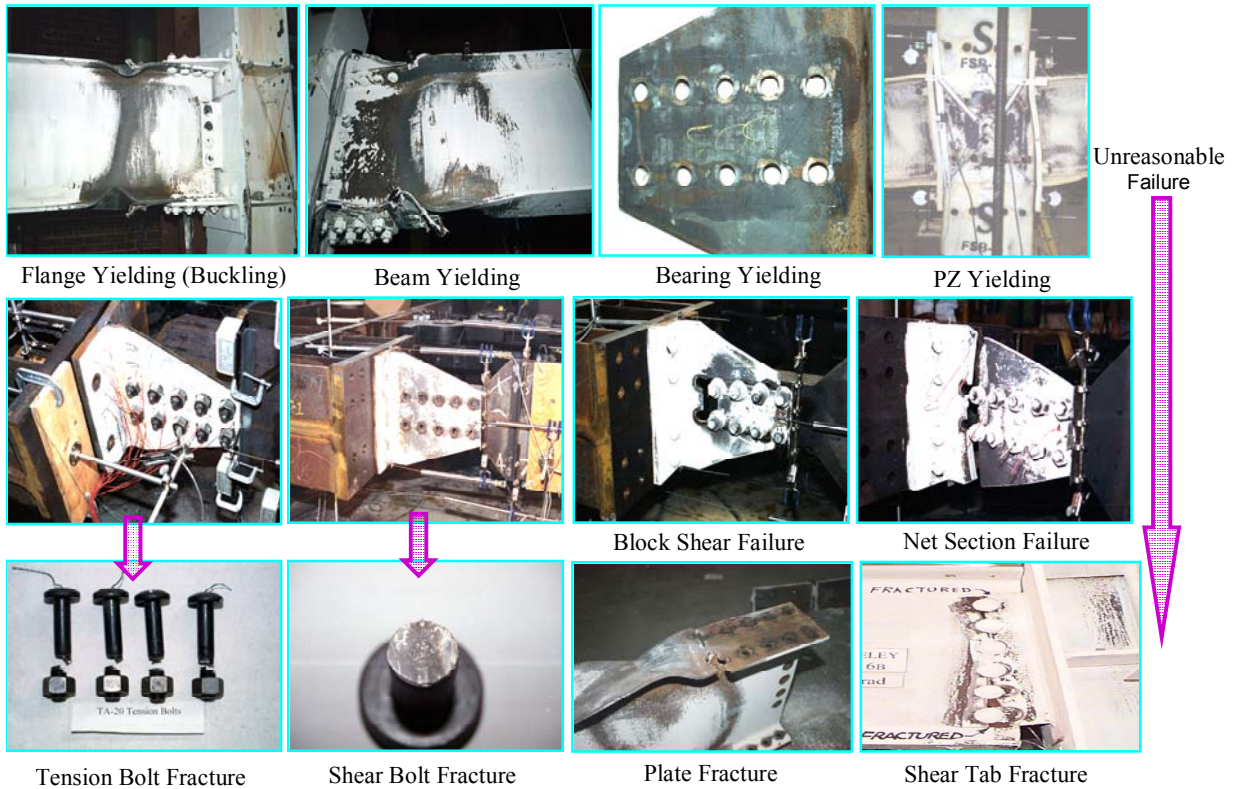


(a) Failure modes for the end-plate connection



(b) Failure modes for the T-stub/clip angle connection

Figure 4.9 Failure modes for SMA PR-CFT connections



(c) Images for the failure modes (Swanson, 2000)

Figure 4.9 Failure modes for SMA PR-CFT connections (Continue)

4.4 Instrumentations

All connection models were discretized such that a variety of measurement points were available to collect data including the displacement, rotations, strains and reactions of the beam-to-column connections. The data from all measurement points was collected using the “Set” function associated with the “History Output” option in ABAQUS 6.6-1. The data was collected and saved automatically for each “Time” (load) step.

The distributions of measurement points for the different connections are shown in Figures 4.10 through 4.12 below. Measurement points collected data from displacement degree of freedoms (DOF U1, U2, and U3) and reaction forces (RF1, RF2, and RF3). The identification of each measurement point is tied the position on each component; for instance, P1 consists of “P” that indicates to “Panel Zone” as shown in each figure.

The total applied force with each displacement increment was transformed into an equivalent axial force in the connection. This axial force corresponds to the bar reaction forces and prying forces shown in Figure 4.13. Based on the force-deformation

mechanism for all connection components, a simple component spring model for each connection model subjected to either monotonic or cyclic loading will be generated (See Chapter 6).

The measurement points for the stress and strain under all time step increments are shown in Figures 4.14 to 4.15.

To summarize, each connection model was “instrumented” so as to identify:

1. the flexural and axial deformations of the important components
2. the overall deformation and relative rotations between the beam and column
3. panel zone deformation
4. response mechanism for all components, and
5. investigation of the failure modes.

Appendix C shows the equations used for the data reduction.

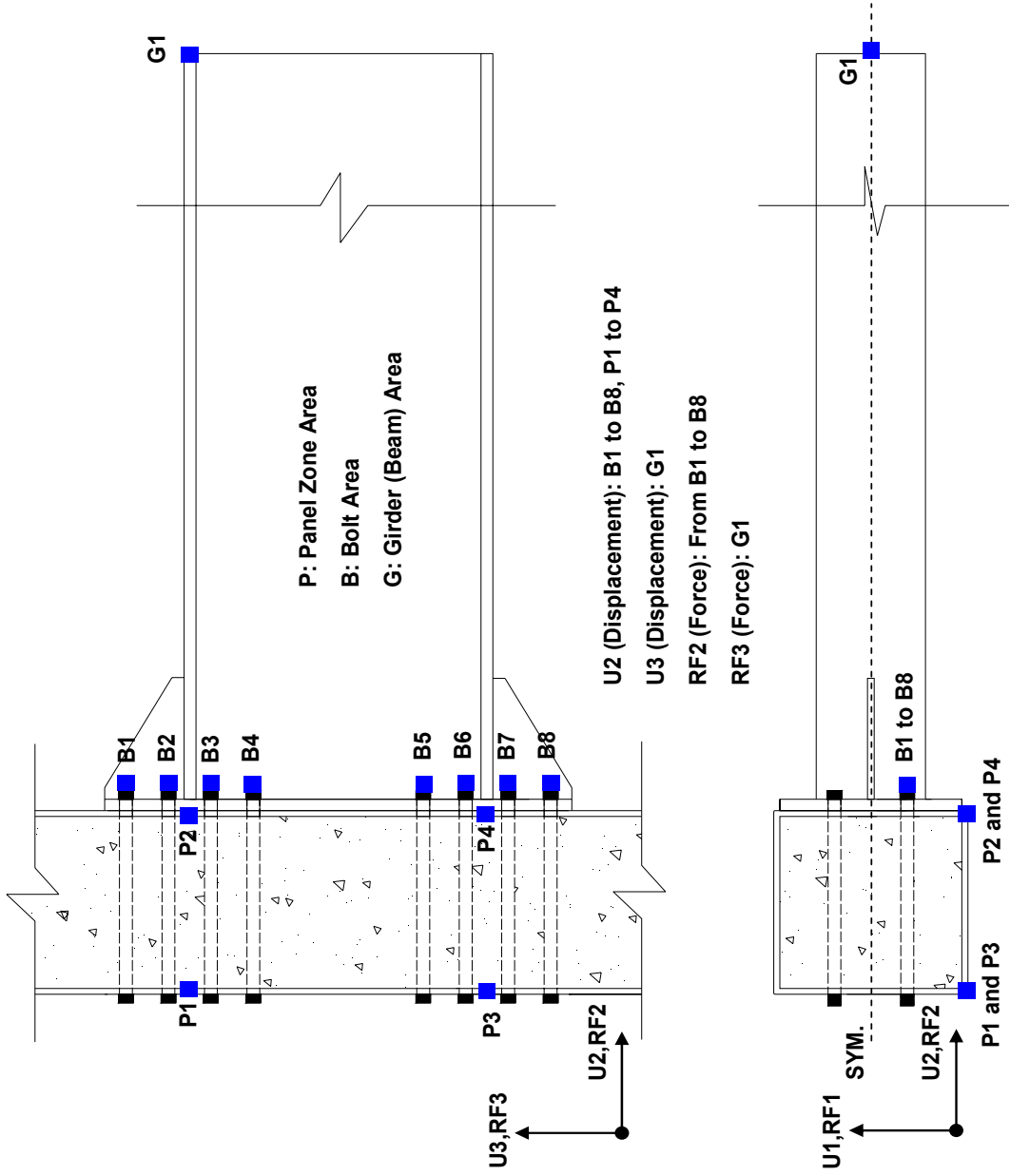


Figure 4.10 Measurement points for the end plate connection (Side and top view)

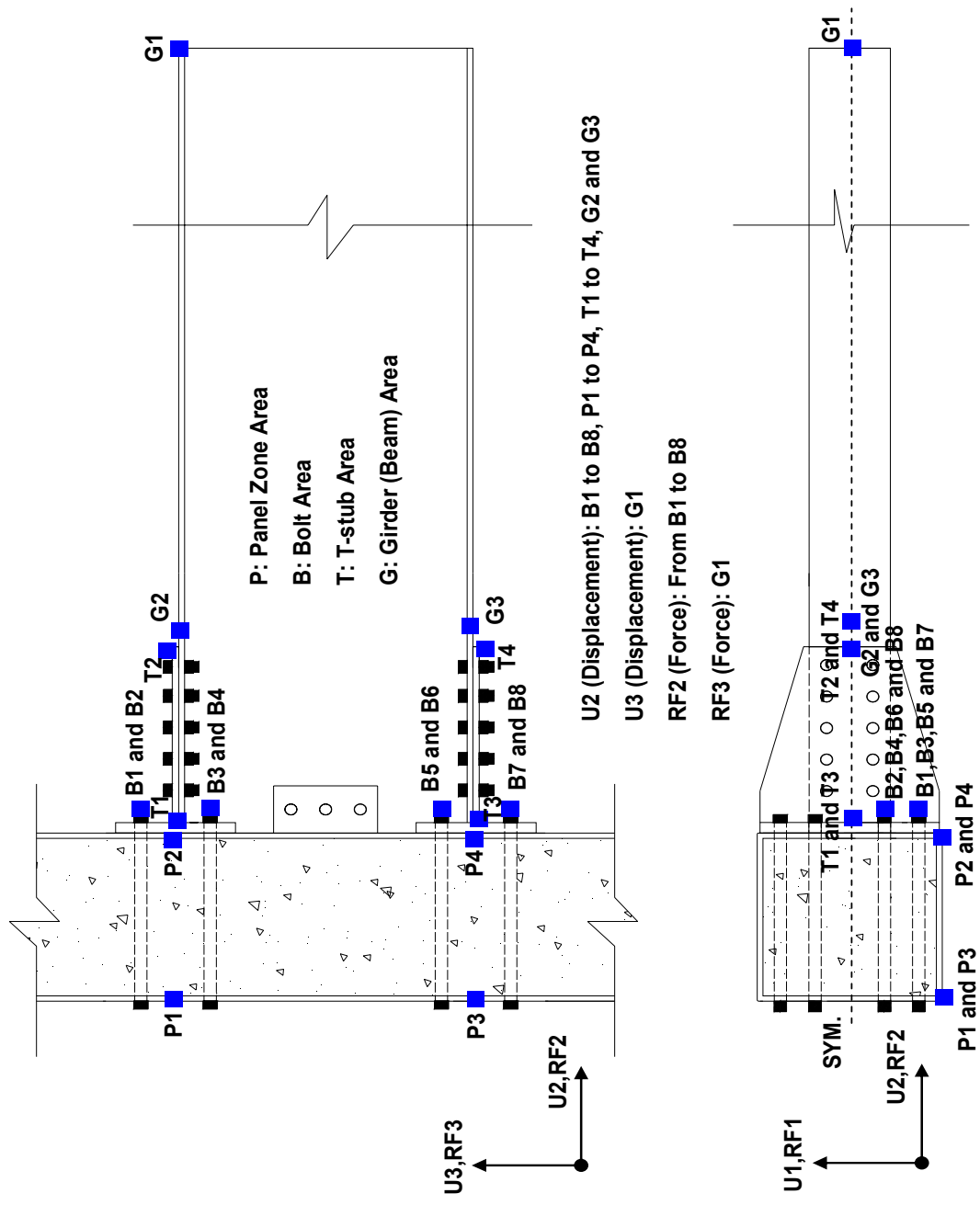


Figure 4.11 Measurement points for the T-stub connection (Side and top view)

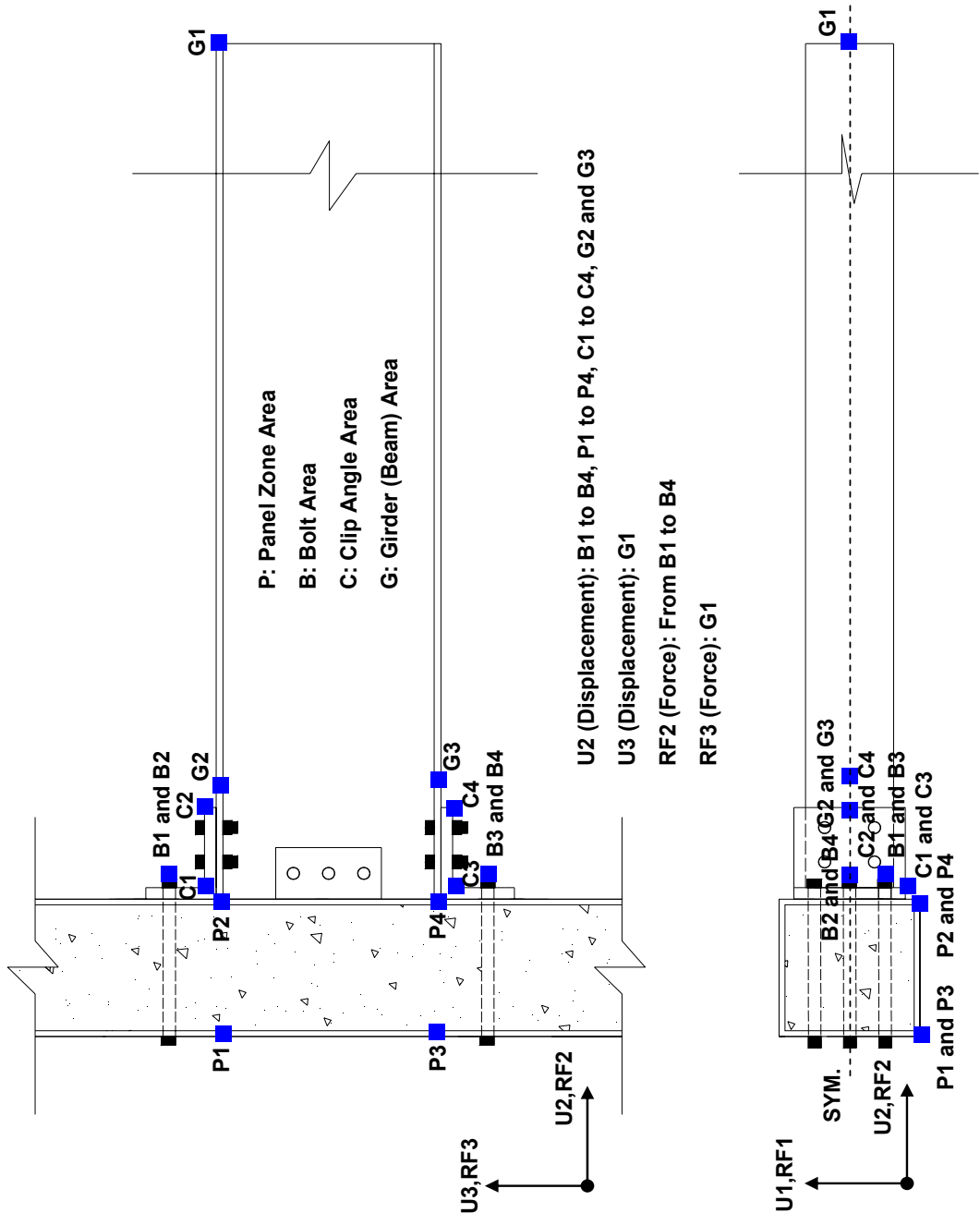


Figure 4.12 Measurement points for the clip angle connection (Side and top view)

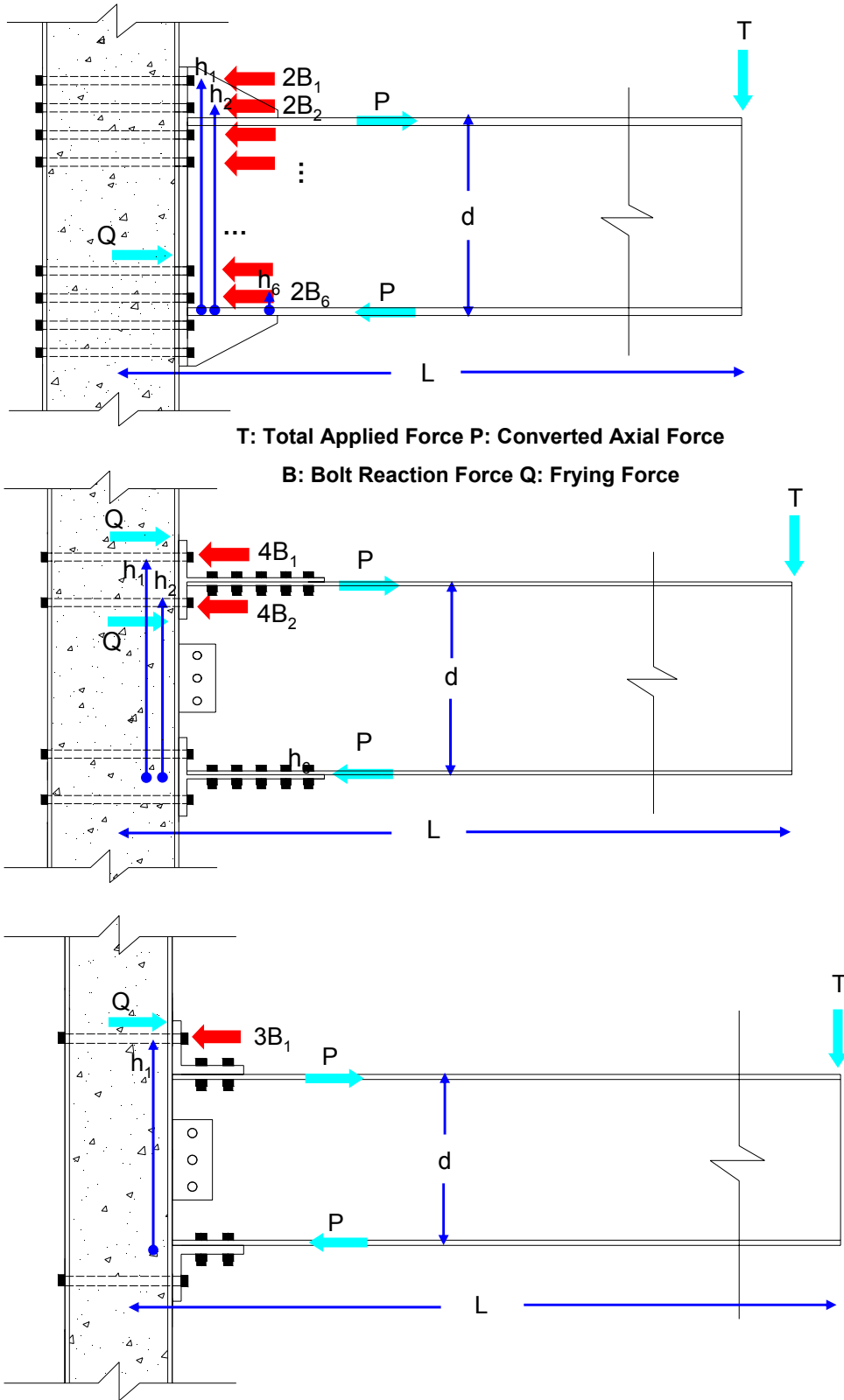


Figure 4.13 Response mechanism for each connection model at ultimate

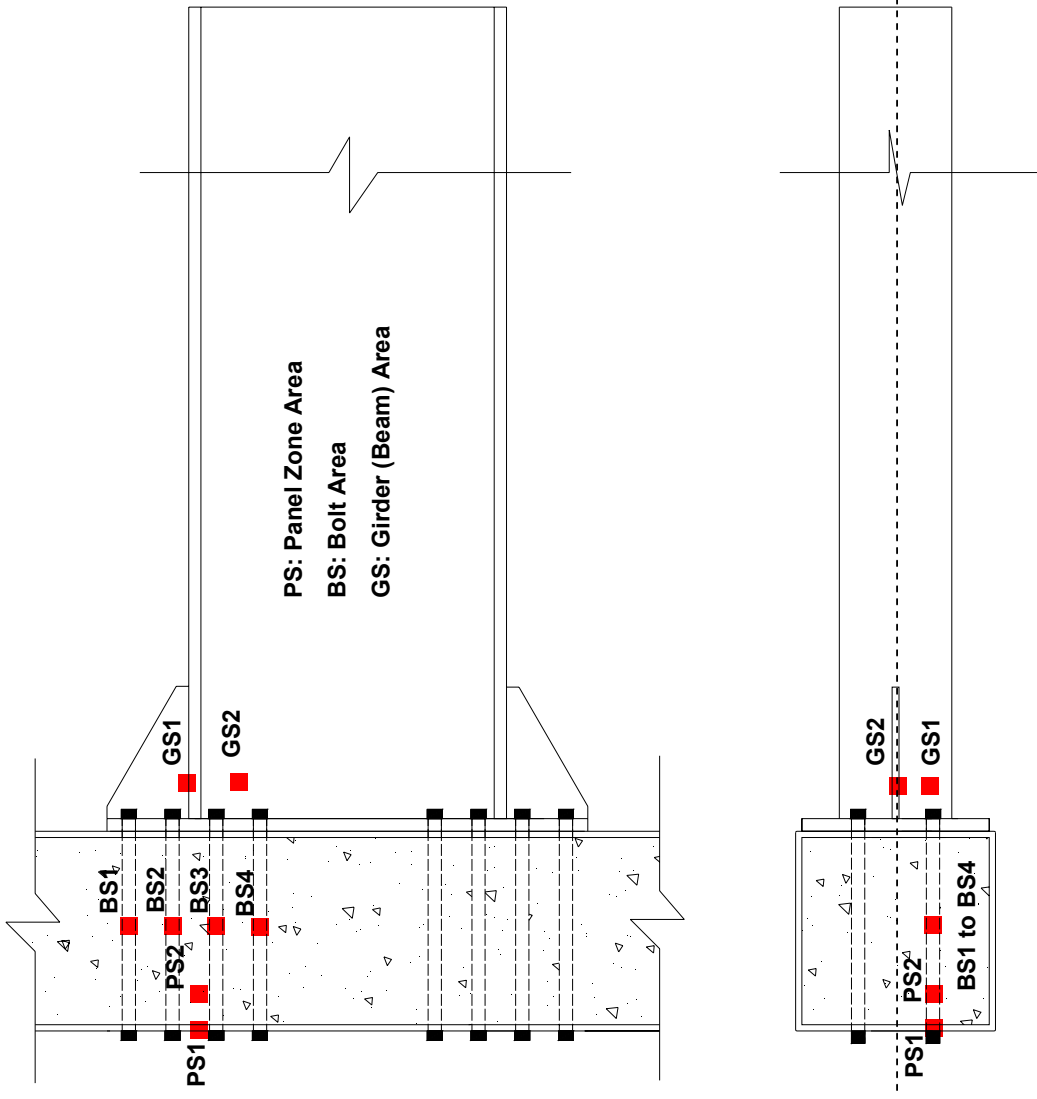


Figure 4.14 Measurement points for the stress and strain for the end plate connection (Side and top view)

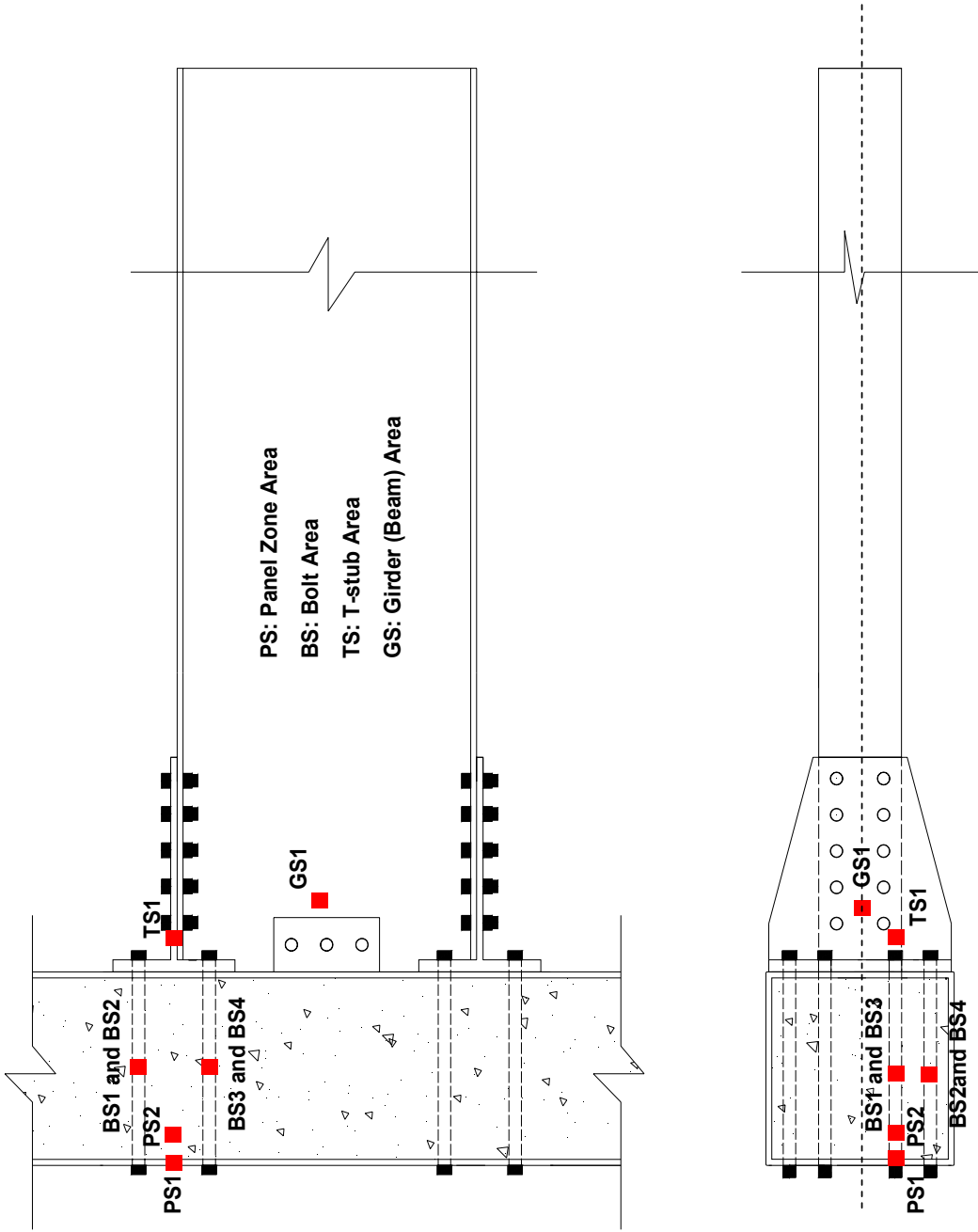


Figure 4.15 Measurement points for the stress and strain for the T-stub connection (Side and top view)

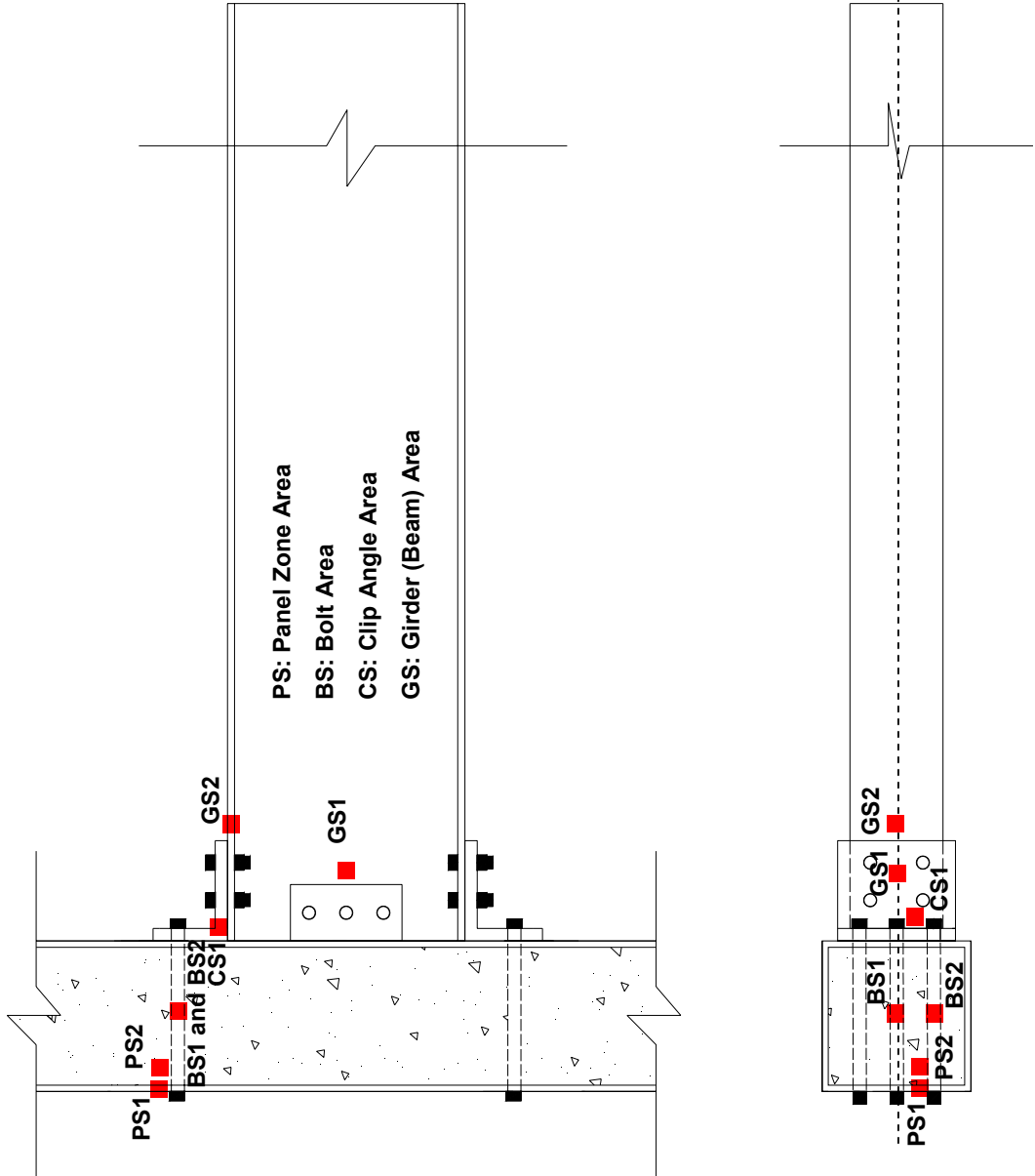


Figure 4.16 Measurement points for the stress and strain for the clip angle connection (Side and top view)

4.5 Summary and Discussion

This chapter discussed the specimen designs for the smart PR-CFT connections. The basic design principles based on achieving the full moment capacity of the beam were introduced in Section 4.1. Structural details related to beam-to-column connection, beam and CFT column designs were provided in Section 4.2. The desirable failure modes (Section 4.3) and instrumentations for the data collection (Section 4.4) were also treated in this chapter. The tests and results of all smart PR-CFT connections using finite element (FE) analyses under static monotonic loading will be presented next (Chapter 5).

Chapter 5

3D Finite Element Modeling

The ABAQUS (ABAQUS *Version* 6.6-1, 2006) finite element code was used to analyze the proposed PR-CFT connections. These numerical models consisted of a combination of elements, springs and constraints conditions. Amongst these were refined 3D solid elements incorporating the full nonlinear material/ geometric properties, contact elements, surface interaction with friction, constraint conditions using equation points, concrete crack conditions and elastic foundation springs. These advanced modeling methods were intended to provide a detailed and accurate understanding of the overall behavior of the connections, including the stress distributions on the contact surfaces in spite of the high computational cost typically associated with this type of data.

This chapter will be structured as follows. First the detail modeling described in the previous paragraph is presented (Section 5.1). The results of the analyses for the FE models, including the stress distribution, final deformation of each component model and comparison of ultimate strength are described next (Section 5.2). Several behavior characteristics under monotonic load are then studied with these models, including the stiffness for all components (Section 5.3). It is then shown that these characteristics have a significant influence on the total behavior of the PR-CFT connections. Failure modes for the PR-CFT connections are then described based on the response of the FE models at different load levels (Section 5.4). The failure strengths obtained by FE model tests are then compared with current design methods. Finally, a summary and discussion about this chapter are presented (Section 5.5). This chapter deals almost exclusively with monotonic behavior.

5.1 3D Solid Modeling Method

FE models for the PR-CFT connections were constructed using the nonlinear FE program ABAQUS 6.6-1. In particular, ABAQUS/CAE was used to generate many of the models. ABAQUS/CAE is a dedicated FE preprocessor that offers powerful and flexible parametric modeling for users familiar with modern computer aided design (CAD)

systems (ABAQUS 2006). In this research, most of the FE work, including the generation of parametric geometries and meshes was done using a version of ABAQUS/CAE incorporating file-based input to provide more advanced modeling options. A typical analysis of a model using a Pentium D 3.00 GHz computer with 1.0 GB of memory required between 12 and 96 hour running time.

5.1.1 Modeling Parts and Elements Adopted

The FE models (i.e. T-stub connections) were subdivided into several independent bodies such as two T-stub members, three web bolts, 10 shear bolt-nuts, one beam, hollow steel column, and interior concrete that interacted with each other via contact definitions (Fig. 5.1). They were modeled as half symmetric models using symmetric boundary conditions (See Section 5.1.5). Shear bolts and nuts were modeled as one body in order to neglect the surface interaction between these two surfaces without slippage. Merging two independent parts made a significant contribution to saving computational cost. The modeling parts of the typical connection with a RCFT column or a CCFT column are shown in Figures 5.1 and 5.2 respectively.

All parts were made up of 3D solid elements. The six basic connection models studied are shown as assemblies of 3D solid elements in Figure 5.3. Close-up views of the corresponding connection areas are shown in Figure 5.4. An exploded view of Figure 5.4-A is shown in Fig. 5.5. In this figure, the meshes for the welded end-plate and stiffeners to the beam were made up of C3D8I elements, 8 node brick elements with the full integration and incompatible modes. These elements provide robust modeling for meshes with elements having large aspect ratios, leading to a considerable reduction in the number of elements and associated computational efficiencies. For all models, beam members also consisted of C3D8I elements. Figure 5.5 shows the component members made up of 3D solid elements. The bolts and bars were made up of C3D6 elements for the inner core and an outer layer of C3D8 elements as shown in Figures 5.5-A and 5.5-B respectively. The two element nodes located on the contact surfaces between the steel column and the interior concrete part had the same initial coordinate positions. Contact interaction with an initial clearance and direction was generated by using a gap element which connects two element nodes. Therefore, the nodal points of all elements located on

the inside steel column surfaces corresponded to those of all elements located on the inside concrete surfaces as shown in Figures 5.5-C and 5.5-D. CCFT columns welded to a rectangular shaped panel zone were modeled using C3D4 elements, a 4 node tetrahedral element. Clip angles and T-stubs were made up of layered C3D8 elements, an 8 node brick element, with the leading edge of the T-stub stem made up of layered C3D6 elements, a 6 node wedge element.

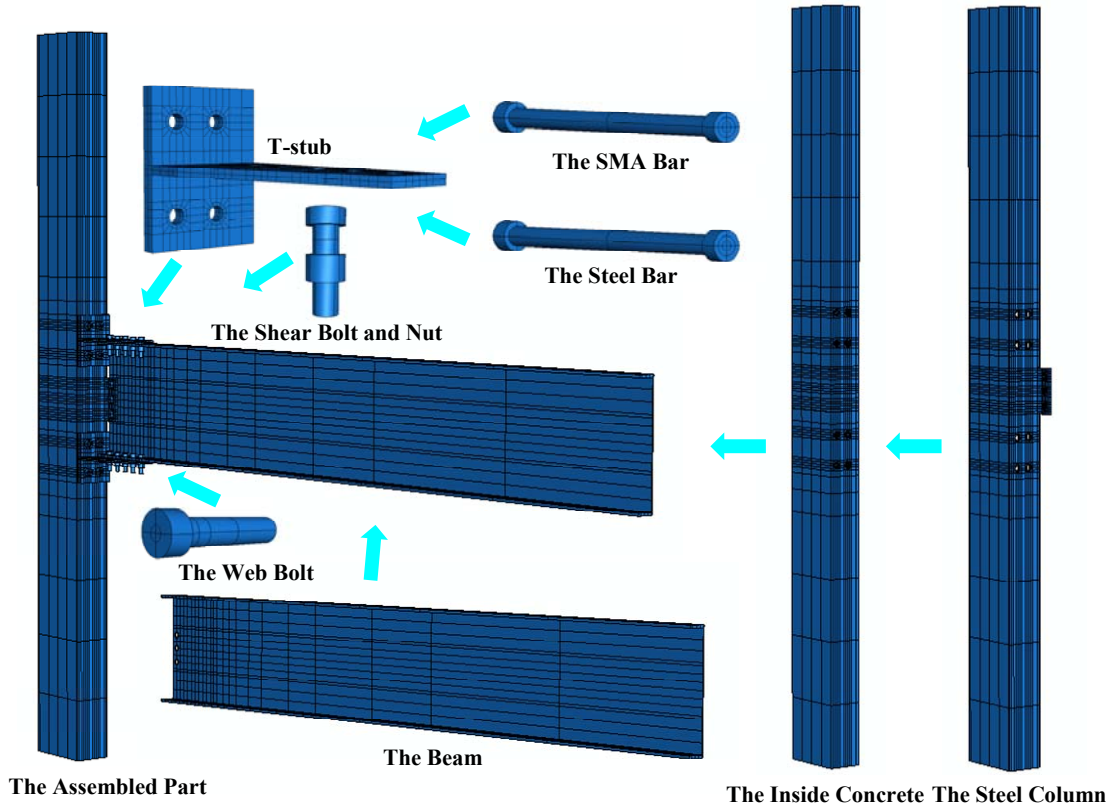


Figure 5.1 Partitioned 3D solid models for the SMA PR-CFT connection (RCFT case)

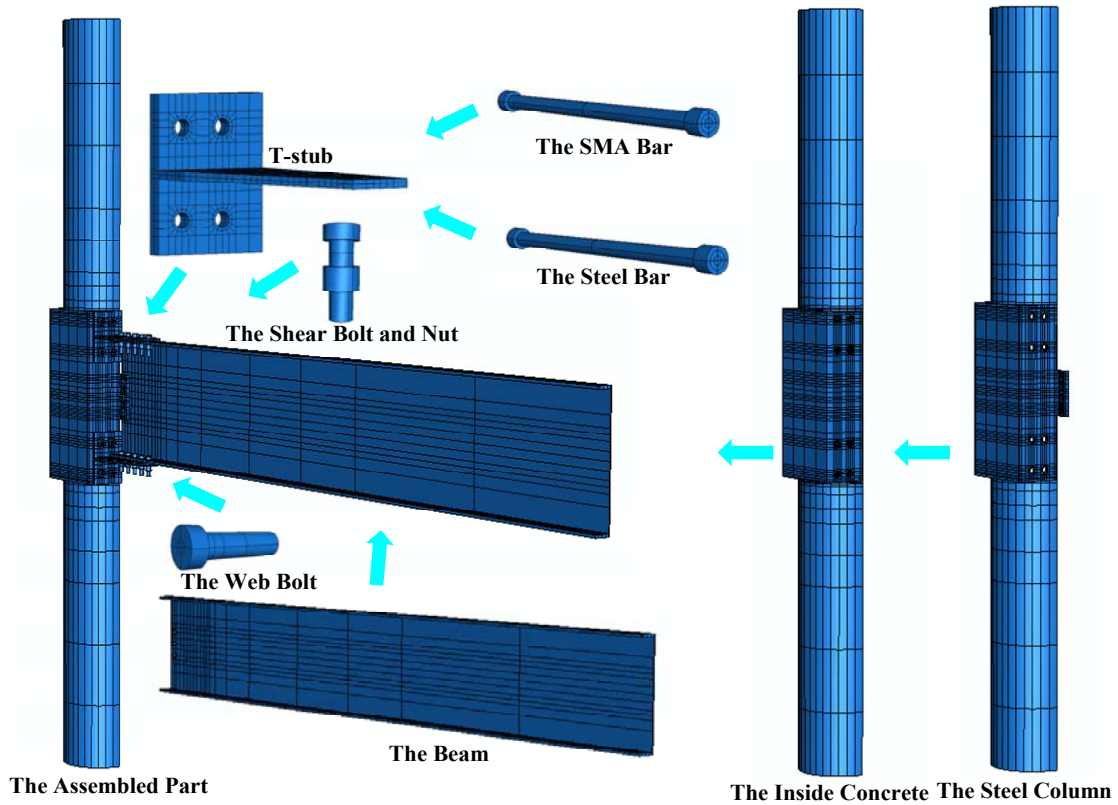


Figure 5.2 Partitioned 3D solid models for the SMA PR-CFT connection (CCFT case)

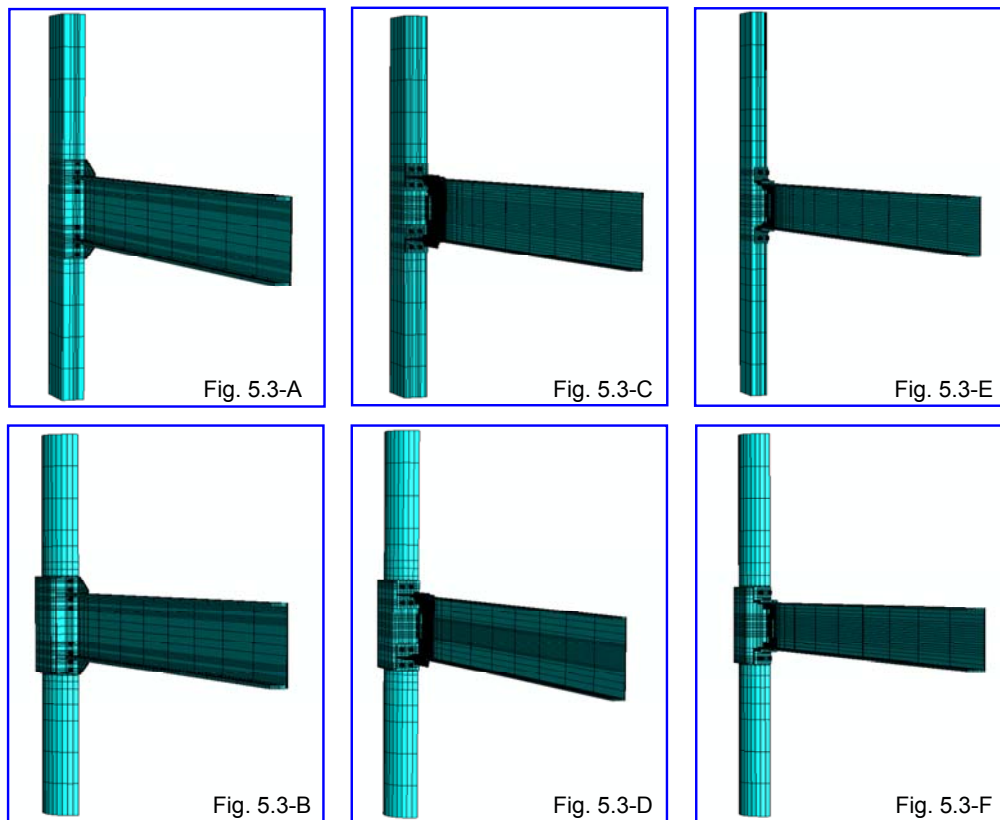


Figure 5.3 3D solid elements for the PR-CFT connections

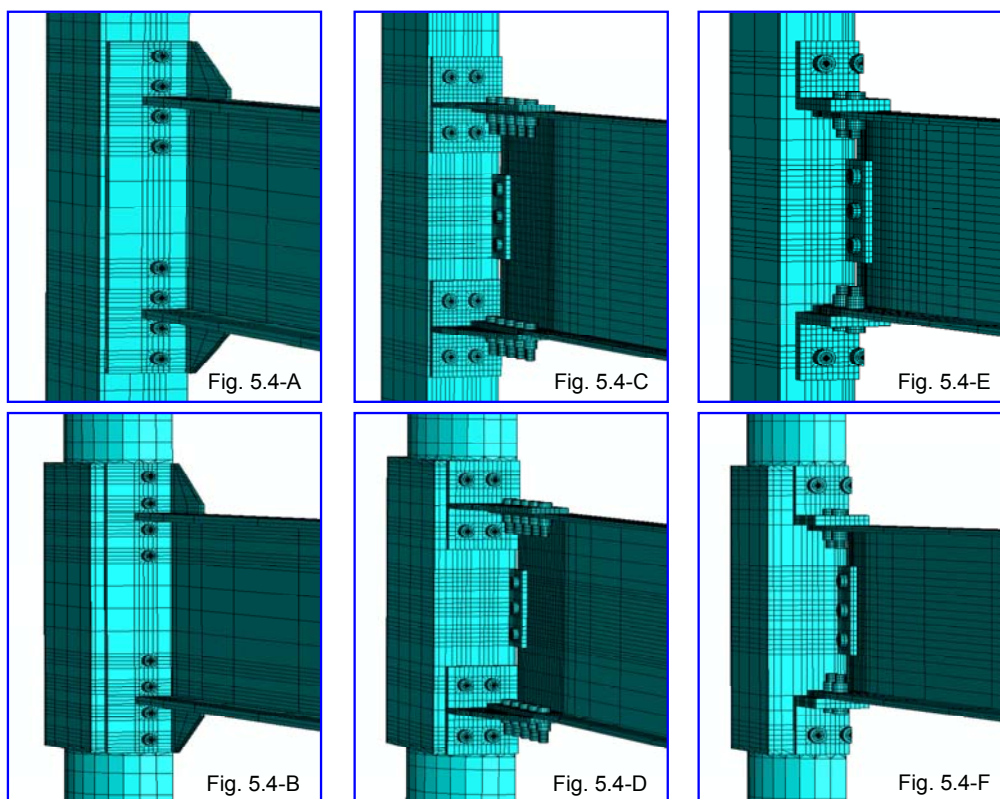


Figure 5.4 3D solid elements for the connection

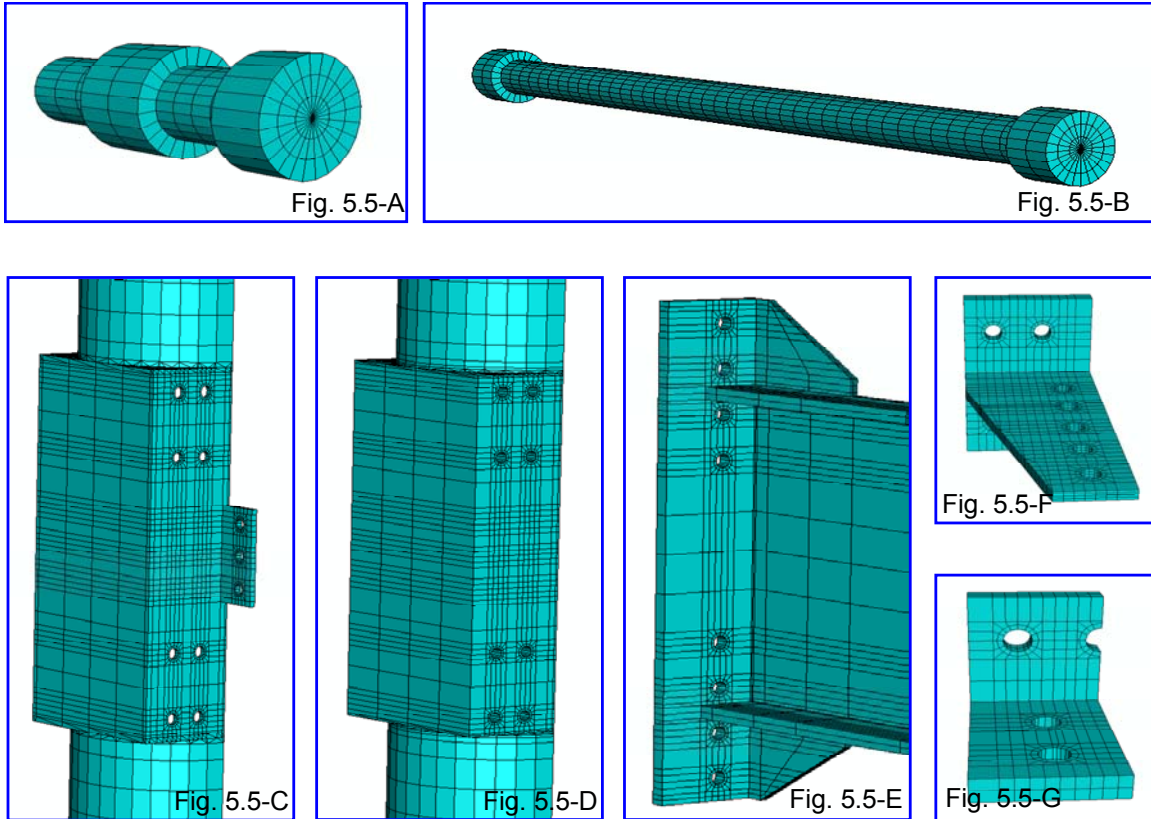


Figure 5.5 3D solid elements for the component members: (A) bolt, (B) bar (C) steel column (D) inside concrete (E) end-plate and steel beam (F) T-stub (G) clip angle

5.1.2 Material Properties

The steel material properties for the component members were modeled after A572-Gr.50 steel with fully nonlinear isotropic characteristics (Figure 5.6 and Table 5.1), while the bolt material properties for the bolts and nuts are modeled after A490 bolt material (Figure 5.7 and Table 5.2). The true stress-logarithmic strain curve from a tensile test was used to specify the plastic part of the isotropic material model for elastic-plastic material model that uses a von Mises yield surface. When defining the plastic material data in ABAQUS, the true stress and true plastic strain should be used as shown in Tables 5.1 and 5.2. The plastic strain is obtained by subtracting the elastic strain, defined as the value of true stress divided by Young's modulus, from the value of total strain (See Figure 5.8).

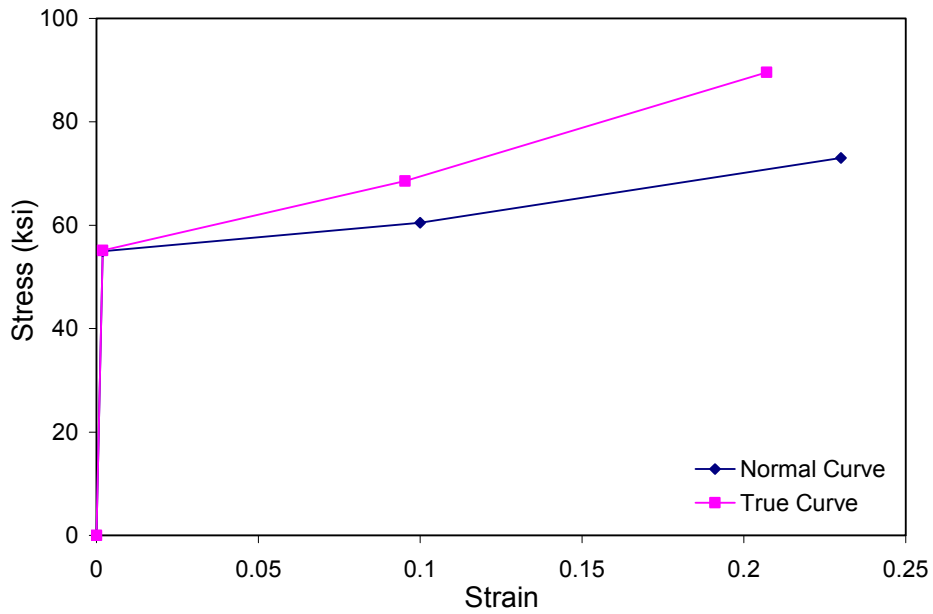


Figure 5.6 Tensile stress-strain curves for A572-Gr. 50 Steel

Table 5.1 ABAQUS Input value for A572-Gr.50 Steel

ABAQUS Input Value

True Stress	True Plastic Strain
55.1 ksi	0
66.55 ksi	0.09302
89.59 ksi	0.204

Nominal Stress Value for Design

Carbon Steel (A572-Gr.50)	Fy	Fu
E=29000 ksi	55 ksi	73 ksi

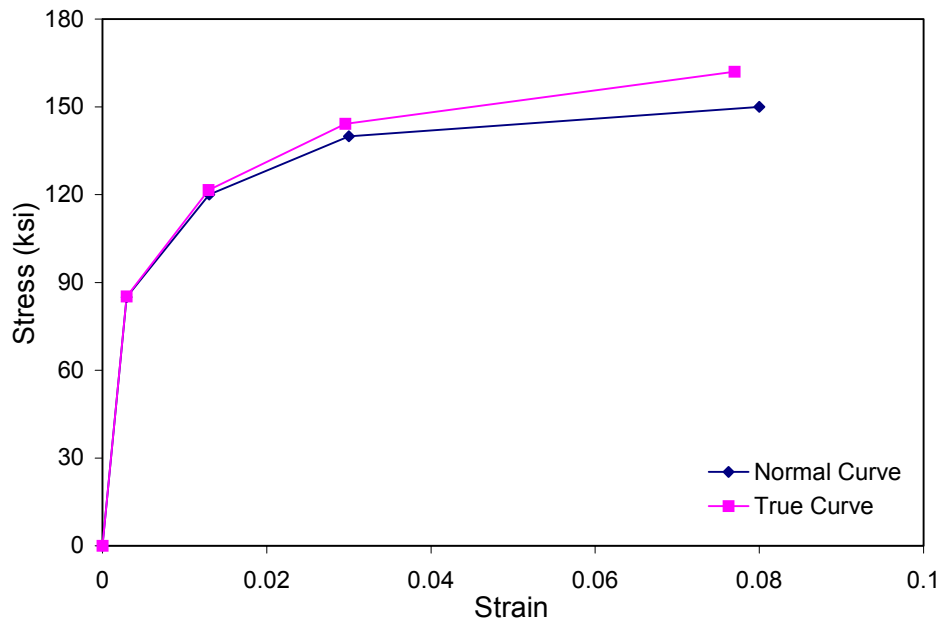


Figure 5.7 Tensile stress-strain curves for A490 bolts

Table 5.2 ABAQUS Input value for A490 bolt
ABAQUS Input Value

True Stress	True Plastic Strain
85.25	0
121.56	0.00872
144.2	0.02459
162	0.07137

Nominal Stress Value for Design

High Strength Bolt (A490)	Fy	Fu
E=29000 ksi	85	150

The constitutive models for confined concrete contain different stress-strain curves for tension and compression response. These models incorporated a damaged concrete plasticity option, one of the material managers available in ABAQUS (ABAQUS 2006). The concrete damaged plasticity model in ABAQUS takes advantage of concepts of isotropic damaged elasticity in combination with isotropic tensile and compressive plasticity to represent the inelastic behavior of concrete. It assumes that the main two failure mechanisms are tensile cracking and compressive crushing of the concrete material. This material model also provides a general capability for other quasi-brittle materials in all types of structures. It can be defined to be sensitive to the rate of straining. Therefore, a small time increment should be used in order to improve the convergence rate after the peak strength of the material property (ABAQUS 2006). The resulting typical stress-strain curves for the concrete material and the formulas involved with confined concrete are shown in Figure 5.9 and Table 5.3.

In this research, an equivalent uniaxial constitutive model for concrete in tension suggested by Torres (Torres et al. 2004) was used. It is simple and easy to implement. In Figure 5.9, f_{ct} and ε_{ct} indicate the mean values of the tensile strength and strain respectively. The slope of the loading is E_c . This model depends only on the dimensionless coefficient α_2 . This coefficient ranges from 1 to infinity.

The material model for confined concrete subjected to an axial compressive force suggested by Hu (Hu et al. 2005) was also used. When concrete is subjected to laterally confining pressure due to the steel tube, the uniaxial compressive strength (f'_{cc}) and the corresponding strain (ε'_{cc}) are much higher than those of unconfined concrete as shown in Figure 5.9. The theoretical equations proposed by Hu et al. are summarized in Table 5.3. The lateral confining effect pressure (f_l) and the material degradation parameter (k_3) are affected by the shape of the CFT column section (RCFT or CCFT) and the axial load ratio (F/F_u). Therefore, the axial load ratio (F/F_u) and the shape of the CFT columns are significant parameters to determine the material constitutive models. For instance, the lateral confining pressure generally increases with increasing axial load ratio and with a decrease of the material degradation parameter. Material examples for RCFT and CCFT with $F/F_u = 0.2$ used in this research are illustrated in Figures 5.10 and 5.11 respectively.

Table 5.4 and Table 5.5 indicate the material input codes of the concrete damage plasticity for ABAQUS.

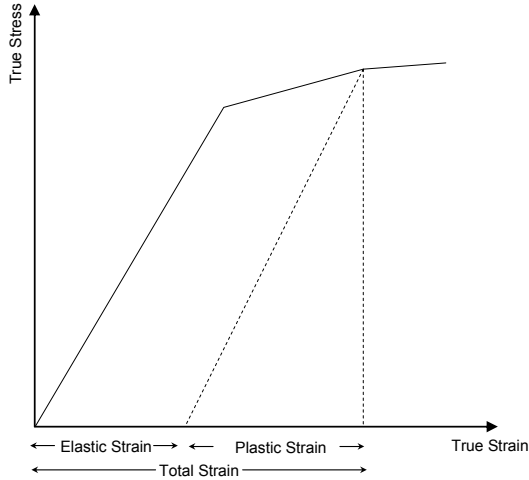


Figure 5.8 Decomposition of the total strain into elastic and plastic strain

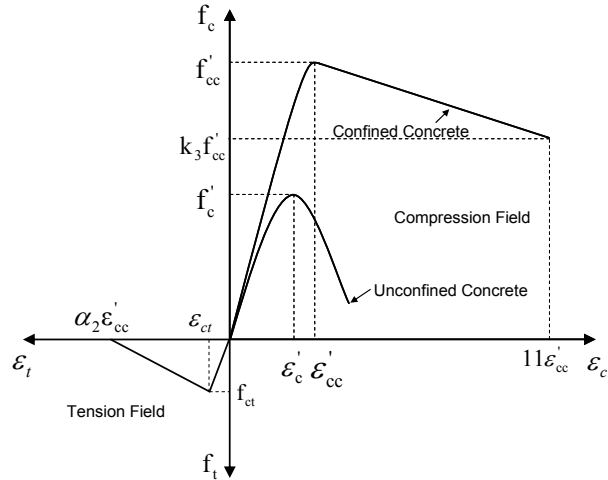


Figure 5.9 Equivalent stress-strain curve for concrete (Hu et al. 2005 and Torres et al.2004)

Table 5.3 Summary of material constitutive models for confined concrete (Refer to Notation and Figure 5.9)

Limit	Stress and Strain for Confined Concrete under Compression	
$\epsilon_c \leq \epsilon'_{cc}$	Value: Unconfined Concrete Property f'_c and ϵ'_c $k_1 = 4.1 \quad k_2 = 20.5$ $f'_{cc} = f'_c + k_1 f_t \quad \epsilon'_{cc} = \epsilon'_c \left(1 + k_2 \frac{f_t}{f'_c} \right)$ $R_\sigma = 4 \quad R_\epsilon = 4$ $E_c = 57000 \sqrt{f'_{cc}} \text{ (psi)}$ $R_E = \frac{E_c \epsilon'_c}{f'_c} \quad R = \frac{R_E (R_\sigma - 1)}{(R_\sigma - 1)^2} - \frac{1}{R_\sigma}$	$f'_c = \frac{E_c \epsilon_c}{1 + (R + R_E - 2) \left(\frac{\epsilon_c}{\epsilon'_{cc}} \right) - (2R - 1) \left(\frac{\epsilon_c}{\epsilon'_{cc}} \right)^2 + R \left(\frac{\epsilon_c}{\epsilon'_{cc}} \right)^3}$
$\epsilon_c > \epsilon'_{cc}$	Rectangular Shape $0 \leq F/F_u \leq 0.23$ $f_t/f_y = 0 \quad k_3 = 1 - 0.304(F/F_u)$ $0.23 \leq F/F_u \leq 0.56$ $f_t/f_y = -0.00859 + 0.0373(F/F_u) \quad k_3 = 1 - 0.304(F/F_u)$ $0.56 \leq F/F_u \leq 0.74$ $f_t/f_y = 0.014 + 0.00333(F/F_u) \quad k_3 = 0.55$	Circular Shape $0 \leq F/F_u \leq 0.34 \quad f_t/f_y = 0$ $0 \leq F/F_u \leq 0.45 \quad k_3 = 0.87 - 0.889(F/F_u)$ $0.34 \leq F/F_u \leq 0.57 \quad f_t/f_y = -0.00517 + 0.0152(F/F_u)$ $0.45 \leq F/F_u \leq 0.57 \quad k_3 = 0.508 - 0.083(F/F_u)$
Limit	Stress and Strain for Confined Concrete under Tension	
$\epsilon_t \leq \epsilon_{ct}$	$f_t = E_c \epsilon_t \quad f_{ct} = 7.5 \sqrt{f'_{cc}}$	
$\epsilon_t > \epsilon_{ct}$	$\alpha_2 \epsilon'_{cc} = 5.5 \epsilon'_{cc}$	

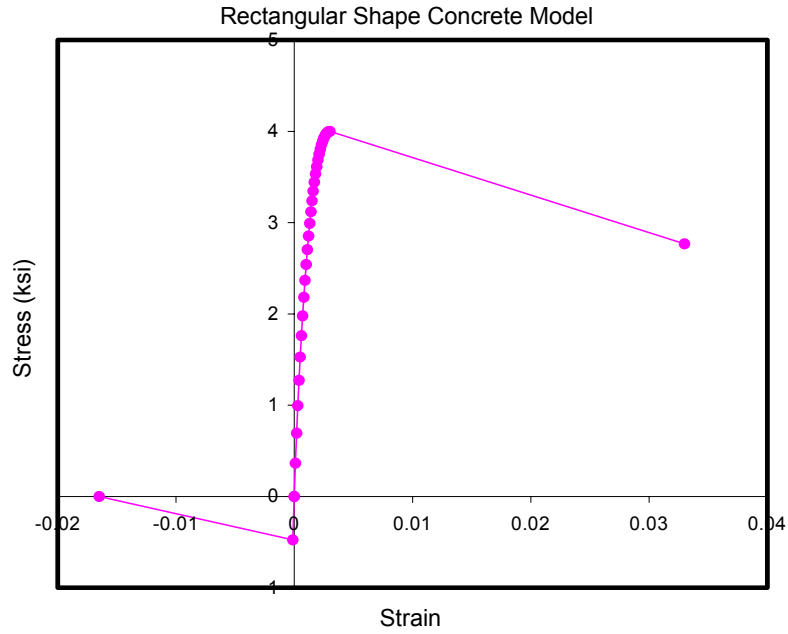


Figure 5.10 Stress-strain curve for confined concrete (RCFT)

Table 5.4 ABAQUS input values for concrete properties

Plastic Stress	Plastic Strain	Compression Damage
2.18 ksi	0.000000	0
2.54 ksi	0.000067	0.01
2.99 ksi	0.000203	0.02
3.54 ksi	0.000504	0.05
3.81 ksi	0.000804	0.1
3.93 ksi	0.001060	0.15
4.00 ksi	0.001533	0.2
3.38 ksi	0.016759	0.5
2.77 ksi	0.031985	0.9

Plastic Stress	Plastic Strain	Tension Damage
0.474 ksi	0	0
0.242 ksi	0.008312	0.5
0.010 ksi	0.016500	0.9

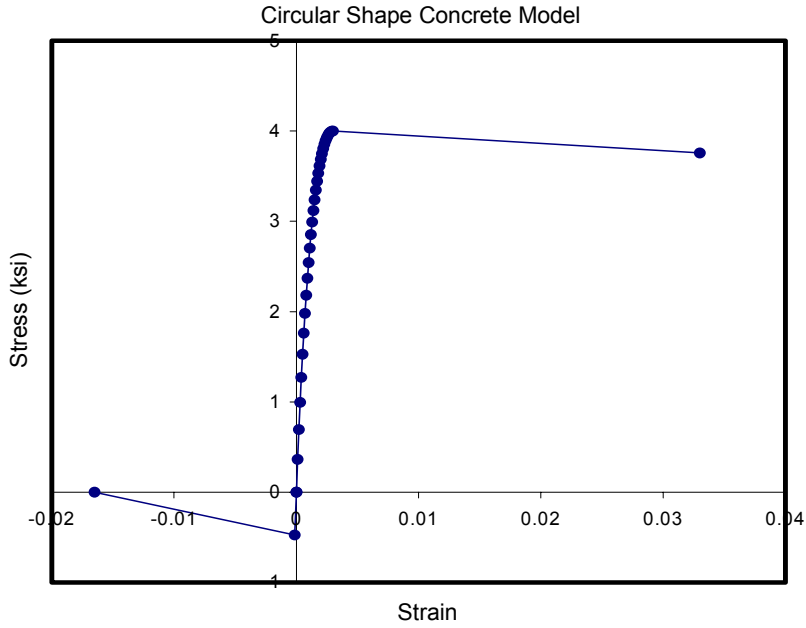


Figure 5.11 Stress strain curve for confined concrete (CCFT)

Table 5.5 ABAQUS input values for concrete properties

Plastic Stress	Plastic Strain	Compression Damage
2.18 ksi	0.000000	0
2.54 ksi	0.000067	0.01
2.99 ksi	0.000203	0.02
3.53 ksi	0.000504	0.05
3.81 ksi	0.000804	0.1
3.93 ksi	0.001060	0.15
4.00 ksi	0.001533	0.2
3.88 ksi	0.016578	0.5
3.76 ksi	0.031622	0.9

Plastic Stress	Plastic Strain	Tension Damage
0.474 ksi	0	0
0.242 ksi	0.008311856	0.5
0.010 ksi	0.0165	0.9

The last set of material properties, those for the SMA bars, was generated from the material properties of super-elastic Nitinol specimens (DesRoches et al. 2004,

McCormick 2006). Figure 5.12 shows a representative stress-strain curve for a 1 inch diameter SMA bar. These quasi-static tensile tests performed on Nitinol specimens provided the required information with respect to deformation under unequal cyclic loading. The complex non-linear behavior shown by SMA materials was idealized as a multi-linear stress-strain in ABAQUS.

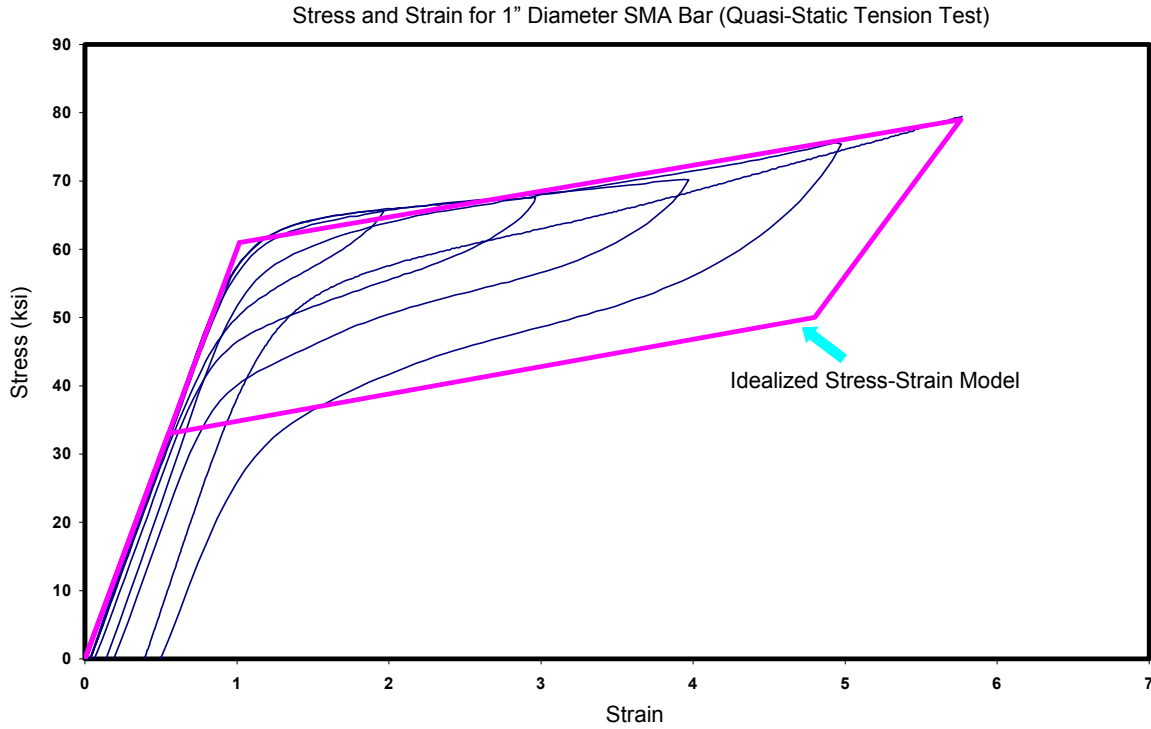


Figure 5.12 Tensile stress-strain curve for super-elastic SMA bar (DesRoches et. al. 2004)

5.1.3 Interface Conditions

All interfaces between two contact surfaces were explicitly modeled. The general contact formulation used in ABAQUS involves a master-slave algorithm (ABAQUS 2006). This formulation considers the interactions for surfaces that are in contact, interpenetrate or slip and imposes a constraint on the nodes of the slave surface in order not to penetrate the master surface (Citipitioglu et al. 2002). Surface interactions with a friction coefficient were defined as shown in Figure 5.13 and as below:

End-Plate Connection – Contact surfaces between:

- The underside of bar heads and end-plate surface surrounding the bolt holes (Surface 1)
- The end-plate and the CFT column (Surface 2)
- The bar shank and the hole surface in the CFT column wall (Surface 3)

T-stub Connection – Contact surfaces between:

- The underside of fastener heads (i.e. bar heads, shear bolt heads, and web bolt heads) and the T-stub/shear tab surface surrounding the bolt holes (Surfaces 1, 2, and 3)
- The T-stub flange and the CFT column (Surface 4)
- The shear tab and the beam (Surface 5)
- The T-stub stem and the beam (Surface 6)
- The bar shank and the hole surface in the CFT column wall (Surface 7)
- The shear bolt shank and the hole surface in the T-stub stem (Surface 8)
- The web bolt shank and the hole surface in the beam web (Surface 9)

Clip Angle Connection– Contact surfaces between:

- The underside of fastener heads (i.e. bar heads, shear bolt heads, and web bolt heads) and the clip angle/shear tab surface surrounding the bolt holes (Surface 1, 2, and 3)
- The clip angle flange and the CFT column (Surface 4)
- The shear tap and the beam (Surface 5)
- The clip angle leg and the beam (Surface 6)
- The bar shank and the hole surface in the CFT column wall (Surface 7)

- The shear bolt shank and the hole surface in the clip angle leg (Surface 8)
- The web bolt shank and the hole surface in the beam web (Surface 9)

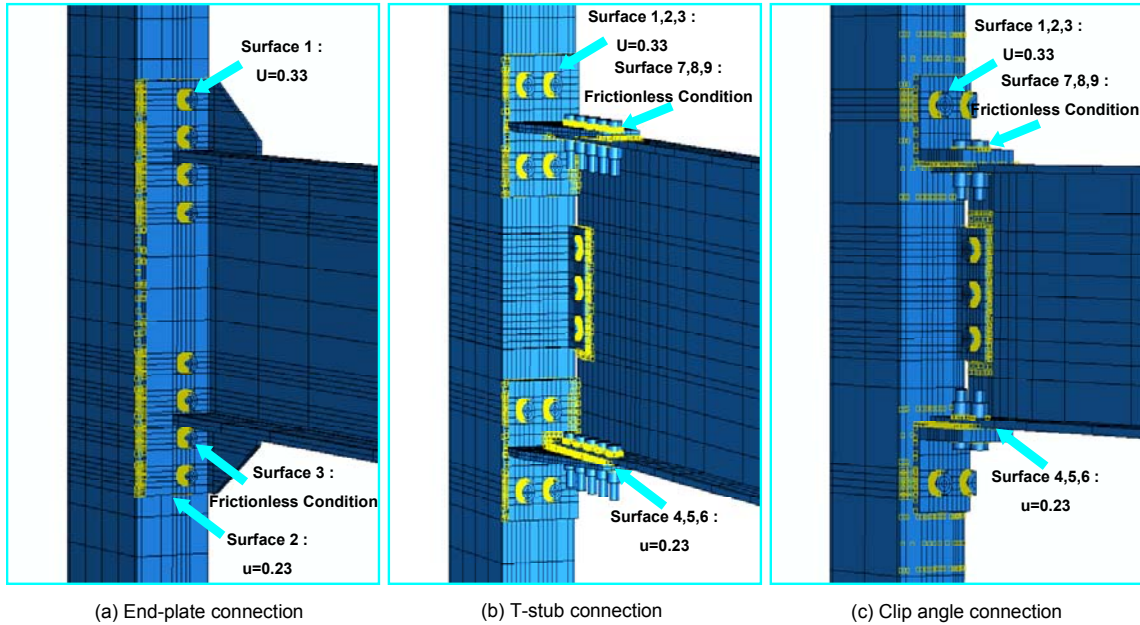
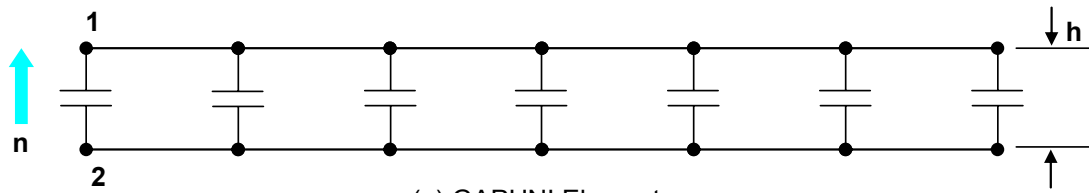


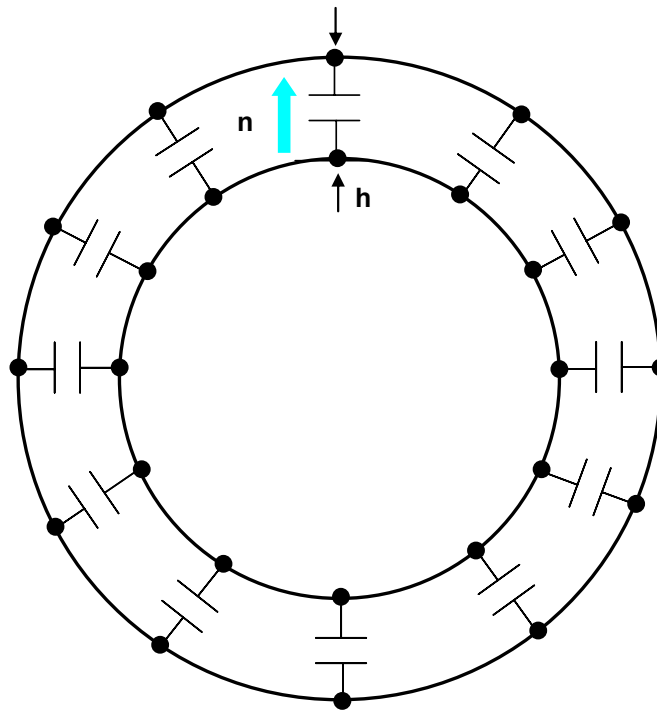
Figure 5.13 Surface interactions with friction coefficient

The contact behavior at the interface between the steel column surface and the interior concrete core was modeled with gap elements. They were defined by specifying two nodes with an initial separation clearance (h) and a contact normal direction (n) as shown in Figure 5.14. The generation of the gap elements benefited from the input file based option in ABAQUS. Microsoft Excel worksheets were used to generate the connections between two nodes having the same coordinate position on the interface. Two different kinds of gap elements, classified according to the contact situation, were used. GAPUNI elements modeled contact between two nodes when the contact direction was fixed in space. For instance, GAPUNI elements were used to model the contact between two flat planes as shown in Figure 5.14 (a). GAPCYL elements modeled contact between two nodes when the contact direction was orthogonal to an axis. For instance, GAPCYL elements were used to model the contact between two circular tubes. As a consequence, the separation and force between the gap elements was provided as an output. While gap elements are defined along the normal direction, surface interactions

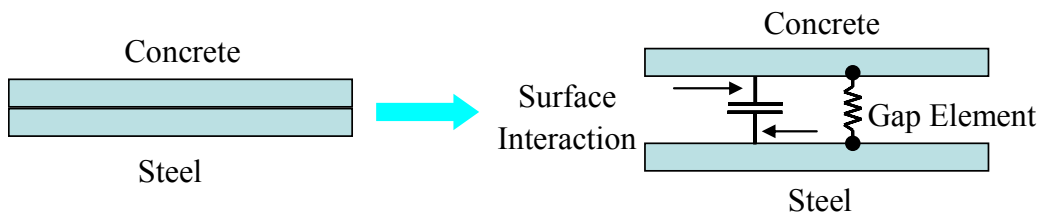
with a friction coefficient are defined along the shear direction in order to generate the real surface condition between steel and concrete interface. The values of the coefficient of friction were taken as 0.3. The interface conditions are depicted in Figure 5.14 (c).



(a) GAPUNI Elements



(b) GAPCYL Elements



(c) The Interface Conditions between Steel and Concrete

Figure 5.14 Contact interactions between steel and concrete

5.1.4 Special Conditions

Crushing of the interior concrete generally localizes in areas under high compressive stresses, such as the bearing surface between the undersides of the bar heads and the bottom flange of the beam. Concrete cracking occurs in the opposite faces to the crushing ones due to tensile strains. The current release of ABAQUS Version 6.6-1 contains modeling options for fracture mechanics analysis. This modeling method requires several fracture specific tools which include those for creating seam cracks, selecting the crack front lines, crack directions, and defining singularities (See Figure 5.15). These fracture tools are usually created in order to estimate a contour integral for a J-integral type or stress intensity factor. The usage of these tools in this research was limited to some crushing areas on the grounds that (a) the interior concrete cracking has a negligible effect on the total behavior of the composite connection and (b) fracture analysis required a considerable amount of computational cost and can result in numerical instabilities. It should be noted in this research that the crushing state could be modeled using the pre-cleavage condition by the “Seem Crack” method available in ABAQUS program.

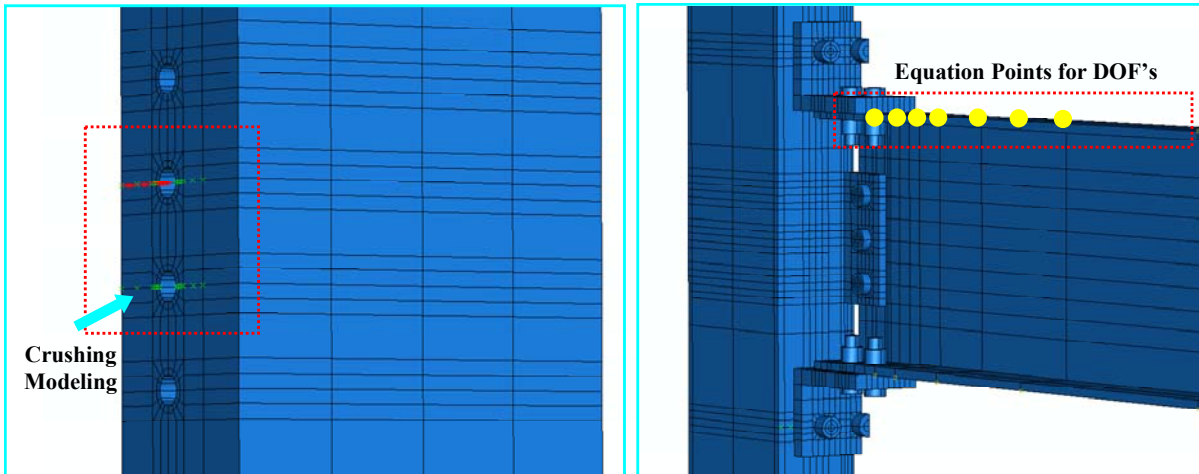


Figure 5.15 Modeling method for concrete cracks (Left)

Figure 5.16 Multi-linear constraint equation points (Right)

In some FE models, the slender beam exhibited extensive distortion when subjected to large displacements at its tip. These distortions made the analysis stop as convergence could not be achieved (i.e. incomplete full step). Multi-linear constraint equations were

used to constrain degree of freedoms (DOF) in the beams to diminish this distortion. Each constraint equation point required a linear combination of nodal variables which was set equal to zero. Figure 5.16 shows the multi-linear constraint equation points introduced at the top of a beam flange.

5.1.5 Initial Conditions

Half of PR-CFT connection was modeled by using symmetry about the centerline of the web, CFT column, and other components. The half models satisfy the precondition that both geometric configurations and loads were perfectly symmetric about the boundary plane. The “type” boundary condition available in ABAQUS/CAE was specified instead of constraining individual degrees of freedom. An example of symmetric boundary conditions for the half model is shown in Figure 5.17. A prescribing boundary condition of type XSYMM to the symmetric plane represents the surface on a plane of symmetry normal to the X Axis. This boundary condition is identical to prescribing a boundary condition using the direct format to degrees of freedom 1, 5, and 6 in the symmetric plane since symmetry about a plane $X=\text{constant}$ indicates $u=0$, $R_y=0$, and $R_z=0$.

The models were loaded in two steps. The first step was used to pretension the bolts while the second step was used to apply the main load with the propagation of the bolt pretension. Great care was taken to attempt model the bolt behavior correctly, including the oversized bolt holes. The all bolts were pre-tensioned by applying an adjustment length/displacement to the center of the bolt shank as shown in Figure 5.18. The direction of the pretension force was taken as the normal axis to the loading surface. The prescribed bolt displacements were calculated by assuming that bolts remain elastic with the axial pretension. In ABAQUS, the prescribed bolt displacement can be converted into the pretension force using the ‘History Output’ tool.

5.1.6 Loading

The second step was used to apply the external displacement. For static loading cases, the load was generated by imposing a support displacement to the tip of the beam as shown in Figure 5.19. A displacement-type boundary condition was used to apply a

prescribed displacement magnitude of $-10.0''$ in the Z direction to the middle of the beam tip. The postprocessor in ABAQUS automatically calculated the equivalent forces for each displacement step. The force-displacement response of the connections was changed into a corresponding moment-rotation response using the equations for the “instruments” described in the previous chapter.

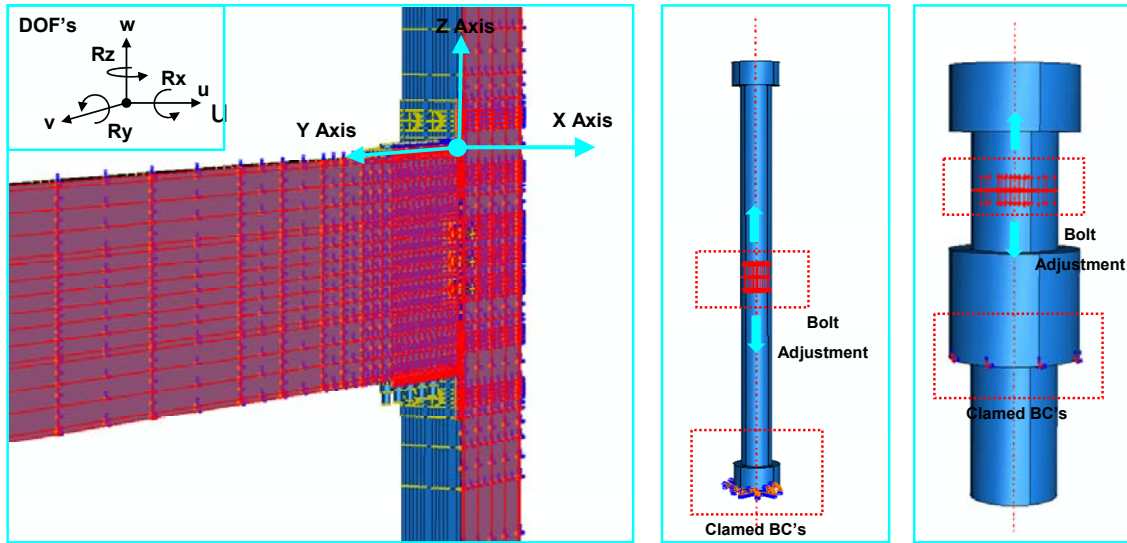


Figure 5.17 Symmetry boundary conditions for half model (Left)

Figure 5.18 Initial pretension force in bars and bolts (Right)

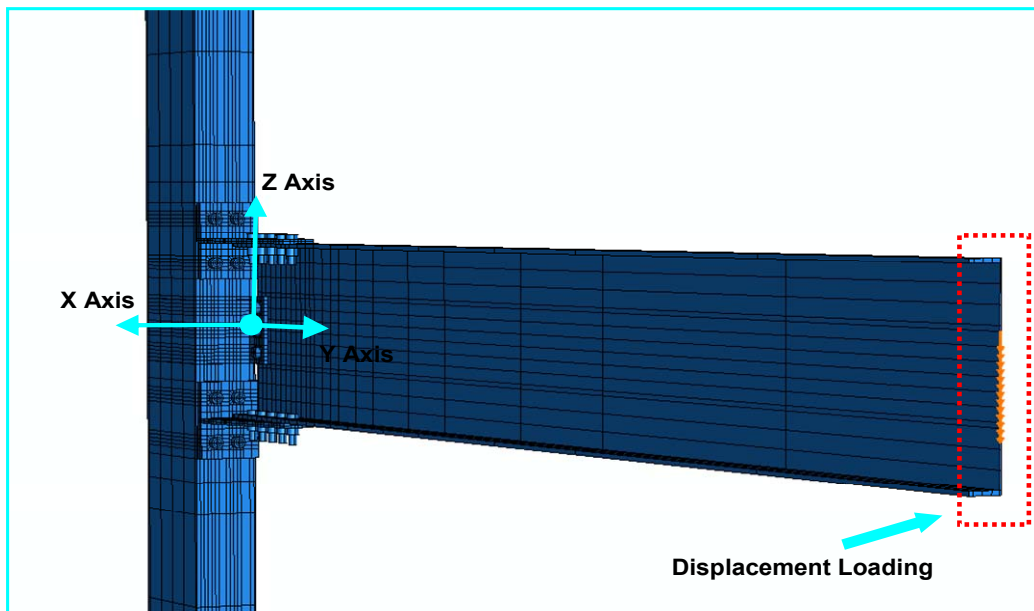


Figure 5.19 Application of the load (end displacement)

5.1.7 Steps and Solution

A sequence of one or more analysis steps had to be defined for each FE model. As noted above, two time steps were required to analyze the bolted connection models with the time increments. This approach was generally used for stable problems and can include linear or nonlinear response but without inertia effects. Multiple analysis steps can be assigned during the analysis as shown in Figure 5.20. For each step in the analysis, the step manager indicates whether the FE model will account for geometric nonlinear effects due to large deformation with the setting of Nlgeom parameter. The initial step was used to define boundary conditions, predefined fields, and interactions which are applicable at the beginning of the analysis.

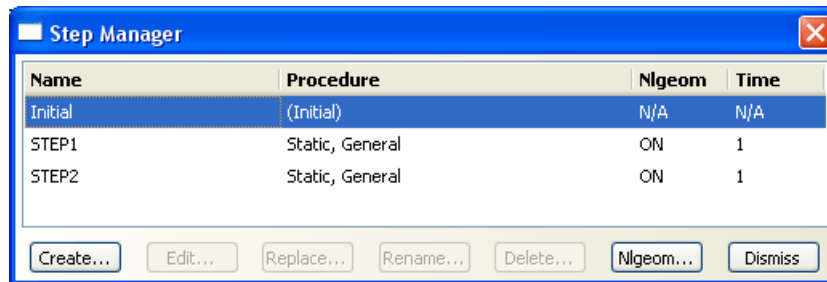


Figure 5.20 Basic step manager

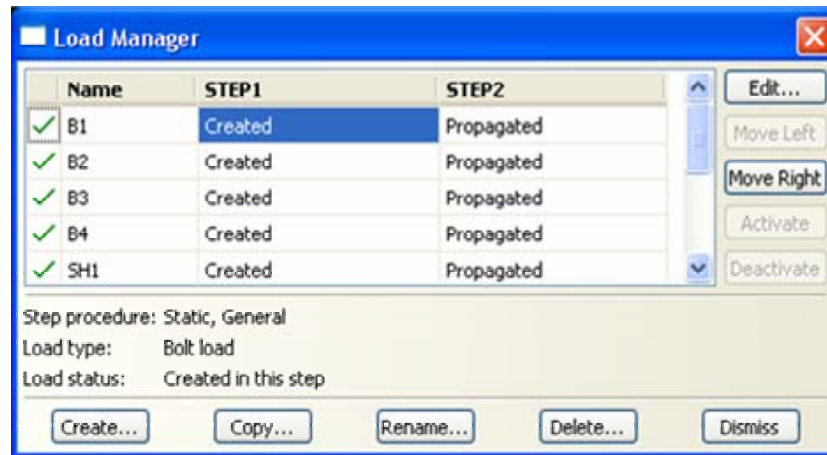


Figure 5.21 Load manager for bolt pretensions incorporated with time steps

After the initial step, several steps were lumped into step 1 to introduce the pretension in the bolts (Figure 5.21). The contact interaction calculations generally converged successfully within the maximum number of allowed iterations, typically taken as 12.

Figure 5.22 shows the analysis solution and control for the computations associated with the step manager. Given the many options available in ABAQUS, this section only highlights some of the most important parameters used. It is felt that this is sufficient to clearly state the procedures followed and allow reproduction of the analyses.

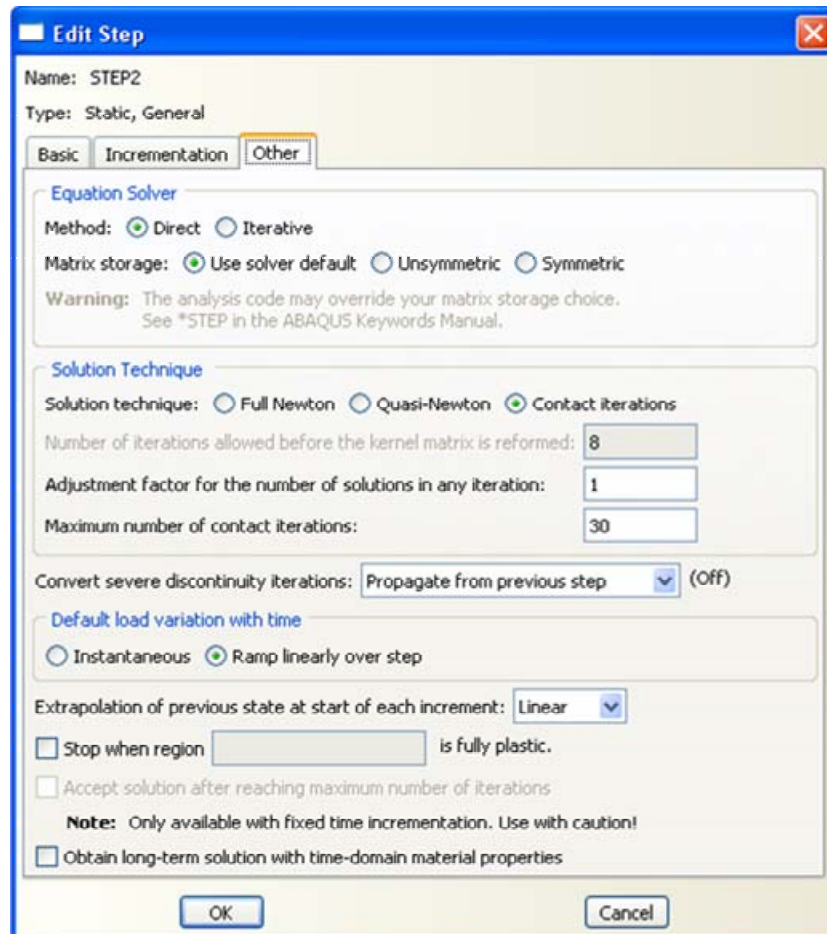


Figure 5.22 Solution and control for the computation associated with step manager

5.1.8 Comparison and Substitution Models

Extra models were generated to carry out parametric studies to investigate the effect of geometric variables. Figure 5.23 shows the first comparison models, divided into concrete-filled (CFT) and hollow steel tube column models. From the results of these studies it was possible to clarify the yielding and failure mechanisms influenced by the presence of concrete in the columns and assess quantitatively the importance of the concrete filling. Figure 5.24 shows another comparison case used to investigate the effect

of the clearance distance between the beam and T-stub flange surfaces. This geometric parameter was found to have an influence on the slip and energy dissipation in the T-stub connection models (See Section 5.2.1).

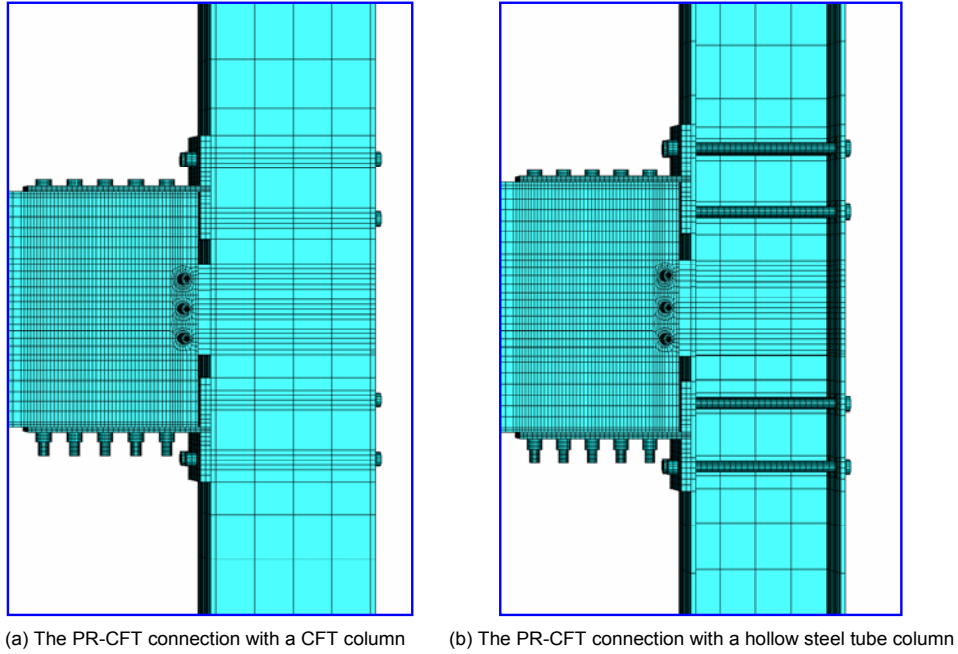


Figure 5.23 Comparison models to investigate the effect of concrete filling

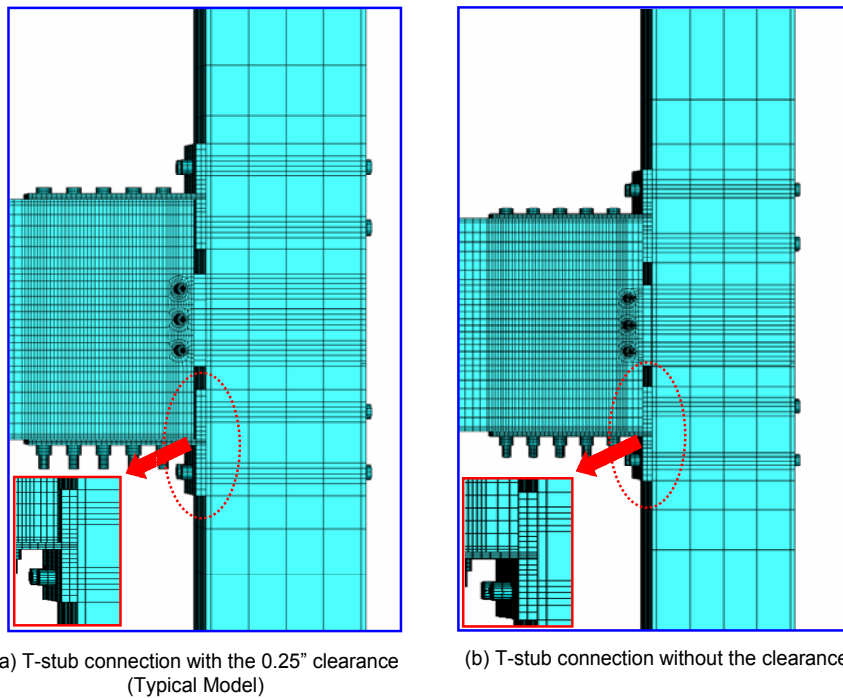


Figure 5.24 Comparison models to investigate the effect of clearance distance

Elastic foundations were modeled by defining the elastic foundation stiffness per unit area of the selected surface as shown in Figure 5.25. The foundation surfaces were only utilized in the bearing area which received most of external force transferred from the beam flange. Use of elastic foundations elements allowed reasonable modeling of behavior in areas of high stress (contact between the concrete and steel in the column directly apposite the beam flange) and avoided numerical convergence difficulties due to high contact compressive strains in the surface between the concrete filling and the hollow steel tube. The unit area stiffness can be determined from a simple simulation for a concrete specimen with a unit area as shown in Figure 5.26. Elastic foundation interactions were created in the initial step.

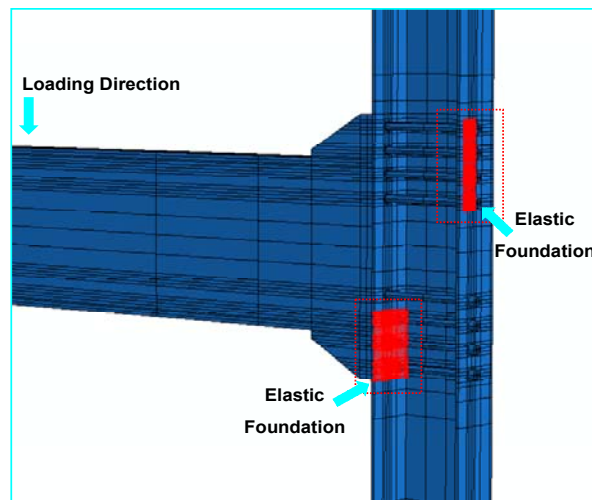


Figure 5.25 Elastic foundation model for the CFT column model

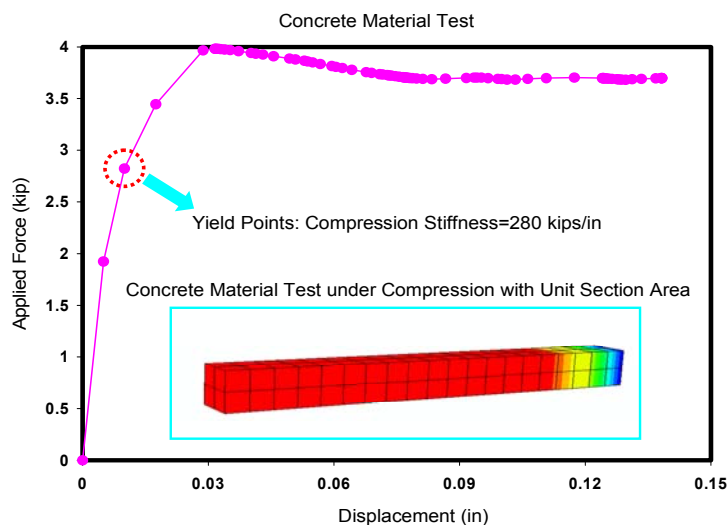


Figure 5.26 Load-deflection curve for confined concrete under compression

5.2 FE Test Results

As noted before, besides the full connection models with the CFT column, additional models with the hollow steel section column were modeled in order to investigate the effect of the confined concrete. This study employs the modeling combinations shown in Table 5.6. FE experiments were performed on 18 full connection models. The constitutive model for the confined concrete was the previously described concrete damaged plasticity one. It can provide accurate stress distributions, account for the weak tensile strength of concrete, and give realistic results for panel zone behavior. However, it results in numerical convergence problems, large memory space demands, and excessive running time. As above mentioned, a properly calibrated elastic foundation model avoids these problems. Comparisons for both models are shown in Table 5.7. A brief summary of the FE test results is described in this section.

Table 5.6 FE model cases for full PR connections

Column Type	End-plate connection	T-stub connection	T-stub without clearance (W/O-C)	Clip-angle connection	Total
Rectangular Hollow (RH)	0	0	0	0	4
Circular hollow (CH)	0	0	0	0	4
RCFT	0	0		0	3
CCFT	0	0		0	3
F-RCFT Substitution (Foundation Spring)	0	0	0		3
F-CCFT Substitution (Foundation Spring)	0				1
Total	6	5	3	4	18

Table 5.7 Comparisons between foundation models and concrete models

Comparison Item	Foundation Model	Concrete Damage Plasticity Model
Running Time	4 - 12 hours	2 – 8 days
Nonlinear Range	Easier to arrive at nonlinear range	Very difficult to arrive at nonlinear range
Save Memory (OBD)	Less than 1 GB	Ave. 3 GB (Max. 5.6 GB)
Accurate (Total Deformation)	A little depend on Elastic Stiffness (Accurate)	Accurate
Panel Zone Behavior	Not Good! (Much Stiffer)	Good

5.2.1 Behavior Curves for All Connection Models

Bending forces are the main contributor to deformations for most FR and PR connections. Thus the main aspects of connection behavior (strength, ductility, and stiffness) can be represented by a moment-rotation ($M-\theta$) curve. For these FE studies, the moment-rotation response of the connections can be calculated by measuring the total applied force-displacement at the tip of beam (See Appendix C). Understanding of the moment-rotation curve for a given connection is a precondition to grasp the mechanisms controlling connection performance.

The load-displacement behavior at the beam end and the $M-\theta$ behavior at the connection for three variations of the end-plate connections is depicted in Figure 5.27. The figures compare the behavior of a connection to a circular (C) and rectangular (R) column, with the column being either steel (H), concrete filled (CFT) and the connection using foundation springs (prefix F) or the damaged concrete plasticity model (no prefix). The behavior is basically bilinear, with the yield transition point reflecting yielding of a connection component: a beam flange, tension bars or the end-plate itself. The load-displacement and moment-rotation curves have very similar shape, indicating the dominance of bending effects.

As far as strength is concerned, connection models with the CFT column show about twice the strength as those with the hollow section column. This implies that the interior concrete can prevent local buckling and yielding of the tube wall under the bar heads. This additional strength and stiffness allows the tension bars to reach their full capacity. For these connections, the absence of any shear faying surface results in no evidence of slip in the moment-rotational curves. Models with foundation springs (prefix F) show almost identical behavior to the ones using concrete damage plasticity models, but the calculation proceeds for a longer time (displacement) for the former. This implies that most of the deformation stems from tensile deformations of the bars rather than panel zone shear deformations for connections with CFT columns.

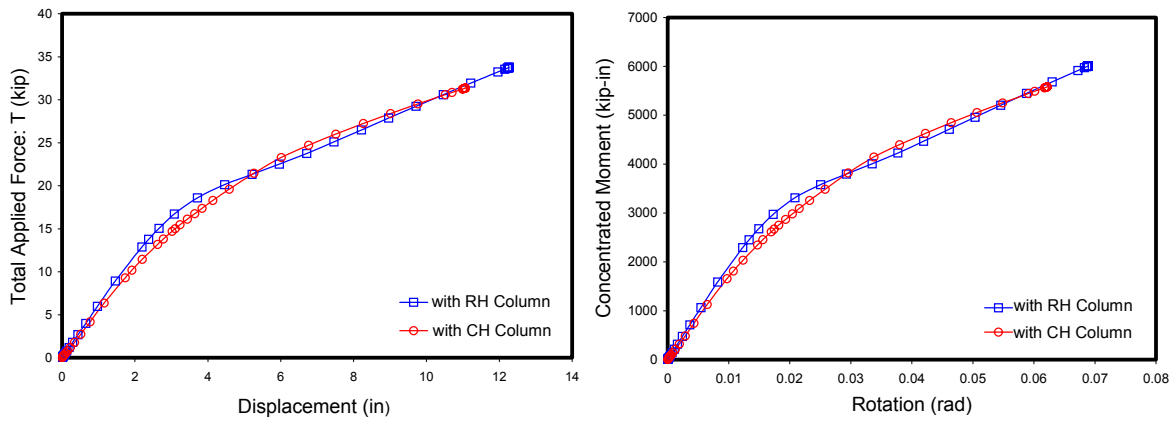
Similar curves for T-stub connections are depicted in Figure 5.28. These compare the behavior of the hollow columns with and without a 0.25 in. clearance in Fig. 5.28(a) and (b). The existence of the shear faying surface generates a horizontal offset (slip distance) in both the load-displacement and $M-\theta$ curves and leads to an increase in deformation

and energy absorption capacity. The friction coefficient is the most significant parameter in determining the strength at which slip occurs (Fig. 5.28(c)). The slip strength for all T-stub connection models is similar because the same friction coefficient was used. The small discrepancy about slip strength levels can be found between connection with RCFT column and that with CCFT column. It is caused because the condition of mesh generation between the master-slave surface interfaces is slightly different. Slippage of bolted components gives rise to a temporary loss of stiffness that acts as a fuse, limiting the force input (See Figure 5.28 (d)). Connection models with the CFT column show slightly higher strength than those with a hollow tube section column.

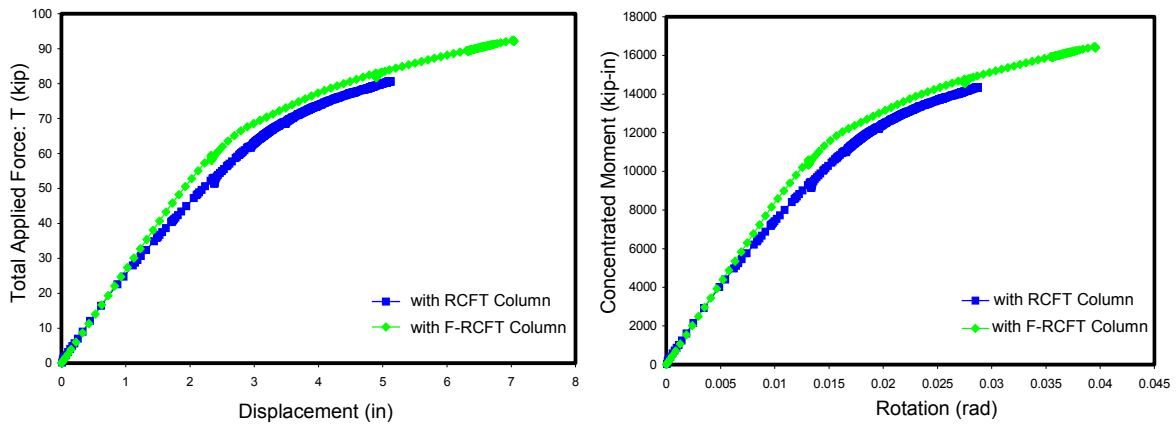
The yielding of the T-stubs stems is the major component contributing to the connection behavior. In addition, for the cases of thin stems a net section failure is likely before either local buckling in the beam or tension bar yielding and hardening are reached.

The curves for clip angle connections are depicted in Figure 5.29. This connection also includes a slip mechanism. The difference in capacity between the connection with or without interior concrete is a product of different failure modes. For the CFTs, the interior concrete prevents local buckling, and the full capacity of the tension bars and thick clip angle-can be utilized.

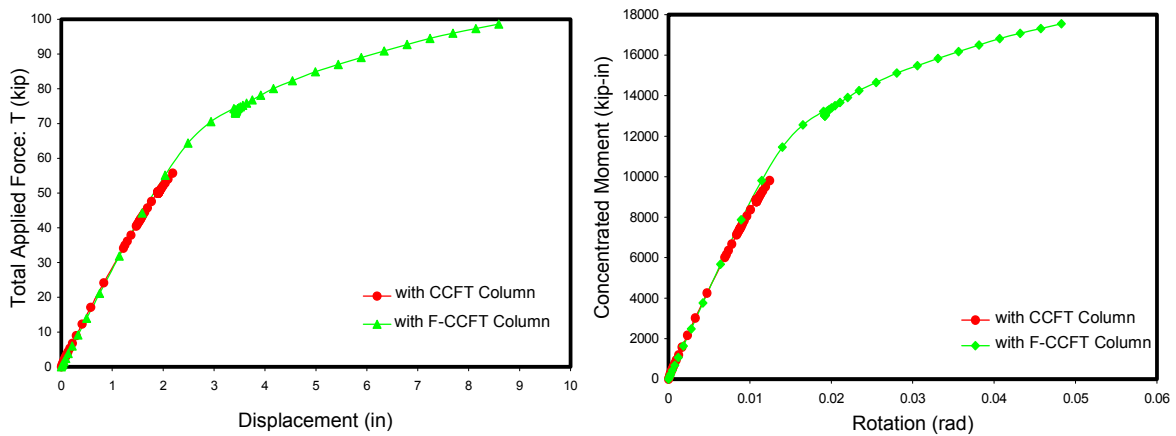
To summarize these results, the behavior curves for all connection models with CFT columns are compared in Figure 5.30. The smallest capacity corresponds to the clip angle connection, with the smallest ultimate strength and a very low stiffness. Although the T-stub connections use the same number of tension bars as the end-plate connections, the strength of the T-stub connection is controlled by the strength of the T-stub stem. The classification of the connection types based on the moment-rotation curves will be described in the next section.



(a) End-plate connection with the hollow section column

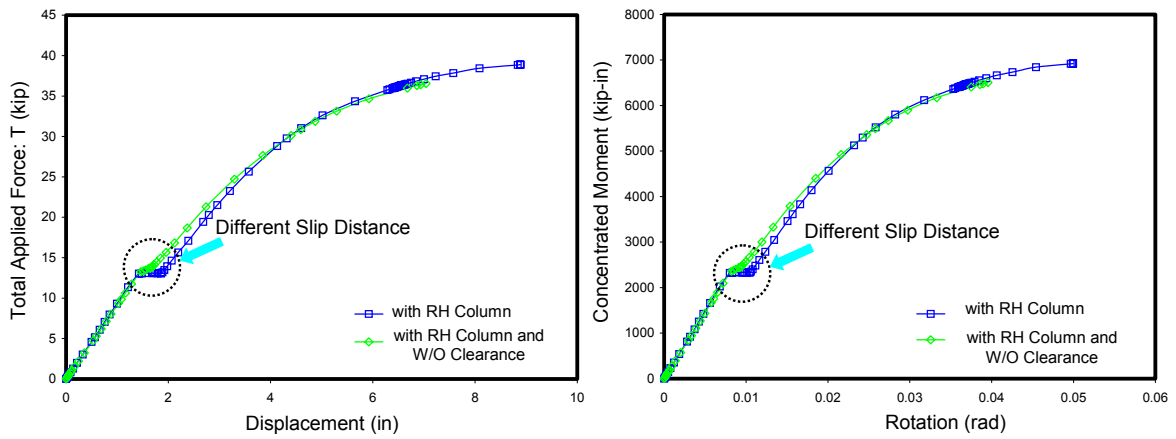


(b) End-plate connection with the RCFT column

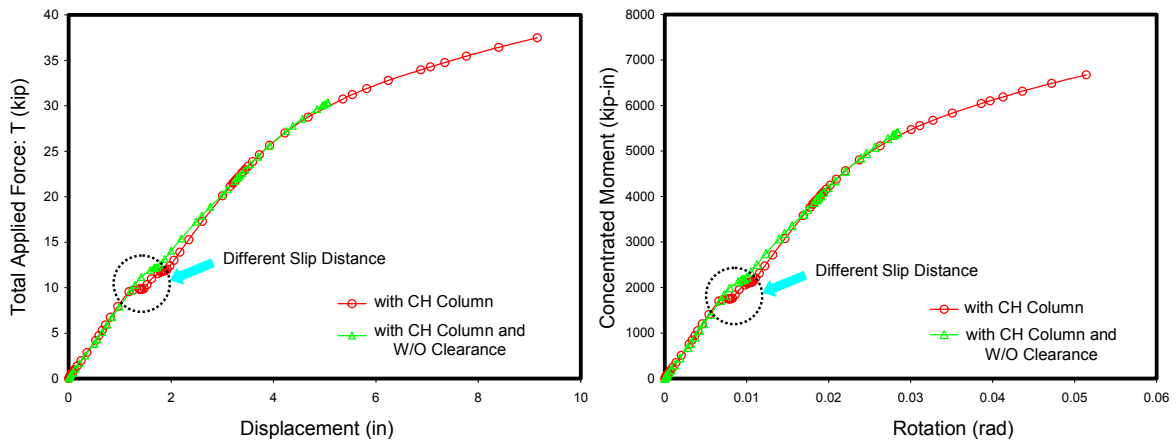


(c) End-plate connection with the CCFT column

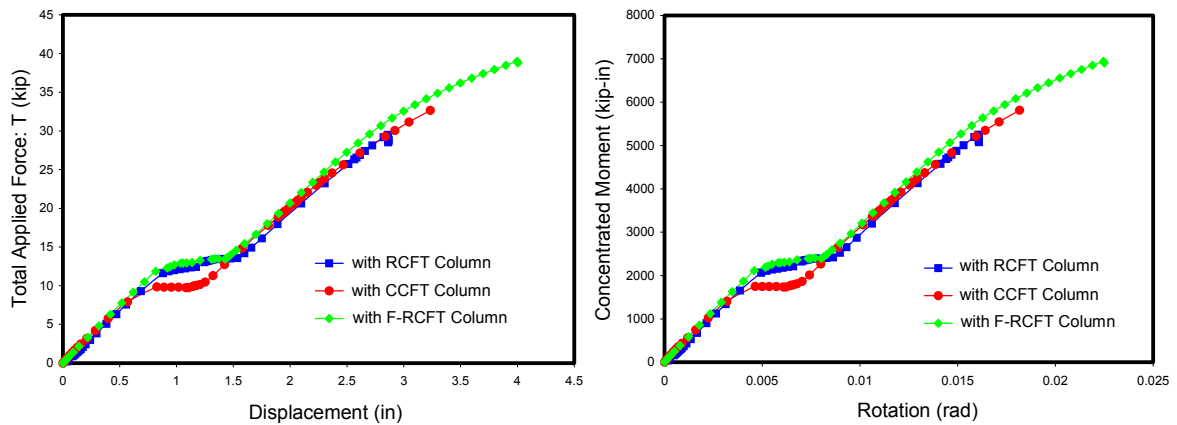
Figure 5.27 Non-linear behavior of end-plate connections



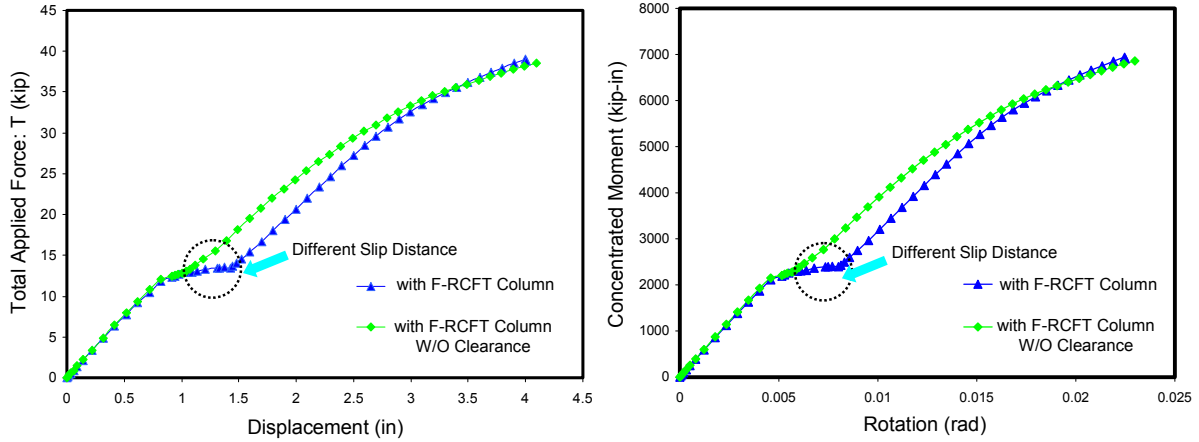
(a) T-stub connection with the rectangular hollow tube section column



(b) T-stub connection with the circular hollow tube section column

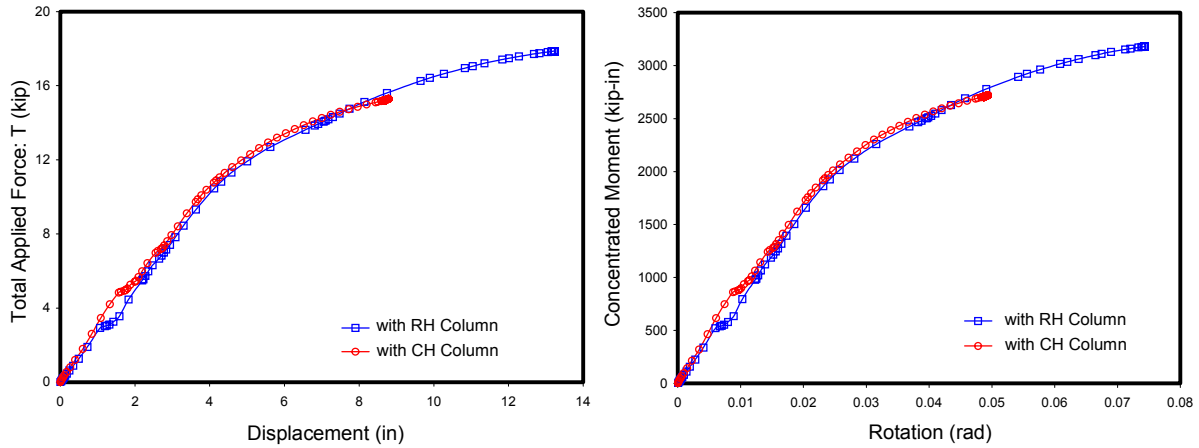


(c) T-stub connection with the CFT column

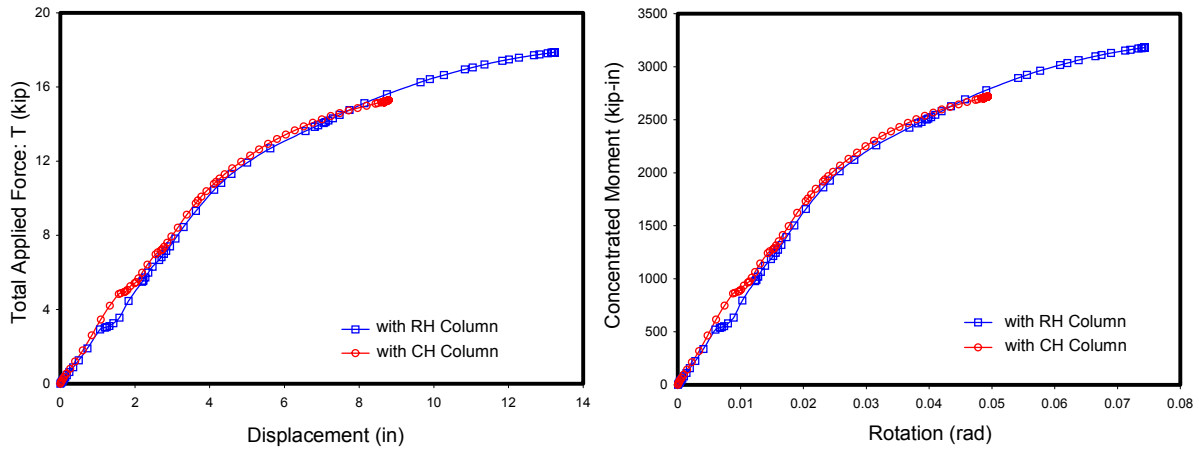


(d) Comparisons of T-stub connection vs. T-stub connection with zero clearance

Figure 5.28 Non-linear behavior of the T-stub connections



(a) Clip angle connection with the hollow tube section column



(a) Clip angle connection with the hollow tube section column

Figure 5.29 Non-linear behavior of the clip angle connection

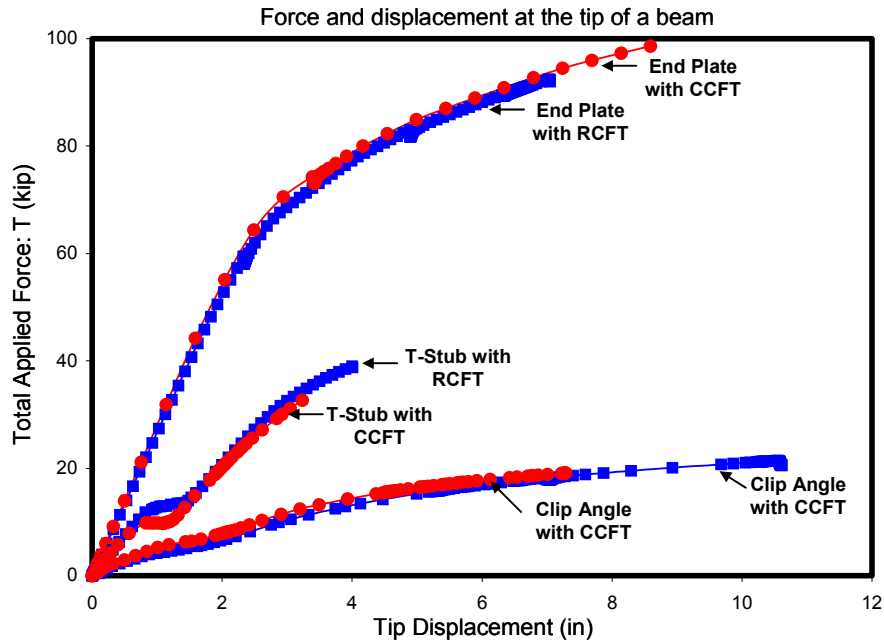
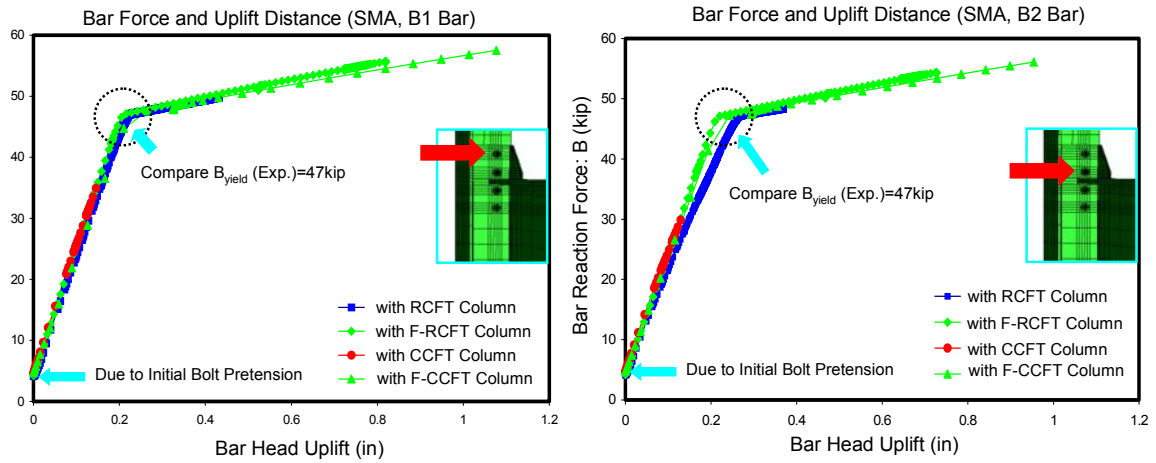


Figure 5.30 Comparisons of behavior for all connection models with the CFT column

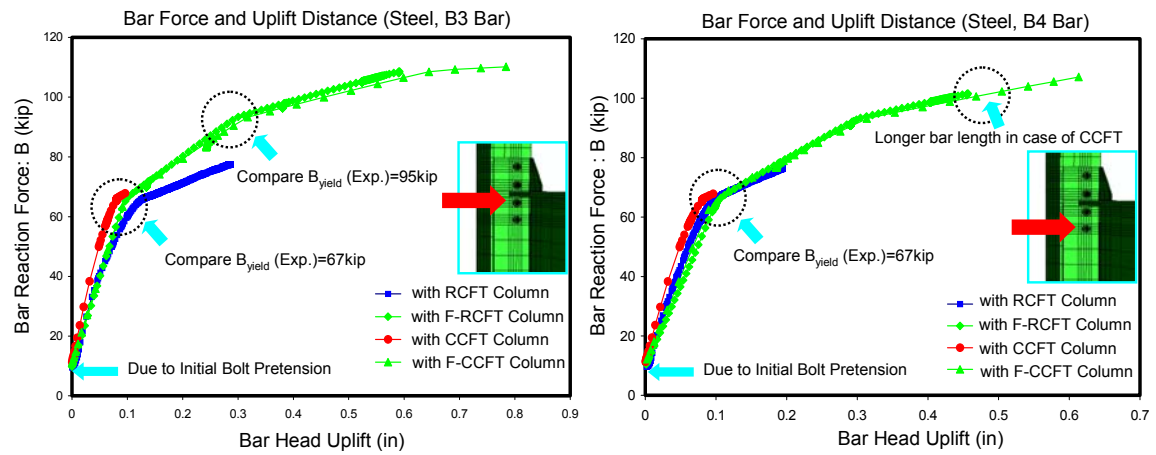
5.2.2 Strength of Tension Bars

Tension bars are the main force transfer component in these connections. Shear and bending moment are assumed not to significantly affect the deformation of tension bars and their effect on the bar performance are also ignored during the design and hand analysis.

Force-deformation curves for tension bars in end-plate connections are shown in Figure 5.31. In these graphs, the values marked as $B_{yield} (exp)$ correspond to the expected yield strength of the bars based on the assumed material properties and the nominal size of the bars. The behavior of tension bars is highly dependent on the material properties and mimics the behavior of a tensile coupon. In these connections, SMA bars should be placed on the bolt holes farthest from the centerline of beam in order to take advantage of their shape memory effect. The forces do not start at zero because the bolts are pretensioned and highly stressed at this point. This connection type was designed to utilize the full plastic capacity of tension bars, and the curves show good agreement with this anticipated behavior.



(a) Force and deformation at the first and second row of tension bars

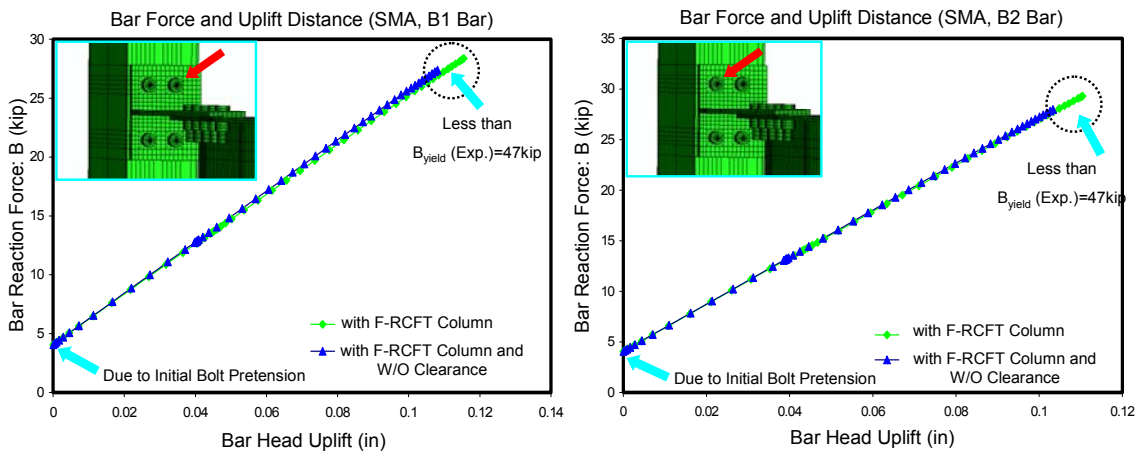


(b) Force and deformation at the third and fourth row of tension bars

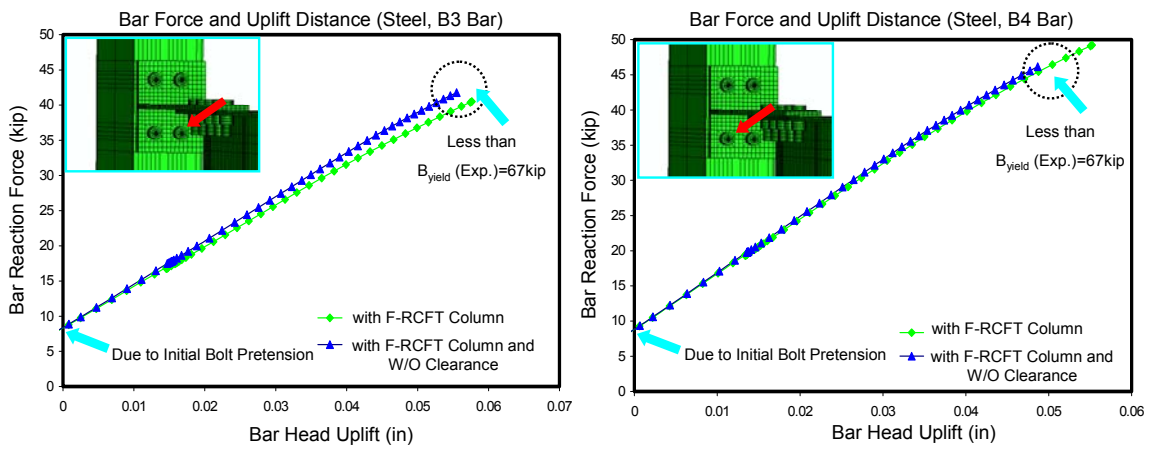
Figure 5.31 Force and deformation in the tension bars (End-plate connections)

Force-deformation curves for tension bars in T-stub connections are shown in the Figure 5.32. The behavior of the bars is almost entirely elastic (i.e. not reaching the expected yield force of 67 kips) because most of the deformation is produced by yielding in the thin T-stub stem. It will be verified by the observation of the force and deformation mechanism for T-stub component at section 5.3.2.

Finally, force-deformation curves for tension bars in the clip angle connections are shown in the Figure 5.33. The large deformations in the angle legs due to their relative flexibility with respect to the end plate and T-stub connections results in a large difference between the behavior of the tension bars in the connection and a typical coupon test.



(a) Force and deformation at the first row of tension bars



(b) Force and deformation at the second row of tension bars

Figure 5.32 Force and deformation in the tension bars (T-stub connections)

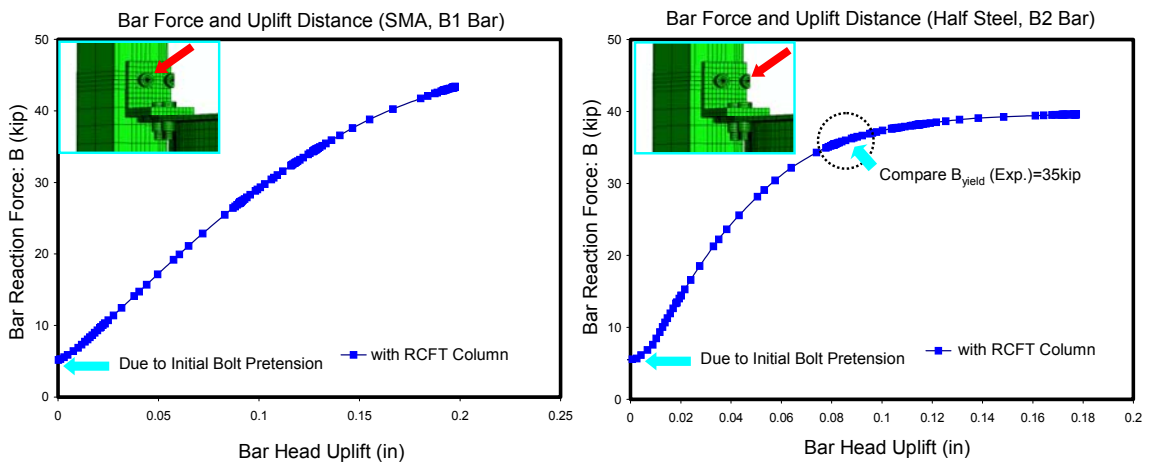


Figure 5.33 Force and deformation in the tension bars (Clip angle connections)

5.2.3 Analyses of Stress Distribution

The areas of stress concentration, likely failure modes and dominant force transfer paths can be gleaned from the stress distributions at the connection. Three parts will be discussed: (1) the steel component (wall of the tube, flanges and stems of steel sections), (2) tension bar, and (3) interior concrete. To facilitate comparison, each part uses the same stress contours based on the used material property (See Figure 5.34).

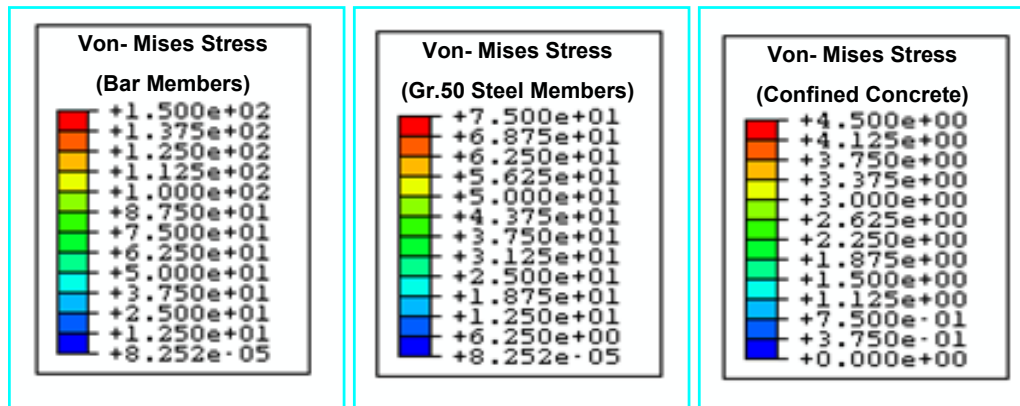
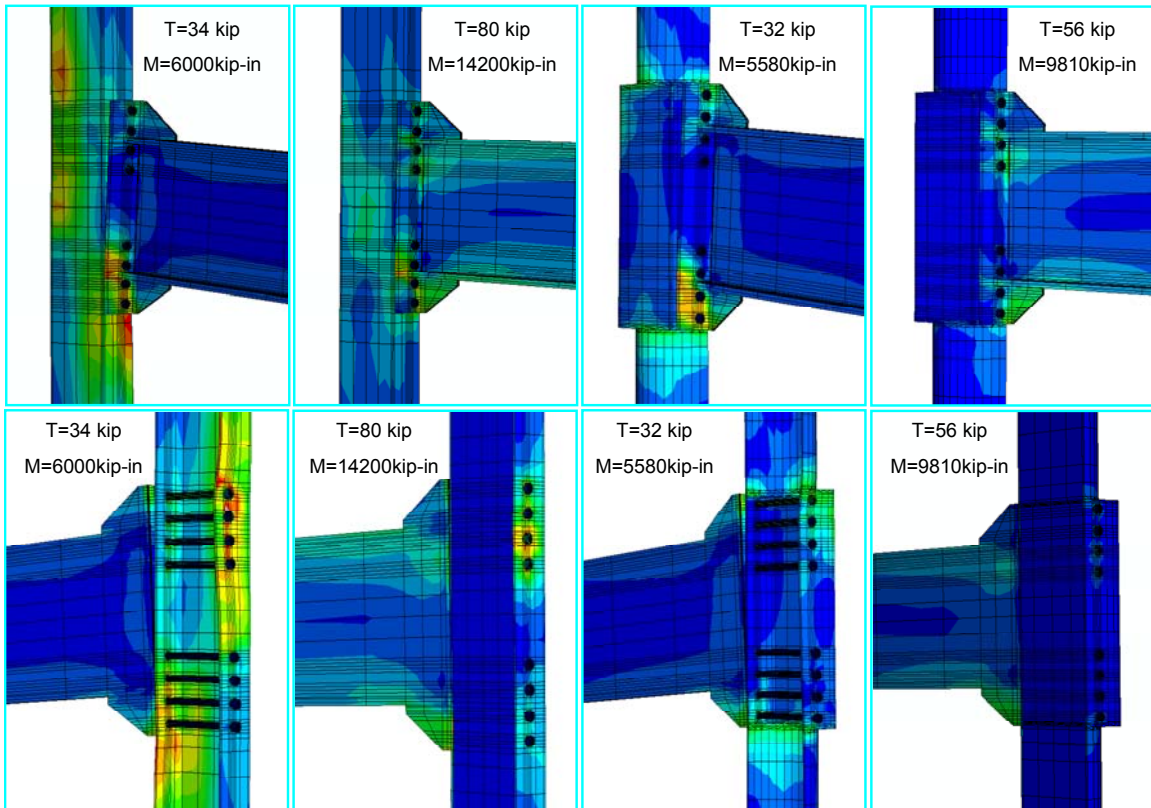


Figure 5.34 Stress contour levels for each material

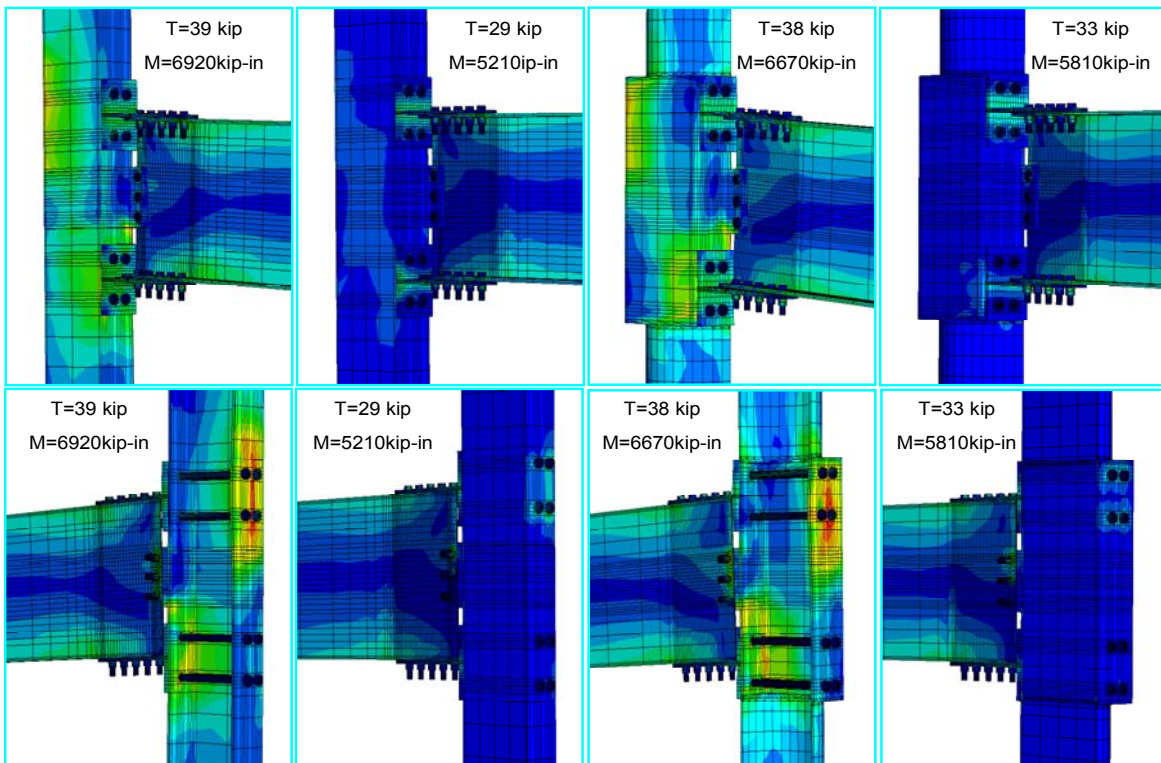
First, the stress distributions on the steel components at the final displacement (time) step are shown in Figures 5.35 to 5.37. Large stress concentration underneath the tension bars, excessive deformation, and high stresses in the panel zone (PZ) can be observed in the connections with hollow tube columns. For end-plate connections, a distinctively high stress distribution in the beam can be found on those models with the CFT columns because of the higher applied force. This implies that the interior concrete effectively limits excessive deformations of the PZ, increases the connection strength capacity and leads to yielding of the beam. This is the preferred mechanism envisioned in the design of end plates.

All T-stub connection cases show high stresses concentrated in the thin T-stem plate. Because this yielding/failure mode is common to all cases, they all show similar ultimate strength values. For the clip angle connections, significant deformations of the angle legs are clear at ultimate. This is the controlling mechanism for these connections with typical moderately thin angles. In this research angles much thicker than those typically used are utilized. These thick angle connections exhibit higher strength and significantly larger stiffness than typical angle connections.



(a) End-Plate with RH (b) End-Plate with RCFT (c) End-Plate with CH (d) End-Plate with CCFT

Figure 5.35 Stress distributions for the end-plate connections at ultimate



(a) T-Stub with RH (b) T-Stub with RCFT (c) T-Stub with CH (d) T-Stub with CCFT

Figure 5.36 Stress distributions for the T-stub connections at ultimate

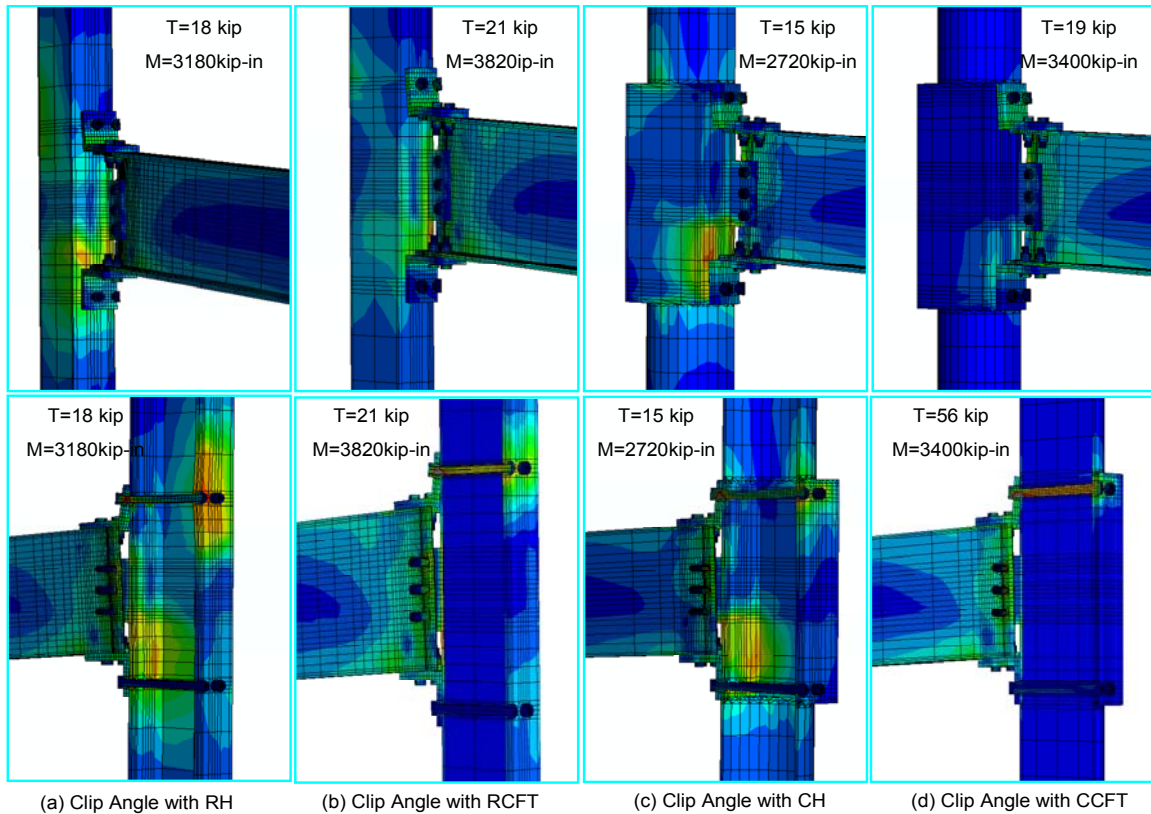


Figure 5.37 Stress distributions for the clip angle connections at ultimate

Second, the stress distributions for the tension bars are shown in Figures 5.38 to 5.40. A linear gradient of the stress distribution over the cross section due to the bending effect can be observed near the bar head. The bending effect is small in comparison with the axial effect. This effect is important if the stresses in the bars are near yield, as that will lead to localized yielding and possible stress concentrations. This effect is highly dependent on the stiffness of the steel components on which the bolts bear. For end-plate and clip angle connections, the interior concrete acts as a stiffener and reduces the rigid body motion for tension bars by preventing the local buckling around the high bearing bar head, so they can be stretched into the plastic range. On the other hand, tension bars for all T-stub connections, even those cases with CFT columns, show an elastic stress state because the tension bars are designed to resist an axial force much greater than can be generated by yielding of the thin T-stub stem.

Finally, stress distributions in the concrete are shown in Figure 5.41. Higher stresses are concentrated on the bearing areas, such as underneath of tension bars and the contact of the beam flange. Crushing due to high compression occurs at some bolt holes.

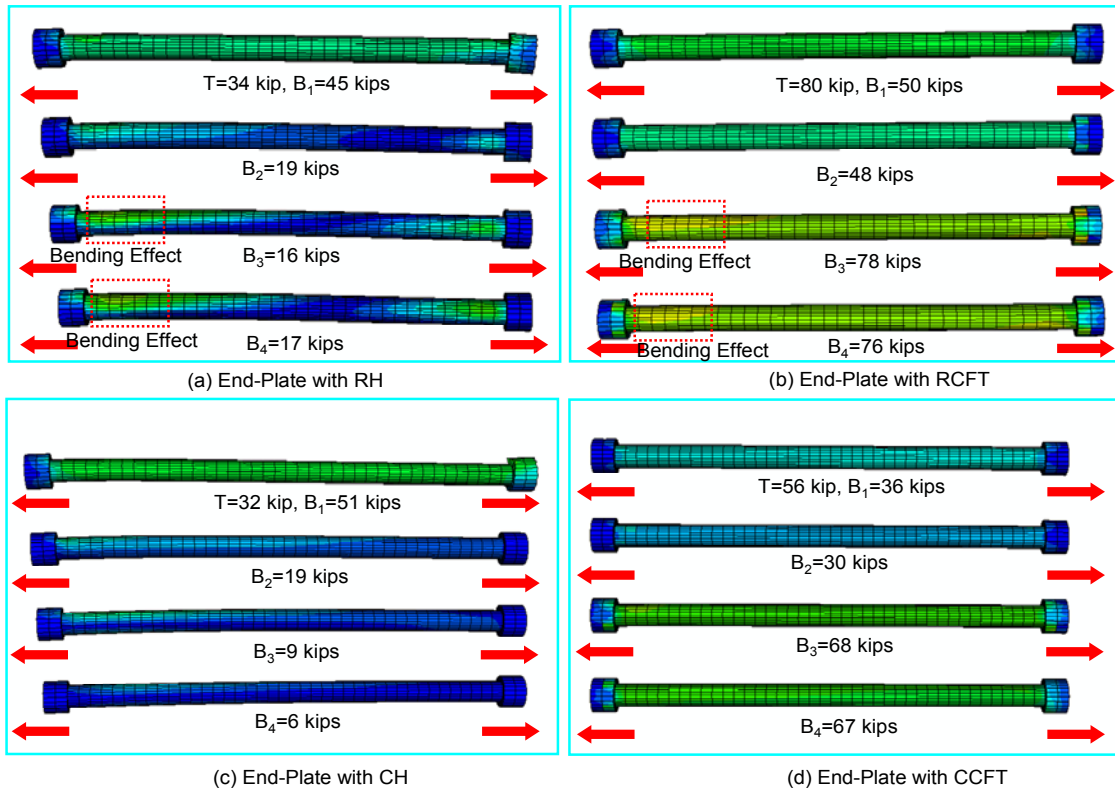


Figure 5.38 Stress distributions for tension bars of end-plate connections at ultimate

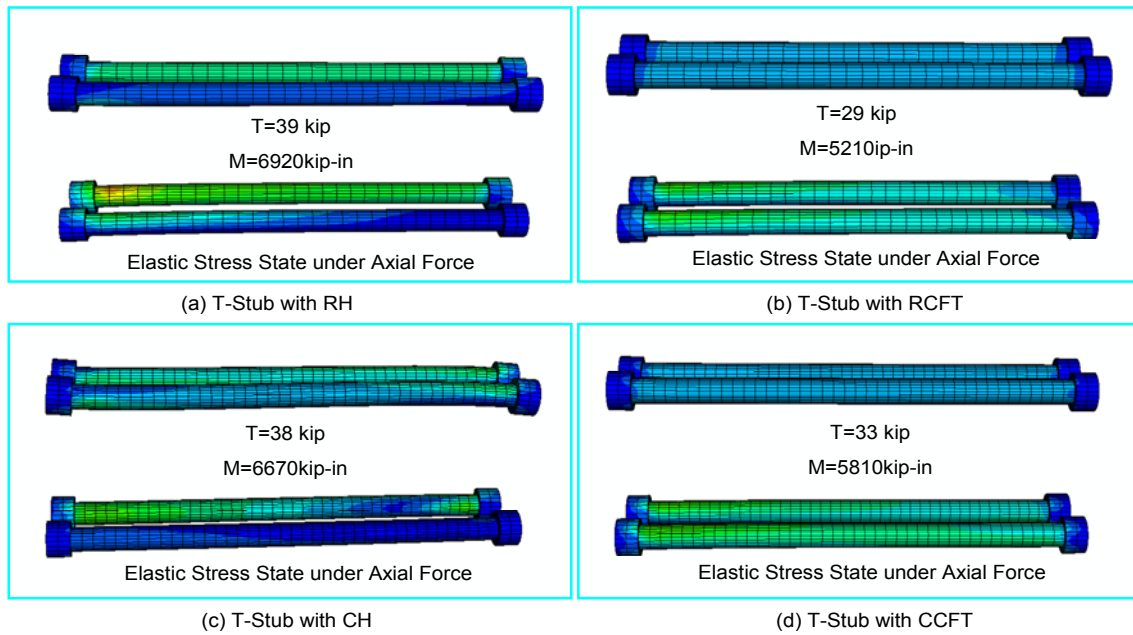


Figure 5.39 Stress distributions for tension bars of T-stub connections at ultimate

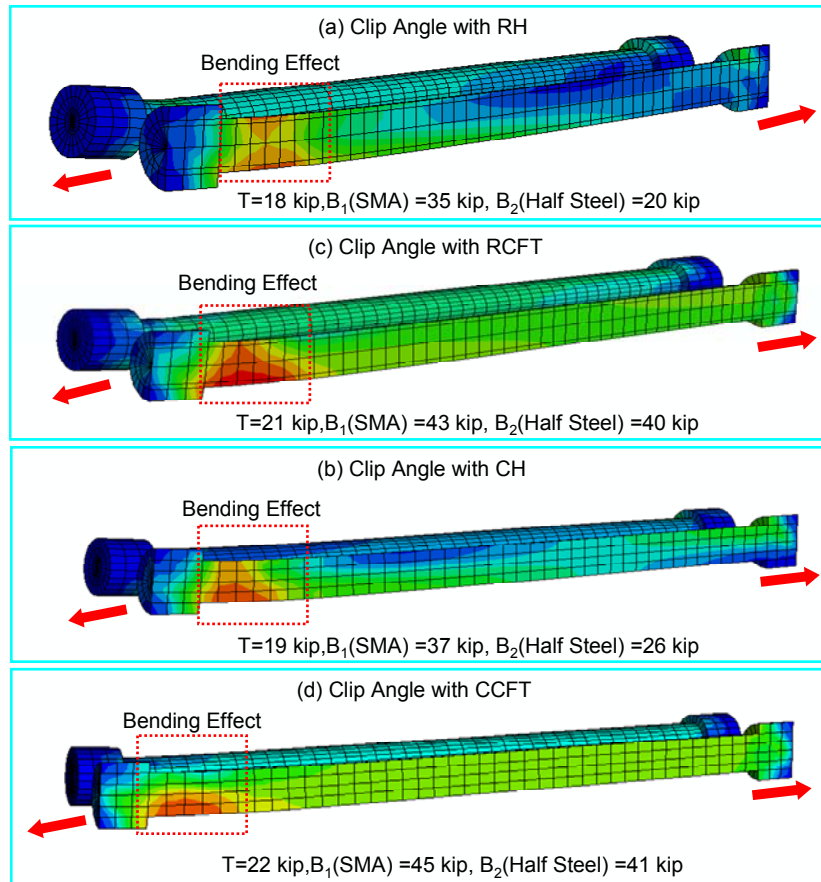
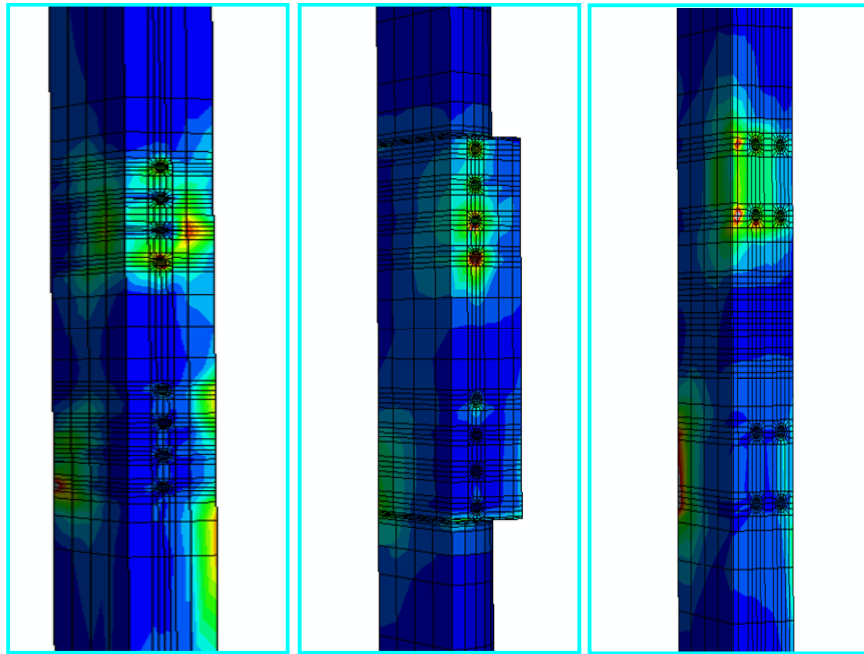
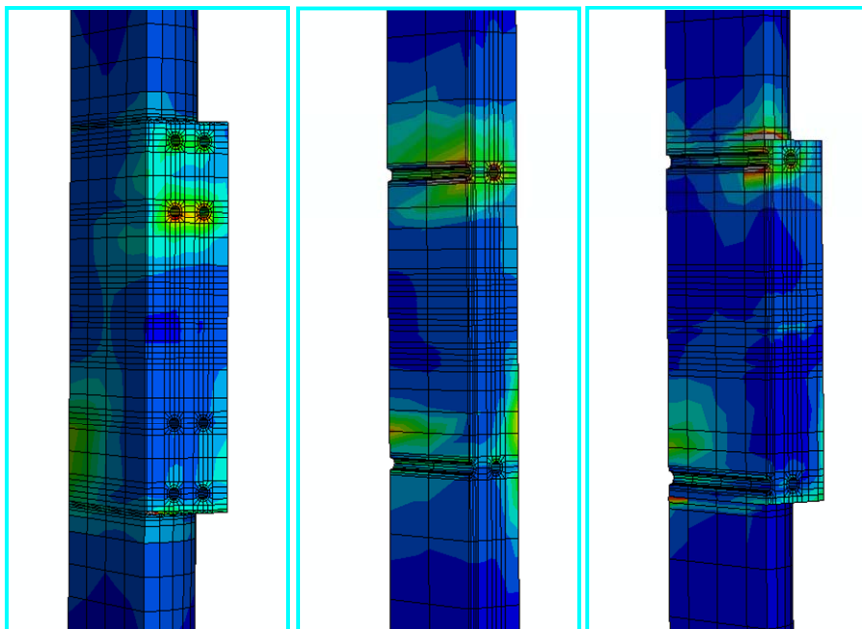


Figure 5.40 Stress distributions for tension bars of clip angle connections at ultimate



(a) End-plate connection with RCFT (b) End-plate connection with CCFT (c) T-stub connection with RCFT



(d) T-stub connection with CCFT (e) Clip angle connection with RCFT (f) Clip angle connection with CCFT

Figure 5.41 Stress distributions for inside concrete at ultimate

5.3 Observations of Monotonic Behavior

For the purpose of these discussions, the total applied force (T) at the tip of beam is converted into a concentrated moment using a first order approximation ($M=TL$). This bending moment is transmitted to the connection as the converted axial forces ($M=Pd$).

5.3.1 End-Plate Connections

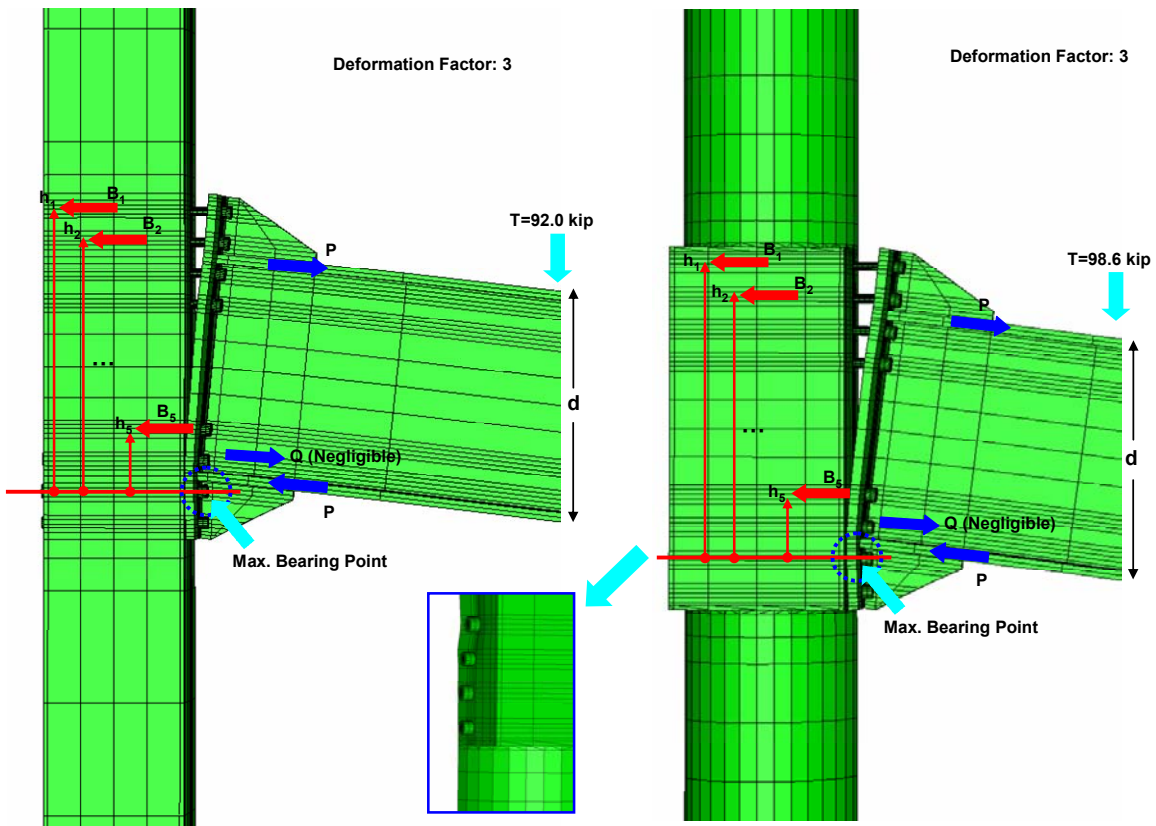


Figure 5.42 Reaction force and deformation for end-plate connections subjected to the maximum force (T) at the tip of beam

The force resisting mechanism for an end-plate connections and associated deformations are shown in Figure 5.42 for two connections at their ultimate load. The converted axial forces consist of tension forces above the centerline of beam and compression forces below the centerline of beam when the total applied force (T) acts in the gravity direction. The tension force corresponds to the summation of bar reaction forces (B), while the compression force corresponds to the bearing force of the beam

flange against the column face. The prying force (Q) acting on the contact between end-plate and column surface is negligible as compared to the other forces.

The PZ behavior of the end-plate connections is shown in Figure 5.43. The detailed calculation procedures for developing these graphs are illustrated in Appendix C. The converted axial force deforms the panel zone. The yield strength at the PZ can be calculated by using Wu's equations (Wu, 2007) which consider the stiffness loss due to bolt holes. For this case, those equations predict shear yielding in the panel zone at a shear of about 1630 and 2060 kips for the RCFT and CCFT connections, respectively. The panel zones remained in the elastic range even under the ultimate applied loading and showed a substantial stiffness.

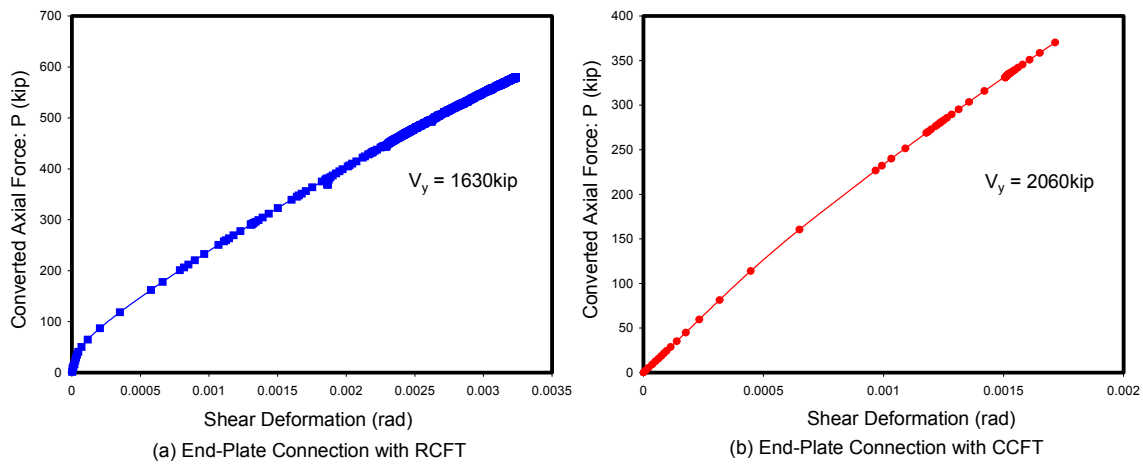
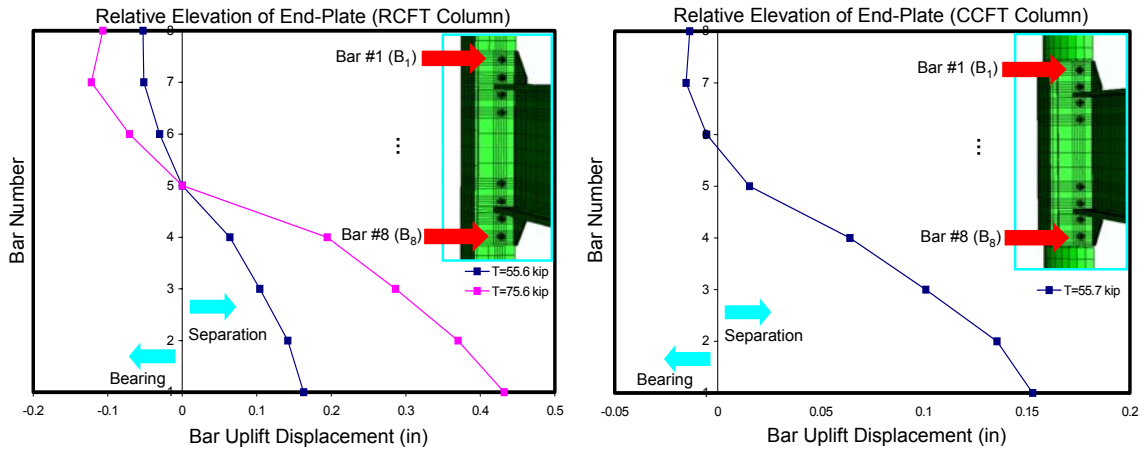


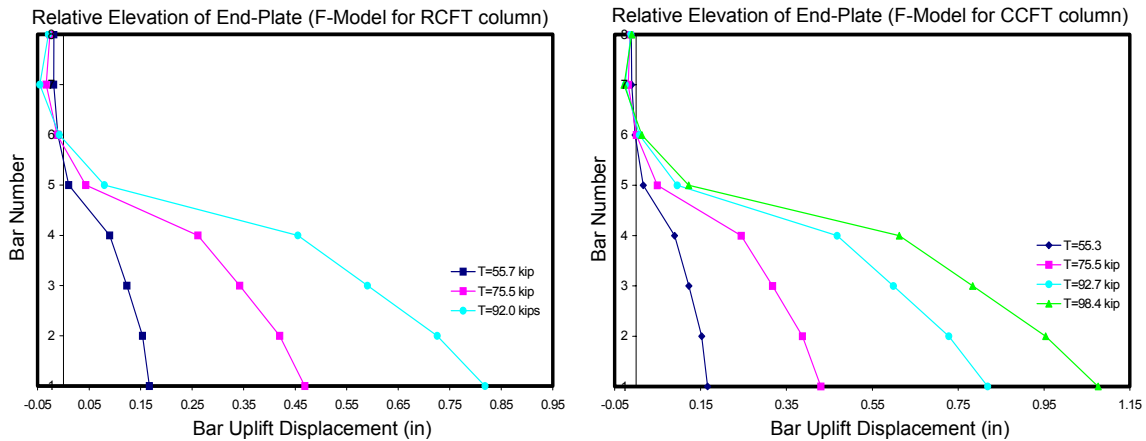
Figure 5.43 Panel zone behavior of the end-plate connections

The bar force and deformation are the major contributing parameters to connection performance. Relative separation of the end-plate from the column face was estimated by subtracting the PZ deformation at the “P2” point (See Figure 4.10) from the displacement of the bar head (Figure 5.44). This separation for the tension bars (ranging from bar number 1 (B_1) to bar number 4 (B_4)) appears to be fairly linear, indicating that the end-plate is basically a rigid plate as assumed in design. While the maximum separation distance is observed at bar number 1 (B_1), the maximum bearing effect is observed in bar number 7 (B_7). Foundation spring models show more bar uplift (30%), less penetration, and a more linear distribution of uplift than the detailed (damaged concrete plasticity

models) models. The more reasonable distribution of the displacements found from the models with the foundation strings was a powerful motivator for selecting this option for most analyses.



(a) Relative elevation of end-plate at the CFT column model made by the concrete damaged plasticity (RCFT,CCFT)

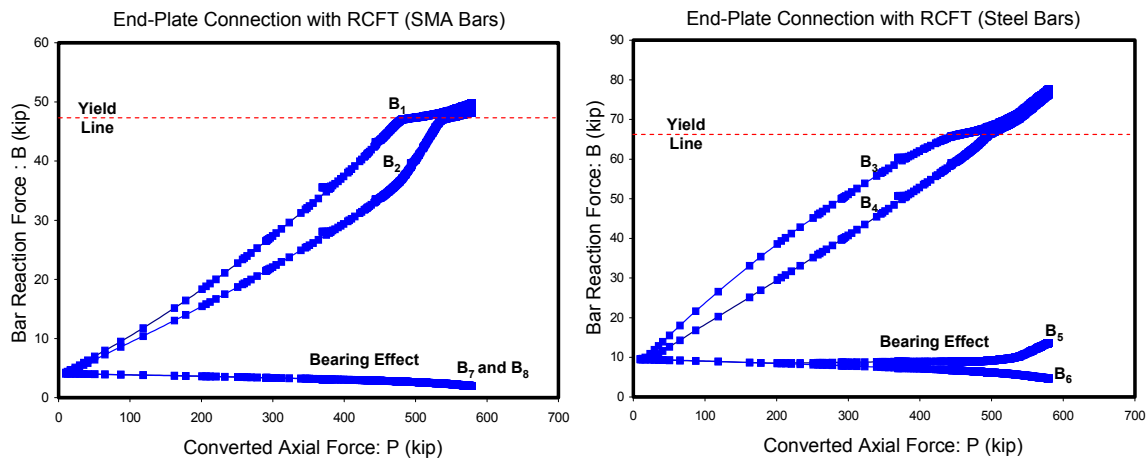


(b) Relative elevation of end-plate at the CFT column model made by the foundation springs (.F-RCFT, F-CCFT)

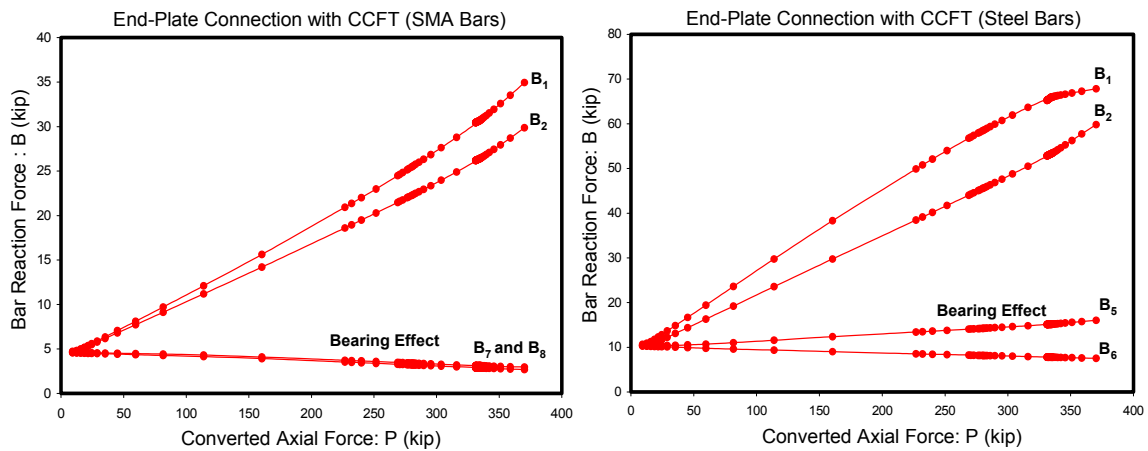
Figure 5.44 Measurement of end-plate uplift displacement at location of tension bars

Forces in the tension bars for the end-plate connections are shown in Figure 5.45. As the total applied force increase, the reaction force in the SMA and steel bars subjected to the tension (i.e. from B_1 to B_5) also increases. Note that only a very slight amount of precompression was present at the beginning of the load history. The bars were not intended to mimic the typical fully-tightened bolt situation, in which the initial pretension would be much higher (close to yield).

The relative elevation of the tension bars aligned above the centerline show the linear slope at each loading step. It is caused by the rigid end-plate effect due to the thick thickness of end-plate component. Though the axial force is increasing, the bearing causes the bars aligned below the centerline (except for B₅) to reduce the bar force to a value lower than the initial pretension force. The B₇ bars shows the maximum bearing effect as given in Figure 5.44, so the moment arm distance (h_i) is taken from this position. The internal moment can be computed by the summation of bar reaction force times its moment arm distance.



(a) Reaction force of tension bars in the end-plate connection with RCFT columns



(b) Reaction force of tension bars in the end-plate connection with CCFT columns

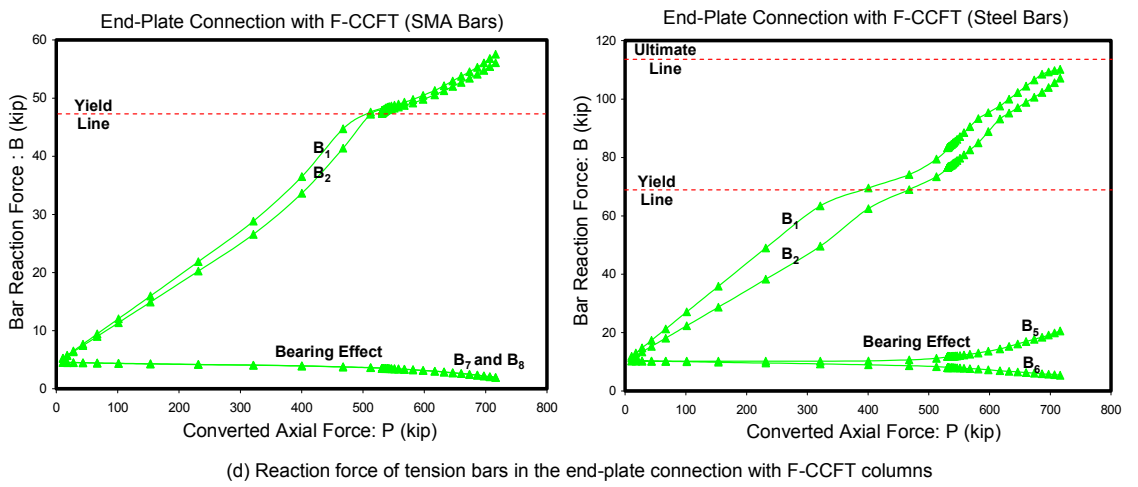
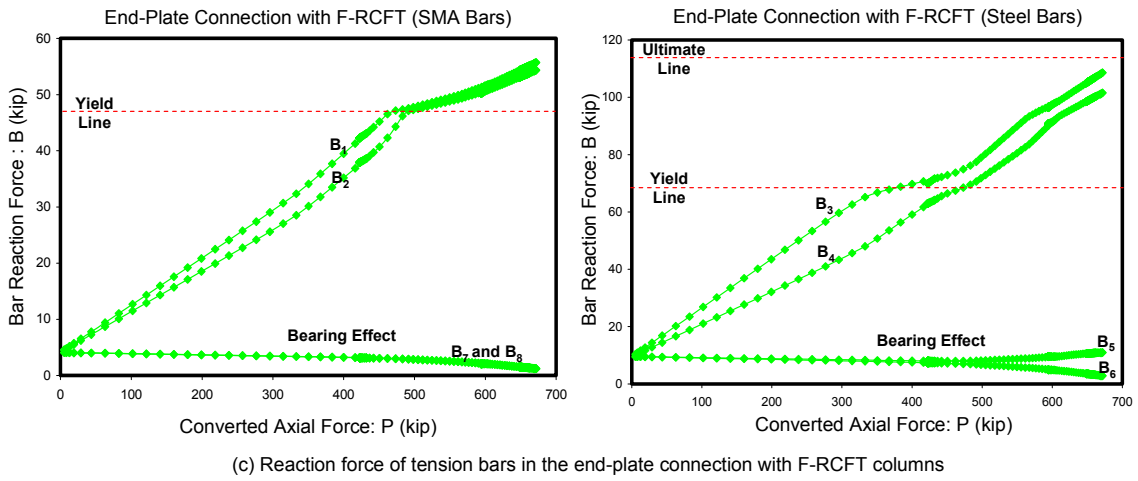
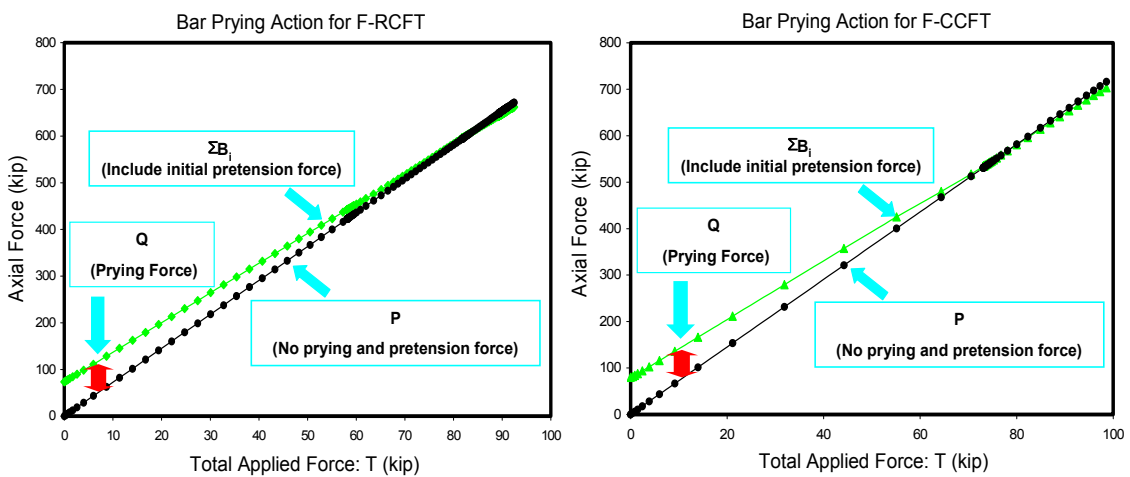


Figure 5.45 Reaction force of tension bars in the end-plate connections



The prying response for the bars in the end-plate connections is shown in Figure 5.46. At the beginning of the loading step, the summation of bar reaction forces, except for tension bars under the bearing area, corresponds to the summation of the converted axial force and prying force ($\sum B_i = P+Q$). However, the effect of prying force is negligible after the force in the tension bars exceeds their yield force. Without the initial pretension of tension bars, the summation of bar reaction force is equal to the converted axial force ($\sum B_i = P$).

This bar prying response has an influence on both the external moment ($M=TL$) and the internal moment ($M = \sum B_i h_i$). Comparisons between the external moment and the internal moments are given in Table 5.8. The prying forces causes the slightly difference shown in the table between the two moments.

Table 5.8 Comparisons between external moment and internal moment including prying response (End-plate connection)

T	P=M/d	$\sum B_i (i=1 \text{ to } 5)$	M = TL	M = $\sum B_i h_i$
55.6 kip	401 kip	421 kip	9840 kip-in	10060 kip-in
75.5 kip	551 kip	554 kip	13500 kip-in	13350 kip-in
92.1 kip	668 kip	660 kip-in	16400 kip-in	15940 kip-in

(a) End-plate with F-RCFT column case

T	P=M/d	$\sum B_i (i=1 \text{ to } 5)$	M = TL*	M = $\sum B_i h_i$
56.3kip	400 kip	420 kip	9820 kip-in	10010 kip-in
75.2 kip	547 kip	548 kip	13400 kip-in	13200 kip-in
92.7 kip	674 kip	667 kip	16500 kip-in	15960 kip-in
98.6 kip	716 kip	704 kip	17600 kip-in	16980 kip-in

L*: Distance from the tip of the beam to the centerline of the CFT column

(b) End-plate with F-CCFT column case

5.3.2 T-Stub Connections

The forces and deformations for two T-stub connections are shown in Figure 5.47.

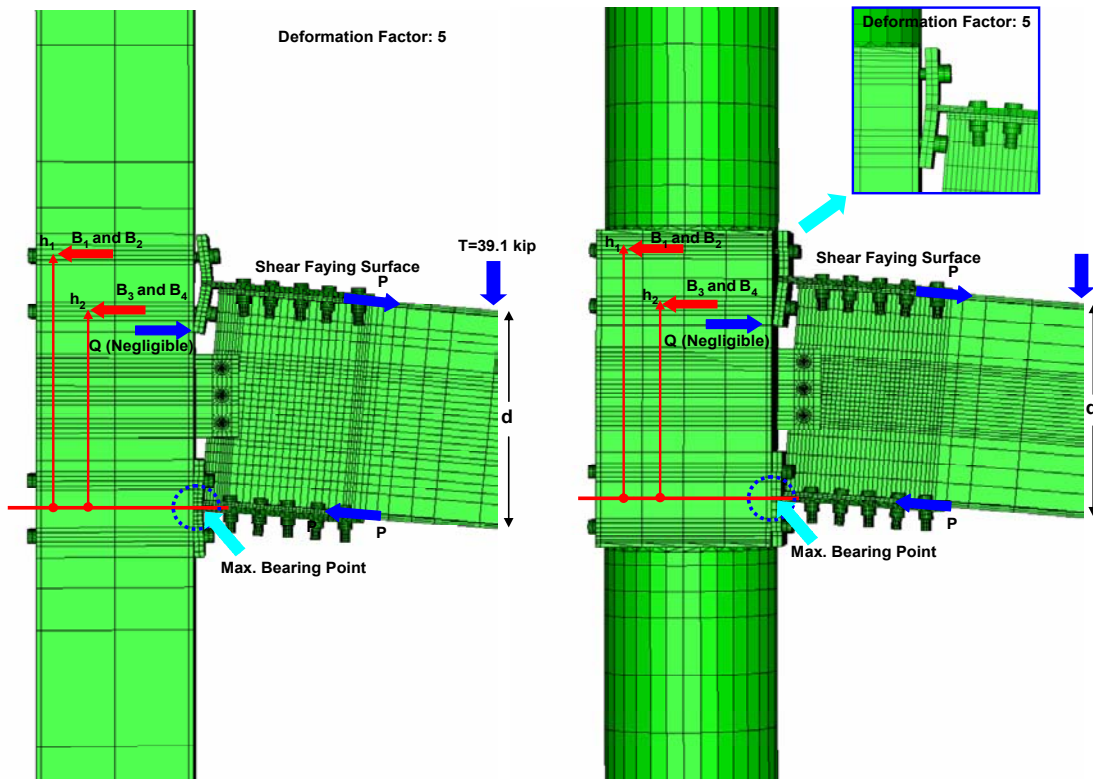
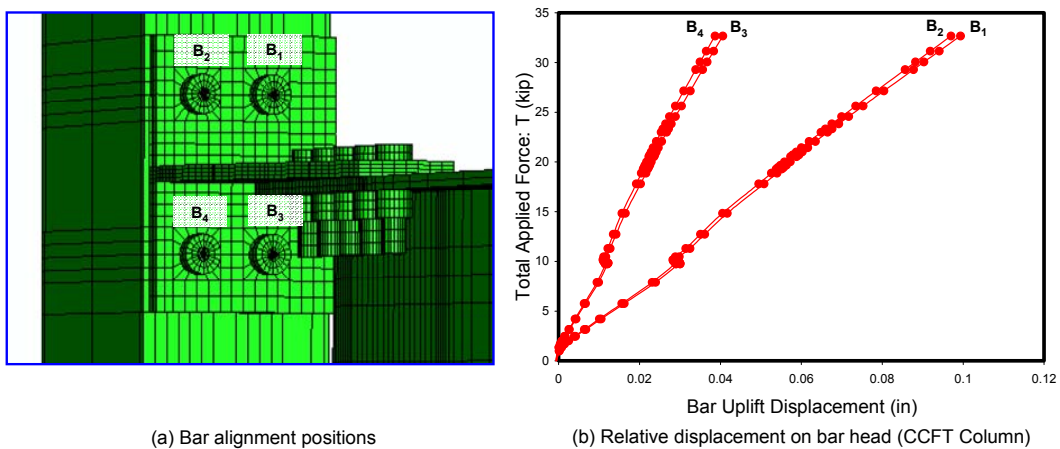


Figure 5.47 Reaction force and deformation for T-stub connections subjected to the maximum force (T) at the tip of beam

T-stub connections were designed with four bars on each row. Bars at the same height show almost identical behavior as shown in Figure 5.48, so tension bars aligned on the same row can be modeled as one equivalent bar by using the parallel system.



(a) Bar alignment positions

(b) Relative displacement on bar head (CCFT Column)

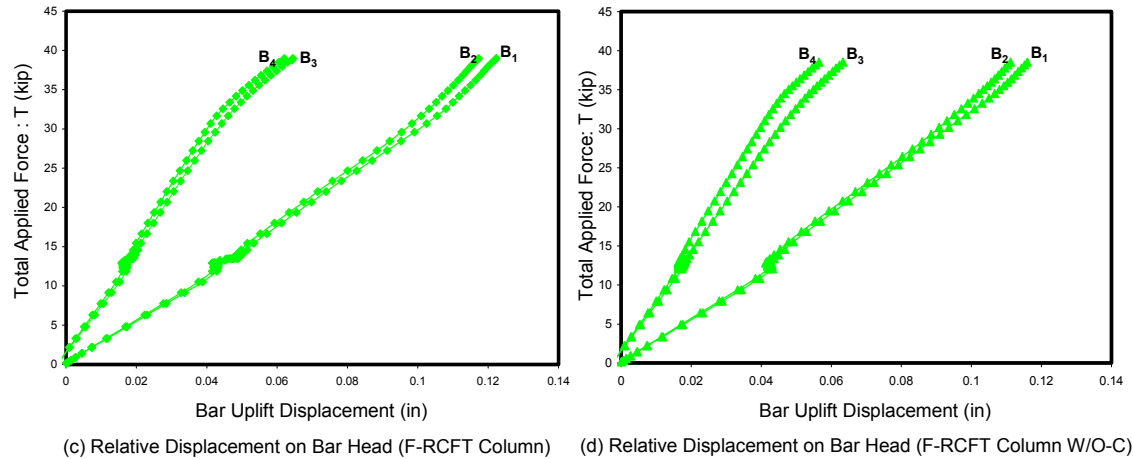


Figure 5.48 Bar alignment position and bar uplift displacement

The force and deformation of T-stub connection components are given in Figure 5.49. The behavior of the T-stub located above the centerline and subjected to the tension force is depicted on the domain with both positive axes, while that of T-stub located below the centerline subjected to the bearing force is depicted on the domain with both negative axes. The shear bolts are perfectly aligned in the center of the bolt holes and these bolt holes are drilled 1/16" larger than the diameter of the shear bolts. The plateau shown in Figure 5.49 (b) indicates the slip along this tolerance distance until the shanks of the shear bolts contact the edge of the bolt holes. At the end of the plateau, the slope increases again due to the effect of bearing. Generally, the slip behavior is symmetrical and the bearing effect is dominant in the T-stub below the centerline of the beam (See Figure 5.49 (b) and Figure 5.49 (c)). The total displacement for the components shown in Figure 5.49 (a) is mostly the result of the addition of the slip distance (Figure 5.49 (b)) and T-stub deformation (Figure 5.49 (c)); These two components are in series and their contributions are directly additive. The PZ behavior shown in Figure 5.49 (d) indicates that the T-stub connection with CCFT column has a steeper initial slope than that with RCFT column because of the larger size of that PZ.

The T-stub connection share the same trends for the bar force and prying response as the end-plate models (See Figures 5.50 and 5.51 and Table 5.9).

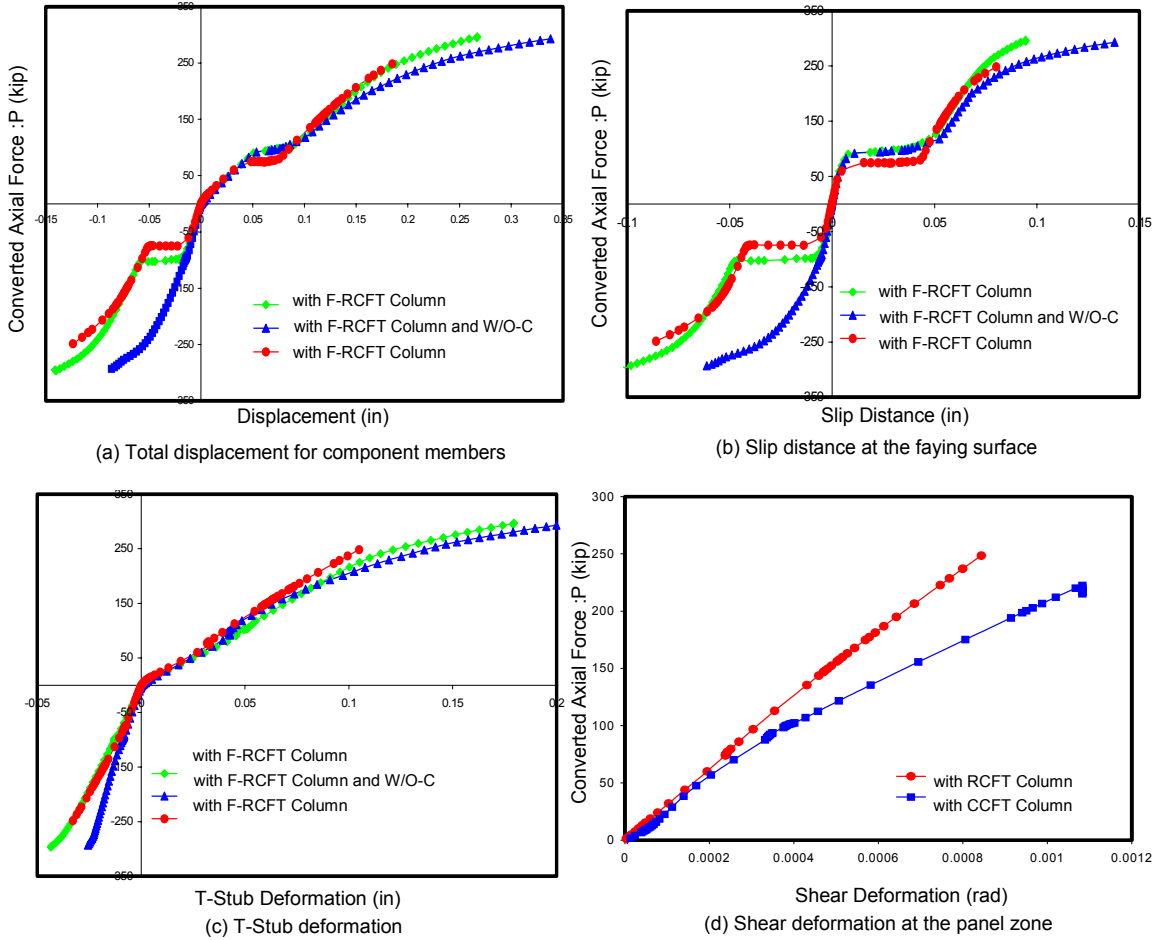
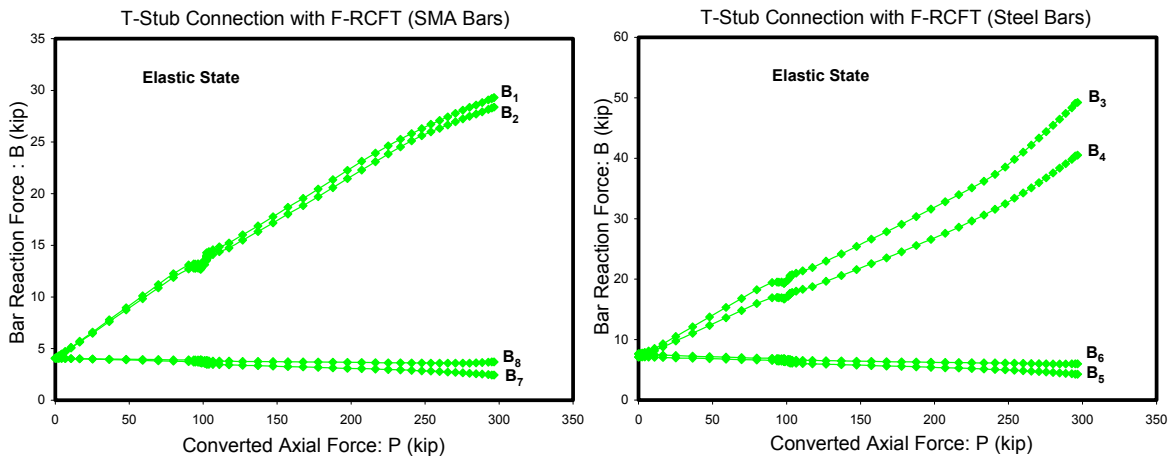
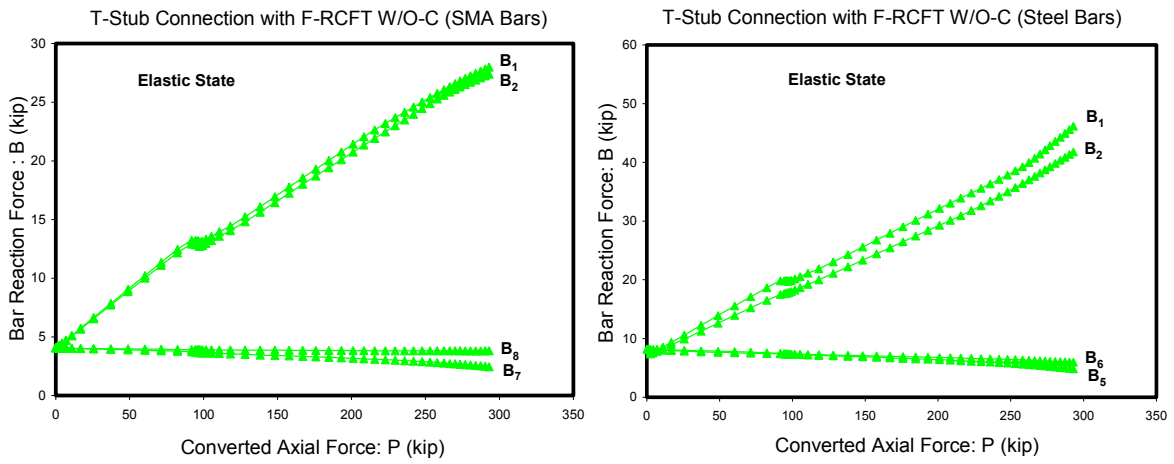
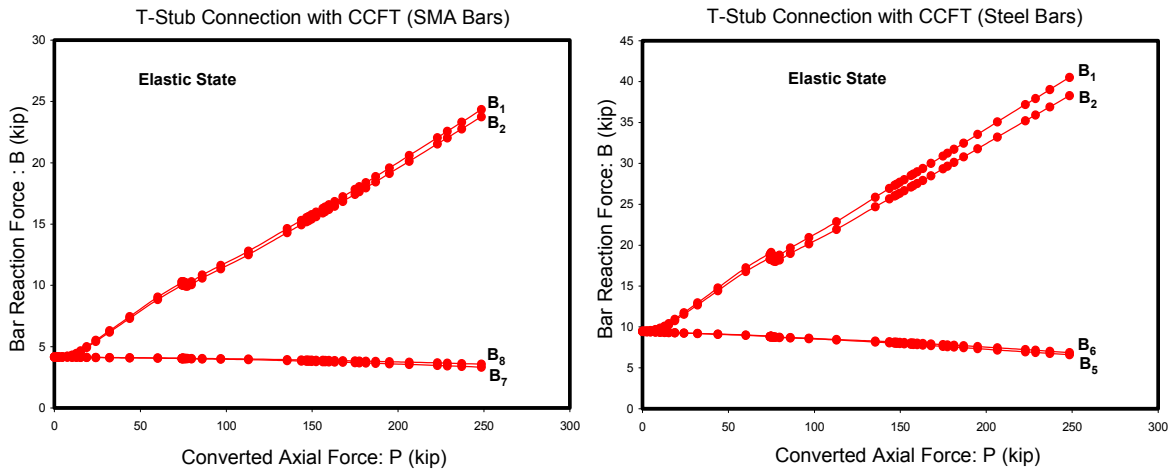


Figure 5.49 Force and deformation of T-stub connection components



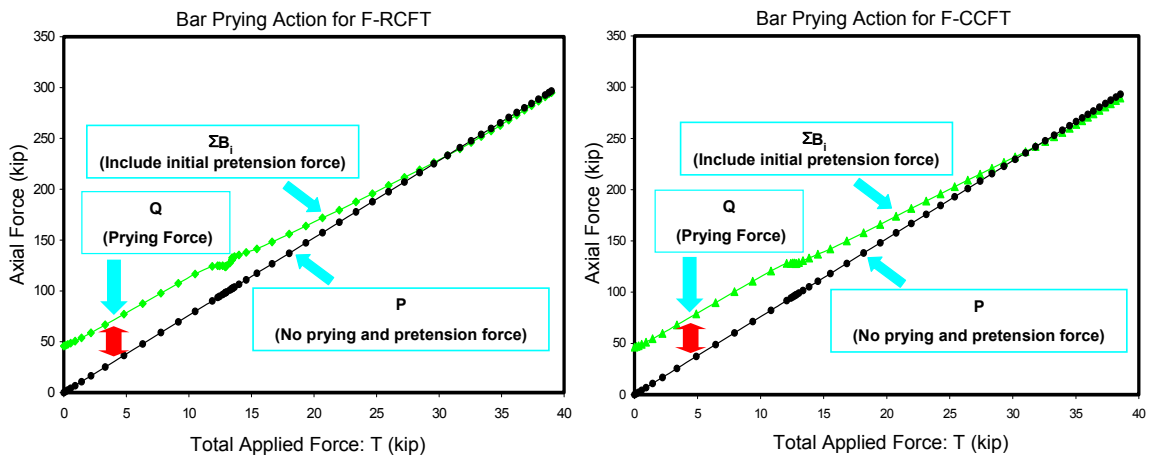


(b) Reaction force of tension bars in the T-stub connection with F-RCFT columns and without clearance



(c) Reaction force of tension bars in the T-stub connection with CCFT columns

Figure 5.50 Reaction force in tension bars of the T-stub connections



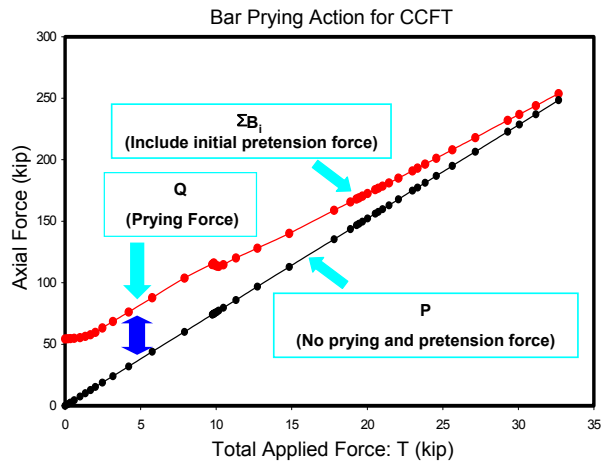


Figure 5.51 Bar prying response for the end-plate connections

Table 5.9 Comparisons between external moment and internal moment including prying response (T-stub connection case)

Case	T	P=M/d	ΣB_i	M = TL	M = $\Sigma B_i h_i$
with F-RCFT	38.8kip	296 kip	294 kip	6900 kip-in	6920 kip-in
with F-RCFT W/O C	38.5 kip	293 kip	287 kip	6860 kip-in	6740 kip-in
with RCFT	32.7kip	248kip	265 kip	5840kip-in	6231 kip-in

5.3.3 Clip Angle Connections

The forces and deformations for two clip angle connections are shown in Figure 5.52. The maximum bearing point occurs near the middle of the clip leg thickness. Forces and deformations for the components are given in Figure 5.53. The behavioral characteristics of clip angle connections have much in common with those of T-stub connections.

The forces in the bars and bar prying response for the clip angle connection are given in Figure 5.54. At the beginning of the loading step (P1), the effect of prying response due to the initial pretension is dominant. The prying force is negligible and the summation of the bar reaction forces is corresponding to the applied axial force ($\sum B_i = P$) at the P2 loading.

After these points (P3 and P4), the axial force is larger than the summation of bar forces in order to keep the equilibrium as the tension bars are aligned in only one row above the beam flange. Comparisons between external moment and internal moment including prying response are given in Table 5.10.

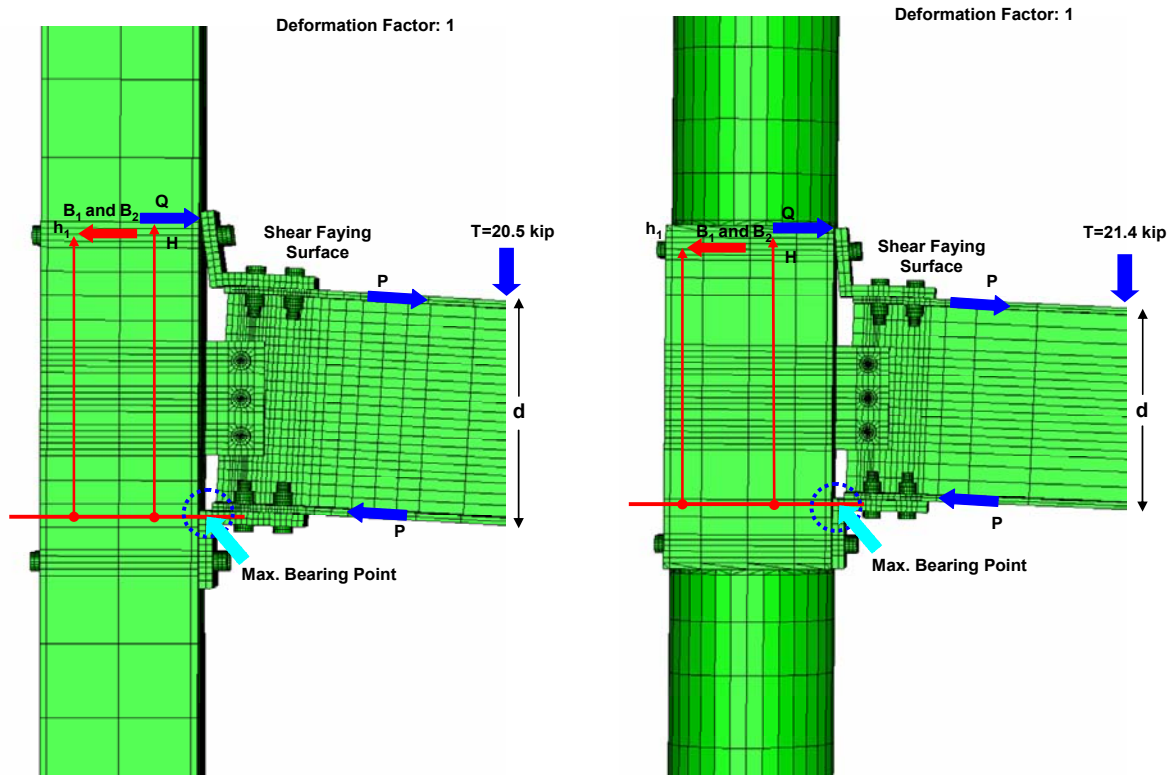


Figure 5.52 Reaction force and deformation for clip angle connections subjected to the maximum force (T) at the tip of beam

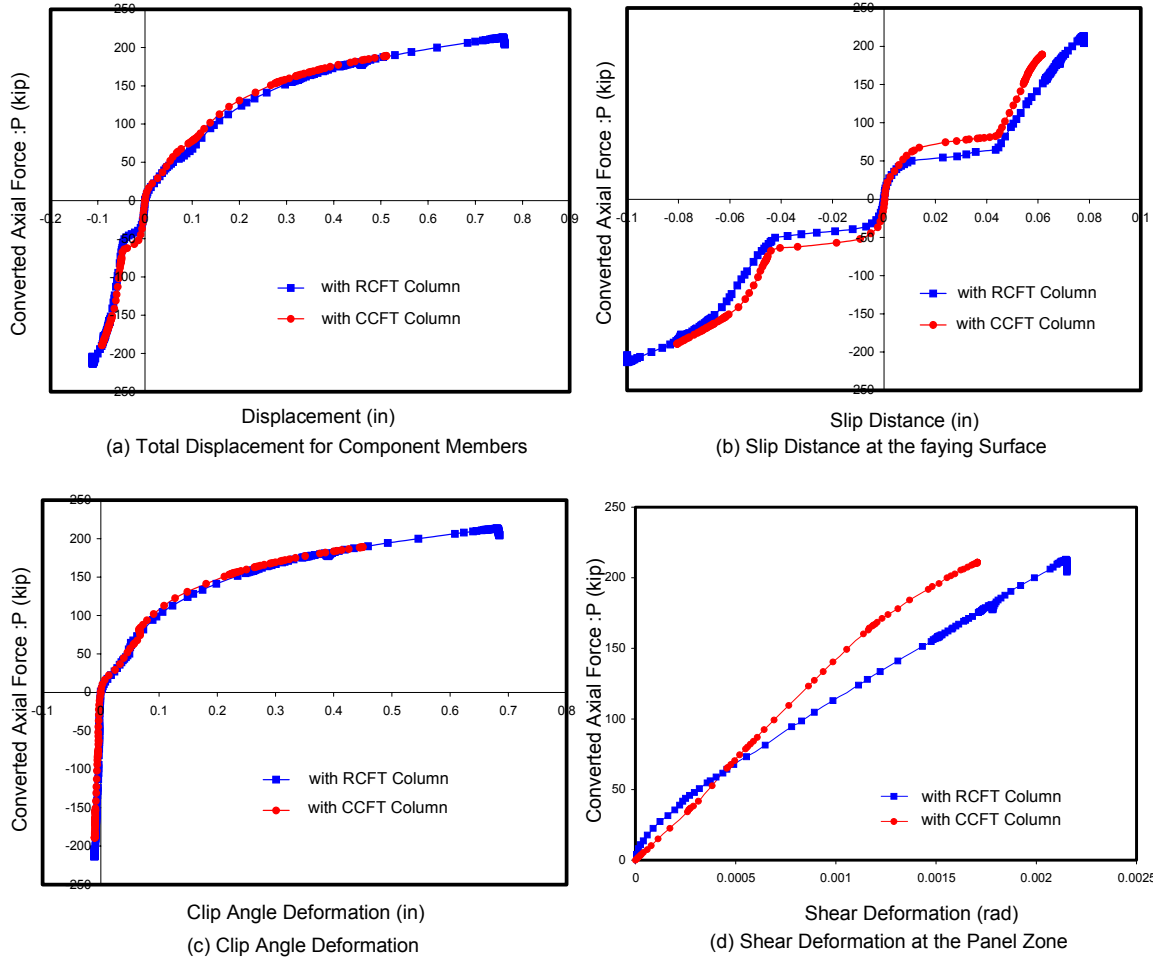


Figure 5.53 Force and deformation of clip angle connection components

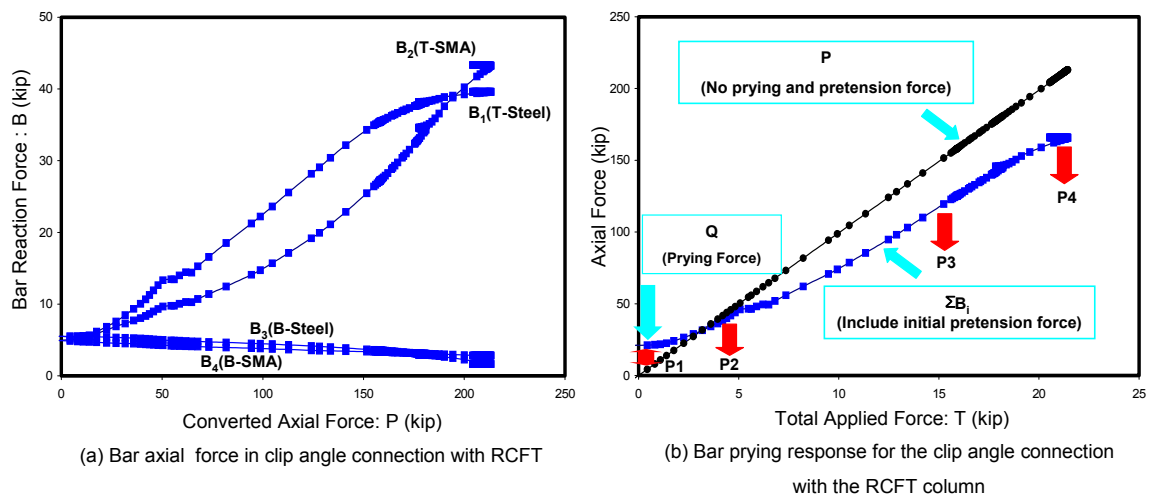


Figure 5.54 Bar prying response of the clip angle connection

Table 5.10 Comparisons between external moment and internal moment including prying response (Clip angle connection case)

Period	T	P=M/d	ΣB_i	Q =RF(ABAQUS)	M = TL	M = $\Sigma B_i h_i$ -QH
P1	0.00kip	0 kip	21.04 kip	18.24 kip	0 kip-in	61.8 kip-in
P2	3.95 kip	39.3 kip	36.22 kip	5.04 kip	708 kip-in	698 kip-in
P3	15.20 kip	152.0 kip	122.1 kip	3.57 kip	2730 kip-in	2692kip-in
P4	21.4 kip	213.1 kip	166.7 kip	1.56 kip	3840 kip-in	3760 kip-in

The failure modes and pictures listed on Figure 4.9 for all three connections will be investigated in this section. As the moment increases, the stresses were monitored at the measuring points given in Figures 4.14 to 4.16.

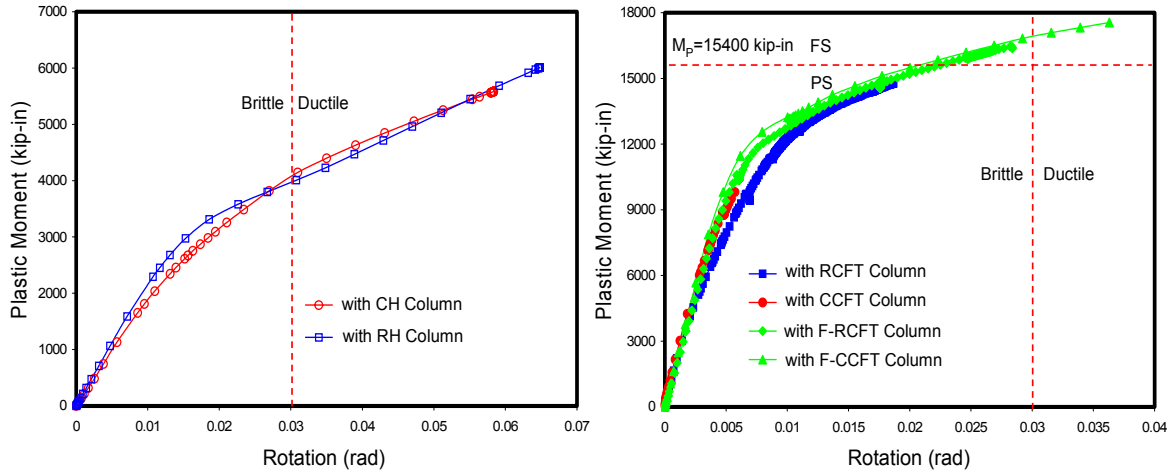
5.4 Observations of Failure Modes

5.4.1 Basic Concepts

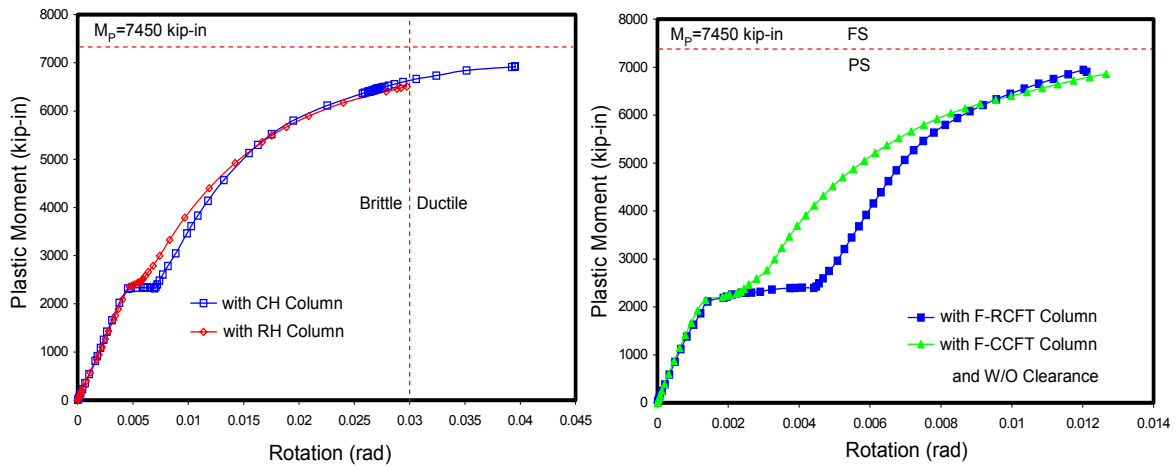
Both the ultimate strength and the rotational capacity of the connections are related to complex failure modes that combine several basic mechanisms. However, the design procedures are governed by a single idealized failure mode. Based on the results of the numerical analyses, the ideal connection design is one in which the design strength is governed by the yielding of the beam, followed by the yielding of other component members, and finally by the fracture at very large deformations. This situation will provide the extra strength to resist the unpredictable seismic demands and the balanced behavior to maximize the deformation capacity after first yielding occurs.

As far as strength is concerned, connections are classified as either full strength (FS) or partial strength (PS) depending on whether they can transmit the full plastic moment ($M_{p,beam}$) of the beam. FS connections take advantage of the ideal yielding mode of beam hinging. The classification and moment-rotation curves for all connection models is shown in Figure 5.55. The nomenclature and basis for this classification are given in Chapter 1. The plastic rotation is obtained by subtracting the elastic rotation from the total rotation (See Appendix C). The design strength of all connection models was based on the full plastic moment of the beam. However, the connection models with the hollow tube section column did not exceed the full plastic moment due to local buckling. For some models with CFT columns, the analysis stopped before reaching the full plastic moment because of numerical problems with the concrete model. The column

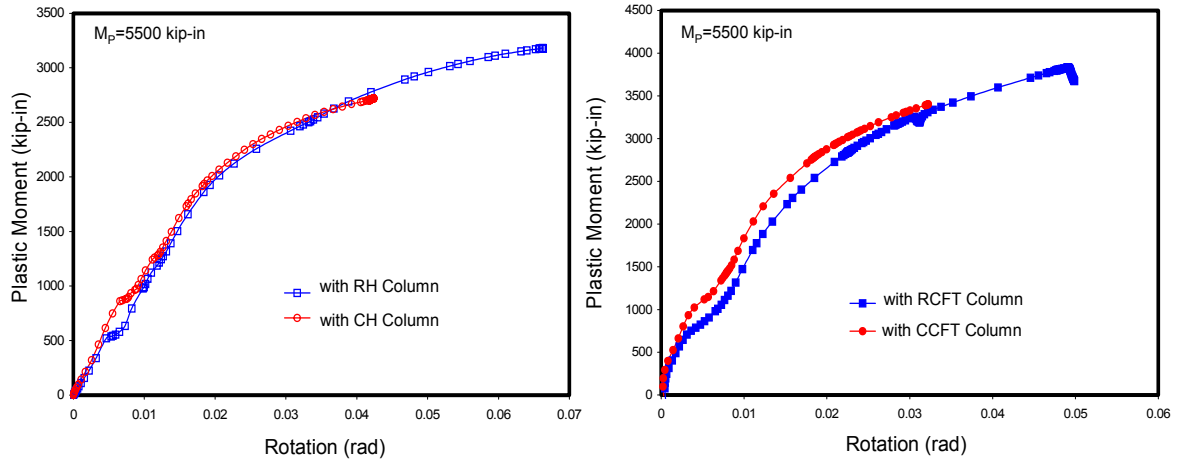
deformation underneath bar heads subjected to the largest bearing force was measured in order to check crippling as shown in Figure 5.56. Note the large difference in the vertical scales (a factor of 8) in Figure 5.56. Excessive deformations of the hollow section tube column degrade the ultimate strength capacity.



(a) Plastic moment and rotation of the end-plate connections

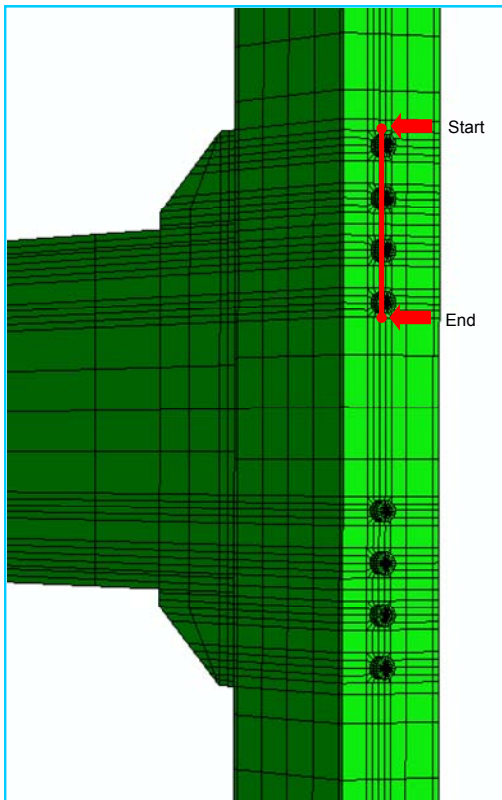


(b) Plastic moment and rotation of the T-stub connections

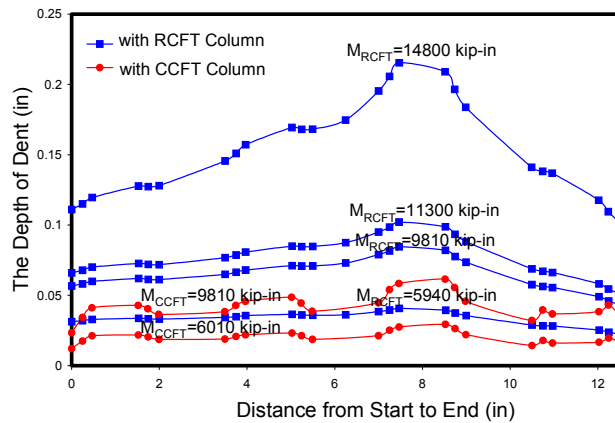
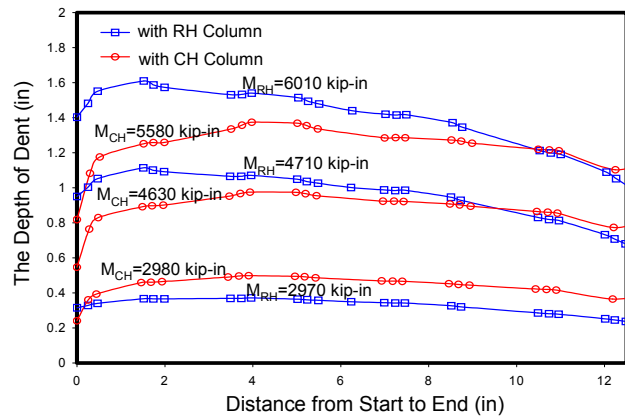


(c) Plastic moment and rotation of the clip angle connections

Figure 5.55 Plastic moment and rotation curves for the connections



(a) The position for the measurement line



(b) The deformations along the measurement line

Figure 5.56 Investigation of local buckling from deformation measurements

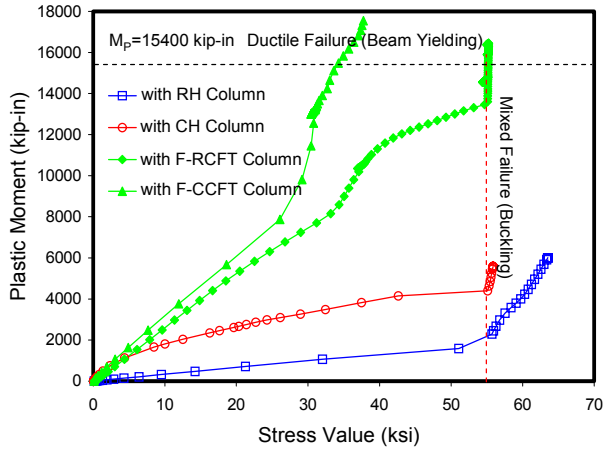
5.4.2 Classifications of Failure Modes

The Von-Mises stress at the column surface, steel tension bars, SMA tension bars, angle, plate, and beam were measured and are given in Figures 5.57 to 5.59. In Figures 5.57 to 5.59, limit states domains calculated from simplified assumptions are also shown. The domains are ductile, mixed, or brittle according to whether the yield or ultimate resistance are reached.

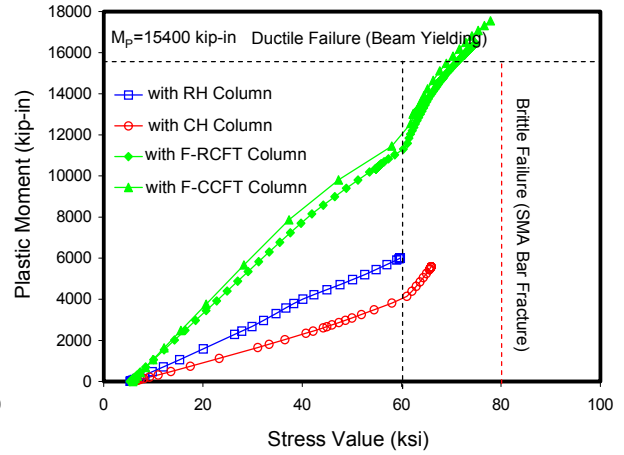
For example, in case of the end-plate connection with the RH column (Figure 5.57 (a)), the stress on the column surface (PS1, see Fig. 4.14) exceeded the yield stress well before the external moment reached the full plastic moment of the beam. This indicates a large local bending strain in the column flange due to the bearing from the bar; the lack of the concrete filling to prevent this behavior mode results in a premature failure (i.e. inability to reach $M_{p,beam}$ as shown in Fig. 5.57(a)). While, stresses on the steel tension bars (BS3 point) and beam (GS1 point) are still elastic and below the full plastic moment of the beam at the ultimate loading step. Therefore, the dominant failure mode of the end-plate connection with RH columns is defined as a mixed failure mode occurring at the panel zone (Refer to Figure 4.9 (a)).

For the end-plate connection with F-CFT column as another example, its Von-Mises stress on the column surface (PS1 point) did not enter the mixed domain at the ultimate loading step and finally enter the ductile domain determined by the beam yielding (See Figure 5.57 (a)). It also avoids passing the brittle domain of tension bars and enters the ductile domain as shown in Figure 5.57 (b) and (c). Therefore, the end-plate connections with F-RCFT column include the ductile failure mode which is one of the ideal failure modes.

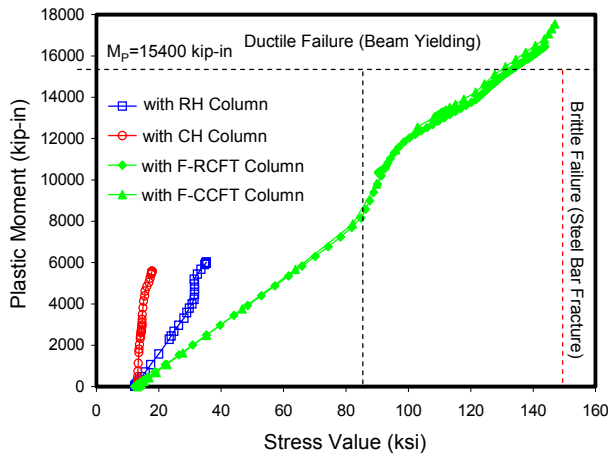
This methodology to determine the dominant failure mode can be applied to other connection models. In case of the connections with the hollow tube column, the stresses on the column surface only enter the mixed domain as shown in Figure 5.58 (e) and Figure 5.59 (c). However, the connections with either RCFT/CCFT column or F-RCFT/F-CCFT column include the stress path on the ductile failure domain or on the closest point to the limit state.



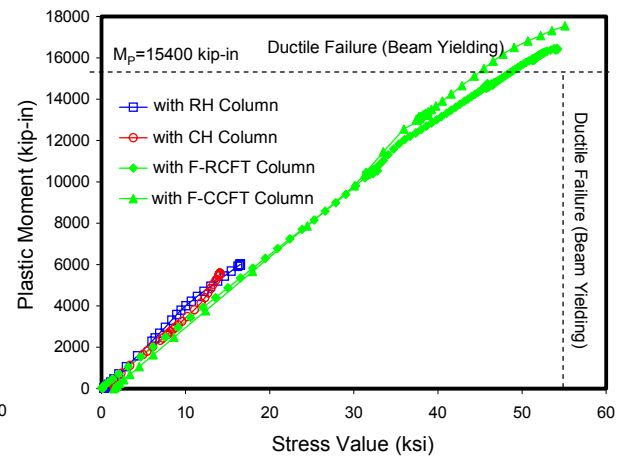
(a) The Von - Mises stress on the PS1 point



(b) The Von - Mises stress on the BS1 point

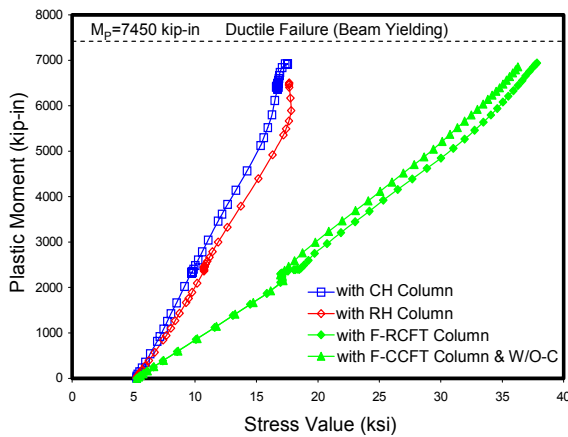


(c) The Von - Mises Stress on the BS3 point

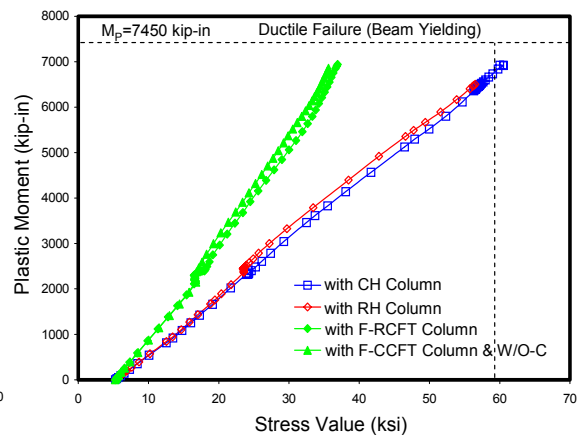


(d) The Von - Mises Stress on the GS1 point

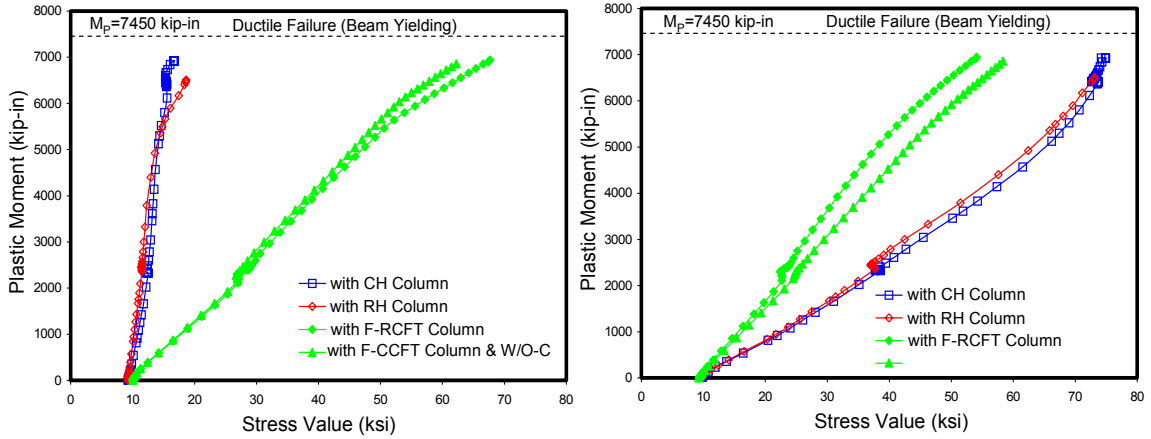
Figure 5.57 Failure modes for end-plate connections based on the stresses



(a) The Von - Mises Stress on the BS1 point

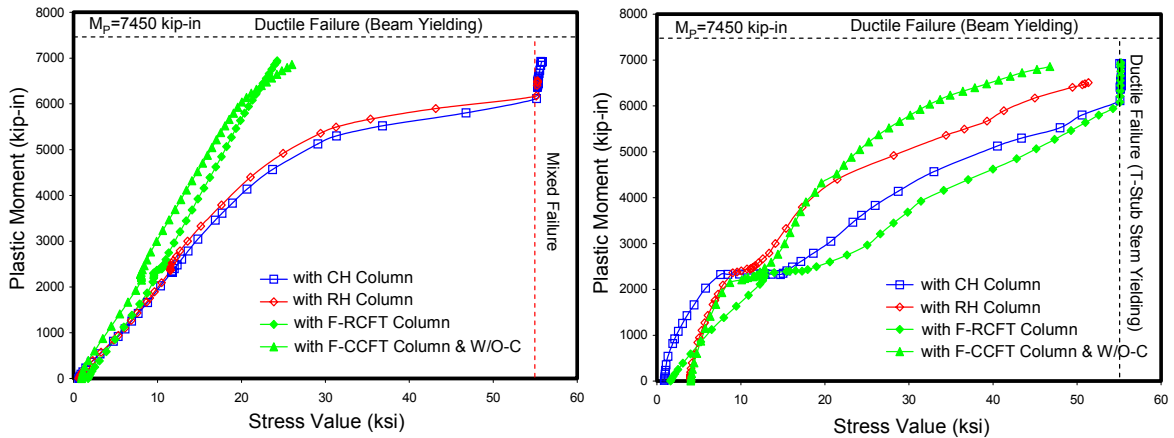


(b) The Von - Mises Stress on the BS2 point



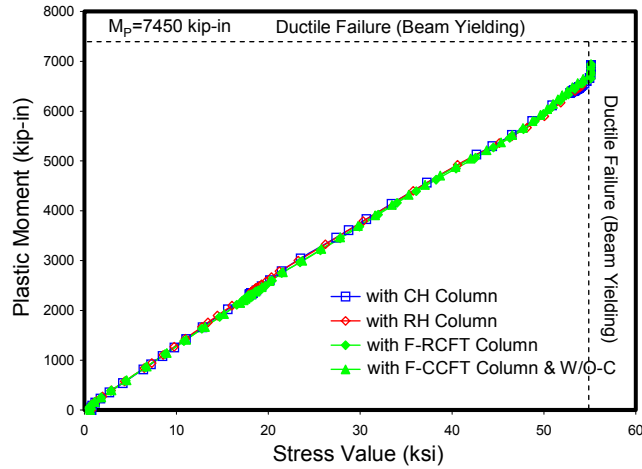
(c) The Von - Mises Stress on the BS3 point

(d) The Von - Mises Stress on the BS4 point



(e) The Von - Mises Stress on the PS1 point

(f) The Von - Mises Stress on the TS1 point



(g) The Von - Mises Stress on the GS1 point

Figure 5.58 Failure modes for T-stub connections based on the stresses

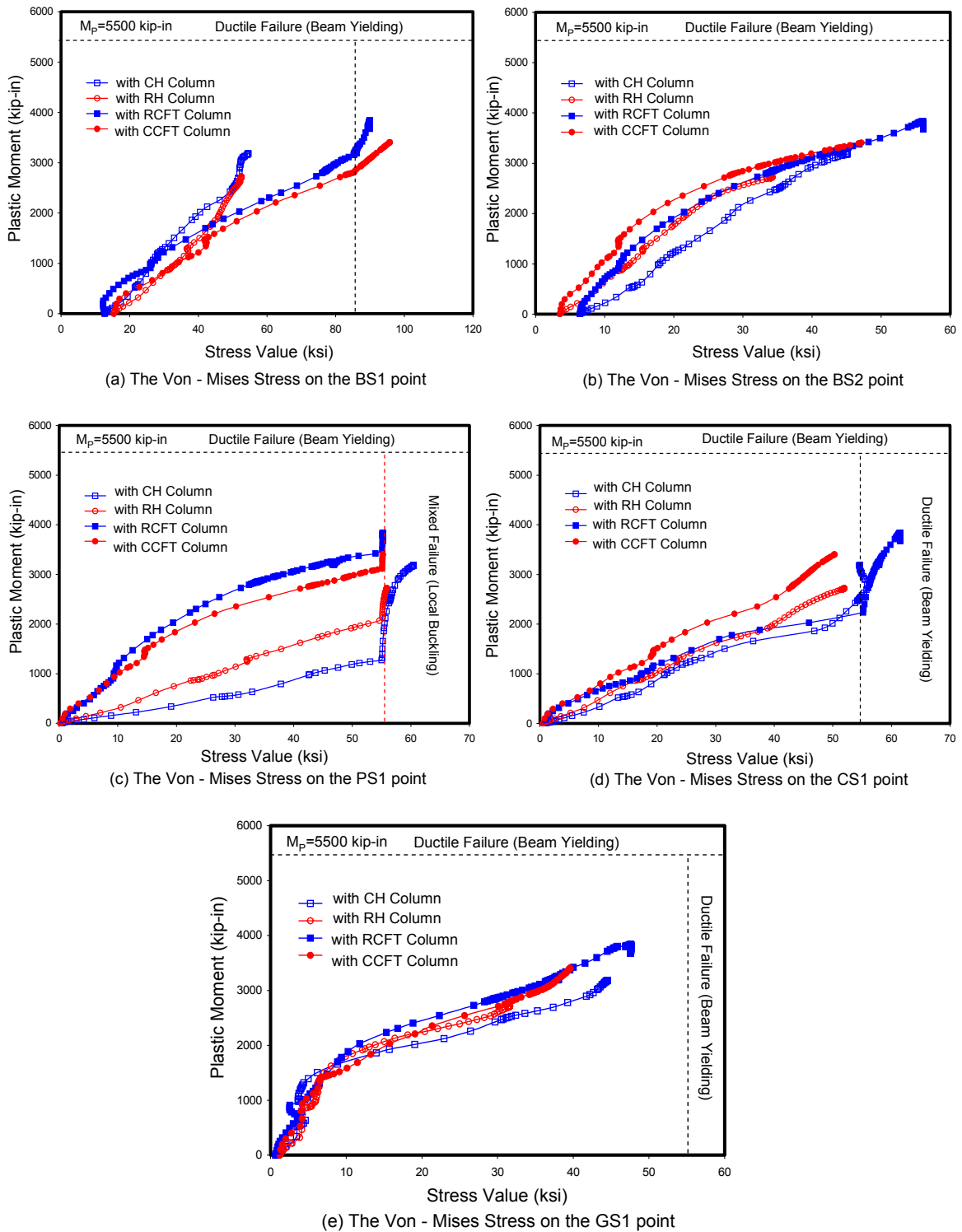


Figure 5.59 Failure modes for clip angle connections based on the stresses

5.5 Summary and Discussion

This chapter discussed the detailed FE analytical models and their results. The detailed modeling procedures were described in Section 5.1. The advanced modeling methods, such as the refined 3D elements, material models based on the 3D plasticity theory, initial pretension, and contact interaction contribute to producing behavior close to that of the real connection. This research depends on numerical “experiments” because of the absence of real test data. Through the FE “tests”, information on innovative structure performance can be obtained economically and efficiently as compared to a real experiment. The key is to have good information on component behavior and robust modeling.

The results of FE tests were described in Section 5.2. The connection models were investigated in terms of their moment vs. rotation behavior (See Figure 5.30). These curves reflect the strength, stiffness and deformation capacity of the connection. Extended end-plate connections have the largest strength. The existence of shear faying surface causes T-stub and clip angle connection to slip, resulting in lower stiffness but equal or greater deformation capacity.

Force and deformation of components were described in Section 5.3. This measurement provides data to calibrate the simplified stiffness models composed of spring elements that will be used in the next chapter.

The occurrence of yielding/failure modes was determined by the observation of the stresses at key measurement points. The methodology to decide the dominant failure mode was described in Section 5.4. All connection models were designed with the design strength based on the full plastic moment capacity of the beam in order to induce the ductile failure mode. This basic design axiom is supported by the measured stresses and strains.

Chapter 6

Connection Modeling under Cyclic Loads

This chapter will investigate analytically the cyclic behavior of the beam-to-column connections to CFT columns proposed in this research. Sections ranging from HSS 12X12X500 to 16X16X500 (RCFT) and from HSS14X500 to HSS18X500 (CCFT) were used in the studies. Based on the observations of the 3D refined FE models subjected to monotonic loads and presented in Chapter 5, simple beam-to-column joint models for the PR-CFT connections were constructed with the nonlinear finite element (FE) program OpenSEES (OpenSEES v. 1.7.3, 2006). These joint models are appropriate for use in 2D frame simulations to estimate the inelastic response of both connections and frames under cyclic loading. The primary objective is the development and implementation of simplified, numerically efficient, and robust joint models reflecting the real connection behavior.

This chapter will be divided as follows. The detailed modeling procedures for spring elements, including the inelastic response of the connection components, are described first (Section 6.1). A joint model is then constructed, consisting of components defined as spring elements. This assemblage of springs can then be modeled as a joint element in the nonlinear FE analyses of entire frames (Section 6.2). The results of cyclic analyses are shown next in and compared with those of selected experiments to verify the validity of the models (Section 6.3.). The next section describes parametric studies aimed at assessing the impact of the number of SMA tension bars (Section 6.4). Finally, a summary and conclusions of this chapter are presented (Section 6.5).

6.1 Joint Model

A frame structure should provide adequate stiffness, strength, and energy dissipation capacity to withstand the lateral as well as gravity loads. This must be achieved within allowable limits of deformation and strength. The dynamic random seismic inertial forces introduced into a building by an earthquake can be converted into the equivalent lateral loads for design. This approach accounts for seismic zoning, site characteristics, and

structural system and configuration at a level suitable for the preliminary sizing of structural members. Figure 6.1 shows the deformed shape for a typical moment frame building and corresponding beam-column sub-assembly under moderate to severe earthquake loading. Typically, the members are deformed in double curvature and the joints by shear as lateral loads dominate. In addition, the first mode is assumed to dominate behavior; higher modes are ignored in design. The modeling described in this chapter is meant to develop connection models that will speed up the non-linear analyses of frames subjected to this type of deformation pattern.

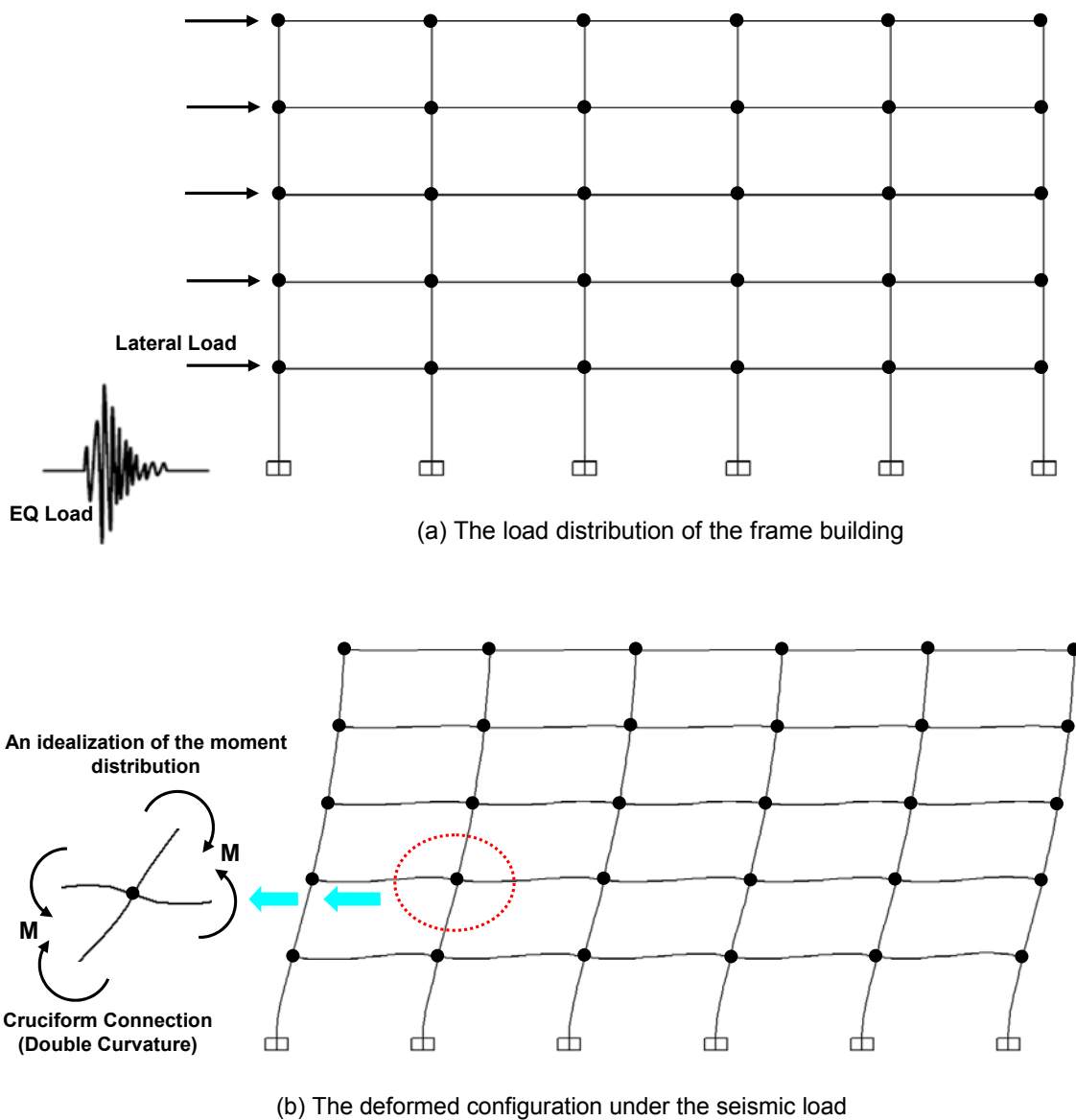


Figure 6.1 Load distribution and deformed configuration of the frame building

6.1.1 Joint Model of the End-Plate Connection

Figure 6.2 show the proposed 2 dimensional idealization for a simplified joint model for an end-plate connection. The connection components designed to yield, such as tension bars and the CFT panel zone, are converted into equivalent spring elements. The end-plate, which is designed as a rigid plate, is shown as rigid elements. Detail explanations on the assemblage of the joint models will be given in Section 6.2.

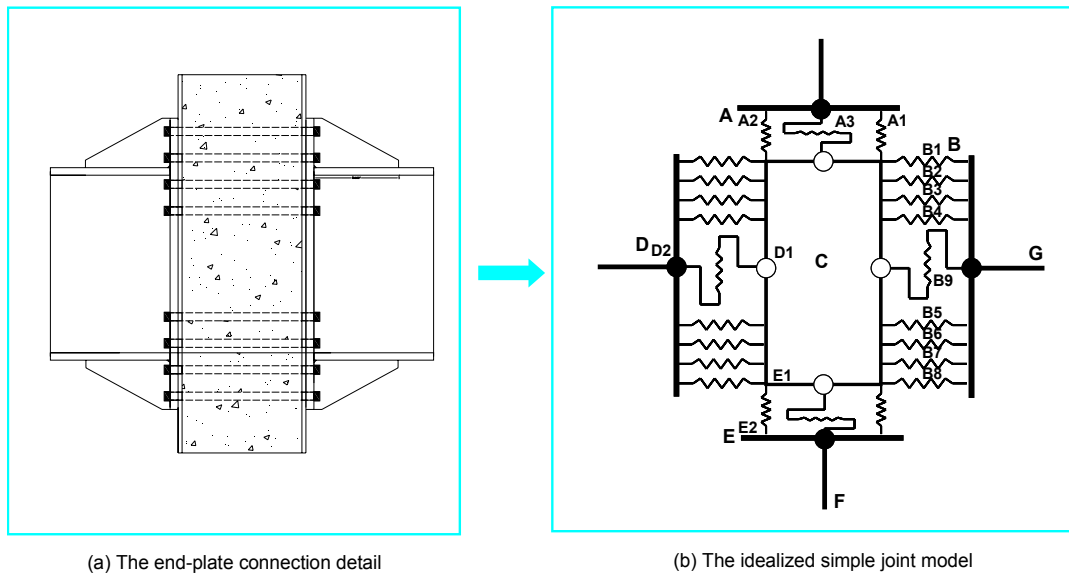


Figure 6.2 Idealized joint model of the end-plate connection

Figure 6.3 show the idealized force distribution at the perimeter of the joint for an end-plate connection subjected to seismic loads. Generally, the beam develops its flexural strength (i.e. plastic hinging) while the column carries the axial gravity loads elastically. These internal member forces are shown as equivalent concentrated forces acting on the joint (blue arrows in Figure 6.3 (a)). The internal reactions in the connection components act against these external forces (green arrows in Figure 6.3 (b)) in order to satisfy equilibrium.

The response of the joint element under the shear deformations resulting from the bending forces in the framing members is shown in Figure 6.4. It is deformed in a scissors-line manner. The internal tension loads are carried by tension bars, which correspond to the top springs on the right side of the connection as shown in Figure 6.4 (a). On the other hand, the internal compression loads resulting from the bearing forces

between the beam flange and the CFT column surface are transferred to the springs on the bottom right. The bars inside the compression zone do not make a significant contribution to the response mechanism of the joint model as shown in Figures 5.42 and 6.4. The end-plate is assumed to behave as a rigid plate, resulting in a linear strain pivoting about the center of bearing. The latter is determined from the advanced 3D analyses. For end plates, it tends to be lower than shown in the sketch.

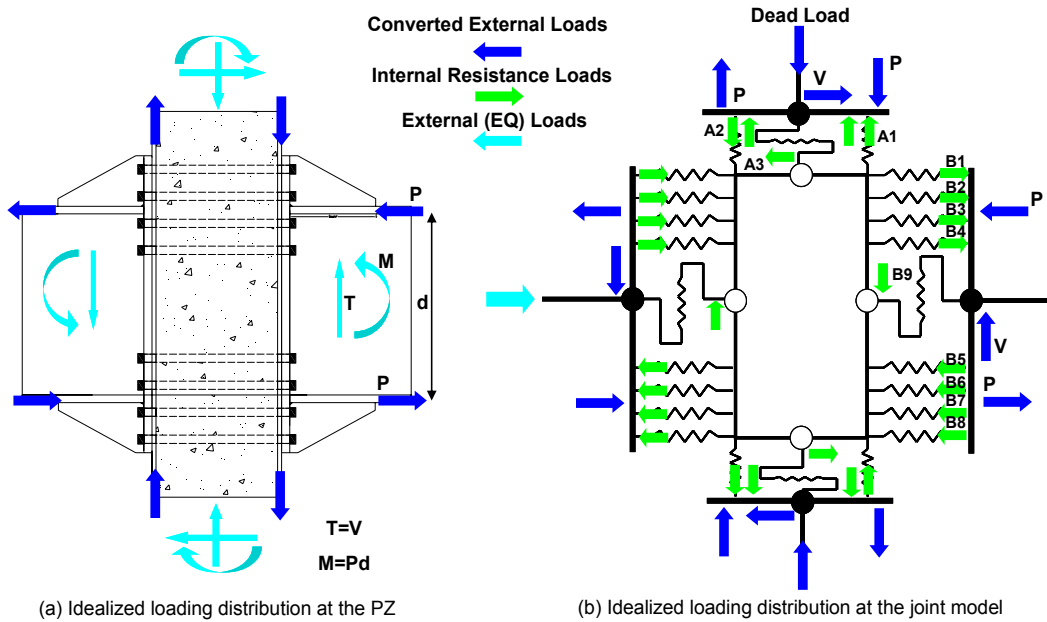


Figure 6.3 External and internal forces at the joint for the end-plate connection

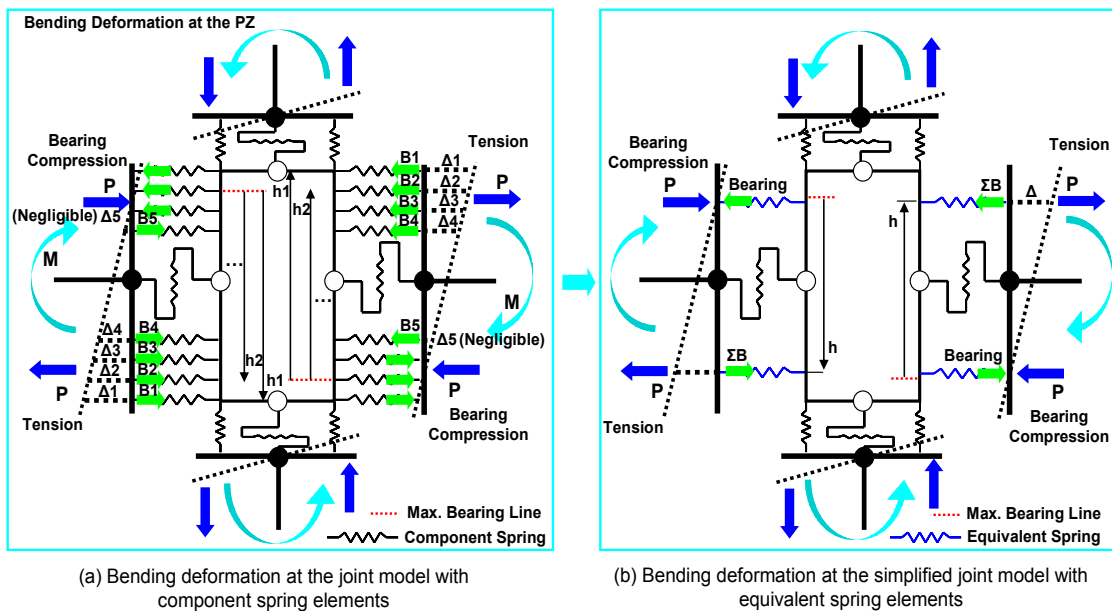


Figure 6.4 Response mechanism of the joint element under bending deformation

The assumptions about strain distribution, basic material stress-strain characteristics, and basic statics (equilibrium of the force resultants) provide the theoretical basis to condense the numerous springs in Figure 6.4(a) into single springs as shown in Figure 6.4 (b) and Figure 6.5. This parallel system is constrained to maintain force equilibrium between the summation of bar reaction force and the converted axial force ($P = \sum B$). The behavior under tension loading is determined by the theoretical equations shown in Figure 6.5 (b), while those under compression (bearing) are determined from observations of the 3D FE model described in Chapter 5. The behavior of the components is depicted in Figure 6.6. The behavior of the steel tension bars and that of the bearing component are generated by using the default material code in the program, with the SMA materials utilizing a user defined material code.

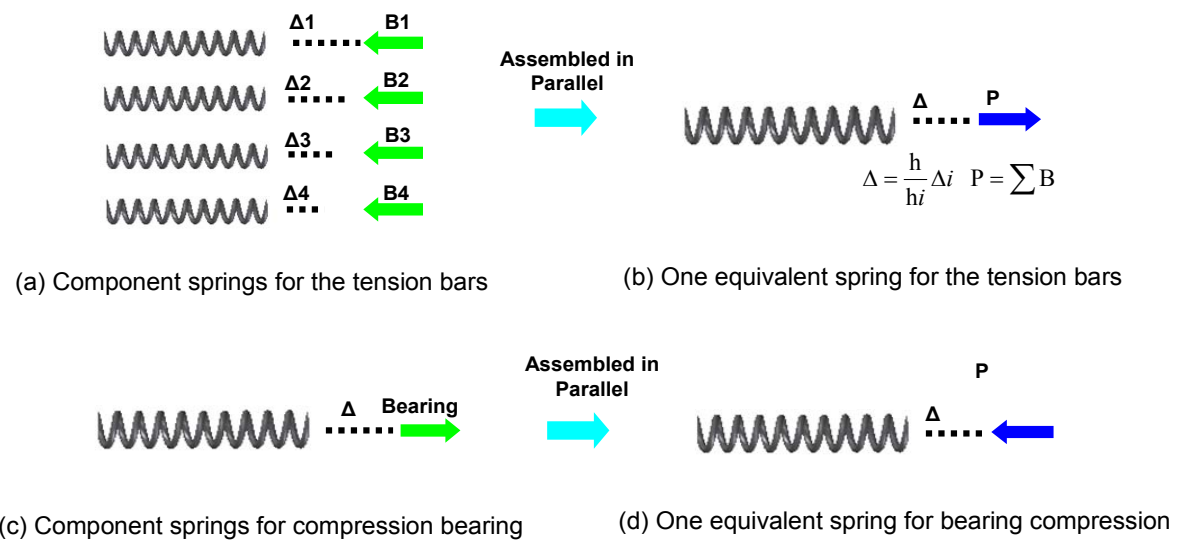


Figure 6.5 Assemblage procedure for spring elements

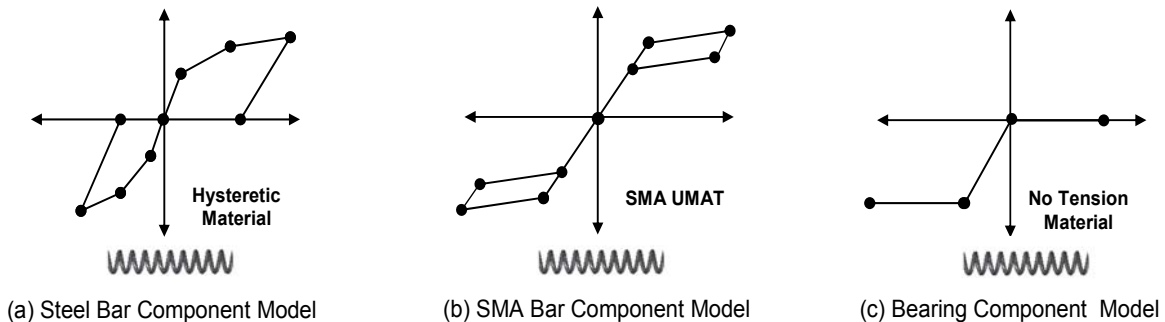


Figure 6.6 Properties of the individual component

An algorithm based on incremental displacement control is appropriate for the theoretical verification of the equivalent spring element formulation (Figure 6.7). For a given displacement of the equivalent spring element, the displacement of each component can be computed by using the simple geometric ratios

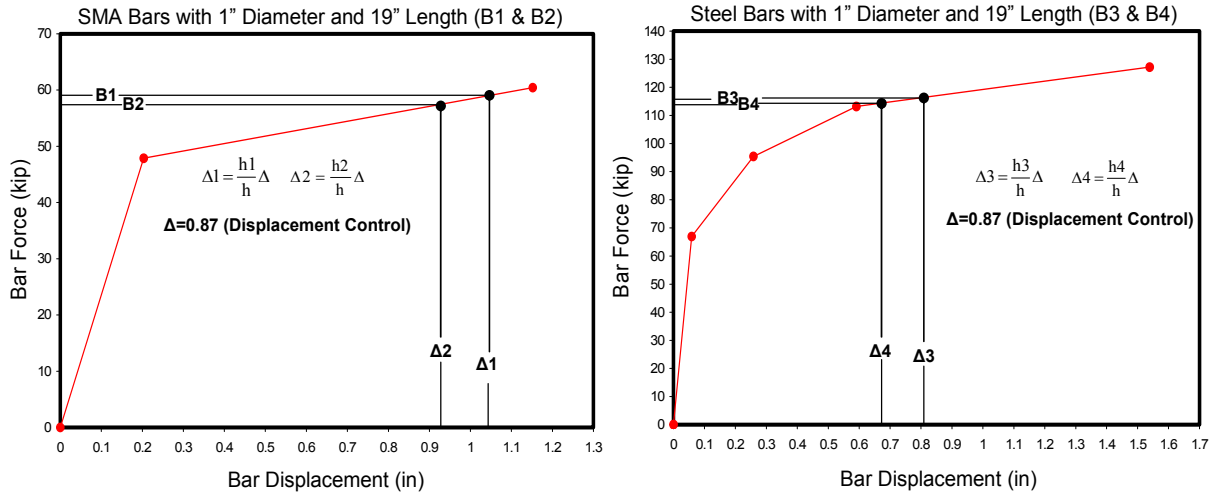


Figure 6.7 Algorithm for the formulation of an equivalent spring element

Comparisons between results of this simple algorithm and those of 3D FE model test (ABAQUS) are given in Table 6.1. The results show a good agreement. The cyclic response of the equivalent spring element is compared with the monotonic envelope from the 3D FE analyses in Figure 6.8. The test results from the 3D FE models show also good agreement with that of the equivalent spring element. In Figure 6.8, the behavior of the equivalent spring element under cyclic loading includes both the shape memory effect that reduces the permanent displacement as well as the effect of bearing.

Table 6.1 Comparisons between results of the simplified model and those of 3D FE

Basic	Algorithm (Δ, Displacement)	ABAQUS (Δ, Displacement)	Algorithm (B, Bolt Force)	ABAQUS (B, Bolt Force)
Δ=0.87"	Δ1=1.05"	Δ1=1.07"	B1=58.8 kip	B1=57.6 kip
	Δ2=0.93"	Δ2=0.96"	B2=57.3 kip	B2=56.2 kip
	Δ3=0.81"	Δ3=0.79"	B3=116.2 kip	B3=110.2 kip
	Δ4=0.68"	Δ4=0.63"	B4=114.5 kip	B4=117.2 kip
			P=2XΣB (i=1 to 4)=693	*2XΣB (i=1 to 4)=682

*2XΣB (i=1 to 5) obtained by ABAQUS analysis was 710 kip.

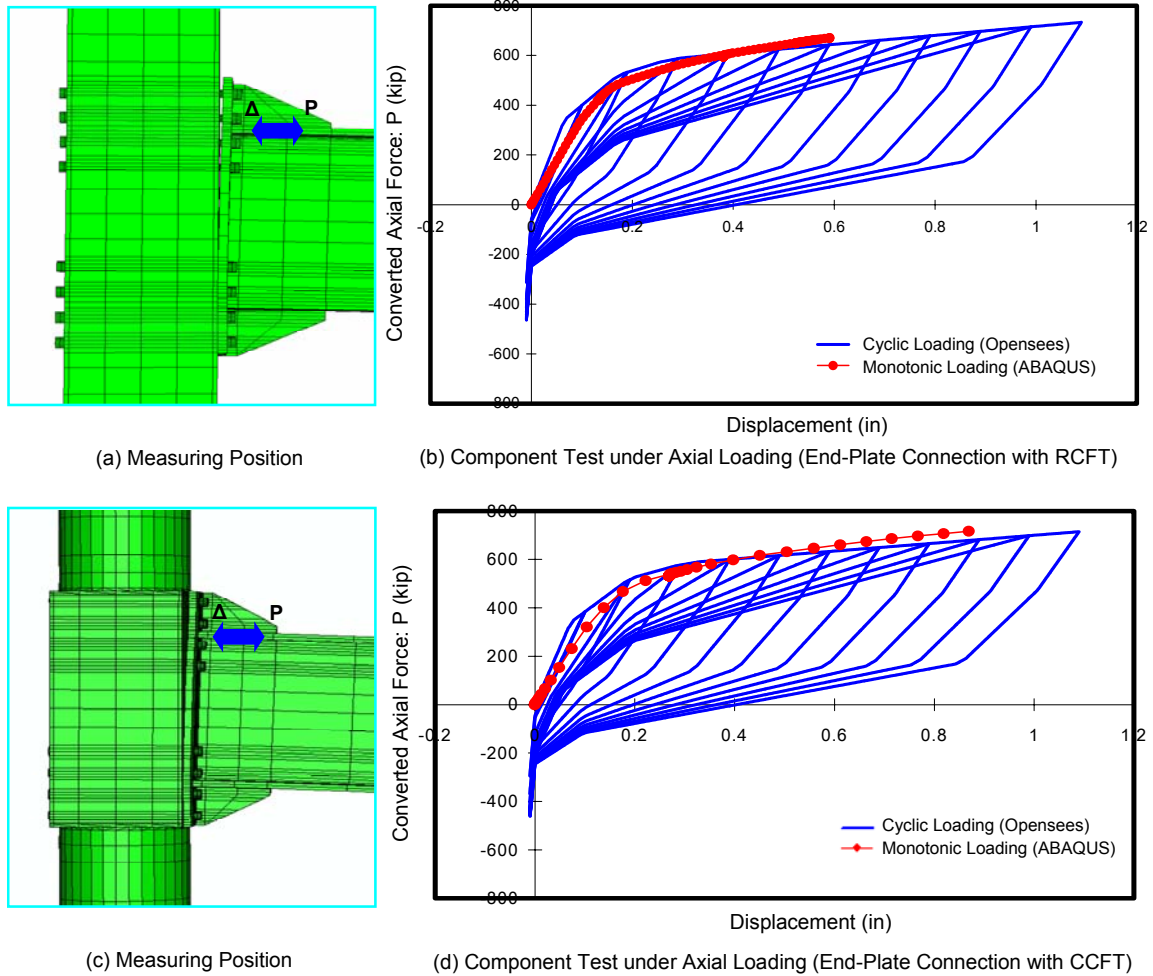


Figure 6.8 Measuring points and comparisons of results between two tests (Cyclic Test vs. Monotonic Test)

6.1.2 Joint Model of the T-Stub Connection

The component model of the T-stub component was developed following similar approaches and procedures to those used for the end plate connection (Section 6.1.1). The force distribution and deformed configuration of the joint model are depicted in Figures 6.9 and 6.10, respectively. Unlike the joint model for the end-plate connection, it contains a rotational spring for the shear tab and includes a sliding component to model slip. The individual spring elements are also assembled into one equivalent spring element.

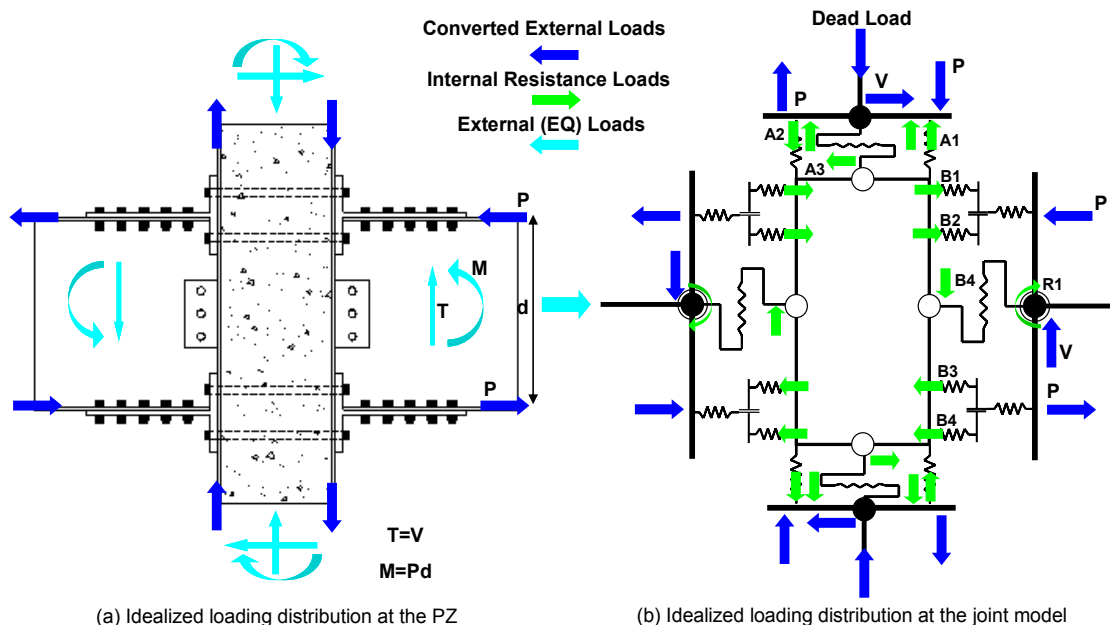


Figure 6.9 External and internal forces in the joint model for the T-stub connection

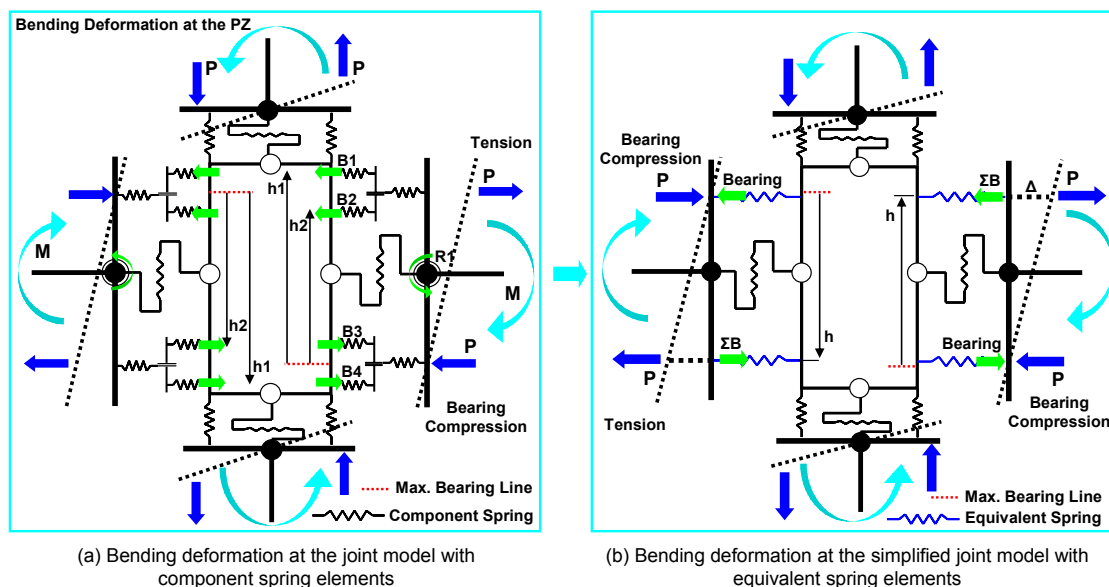


Figure 6.10 Response mechanism of the joint element under bending deformation

The component model for the OpenSEES program is shown in Figure 6.11. The data obtained from comprehensive experiments on T-stub components (Swanson 1999), such as that for fracture of the T-stem shown in Figure 6.12, was used to develop the component springs.

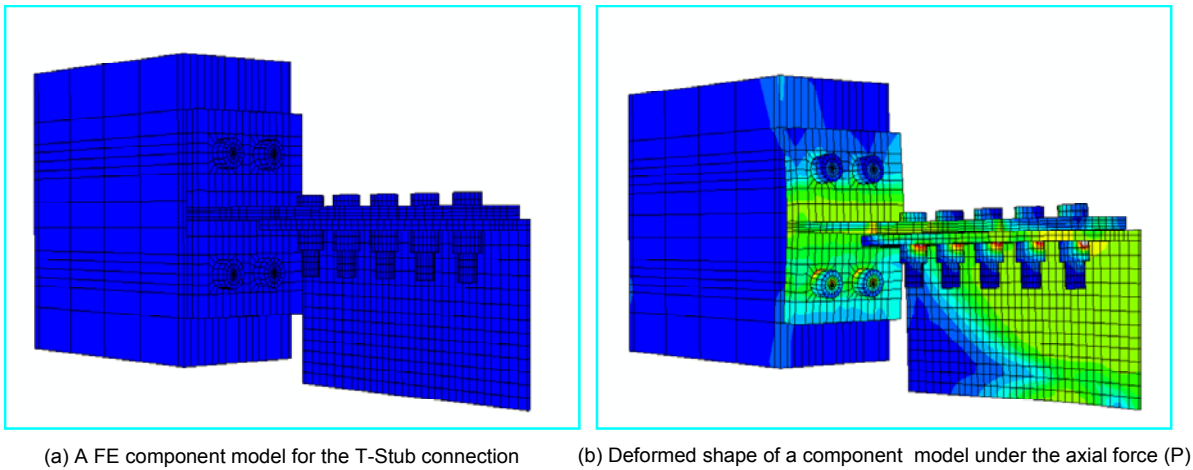


Figure 6.11 Component model for the 3D FE T-stub and its deformed Configuration under axial force

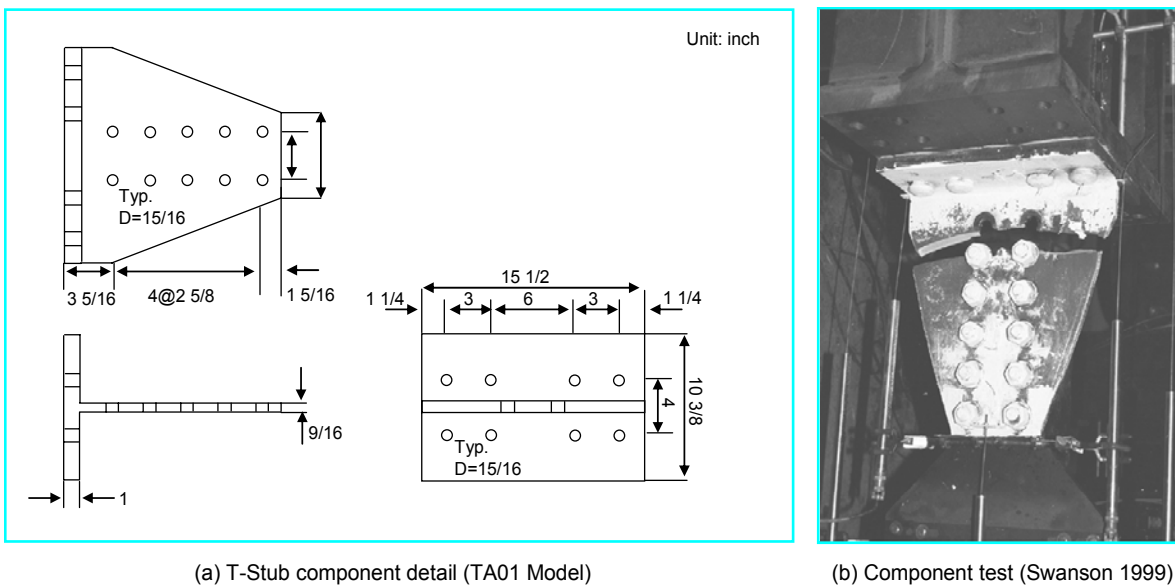


Figure 6.12 Specimen details of T-stub component model

The total force vs. deformation behavior is given in Figure 6.13(d). The total displacement is due primarily to three basic mechanisms: (a) bar yielding/uplift and flexural deformation of the T-flange (Figure 6.13(a)), (b) T-stem deformation (Figure 6.13(b)), and (c) slip (Figure 6.13(c)). The bar uplift resultant is produced by assembling all spring elements modeling bar components in the parallel system. The cyclic analytical

and experimental data performed by Swanson (1999) result in a good visual match of the shape of the hysteresis loops.

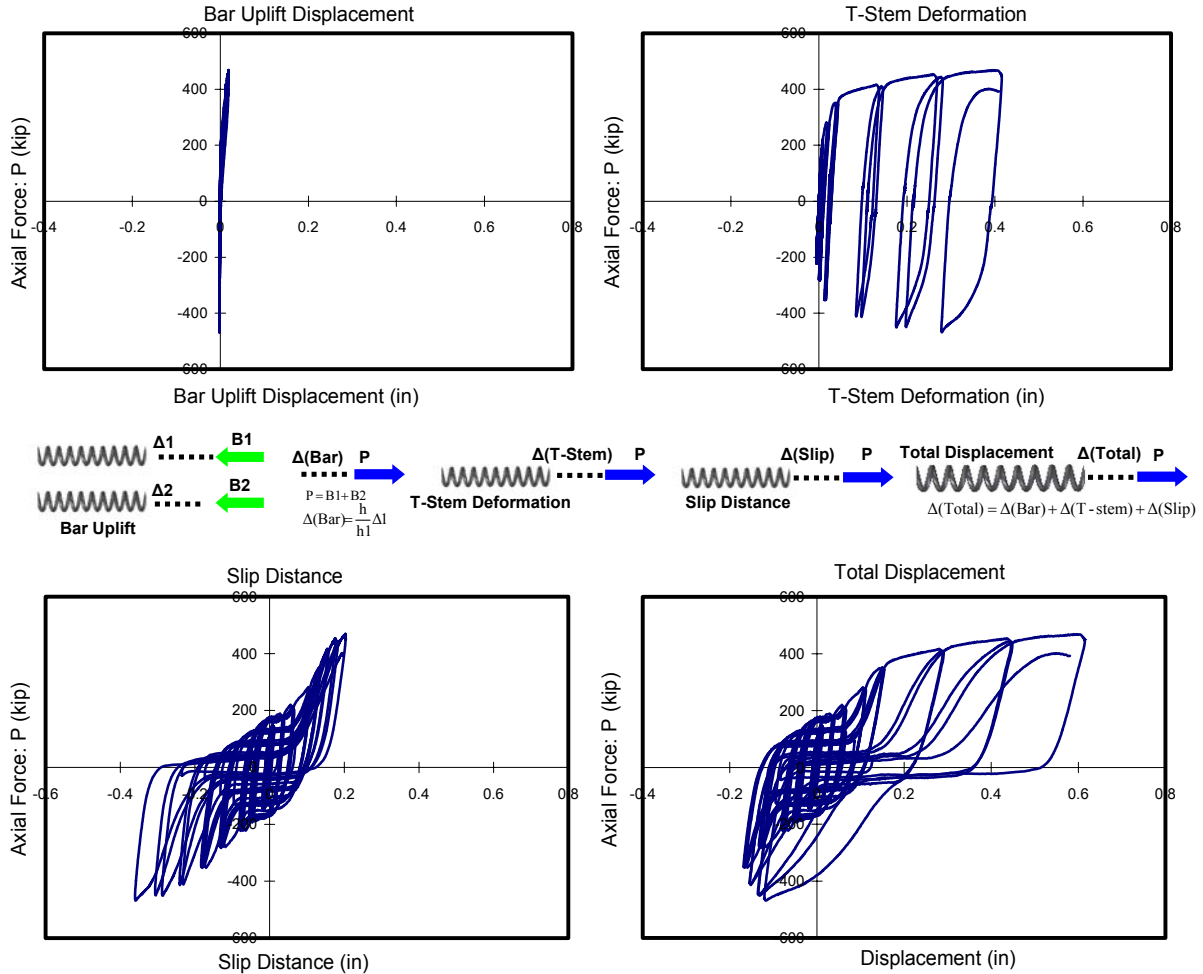


Figure 6.13 Force vs. deformation of T-stub component model

The behavior of each component is shown in Figure 6.14. The stiffness for each component was developed by observations of experimental results. The bar uplift model considers the prying action and yield lines in the flange and results in a tri-linear backbone curve: initial elastic behavior, followed by the formation of two yield lines and/or yielding of the tension bolts. The stem component has an elastic-hardening model for the base material coupled with a slip one to mimic the sliding due to the oversize of the holes. The bearing on the column flange is modeled with a compression-only spring.

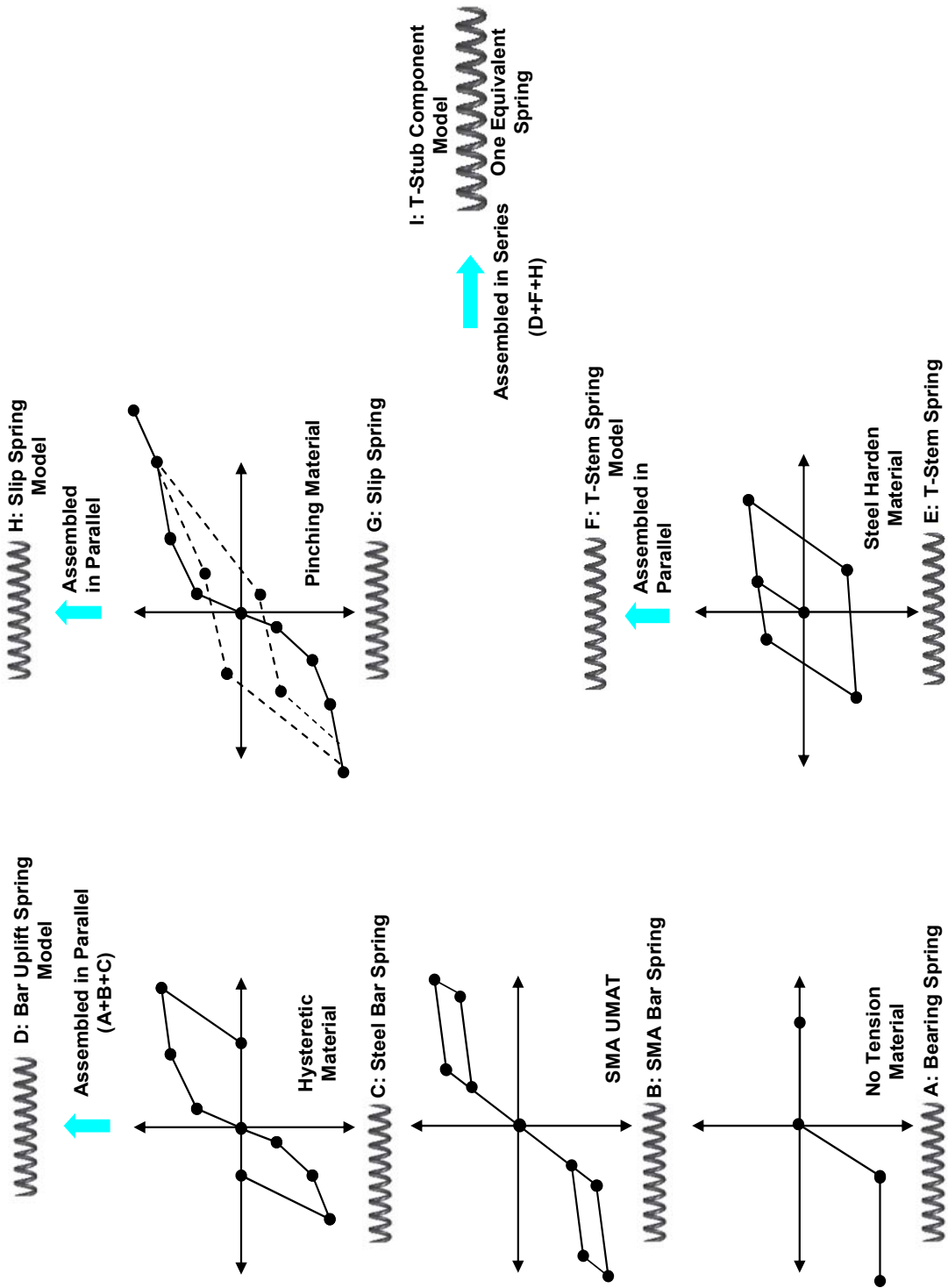


Figure 6.14 Properties of the individual component model

Comparisons between results of T-stub experiments and those of components are shown in Figure 6.15. Again, the results show good agreements in terms of initial stiffness, shape of the envelope, ultimate capacity, and even location of pinching points. The model is not capable of tracking the softening behavior shown in the last cycle of the test as this was due to the propagation of the fracture in the stem; this behavior cannot be modeled by the simple springs used here. Attempts to model this by some summation of total strains (rain flow counting) and similar simple techniques proved unworkable.

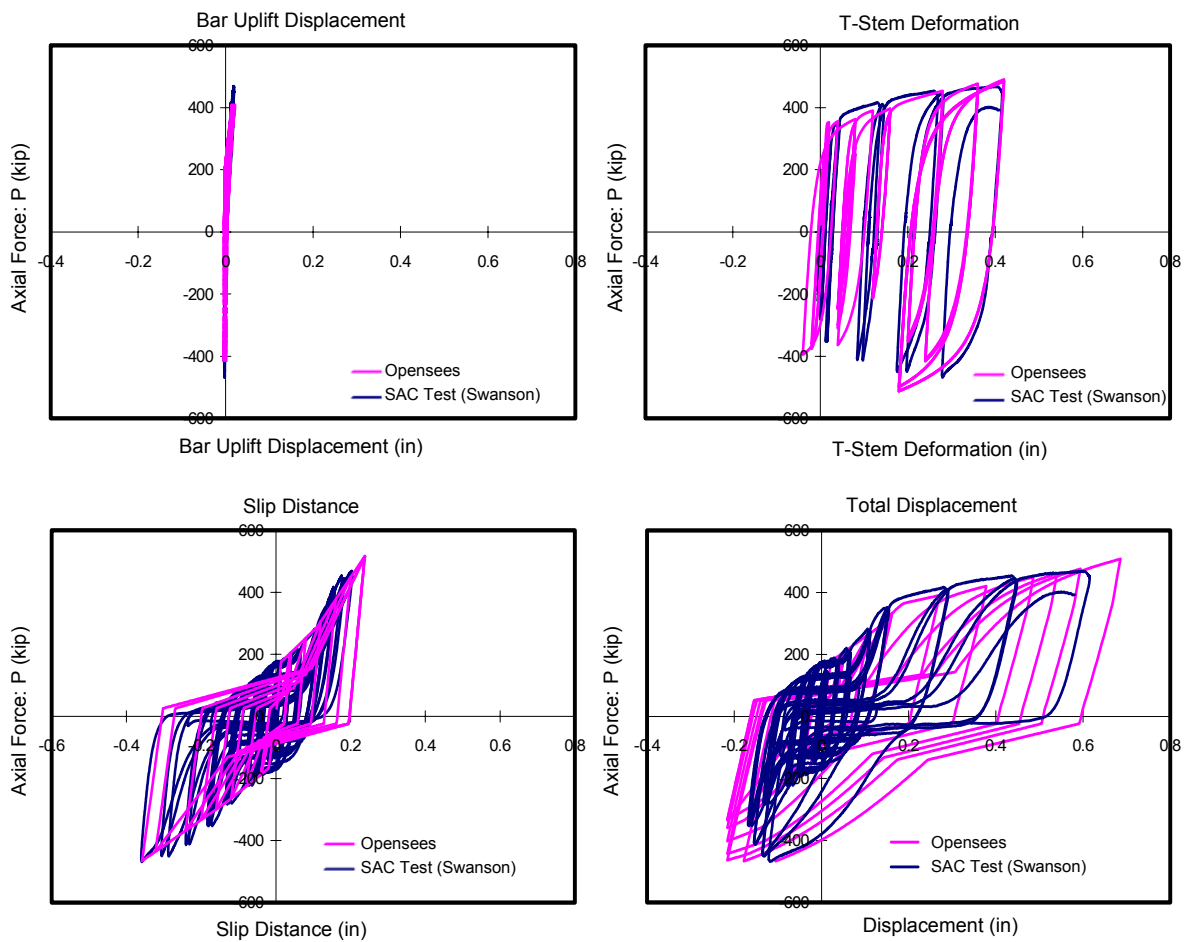


Figure 6.15 Comparisons between results of T-stub experiments and those of element tests

6.1.3 Joint Model of the Clip Angle Connection

The component model of the clip angle is shown in Figures 6.16 and 6.17 following the same principles outlined for the end-plate and T-stub connections. Figure 6.18 shows a typical clip angle connection, with the large gaps forming at the heel of the angle (Figure 6.18(b)). The deformation components are shown in Fig. 6.19 (Swanson 1999). The main behavior difference, the formation of the gap at the heel of the angle, is modeled with the help of an elastic gap element. This gap, which results in appreciable vertical displacements, results from the slip of the shanks of the shear bolts before they come into contact with the bolt holes.

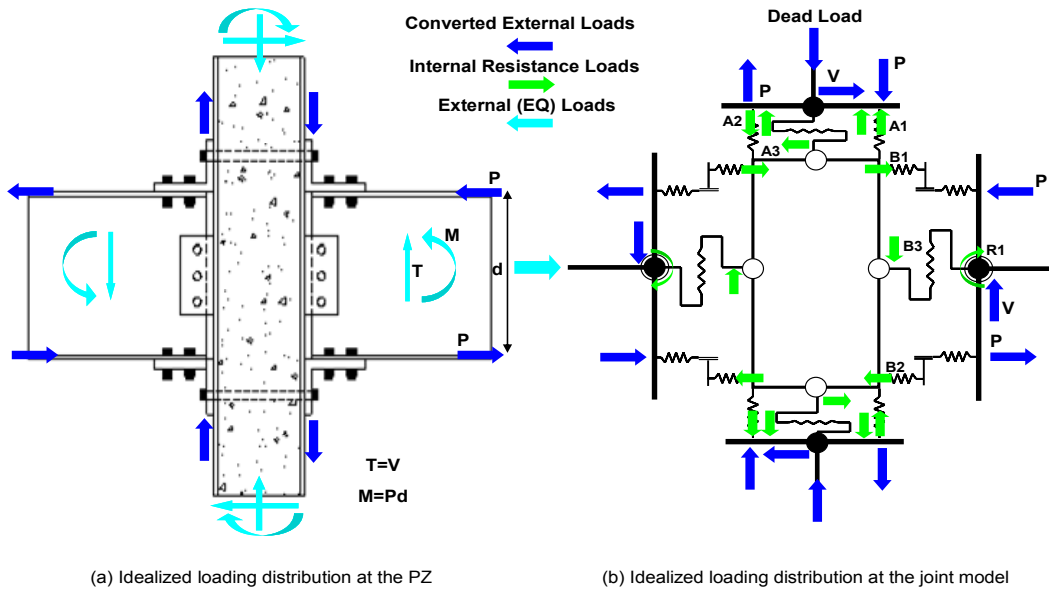


Figure 6.16 External and internal forces for the joint model of the clip angle connection

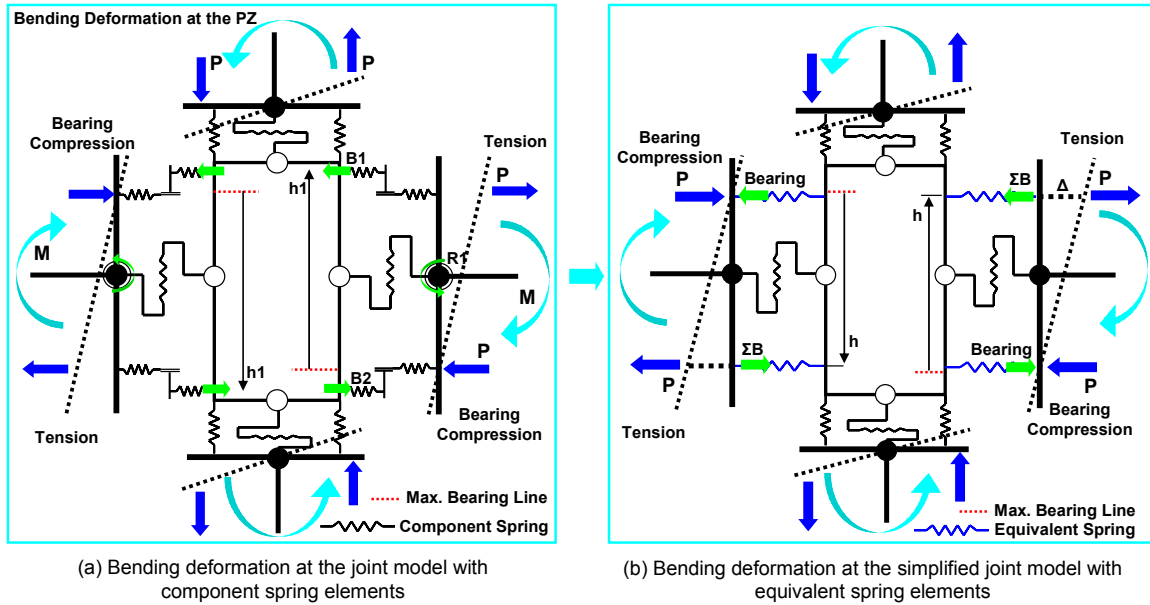


Figure 6.17 Response mechanism of the joint element under bending deformation

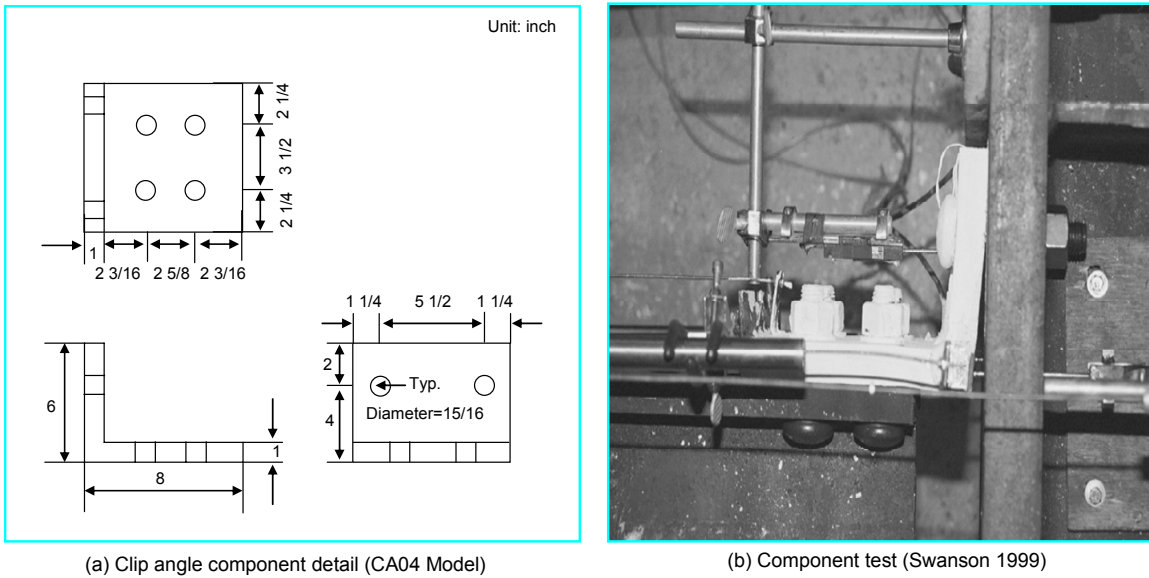


Figure 6.18 Specimen details for the clip angle component model

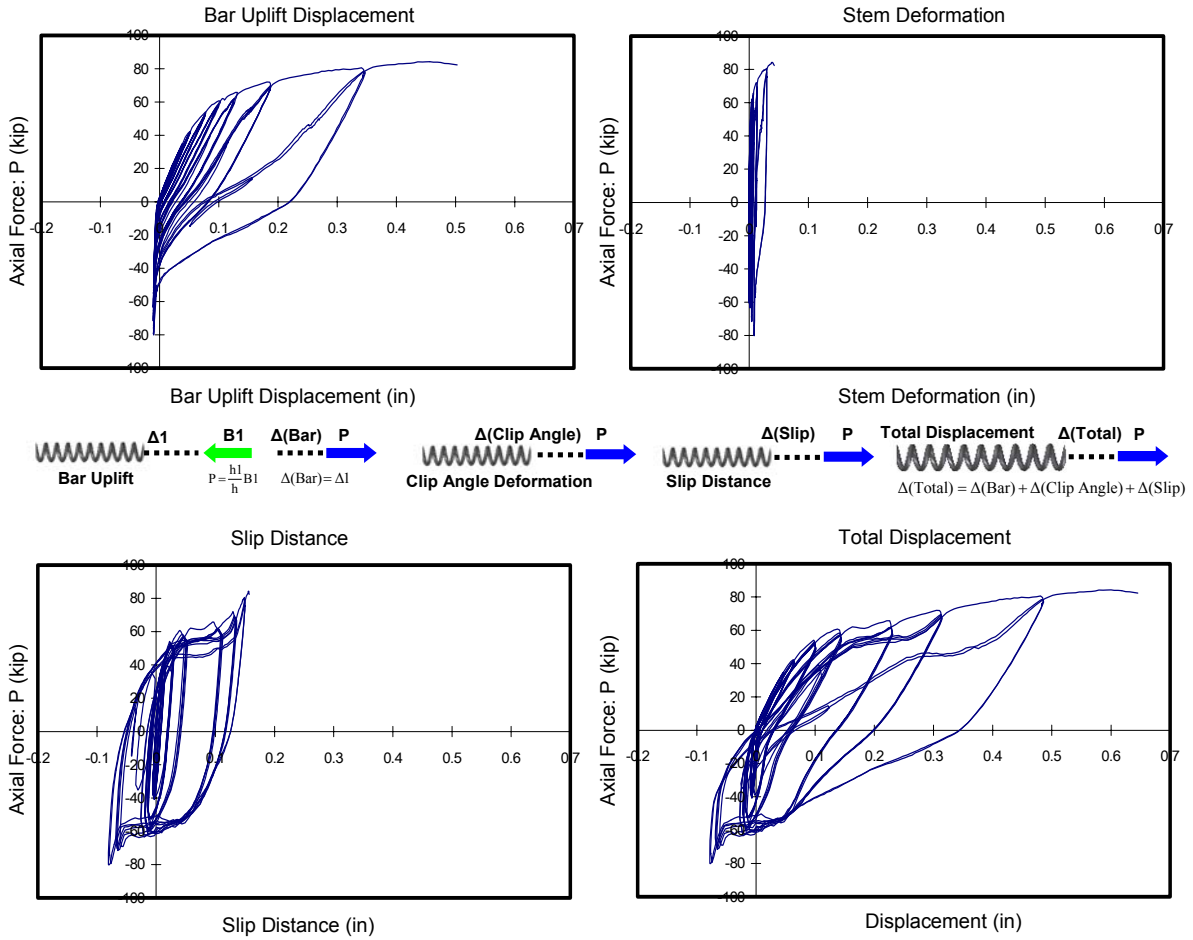


Figure 6.19 Force vs. deformation of clip angle component model

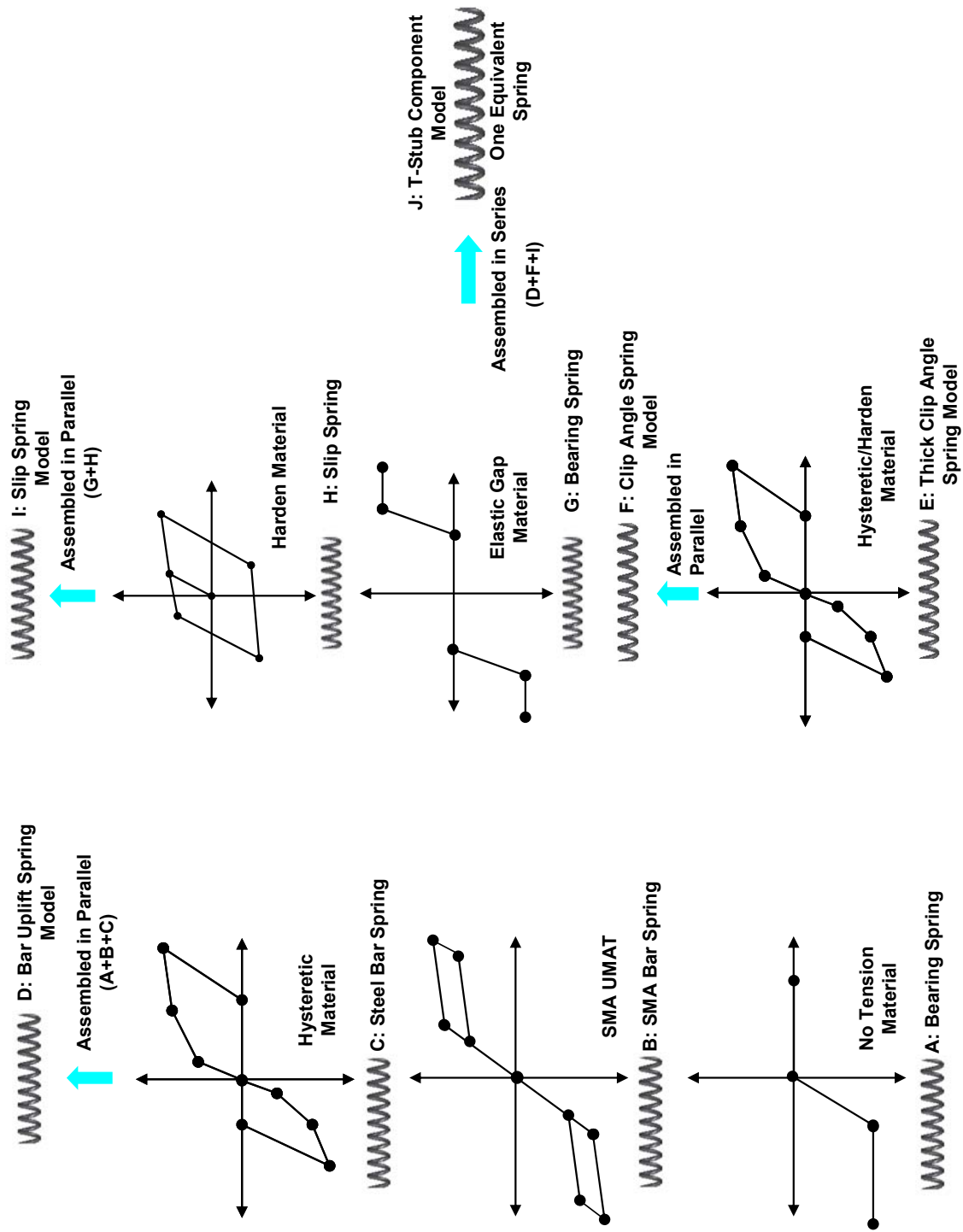


Figure 6.20 Properties of the individual components

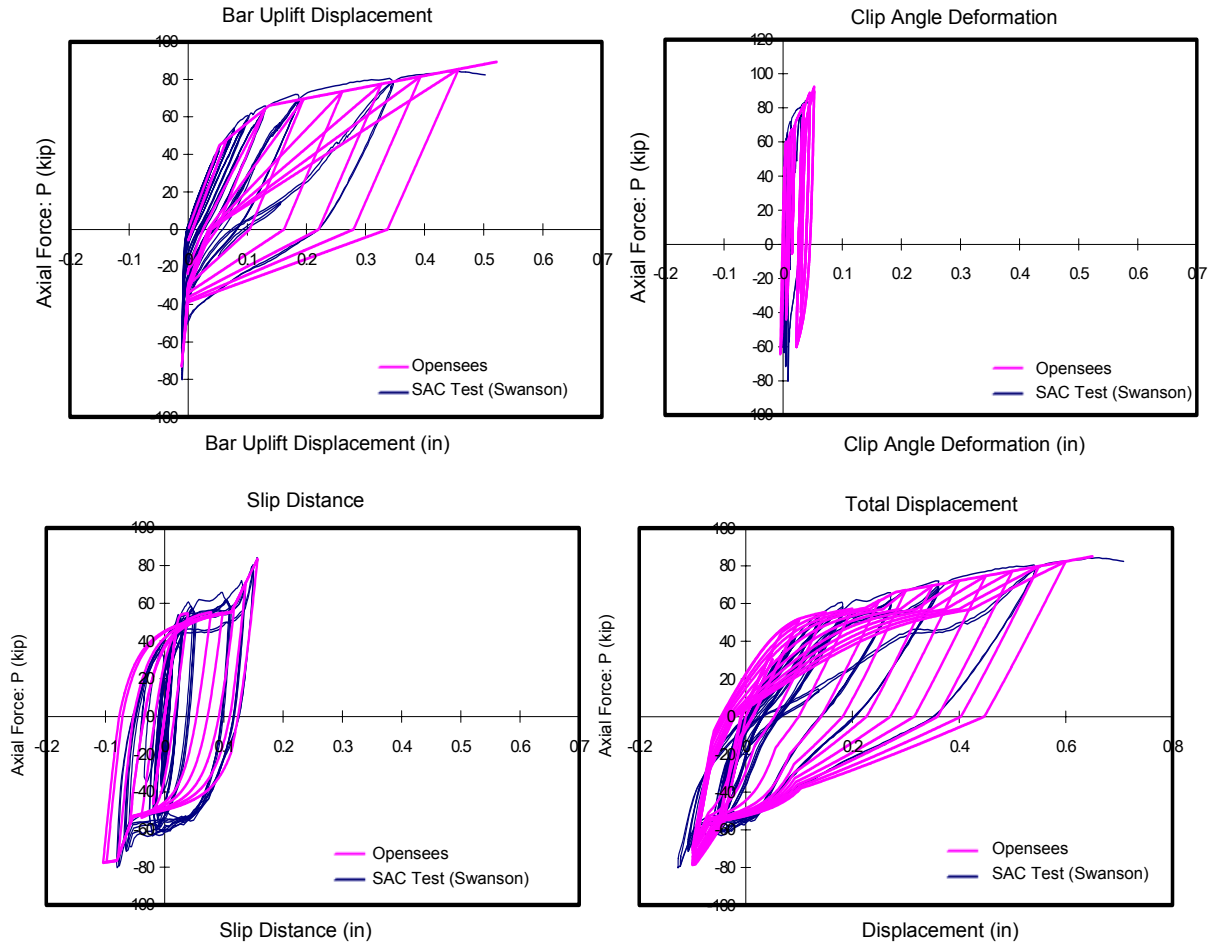


Figure 6.21 Comparisons between results of clip angle experiments and those of element tests

6. 2 Joint Elements

The joint models presented above were introduced as 2D joint elements into OpenSEES. Figure 6.22 shows the composition of the joint element for a general cruciform connection. This element includes (1) four equivalent spring elements (S1) which are intended to reproduce the deformations due to the bending forces from the framing members; (2) four internal spring elements (S2) which are intended to reproduce the axial deformations of the CFT column; (3) four internal shear springs (S3) which are intended to reproduce the shear deformations of the panel zone of the CFT column; and (4) one shear panel element (C) which is intended to reproduce the failure of the panel zone under severe loading. The behavior of the shear panel zone was obtained by observation of 3D FE test (See Figure 5.43). Rotational spring elements (R1) are used if a shear tab is present.

- A: External nodal points
- B: Internal nodal points
- C: Panel zone
- D: Rotational spring for panel zone deformation
- E: External rigid plane
- F: Internal rigid plane
- G: Nonlinear beam column element with fiber section
- S1: Equivalent spring for the component members with zero-length element
- S2: Internal axial spring with zero-length element
- S3: Internal shear spring with zero-length element
- R1: Rotational spring for the shear tab with zero-length element

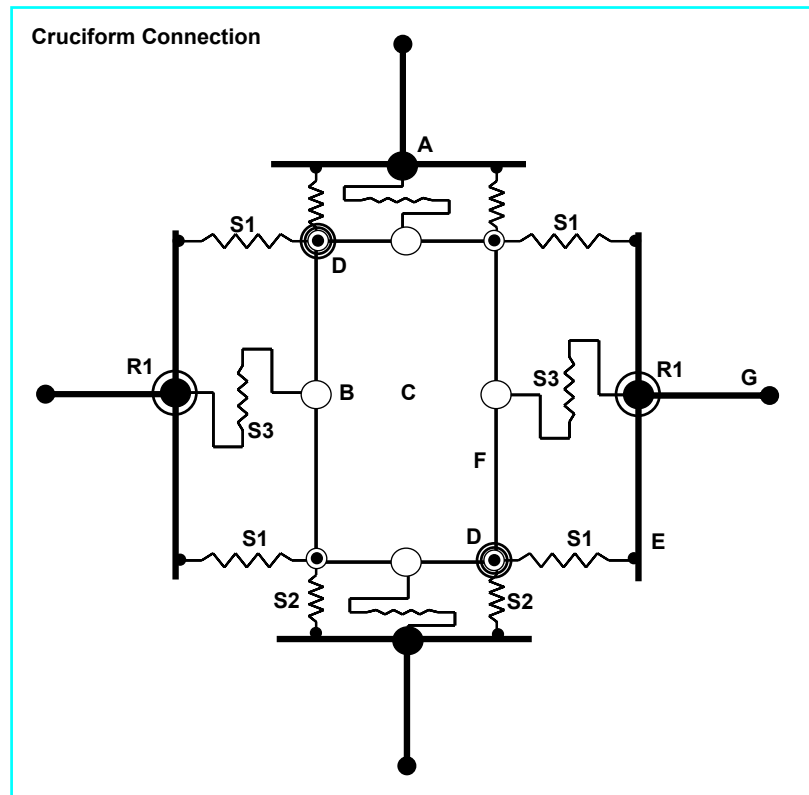


Figure 6.22 Typical joint element for a joint model (Cruciform Connection)

The joint element is condensed into four external and four internal nodes. Contrary to the typical displacement-controlled element formulation in which the displacement at the external nodes uniquely defines the deformation of the element, the deformation state of this joint element is defined based on both the displacements of external and internal nodes (Lowe 2003 and Mazzoni 2006). Each external node includes two translational displacements and one rotation as available degrees of freedom (DOF), while each internal node includes one translational displacement of the panel zone as shown in Figure 6.23. This element formulation is appropriate for use in an incrementally displacement controlled algorithm as it enables to compute the DOF of each nodal point with the load based equilibrium of the element. The spring elements are implemented with the interior and exterior planes coincident (zero-length element).

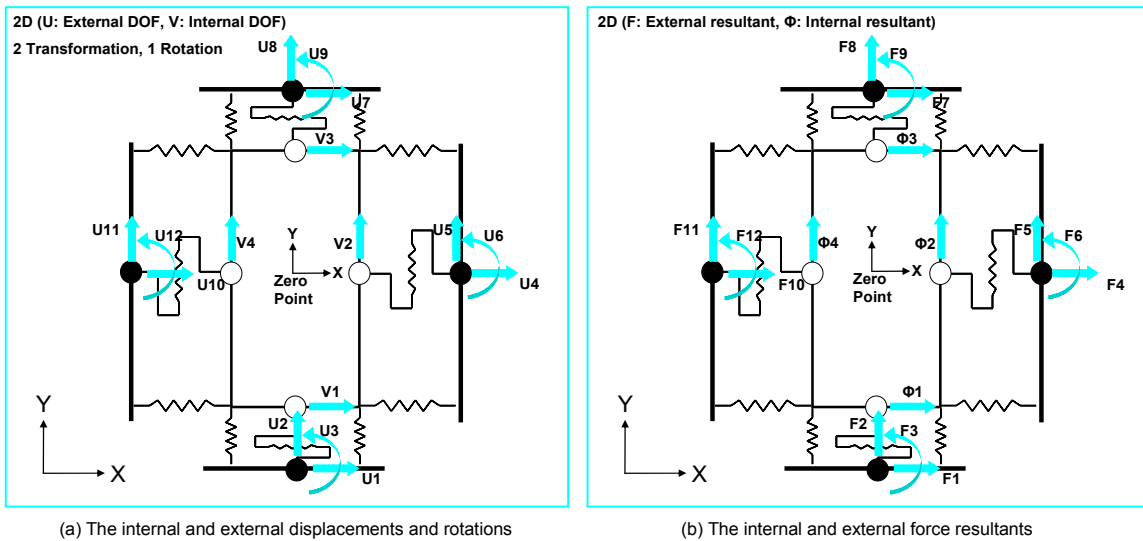
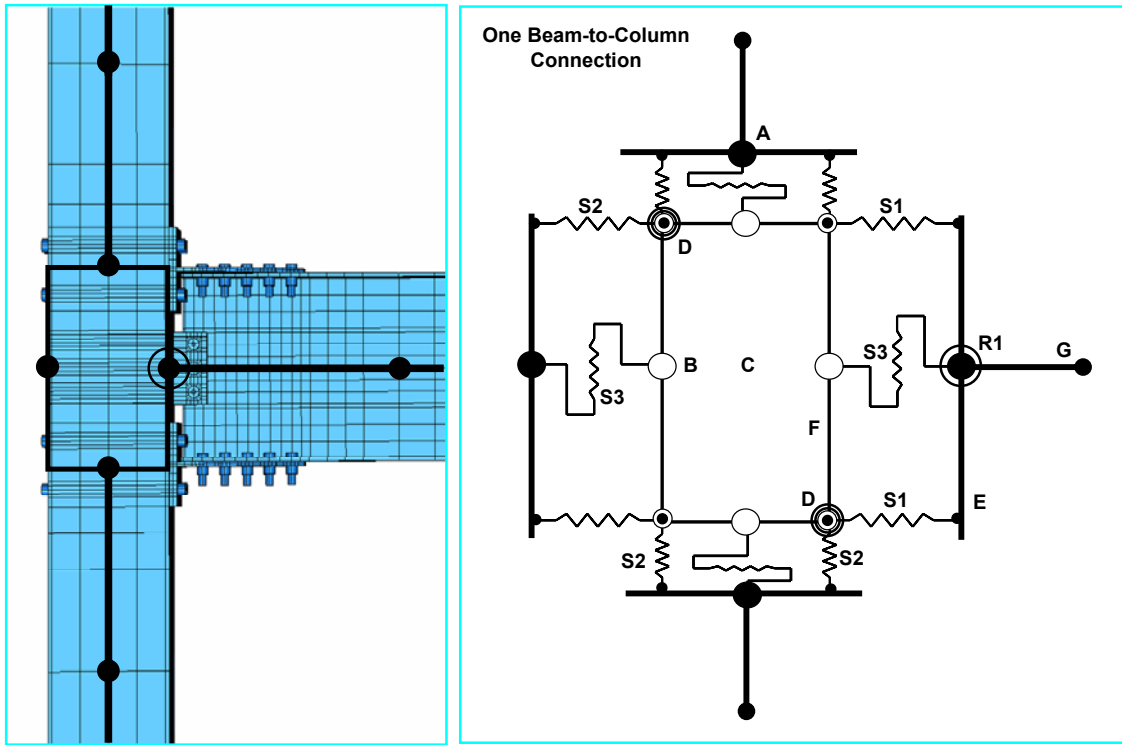


Figure 6.23 Internal and external displacements and forces

The element formulation and joint element of one beam-to-column connection are shown in Figure 6.24. The typical beam and CFT column are modeled as nonlinear beam-column elements with 2D fiber sections (See Figure 6.25). One nonlinear beam-column element includes the integration points in which displacement and resultant force are measured. 2D fiber sections are also assigned in these points. The characteristics of the cross section such as fiber stress, internal fiber force, fiber strain, and curvature are also measured. These fiber sections follow the material models shown in Figure 6.26. The

monotonic and cyclic material models are assigned to 3D finite elements and to the nonlinear beam-column element with 2D fiber sections, respectively.



(a) The element formulation on the connection (b) The joint element of one beam-to-column connection

Figure 6.24 Typical joint element for a joint model (One Beam-to-Column Connection)

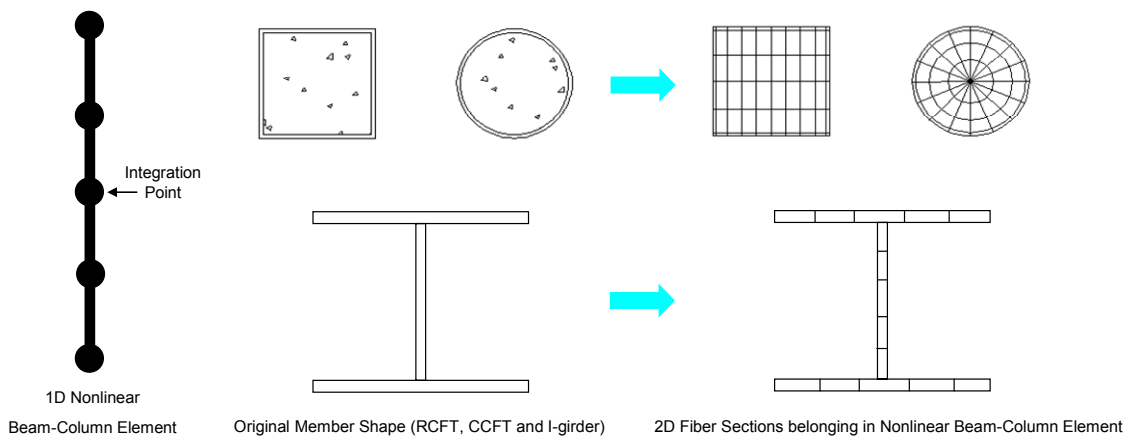
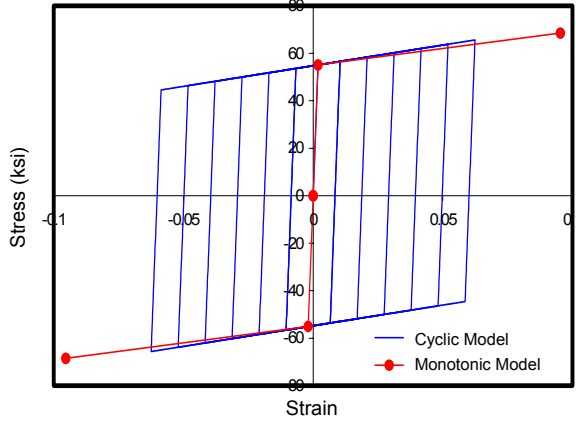
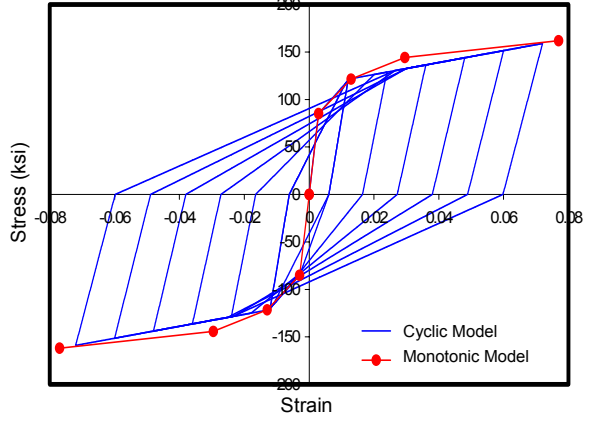


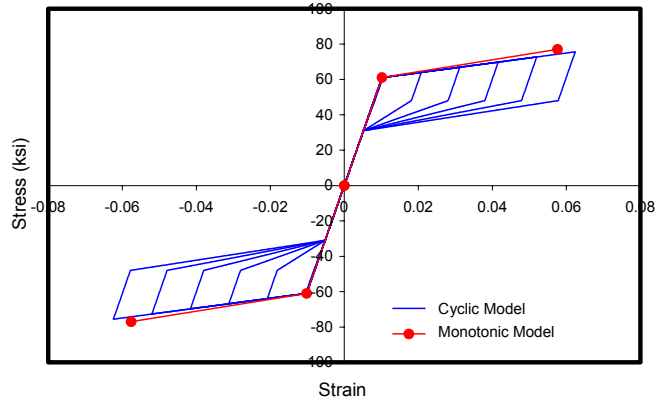
Figure 6.25 Nonlinear beam-column element and 2D fiber sections



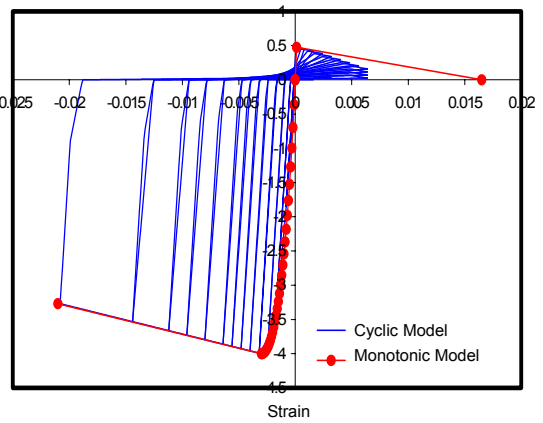
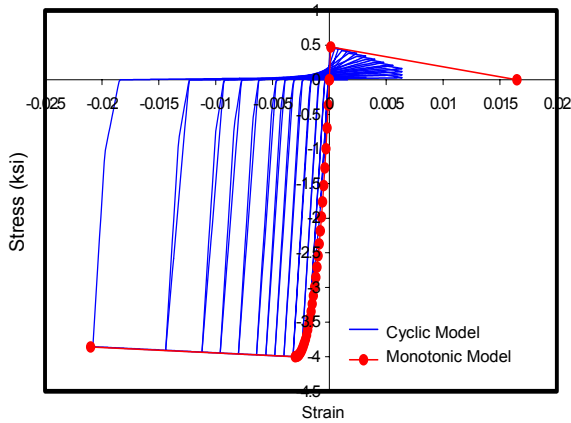
(a) Stress and Strain Curve for A572-Gr. 50 Steel



(b) Stress and Strain Curve for A490 High Strength Bolt



(c) Stress and Strain Curve for Super-elastic SMA



(d) Stress and Strain Curve for Confined Circular Shape Concrete (e) Stress and Strain Curve for Confined Rectangular Shape Concrete

Figure 6.26 Material properties for the analyses

6.3 Cyclic Behavior

The 2D joint element models for the full scale connections consisted of either Smart SMA PR-CFT connections, Steel PR connections, or a combination thereof. These models were analyzed under cyclic loads using OpenSEES. For calibration of these 2D models, results from the 3D FE connection models under monotonic loads described in the previous chapters and SAC test models (Swanson, 2000) under cyclic loads were used. A diagram of a full-scale test and the resulting response at ultimate are shown in Figure 6.27. All loads were applied to the tip of the beam corresponding to the position of a loading actuator. The connection details shown in Figure 4.2 to 4.7 were applied to joint element models and 3D FE models for comparison.

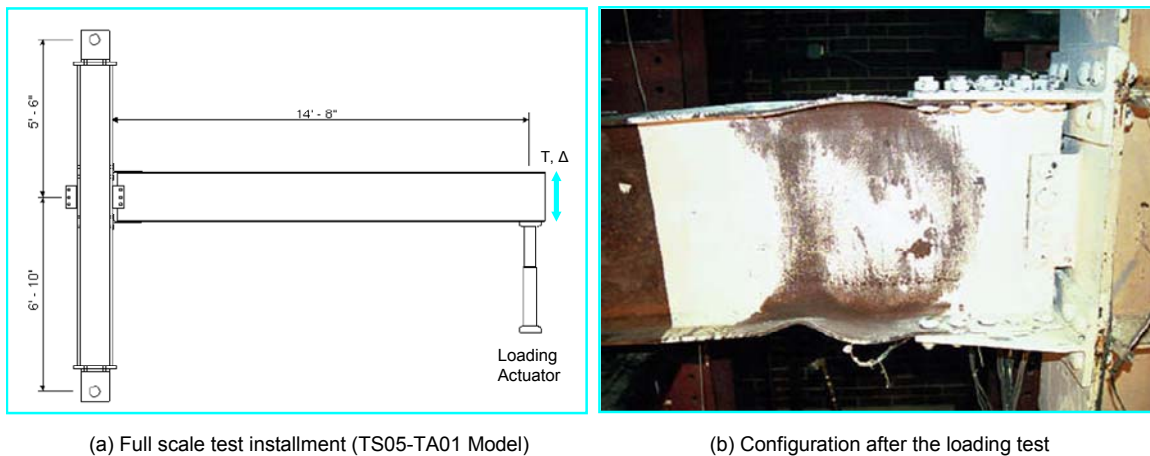


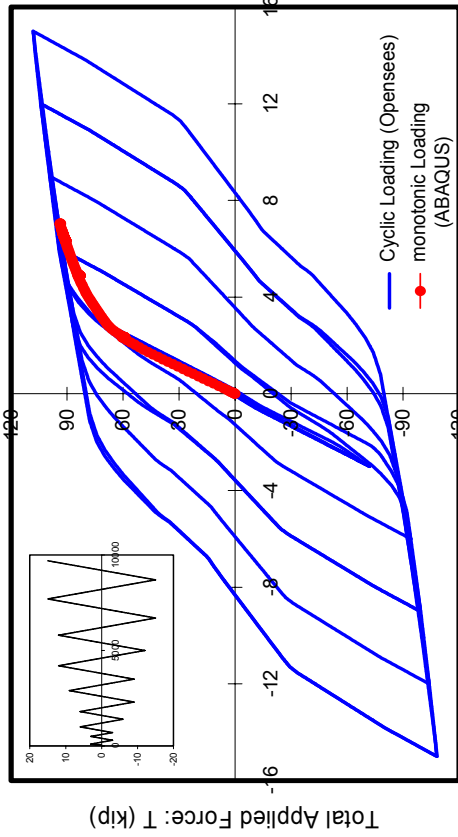
Figure 6.27 Test setup for a full scale connection (Swanson, 2000)

Comparisons between the monotonic results from the 3D FE models and the cyclic results from the 2D joint models are shown in Figure 6.28. These models are for end-plate connections illustrated in Figure 4.2 and 4.3. The inset figure indicates the loading history. The monotonic 3D FE model was performed using ABAQUS as mentioned in Chapter 5. For the 2D joint model, the detailed modeling procedures were described in Section 6.1.1. The test results show good agreement in terms of initial stiffness, ultimate strength and overall envelope. It should be noted that the terminology “good” agreement used in this dissertation is meant to indicate that the governing behavior modes and controlling points in the monotonic force-deformation and moment-rotation curve match well (within 15% for the controlling points). On the other hand, for the cyclic tests,

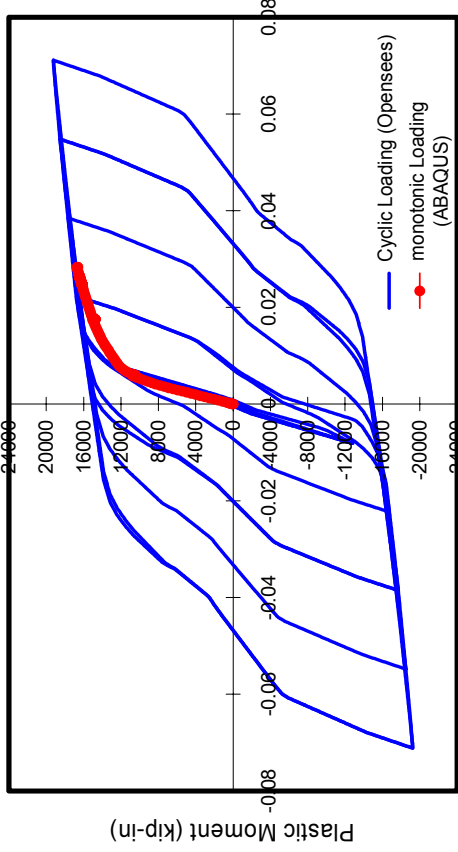
“good” means that the superposition of the cyclic analytical and experimental data results in a good visual match of the shape of the hysteresis loops. Attempts to match test data exactly were not carried out as the intent was to verify the general robustness of the models.

Comparisons for moment and rotation curves are given in Figure 6.29 and 6.30 for T-stub connections. For the joint model, the detailed modeling procedures for the T-stub components were described in Section 6.1.2. Figure 6.29 shows comparisons for the TA01 T-stub from Swanson (1999), in which beam and stem yielding are the major failure modes. The details for the T-stub connections from the SAC programs were illustrated in Figure 3.5(a). The results also show good agreement. Comparisons between the monotonic result from the 3D FE model and the cyclic result from 2D joint element model are given in Figure 6.30 for T-stub connection specimen illustrated in Figure 4.4. Force and deformation for connection components (i.e. T-stub and tension bars) can be also measured for both models and experiments. Comparisons for component behavior are given in Figure 6.31. They also show good agreement.

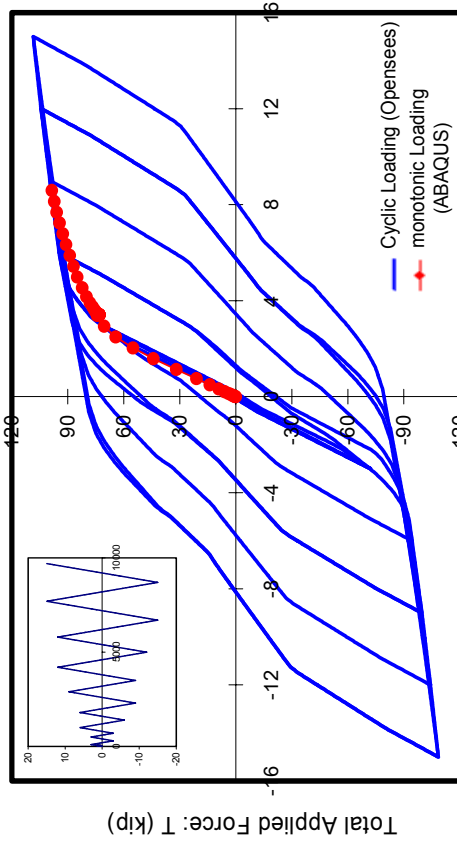
Finally, comparisons for moment and rotation curves are given in Figure 6.32 and 6.33 for clip angle connections. For the joint model, the detailed modeling procedures for the clip angle components were described in Section 6.1.3. Figure 6.32 shows comparisons for the CA04 clip angle from Swanson (1999), for which beam yielding is the major failure mode. The design details for a clip angle connection from the SAC programs were illustrated in Figure 3.5 (b). Comparisons between the monotonic result from the 3D FE model and the cyclic result from 2D joint element model for this test are shown in Figure 6.33 for clip angle connection specimen illustrated in Figure 4.6. Comparisons for component behavior are given in Figure 6.34. They also show good agreement.



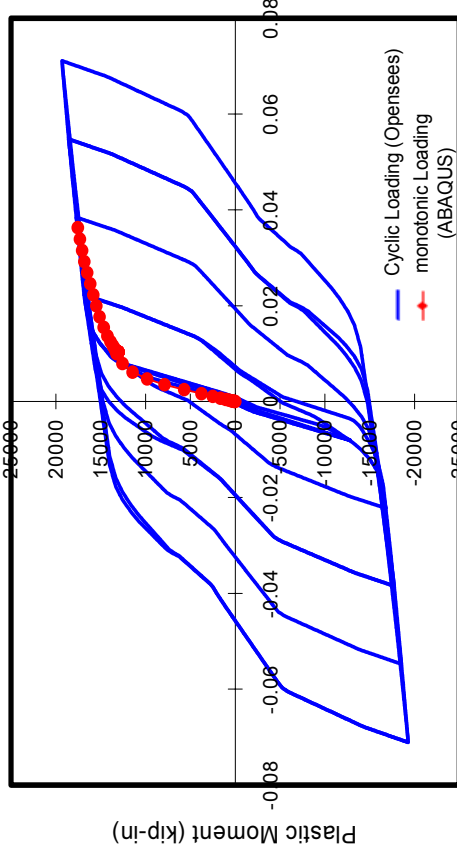
(a) Total Applied Force (T) and Displacement (End-Plate Connection with RCFT)



(b) Plastic Moment and Rotation (End-Plate Connection with RCFT)

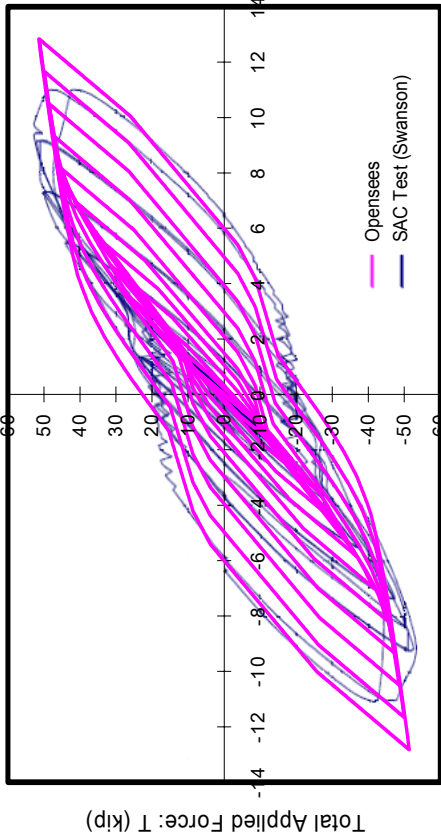


(c) Total Applied Force (T) and Displacement (End-Plate Connection with CCFT)

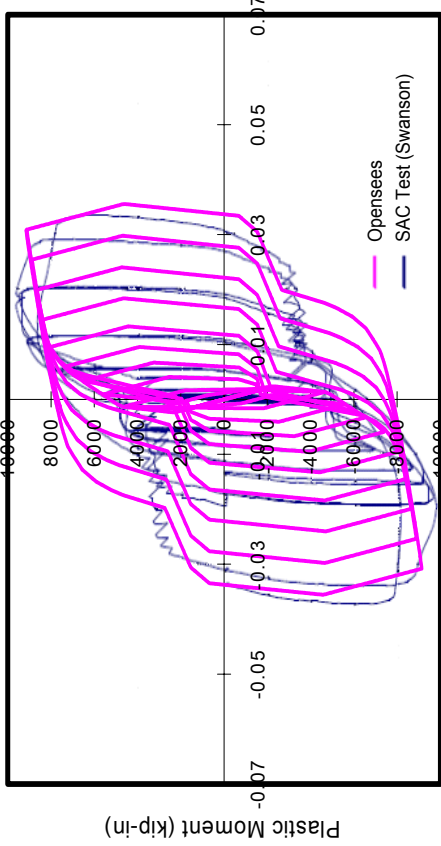


(d) Plastic Moment and Rotation (End-Plate Connection with CCFT)

Figure 6.28 Comparisons between monotonic loading of a 3D FE model and cyclic loading of the joint element

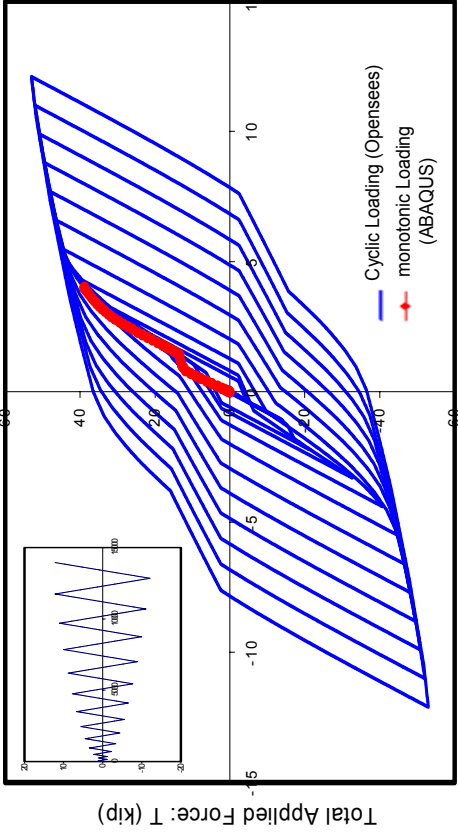


(a) Total Applied Force (T) and Displacement (T-Stub Connection FS05-TA01)

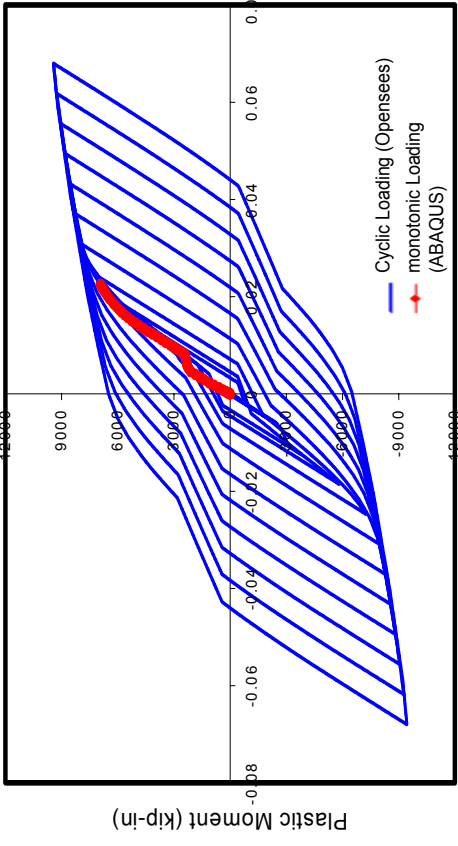


(b) Plastic Moment and Rotation (T-Stub Connection FS05-TA01)

Figure 6.29 Comparisons between the cyclic loading test of the SAC experiment model and the cyclic loading test



(a) Total Applied Force (T) and Displacement (T-Stub Connection with RCFT)



(b) Plastic Moment and Rotation (T-Stub Connection with RCFT)

Figure 6.30 Comparisons between the monotonic loading test of a 3D FE model and the cyclic loading test (Monotonic Test vs. Cyclic Test)

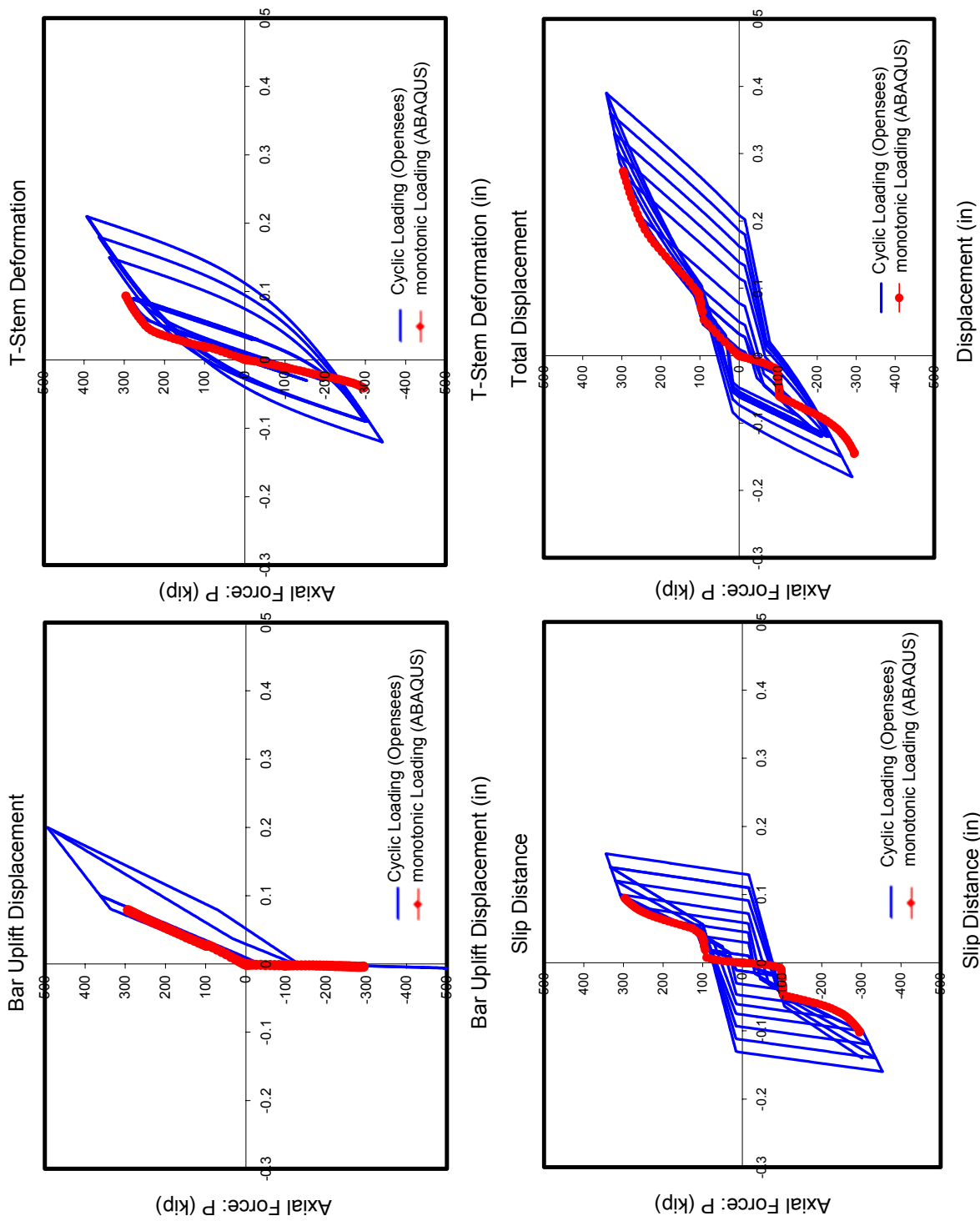
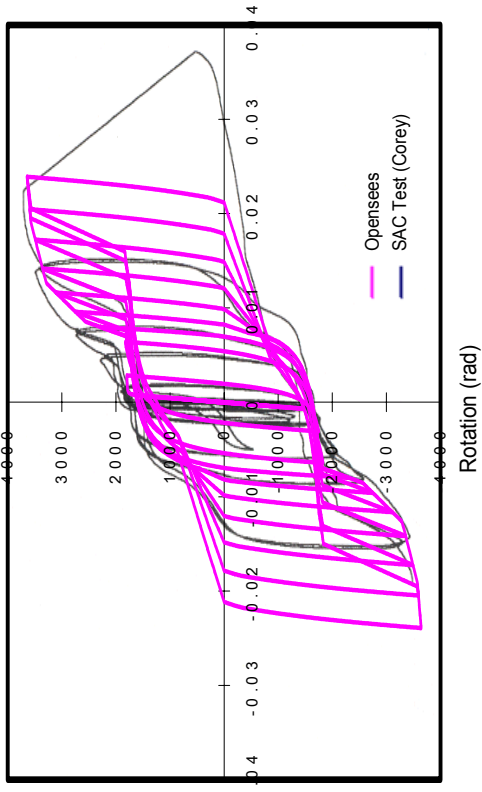
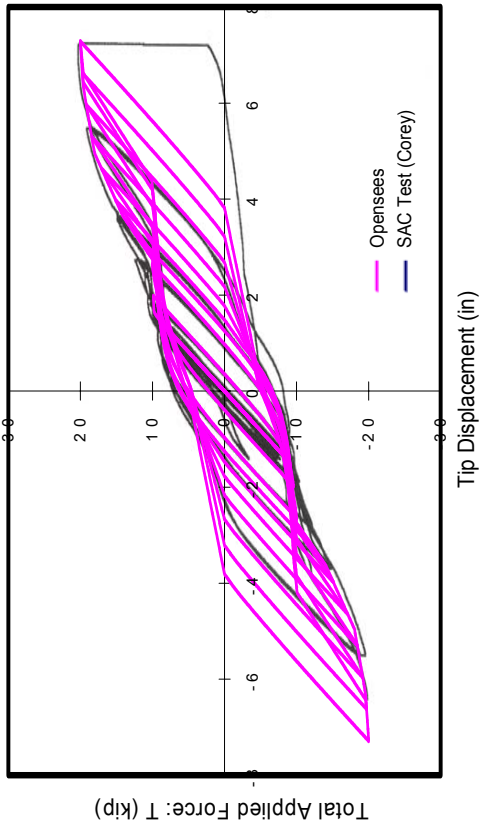


Figure 6.31 Generation of the behavioral properties of components through observations of 3D FE test (Monotonic Test vs. Cyclic Test)



(a) Total Applied Force (T) and Displacement (Clip Angle Connection, FS02-CA04)

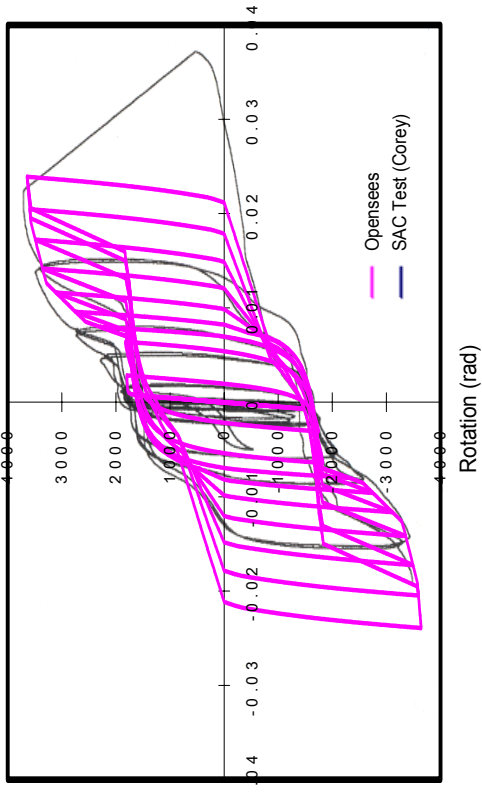
Figure 6.32 Comparisons between the cyclic loading test of SAC experiment model and the cyclic loading test (SAC Experimental Test vs. Cyclic Test)



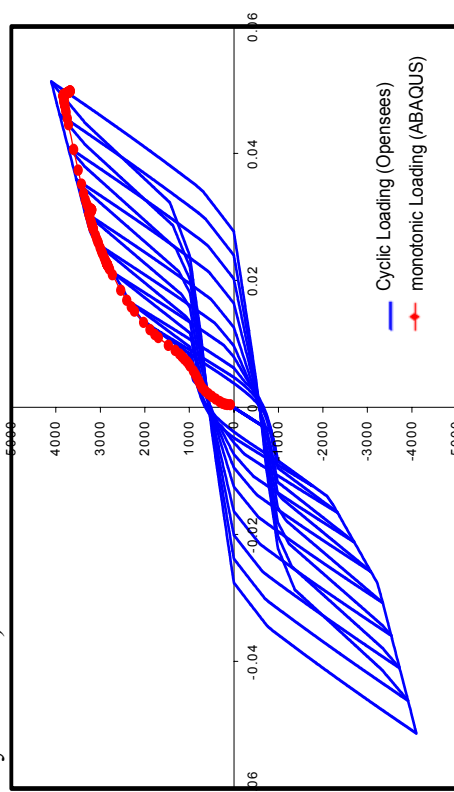
Tip Displacement (in)

Tip Displacement (in)

(a) Total Applied Force (T) and Displacement (Clip Angle Connection with RCFT)



(b) Plastic Moment and Rotation (Clip Angle Connection, FS02-CA04)



Rotation (rad)

(b) Plastic Moment and Rotation (Clip Angle Connection with RCFT)

Figure 6.33 Comparisons between the monotonic loading test of 3D FE model and the cyclic loading test (Monotonic Test vs. Cyclic Test)

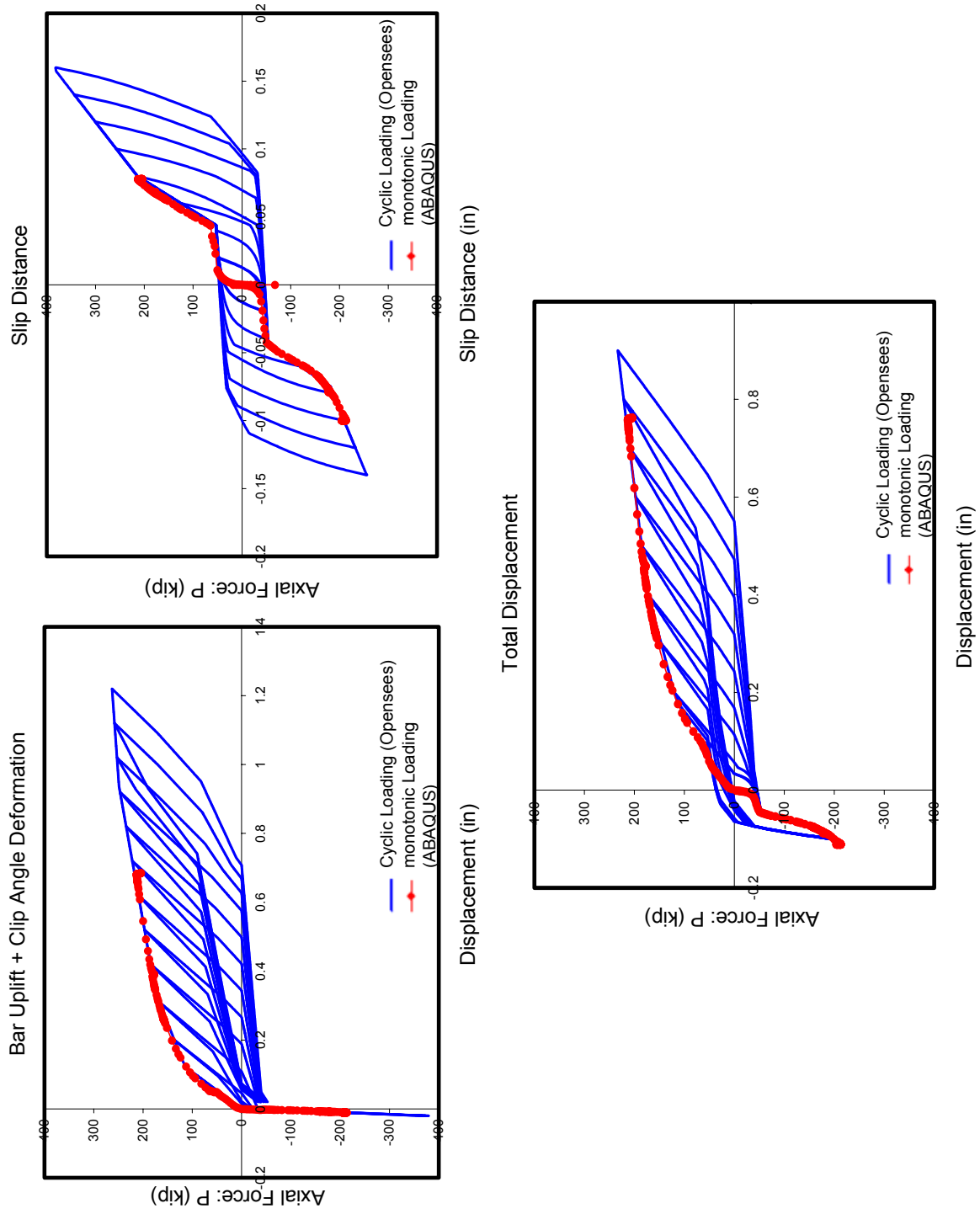


Figure 6.34 Generation of the behavioral properties of component models through observations of 3D FE test (Monotonic Test vs. Cyclic Test)

6.4 Observations of Model Tests

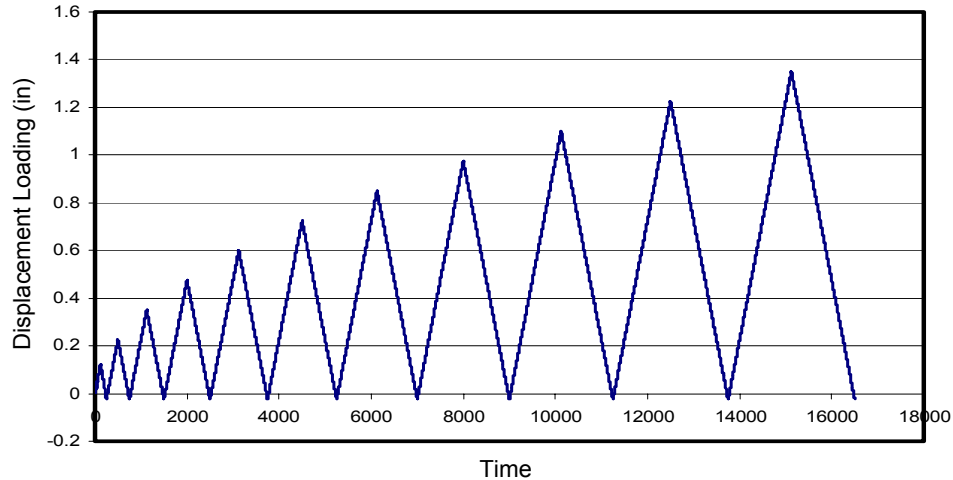
Based on the study of the component analyses described in the previous sections, parametric studies, especially for the steel and SMA tension bars, will be described in this section. Three different combinations of steel tension bars and SMA tension bars were chosen: (1) all SMA bars, (b) 50% SMA and 50% steel, and (c) all steel. The second option was based on parametric studies that showed that a range between 40%-60% and 60%-40% for the steel-to-SMA bar ratio by force provided the best compromise between recentering and energy dissipation. Two types of analyses were run. In the first type, a cyclic axial force was applied in the longitudinal direction of the equivalent spring element in order to investigate the behavior of different components. In the second type of analyses, the cyclic force was applied to the tip of the beam element in the 2D joint in order to investigate the behavior of the full connection. The equivalent spring element and joint element for these parametric studies were designed with the component and connection details shown in Figures 4.2 to 4.7.

6.4.1 Observations on End-Plate Connections

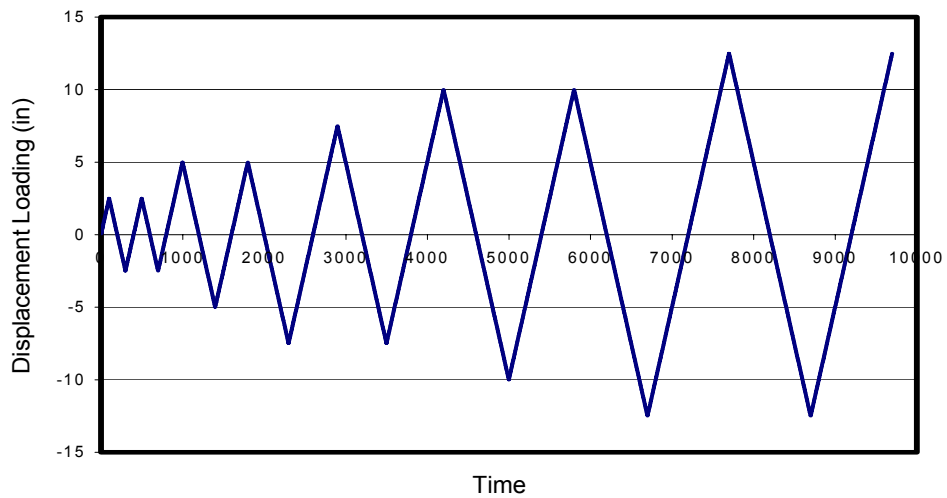
The displacement loading histories used are given in Figure 6.35. The connection details were illustrated in Figure 4.2. Due to the large bearing stiffness assigned to the equivalent spring element, the displacement in the direction of bearing (negative value) is much smaller than that in the direction of tension (positive value) as shown in Figure 6.35 (a). The displacement loading history for the full connection is symmetric (Figure 6.35(b)).

Results for three cases of end-plate connections are given in Figure 6.36. The red dashed lines in this figure indicate the plastic limits defined as the plastic axial force (P_p) and the full plastic moment of the beam (M_p) respectively. Figures 6.36 (a) and (b) clearly show the strong recentering effect of the SMA bars, the phase transformation plateau (“yielding”) well below the plastic capacity of the beam, the large deflections possible at low loads, and the relatively small energy dissipation capacity. Almost the opposite can be said for the all steel case (Figures 6.36(e) and (f)), where large permanent deformations, high initial stiffness, and good energy dissipation capacity are seen. The

intermediate case (Figure 6.36 (c) and (d)) shows the potential for a combination of the two types of tension bars: some reentering and some energy adsorption capacity.



(a) Displacement loading history for the full test of the equivalent spring element



(b) Displacement loading history for the test of the joint element model

Figure 6.35 Displacement loading history for the models

As stated in Section 6.1.1, component models for tension bars are assembled as a parallel system in order to obtain one equivalent spring element. Based on the incrementally displacement controlled algorithm, analytical predictions for the force vs. displacement of this element subjected to cyclic axial loading are calculated based on constitutive models that incorporate observations on behavior from tests. One such

analytical prediction, for the case of a connection with 50% SMA and 50% steel bars, is given in Figure 6.37. Each prediction point shown in Figure 6.37(a) corresponds to a change in individual behavior of a component model. The prediction points correspond to:

1. The first yielding (points 1 and 2 or P1 and P2 in Figure 6.37 (a)), which occurs in the steel tension bars (B3 and B4). B3 yields first as it is the farthest steel bar from the center of rotation, but B4 yields almost immediately after. It is almost impossible to tell the difference between the two points in graphs to the scale shown. Note that because the SMA bars begin their phase transformation at a higher strain, it is the steel that “yields” first.
2. After steel bars yield, the SMA bars reach their phase transformation point at P3 and P4.
3. The components reach the maximum deformation at P5; and unloading point (p6) is also shown.

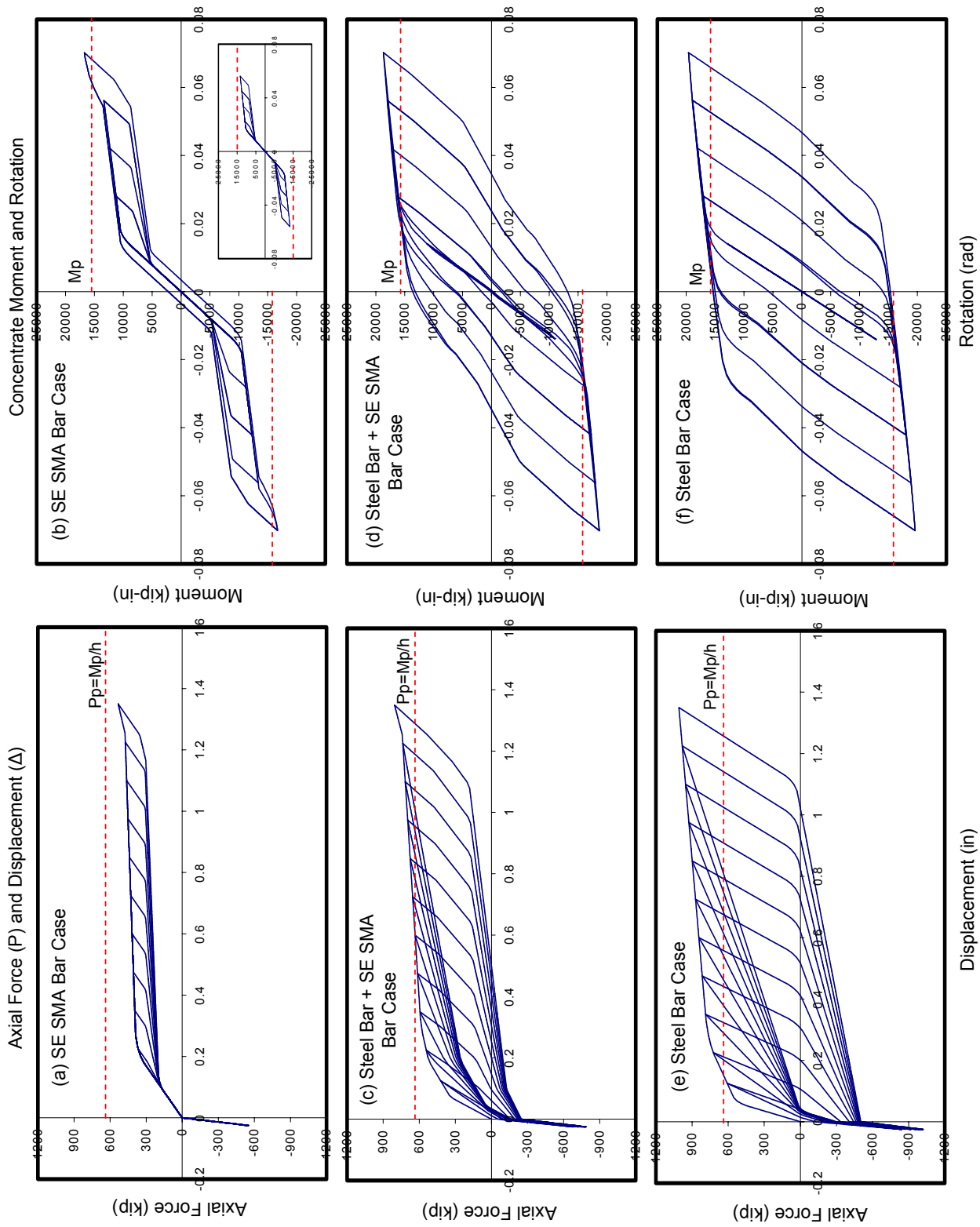
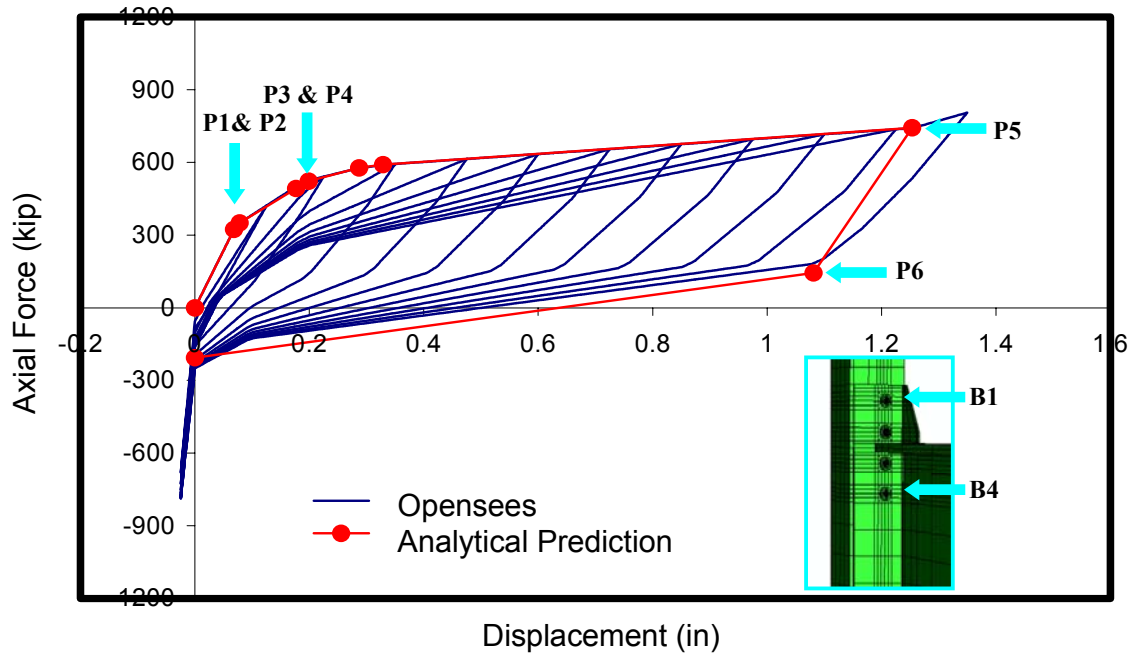
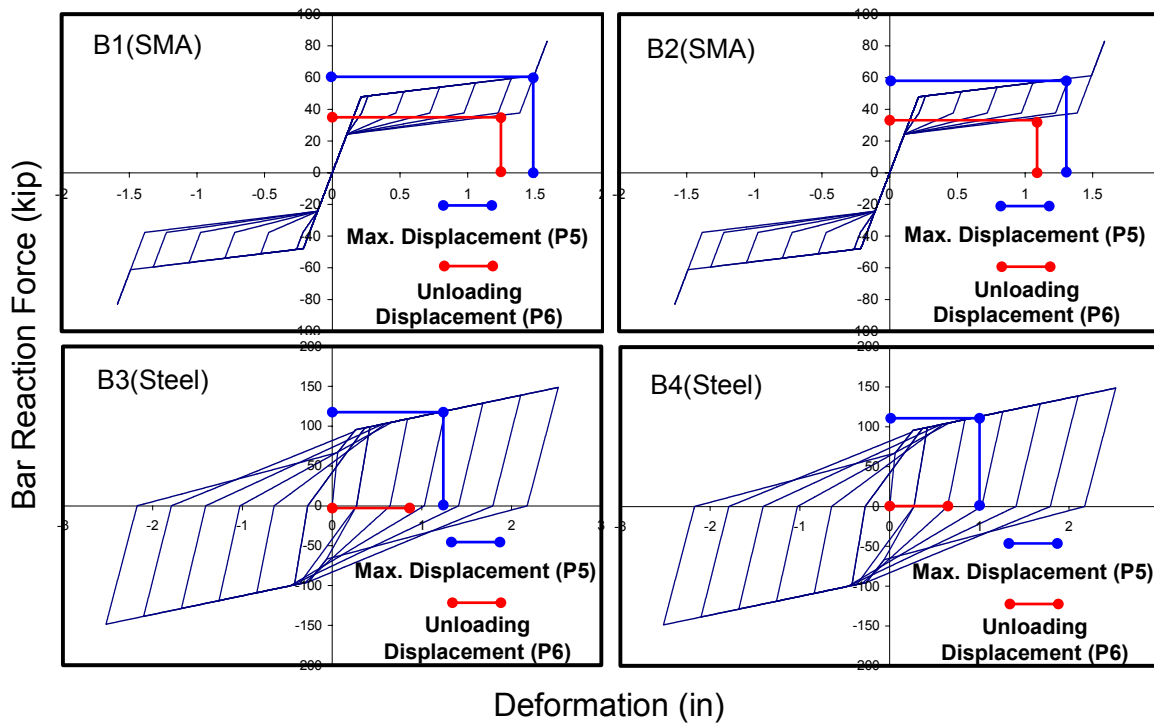


Figure 6.36 Results of tests for end-plate connections with different combinations of tension bars



(a) Axial Force (P) vs. displacement (Δ) points computed by the analytical observations of the behavioral property of the component model

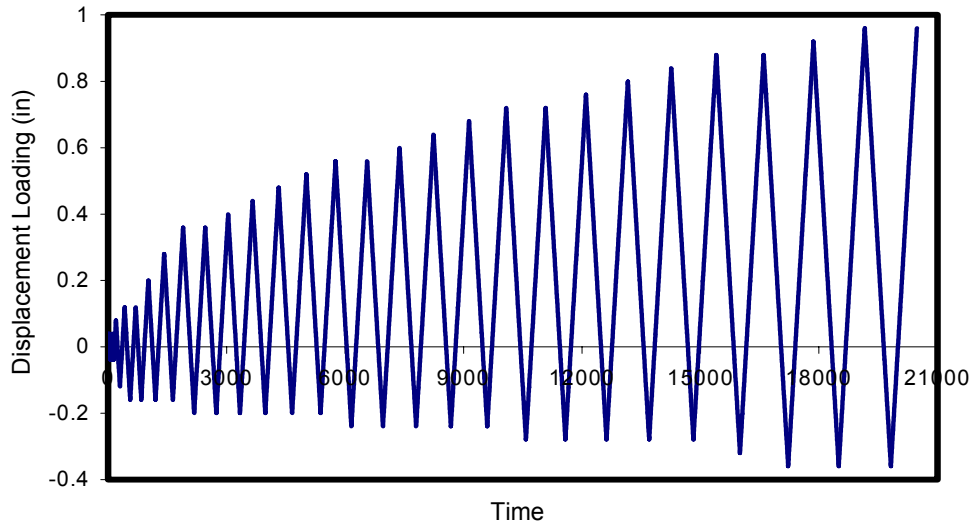


(b) The analytical observations of the behavioral property of the component model

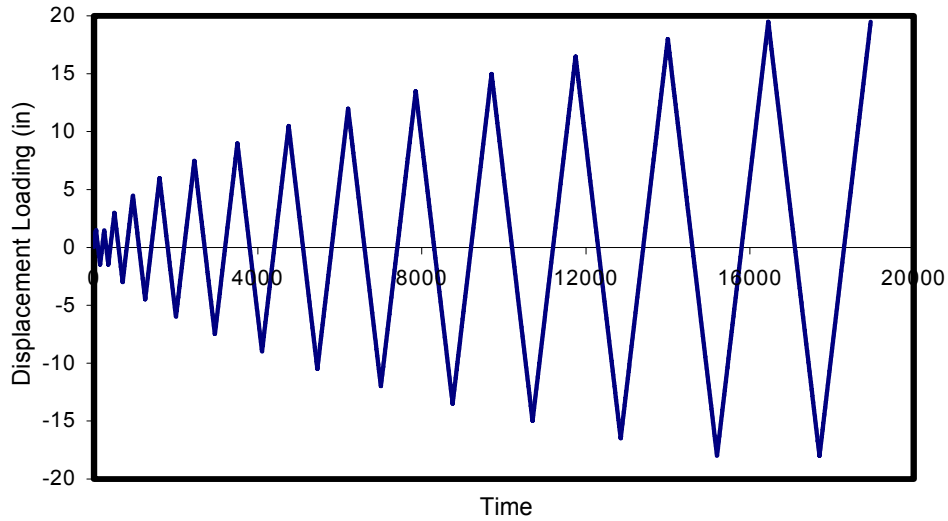
Figure 6.37 Analytical predictions for the behavior of the component models

6.4.2 Observations of Model Tests for T-stub Connections

The displacement loading histories for the T-stub connections are given in Figure 6.38. The connection details were illustrated in Figure 4.4. The connection behavior was compared with respect to three different combinations for tension bar installations. The format of these loading histories is the same as that of displacement loading histories for the end-plate connection models.



(a) Displacement loading history for the full test of the equivalent spring element



(b) Displacement loading history for the test of the joint element model

Figure 6.38 Displacement loading history for the model tests

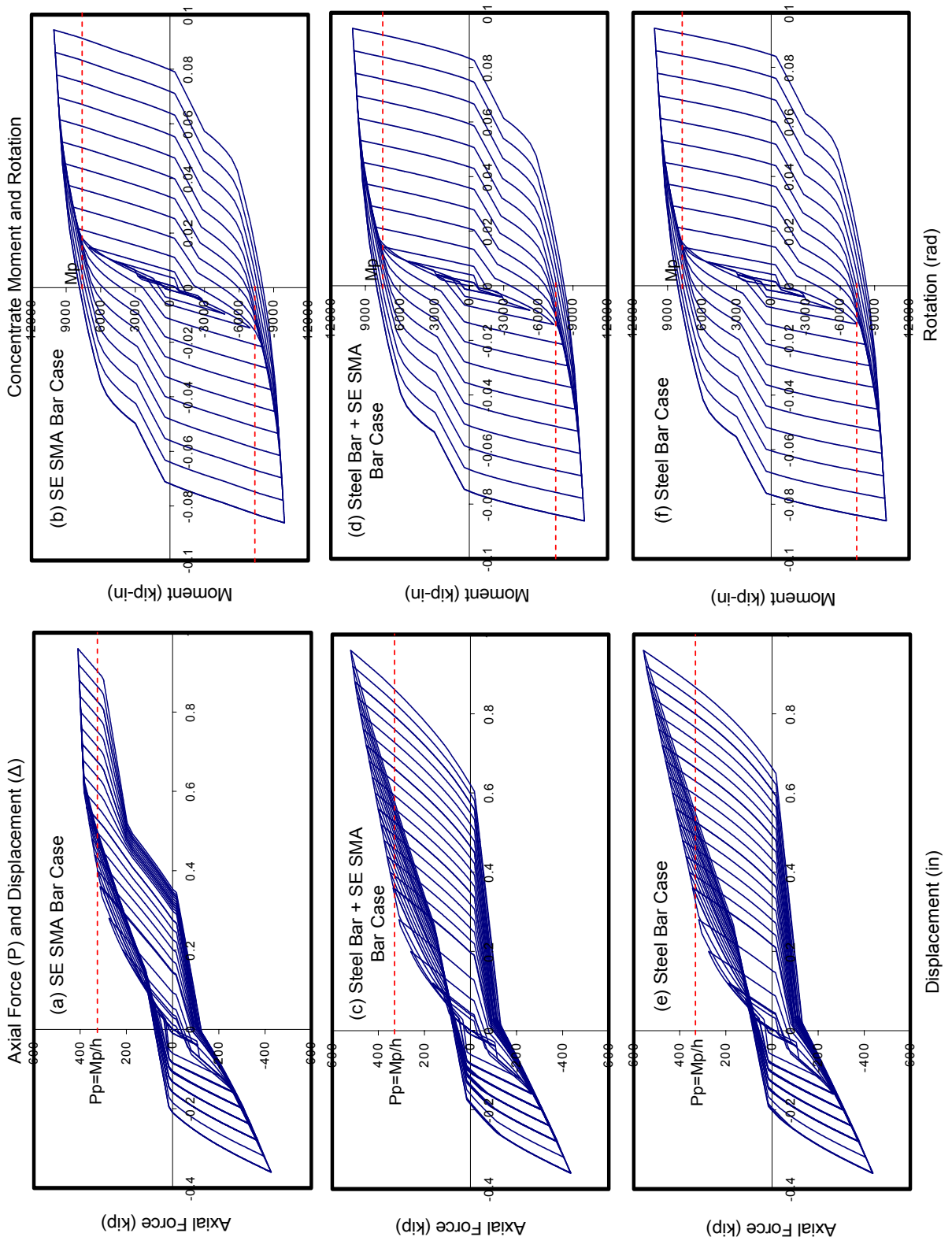
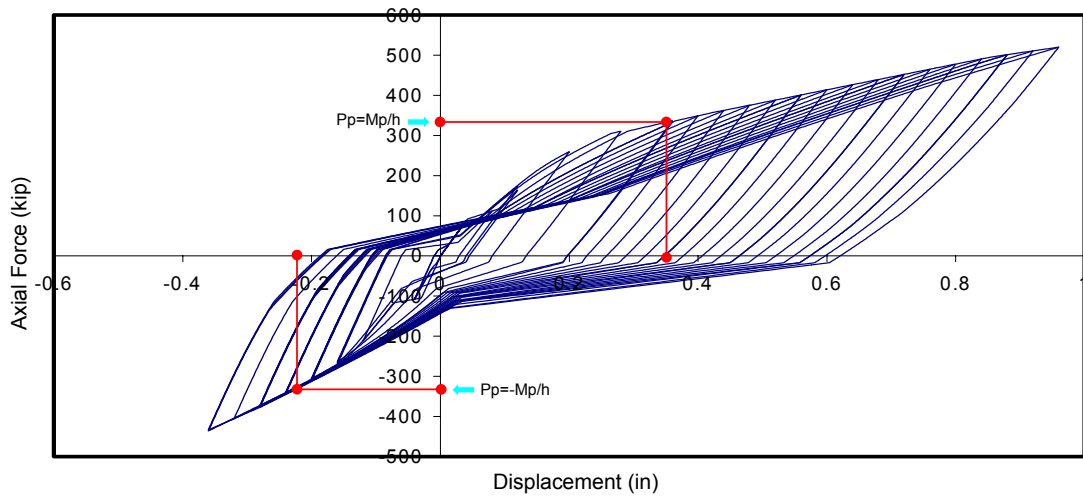


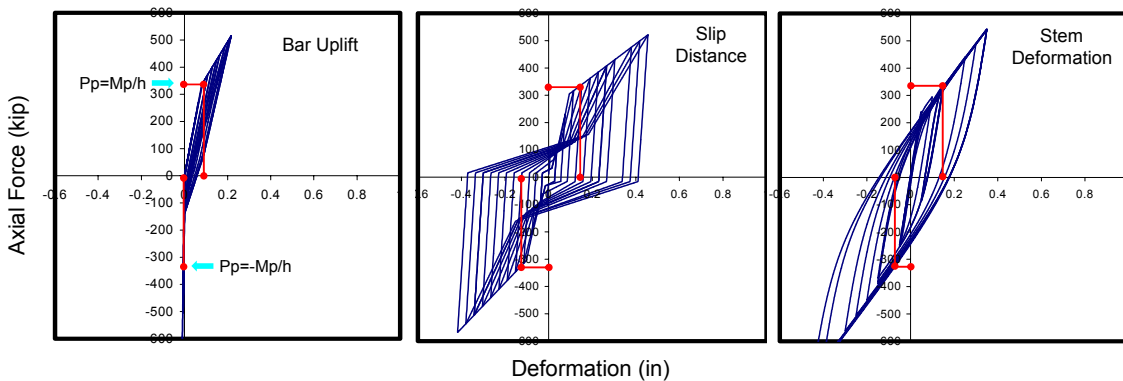
Figure 6.39 Results of model tests for T-stubs connections with different combinations of tension bars

Results of model tests for T-stub connections are given in Figure 6.39. Although both steel and SMA tension bars are used in the case shown in Figures 6.39(a) and (b), there are significant permanent deformation and much of the recentering capability shown in the end plate connection is lost. This is a direct result of the design procedure which allows (encourages) yielding of the T-stem. This deformation is not recoverable, but leads to high energy dissipation. Yielding of the beam is also reflected in the plastic deformation at the moment vs. rotation curve. In many cases, the tension bars remain in the elastic state.

An example of an analytical prediction is given in Figure 6.40. Since the assembly consists of a series of springs in series, the total displacement (Δ) is equal to the summation of three component deformations (See Figure 6.13).



(a) Axial Force (P) vs. displacement (Δ) point computed by the analytical observations of the behavioral property of the component model

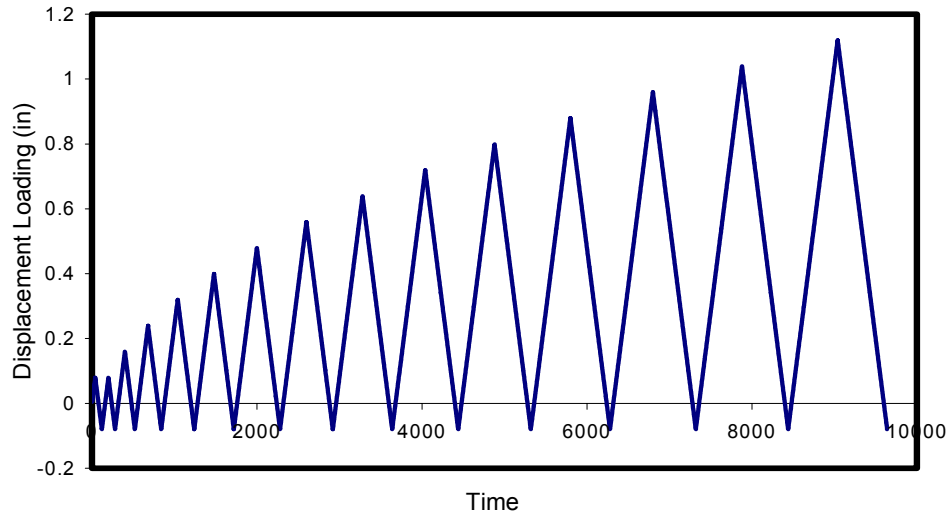


(b) The analytical observations of the behavioral property of the component model

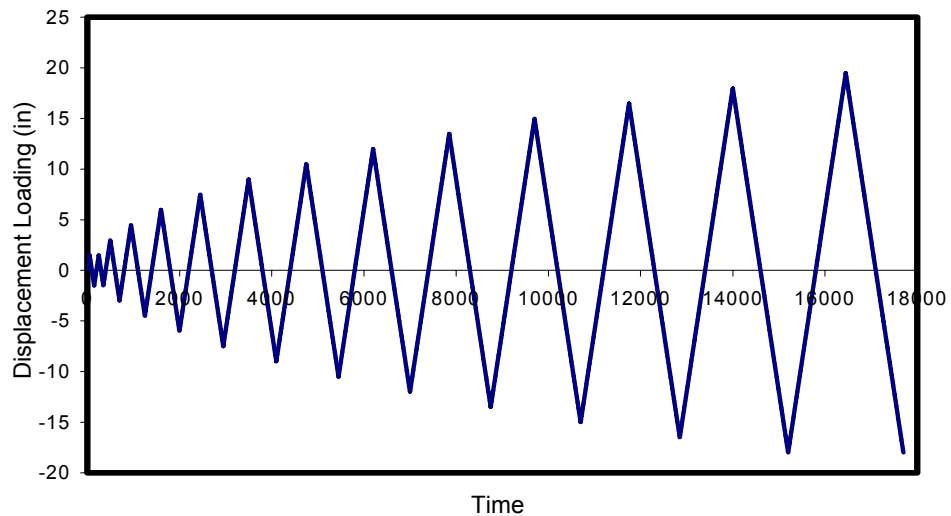
Figure 6.40 Analytical predictions for the behavior of the component models

6.4.2 Observations of Model Tests for Clip Angle Connections

The displacement loading histories and results for clip angle connections are given in Figures 6.41 and 6.42 respectively. The details of the clip angle geometry were illustrated in Figure 4.6. A detailed example of the analytical prediction is given in Figure 6.43.



(a) Displacement loading history for the full test of the equivalent spring element



(b) Displacement loading history for the test of the joint element model

Figure 6.41 Displacement loading history for the models

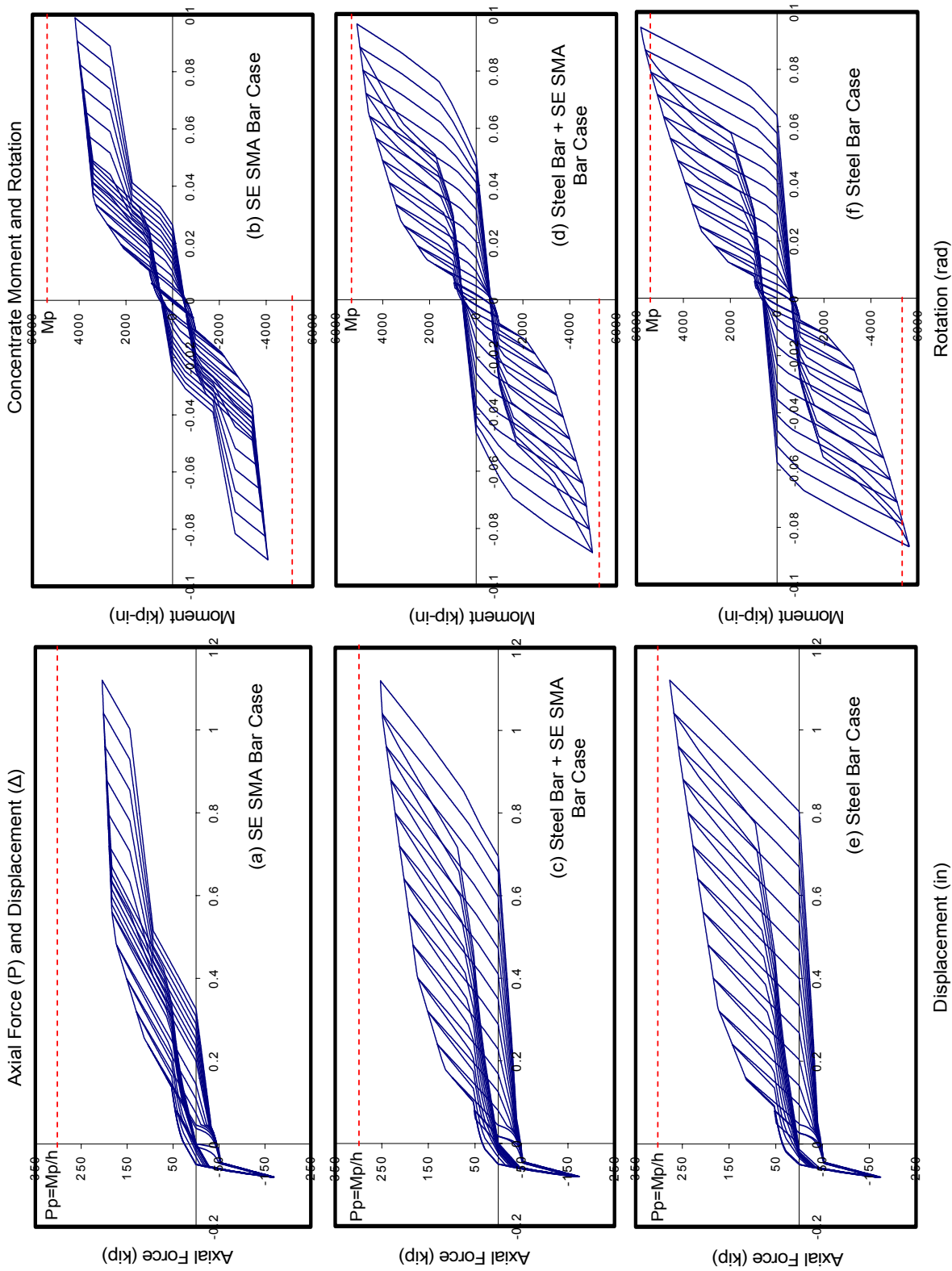
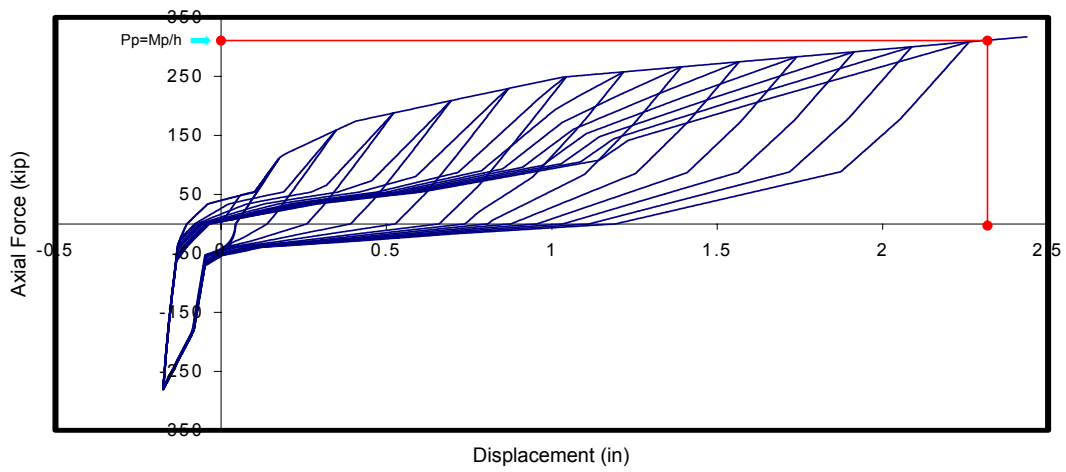
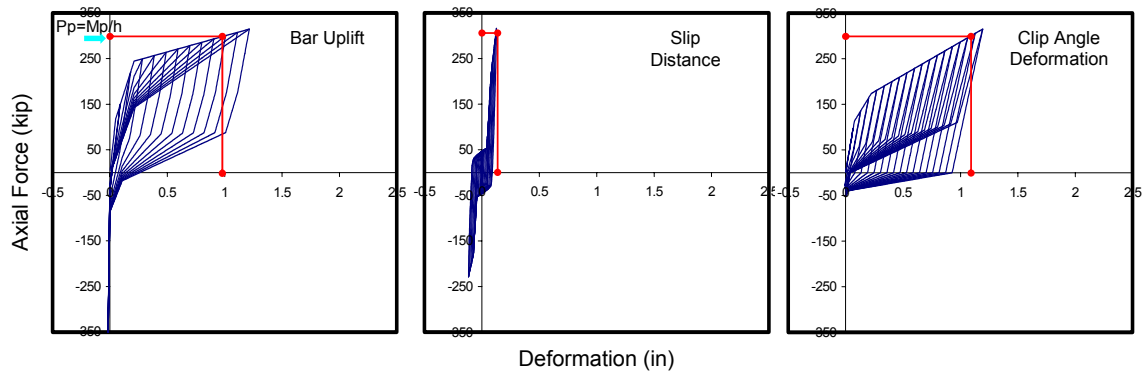


Figure 6.42 Results of model tests for clip-angle connections with different combination of tension bars



(a) Axial Force (P) vs. displacement (Δ) point computed by the analytical observations of the behavioral property of the component model



(b) The analytical observations of the behavioral property of the component model

Figure 6.43 Analytical predictions for the behavior of the component models

6.5 Summary and Discussion

This chapter discussed the cyclic modeling of the joints developed in this research and some selected test results. The component models were investigated in Section 6.1. The component model was assigned to a spring element whose properties were defined by either its material behavior (tension) or the observation of 3D FE test (compression/bearing). Groups of these springs are assembled in series or parallel system to simulate the joint behavior.

The formation of the 2D joint element for a typical PR connection was described in Section 6.2. This joint element includes the behavioral properties of the components in the form of a simplified model that aims to reflect the global stiffness, strength and deformation capacity of the actual connection. This type of joint model results in significant savings in running time for frame analyses.

In Section 6.3, the exact behavior of the connections including slippage, Bauschinger effect, and even shape memory effect were observed on the cyclic curves. Comparisons between test results and numerical simulations showed good agreement.

Parametric studies on the effect of different combinations of steel and SMA tension bars on the cyclic behavior characteristics were described in Section 6.4. The shape memory effect and yielding of other component members were affected by variations in this parameter. The decomposition of the contributions to joint deformation provided the opportunity to understand the response mechanism of the component models of the connection. Up to this chapter, the design procedures, computational modeling, and simulation focused only on the local connection models. Based on these previous studies, the direction of research will now shift to the analyses of entire composite frames with these connection models.

Chapter 7

Design of Composite Moment Frames with Smart SMA PR-CFT Connections

Three sets of prototype composite partially restrained moment frames (C-PRMF) were designed – one with end-plate, one with T-stub, and one with clip angle connections. In addition, companion composite special moment frames (C-SMF) with fully rigid (FR) welded connections were also designed in order to compare the behavior of both types (partially (PR) and fully restrained (FR)) composite frames. All composite moment frames presented here are designed in accordance with the *AISC 2005 Seismic Provisions* (AISC 2005 Seismic Provisions) and the *IBC 2003* (IBC 2003) for lateral and gravity loads, respectively. The gravity and lateral loads were determined following the ASCE 7-05 guidelines (ASCE 2005). Design limits, system requirements, and seismicity factors for these building located on a high seismicity area were determined by these guidelines.

This chapter will be structured as follows. Typical characteristics of these frames are described in Section 7.1. Descriptions of the PR building configurations used in this study are given in Section 7.2. Seismic design methods, design limits, and the equivalent lateral forces are described in Section 7.3. This section is associated with Appendix D, which includes the detailed procedures for computing the equivalent lateral forces. The design of the C-SMF specimens is given in Section 7.4. Key attributes for the numerical models are described in Section 7.5. The procedure for the numerical modeling of the deformations of the panel zones is described in Appendix E. Finally, summary and discussion of these frame models are given in Section 7.6.

7.1 Characteristics of Composite Moment Frames

The frame designs are governed by the *AISC 2005 Seismic Provisions*. Four general classes of composite moment frame (C-MF) are identified in Part II of the *AISC 2005 Seismic Provisions* (AISC 2005 Seismic Provisions) as shown in Table 7.1. The buildings were designed to the loads prescribed by ASCE 7-05 (ASCE 2005). The primary purpose of the ASCE 7-05 standard is to provide information useful to determine the required

strength, maximum inter-story drift, and seismic use groups for a given structure type and geographical location. The seismic design category (SDC) assigned to a building is a classification based upon the occupancy class (type of occupation and consequences to human life in case of collapse) and the seismicity of the site. SDC A, B and C generally correspond to structures in zones of low to moderate seismicity or low importance, while SDC D, E, and F require special seismic detailing as they address structures in areas of high seismic risk and/or critical structures (hospitals, fire stations, emergency response centers, for example). For this study, composite PR moment frames (C-PRMF), a moderately ductile system, and composite special moment frames (C-SMF), one of the most ductile systems, were selected for the trial design of several low-rise (4 to 6 stories) moment frames. The designs herein satisfy all the design requirements of C-PRMF or C-SMF for SDC D, E, or F.

Table 7.1 General classes of composite moment frame (C-MF)

The type of C-MF	Main deformation/yield shape	A total inter-story drift angle	SDC	Special system requirements
C-PRMF	Limited yielding in column base Main yielding in the ductile components	0.04 radian	C or below	A nominal strength is at least equal to 50 percent of M_p
C-SMF	Main yielding in the beams Limited inelastic deformations in the columns and/or connections	0.04 radian	D and above	The required strength shall be determined with the flexural strength (LRFD: $R_y M_n$)
C-IMF	Main yielding in the beams Moderate inelastic deformations in the columns and/or connections	0.03 radian	C and below	-
C-OMF	The limited inelastic action will occur in the beam, columns and/or connections	-	A and B	-

Typical composite partially restrained frames (C-PRMF) are composed of I-shape steel columns and composite steel beams which are interconnected with PR composite connections (Leon and Kim 2004; Thermou, Elnashai, Plumier, and Doneaux 2004). However, composite PR frames with concrete filled tube columns and steel beams with PR composite connections have been recently proposed (Tsai et al. 2004 and Wu et al. 2006). PR composite connections use traditional shear and bottom flange connections, but take advantage of the floor slab to provide the top connection. Composite connections use shear studs to the beams and slab reinforcement in the negative moment regions to

provide additional strength and stiffness as shown in Figure 7.1. A PR composite connection has many beneficial characteristics including:

- The floor slab system results in a more efficient distribution of strength and stiffness between negative moment and positive moment regions of the beam. It also contributes to the redistribution of loads under inelastic state.
- In the design of PR composite connections, applied loads can be considered separately, with the bending moment assigned to the steel reinforcement in the slab and a clip angle or plate on the bottom flange, and the shear force assigned to the web angle or plate.
- PR composite connections can undergo large deformations without fracture. The connections are generally designed for less than the full plastic strength of the beam. The ductility of the connection comes from deformations of its many components. The intent is to delay the occurrence of brittle failures such as web crippling, bolt or weld failures, and net section failures. If these brittle failures are avoided, the large available connection ductility can guarantee excellent frame performance under large inelastic deformations.
- PR moment frames are better at mitigating the effects of seismically induced loads as the lengthening of the natural period due to both the flexibility of the connection and its gradual yielding and stable hysteretic behavior of the connections.

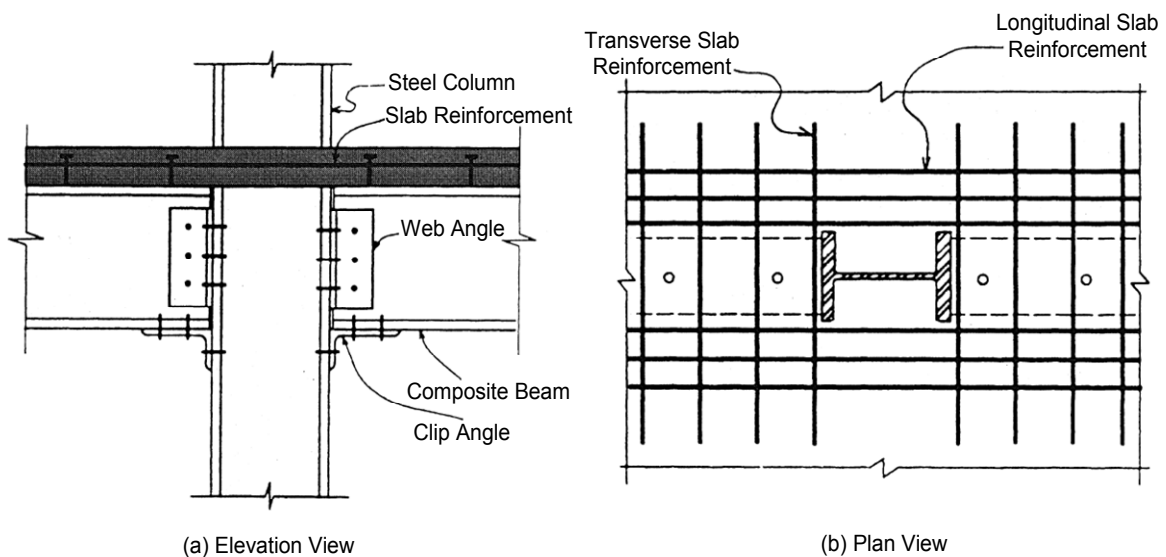


Figure 7.1 Typical composite partially restrained moment connection
(AISC 2005 Seismic Provisions)

C-PRMF were originally conceived for areas of low to moderate seismicity in SDC C and below. However, C-PRMF can be used in areas of higher seismicity (Leon 1990) with appropriate detailing and analyses. In addition, the recently developed bidirectional bolted connections for CFT columns and I-beams provide superior earthquake performance in terms of in stiffness, strength, ductility, and energy dissipation. Recent studies demonstrate that the seismic resistance exceeds those requirements specified in the seismic design codes of Taiwan and the US (Wu et al. 2007). The structural configurations of those connections are very similar to those of end-plate connections presented in this research (See Figure 7.2). Therefore, C-PRMF with those connection models have excellent seismic resistance, and this structural system can perform well and be put into practice.

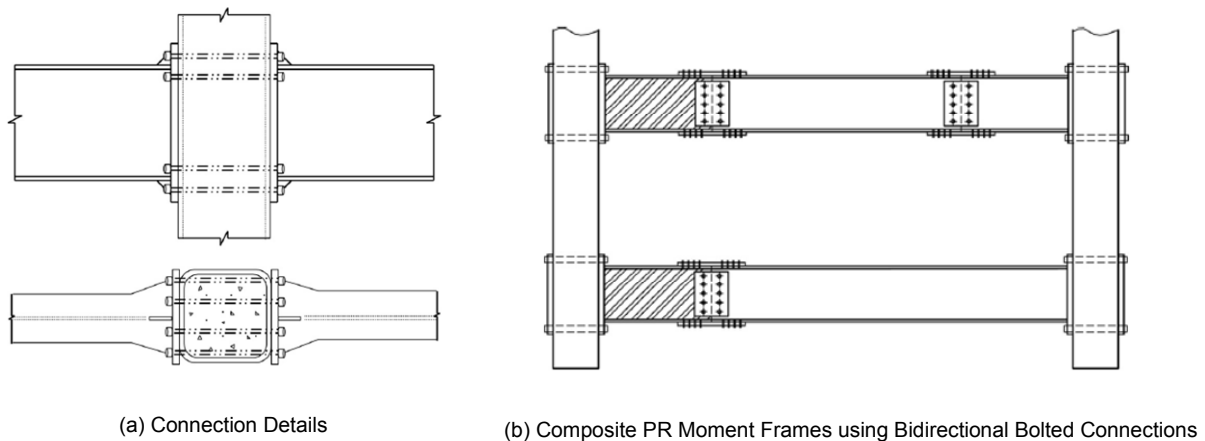
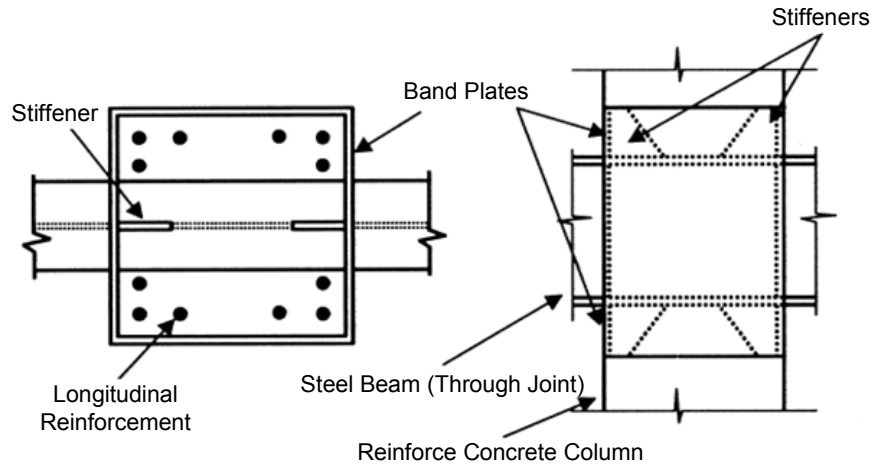


Figure 7.2 Bidirectional bolted connections between CFT columns and H-beams

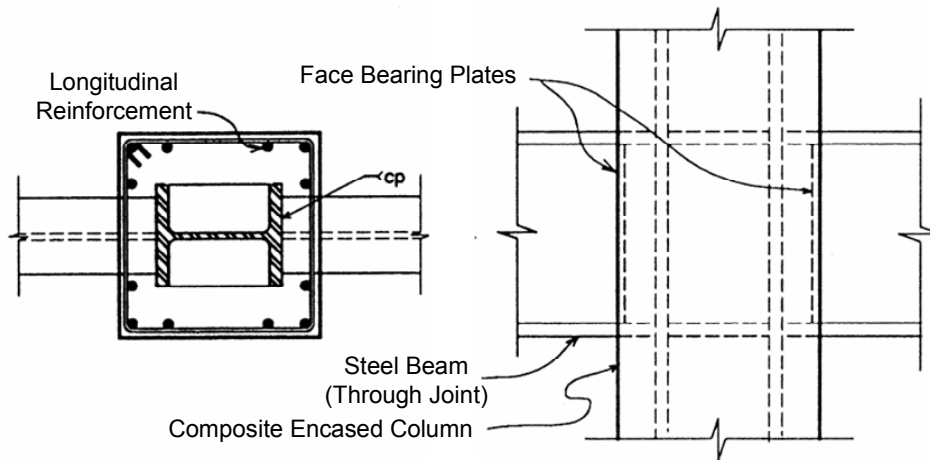
(Wu et al., 2007)

Composite special moment frames (C-SMF) are composed of a variety of configurations where structural steel or composite beams are combined with either reinforced concrete or composite columns. Schematic connection drawings for C-SMF are shown in Figure 7.3. In order to avoid the need for field welding of the beam flange adjacent to the critical beam-to-column junction, the steel beam can run continuously through the reinforcement concrete column as shown in Figure 7.3 (a). The steel band plates attached to the beam are one of possible ways to strengthen the joint by providing good confinement to the concrete. As shown in Figure 7.3 (b), connections between steel

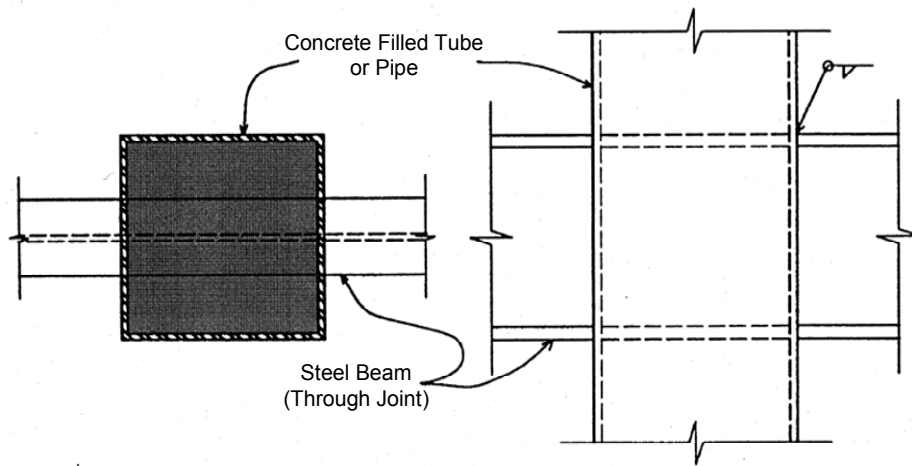
beams and encased composite columns have been used and tested extensively in Japan. One disadvantage of this connection detail is that it requires welding of the beam flange to the encased steel column. Composite filled tube column-to-steel beam connections as shown in Figure 7.3 (c) have been used less frequently but there has been recent research resulting in practical design recommendations (Azizinamini and Schneider 2004). Based on ASCE 7-05, C-SMF were originally designed for use in SDC D and above. C-SMF shall be designed with assumption that significant inelastic deformation will occur under the design earthquake, primarily in the beams, but with limited inelastic deformation in the columns and connections. Therefore, connections in C-SMF satisfy the story drift capacity of 0.04 radian as specified in the *AISC 2005 Seismic Provisions* (AISC 2005 Seismic Provisions) so that they are not susceptible to weld fracture.



(a) Reinforce concrete column-to-steel beam connection



(b) Composite encased column-to-steel beam connection



(c) Composite filled tube column-to-steel beam connection

Figure 7.3 Typical composite special moment connection
(AISC 2005 Seismic Provisions)

7.2 Building Configurations

This section describes the building configurations for C-PRMF and C-SMF used in this study. C-PRMF were designed with three types of moment connections: end-plate, T-stub, and clip angle connections. The rest of the system comprises structural steel beams and CFT columns. On the other hand, C-SMF were designed with welded moment connections between composite filled tube columns and steel beams

Table 7.2 Location, loads, and structural classifications common to all frames

Located Area	Gravity Loads	SDC	Occupancy Category
LA Area	Dead: 100 psf Live: 80 psf	D Class	Ordinary Structures

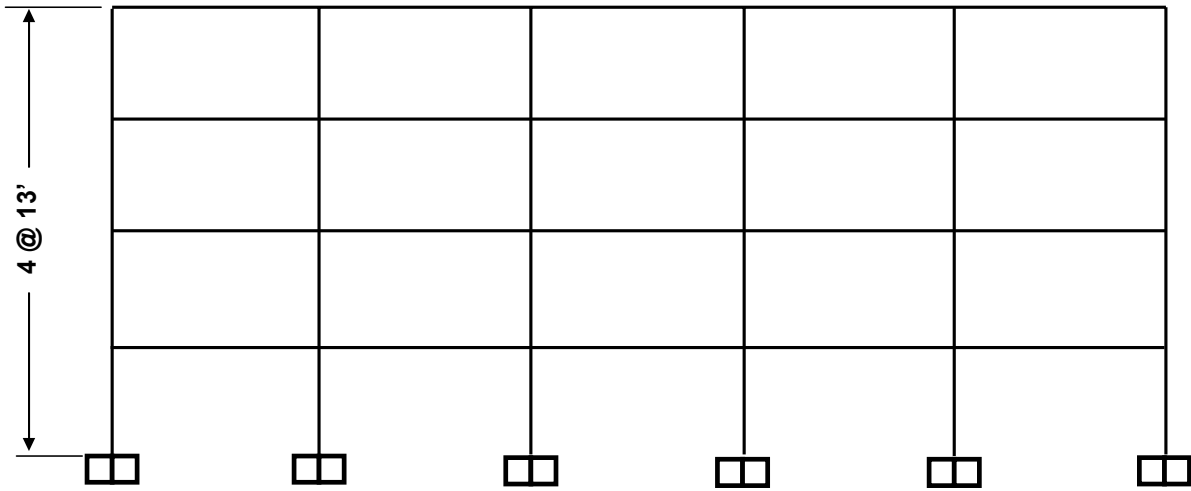
Building configurations, materials, and modeling conditions were the same for both the C-PRMF and C-SMF in order to compare their inelastic behavior. Four and six story configurations with 3 by 5 long bays were used throughout this research. Perimeter moment resisting frame systems were used because the intent is to demonstrate the economy of this system for a market segment that constitutes about 90 percent of the steel frame construction in the USA. Most of all, these moment resisting frames have

been very popular in many regions of high seismicity because of high ductility and excellent architectural versatility. Identical dead loads, live loads, seismic design, and occupancy category are used with all buildings, as given in Table 7.2. More detailed descriptions are given in the following sub-sections.

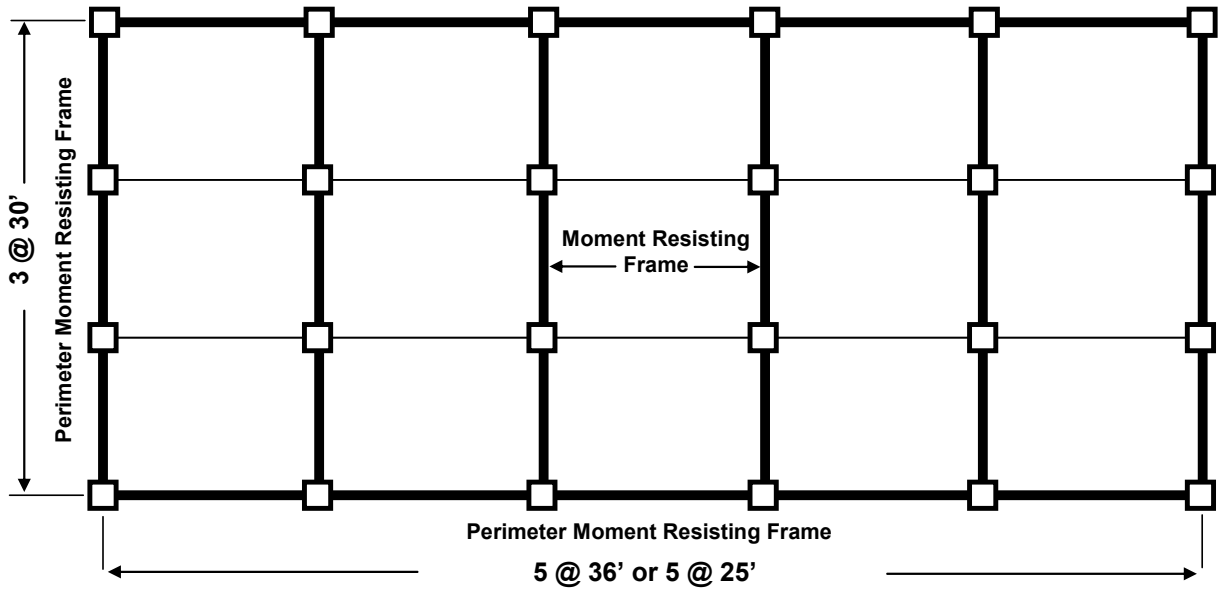
7.2.1 Building Description for 4 Story Building

The configuration for the 4 story buildings is shown in Figure 7.4. The total height is 52 ft., with a constant height 13 ft. for all stories. This building has 3 bays by 5 bays. There are two bay lengths according to the PR moment connections used. Bays with end-plate connections (5 @ 36') have longer bay lengths than those with clip angle connections (5 @ 25') because the former connections consist of larger beam and columns (Table 7.2). C-SMF having welded moment connections were also designed with 36 ft. (5 @ 36') and 25 ft. (5 @ 25') bay lengths. In addition, the same member size for each C-PRMF was used in the corresponding C-SMF in order to compare the behavior of both composite frames.

Resistance against lateral forces is provided primarily by rigid frame action in the perimeter frames. These perimeter frames utilize composite PR connections between the CFT columns and beams while the interior CFT columns and beams aligned in one direction are interconnected by pinned connections. For the C-SMF, FR connections are used in the perimeter frames instead of PR connections. The moment resistant frames with either PR or FR connections are presented as thick lines in the building plans for each frame type shown in Figure 7.4. The moment connections used in the moment resistant frames of the 4 story buildings are given in Figure 7.5.

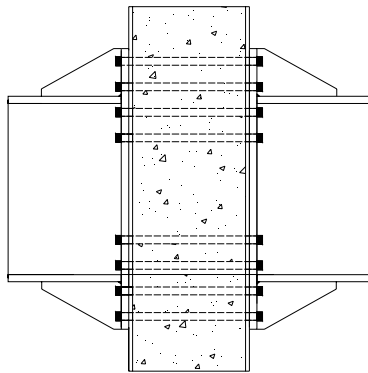


(a) Building Elevation View

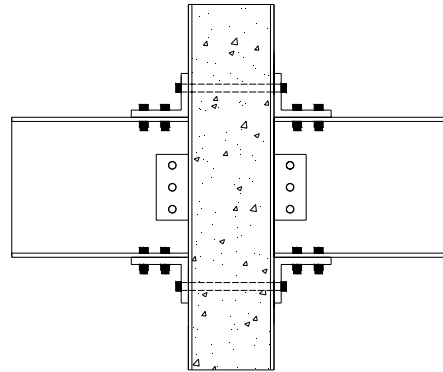


(b) Building Plan View

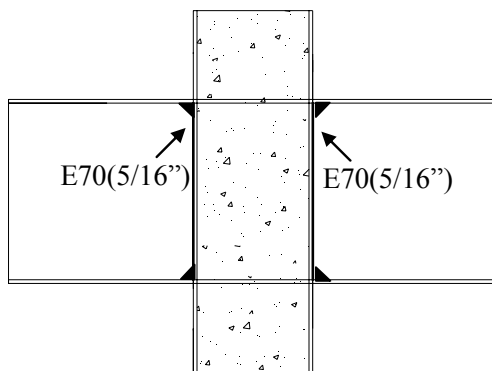
Figure 7.4 Building elevation and plan view for the 4 story building



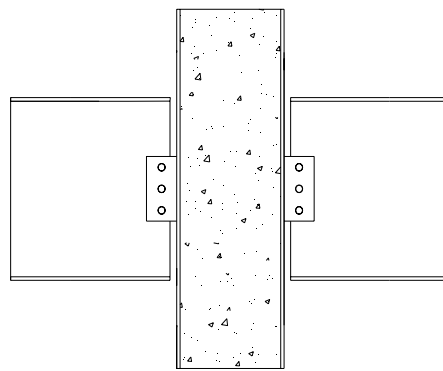
(a) PR Moment Connection
(End Plate Connection)



(b) PR Moment Connection
(Clip Angle Connection)



(c) FR Moment Connection (Composite
Welded Connection)



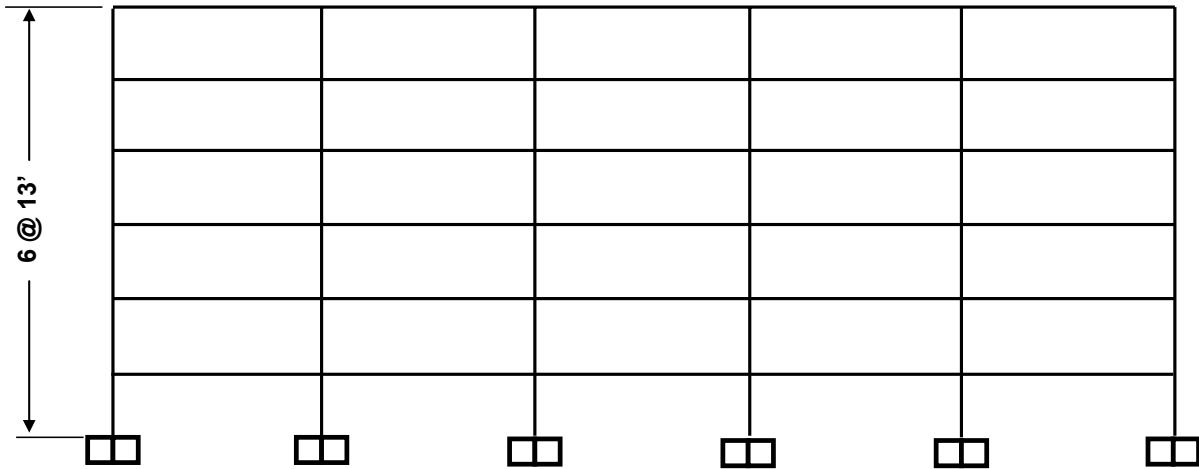
(d) Pinned Connection (Shear
Tab Connection)

Figure 7.5 Cruciform connection details for moment frames (4 story building)

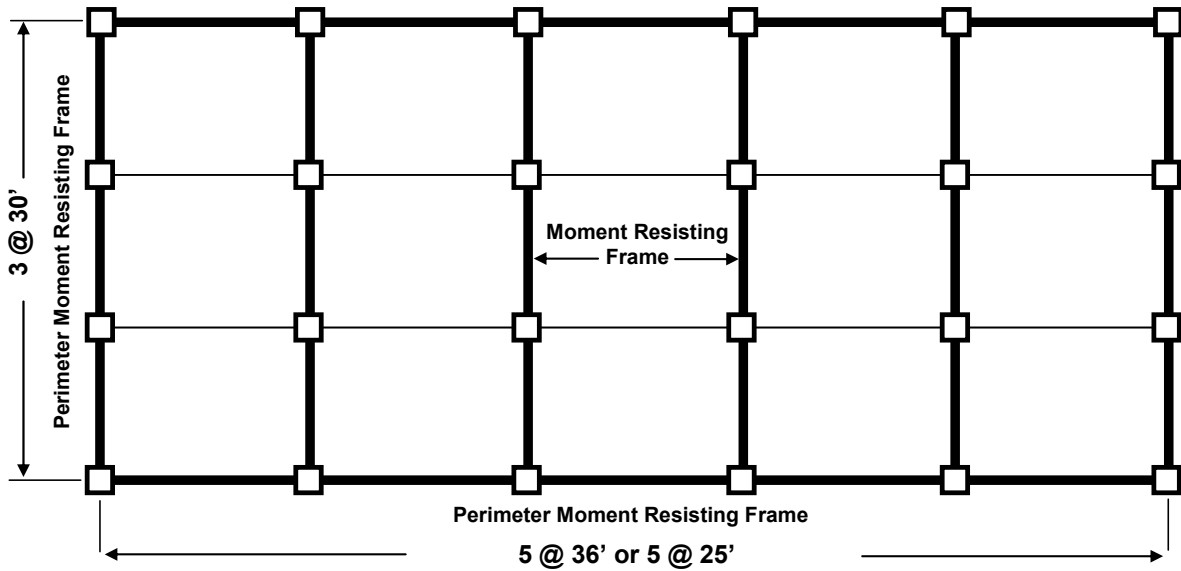
7.2.2 Building Description of 6 Story Building

The configuration for the 6 story buildings is shown in Figure 7.6. The total height is 78 ft in the elevation, with uniform 13 foot heights. This building also has 3 bays by 5 bays. There are two kinds of bay lengths determined according to the PR moment connections used. The bays with end-plate connections (5 @ 36') have longer bay lengths than those with T-stub connections (5 @ 25') because the former connections consist of larger beam and columns. The plan for the 6 story building is the same as that of 4 story building. Both buildings share the same conditions given in Table 7.2. C-SMF having welded moment connections were designed with five 36 ft. (5 @ 36') and five 25 ft. (5 @ 25') bay lengths. As for the 4 story buildings, the same member size within each C-PRMF was used in the corresponding C-SMF in order to compare the behavior of both composite frames.

Thick lines in the building plan Figure 7.6) indicate the moment resisting frames. The moment resisting frames in 6 story building were located in the same positions as those in the 4 story building. However, T-stub connections were used as the PR connections in the five 25 ft. (5 @ 25') bay lengths. T-stub connections provide less inter-story drift as well as more resistance against to the lateral loads in comparison with clip angle connections. For this higher building system, T-stub connections are a better structural system than clip angle connections under the same modeling conditions for plan and component members. The moment connections use in the moment resistant frames for the 6 story buildings are given in Figure 7.7. The detailed design procedures for all frame specimens will be described in the next section where the use of the SAP2000 programs (CSI, 1984-2004) is described.

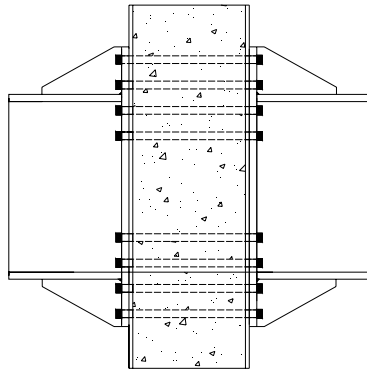


(a) Building Elevation View

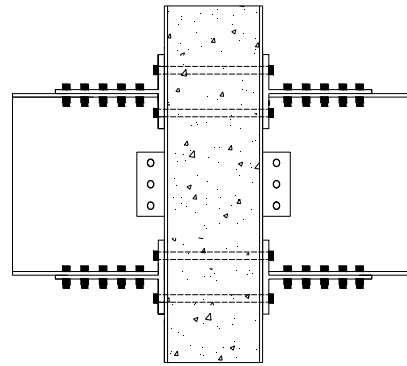


(b) Building Plan View

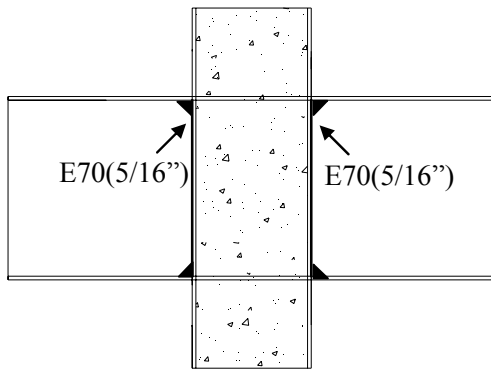
Figure 7.6 Building elevation and plan view for the 6 story building



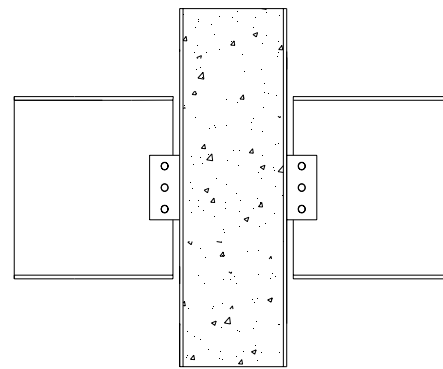
(a) PR Moment Connection
(End Plate Connection)



(b) PR Moment Connection
(T-Stub Connection)



(c) FR Moment Connection (Composite
Welded Connection)



(d) Pinned Connection (Shear
Tab Connection)

Figure 7.7 The cruciform connection details for moment frames (6 story building)

7.3 Seismic Design Method

As stated above, the connections and the composite frames were designed as structures located in the L.A area in accordance with *AISC LRFD* (AISC 2001) and *AISC 2005 Seismic Provisions* (ANSI/AISC 341-05) respectively. The design of the prototype buildings was checked with the SAP 2000 design checking tool (SAP 2000, ver 11, 2007). Only Dead (D), live (L), and earthquake (E) loads are considered in this research as earthquakes dominate over wind in the L.A. area. The equivalent lateral loads (E) for these composite frames are calculated by using 2003 International Building Codes (IBC 2003).

7.3.1 Load Combinations

The design dead and live loads for the composite frames are assumed as 100 psf and 80 psf respectively. A572 Grade 50 steel was used for beams and steel section of CFT columns. ASCE 7-05 and LRFD design guidelines for load factors and combinations were used, as follows:

- Load Combination 1: 1.4D
- Load Combination 2: 1.2D + 1.6L + 0.5L
- Load Combination 3: 1.2D + 1.6S + (0.5L or 0.8W)
- Load Combination 4: 1.2D + 1.6W + L + 0.5S
- Load Combination 5: 1.2D + 1.0E + L
- Load Combination 6: 0.9D + 1.6W
- Load Combination 7: 0.9D + 1.0E

The terms related snow load (S) and wind load (W) were ignored in the above combinations. The earthquake effect includes the components from both vertical and horizontal accelerations. Based on the load combinations, load combination 5 dominated over other load combinations.

7.3.2 Equivalent Lateral Loads

Composite moment frames should provide adequate strength, stiffness, and energy capacity so that they can withstand not only the lateral loads but also the gravity loads within specified limits of deformation and strength. The design utilized equivalent lateral load procedures as introduced in the ASCE 7-05 and the IBC2003 codes. The equivalent lateral load approach is based on a set of static lateral loads that corresponds to the 1st mode shape of deformation. For frame structures, the first mode generally contributes upwards of 90% of the effective seismic mass and dominates the behavior of the structure. Therefore, those procedures may not always be valid when higher mode shapes contribute more than 10% of the effective seismic mass. More details on the calculation procedures for equivalent lateral loads are given in Appendix D.

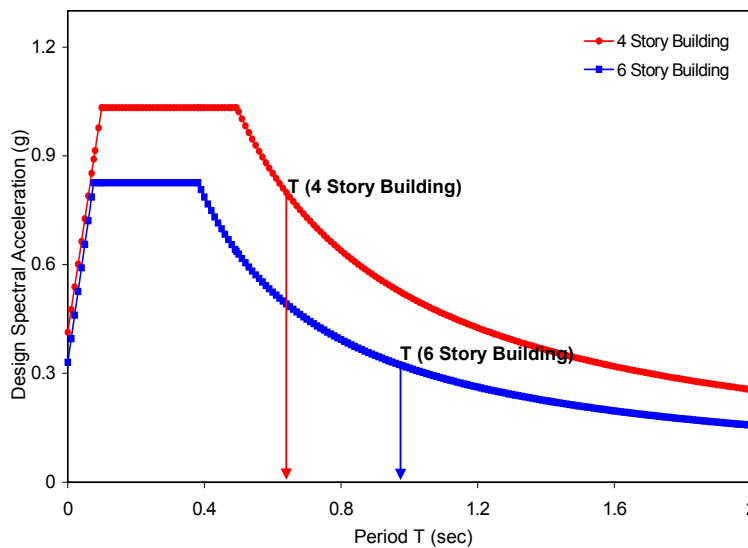


Figure 7.8 Design response spectra for CMF in LA area

The design response spectra for these composite moment frames (CMF) in the LA area are summarized in Table 7.3 and Figure 7.8. The site class for the area on which the building is located is one of the factors that determine the seismic response coefficients. A site class A for 4 story building or C for 6 story building, which corresponds to hard rock area or soft rock area respectively, was used in these designs. The fundamental time period of the building is computed by simplified analysis based on the code equations (ASCE 7-05 Sec. 9.5.4 and IBC2003 Sec.1617.5). Therefore, the same value of fundamental time period can be applied to the buildings with same number of stories and

heights regardless of the connection type. The final calculations for the equivalent lateral loads are summarized in Table 7.4. The vertical distribution of the equivalent lateral load is proportional to the area of the building plan which determines the weight of each story level.

Table 7.3 Design response spectra for CMF in LA area

	4 Story Frame	6 Story Frame
Area	90045 LA Area	90045 LA Area
Site Class	C	A
S_s	1.5491	1.5491
S_1	0.5897	0.5897
F_a	1.0	0.8
F_v	1.3	0.8
S_{ms}	1.5491	1.2393
S_{m1}	0.7666	0.4718
S_{Ds}	1.033	0.8262
S_{D1}	0.511	0.3146
T_0	0.099	0.076
T_s	0.495	0.381
T	0.661	0.914

Table 7.4 Design loads for all composite moment frames

Story	Dead Load (D)	Live Load (L)	Equivalent Lateral Load (E)
1	100 psf	80 psf	36.3 kip
2	100 psf	80 psf	57.6 kip
3	100 psf	80 psf	59.5 kip
4	100 psf	80 psf	40.6 kip

(a) The design loads for 4 story composite frame with end-plate connections (5 @ 36' bay length)

Story	Dead Load (D)	Live Load (L)	Equivalent Lateral Load (E)
1	100 psf	80 psf	21.02 kip
2	100 psf	80 psf	33.34 kip
3	100 psf	80 psf	34.44 kip
4	100 psf	80 psf	23.50 kip

(b) The design loads for 4 story composite frame with clip angle connections (5 @ 25' bay length)

Story	Dead Load (D)	Live Load (L)	Equivalent Lateral Load (E)
1	100 psf	80 psf	19.62 kip
2	100 psf	80 psf	37.73 kip
3	100 psf	80 psf	49.24 kip
4	100 psf	80 psf	52.26 kip
5	100 psf	80 psf	45.61 kip
6	100psf	80 psf	28.42 kip

(c) The design loads for 6 story composite frame with end-plate connections (5 @ 36' bay length)

Story	Dead Load (D)	Live Load (L)	Equivalent Lateral Load (E)
1	100 psf	80 psf	11.35 kip
2	100 psf	80 psf	26.20 kip
3	100 psf	80 psf	34.20 kip
4	100 psf	80 psf	36.29 kip
5	100 psf	80 psf	26.39 kip
6	100psf	80 psf	16.45 kip

(d) The design loads for 6 story composite frame with T-stub connections (5 @ 25' bay length)

7.3.3 Regulations and Limits

The IBC 2003 code is designed to protect public health and welfare in all communities through model code regulations. Minimum regulations for building systems using both prescriptive and performance based provisions are specified in this comprehensive building code.

IBC 20043 requires that the design story drift (Δ) should not exceed the allowable story drift (Δ_a) as obtained from Table 1617.3 of the IBC2003 for any story level. The design story drift can be calculated as the difference of the deflections (δ_x) at the center of mass at the top and bottom of the story. The deflections (δ_x) of each story level x and allowable story drift are determined as following equations:

$$\delta_x = \frac{C_d \delta_{xe}}{I_E} \quad (\text{EQ 7.1})$$

$$\Delta_a = 0.02 h_{xe} \quad (\text{EQ 7.2})$$

where,

C_d : the deflection amplification factor ($C_d=5.5$ for C-SMF system)

δ_{xe} : the deflections determined by an elastic analysis for C-SMF system

I_E : the occupancy importance factor ($I_E=1.0$ for an ordinary occupancy)

h_{xe} : the story height at each story level x

The P- Δ effects on the story shears and moments, the resulting member forces and moments and the story drift caused by these effects need not be considered when the stability coefficient (θ) is equal to or less than 0.1. The stability coefficient is determined by:

$$\theta = \frac{P_x \Delta}{V_x h_{sx} C_d} \quad (\text{EQ 7.3})$$

where,

P_x : total un-factored vertical design load at and above story level x

V_x : the seismic lateral force between story level x and story level $x-1$

Δ : the design story drift occurring simultaneously with V_x

The stability coefficient shall not exceed θ_{\max} determined as below:

$$\theta_{\max} = \frac{0.5}{\beta C_d} \leq 0.25 \quad (\text{EQ 7.4})$$

where, β is the ratio of shear demand to shear capacity for the story between story level x and story level $x-1$, generally taken as 1.0.

Based on these limits, the design checks for deflection and drift limits for the composite frames can be conducted by comparing the factored deflections obtained by Equation 7.1 and the stability coefficient obtained by Equation 7.3 with the allowable story drift and the stability coefficient limit (0.1 or θ_{\max}) respectively. The design checks of deflection and drift limit for C-SMF subjected to the dominant Load Combination 5 will be shown after the initial selection of member sizes using the SAP2000 programs (SAP2000).

7.4 Design of Composite Moment Frame Specimens

The design for all buildings that consist of structural composite columns and steel beams are summarized in Table 7.5. As mentioned above, material for all steel component members is assumed as A572 Gr. 50. The prototype building has nine variations according to the different combinations of connection types and column systems. A uniform size for all column members was selected because of fabrication and economy considerations. This means that the behavior of the lower columns is anticipated as the controlling factor, as the column sizes generally decrease with height. On the other hands, smaller beam sizes were selected for the higher stories in order to achieve an economical design. In addition, beam and column sizes presented in here are very close to those presented in the 3D FE models described in previous chapters in order to maintain the ideal failure modes. Other connection details follow those of the 3D FE connection models.

Structural models of both the 4 and 6 story buildings have symmetric configurations at all story levels. Because of the assumption that the composite floors behave as rigid diaphragms, the perimeter composite moment frames (C-MF) work together with the internal frames in resisting the lateral loads. Thus, analyses of a 2D perimeter composite moment frame can used to simulate the behavior of the buildings, avoiding the need for 3D analyses. Figure 7.9 show plan views of the 3D building and perimeter moment frames of interest (C-SMF). Moment frames along the W-E direction deform more under the equivalent lateral loads because of the larger number of panel zones and members. The red dashed rectangular indicate the perimeter C-SMF modeled as 2D models on a SAP2000 program.

Analyses performed by OpenSEES and SAP2000 were used to estimate story drift, deflections, and P-Delta effects. After this initial analysis, a design check was run by using an AISC-LRFD 2001 code which is available on the design check menu of SAP2000. Figure 7.10 shows the results of the design check for structural frame models with combined RCFT and CCFT columns. These design checks are described in terms of a strength ratio (capacity used/capacity available). The strength ratios are shown on the beam elements. The beam elements are deformed by the bending moments as well as the axial forces. Therefore, these strength ratios for the beams should include the available

strength of the members as beam-columns. Larger negative moments adjacent to the panel zone are the cause that the strength ratios acting on one end of beam elements are generally larger than those acting on the middle of beam elements as shown in Figure 7.10 (a-1). Other figures ranging from Figure 7.10 (a-2) to Figure 7.10 (d) show the largest strength ratio on each beam element. The design check function in SAP 2000 is only available for steel sections, so the design check for the composite columns will be calculated by other methods presented in Chapter 9.

Table 7.5 Design results for composite frame buildings

Model ID	Connection Type	Column System	Column Size (All Stories)	Beam Size	
				1 st and 2 nd Story	3 rd and 4 th Story
4END-C1	End Plate	RCFT	HSS16X16X500	W24X103	W24X84
4END-C2	End Plate	CCFT	HSS18X500	W24X103	W24X84
4END-C3	End Plate	RCFT+CCFT	HSS16X16X500,HSS18X500	W24X103	W24X84
4END-C4	End Plate	RCFT	HSS16X16X500	W24X103	W24X84
4END-C5	End Plate	CCFT	HSS18X500	W24X103	W24X84
4END-C6	End Plate	RCFT+CCFT	HSS16X16X500,HSS18X500	W24X103	W24X84
4END-C7	Welding	RCFT	HSS16X16X500	W24X103	W24X84
4END-C8	Welding	CCFT	HSS18X500	W24X103	W24X84
4END-C9	Welding	RCFT+CCFT	HSS16X16X500,HSS18X500	W24X103	W24X84

(a) 4 story building with 5 @ 36' bays and end-plate or welding connections

Model ID	Connection Type	Column System	Column Size (All Stories)	Beam Size	
				1 st and 2 nd Story	3 rd and 4 th Story
4CLI-C1	Clip Angle	RCFT	HSS14X14X500	W18X50	W18X50
4CLI-C2	Clip Angle	CCFT	HSS16X500	W18X50	W18X50
4CLI-C3	Clip Angle	RCFT+CCFT	HSS14X14X500,HSS16X500	W18X50	W18X50
4CLI-C4	Clip Angle	RCFT	HSS14X14X500	W18X50	W18X50
4CLI-C5	Clip Angle	CCFT	HSS16X500	W18X50	W18X50
4CLI-C6	Clip Angle	RCFT+CCFT	HSS14X14X500,HSS16X500	W18X50	W18X50
4CLI-C7	Welding	RCFT	HSS14X14X500	W18X50	W18X50
4CLI-C8	Welding	CCFT	HSS16X500	W18X50	W18X50
4CLI-C9	Welding	RCFT+CCFT	HSS14X14X500,HSS16X500	W18X50	W18X50

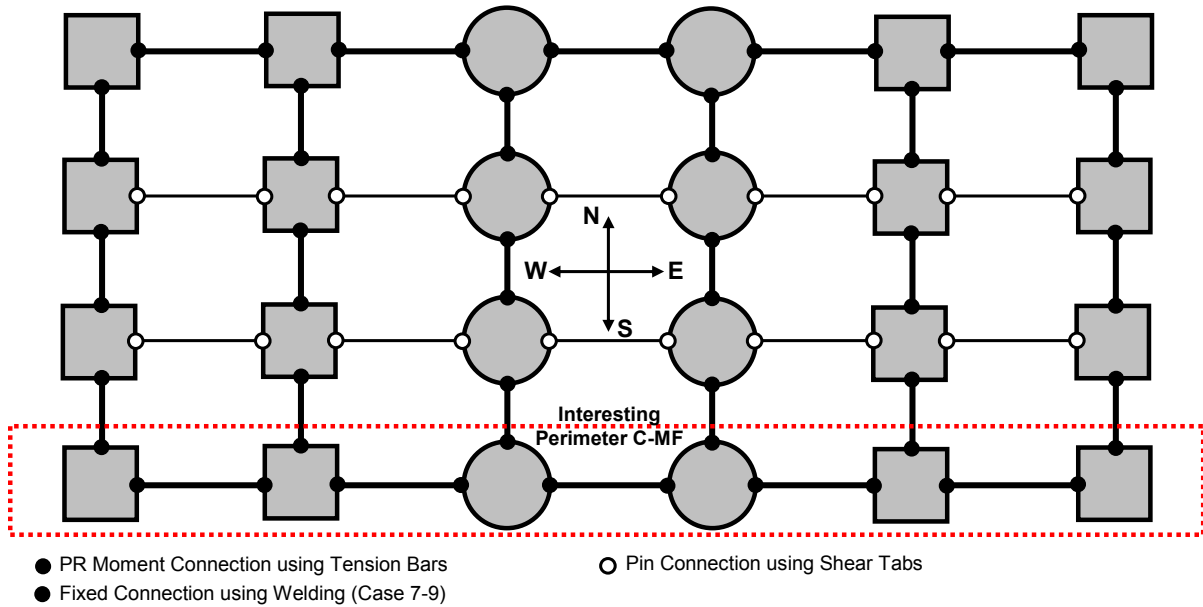
(b) 4 story building with 5 @ 25' bays and clip angle or welding connections

Model ID	Connection Type	Column System	Column Size (All Stories)	Beam Size	
				1st to 3rd Story	4th and 6th Story
6END-C1	End Plate	RCFT	HSS16X16X500	W24X103	W24X84
6END-C2	End Plate	CCFT	HSS18X500	W24X103	W24X84
6END-C3	End Plate	RCFT+CCFT	HSS16X16X500, HSS18X500	W24X103	W24X84
6END-C4	End Plate	RCFT	HSS16X16X500	W24X103	W24X84
6END-C5	End Plate	CCFT	HSS18X500	W24X103	W24X84
6END-C6	End Plate	RCFT+CCFT	HSS16X16X500, HSS18X500	W24X103	W24X84
6END-C7	Welding	RCFT	HSS16X16X500	W24X103	W24X84
6END-C8	Welding	CCFT	HSS18X500	W24X103	W24X84
6END-C9	Welding	RCFT+CCFT	HSS16X16X500, HSS18X500	W24X103	W24X84

(c) 6 story building with 5 @ 36' bays and end-plate or welding connections

Model ID	Connection Type	Column System	Column Size (All Stories)	Beam Size	
				1st to 3rd Story	4th and 6th Story
6TSU-C1	T-Stub	RCFT	HSS16X16X375	W24X62	W24X55
6TSU-C2	T-Stub	CCFT	HSS18X375	W24X62	W24X55
6TSU-C3	T-Stub	RCFT+CCFT	HSS16X16X375, HSS18X375	W24X62	W24X55
6TSU-C4	T-Stub	RCFT	HSS16X16X375	W24X62	W24X55
6TSU-C5	T-Stub	CCFT	HSS18X375	W24X62	W24X55
6TSU-C6	T-Stub	RCFT+CCFT	HSS16X16X375, HSS18X375	W24X62	W24X55
6TSU-C7	Welding	RCFT	HSS16X16X375	W24X62	W24X55
6TSU-C8	Welding	CCFT	HSS18X375	W24X62	W24X55
6TSU-C9	Welding	RCFT+CCFT	HSS16X16X375, HSS18X375	W24X62	W24X55

(d) 6 story building with 5 @ 25' bays and T-stub or welding connections



(a) The plan view of the building with combined RCFT and CCFT columns

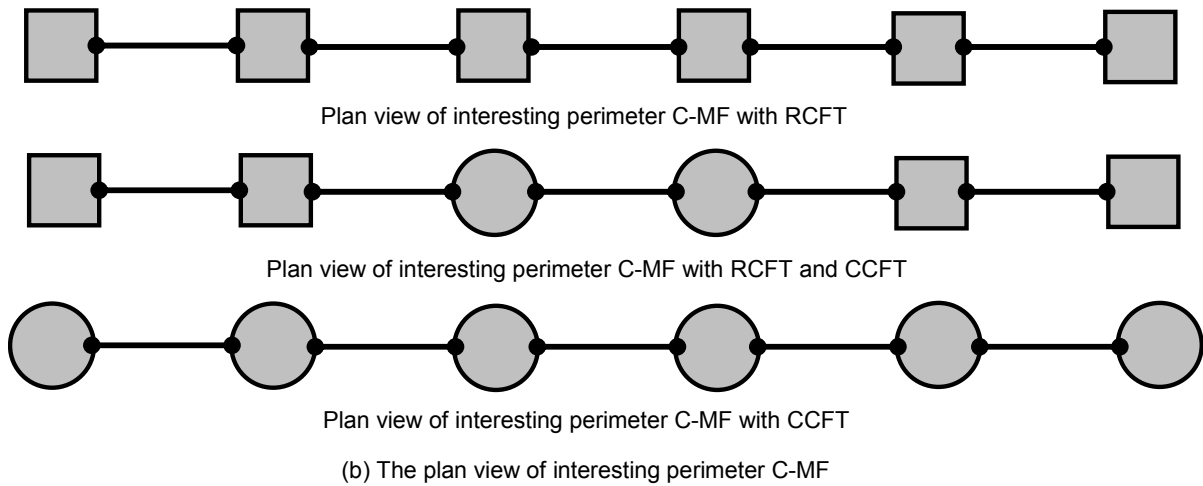
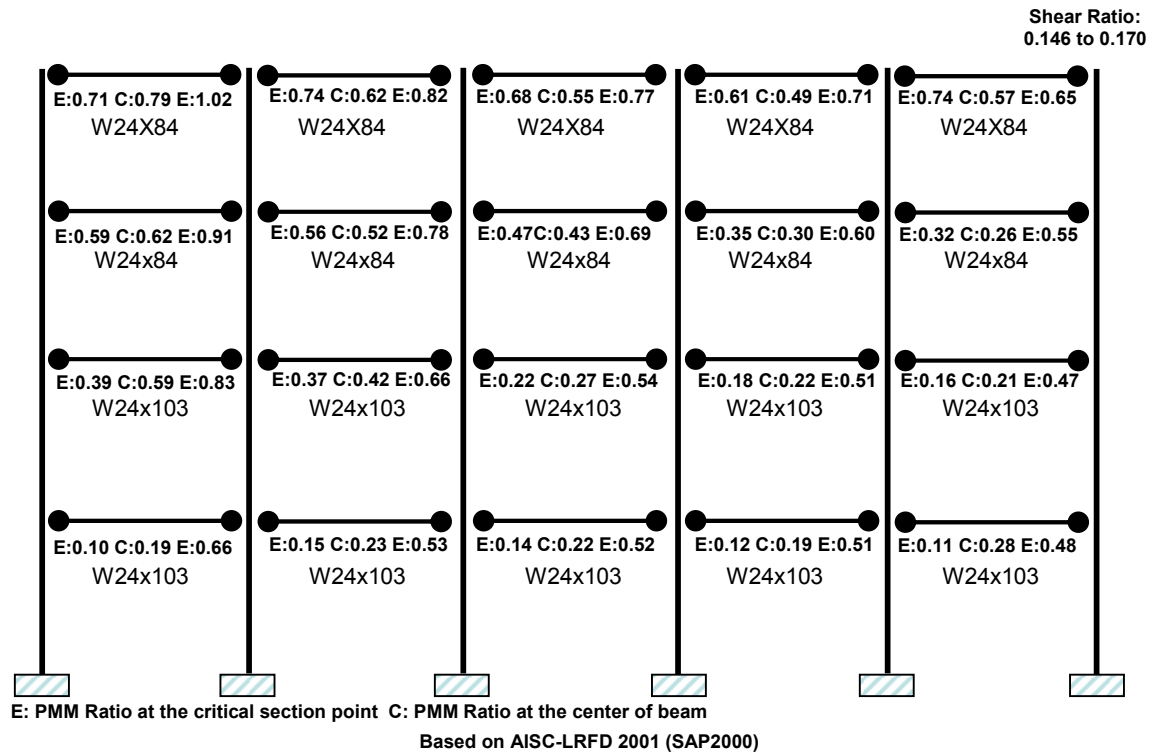
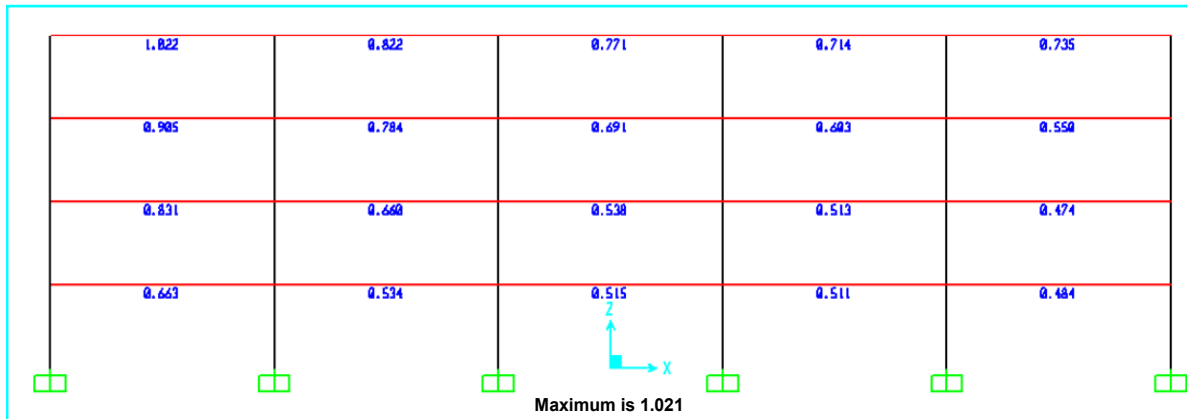


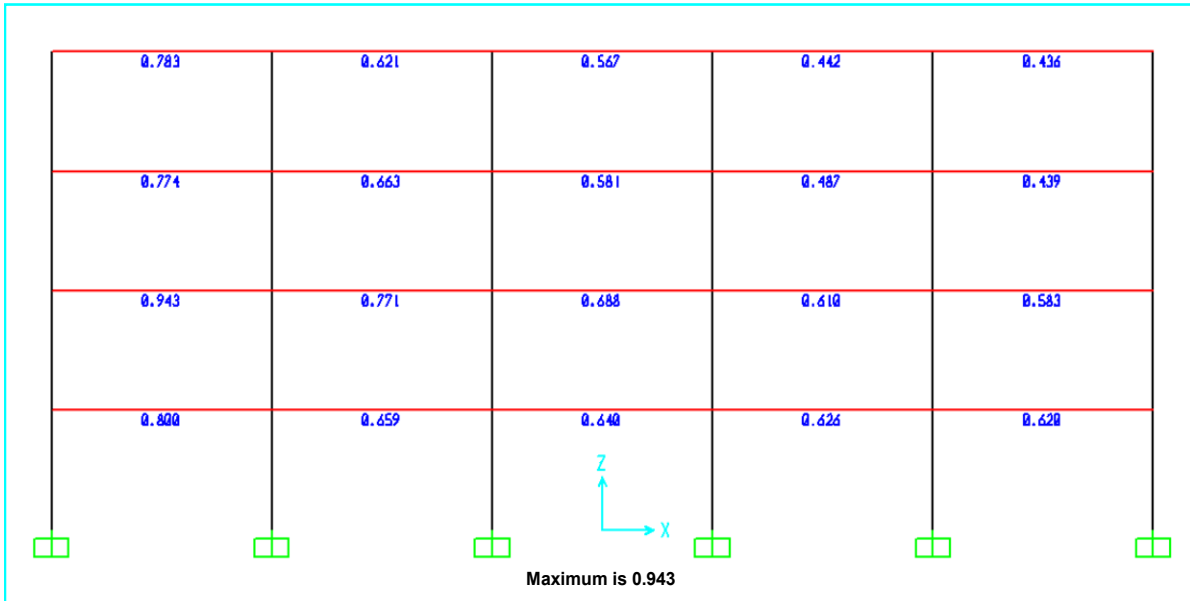
Figure 7.9 Plan views of the 3D building and perimeter composite moment frames (C-MF)



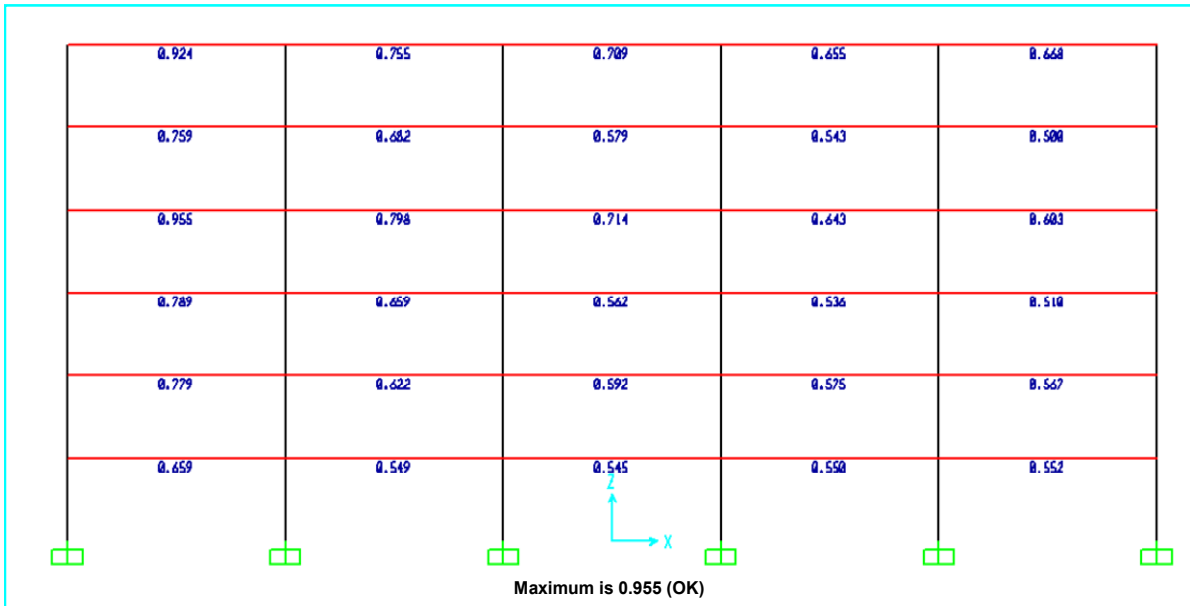
(a-1) Moment interaction ratio for beam members under dominant load combination 5 (SAP2000 PMM Ratio, 4END-C9)



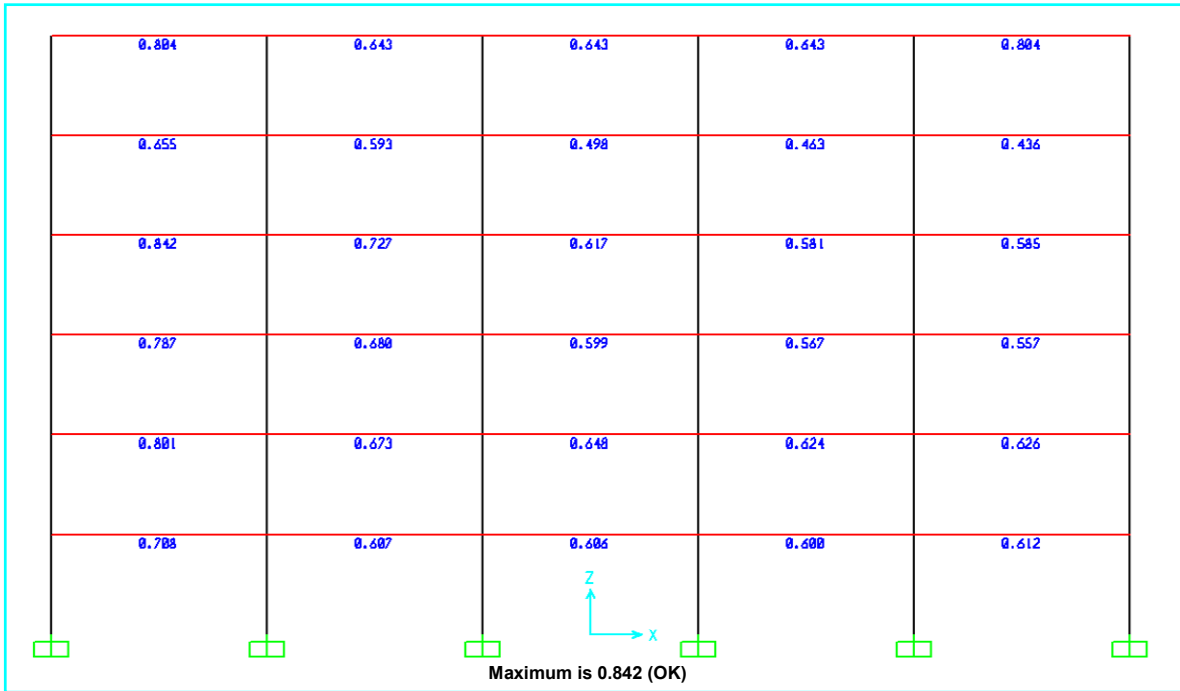
(a-2) Moment interaction ratio for beam members under dominant load combination 5 (SAP2000 PMM Ratio, 4END-C9)



(b) Moment interaction ratio for beam members under dominant load combination 5 (SAP2000 PMM Ratio, 4CLI-C9)



(c) Moment interaction ratio for beam members under dominant load combination 5 (SAP2000 PMM Ratio, 6END-C9)



(d) Moment interaction ratio for beam members under dominant load combination 5 (SAP2000 PMM Ratio, 6TSU-C9)

Figure 7.10 Moment interaction ratio for beam members under load combination 5

Design checks for deflection and drift ratios specified in Chapter 7.3.3 of (what reference) are given in Table 7.6. The dominant load combination was applied to all frame models. All values from static analyses using the SAP2000 are less than the allowable limits. The model trees for all frame specimens are shown in Figure 7.11.

Table 7.6 Design checks for deflection and drift ratio

Story	Factored Story Drift (Δ)	Allowable Story Drift (Δ_a)	Stable Coefficient (θ)	Max. Stable Coefficient (θ_{max})	Decision
4	7.48	12.48	0.004	0.091	OK
3	6.49	9.36	0.008	0.091	OK
2	4.67	6.24	0.015	0.091	OK
1	1.99	3.12	0.026	0.091	OK

(a) Design checks for deflection and drift ratio (4END-C7)

Story	Factored Story Drift (Δ)	Allowable Story Drift (Δ_a)	Stable Coefficient (θ)	Max. Stable Coefficient (θ_{max})	Decision
4	7.32	12.48	0.004	0.091	OK
3	6.38	9.36	0.008	0.091	OK
2	4.63	6.24	0.015	0.091	OK
1	2.10	3.12	0.027	0.091	OK

(b) Design checks for deflection and drift ratio (4END-C8)

Story	Factored Story Drift (Δ)	Allowable Story Drift (Δ_a)	Stable Coefficient (θ)	Max. Stable Coefficient (θ_{max})	Decision
4	8.96	12.48	0.005	0.091	OK
3	7.81	9.36	0.010	0.091	OK
2	5.55	6.24	0.018	0.091	OK
1	2.26	3.12	0.028	0.091	OK

(c) Design checks for deflection and drift ratio (4CLI-C7)

Story	Factored Story Drift (Δ)	Allowable Story Drift (Δ_a)	Stable Coefficient (θ)	Max. Stable Coefficient (θ_{max})	Decision
4	8.85	12.48	0.005	0.091	OK
3	7.71	9.36	0.010	0.091	OK
2	5.50	6.24	0.018	0.091	OK
1	2.31	3.12	0.029	0.091	OK

(d) Design checks for deflection and drift ratio (4CLI-C8)

Story	Factored Story Drift (Δ)	Allowable Story Drift (Δ_a)	Stable Coefficient (ϵ)	Max. Stable Coefficient (ϵ_{max})	Decision
6	13.86	18.72	0.002	0.091	OK
5	13.14	15.6	0.006	0.091	OK
4	11.57	12.48	0.009	0.091	OK
3	9.22	9.36	0.015	0.091	OK
2	6.14	6.24	0.026	0.091	OK
1	2.56	3.12	0.042	0.091	OK

(e) Design checks for deflection and drift ratio (6END-C7)

Story	Factored Story Drift (Δ)	Allowable Story Drift (Δ_a)	Stable Coefficient (ϵ)	Max. Stable Coefficient (ϵ_{max})	Decision
6	13.72	18.72	0.002	0.091	OK
5	13.02	15.6	0.006	0.091	OK
4	11.49	12.48	0.009	0.091	OK
3	9.20	9.36	0.015	0.091	OK
2	6.22	6.24	0.026	0.091	OK
1	2.71	3.12	0.044	0.091	OK

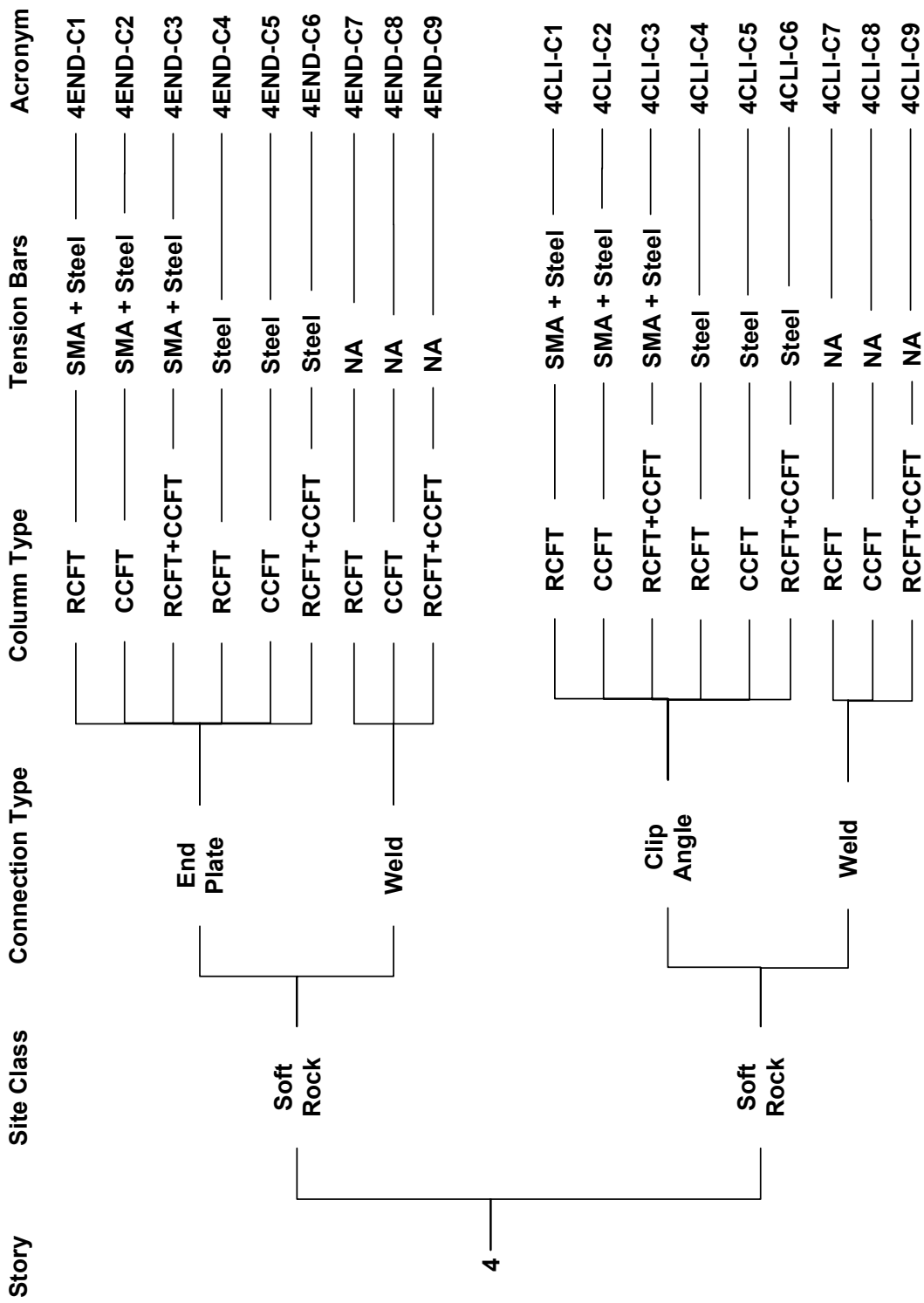
(f) Design checks for deflection and drift ratio (6END-C8)

Story	Factored Story Drift (Δ)	Allowable Story Drift (Δ_a)	Stable Coefficient (ϵ)	Max. Stable Coefficient (ϵ_{max})	Decision
6	10.84	18.72	0.002	0.091	OK
5	10.33	15.6	0.004	0.091	OK
4	9.19	12.48	0.007	0.091	OK
3	7.36	9.36	0.012	0.091	OK
2	4.87	6.24	0.021	0.091	OK
1	1.99	3.12	0.032	0.091	OK

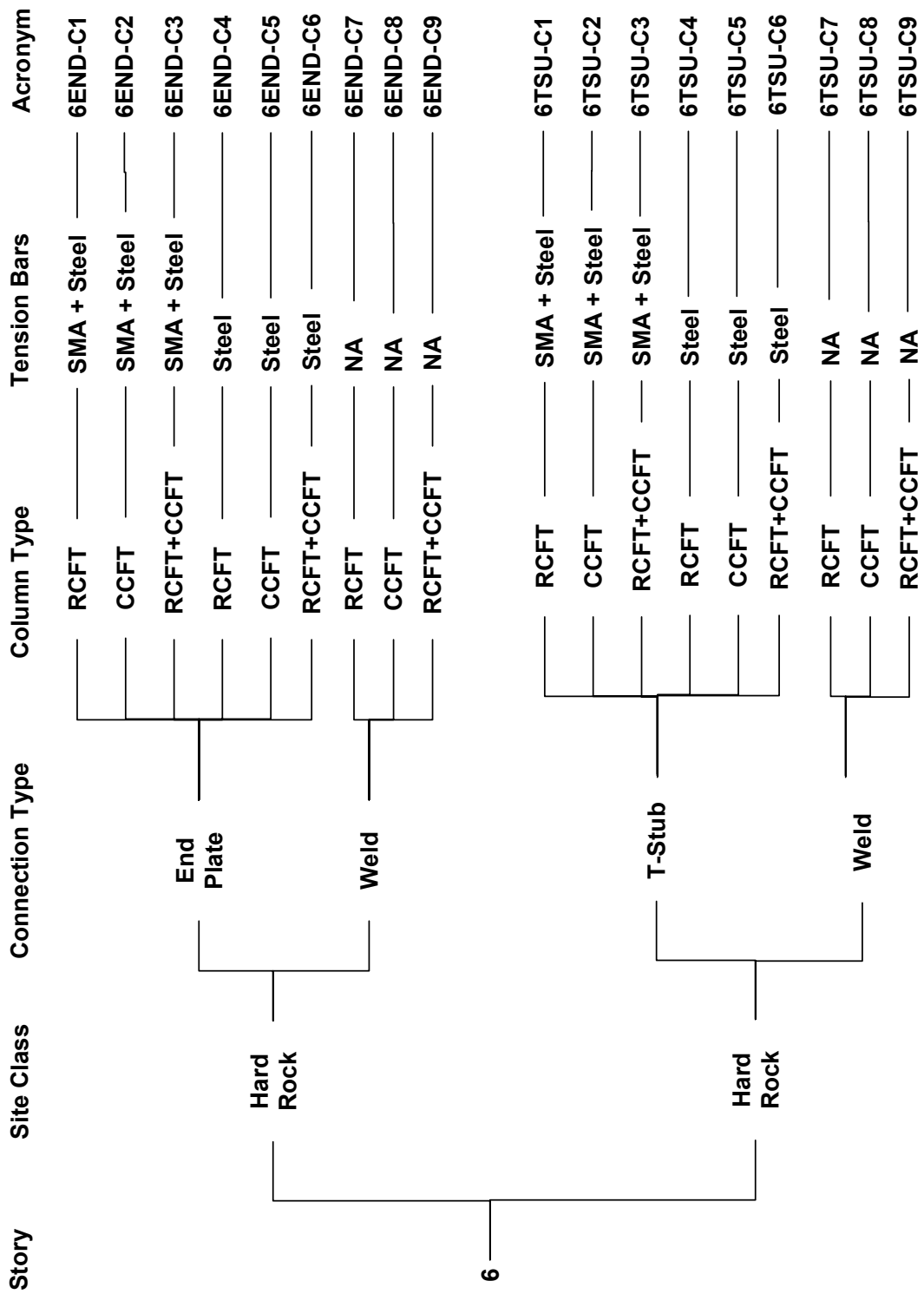
(g) Design checks for deflection and drift ratio (6TSU-C7)

Story	Factored Story Drift (Δ)	Allowable Story Drift (Δ_a)	Stable Coefficient (ϵ)	Max. Stable Coefficient (ϵ_{max})	Decision
6	10.83	18.72	0.002	0.091	OK
5	10.34	15.6	0.004	0.091	OK
4	9.23	12.48	0.007	0.091	OK
3	7.45	9.36	0.012	0.091	OK
2	5.02	6.24	0.021	0.091	OK
1	2.17	3.12	0.035	0.091	OK

(h) Design checks for deflection and drift ratio (6TSU-C8)



(a) The model trees for 4 story composite moment frames



(b) The model trees for 6 story composite moment frames

Figure 7.11 Model trees for all composite moment frame specimens

7.5 Modeling Attributes for the Numerical Frame Models

In this section, the modeling attributes for the 2D numerical frame models which will be used for nonlinear analyses are described. This includes, in particular, panel zone modeling following mostly OpenSEES (OpenSEES 1.7.3). The general modeling methods for the numerical frame models are also introduced in the guidelines given in FEMA 355C (FEMA, 2000).

The composite columns and steel beams were modeled as nonlinear beam-column elements. 2D discrete fiber sections placed in the nonlinear beam-column elements simulate the columns and beams cross sections as shown in Figure 6.25. The expected material strengths were used in accordance with the previous material property models shown in Figure 6.26. Nonlinear materials were assigned into these nonlinear elements with the 2D discrete fiber sections. All nonlinear analyses were carried out under the same condition with the following assumptions:

- A mass corresponding to 1.0DL (Dead Load) + 0.2 LL (Live Load) was applied for the nonlinear dynamic analyses
- Steel material properties included a 1.5% strain hardening
- A 2.5 % Rayleigh damping was used in the first mode
- Soil-structure interaction at the ground support was neglected
- The beams and columns extended from centerline to centerline
- The uniform loads on the beams were converted into equivalent point loads
- A beam was modeled as many nonlinear beam-column elements subjected to the equivalent point loads
- Dimensions, strength and stiffness of panel zones are considered

The most significant characteristic of the frame analyses presented in this study is the careful consideration of the panel zone modeling. The behavior of composite PR connections can be simulated by using the more precise joint elements shown in Figure 6.22. Nodes and elements located on this numerical frame model are given in Figure 7.12. Rectangular boxes labeled from P1 to P24 indicate joint elements for composite PR connections. The structural details of the joint element are given in Figure 7.13. The

procedures to determine panel zone dimensions, stiffness, and strength are dependent upon the previous study for a local joint element model under cyclic loads (See Sections 6.1 and 6.2). In addition, the properties of panel zones was defined as a tri-linear model as shown in Figure 7.14. The joint element includes this panel zone spring. Required information for this tri-linear model such as initial stiffness, yield shear, and ultimate shear strength were generated by using the equations proposed by Wu (Wu et al., 2007). This tri-linear model can be simulated by using the hysteretic material in the OpenSEES program. The detail descriptions of calculation procedures to determine the properties of panel zones are given in Appendix E. The properties of panel zones for all frame model connections are summarized in Table 7.7.

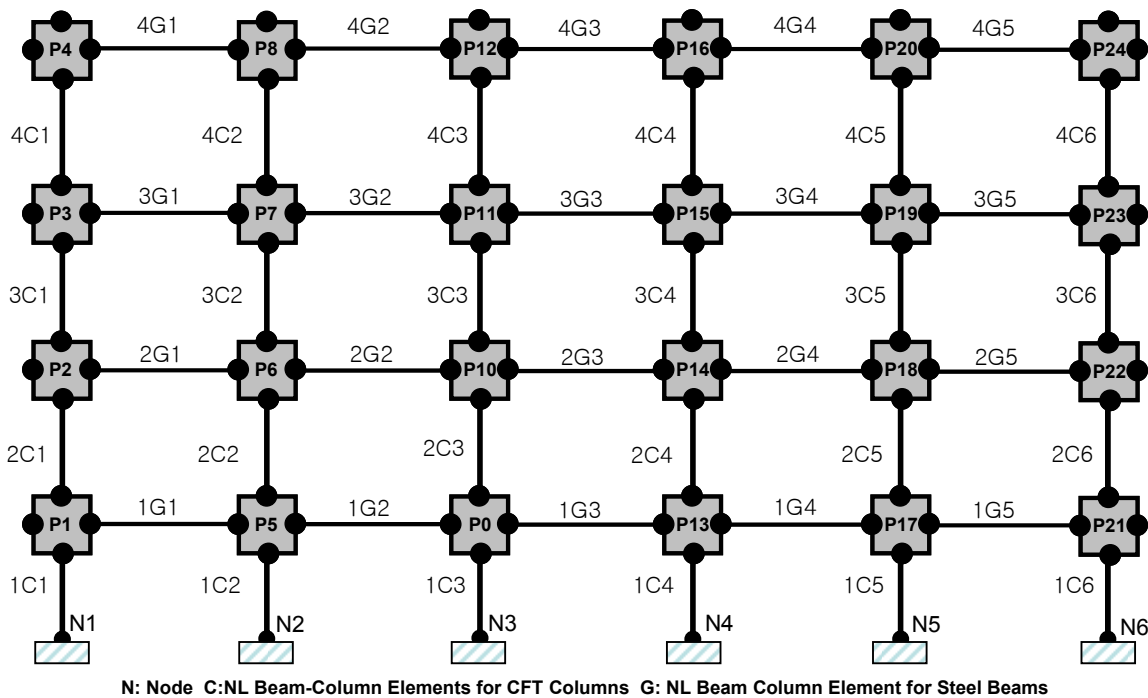


Figure 7.12 Numerical frame model composed of joint and nonlinear elements (C-PRMF case)

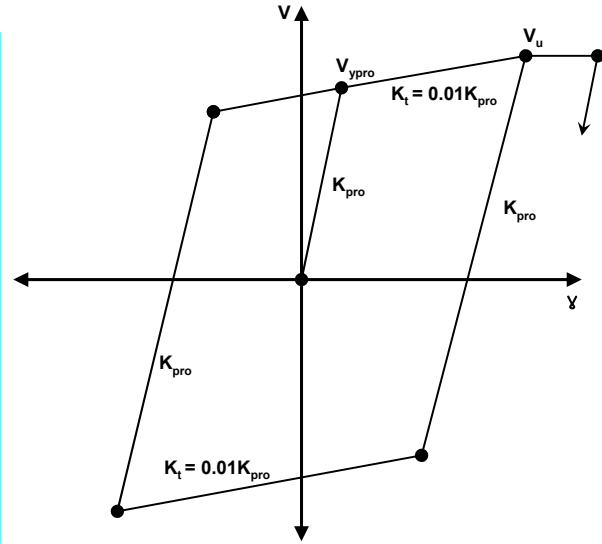
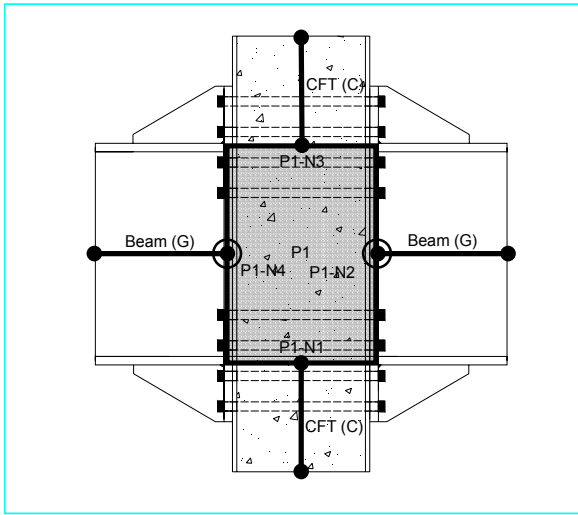


Figure 7.13 Structural details of a joint element (Left)

Figure 7.14 Tri-linear model of the panel zone (Right)

The numerical frame models for C-SMF were only composed of nonlinear beam-column elements without joint elements as shown in Figure 7.15. The beam and columns extend from centerline to centerline and meet together at the panel zone. Therefore, panel zone dimensions and shear distortions are neglected in these frames. The numerical modeling of a panel zone for the welded connections is shown in Figure 7.16.

Table 7.7 Properties of panel zones for all frame model connections

Unit: kips, rad and in

Connection Type	Beam Size	Column Size	PZ Size*	V_{ypro}	K_{ypro}	V_u	K_t
End-Plate	W24X103	HSS16X16X500	16X16" (0.5")	1.758×10^3	6.820×10^5	1.866×10^3	$0.01K_{ypro}$
End-Plate	W24X103	HSS18X500	18X18" (0.5")	2.108×10^3	8.055×10^5	2.222×10^3	$0.01K_{ypro}$
End-Plate	W24X84	HSS16X16X500	16X16" (0.5")	1.742×10^3	6.755×10^5	1.851×10^3	$0.01K_{ypro}$
End-Plate	W24X84	HSS18X500	18X18" (0.5")	2.139×10^3	8.068×10^5	2.253×10^3	$0.01K_{ypro}$
Clip Angle	W18X50	HSS14X14X500	14X14" (0.5")	1.219×10^3	5.429×10^5	1.366×10^3	$0.01K_{ypro}$
Clip Angle	W18X50	HSS16X500	16X16" (0.5")	1.642×10^3	6.981×10^5	1.787×10^3	$0.01K_{ypro}$
T-Stub	W24X62	HSS16X16X375	16X16" (0.375")	1.693×10^3	7.773×10^5	1.833×10^3	$0.01K_{ypro}$
T-Stub	W24X62	HSS18X375	18X18" (0.375")	1.932×10^3	8.531×10^5	2.075×10^3	$0.01K_{ypro}$
T-Stub	W24X55	HSS16X16X375	16X16" (0.375")	1.687×10^3	7.443×10^5	1.827×10^3	$0.01K_{ypro}$
T-Stub	W24X55	HSS18X375	18X18" (0.375")	1.925×10^3	8.499×10^5	2.068×10^3	$0.01K_{ypro}$

*() indicate the thickness of steel tube section

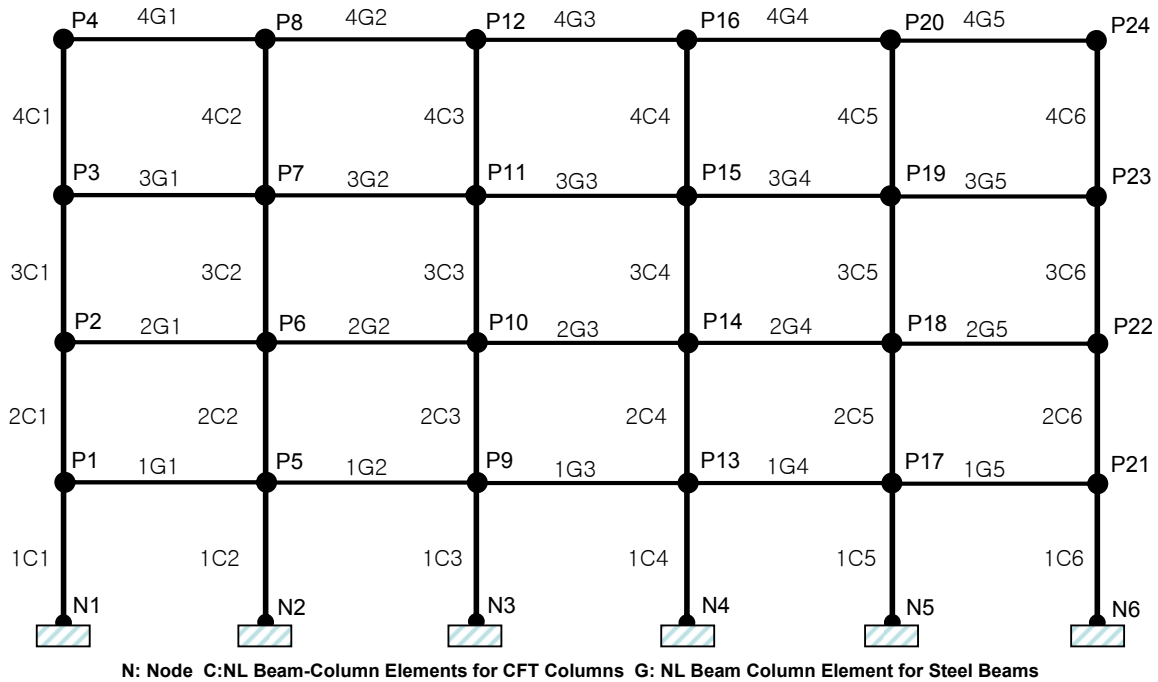


Figure 7.15 Numerical frame model composed of nonlinear beam-column elements (C-SMF case)

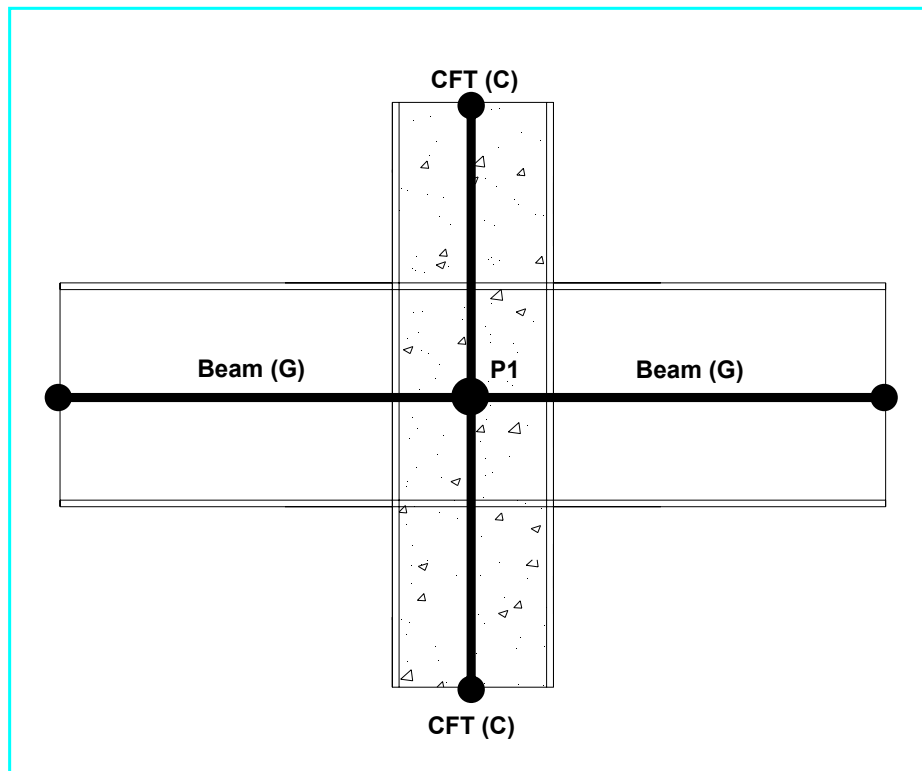


Figure 7.16 Numerical modeling of a panel zone for the welding connection

7.6 Summary and Discussion

This addressed three issues: (a) an introduction to the design methodology for the composite moment frames, (2) design results and checks for composite moment frames and (3) the numerical model attributes including the panel zone models. Four different prototypes of composite perimeter moment frames with either PR connections or FR connections were designed. Each prototype broke down into nine model cases according to the possible combinations of connection types and column systems as shown in Figure 7.11.

The characteristics and design for composite moment frames were described in Section 7.1. Two types of composite moment frames (C-PRMF and C-SMF) were selected in this study. C-PRMF were designed with three different types of PR moment connections (end-plate, T-stub, and clip angle connections), while C-SMF were designed with welded composite column to steel beam connections as the single FR connection system.

The prototype building configurations were described in Section 7.2, while the load generation and design regulations were described in Section 7.3. Design results and checks for frame specimens were described in Section 7.4. Modeling attributes for the 2D numerical frame models were described in Section 7.5, including panel zone modeling. These numerical models will be utilized in the nonlinear analyses presented in the next chapter.

Chapter 8

Nonlinear Analyses of Composite Moment Frames

For the purpose of generating the behavioral models for smart SMA PR-CFT connections, refined 3D FE models and simplified 2D joint models were studied in Chapters 5 and 6, respectively. Based on these modeling strategies, building configurations and models for entire moment frames were described in Chapter 7. In this chapter, the results of both nonlinear pushover and dynamic analyses conducted using a current version of the OpenSEES program are described. The frame response for both C-PRMF and C-SMF subjected to a set of 10 ground motions each for the Los Angeles (LA) and Seattle (SE) areas were examined and results will be discussed. After assessing these nonlinear analyses results, the seismic performance and damage evaluation for these systems will be described in Chapter 9.

The primary data collected and nonlinear analysis methods used are described in Section 8.1. The results of nonlinear pushover analyses with either monotonic or reversed loading are discussed and compared in Section 8.2. The nonlinear dynamic analyses are described in Section 8.3. In both Sections 8.2 and 8.3, inter story drift, panel zone deformation, and plastic yielding are used as the main indices to compare performance of the different structural systems. Finally, a summary and conclusions are given in Section 8.4.

8.1 Introduction to Nonlinear Analyses

Numerical frame models which include the 2D joint models described in previous chapters are assumed to be accurate and able to replicate the real behavior of PR frames. The programs could not model fracture of the connections and connection rotational ductility was assumed as infinite; however, peak rotations were checked to ensure that they did not reach unusual levels (0.07 radians).

The overall analysis program and types of data collected are summarized in Table 8.1 and Figure 8.1. The expected strength and deformation demands for composite frame

systems can be estimated by these nonlinear frame analyses. A total of 72 pushover and 320 non-linear dynamic analyses were carried out.

The performance data selected for comparisons are the inter story drift ratios (ISDR), panel zone rotation angles (PZRA), forces, deformations and fiber stresses for key members and nodal displacement. In particular, member forces and deformations measured at the integration points of the nonlinear beam-column elements will be used for calculating elastic strength ratios (ESR) and inelastic curvature ductility ratios (ICDR) in the next chapter.

Table 8.1 Overall frame analyses and data measurements

(a) Frame Analysis (Second Order Inelastic Analysis)
The nonlinear pushover analysis with the equivalent lateral loads The nonlinear dynamic analysis with the ground motion
(b) Measurement
Inter story drift ratio (ISDR) Panel zone rotation angle (PZRA) Member force and deformation Fiber stress and strain Nodal displacement

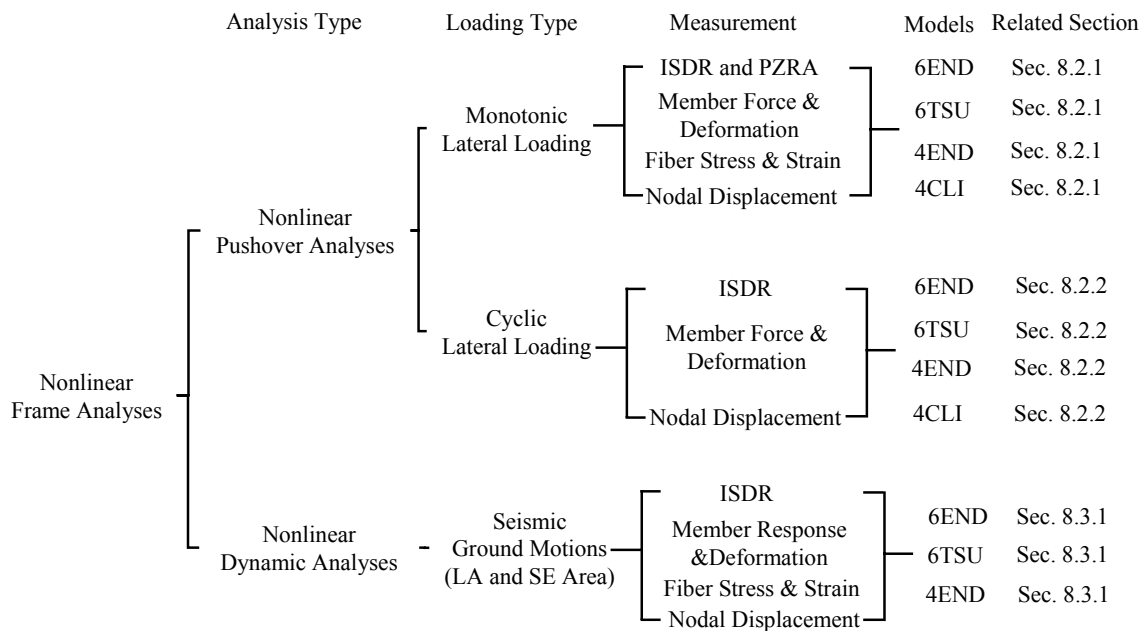


Figure 8.1 Detail information for frame analysis and measurement cases

The dominant load combination, Load Combination 5 (See Section 7.3.1), was used to perform the nonlinear pushover analyses. The detailed load profiles for each frame model are shown in Table 7.4. Equivalent point loads, simulating the uniform dead and live loads, were applied to the beam elements in the gravity direction using the Constant Time Series function associated with the load pattern in OpenSEES. The equivalent lateral loads on the joints were simulated by using the Linear Time Series function, so these loads can be applied in a linearly incremental fashion associated with a predefined time step. For each time step, a static analysis was performed through a displacement control algorithm.

Ground motions selected from the SAC suite of ground motions (Somerville et al. 1997) were used to perform the nonlinear dynamic analyses. Some selected ground motions are shown in Figure 8.2. More information on the ground motions used in this research is given in Appendix F. For each time step, a transient analysis was performed using the Newmark method (Newmark 1959). A value of 2.5 percent was used for the structural damping as defined by the Rayleigh command in OpenSEES. In order to include second order effects (P-Delta effect) due to dead and live loads along the gravity direction, these loads were also applied to the beam elements. In addition to the gravity loads to model the P-Delta effects, lumped masses were assigned to nodes so as to generate the story shear force due to the ground acceleration. Lumped masses consisted of 1.0 times dead loads plus 0.2 times live loads. The calculation of the lumped mass is described in Appendix D.

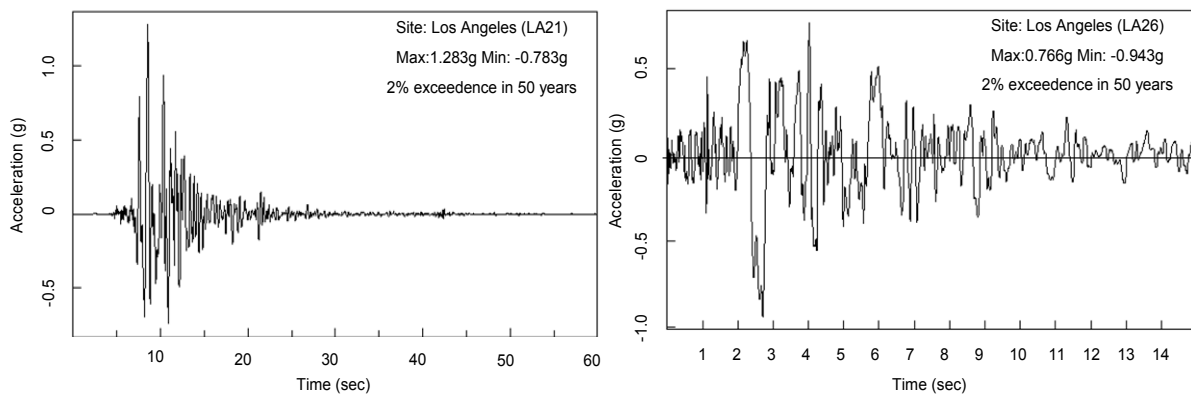


Figure 8.2 Ground motions used in nonlinear dynamic analysis

From these nonlinear analyses, the primary response data were collected by utilizing recorder commands in the OpenSEES program. A schematic view of the data collected for the composite frame performance is depicted in Figure 8.3. Two types of data recorder

commands, Node Recorder and Element Recorder, were used to collect the data of interest. The Node Recorder function was used to record the response of the global nodes, while the Element Recorder function collected data on the local response of members and fiber sections. For example, displacement, velocity, acceleration, and reaction force at the Record 1 or Record 2 position as shown in Figure 8.3 was monitored by the Node Recorder. On the other hand, member forces, deformations, fiber stresses, and strains at Record 3 to Record 5 positions were monitored by the Element Recorder. The ISDA shown in Figure 8.3 (a) was calculated by observations of the global response data. The base shear force (V_{base}) is the summation of the reaction forces at the column bases, and is another example of a global measurement. On the other hand, both the PZRA and stress hinge sequences are derived from monitoring local response data.

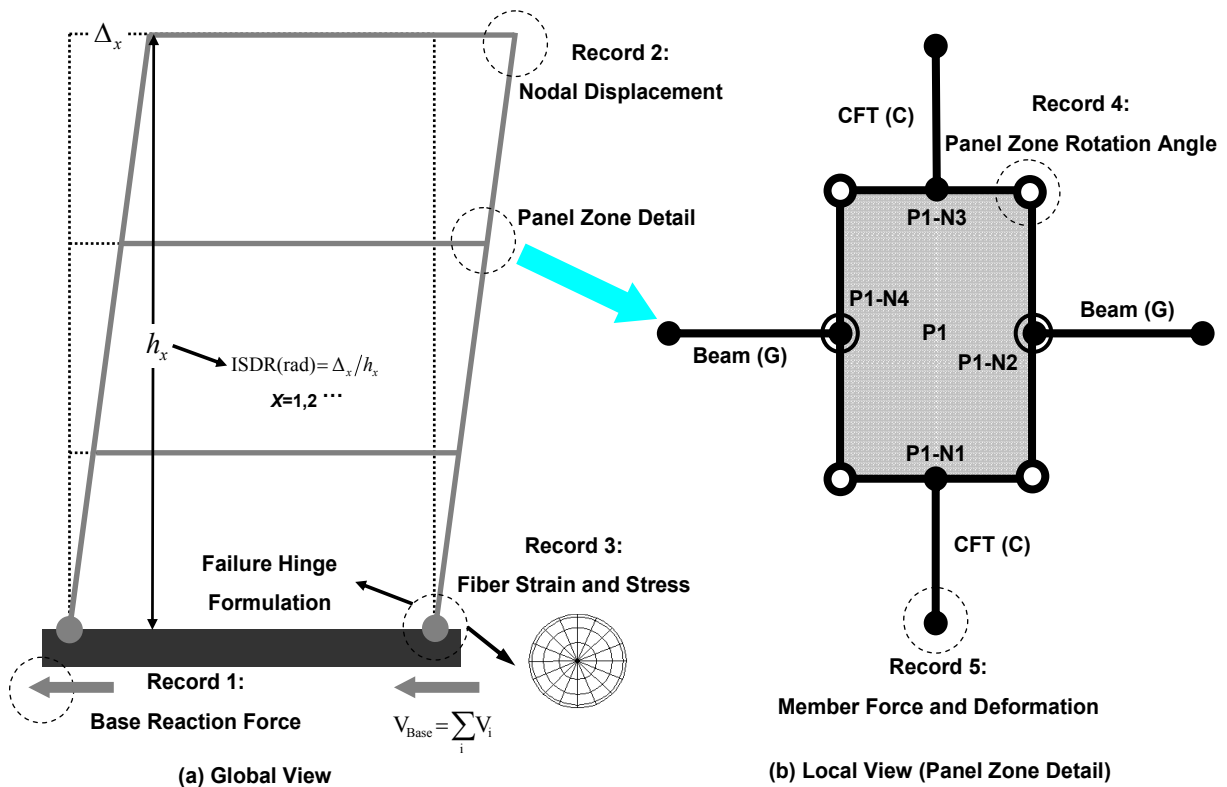


Figure 8.3 The schematic view of data collections

The overall composite moment frame models used to perform the nonlinear analyses are shown in Figure 7.11. All models were analyzed for the western US ground motions with 2% probability of exceedence in 50 years. The first number of the acronym shown in

Figure 7.11 indicates the total numbers of stories (4 or 6). The letter of the acronym following this number represents the connection type (END: End-plate connections, TSU: T-stub connections and CLI: Clip angle connections). The last letter indicates the cases determined by the model combinations due to column systems, tension bars and connection types (See Table 7.5). For instance, the 6 story composite moment frame with end-plate connections having CCFT + RCFT column systems and SMA + Steel tension bars is expressed as 6END-C1.

8.2 Nonlinear Pushover Analyses

2D nonlinear pushover analyses were performed to estimate the maximum strength and deformation capacities of the composite moment frames designed in the previous chapter. The collapse mechanisms were also investigated by tracking the yield or ultimate stress state of the prescribed fiber sections. The second order (P-Delta) effects due to the constant dead and live loads were tracked by using the Corotational Transformation Command available in OpenSEES

8.2.1 Monotonic Pushover Curves

The resulting monotonic pushover curves plotted in terms of interstory drift ratio vs. the normalized base shear force are shown in Figures 8.4 to 8.7. The normalized base shear corresponds to the base shear force measured by the Node Recorder. The ISDR on the X-axis is defined as the roof displacement divided by the total frame height. The design base shear force (V_{design}) is defined as the summation of the equivalent lateral loads shown in Figure 7.4. These figures show comparisons of pushover curves for frames with the same composite column systems but different connection types, including variations in the type and layout of the tension bars.

In all pushover curves shown in Figures 8.4 through 8.7, there are some important transition points in the curves which can be related to the ISDR. The limits to determine these transition points consist of the elastic range (proportional limit), initial yielding, initiation of hardening, ultimate strength, and strength degradation or the stability limit. For example, the 6END-C1 model indicates that an ISDR of 0.01 radians is the limit for the

elastic range, that 0.02 corresponds to the yielding point, that 0.03 corresponds to strength hardening, that 0.05 corresponds to the ultimate strength, and at an approximate value of 0.09 is the stability limit.

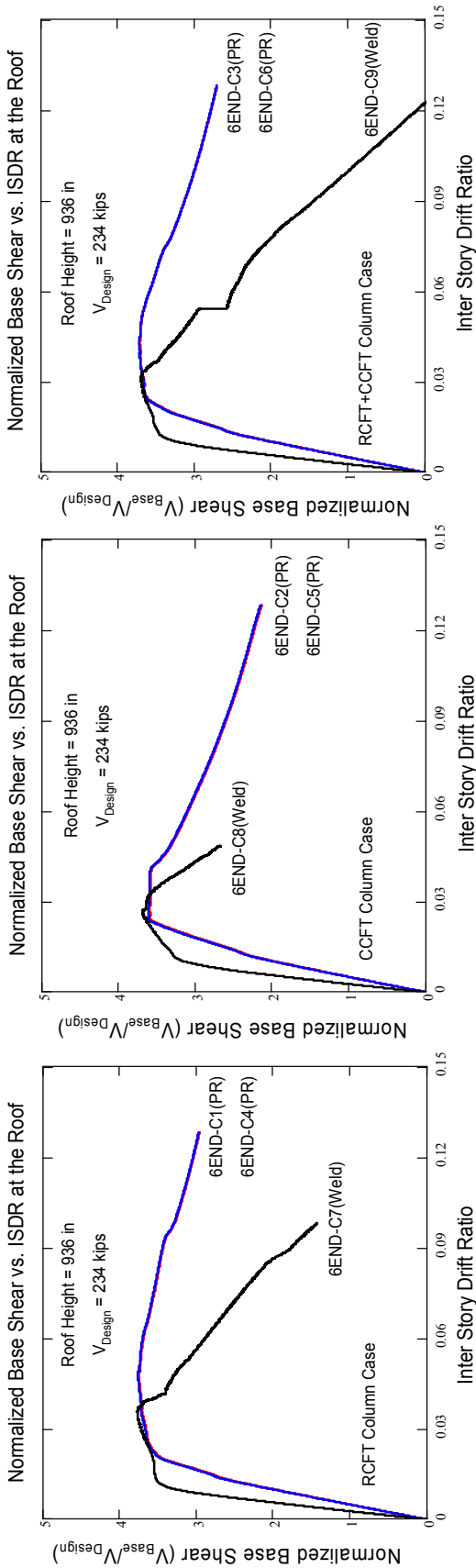
Overall, composite frames with the same PR connections exhibit almost identical pushover curves regardless of the parameters for tension bars (i.e. 6END-C1 vs. 6END-C4). This implies that the materials in the tension bars result in an insignificant change in the behavior of the composite frame. However, changes in panel zones and composite columns type give rise to significant behavioral differences.

From all curves, the initial slope of the composite moment frames with welded connections is steeper than that of the composite moment frames with PR connections (i.e. 6END-C1 vs. 6END-C7). The stiffness loss due to the oversize bolt holes in the panel zone and the structural characteristics of PR connections cause the composite moment frames with PR connections (i.e. 6END-C1 and 6END-C2) to have lower initial stiffness. Although the three frame models evidence similar ultimate strength, the strength of the composite moment frames with welded connections generally deteriorates more rapidly than that of the composite moment frames with PR connections after reaching the ultimate strength. The welded connections fail by brittle fracture of the welds and increased P-Delta effects. In fact, these frames appear to have reached their stability limit. In contrast, connections with the more flexible tension bars provide more ductility. Therefore, the composite frames with PR connections show more gradual strength degradation after reaching their ultimate strength.

The strength of the composite columns has a major effect on the performance of the frames. The axial force and bending moment interaction capacity (P-M interaction) for all composite columns is given in Appendix A. Composite frames with end-plate connections have larger steel areas and reinforcement (roughly 33% higher) than those with T-stub connections (i.e. 6END-C1 vs. 6TSU-C1). These larger column sizes obviously increase the resistance against lateral loads. Generally, the capacity of the CCFT columns is identical or slightly smaller than that of the RCFT columns. Therefore, the strength of composite frames with CCFT columns is identical or slightly smaller than that of composite frames with RCFT columns (i.e. 6END-C1 vs. 6END-C2). Composite moment frames with CCFT columns are susceptible to stress concentration at the panel zone

because the rectangular shape panel zone is welded to the circular columns. This characteristic of panel zones causes the strength to deteriorate more rapidly.

Finally, the strength of the taller frames deteriorates more rapidly than that of the shorter frame due to the larger P-Delta effect. Comparisons between the pushover curves for 6END-C9 and those for 4END-C9 provide good examples to verify this argument (see Figures 8.4 and 8.6).

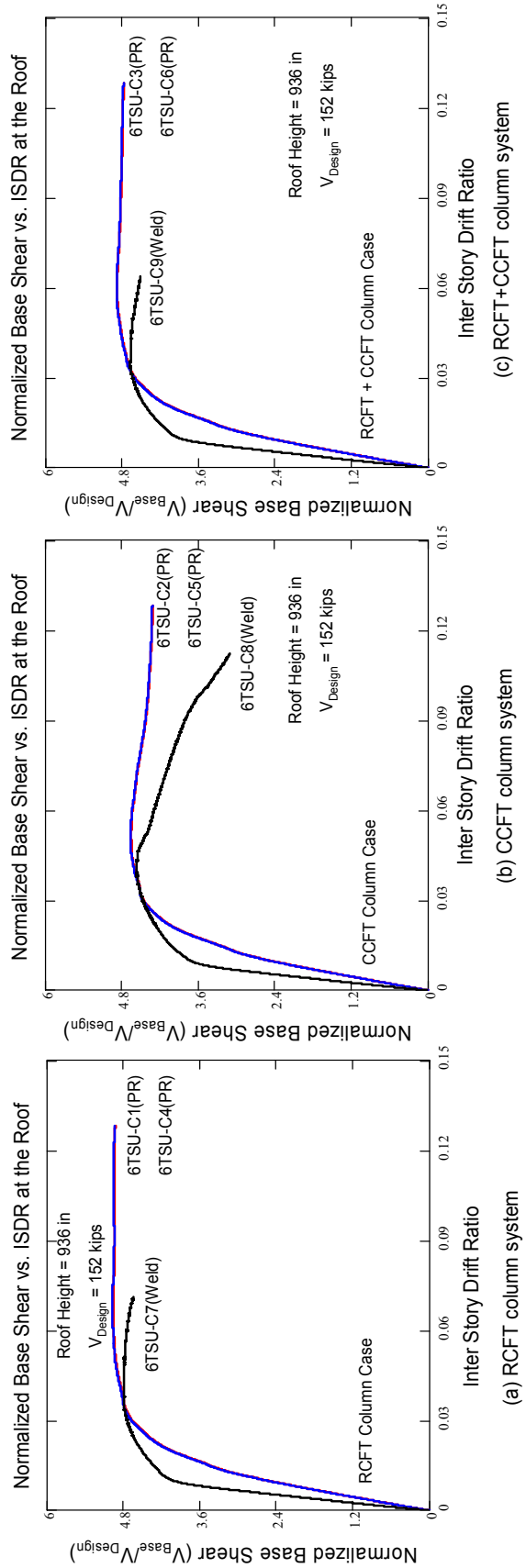


(a) RCFT column system

(b) CCFT column system

(c) RCFT+CCFT column system

Figure 8.4 Nonlinear monotonic pushover curves for C-MF with end-plate and welded connections (6END)



(a) RCFT column system

(b) CCFT column system

(c) RCFT+CCFT column system

Figure 8.5 The nonlinear monotonic pushover curves for C-MF with T-stub and welded connections (6TSU)

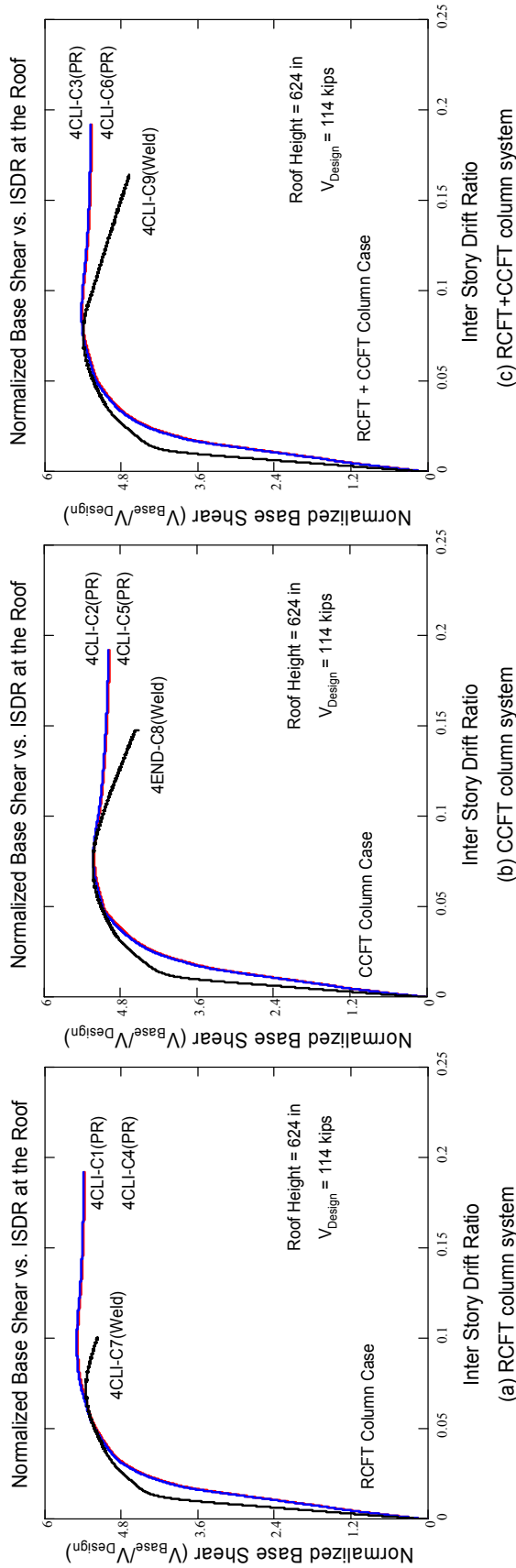


Figure 8.6 The nonlinear monotonic pushover curves for C-MF with end-plate and welded connections (4END)

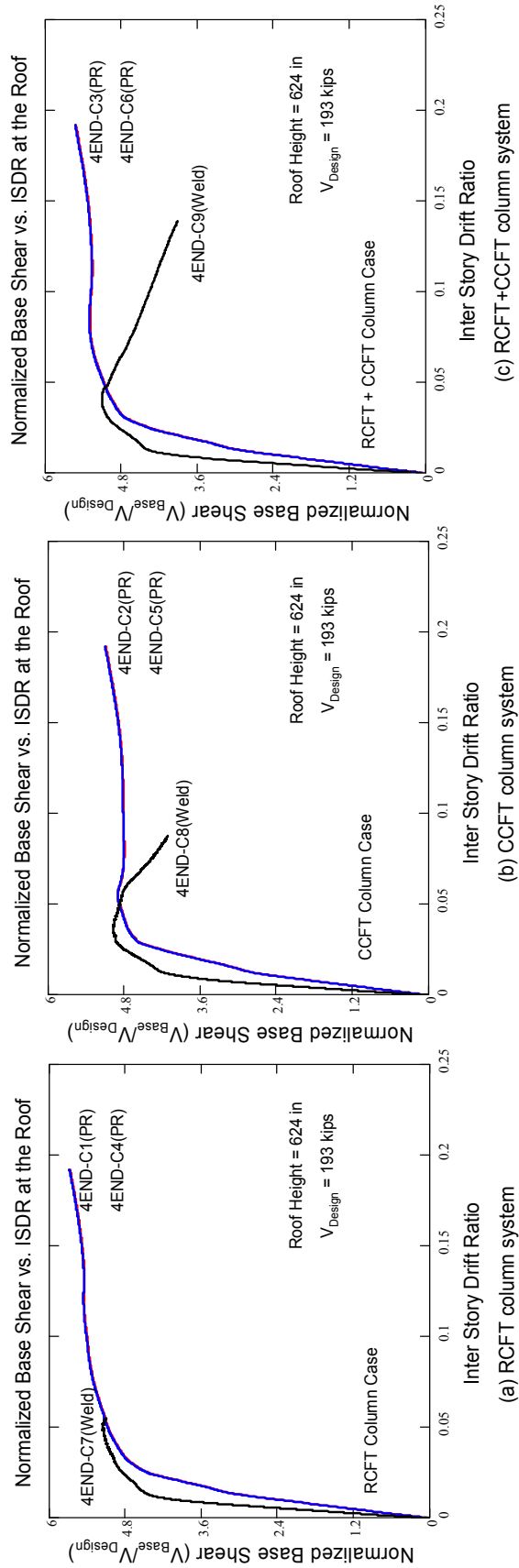


Figure 8.7 Nonlinear monotonic pushover curves for C-MF with clip angle and welded connections (4CLI)

8.2.2. Cyclic Pushover Curves

The same numerical models that were tested monotonically were also used for cyclic pushover analyses. The modeling decisions and data collected, where possible, were identical to those for the monotonic pushover tests.

Figure 8.8 shows the displacement load history for the nonlinear cyclic pushover analyses. This load history was applied to the roof of all composite moment frames. The use of only one load history aimed at simplifying comparisons for strength, stiffness and energy capacity.

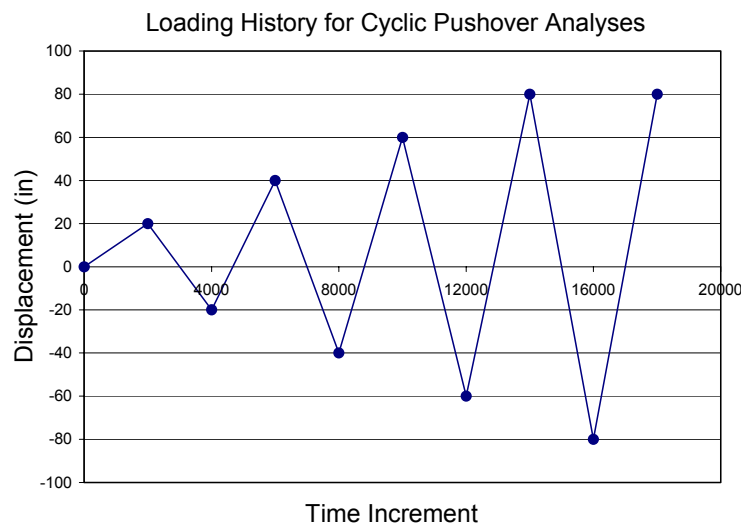


Figure 8.8 Displacement history for the nonlinear cyclic pushover analysis

The cyclic pushover curves for all composite moment frames are shown in Figures 8.9 to 8.12. Overall, the envelope of the monotonic curve corresponds to that of the cyclic curve when the same models are tested. As expected, all transition points and limits obtained by the monotonic pushover test are equal to those obtained by the cyclic pushover test. This illustrates an important limitation of these analyses, which cannot capture substantial degradation unless the monotonic ultimate strength is reached.

From all cyclic curves, the unloading slopes were taken as equal to the initial slope. Composite moment frames with PR connections show smaller residual displacement during unloading than those with welded connections. Similarly, composite frames with PR connections show gentler strength degradation after reaching their ultimate strength (See

Figure 8.9 (b) and Figure 8.9 (d)). This results in an increase in the energy absorption capacity. Moreover, composite frames with the same PR connection systems evidence almost identical cyclic curves regardless of the parameters for tension bars (See Figure 8.9 (a), (c), and (e)).

The cyclic pushover curves for 6END models show distinct strength degradation due to the large P-Delta effect in comparison with those for 4END models (i.e. 6END-C7 vs. 4END-C7). A slight slippage during reloads can be found on some cyclic curves as shown in Figure 8.12. This implies that the detailed component approach undertaken in this research is capable of detecting this subtle but important behavior mode.

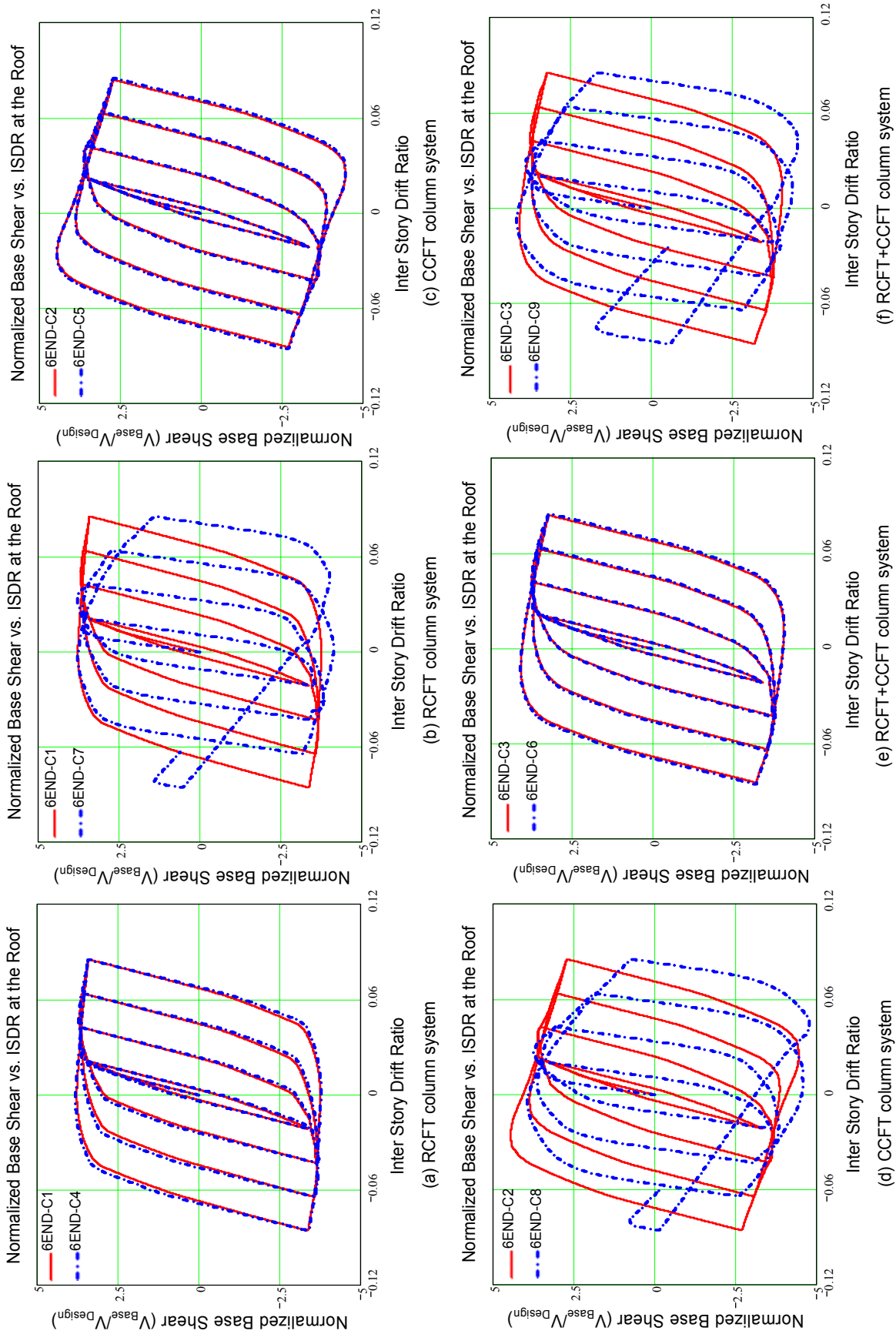


Figure 8.9 Nonlinear cyclic pushover curves for C-MF with end-plate and welded connections (6END)

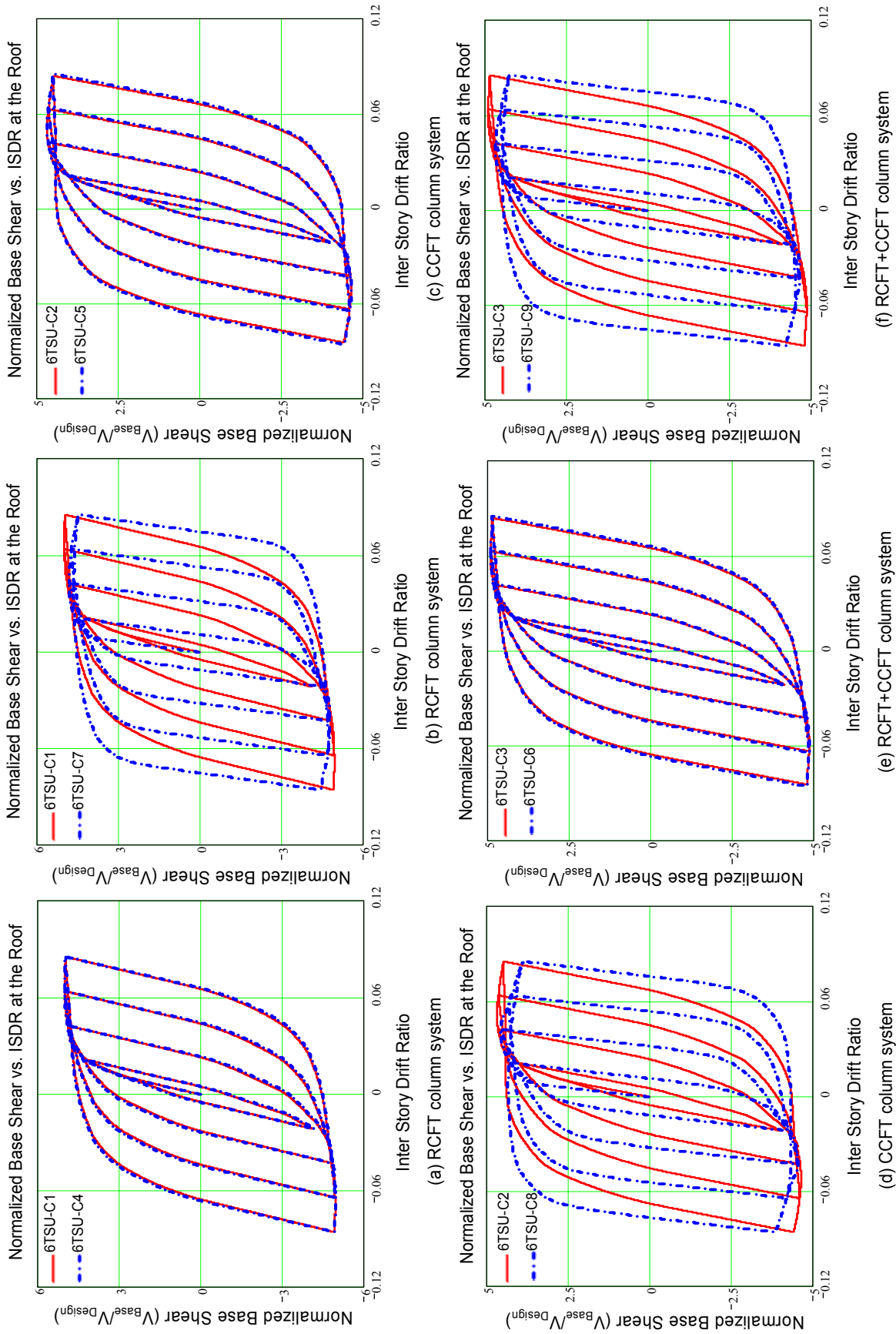


Figure 8.10 The nonlinear cyclic pushover curves for C-MF with T-stub and welded connections (6TSU)

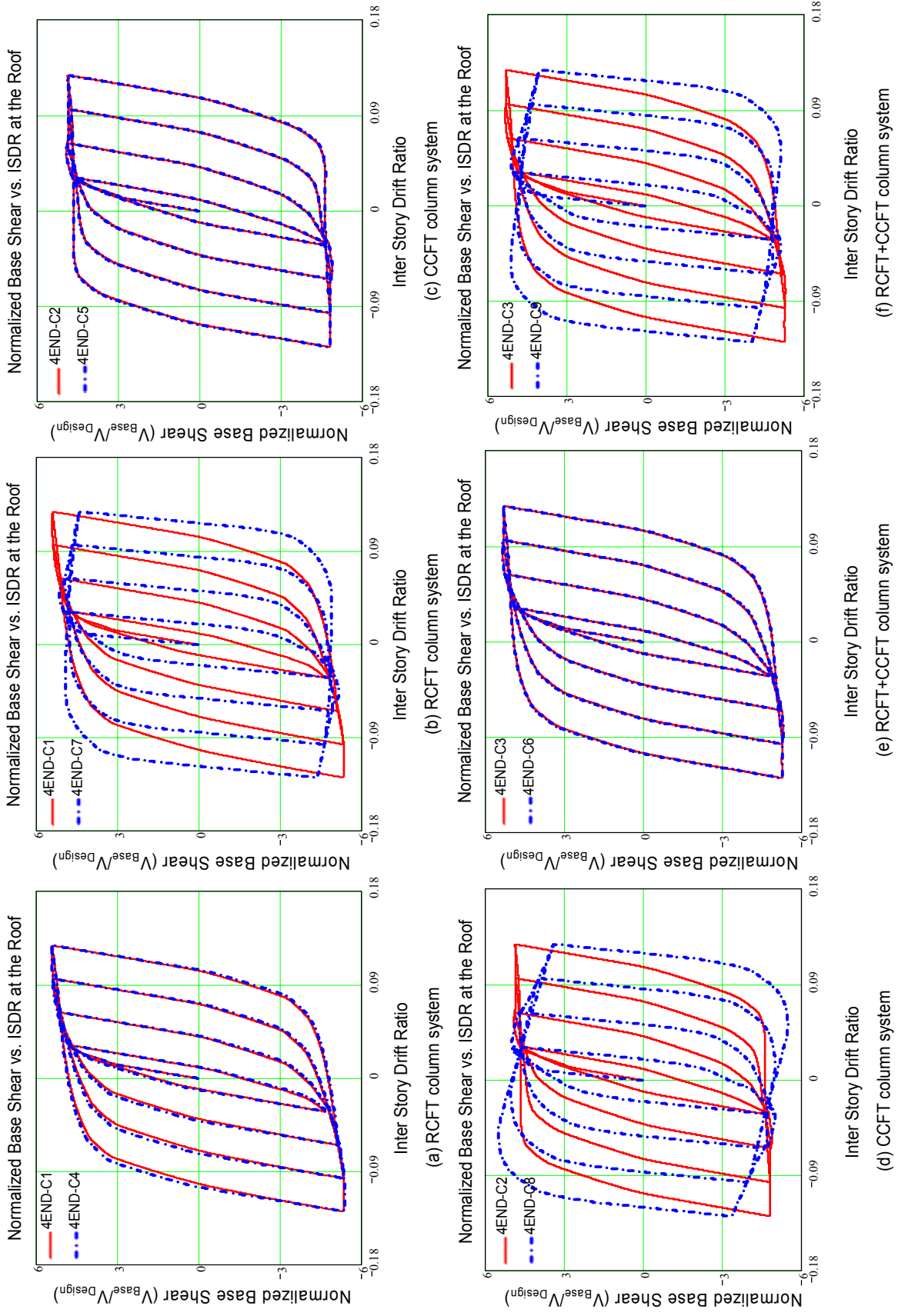


Figure 8.11 The nonlinear cyclic pushover curves for C-MF with end-plate and welded connections (4END)

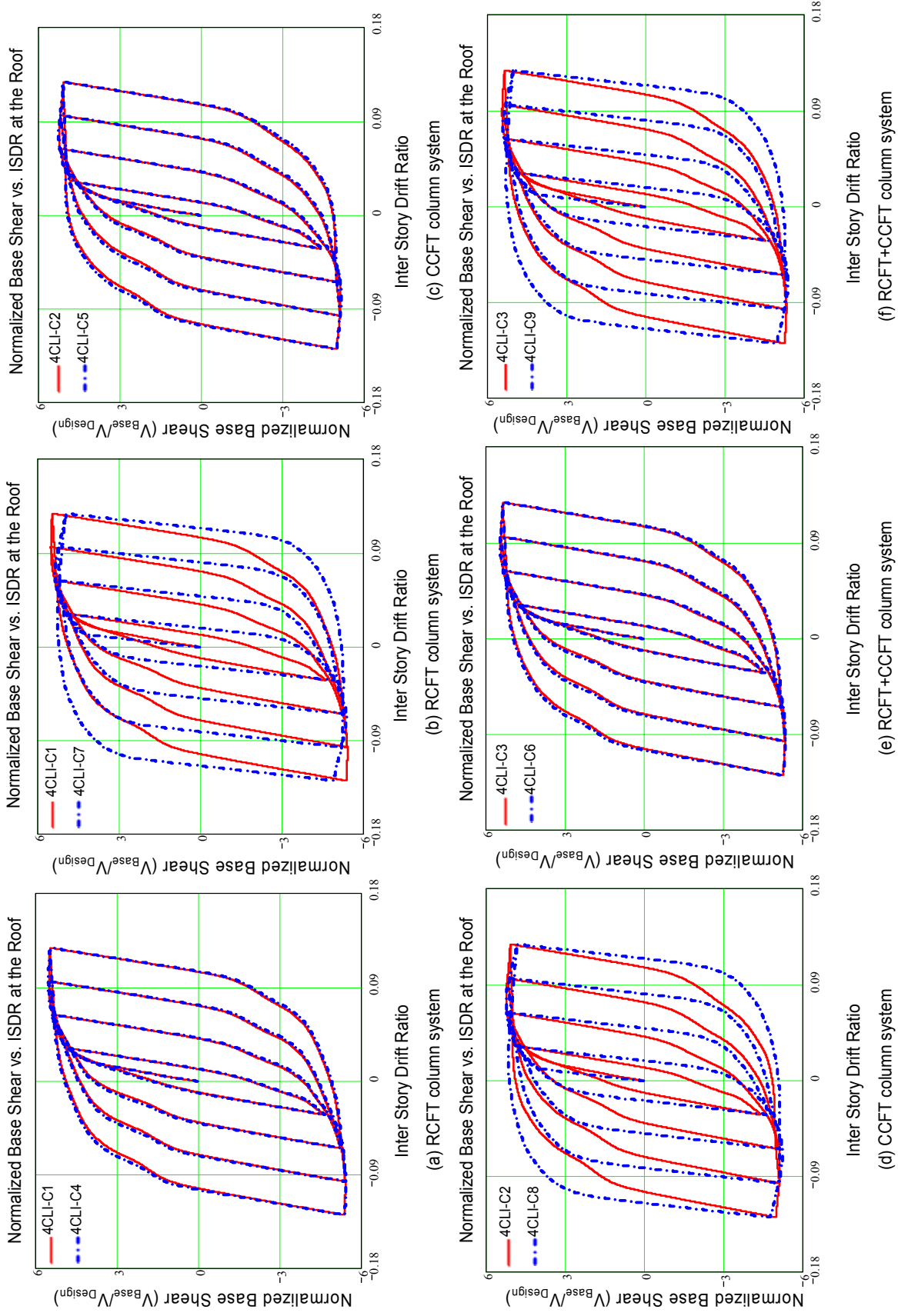


Figure 8.12 The nonlinear cyclic pushover curves for C-MF with end-plate and welded connections (4CLI)

8.2.3 Results of Nonlinear Pushover Analyses

The performance levels were defined from the monotonic pushover curves. The performance levels result from three transition points on these pushover curves: the Design Point, Yield Point, and Ultimate Point as shown in Figure 8.13. The monotonic pushover curves measured at the first floor were selected to determine the measurement points because the composite columns at this level are the most susceptible to the yielding and collapse (i.e., formation of a soft story). ISDR and PZRA at all floors under each performance level are investigated in this section.

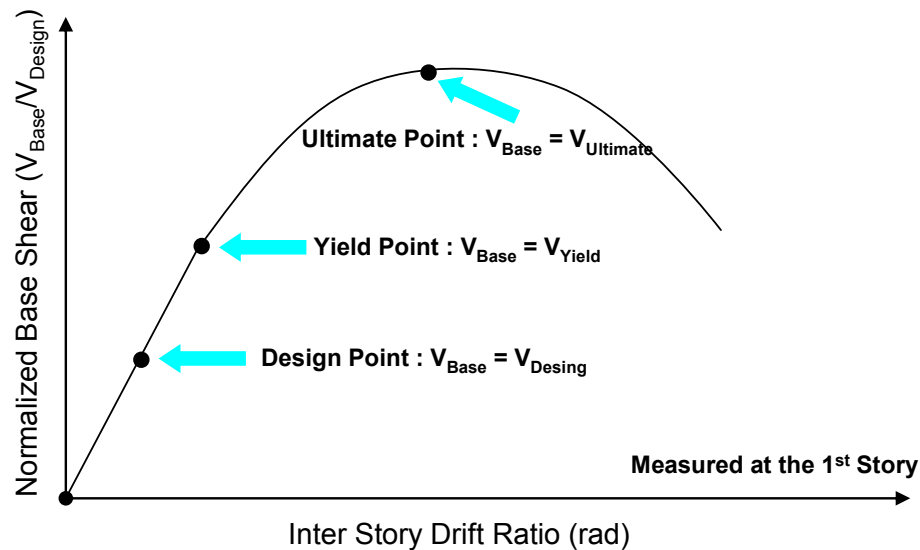


Figure 8.13 Measurement points for the performance levels

The ISDA at the design, yield and ultimate level are shown in Figures 8.14 to 8.17. The material properties of the tension bars rarely affected the pushover curves, so composite moment frame models with only steel tension bars were omitted in these figures. The design story drift shall not exceed the allowable story drift defined as by EQ (7.2). The allowable story drift checks for composite moment frames with welded connections (C-SMF) are shown in Figures 8.14 (a) and 8.15 (a). All stories satisfy the allowable drift limits.

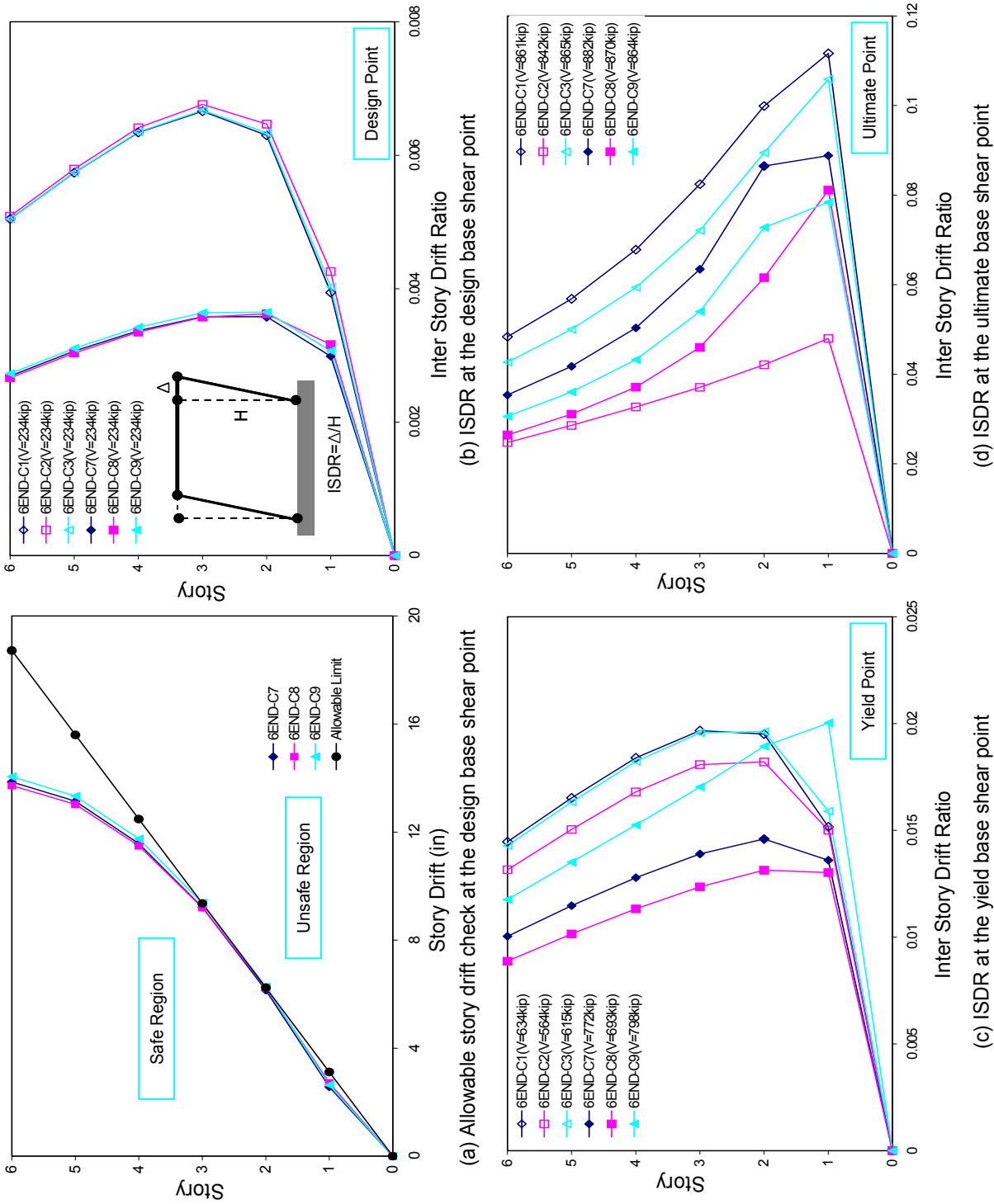
As expected from the design approaches used, all frames are stable up to the yield point level. After reaching the ultimate point level, plastic deformations due to bending increase

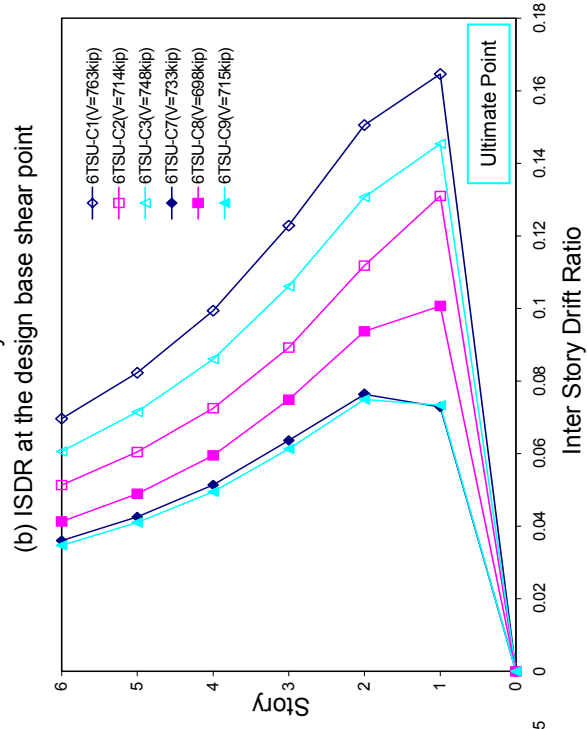
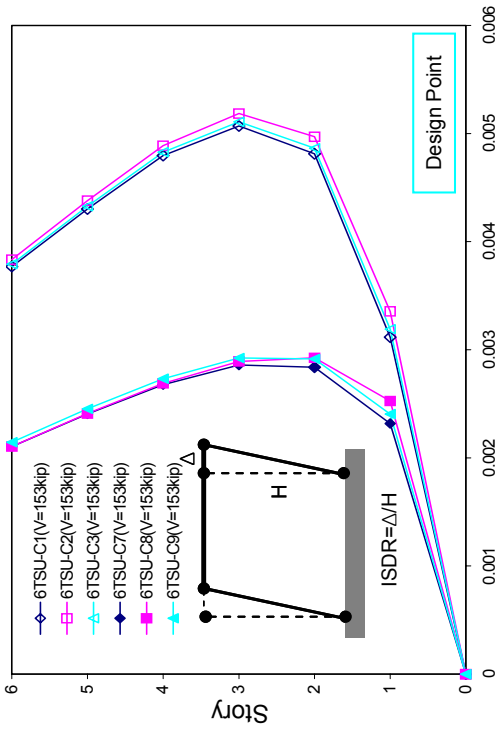
significantly and concentrate on the lower stories as shown in Figures 8.14 (d) and 8.15 (d). The maximum ISDR for the 6 story frames occur at the 3rd story until the yield point level, but it gradually moves to the lowest level as the lateral loads increased. The increased plastic deformations at the lower story cause this phenomenon (See next Section 8.2.4).

The composite moment frames with welded connections show a stiffer initial slope than those with bolted PR connections in the nonlinear pushover curves. Thus, the composite moment frames with welded connections show smaller inter-story drift than those with bolted PR connections within the elastic range of the pushover curves. Two performance levels which are design and yielding point level belong to the elastic range of the pushover curve. Therefore, the welded connection systems cause lower ISDR than the PR connection systems at both performance levels. For example, the average ISDR for the frames with welded connections is about 0.003, while the corresponding ISDR for those with PR connections is 0.006 at the design point level (See Figure 8.14 (b)). At the yielding performance level (See Figure 8.14 (c) and Figure 8.15 (c)), the value of ISDR at the lower story levels starts to increase. The scatter of ISDR at the each story level also start to increase.

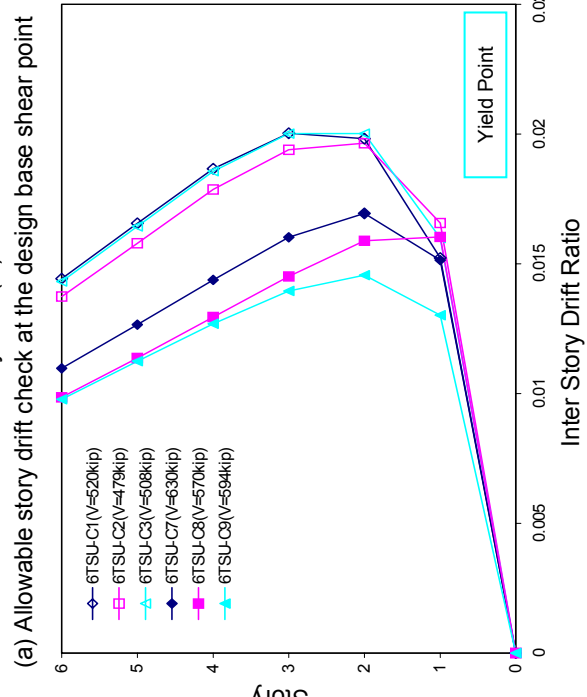
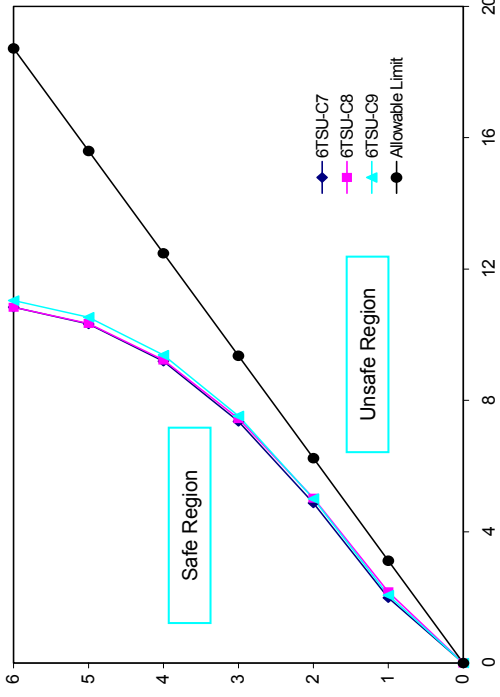
For the 4 story frame cases (Figures 8.16 and 8.17), the ISDR at the ultimate point level can not be reliably estimated because of the continuous strain hardening of the monotonic pushover curves. This implies that the ISDR at the ultimate point level increases significantly for shorter buildings. In addition, it is worthwhile to notice that the ISDR for the 4 story frames are generally smaller than those of the 6 story frames at both the design and the yield point level due to the smaller P-Delta effects.

The PZRA show the same trend as ISDR for all composite moment frames. The PZRA for the 6 story moment frames are shown in Figures 8.18 and 8.19. Circular columns had rectangular shapes welded to the panel zone to facilitate the fabrication of the connection (See Figure 4.8). This detail gave rise to stress concentrations, so the PZRA of 6END-C2 deteriorated rapidly, as shown in Figure 8.18 (a). Similarly to the ISDR, all frames exhibit stable PZRA behavior up to the yield point level. After reaching the ultimate point level, plastic rotations due to bending localize on the lowest story level as shown in Figure 8.18 (d) and Figure 8.19 (d).



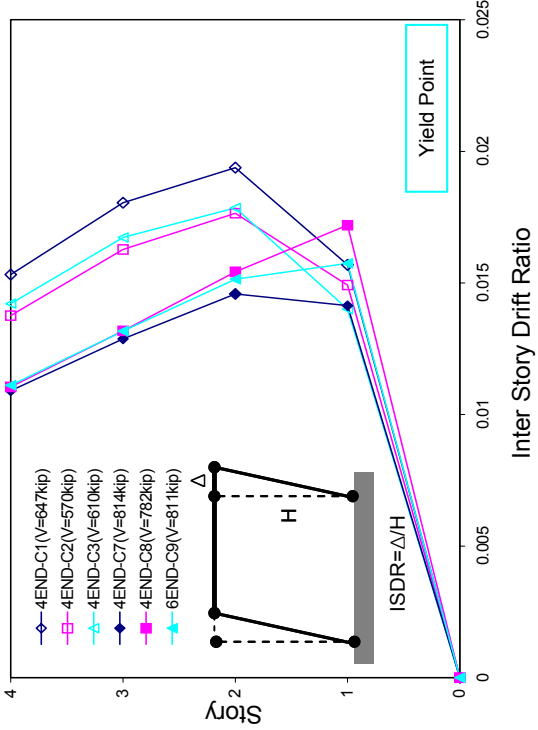


(b) ISDR at the ultimate base shear point



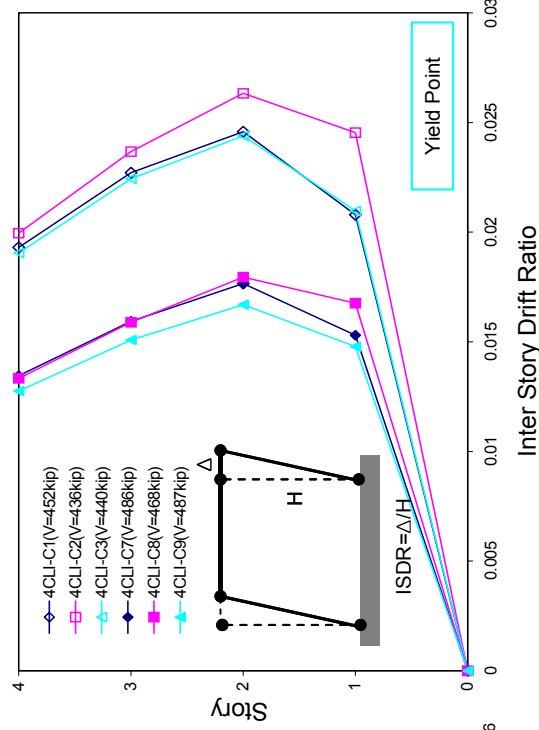
(c) ISDR at the yield base shear point

Figure 8.15 Allowable story drift check and inter story drift ratio at the measurement points (6TSU)

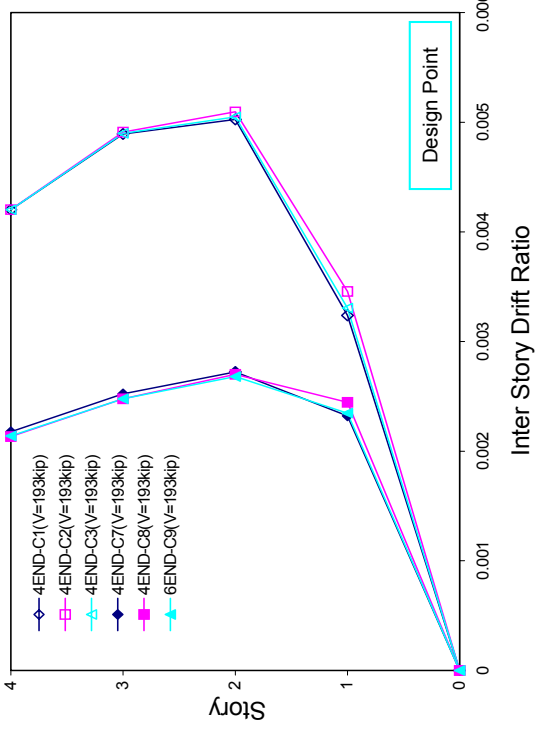


(a) ISDR at the design base shear point

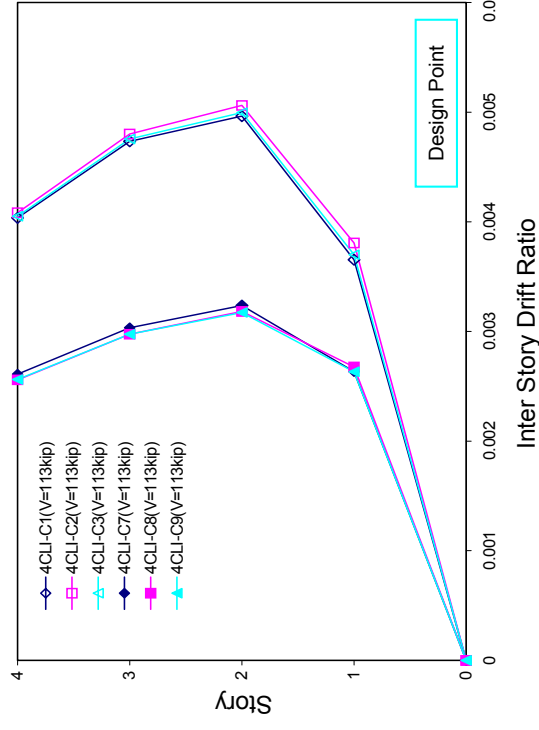
Figure 8.16 Interstory drift ratio at the measurement points (4END)



(b) ISDR at the yield base shear point



(a) ISDR at the design base shear point



(b) ISDR at the yield base shear point

Figure 8.17 Interstory drift ratio at the measurement points (4CLJ)

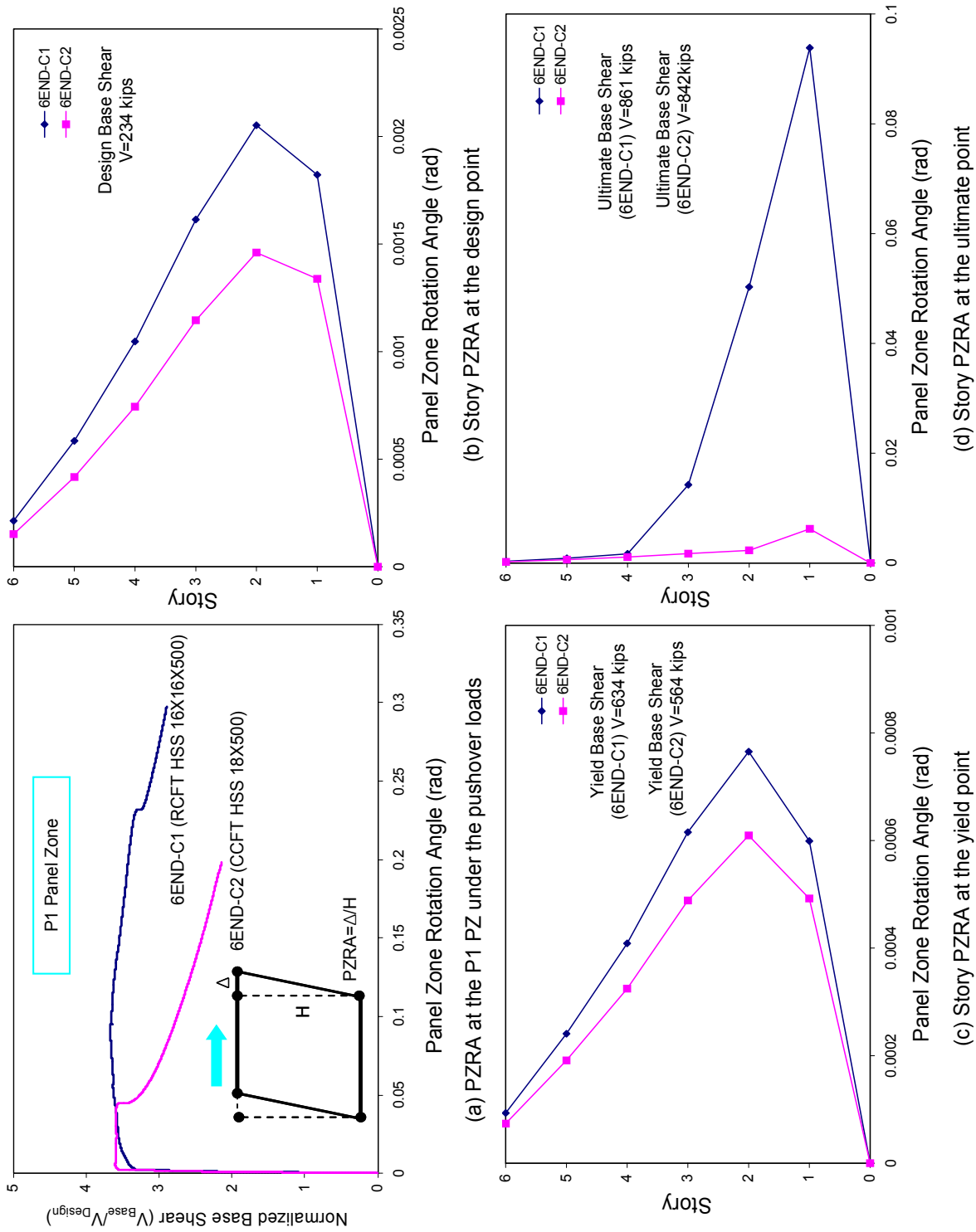


Figure 8.18 Story panel zone rotation angle at the measurement points (6END)

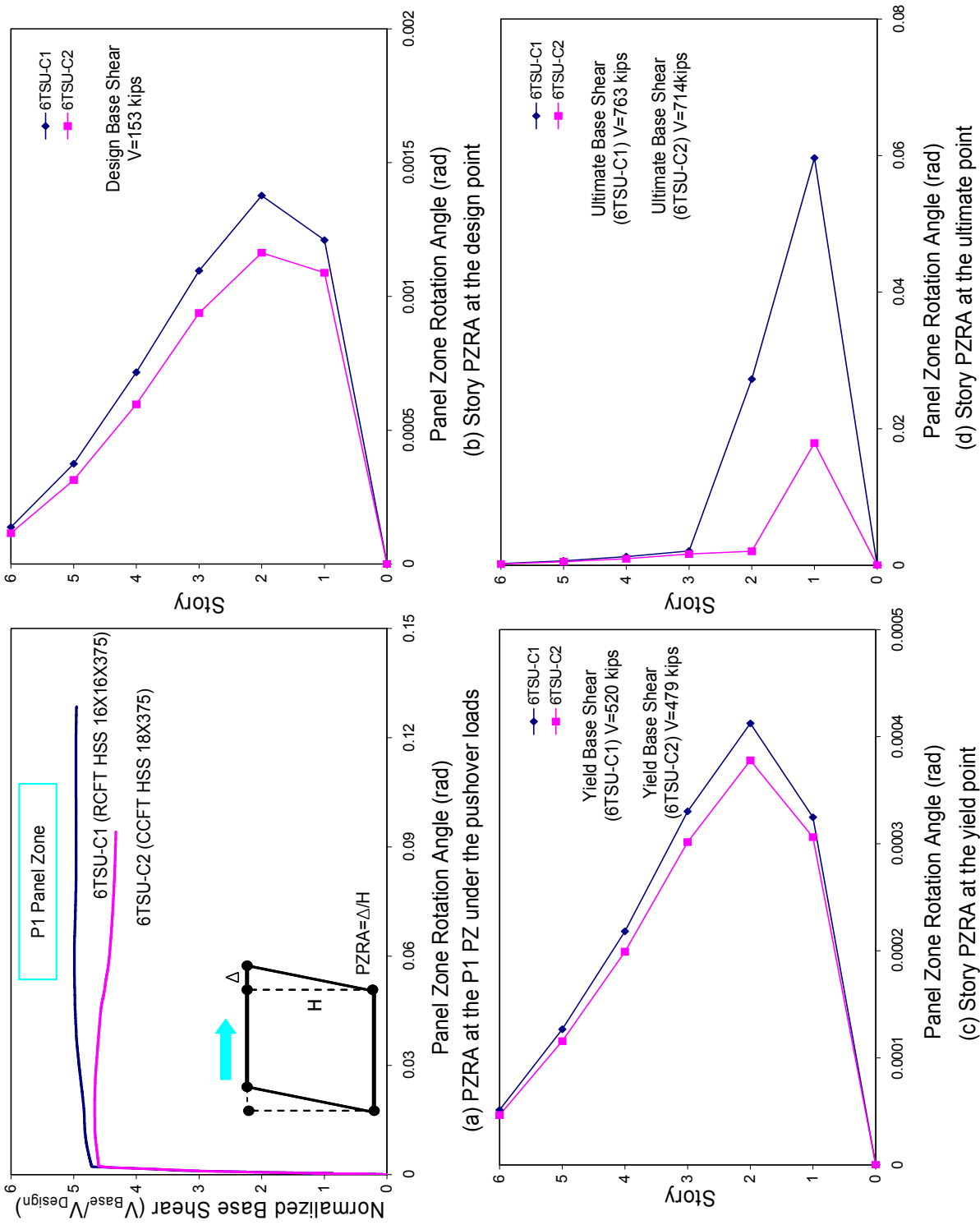


Figure 8.19 Story panel zone rotation angle at the measurement points (6TSU)

8.2.4 Failure Mechanism for Composite Frame Models

From the pushover results, it can be shown that hinges occurs at the bottom of the composite columns as well as other column locations. The occurrence of a hinge, and its increasing rotations, can be detected by measuring the stresses and strains in the sections during the pushover analysis.

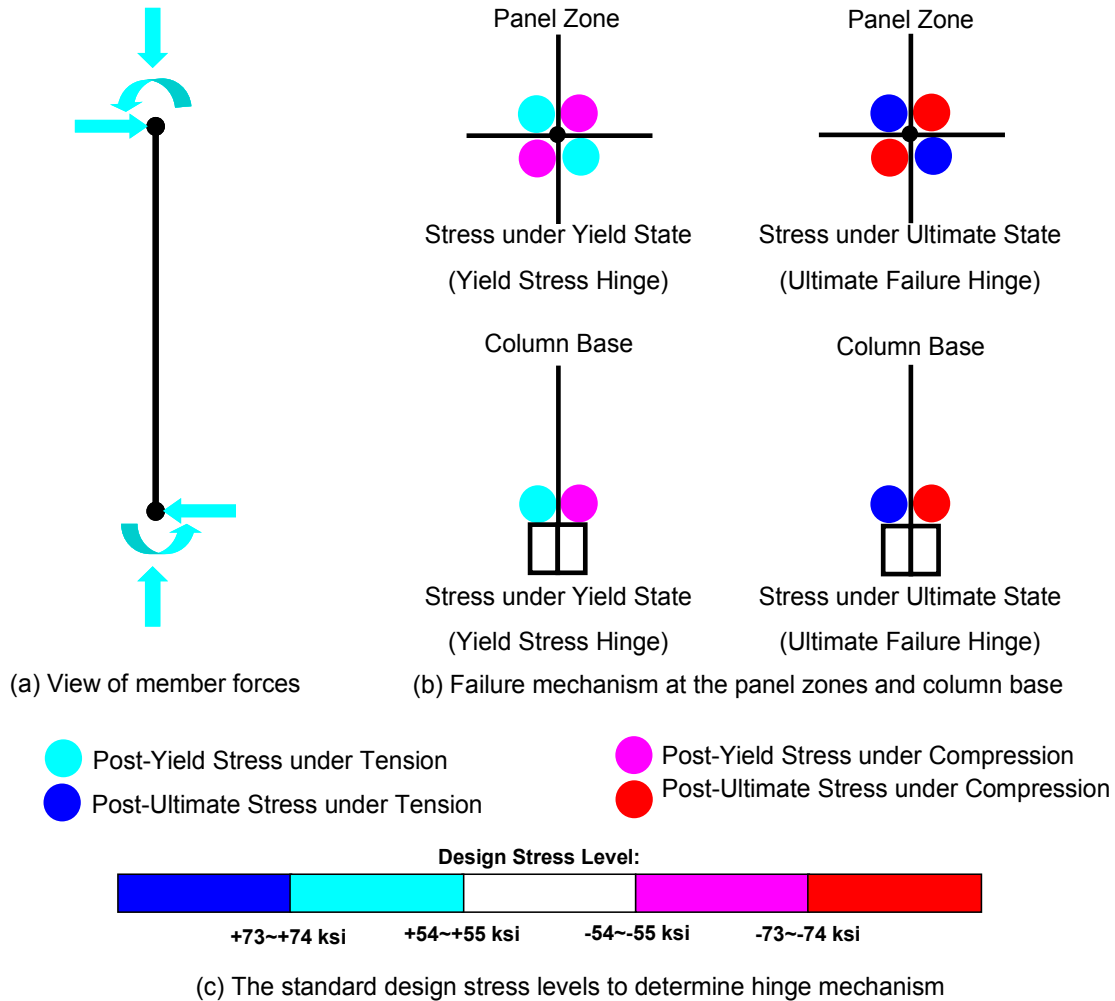


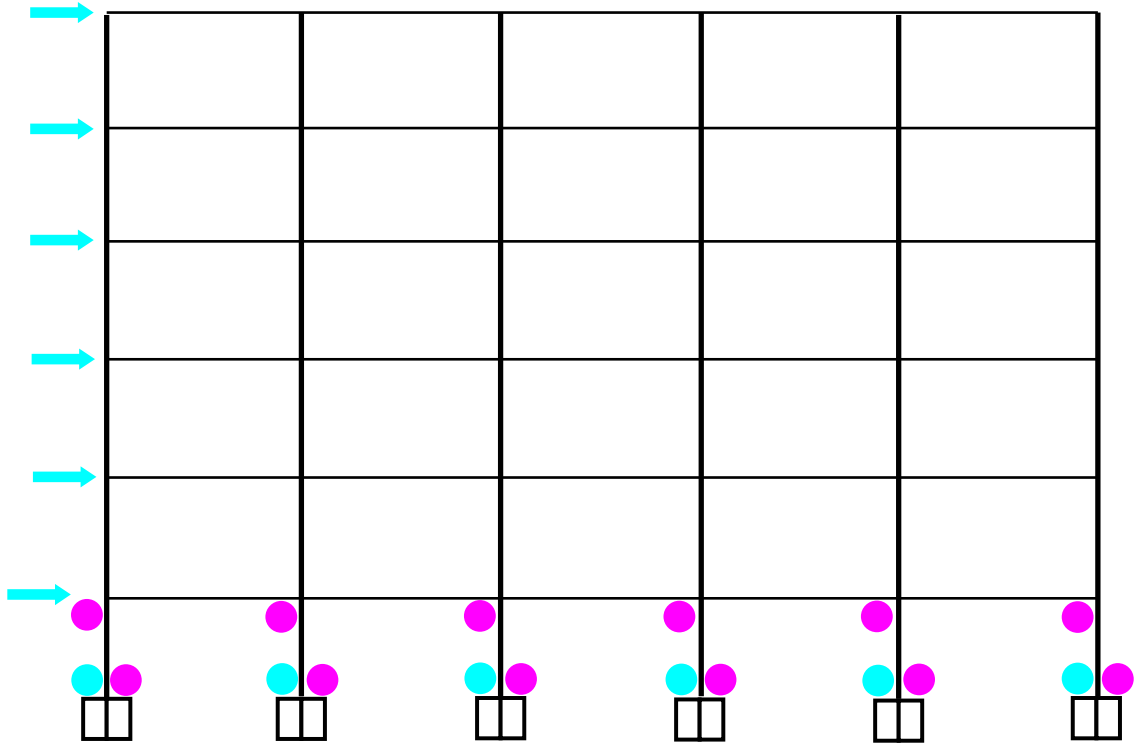
Figure 8.20 Determination of the failure mechanism using the failure hinge

The composite columns subjected to lateral loads accommodate the imposed frame deformations through a double curvature deflection mode. The member forces acting on the composite frames are shown in Figure 8.20 (a). As the applied lateral loads are increased, the bending moments are also increasing at the ends of composite columns. The bending

stress due to the bending moments contributes to creating the hinges as shown in Figure 8.20 (b). Generally, the shear stresses in the members are negligible in a frame analysis. Both hinge levels are defined in Figure 8.20 (c). The yield stress hinge is determined when the design yield stress (55 ksi). The ultimate failure hinge is determined when the post design ultimate stress (74 ksi) is reached. The design stress level was based on the steel materials used in the composite columns.

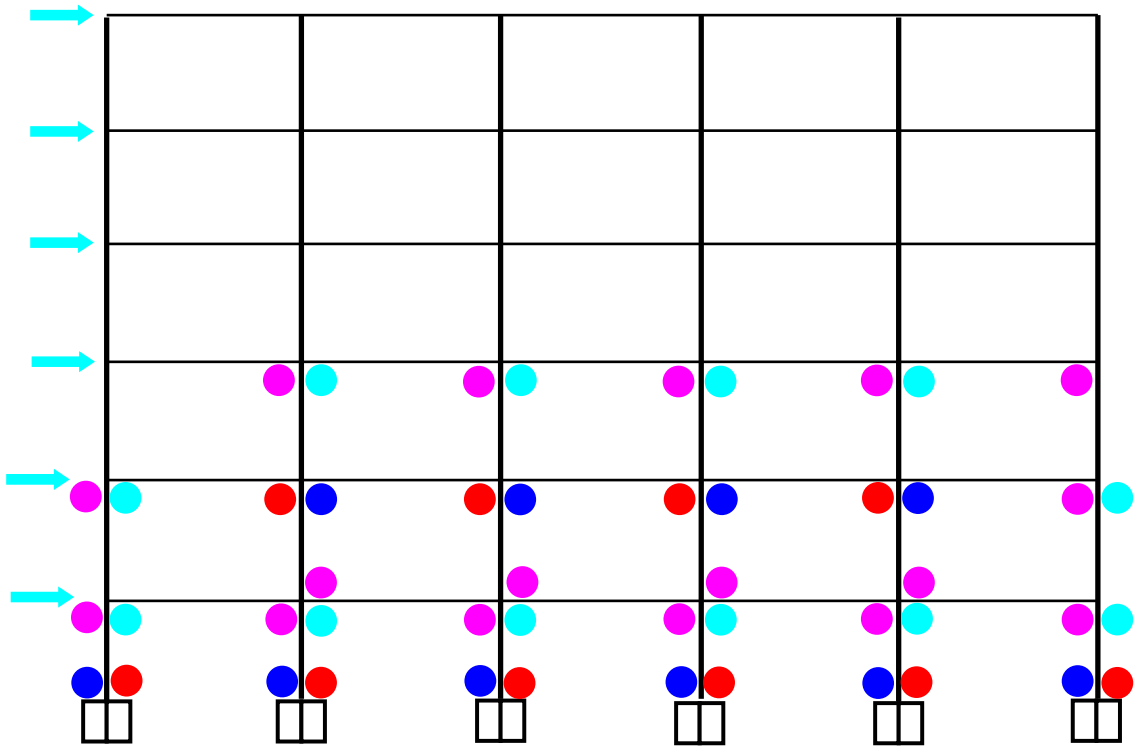
The hinging during the nonlinear pushover analysis is shown in Figure 8.21 to Figure 8.24. Only two performance levels (the yield point and the ultimate points) are shown because no yielding occurred at the design point. Hinges start to occur at the column bases and extend to the upper stories. The hinges occur due to the combination of axial and bending stresses. At the yield base shear force, the number of hinge points due to compression is more than that of hinge points due to tension because of the axial stresses generated by the gravity loads. However, as the applied lateral loads are increased, the bending stresses generated by the bending moments become dominant. Remember, that as noted in Figure 9.5, the beam hinges are not shown. Moreover, while many hinges are shown in the columns, no complete story mechanisms form, so the structures are still stable.

Overall, the interior composite columns are more susceptible to failure than the external composite columns due to the larger P-Delta effect. The positions of hinges are symmetric to the center of the moment frame. Composite moment frames with welded connections show more hinges than those with PR connections at the yield point because of the sudden brittle failure.



Double Curvature (Check Local Coordinates for the fiber section)

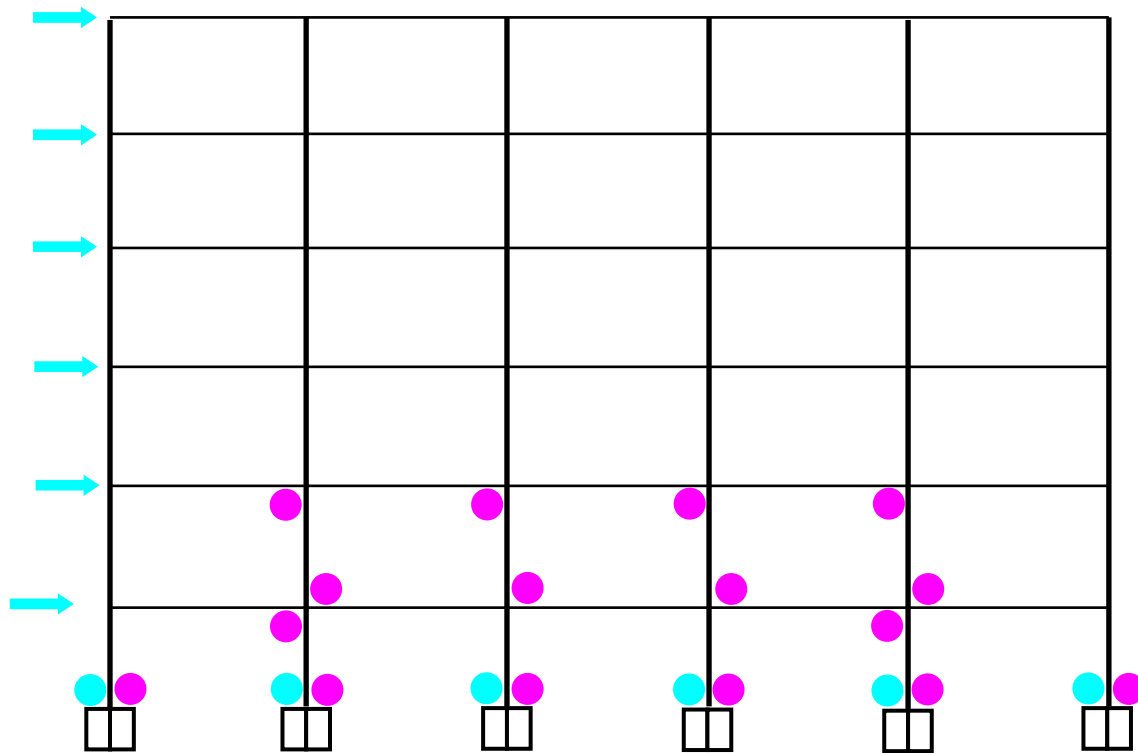
(a) Failure hinge formation for 6END-C1 model under yield base shear force ($V=634$ kip)



Double Curvature (Check Local Coordinates for the fiber section)

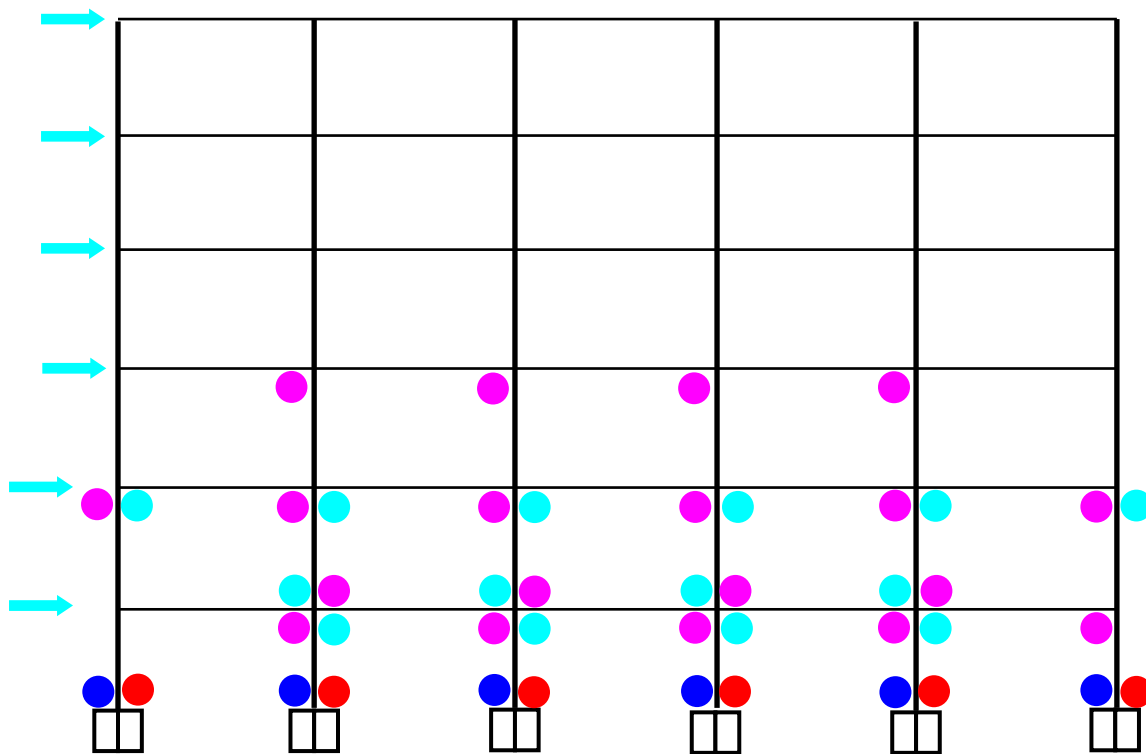
(b) Failure hinge formation for 6END-C1 model under ultimate base shear force ($V=861$ kip)

Figure 8.21 Failure hinge formation during the nonlinear monotonic pushover analysis (6END-C1)



Double Curvature (Check Local Coordinates for the fiber section)

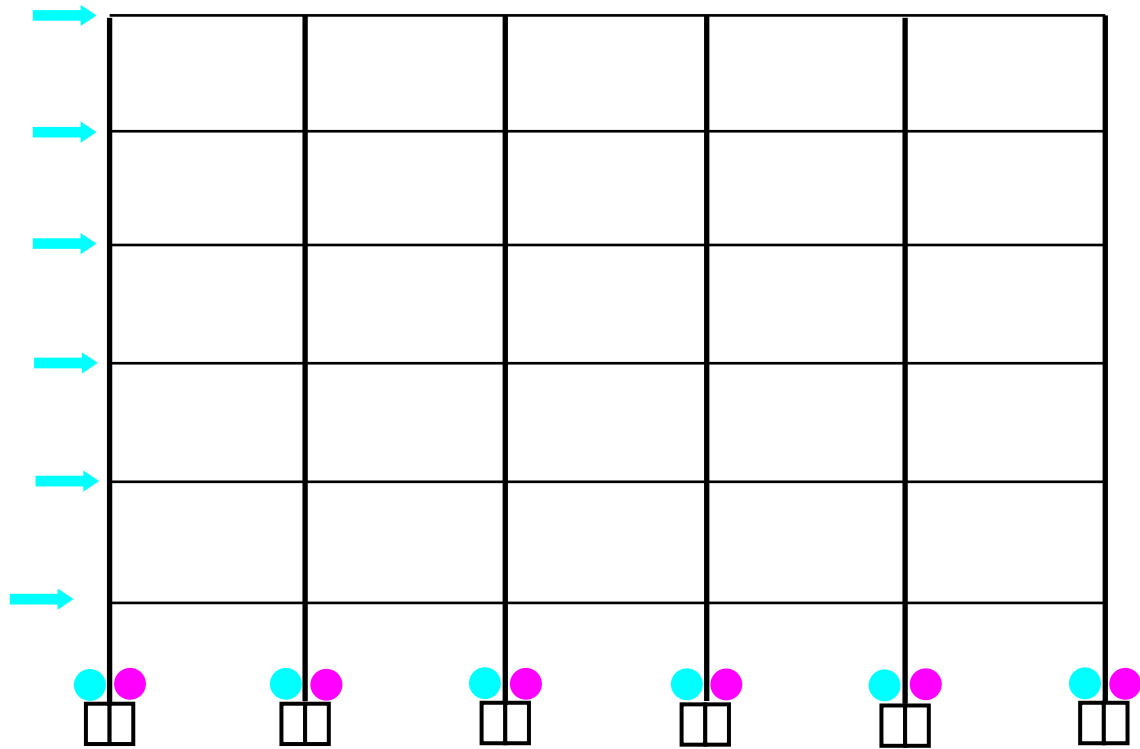
(a) Failure hinge formation for 6END-C7 under yield base shear force ($V=772$ kip)



Double Curvature (Check Local Coordinates for the fiber section)

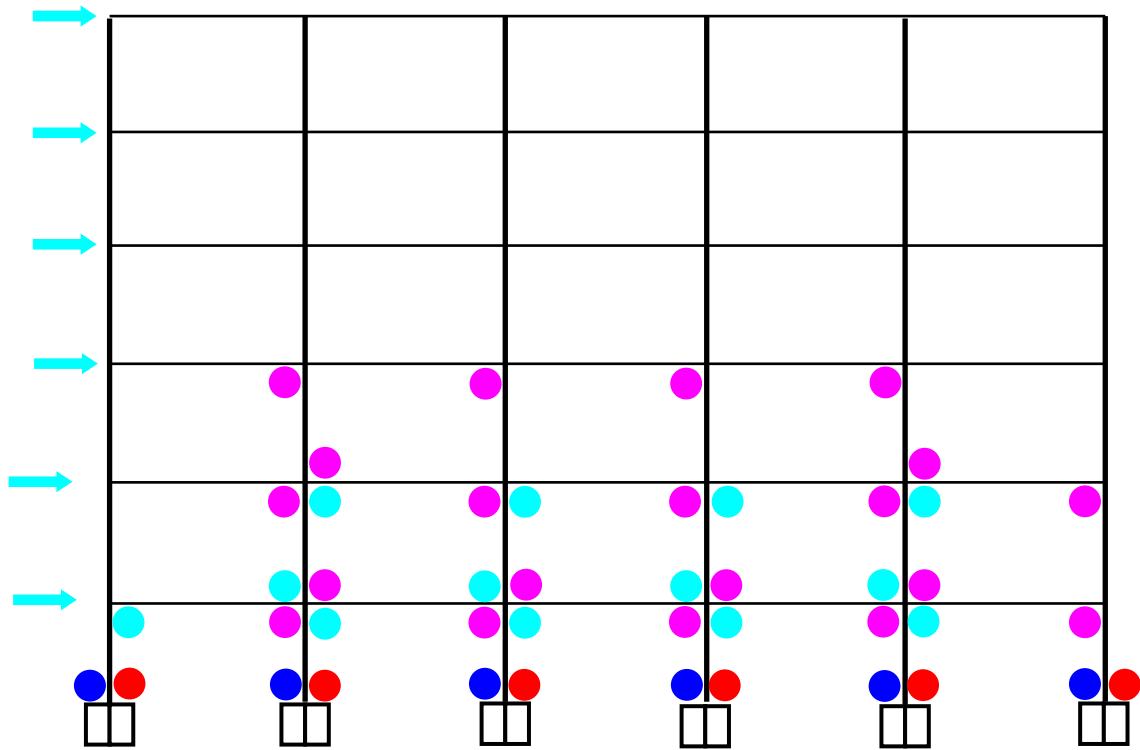
(b) Failure hinge formation for 6END-C7 under ultimate base shear force ($V=882$ kip)

Figure 8.22 Failure hinge formation during the nonlinear monotonic pushover analysis (6END-C7)



Double Curvature (Check Local Coordinates for the fiber section)

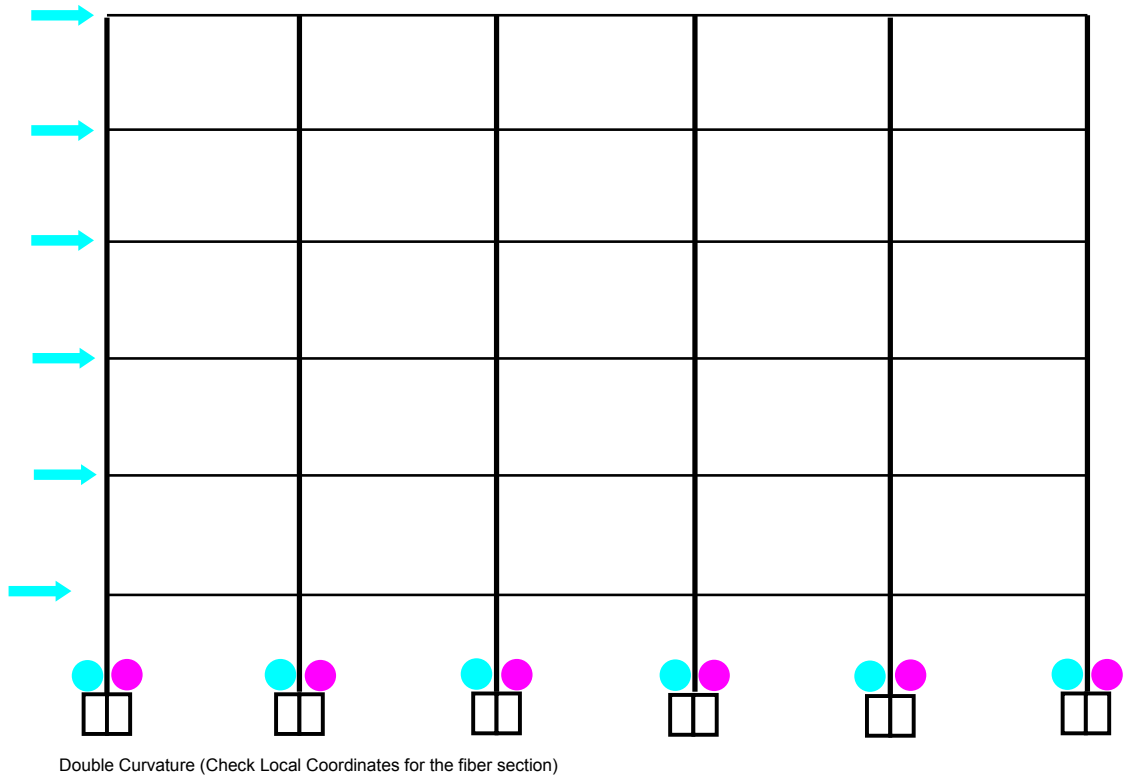
(a) Failure hinge formation for 6END-C2 under yield base shear force ($V=564$ kip)



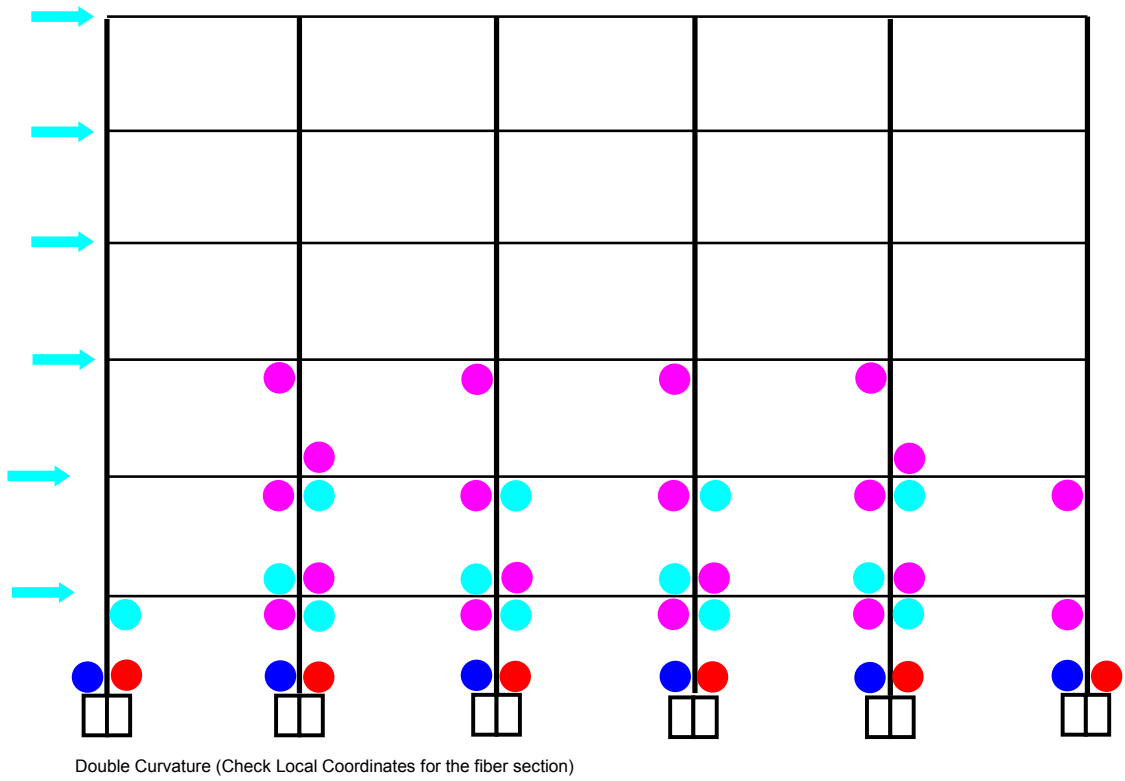
Double Curvature (Check Local Coordinates for the fiber section)

(b) Failure hinge formation for 6END-C2 under ultimate base shear force ($V=843$ kip)

Figure 8.23 Failure hinge formation during the nonlinear monotonic pushover analysis (6END-C3)



(a) Failure hinge formation for 6END-C2 under yield base shear force ($V=564$ kip)



(b) Failure hinge formation for 6END-C2 under ultimate base shear force ($V=843$ kip)

Figure 8.24 Failure hinge formation during the nonlinear monotonic pushover analysis (6END-C8)

8.3 Nonlinear Dynamic Analyses

The nonlinear dynamic analyses consisted of two suites of 20 earthquake ground motions with 2% probability of exceedence in 50 years for the western USA area (LA21 to LA30 and SE21 to SE30, Somerville et al., 1997). Information on the ground motions is given in Table 8.2 and Appendix F.

Table 8.2 Earthquake ground motions with 2% probability of exceedence in 50 years

SAC Name	Record	Earthquake Magnitude	Distance (km)	Scale Factor	Number of Points	DT (sec)	Duration (sec)	PGA (g)
LA21	1995 Kobe	6.9	3.4	1.15	3000	0.02	59.98	1.283
LA22	1995 Kobe	6.9	3.4	1.15	3000	0.02	59.98	0.92069
LA23	1989 Loma Prieta	7	3.5	0.82	2500	0.01	24.99	0.418097
LA24	1989 Loma Prieta	7	3.5	0.82	2500	0.01	24.99	0.472976
LA25	1994 Northridge	6.7	7.5	1.29	2990	0.005	14.945	0.868544
LA26	1994 Northridge	6.7	7.5	1.29	2990	0.005	14.945	0.943678
LA27	1994 Northridge	6.7	6.4	1.61	3000	0.02	59.98	0.926758
LA28	1994 Northridge	6.7	6.4	1.61	3000	0.02	59.98	1.330016
LA29	1974 Tabas	7.4	1.2	1.08	2500	0.02	49.98	0.809218
LA30	1974 Tabas	7.4	1.2	1.08	2500	0.02	49.98	0.991908

(a) Earthquake ground motions in LA area (LA Motions)

SAC Name	Record	Earthquake Magnitude	Distance (km)	Scale Factor	Number of Points	DT (sec)	Duration (sec)	PGA (g)
SE21	1992 Mendocino	7.1	8.5	0.98	3000	0.02	59.98	0.7551332
SE22	1992 Mendocino	7.1	8.5	0.98	3000	0.02	59.98	0.4852179
SE23	1992 Erzincan	6.7	2	1.27	4156	0.005	20.775	0.6048157
SE24	1992 Erzincan	6.7	2	1.27	4156	0.005	20.775	0.5390563
SE25	1949 Olympia	6.5	56	4.35	4000	0.02	79.98	0.8948236
SE26	1949 Olympia	6.5	56	4.35	4000	0.02	79.98	0.8209028
SE27	1965 Seattle	7.1	80	10.04	4092	0.02	81.82	1.7549437
SE28	1965 Seattle	7.1	80	10.04	4092	0.02	81.82	1.3904852
SE29	1985 Valpariso	8	42	2.9	4000	0.025	99.975	1.6358349
SE30	1985 Valpariso	8	42	2.9	4000	0.025	99.975	1.5726635

(b) Earthquake ground motions in Seattle Area (SE Motions)

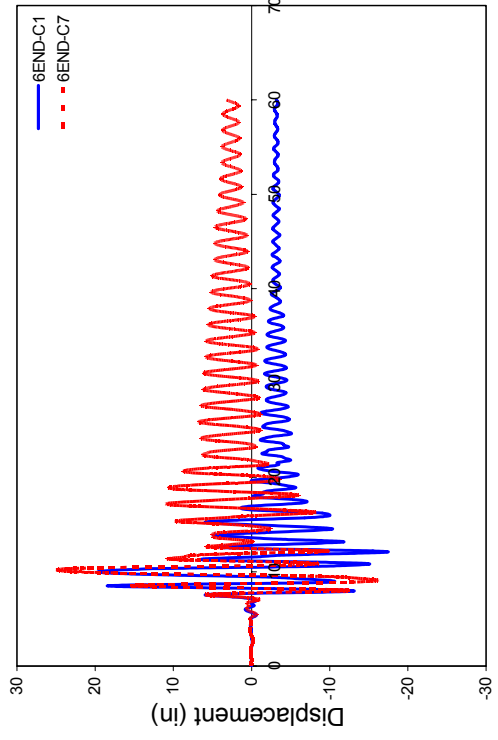
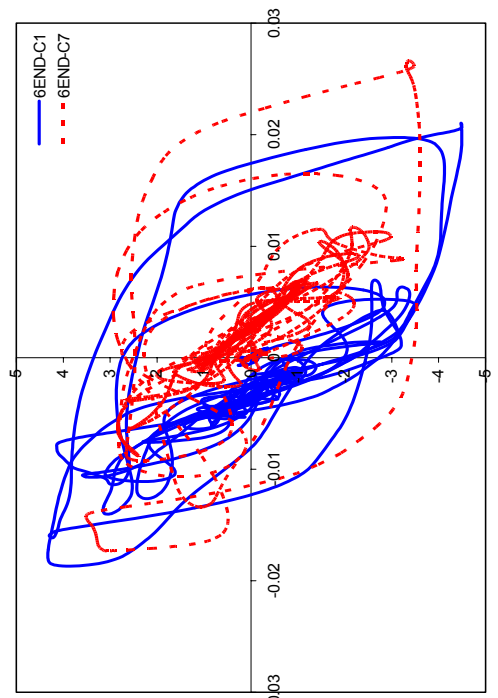
Displacements and interstory drift ratios are investigated in this section. As the amount of data generated in these analyses was enormous, only the peak responses for some composite moment frame models subjected to all ground motions are summarized here.

8.3.1 Nonlinear Dynamic Behavior

For a comparison between the behavior of the PR and that of the welded FR frames, two ground motions (LA21 and LA26) were selected. The LA 21 ground motion has energy concentrated a relatively long period (60 sec.), while the LA 26 ground motion has energy concentrated at a relatively short period (15 sec., See Figure 8.2).

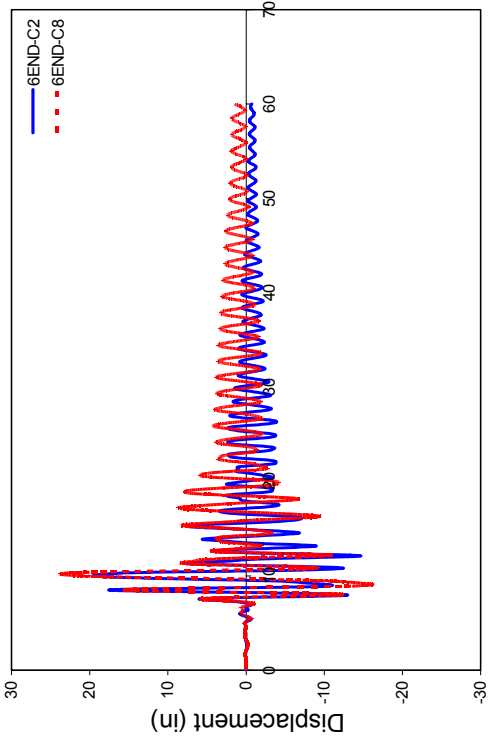
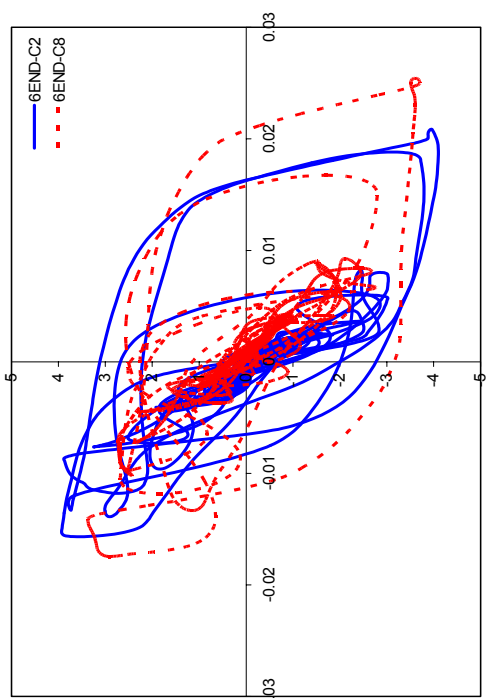
Displacements at the roof level and inter-story drift ratios are shown in Figures 8.25 to 8.27. The figures compare the behavior of two frame models with different connection types. Generally, composite moment frames with PR connections show smaller maximum displacements than those with welded FR connections.

The cyclic behavior of composite frame structures under ground motions will be plotted as the normalized shear forces versus interstory drift ratio at the roof. These plots show the influence of the applied ground motion and P-Delta effect. In general, the 6 story frames show higher maximum base shear than the 4 story frames; this is expected given the additional height and mass. There are significant permanent displacements at the ends of the analyses for several of the analyses.



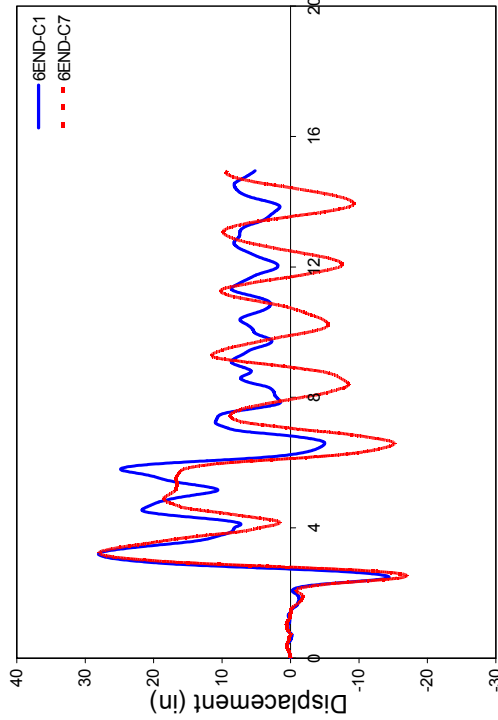
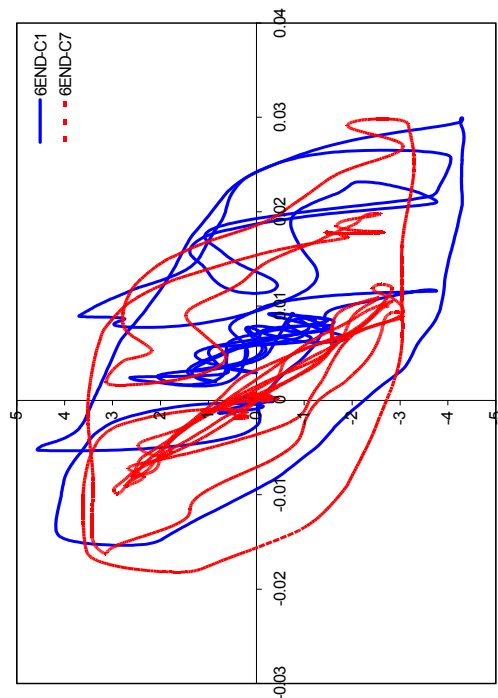
Inter Story Drift Ratio

(a) Displacement at the Roof under LA21 Ground Motion (6END-C1 vs. 6END-C7)

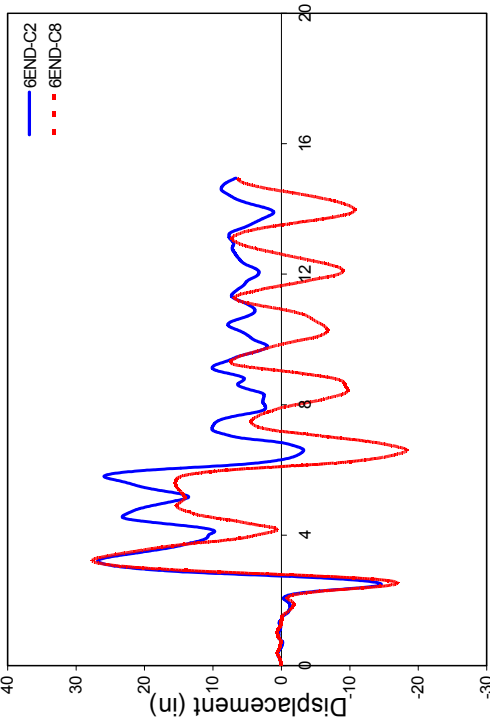
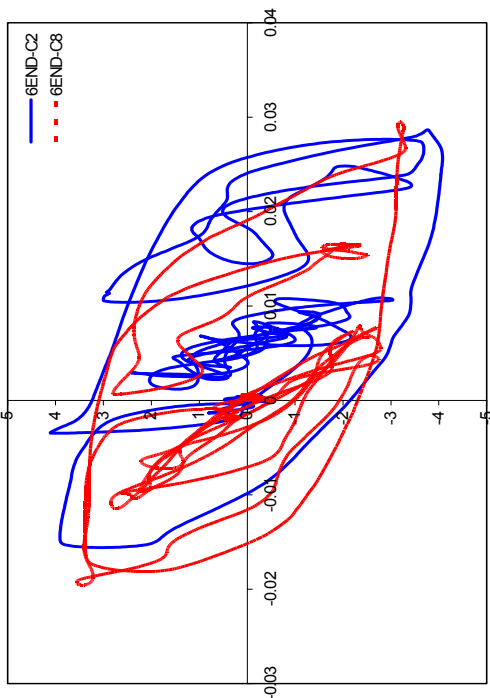


Inter Story Drift Ratio

(b) Displacement at the Roof under LA21 Ground Motion (6END-C2 vs. 6END-C8)

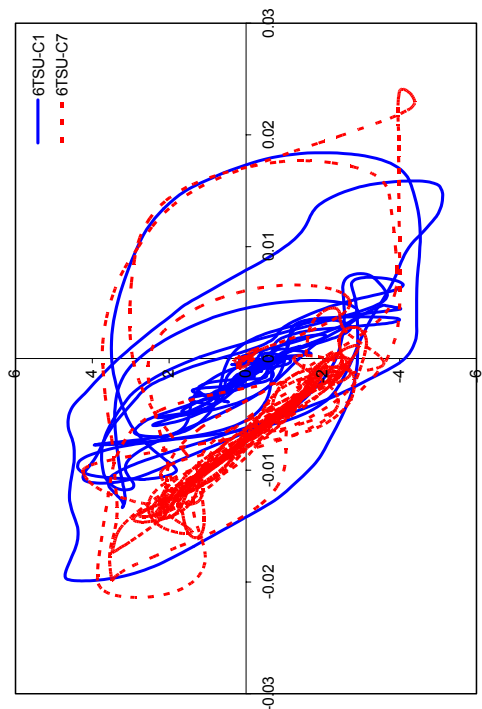


(c) Displacement at the Roof under LA26 Ground Motion (6END-C1 vs. 6END-C7)



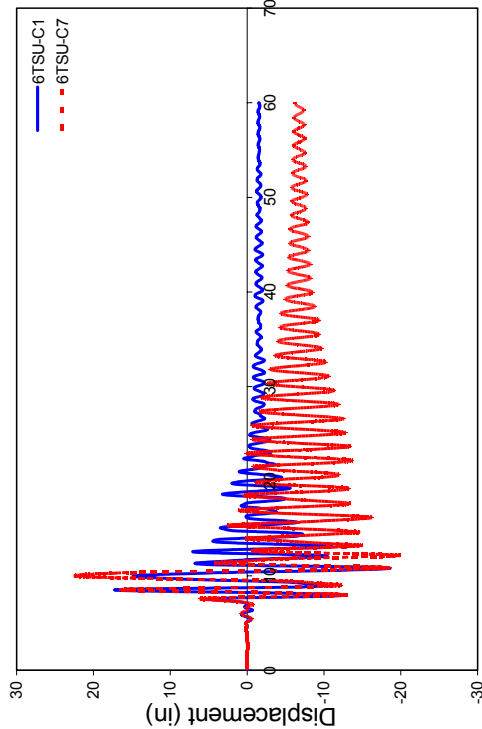
(d) Displacement at the Roof under LA26 Ground Motion (6END-C2 vs. 6END-C8)

Figure 8.25 Displacement at the roof level under ground motions (6END))

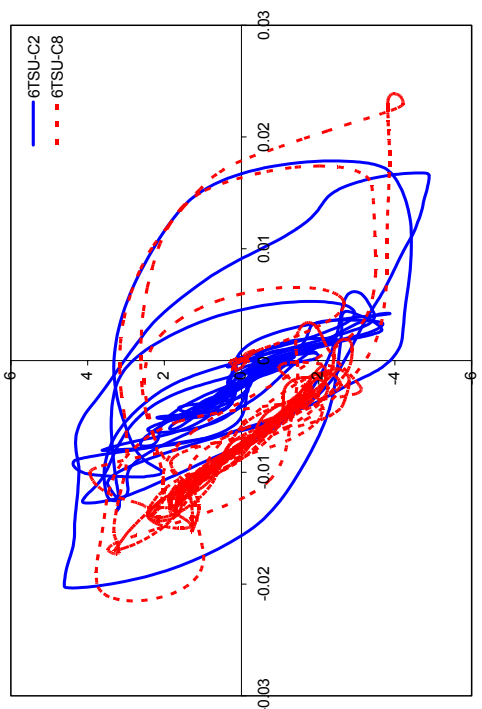


Inter Story Drift Ratio

(a) Displacement at the Roof under LA21 Ground Motion (6TSU-C1 vs. 6TSU-C7)

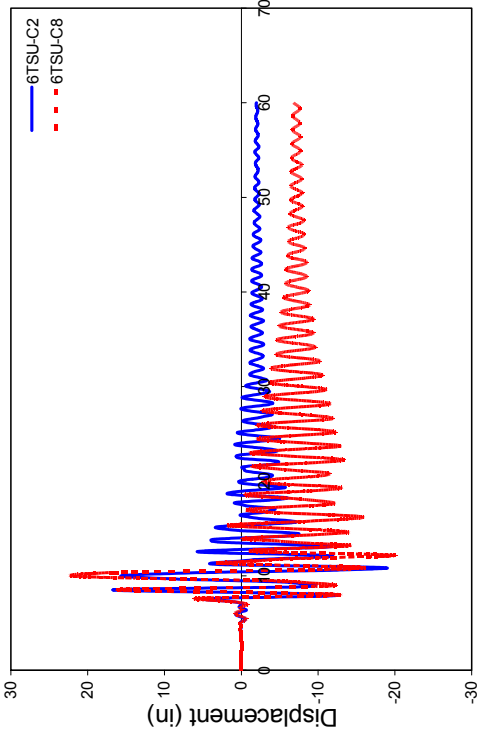


Time (sec)

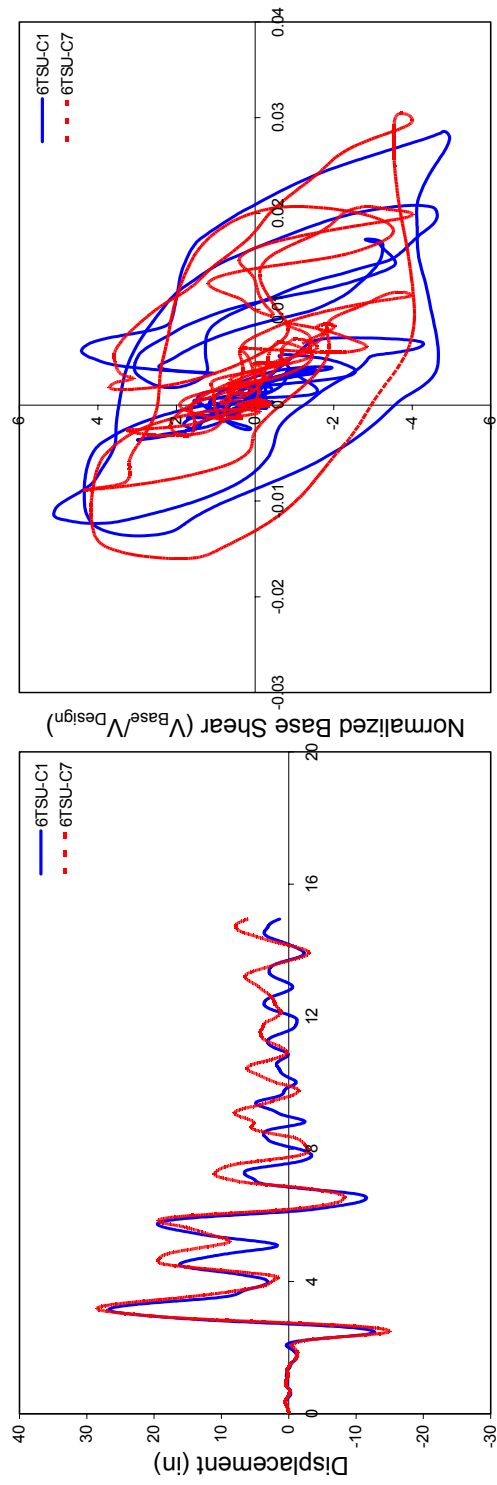


Inter Story Drift Ratio

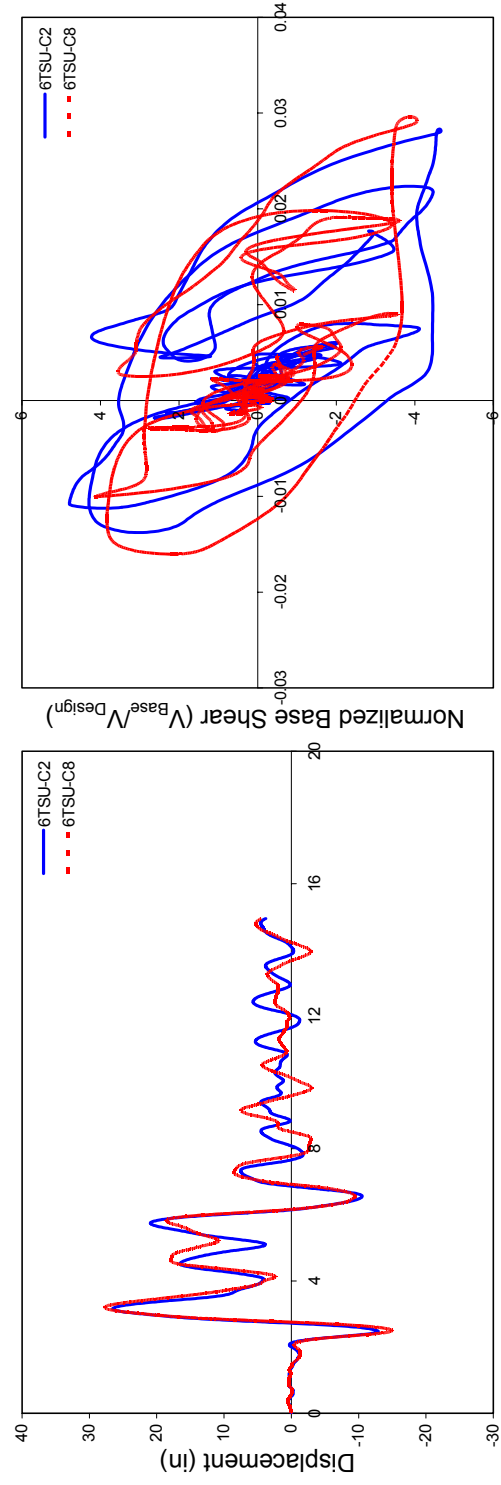
(b) Displacement at the Roof under LA21 Ground Motion (6TSU-C2 vs. 6TSU-C8)



Time (sec)

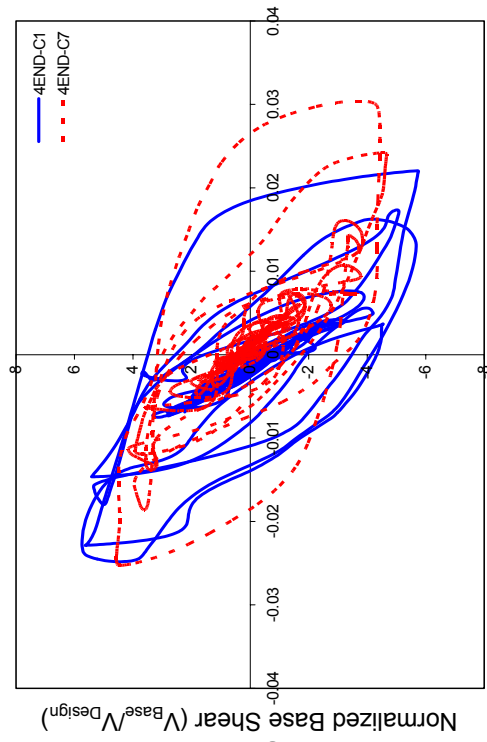


(c) Displacement at the Roof under LA26 Ground Motion (6TTSU-C1 vs. 6TTSU-C7)



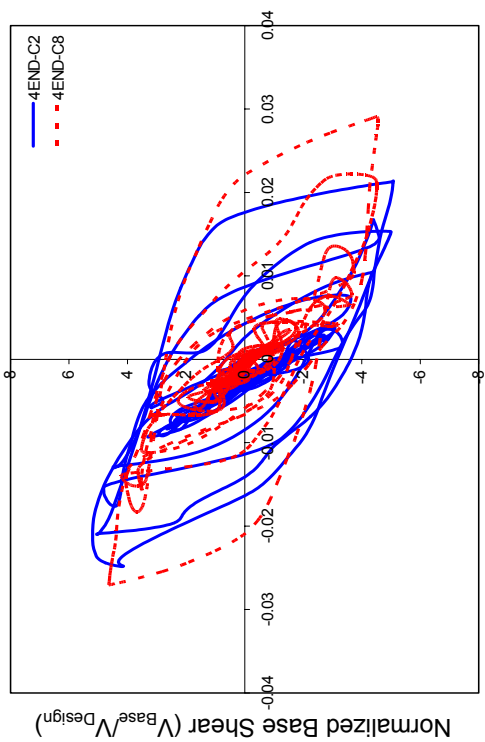
(d) Displacement at the Roof under LA26 Ground Motion (6TTSU-C2 vs. 6TTSU-C8)

Figure 8.26 Displacement at the roof level under ground motions s (6TTSU)



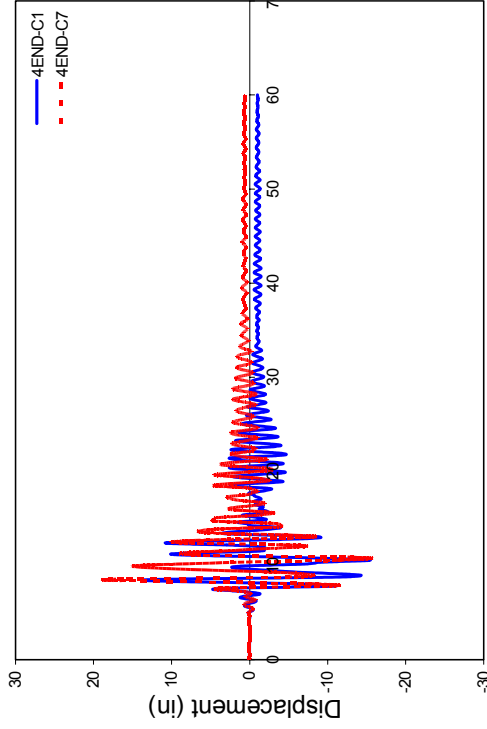
Inter Story Drift Ratio

(a) Displacement at the Roof under LA21 Ground Motion (4END-C1 vs. 4END-C7)



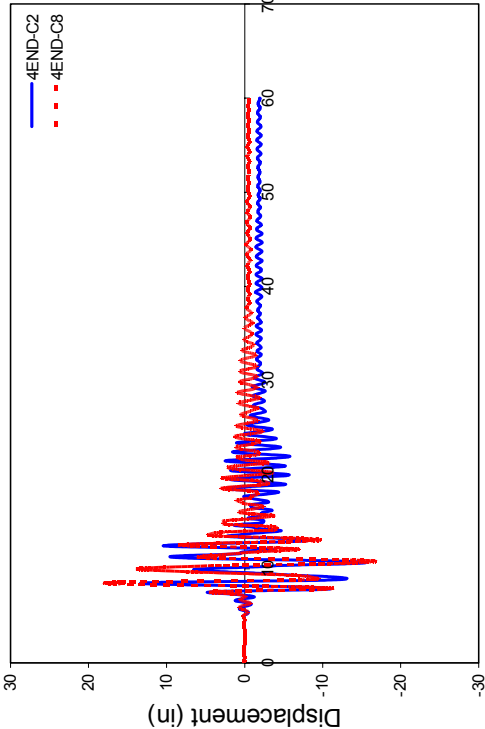
Inter Story Drift Ratio

(b) Displacement at the Roof under LA21 Ground Motion (4END-C2 vs. 4END-C8)



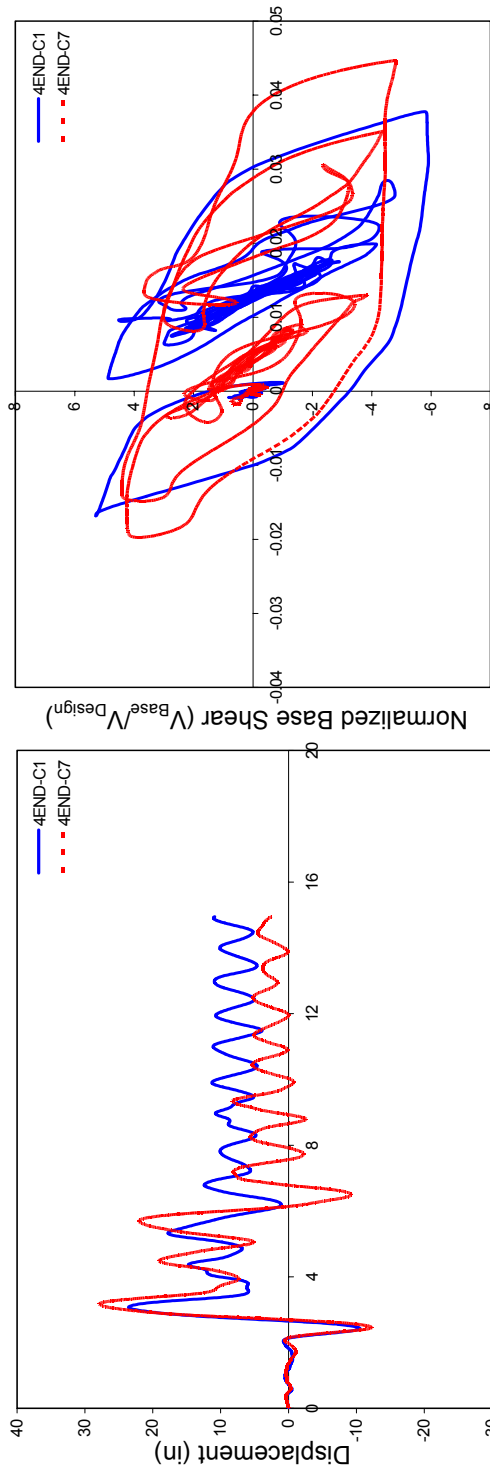
Time (sec)

(a)

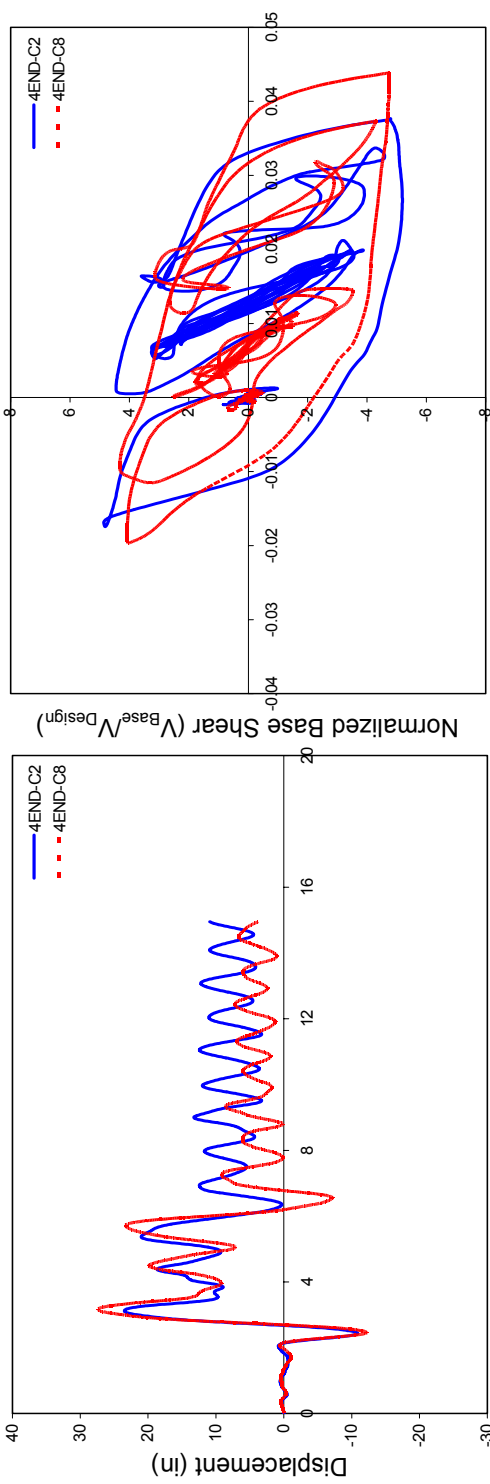


Time (sec)

(b)



(c) Displacement at the Roof under LA26 Ground Motion (4END-C1 vs. 4END-C7)



(d) Displacement at the Roof under LA26 Ground Motion (4END-C2 vs. 4END-C8)

Figure 8.27 Displacement at the Roof under Ground Motions (4END)

8.3.2 Peak Responses

In order to examine the dynamic performance and evaluation effectively, the peak responses were investigated. The peak responses acting on the composite moment frame models are listed in Tables 8.3 to 8.16. These tables show the results of applying all 20 ground motions to selected frames. In general, maximum displacement, velocity, and pseudo-acceleration occur at the roof level. The occurrence time for each peak value was slightly different for the different frames and lagged behind the peak ground acceleration (PGA). The maximum base shear force obtained by the nonlinear dynamic test is approximately 5 to 10 percent larger than the ultimate base shear force obtained from the nonlinear pushover test. This numerical discrepancy results from the use of lumped masses. The 6 story frames have a larger maximum base shear force than the 4 story building due to the larger mass effect (i.e. Table 8.3 vs. Table 8.11). The largest maximum pseudo-acceleration occurs for the record with the strongest PGA (SE27). The bold letters in the tables indicate the largest value.

The graphs of the scatter data for peak inter story drift ratios (ISDR) shown in the tables (i.e. Table 8.4) are provided in Figures 8.28 to 8.34. These graphs show the average and 84 percentile ISDR together with individual peak data points. The values of the 84 percentile employed from here on to indicate the statistical values of the peak ISDR as defined in FEMA 355C. Similarly to the ISDR at the ultimate point obtained by the nonlinear pushover analysis, the peak ISDR obtained from the dynamic analysis show the largest values at the first story level. They are also decrease as one moves up the frame. This implies that the composite columns located in the lower story levels are susceptible to severe plastic deformations under these ground motions. In addition to the PGA, the lumped masses have an influence on the peak ISDR. The larger lumped masses can increase the values of the peak ISDR. For example, the average of the peak first story ISDR for the 6END-C7 approaches 0.043, while the same parameter at the 6TSU-C7 approaches 0.032 (See Figure 8.29 and Figure 8.30).

Table 8.3 Peak response of the 6END-C1 case under various EQ motions

EQ Motion	Max. PGA(g)	Max. Base Shear (kip)	Max. Displ.(in)	Max. Vel.(in/sec)	Max. Pseudo-Accel.(g)
LA21	1.283	1076	19.68	112.53	2.21
LA22	0.921	1017	17.53	98.68	1.83
LA23	0.418	982	11.67	62.42	1.06
LA24	0.473	1099	24.54	84.24	1.42
LA25	0.869	1043	18.36	102.41	1.79
LA26	0.944	1094	27.89	120.18	1.57
LA27	0.927	1067	27.51	85.35	1.41
LA28	1.330	1120	24.12	96.18	1.92
LA29	0.809	1034	12.81	60.77	1.76
LA30	0.992	1084	19.75	60.92	2.28
SE21	0.755	1100	24.06	68.05	1.39
SE22	0.485	939	9.15	56.21	0.95
SE23	0.605	1089	14.21	77.83	1.45
SE24	0.539	1090	22.12	72.05	0.88
SE25	0.895	1068	15.07	70.76	1.58
SE26	0.821	1012	10.20	69.40	1.45
SE27	1.755	1093	32.39	112.98	2.43
SE28	1.390	1074	13.72	106.32	2.12
SE29	1.636	1060	16.34	83.22	2.41
SE30	1.573	1063	15.48	95.81	2.38
Average	0.9709	1060.20	18.83	84.82	1.71
Standard Dev.	0.4006	44.54	6.40	19.77	0.48

Table 8.4 Peak inter-story drift ratio of the 6END-C1 case under various EQ motions

EQ Motion	Time	1	2	3	4	5	6
LA21	10.06	0.0665	0.0518	0.0392	0.0302	0.0243	0.0205
LA22	8.88	0.0202	0.0218	0.0228	0.0227	0.0211	0.0187
LA23	10.62	0.0229	0.0195	0.0170	0.0154	0.0139	0.0124
LA24	10.14	0.0843	0.0604	0.0447	0.0360	0.0303	0.0261
LA25	3.15	0.0329	0.0321	0.0288	0.0251	0.0217	0.0185
LA26	3.23	0.0714	0.0625	0.0509	0.0417	0.0350	0.0298
LA27	7.22	0.0752	0.0613	0.0493	0.0407	0.0341	0.0288
LA28	4.92	0.0754	0.0581	0.0447	0.0358	0.0299	0.0257
LA29	12.28	0.0292	0.0237	0.0196	0.0169	0.0147	0.0129
LA30	11.72	0.0627	0.0458	0.0346	0.0284	0.0243	0.0211
SE21	3.34	0.0753	0.0603	0.0458	0.0365	0.0302	0.0256
SE22	7.52	0.0165	0.0148	0.0132	0.0120	0.0109	0.0098
SE23	3.72	0.0403	0.0310	0.0250	0.0206	0.0173	0.0149
SE24	3.71	0.0732	0.0547	0.0413	0.0331	0.0276	0.0236
SE25	19.94	0.0344	0.0275	0.0228	0.0201	0.0180	0.0159
SE26	9.4	0.0183	0.0164	0.0147	0.0133	0.0118	0.0103
SE27	8.82	0.0662	0.0607	0.0537	0.0466	0.0403	0.0345
SE28	10.76	0.0281	0.0260	0.0228	0.0199	0.0171	0.0147
SE29	31.65	0.0335	0.0299	0.0255	0.0218	0.0188	0.0162
SE30	30.05	0.0482	0.0368	0.0283	0.0229	0.0191	0.0161
Average		0.0487	0.0398	0.0322	0.0270	0.0230	0.0198
Standard Dev.		0.0233	0.0174	0.0130	0.0101	0.0083	0.0069

Table 8.5 Peak response of the 6END-C2 case under various EQ motions

EQ Motion	Max. PGA(g)	Max. Base Shear (kip)	Max. Displ.(in)	Max. Vel(in/sec)	Max. Pseudo-Accel.(g)
LA21	1.283	936	19.52	105.76	2.07
LA22	0.921	922	18.03	94.29	1.79
LA23	0.418	903	11.59	56.12	0.99
LA24	0.473	981	24.57	79.82	1.28
LA25	0.869	956	15.94	93.93	1.75
LA26	0.944	937	26.79	117.82	1.52
LA27	0.927	938	29.36	82.59	1.23
LA28	1.330	978	26.09	98.62	1.88
LA29	0.809	928	11.72	55.90	1.49
LA30	0.992	972	18.70	59.61	2.21
SE21	0.755	973	24.45	69.83	1.12
SE22	0.485	835	9.82	55.34	0.90
SE23	0.605	962	14.42	75.14	1.42
SE24	0.539	940	23.35	71.43	0.85
SE25	0.895	961	15.25	64.90	1.79
SE26	0.821	912	9.83	65.95	1.55
SE27	1.755	973	31.39	120.43	2.48
SE28	1.390	952	14.03	99.75	2.38
SE29	1.636	935	16.38	76.47	2.42
SE30	1.573	945	15.18	88.75	2.40
Average	0.9709	941.95	18.82	81.62	1.68
Standard Dev.	0.4006	33.48	6.56	20.14	0.53

Table 8.6 Peak inter-story drift ratio of the 6END-C2 case under various EQ motions

EQ Motion	Time	1	2	3	4	5	6
LA21	10.12	0.0747	0.0529	0.0394	0.0300	0.0240	0.0204
LA22	8.92	0.0217	0.0233	0.0243	0.0236	0.0216	0.0189
LA23	10.66	0.0259	0.0200	0.0171	0.0154	0.0139	0.0124
LA24	10.12	0.1036	0.0640	0.0459	0.0362	0.0300	0.0255
LA25	3.1	0.0309	0.0291	0.0256	0.0222	0.0194	0.0168
LA26	3.26	0.0879	0.0648	0.0500	0.0402	0.0335	0.0283
LA27	9.06	0.1035	0.0701	0.0534	0.0436	0.0367	0.0311
LA28	7.68	0.0983	0.0658	0.0483	0.0386	0.0322	0.0274
LA29	12.36	0.0340	0.0241	0.0192	0.0164	0.0144	0.0125
LA30	11.72	0.0667	0.0464	0.0346	0.0279	0.0234	0.0200
SE21	3.44	0.0873	0.0604	0.0449	0.0362	0.0303	0.0259
SE22	7.58	0.0216	0.0172	0.0146	0.0130	0.0116	0.0103
SE23	4.03	0.0463	0.0313	0.0244	0.0205	0.0177	0.0154
SE24	3.82	0.0951	0.0626	0.0457	0.0360	0.0294	0.0248
SE25	20.2	0.0430	0.0319	0.0253	0.0212	0.0182	0.0159
SE26	9.4	0.0210	0.0170	0.0147	0.0131	0.0116	0.0102
SE27	8.86	0.0800	0.0643	0.0539	0.0459	0.0394	0.0335
SE28	10.72	0.0295	0.0252	0.0218	0.0194	0.0170	0.0147
SE29	33.32	0.0386	0.0321	0.0266	0.0228	0.0199	0.0175
SE30	30.05	0.0482	0.0368	0.0283	0.0229	0.0191	0.0161
Average		0.0579	0.0420	0.0329	0.0273	0.0232	0.0199
Standard Dev.		0.0306	0.0191	0.0135	0.0104	0.0084	0.0070

Table 8.7 Peak response of the 6END-C7 case under various EQ motions

EQ Motion	Max. PGA(g)	Max. Base Shear (kip)	Max. Displ.(in)	Max. Vel(in/sec)	Max. Pseudo-Accel.(g)
LA21	1.283	828	24.89	102.96	1.94
LA22	0.921	831	21.12	88.54	1.90
LA23	0.418	837	11.58	66.12	1.09
LA24	0.473	889	30.07	90.93	1.16
LA25	0.869	842	18.83	92.84	1.54
LA26	0.944	833	27.92	120.81	1.42
LA27	0.927	880	37.27	95.97	1.31
LA28	1.330	856	26.59	89.72	1.97
LA29	0.809	832	17.22	52.29	1.56
LA30	0.992	849	22.08	62.88	1.64
SE21	0.755	866	30.62	85.82	1.19
SE22	0.485	833	12.89	52.89	0.98
SE23	0.605	886	19.84	80.62	1.18
SE24	0.539	876	31.08	84.97	0.89
SE25	0.895	833	15.26	66.81	1.31
SE26	0.821	867	18.45	57.66	1.07
SE27	1.755	850	24.32	108.42	2.24
SE28	1.390	848	14.52	65.29	2.09
SE29	1.636	830	18.94	81.87	1.92
SE30	1.573	830	17.84	81.67	1.77
Average	0.9709	849.80	22.07	81.45	1.51
Standard Dev.	0.4006	20.58	6.86	18.65	0.41

Table 8.8 Peak inter-story drift ratio of the 6END-C7 case under various EQ motions

EQ Motion	Time	1	2	3	4	5	6
LA21	10.22	0.0493	0.0544	0.0483	0.0392	0.0316	0.0266
LA22	10.86	0.0153	0.0211	0.0244	0.0272	0.0259	0.0225
LA23	10.18	0.0195	0.0178	0.0160	0.0147	0.0135	0.0120
LA24	11.52	0.0982	0.0681	0.0535	0.0445	0.0372	0.0316
LA25	2.53	0.0468	0.0377	0.0307	0.0264	0.0231	0.0202
LA26	3.19	0.0221	0.0337	0.0394	0.0391	0.0346	0.0296
LA27	7.54	0.0749	0.0744	0.0650	0.0553	0.0469	0.0397
LA28	4.98	0.0572	0.0612	0.0497	0.0406	0.0338	0.0284
LA29	12.44	0.0341	0.0304	0.0257	0.0229	0.0208	0.0184
LA30	11.52	0.0509	0.0421	0.0347	0.0299	0.0267	0.0234
SE21	3.36	0.0745	0.0706	0.0555	0.0454	0.0383	0.0327
SE22	4.12	0.0182	0.0160	0.0148	0.0142	0.0137	0.0127
SE23	4.11	0.0616	0.0456	0.0352	0.0292	0.0246	0.0210
SE24	3.86	0.0748	0.0726	0.0580	0.0472	0.0390	0.0329
SE25	5.26	0.0362	0.0302	0.0247	0.0210	0.0185	0.0162
SE26	9.72	0.0535	0.0381	0.0302	0.0258	0.0226	0.0197
SE27	8.94	0.0179	0.0247	0.0308	0.0327	0.0299	0.0259
SE28	29.92	0.0189	0.0202	0.0194	0.0181	0.0167	0.0148
SE29	31.7	0.0231	0.0258	0.0275	0.0258	0.0228	0.0198
SE30	30.8	0.0145	0.0179	0.0210	0.0226	0.0210	0.0184
Average		0.0431	0.0401	0.0352	0.0311	0.0271	0.0233
Standard Dev.		0.0249	0.0201	0.0149	0.0115	0.0091	0.0074

Table 8.9 Peak response of the 6TSU-C1 case under various EQ motions

EQ Motion	Max. PGA(g)	Max. Base Shear (kip)	Max. Displ.(in)	Max. Vel(in/sec)	Max. Pseudo-Accel.(g)
LA21	1.283	801	18.64	116.98	2.05
LA22	0.921	752	15.42	94.98	1.86
LA23	0.418	678	8.51	53.13	1.08
LA24	0.473	814	20.26	72.96	1.28
LA25	0.869	771	20.18	106.05	1.68
LA26	0.944	806	26.6	108.61	1.68
LA27	0.927	821	25.34	69.34	1.26
LA28	1.330	819	19.56	79.15	1.54
LA29	0.809	746	10.87	59.93	1.47
LA30	0.992	828	17.32	61.62	2.16
SE21	0.7551332	805	21.99	82.08	1.95
SE22	0.4852179	557	8.21	56.91	1.28
SE23	0.6048157	784	13.42	72.39	1.22
SE24	0.5390563	824	20.31	68.14	1.25
SE25	0.8948236	751	10.19	77.37	1.27
SE26	0.8209028	714	10.37	59.85	1.52
SE27	1.7549437	752	19.88	82.36	2.44
SE28	1.3904852	743	13.67	76.28	2.05
SE29	1.6358349	737	13.88	98.71	2.24
SE30	1.5726635	810	15.56	79.6	2.06
Average	0.9709	765.65	16.51	78.82	1.67
Standard Dev.	0.4006	64.27	5.36	18.07	0.41

Table 8.10 Peak inter-story drift ratio of the 6TSU-C1 case under various EQ motions

EQ Motion	Time	1	2	3	4	5	6
LA21	10.76	0.0314	0.0309	0.0284	0.0255	0.0226	0.0198
LA22	8.88	0.0182	0.0210	0.0219	0.0210	0.0188	0.0165
LA23	11.49	0.0157	0.0152	0.0134	0.0117	0.0103	0.0091
LA24	8.92	0.0464	0.0437	0.0361	0.0297	0.0250	0.0214
LA25	3.09	0.0354	0.0352	0.0327	0.0288	0.0248	0.0214
LA26	3.18	0.0531	0.0523	0.0464	0.0394	0.0333	0.0284
LA27	7.22	0.0520	0.0496	0.0436	0.0371	0.0314	0.0267
LA28	4.82	0.0384	0.0367	0.0317	0.0275	0.0236	0.0202
LA29	11.34	0.0209	0.0196	0.0171	0.0149	0.0131	0.0116
LA30	11.48	0.0371	0.0346	0.0288	0.0245	0.0211	0.0183
SE21	3.26	0.0472	0.0458	0.0392	0.0322	0.0269	0.0229
SE22	3.52	0.0070	0.0088	0.0097	0.0098	0.0095	0.0087
SE23	3.63	0.0262	0.0247	0.0219	0.0188	0.0162	0.0141
SE24	3.57	0.0463	0.0433	0.0361	0.0300	0.0253	0.0215
SE25	4.88	0.0181	0.0175	0.0157	0.0138	0.0121	0.0106
SE26	11.18	0.0216	0.0203	0.0172	0.0144	0.0122	0.0105
SE27	8.72	0.0323	0.0332	0.0315	0.0284	0.0247	0.0212
SE28	10.66	0.0298	0.0283	0.0243	0.0205	0.0173	0.0146
SE29	35.13	0.0165	0.0183	0.0188	0.0179	0.0162	0.0143
SE30	29.93	0.0333	0.0310	0.0267	0.0226	0.0193	0.0166
Average		0.0313	0.0305	0.0271	0.0234	0.0202	0.0174
Standard Dev.		0.0133	0.0123	0.0102	0.0083	0.0068	0.0057

Table 8.11 Peak response of the 4END-C1 case under various EQ motions

EQ Motion	Max. PGA(g)	Max. Base Shear (kip)	Max. Displ.(in)	Max. Vel(in/sec)	Max. Pseudo-Accel.(g)
LA21	1.283	1157	15.48	119.07	2.02
LA22	0.921	1138	15.44	96.07	1.58
LA23	0.418	1013	8.75	61.58	1.27
LA24	0.473	1157	10.46	63.57	1.24
LA25	0.869	1181	18.76	86.32	1.68
LA26	0.944	1171	23.54	94.02	1.27
LA27	0.927	1201	14.94	73.57	1.76
LA28	1.330	1160	14.17	79.77	2.17
LA29	0.809	1019	8.08	60.08	1.35
LA30	0.992	1122	10.76	60.77	2.05
SE21	0.7551332	1185	13.74	89.51	1.56
SE22	0.4852179	1006	8.73	61.88	1.51
SE23	0.6048157	1157	11.64	60.83	1.07
SE24	0.5390563	1175	11.46	58.69	0.97
SE25	0.8948236	1026	8.2	63.38	1.98
SE26	0.8209028	1021	6.67	63.49	1.71
SE27	1.7549437	1189	20.38	79.37	2.33
SE28	1.3904852	1138	10.56	69.12	2.12
SE29	1.6358349	1106	16.08	81.57	2.17
SE30	1.5726635	1130	11.39	74.28	2.05
Average	0.9709	1122.60	12.96	74.85	1.69
Standard Dev.	0.4006	66.77	4.44	15.98	0.41

Table 8.12 Peak inter-story drift ratio of the 4END-C1 case under various EQ motions

EQ Motion	Time	1	2	3	4
LA21	10.54	0.0496	0.0388	0.0302	0.0245
LA22	8.84	0.0527	0.0415	0.0312	0.0246
LA23	10.61	0.0212	0.0191	0.0164	0.0139
LA24	9.89	0.0409	0.0279	0.0210	0.0168
LA25	2.98	0.0723	0.0520	0.0383	0.0300
LA26	3.07	0.0971	0.0668	0.0482	0.0377
LA27	7.12	0.0606	0.0413	0.0303	0.0239
LA28	3.82	0.0546	0.0393	0.0290	0.0227
LA29	8.84	0.0239	0.0193	0.0157	0.0129
LA30	11.42	0.0357	0.0265	0.0211	0.0172
SE21	3.24	0.0548	0.0376	0.0279	0.0220
SE22	3.46	0.0222	0.0193	0.0163	0.0138
SE23	3.43	0.0455	0.0318	0.0236	0.0186
SE24	3.38	0.0450	0.0311	0.0233	0.0184
SE25	7.5	0.0218	0.0181	0.0153	0.0130
SE26	9.04	0.0190	0.0154	0.0128	0.0107
SE27	8.72	0.0704	0.0554	0.0416	0.0327
SE28	10.54	0.0388	0.0272	0.0207	0.0166
SE29	35.08	0.0471	0.0390	0.0317	0.0258
SE30	30.45	0.0382	0.0280	0.0221	0.0182
Average		0.0456	0.0338	0.0258	0.0207
Standard Dev.		0.0199	0.0136	0.0094	0.0071

Table 8.13 Peak response of the 4END-C2 case under various EQ motions

EQ Motion	Max. PGA(g)	Max. Base Shear (kip)	Max. Displ.(in)	Max. Vel(in/sec)	Max. Pseudo-Accel.(g)
LA21	1.283	1025	15.51	112.3	1.87
LA22	0.921	1004	15.64	90.04	1.47
LA23	0.418	876	8.39	56.43	1.17
LA24	0.473	965	8.55	61.42	1.16
LA25	0.869	1018	18.56	84.82	1.46
LA26	0.944	1017	23.46	94.35	1.31
LA27	0.927	1025	15.22	68.48	1.67
LA28	1.330	1018	15.72	65.96	1.7
LA29	0.809	904	7.91	56.37	1.29
LA30	0.992	994	9.92	62.89	1.76
SE21	0.7551332	1031	14.97	81.05	1.49
SE22	0.4852179	882	8.26	53.68	1.29
SE23	0.6048157	1017	11.77	60.54	0.97
SE24	0.5390563	1028	13.15	58.58	0.93
SE25	0.8948236	925	8.27	56.35	1.93
SE26	0.8209028	897	7.24	60.92	1.45
SE27	1.7549437	1026	19.91	76.84	2.26
SE28	1.3904852	1012	10.89	62.37	2.08
SE29	1.6358349	997	15.4	74.22	2.15
SE30	1.5726635	1024	13.2	65.77	2.1
Average	0.9709	984.25	13.10	70.17	1.58
Standard Dev.	0.4006	54.62	4.49	15.45	0.40

Table 8.14 Peak inter-story drift ratio of the 4END-C2 case under various EQ motions

EQ Motion	Time	1	2	3	4
LA21	10.64	0.0569	0.0405	0.0310	0.0249
LA22	8.84	0.0584	0.0437	0.0321	0.0250
LA23	10.62	0.0218	0.0186	0.0157	0.0133
LA24	8.84	0.0344	0.0226	0.0172	0.0137
LA25	3.01	0.0803	0.0533	0.0382	0.0297
LA26	3.14	0.1112	0.0697	0.0490	0.0376
LA27	7.14	0.0693	0.0439	0.0314	0.0244
LA28	3.84	0.0641	0.0417	0.0301	0.0234
LA29	8.86	0.0253	0.0191	0.0154	0.0126
LA30	11.44	0.0353	0.0251	0.0196	0.0159
SE21	3.26	0.0704	0.0425	0.0307	0.0240
SE22	3.48	0.0223	0.0185	0.0155	0.0131
SE23	3.46	0.0507	0.0332	0.0241	0.0189
SE24	3.46	0.0543	0.0354	0.0265	0.0210
SE25	4.76	0.0281	0.0203	0.0158	0.0128
SE26	9.08	0.0246	0.0178	0.0142	0.0116
SE27	8.72	0.0774	0.0560	0.0410	0.0319
SE28	10.56	0.0470	0.0303	0.0222	0.0174
SE29	35.1	0.0505	0.0397	0.0307	0.0245
SE30	30.55	0.0521	0.0346	0.0263	0.0212
Average		0.0517	0.0353	0.0263	0.0208
Standard Dev.		0.0232	0.0143	0.0096	0.0072

Table 8.15 Peak response of the 4END-C7 case under various EQ motions

EQ Motion	Max. PGA(g)	Max. Base Shear (kip)	Max. Displ.(in)	Max. Vel(in/sec)	Max. Pseudo-Accel.(g)
LA21	1.283	932	18.97	119.08	1.86
LA22	0.921	893	14.89	95.39	1.59
LA23	0.418	852	8.05	54.27	0.97
LA24	0.473	820	17.32	71.18	1.14
LA25	0.869	887	20.04	101.3	1.3
LA26	0.944	963	27.86	108.69	1.55
LA27	0.927	961	22.05	64.95	1.23
LA28	1.330	915	16.78	74.13	1.69
LA29	0.809	862	9.62	60.42	1.3
LA30	0.992	912	11.96	55.28	1.41
SE21	0.7551332	958	18.57	80.42	1.85
SE22	0.4852179	724	8.73	59.16	1.31
SE23	0.6048157	883	14.38	72.83	1.14
SE24	0.5390563	951	17.95	65.19	0.95
SE25	0.8948236	886	10.61	72.88	1.42
SE26	0.8209028	892	11.11	60.62	1.4
SE27	1.7549437	889	16.64	81.44	2.38
SE28	1.3904852	918	14.03	72.48	1.88
SE29	1.6358349	879	16.01	95.86	2.19
SE30	1.5726635	916	13.64	72.13	1.92
Average	0.9709	894.65	15.46	76.89	1.52
Standard Dev.	0.4006	55.02	4.86	18.28	0.39

Table 8.16 Peak inter-story drift ratio of the 4END-C7 case under various EQ motions

EQ Motion	Time	1	2	3	4
LA21	8.46	0.0452	0.0446	0.0370	0.0301
LA22	8.9	0.0217	0.0334	0.0287	0.0234
LA23	11.88	0.0180	0.0172	0.0151	0.0129
LA24	8.93	0.0692	0.0468	0.0349	0.0277
LA25	3.04	0.0530	0.0539	0.0422	0.0331
LA26	3.17	0.0810	0.0770	0.0571	0.0446
LA27	7.14	0.0699	0.0613	0.0457	0.0353
LA28	4.91	0.0555	0.0445	0.0337	0.0267
LA29	9.32	0.0148	0.0182	0.0174	0.0154
LA30	11.42	0.0421	0.0300	0.0233	0.0188
SE21	3.28	0.0683	0.0515	0.0380	0.0298
SE22	3.52	0.0104	0.0152	0.0156	0.0144
SE23	3.48	0.0338	0.0346	0.0282	0.0230
SE24	3.58	0.0627	0.0484	0.0365	0.0288
SE25	15.94	0.0142	0.0184	0.0191	0.0170
SE26	9.16	0.0190	0.0222	0.0206	0.0178
SE27	8.72	0.0384	0.0380	0.0325	0.0267
SE28	10.61	0.0468	0.0368	0.0285	0.0225
SE29	35.13	0.0311	0.0337	0.0302	0.0256
SE30	29.9	0.0456	0.0363	0.0276	0.0217
Average		0.0420	0.0381	0.0306	0.0248
Standard Dev.		0.0214	0.0160	0.0107	0.0078

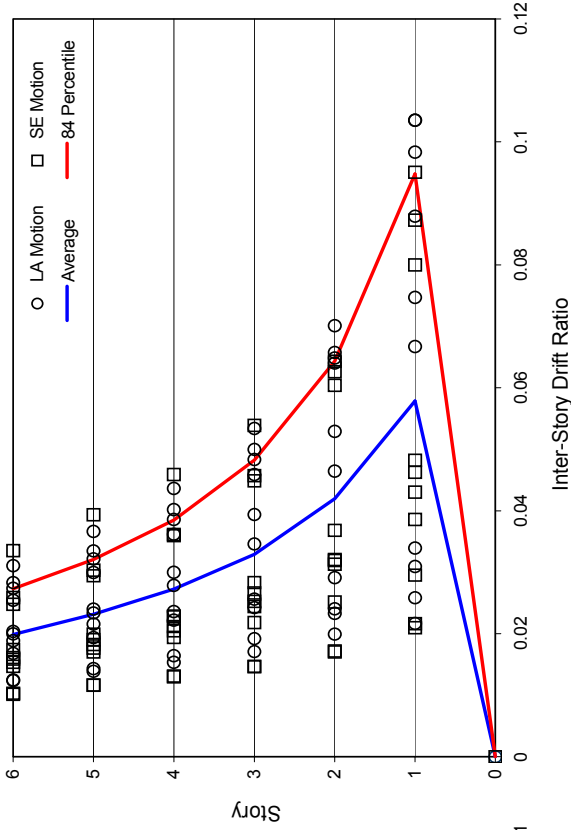


Figure 8.29 The peak ISDR for the 6END-C2 case

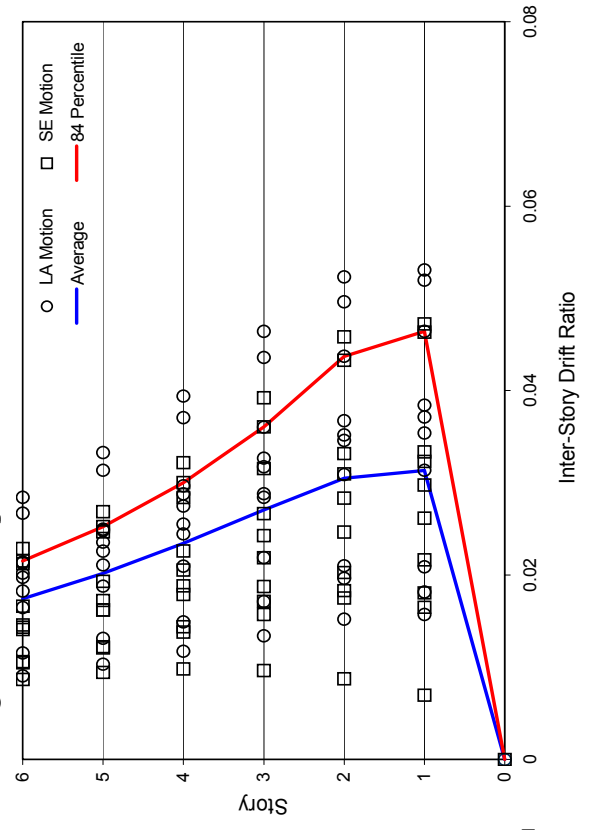


Figure 8.30 Peak ISDR for the 6END-C1 case

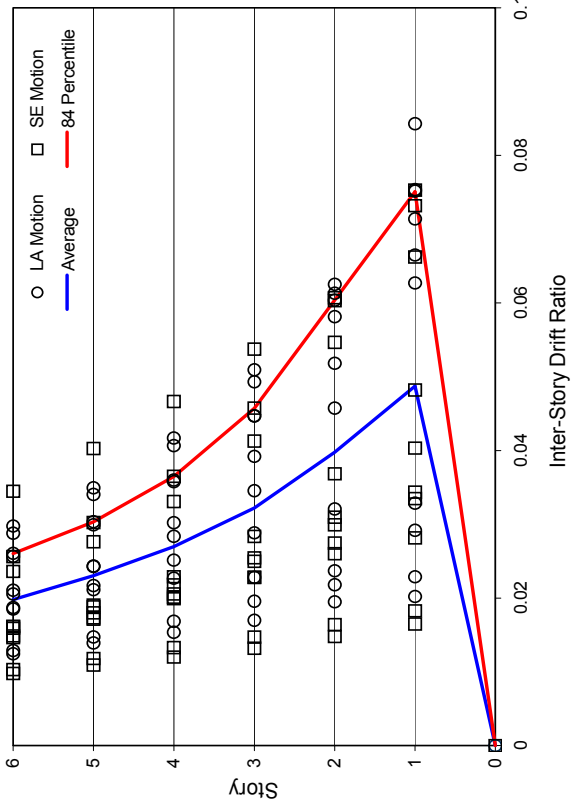


Figure 8.28 Peak ISDR for the 6END-C1 case

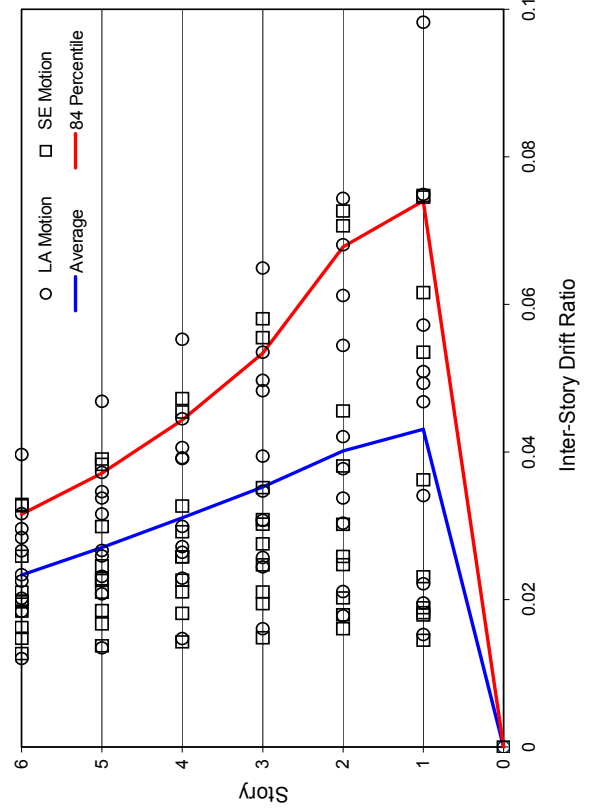


Figure 8.31 Peak ISDR for the 6TSU-C1 case

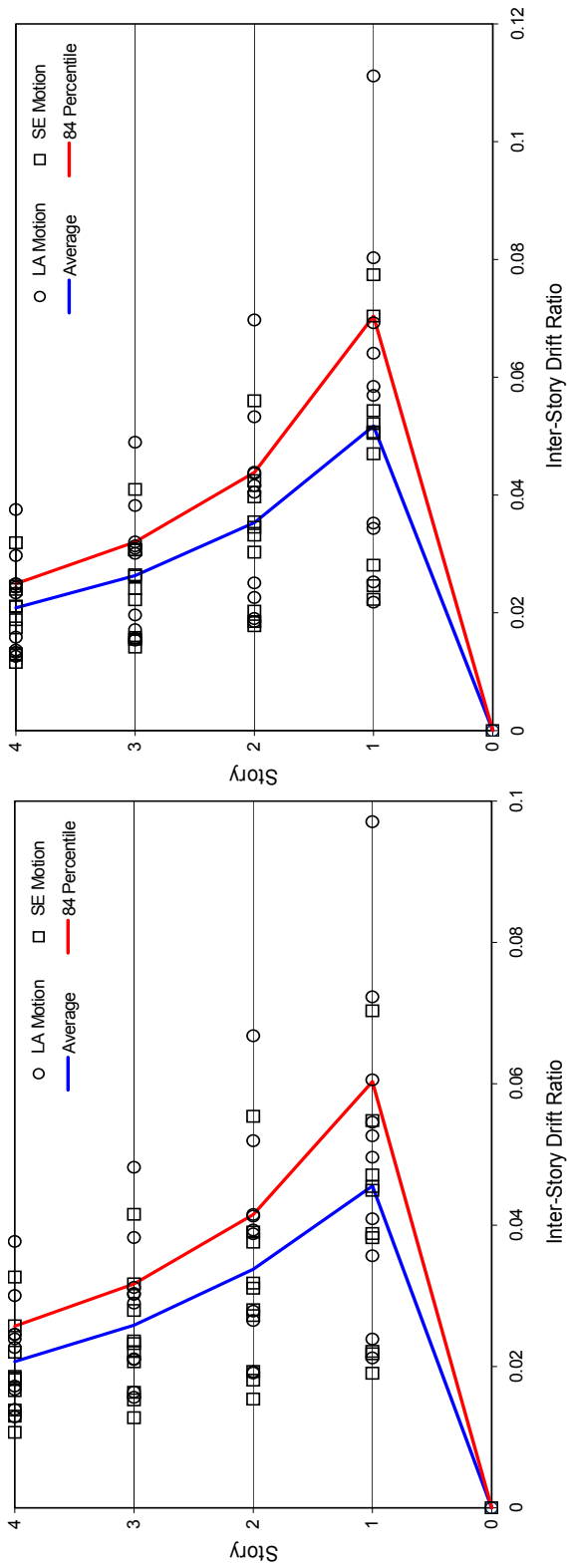


Figure 8.32 Peak ISDR for the 4END-C1 case

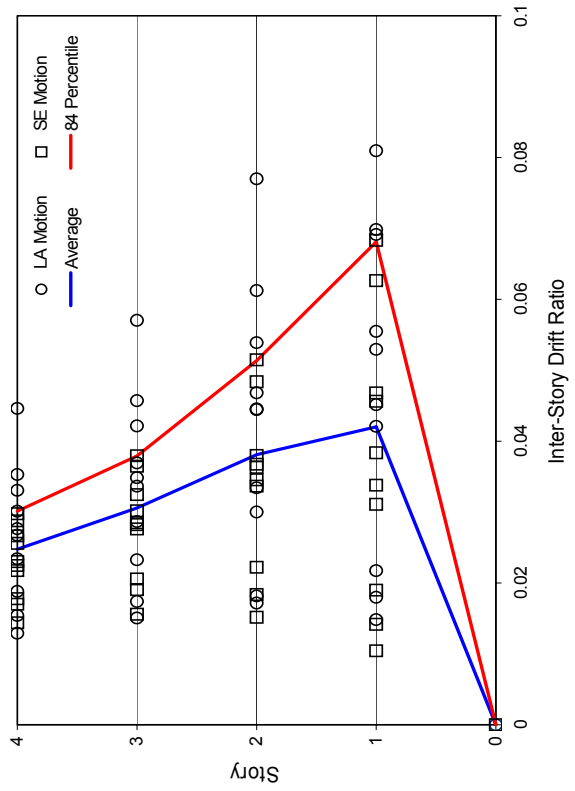


Figure 8.33 Peak ISDR for the 4END-C2 case

Figure 8.34 Peak ISDR for the 4END-C7 case

To obtain more insight into the behavior of these frames, all composite moment frame models were subjected to two ground motions, LA21 (relatively strong PGA = 1.283 g) and LA23 (the relatively weak PGA = 0.418 g). The peak responses and the peak ISDR under the selected ground motions are shown in Table 8.17 to Table 8.20 and Figure 8.35 to Figure 8.38, respectively. The peak responses obtained between the PR connection frame and the welded FR connection frame are compared in these tables and figures. The maximum base shear forces for the end-plate connection frames are larger than those of the welded connection frames as listed in tables. This holds regardless of the PGA. The maximum pseudo-accelerations show the same trend. In the nonlinear pushover analyses, welded connection frames have the steep initial slope of the pushover curves and show the rapid strength degradation after the ultimate point.

As expected, within the elastic range of the pushover curves, the composite moment frames with welded connections show a faster initial slope for the same ISDR than those with PR connections. However, these frames also show faster strength degradation after reaching their stability point. Owing to these structural characteristics, composite moment frames with welded connections reach larger ISDR under relatively strong ground motion (LA21) and smaller ISDR under relatively weak ground motion (LA23) in comparison with the ISDR of the PR connection frames. It can be concluded that welded frames are relatively stiffer under the ground motion with weak PGA in comparison with PR connection frames and that the amount of PGA divided by the building mass (i.e. elastic behavior) for nonlinear analyses is equivalent to that of base shear force. However, welded connection frames are more susceptible to deformation and rapid strength degradation under ground motions with a large PGA. This indicates a susceptibility to complete collapse for this structural system under severe external forces.

Table 8.17 Peak response of the 6END case under the LA21 motion
with relatively strong PGA

Model	Max. PGA(g)	Max. Base Shear (kip)	Max. Displ.(in)	Max. Vel(in/sec)	Max. Pseudo-Accel.(g)
6END-C1	1.283	1076	19.68	112.53	2.21
6END-C7	1.283	828	24.89	102.96	1.94
6END-C2	1.283	936	19.52	105.76	2.07
6END-C8	1.283	849	23.78	102.31	1.97
6END-C3	1.283	1028	19.68	110.12	2.12
6END-C9	1.283	870	24.18	103.24	1.96

Table 8.18 Peak response of the 6END case under the LA23 motion
with relatively weak PGA

Model	Max. PGA(g)	Max. Base Shear (kip)	Max. Displ.(in)	Max. Vel(in/sec)	Max. Pseudo-Accel.(g)
6END-C1	0.418	982	11.67	62.42	1.06
6END-C7	0.418	837	11.58	66.12	1.09
6END-C2	0.418	903	11.59	56.12	0.99
6END-C8	0.418	792	11.68	63.66	1.05
6END-C3	0.418	960	11.74	59.28	1.06
6END-C9	0.418	830	11.71	66.1	1.08

Table 8.19 Peak response of the 4END case under the LA21 motion
with relatively strong PGA

Model	Max. PGA(g)	Max. Base Shear (kip)	Max. Displ.(in)	Max. Vel(in/sec)	Max. Pseudo-Accel.(g)
4END-C1	1.283	1157	15.48	119.07	2.02
4END-C7	1.283	932	18.97	119.08	1.86
4END-C2	1.283	1025	15.51	112.3	1.87
4END-C8	1.283	929	18.16	109.36	1.91
4END-C3	1.283	1114	15.45	117.08	2.07
4END-C9	1.283	928	18.87	110.5	1.88

Table 8.20 Peak response of the 4END case under the LA23 motion
with relatively weak PGA

Model	Max. PGA(g)	Max. Base Shear (kip)	Max. Displ.(in)	Max. Vel(in/sec)	Max. Pseudo-Accel.(g)
4END-C1	0.418	1013	8.75	61.58	1.27
4END-C7	0.418	852	8.05	54.27	0.97
4END-C2	0.418	876	8.39	56.43	1.17
4END-C8	0.418	818	8.16	51.22	0.99
4END-C3	0.418	970	8.62	59.55	1.25
4END-C9	0.418	845	7.98	53.28	0.99

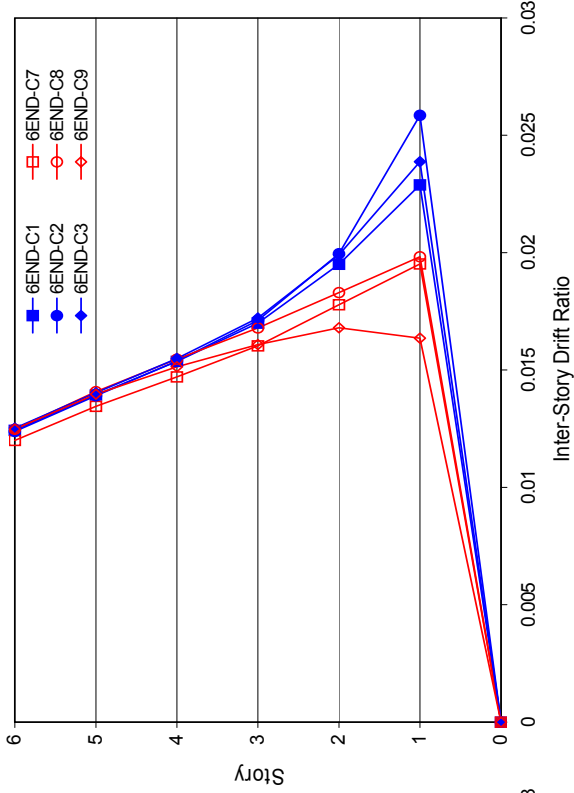


Figure 8.36 Peak ISDR under the LA23 motion

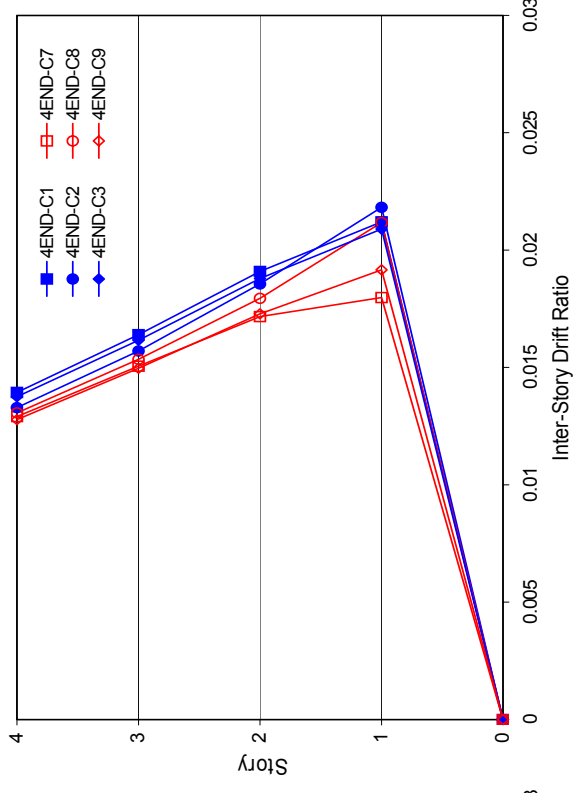


Figure 8.38 Peak ISDR under the LA23 motion

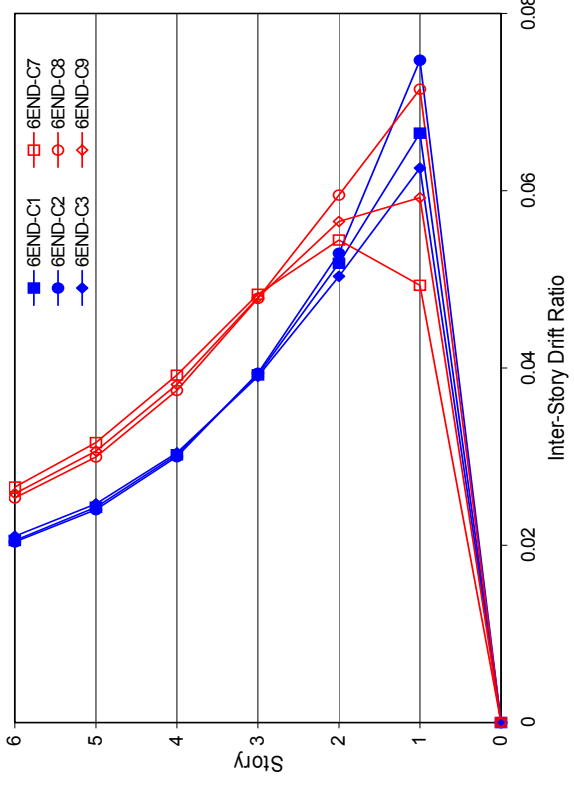


Figure 8.35 Peak ISDR under the LA21 motion

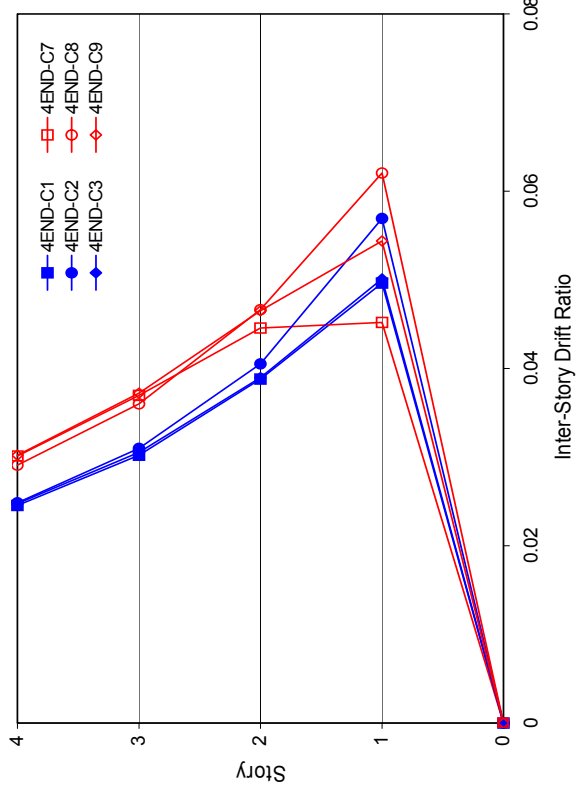


Figure 8.37 Peak ISDR under the LA21 motion

8.3.3 Failure Mechanism for Composite Frame Models

The damage to composite moment frames under large ground motions can be investigated by tracing the failure hinge sequence. Similar to the pushover analyses, the hinge formations were investigated in only CFT column sections. Hinge points for some selected frame models at the columns are shown in Figures 8.39 to 8.40. The most severe damage occurs immediately after the occurrence of the PGA. The hinge shown in the figures are computed at the time of the highest demand on the frame. The determination of the failure hinge level is also shown in Figure 8.20. Similarly to results of the pushover analyses at the ultimate point, the composite columns located on the lower story undergo the most severe damage and plastic deformation. A larger number of hinges were found in the dynamic analyses. The position of the hinge points is also symmetric to the center of the composite moment frame.

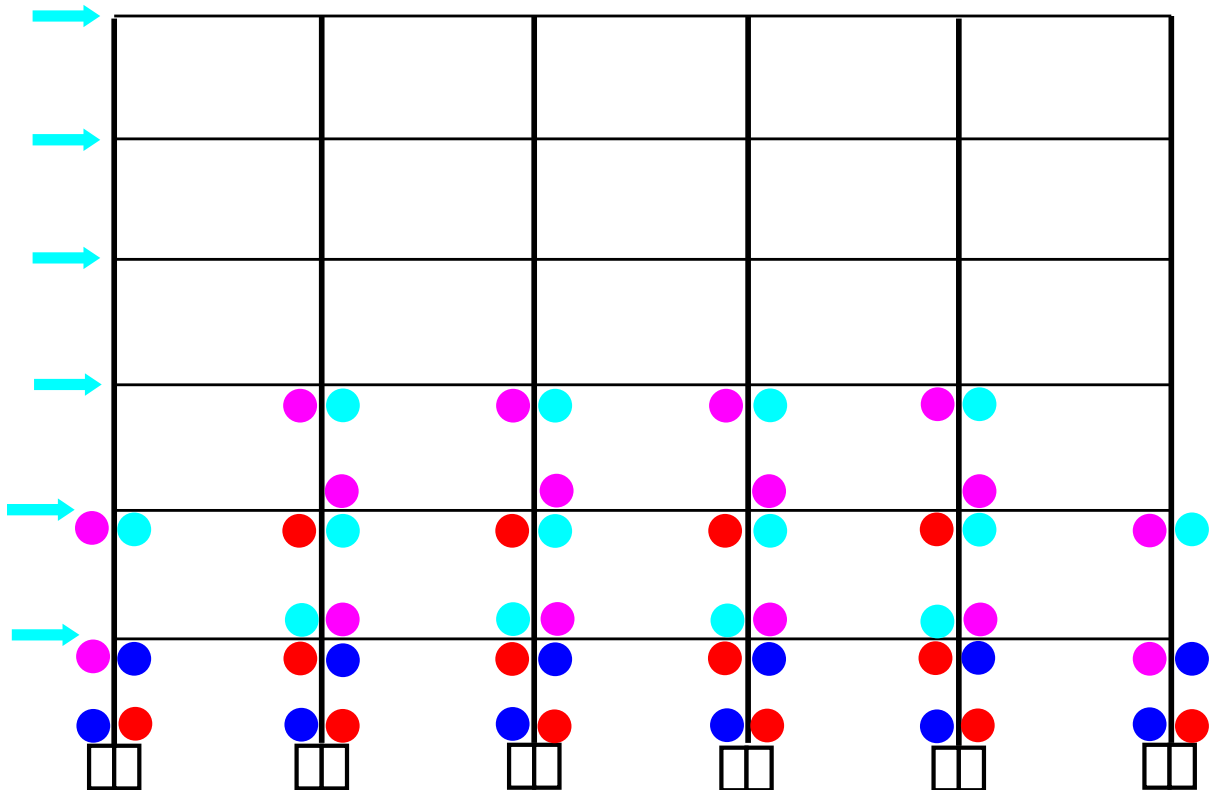


Figure 8.39 Hinges for 6END-C1 at RCFT columns under LA21 Motion (t=10.04sec)

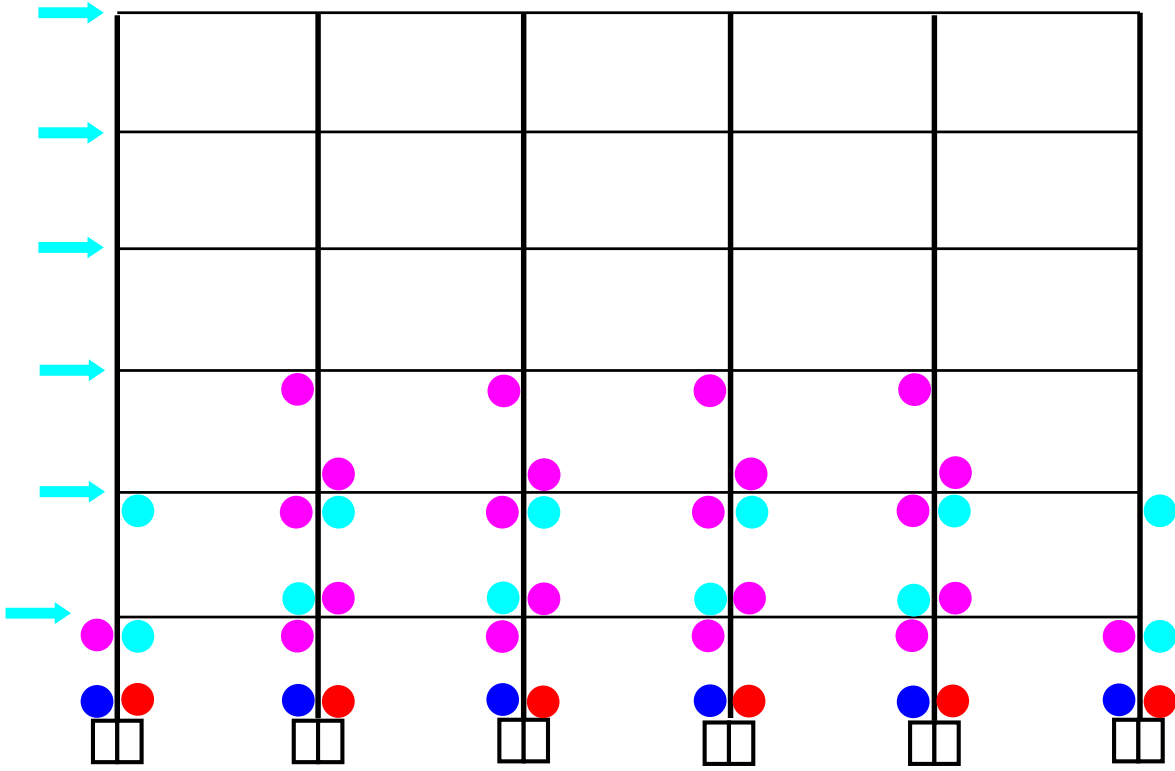


Figure 8.40 Hinges for 6END-C7 at RCFT columns under LA21 Motion (t=10.22sec)

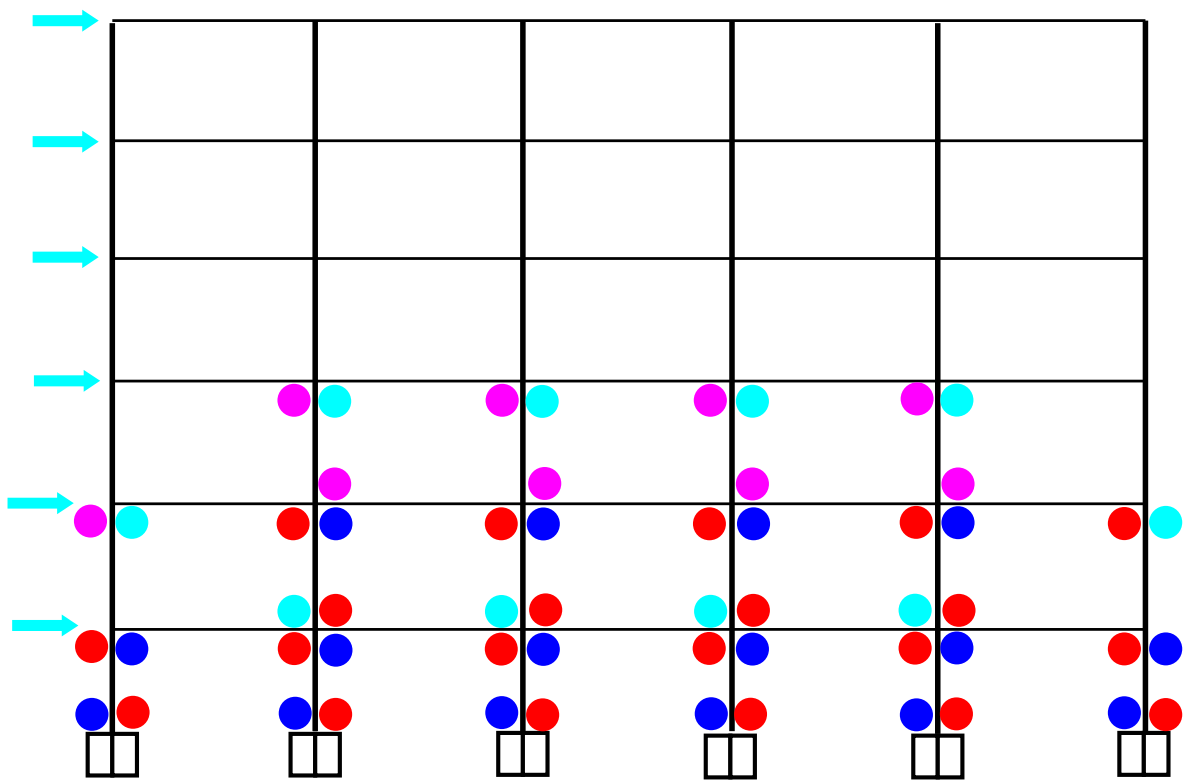


Figure 8.41 Hinges for 6END-C2 at CCFT columns under LA21 Motion (t=9.96sec)

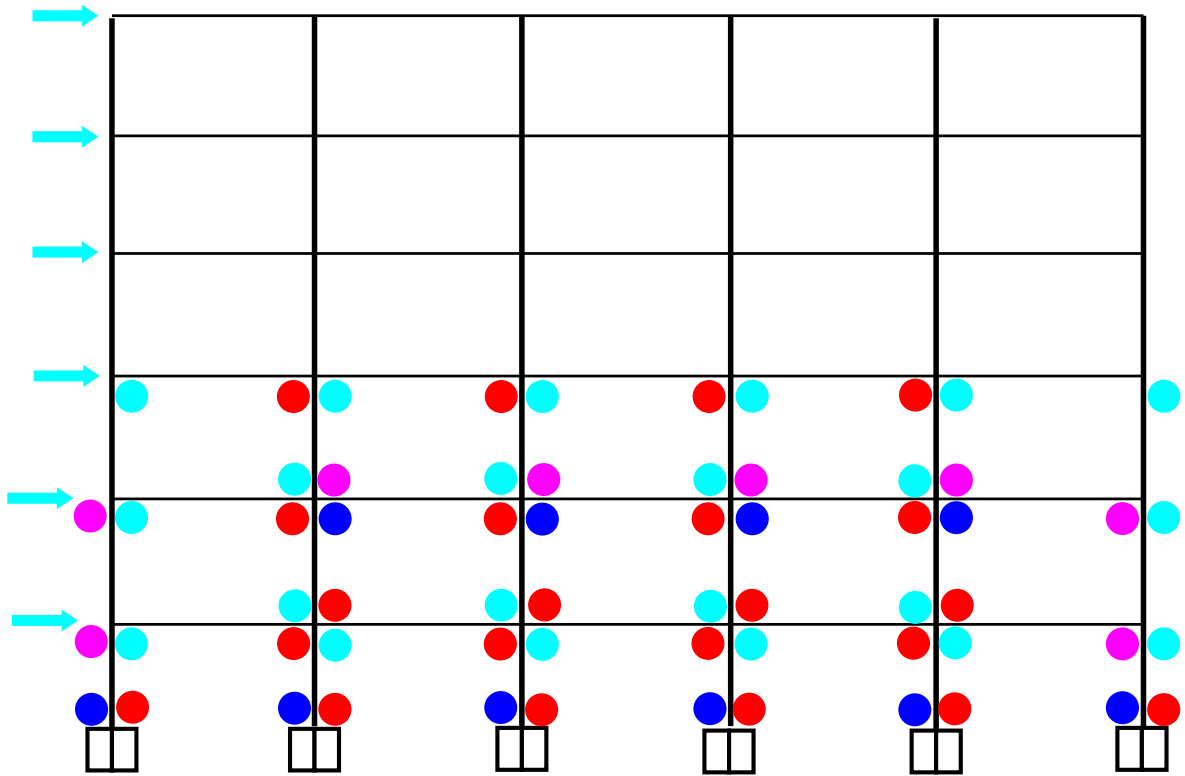


Figure 8.42 Hinges for 6END-C1 at RCFT columns under LA26 Motion ($t=3.10\text{sec}$)

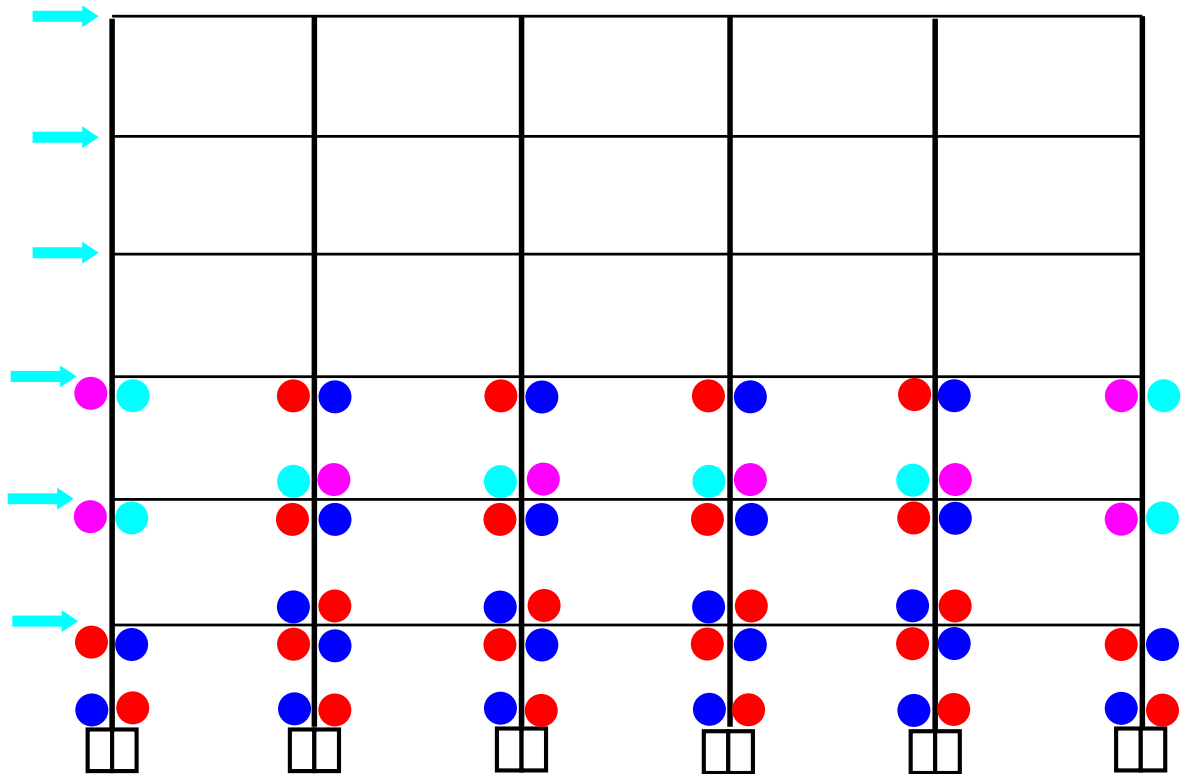


Figure 8.43 Hinges for 6END-C2 at CCFT columns under LA26 Motion ($t=3.10\text{sec}$)

8.4 Summary and Discussion

Two types of nonlinear analyses, (1) nonlinear pushover analyses and (2) nonlinear dynamic analyses, were performed by using 2D simplified frame models. This chapter mainly focused on analysis of the data collected from these analyses, the behavior of frame models, summaries of the peak responses, and investigations of the failure mechanism after analyses. These are preliminary steps to conduct the performance and damage evaluations which will be shown in next chapter.

From the nonlinear pushover analyses, structural characteristics of welded connection frames were compared with those of PR connection frames. From the cyclic pushover tests, as well as the monotonic pushover curves, it is shown that the connection types play a significant role. PR frames showed more flexible behavior at the design and yield level. More gradual strength degradation was evident for these composite moment frames when compared to fully welded ones.

From the nonlinear dynamic analyses treated in Section 8.3, it was shown that considerable plastic deformations occurred at the lower story composite columns immediately after the PGA of the ground motions had been reached. When welded connection frames were compared with PR ones, welded frames show stiffer behavior and larger resistance at low to moderate base shears but they collapse rapidly after reaching their ultimate resistance.

With the data obtained by these nonlinear analyses, the performance and damage evaluations for the composite columns are described in Chapter 9.

Chapter 9

Seismic Performance and Damage Evaluation

The principal objective in conventional seismic design is to provide sufficient strength and deformation capacity on a member-by-member basis so that collapse does not occur under the maximum credible ground motion. It should be noted that seismic design addresses this objective primarily through prescriptive strength design provisions and requires neither local checks for deformation capacity of the members nor a complete structural system approach to the design. Because conventional design software does not deal with composite members, this chapter begins with an examination of the significance of pseudo-elastic design interaction equations and the plastic ductility demand ratios due to combined axial compressive force and bending moment in composite members. The member demands expressed as the local forces and deformations are obtained from the nonlinear analyses described in Chapter 8. The specific levels of building damage will be evaluated based on the ratios of the required member response to the applicable strength capacity of the member section. The primary purpose of this chapter is to investigate both building performance and damage for four prototype composite moment frames (C-MF).

The chapter is organized as follows. Section 9.1 presents the basic definition and background for the limit states, seismic performance, and damage evaluation. Based on results of the nonlinear analyses in Chapter 8, the seismic performance and the damage evaluations for all composite moment frames are discussed in Section 9.2 and Section 9.3. Comparisons of structural damage between frames with welded and PR connections are described in Section 9.4. Finally, a summary and discussion of these frame models are given in Section 9.5.

9.1 Introduction

The basic design objective for the frames designed in this research was to enforce a strong column-weak beam mechanism, i.e., reaching the full plastic moment capacity of the steel beam before any other failure mode was reached. In addition to strength, this

requires large hinge rotational capacity in the critical sections. Exceedance of any ultimate limit state in the columns indicates the most severe type of damage for the building as it can lead to complete collapse. Therefore, a careful investigation of the structural damage for the composite columns is emphasized in this chapter.

The more popular available design-oriented programs do not provide, in general, the correct design checks for the beam-columns and composite sections in particular. The checks provided for beam-columns are generally very conservative and strength based as this process requires subjective judgment and is thus impossible to automate. Even if it were possible to automate them, these checks would not provide any information on actual performance. Finally, it should be noted that there were no investigations on either seismic performance or damage evaluation for composite moment frames similar to those studied here found in the technical literature. This chapter will focus on the seismic performance and the damage evaluation for the composite CFT columns because of these reasons.

There are two major steps in order to perform the damage evaluation, one associated with determining the capacity and the other with assessing the demand. In the first step, the cross-sectional capacity of the hinging regions must be carefully determined. In the second step, the demand at these critical sections must be established from careful numerical and detailed analyses of entire structures subjected to large ground motions. To accomplish the first step, monotonic and cyclic behavior of CFT beam-columns subjected to combined axial and moment loading was studied in an attempt to estimate both the maximum strength and ductility for doubly-symmetric and axis-symmetric composite cross sections. From these studies it can be shown that design ultimate capacities for rectangular/circular CFT beam-columns can be estimated with reasonable accuracy using the simplified axial and moment (P-M) interaction formulas provided by *2005 AISC Specification* for composite systems. The P-M interaction formations are given in Appendix A.

To accomplish the second step, advanced computational simulations were carried out on a series of composite moment resisting frames. The structural damage was evaluated in this research through the comparison of elastic strength ratios (ESR) and the inelastic curvature ductility ratios (ICDR). ESR are defined as the ratios of the member response

to the strength capacity for the member cross section. ICDR are defined as the ultimate required rotation divided by the rotation at the nominal yield point, as taken from the moment-ductility curve for the member cross section. ESR and ICDR can be calculated by using the analytical studies of CFT cross-sectional strength and ductility, respectively. These concepts are taken from the work by Hajjar et al. (Hajjar 1998).

The P-M interaction diagram for a composite section based on a full plastic stress distribution can be generated as a linear interpolation between five points. The theoretical background for determining these five points were given in Section 3.1.1 (See Figure 3.2 and Table 3.1). For the damage evaluation, a simplified bilinear interpolation may be used between three points as shown in Figure 9.1. The simplified expressions shown as Equations 3.8 and 3.9 can be used for determining the member capacity to use in the calculation of the elastic strength ratios (ESR) for composite columns. This approach is reasonably accurate for steel columns and should provide a conservative estimation for composite structures.

The value of ESR can be determined by the position of the required strength on the domain of a simplified P-M interaction diagram. Two regions can be identified insofar as axial strength is concerned. If the axial load is low (R1), the behavior is controlled by yielding in tension due to bending and will be very ductile if the cross-section is properly detailed. If the axial load is high (R2), the behavior will be dominated by compression due to the axial loads and will result in only limited ductility even for a well-detailed member. A poorly detailed member in R2 is likely to fail in a brittle, catastrophic manner. If the required strength exceeds the member resistance capacity ($ESR > 1.0$), the possibility of failure is high and both the inelastic rotational demand and the ability of the column to sustain axial loads must be carefully established. It should be noted that the term elastic as used in the ESR definition is a misnomer as it assumes a bilinear elasto-plastic behavior and not to the capacity when the cross-section first exceeds the proportional limit.

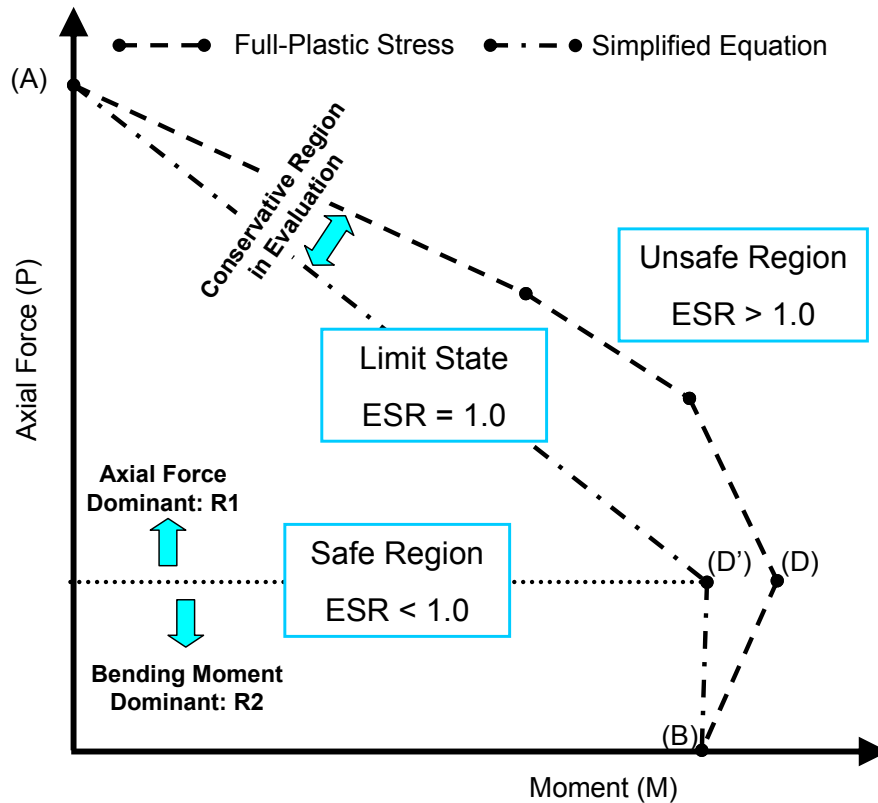


Figure 9.1 Basic concept for the elastic strength ratio (ESR)

As another index of damage, the concept of the inelastic curvature ductility ratio (ICDR) is illustrated in Figure 9.2. The ICDR is based on the monotonic moment-curvature diagram for a section. This envelope is used to determine the ultimate moment capacity (M_u), the initial flexural stiffness (K_i) and the Inelastic Curvature Ductility Ratios (ICDR). K_i is defined as the initial secant stiffness corresponding to the serviceability level of moment (arbitrarily taken as $0.6M_u$). ICDR are defined as ϕ_u divided by ϕ_y . ϕ_y indicates the curvature at nominal yield, defined as M_u divided by K_i . Under large rotations due to bending, the ultimate curvature (ϕ_u) is located on the post-peak path generated by the hardening effect of the composite materials. The ultimate curvature may change according to cross-sectional and material properties as well as the type of loading.

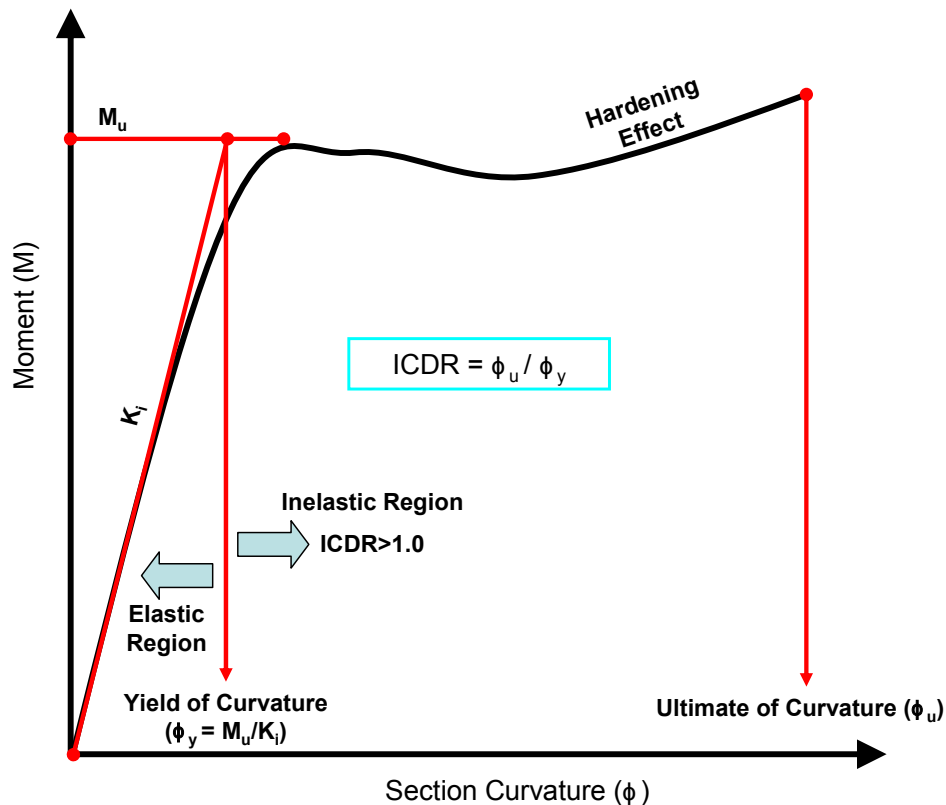


Figure 9.2 Basic concept for the inelastic curvature ductility ratio (ICDR)

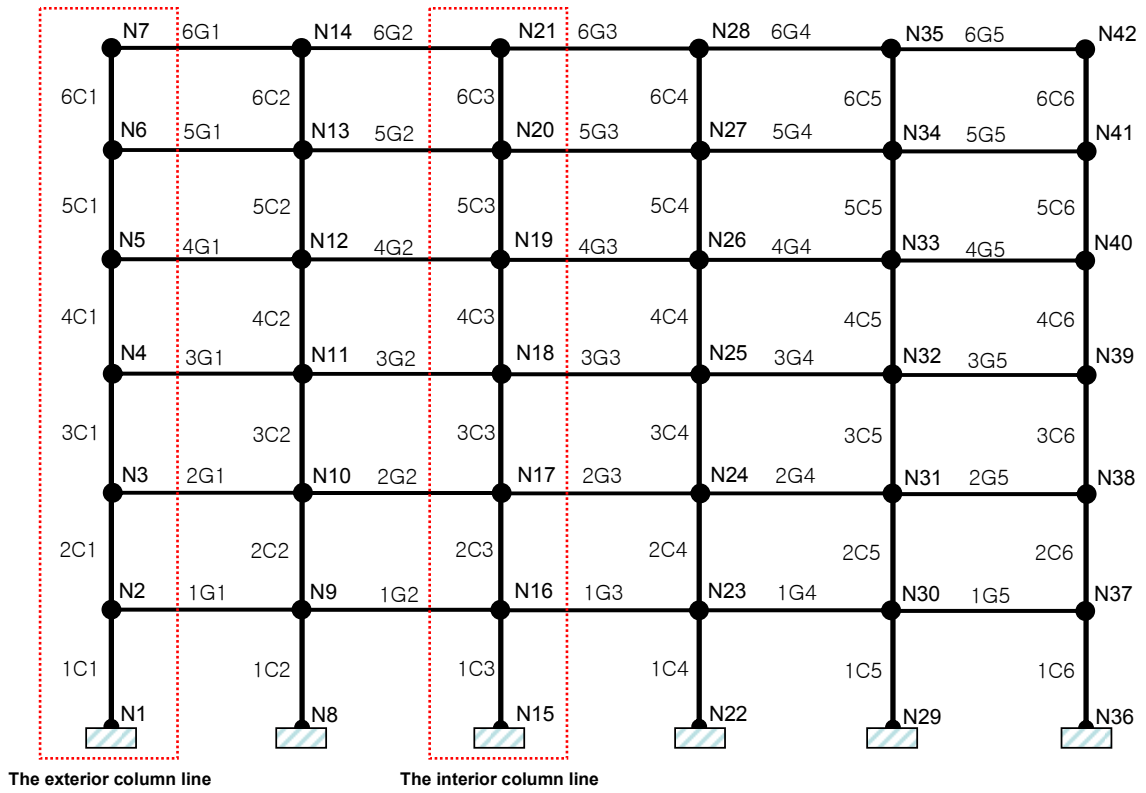
The available limit states to conduct the damage evaluations are listed in Table 9.1. Three performance levels as shown in Figure 8.13 were used to estimate the ESR for the pushover analyses. Overall, the composite cross sections stay in the elastic level without any plastic deformation up to the design point level, so ISDR are available only at other two levels as shown in the table. For the dynamic analyses, it was impossible to check each and every time step. Arbitrarily, but based on selected examination of the data, the evaluation was made at the time of occurrence of the maximum base shear.

In addition, only data at some key locations can be examined in detail. Identification for nodes and members to be used in this discussion are given in Figure 9.3. The distribution of the damage ratios was determined according to the structural shape (CCFT vs. RCFT) and the loading type (monotonic vs. seismic). All frame models are symmetric in plan and subjected to uniform gravity loads along all bays and stories. As a result, the values for damage evaluation show a similar distribution along the representative lines of

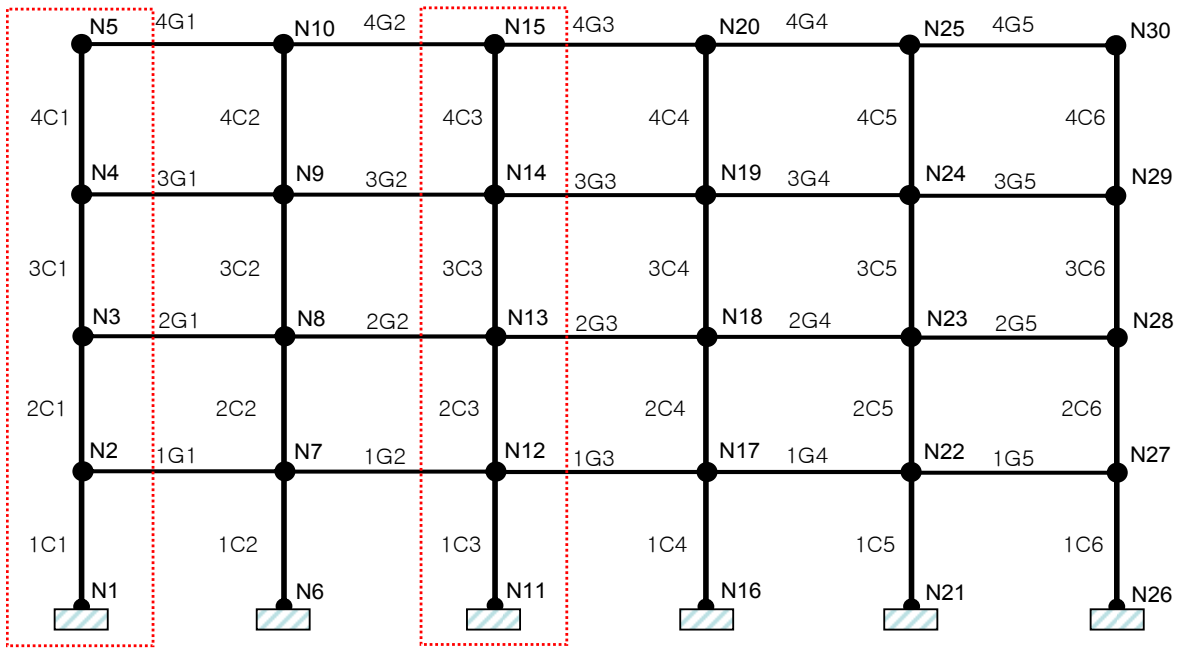
the composite columns. For example, the column line connected by interior columns 1C3, 2C3, 3C3, and 4C3 shown in Figure 9.3 (b) results in data representative of the same results along other interior column lines such as that for columns 1C2, 2C2, 3C2, and 4C2. Therefore, ESR and ICDR along typical column lines boxed by the red lines in Figure 9.3 can be considered representative of damage to the whole frame.

Table 9.1 Available information on damage evaluations for the composite columns

Evaluation	Analysis	Measuring Points (Base Shear)		
		Design	Yield	Ultimate
ESR	Pushover	Design	Yield	Ultimate
	Dynamic	-	-	Ultimate
ICDR	Pushover	-	Yield	Ultimate
	Dynamic	-	-	Ultimate



(a) Nodes and Elements on the Frame Model for 6 Story C-MF



N: Node C:NL Beam-Column Elements for CFT Columns G: NL Beam Column Element for Steel Beams-

(b) Nodes and Elements on the Frame Model for 4 Story C-MF

Figure 9.3 Identification for nodes and elements on the composite moment frames

9.2 Seismic Performance and Damage Evaluation

The two dimensional composite moment frames designed for this research were first evaluated using an equivalent static lateral load procedure (pushover) and then using nonlinear dynamic analysis for the LA21 ground motion (1995 Kobe earthquake). Based on the analytical results, the available damage evaluations for the whole frames were conducted based on the limit states given in Table 9.1. Detailed explanations for the computation of the damage ratios will be presented in the form of examples. In addition, the distribution of the damage ratios on the frames will also be investigated in this section.

As mentioned above, ESR are defined as the ratio of the required member strength to the member capacity under combined axial force and bending moment. Specific examples for ESR calculations are given in Figure 9.4 for several members in a 6-story frame with end plate connections and RCFT columns (Frame 6END-C1). The required member forces corresponding to each performance level were obtained by collecting the local member forces from the pushover tests, and the values corresponding to each ESR are shown by a blue star (design point level), magenta star (yield point level) and a red star (ultimate point level). For the ultimate level, in particular, note that the ESR can exceed the value of 1.0 because the denominator of the ESR is based on a simplified biaxial approximation to the real interaction surface (see region marked as conservative in Fig. 9.1 – the difference between the surfaces can be quite significant).

The required member forces acting on the composite columns consist of a combined axial force and bending moment (P-M). ESR corresponding to the local member forces were calculated by using the simplified equations (See Equations 3.8 and 3.9). The ESR can not exceed the applicable limit state at the design point level, so values less than or equal to 1.0 must be obtained at this stage. The interior columns hold larger gravity loads than the exterior columns. Thus, P-M interaction forces for the interior columns (See Figure 9.4 (b) and Figure 9.4 (d)) are the higher on the P-M interaction diagram in comparison with those for the exterior columns (See Figure 9.4 (a) and Figure 9.4 (c)). Thus the ESR for the interior columns are generally larger than those for the exterior columns. Similarly, the ESR for the first floor columns are larger than those for the second (and upper) floor columns due to the larger gravity load effect (Figure 9.4 (b) vs. Figure 9.4 (d)). As the pushover loads increase, the local moment acting on the composite

columns increases significantly as compared to the axial load because of drift and second-order effects. As a result, the star signs under performance levels become aligned with the horizontal axis. P-M interaction forces acting on the composite columns under either the yield point level or the ultimate point level exceed the limit state, so the values of ESR result in more 1.0.

The relationship between ESR values at the basement of interior CFT column and hinge progression is illustrated in Figure 9.5. For combinations at axial loads and bending moments, the ESR can be defined as:

If $P_r \leq P_D$

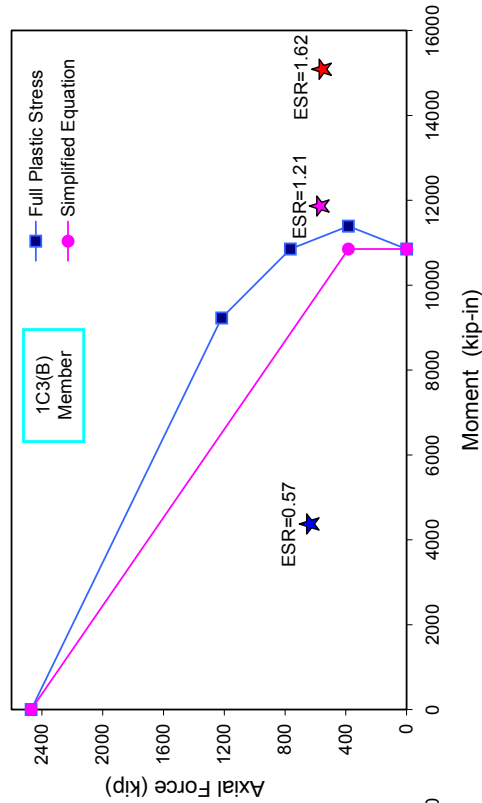
$$ESR = \frac{M}{M_B} \quad (EQ 9.1)$$

otherwise,

$$ESR = \frac{P - P_D}{P_A - P_D} + \frac{M}{M_B} \quad (EQ 9.2)$$

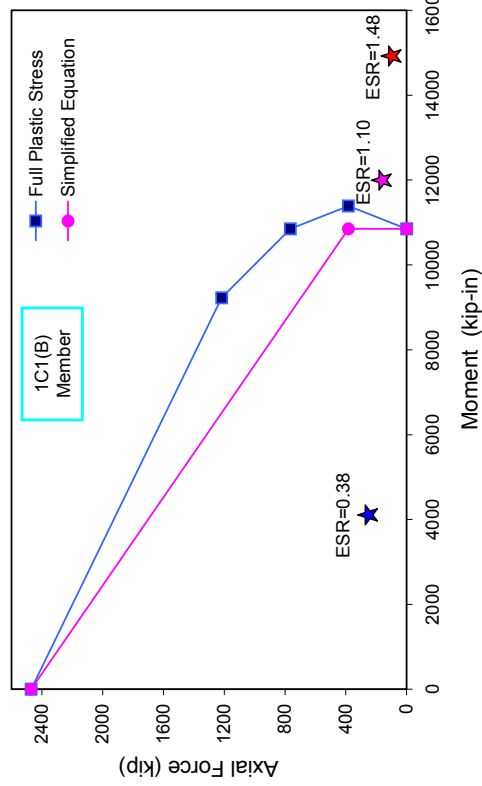
Because the simplified equation line is taken conservatively as being bilinear instead of multi-linear, the value of ESR from the analysis can exceed 1.0 as the design level is exceeded. As shown by the lines labeled “Fiber Yield” and “Fiber Ultimate” in Figure 9.5, large differences in capacity can be found between the normal design (“Bilinear Conservative”) and conditions that more closely reflect the initial plastic stress (“Fiber Yield”) and ultimate strength (“Fiber Ultimate”). The latter includes strain hardening and the only limited deterioration of the concrete strength as the sections are well confined.

Because it was of interest to study the connection behavior, beam hinges are not shown in Figure 9.5. Since the frames were designed with a strong-column weak-beam philosophy, all beams adjacent to where column yielding is shown are well into their inelastic range.

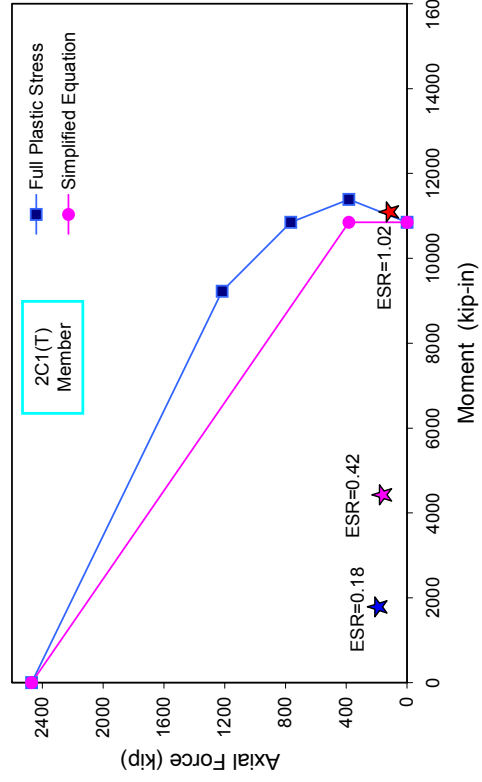


(a) ESR calculations at 1C1(B) position (Exterior Column)

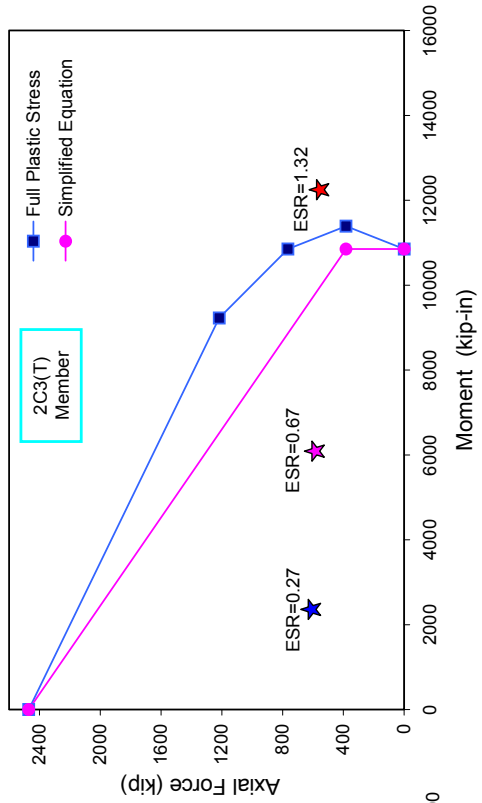
ESR at the design point ★ ESR at the yield point ★ ESR at the ultimate point ★



(b) ESR calculations at 1C3(B) position (Interior Column)



(c) ESR calculations at 2C1(T) position (Exterior Column)



(d) ESR calculations at 2C3(T) position (Interior Column)

Figure 9.4 Specific examples for ESR calculations (6END-C1 Model)

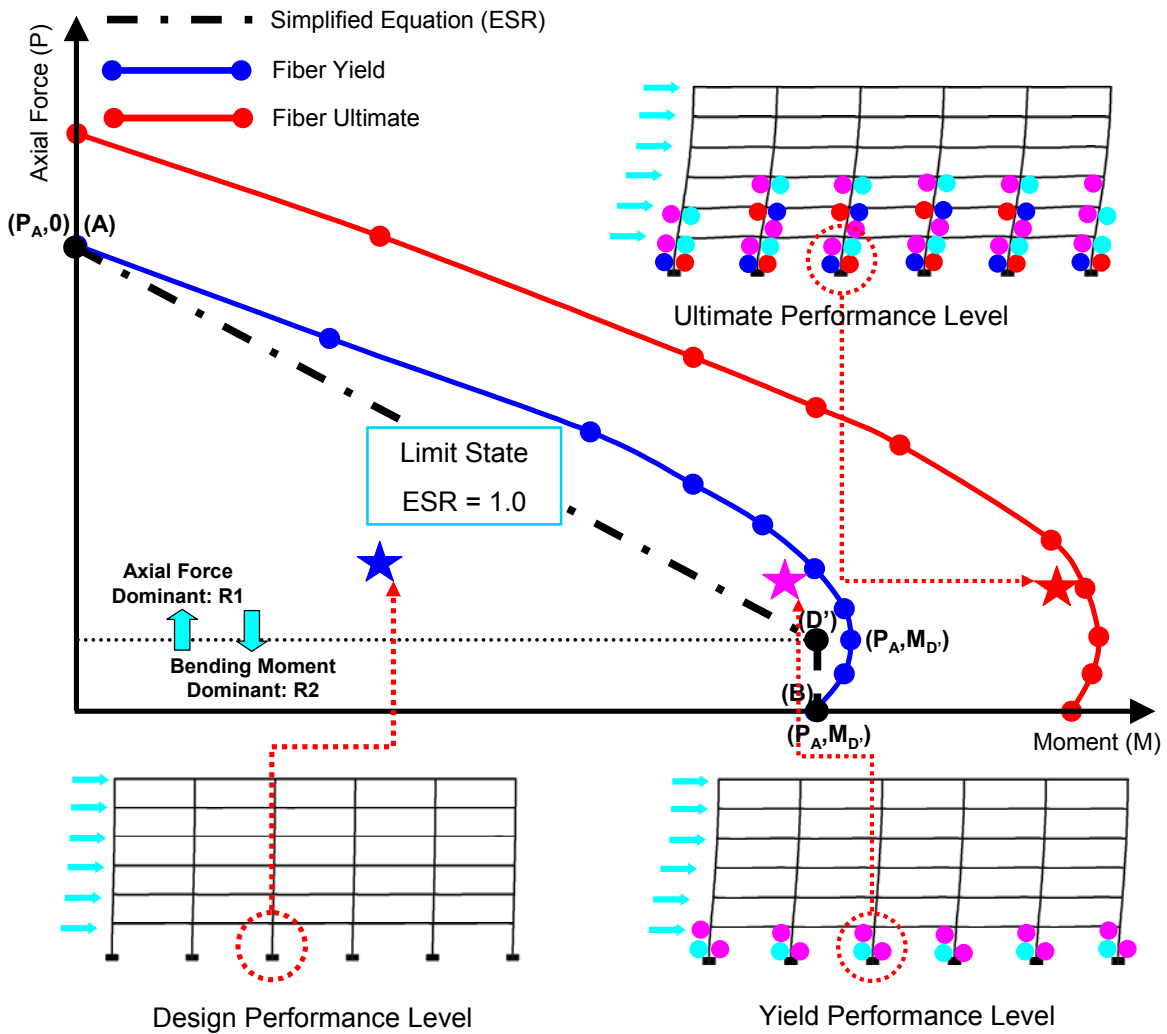
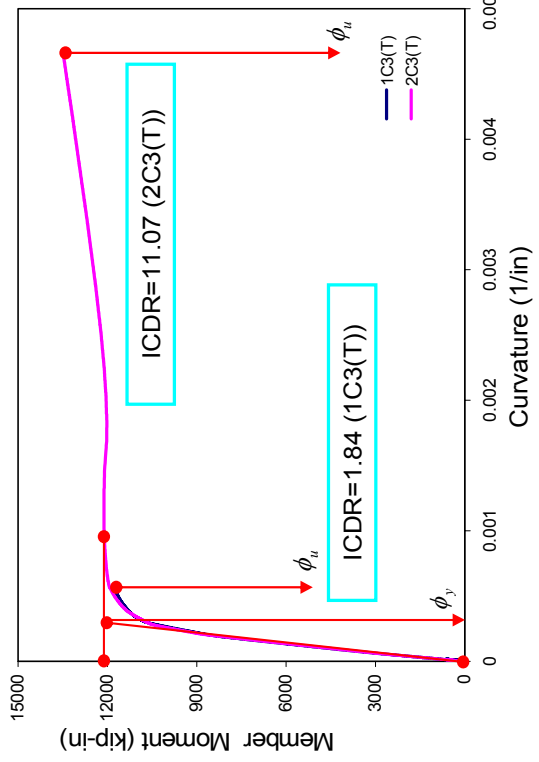
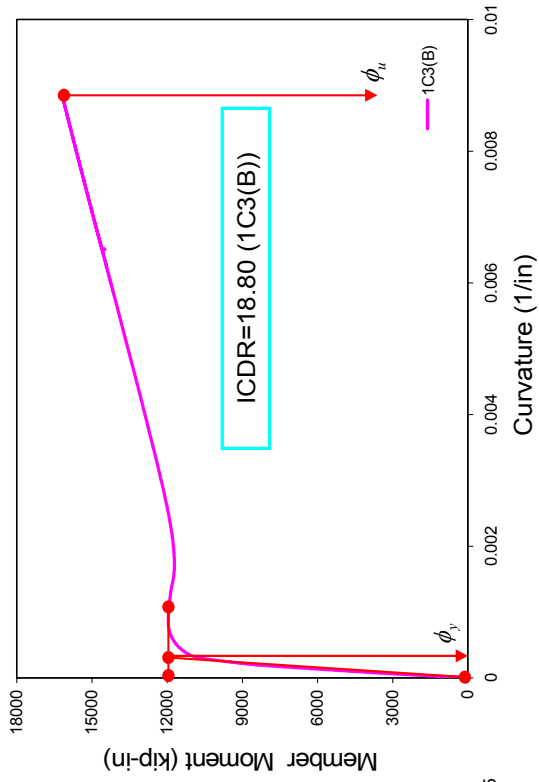


Figure 9.5 Relationship between ESR values at the basement of interior column lines and hinge formation

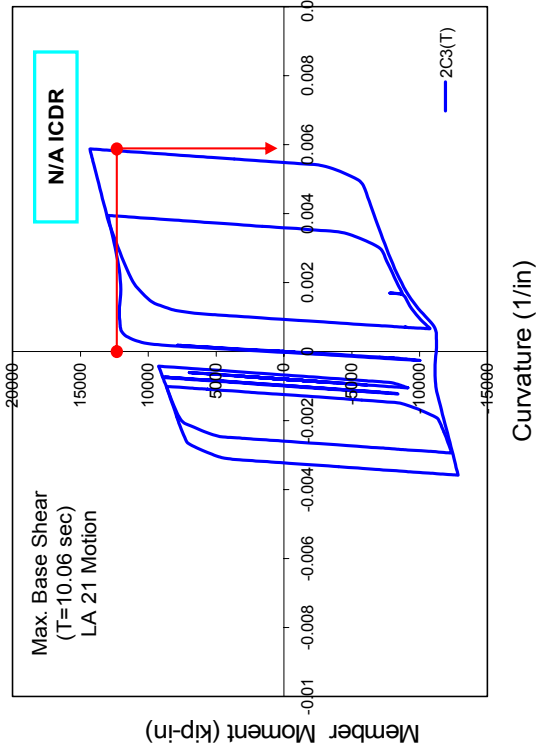
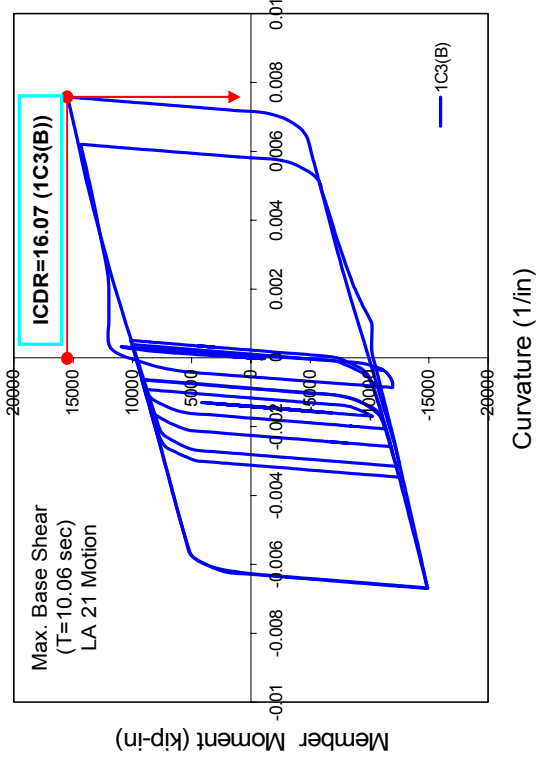
ICDR are defined as the ratio of the current ultimate member curvature (ϕ_u) to the nominal yield curvature (ϕ_y). Specific examples for ICDR calculations are given in Figure 9.6. Figure 9.6 (a) shows the curve for monotonic pushover loads, while Figure 9.6 (b) shows the hysteretic loops under the given ground motion. The largest curvature occurs at the column base of the first floor shown for 1C3(B). Except for the column bases, the curvature is not always at its maximum at the time of the maximum base shear force. Overall, the members which undergo significant deformations show larger value of ESR and ICDR.

The most severe damage occurs at the column bases of the first floor. The damage evaluations along the column bases are given in Tables 9.2 to 9.5. The interior columns undergo more severe damage than the external columns under the same performance levels as shown in the computation examples. The ESR for the interior column bases of the first floor are more than 1.55 for the ultimate point level. A high ESR is often accompanied by a high ICDR at the same performance level. The considerable amount of curvature due to the increasing external forces causes these damage ratios to increase very rapidly.

PMM ratios were computed by using the design check tool in SAP 2000 at the design point level. PMM are moment interaction ratios for beam members under combined axial and bending forces. The values of ESR for the column bases at the design point level are smaller than the average PMM ratios for the steel beams as shown in Figure 7.10. It can be shown that the design strength for the composite frame is based on the plastic strength of the beam.



(a) ICDR calculations at the ultimate point (Pushover Analyses)



(b) ICDR calculations at the occurrence time for the maximum base shear force (Dynamic Analyses)

Figure 9.6 Specific examples for ICDR calculations (6END-C1 Model)

Table 9.2 Damage evaluations for RCFT columns (HSS 16X16X500)
for the 6END-C1 model case

Model	Member	Evaluation	Analysis	Measuring Points (Base Shear)		
				Design	Yield	Ultimate
6END-C1	1C1(B)	ESR	Pushover	0.38	1.10	1.48
			Dynamic	-	-	1.43
		ICDR	Pushover	-	1.81	15.41
			Dynamic	-	-	14.2
Model	Member	Evaluation	Analysis	Measuring Points (Base Shear)		
6END-C1	1C2(B)	ESR	Pushover	0.58	1.21	1.63
			Dynamic	-	-	1.56
		ICDR	Pushover	-	3.41	18.81
			Dynamic	-	-	16.13
Model	Member	Evaluation	Analysis	Measuring Points (Base Shear)		
6END-C1	1C3(B)	ESR	Pushover	0.57	1.21	1.62
			Dynamic	-	-	1.55
		ICDR	Pushover	-	3.24	18.8
			Dynamic	-	-	16.07

Model	Member	Evaluation	Analysis	Measuring Points (Base Shear)		
				Design	Yield	Ultimate
6END-C1	1C4(B)	ESR	Pushover	0.58	1.21	1.62
			Dynamic	-	-	1.55
		ICDR	Pushover	-	3.27	18.81
			Dynamic	-	-	16.1
Model	Member	Evaluation	Analysis	Measuring Points (Base Shear)		
6END-C1	1C5(B)	ESR	Pushover	0.57	1.20	1.62
			Dynamic	-	-	1.55
		ICDR	Pushover	-	3.38	19.21
			Dynamic	-	-	16.15
Model	Member	Evaluation	Analysis	Measuring Points (Base Shear)		
6END-C1	1C6(B)	ESR	Pushover	0.37	1.18	1.60
			Dynamic	-	-	1.51
		ICDR	Pushover	-	2.35	17.07
			Dynamic	-	-	15.61

LA21 ground motion was used in case of dynamic analysis

B: The bottom of CFT column members

Table 9.3 Damage evaluations for CCFT columns (HSS 18X500)
for the 6END-C2 model case

Model	Member	Evaluation	Analysis	Measuring Points (Base Shear)		
				Design	Yield	Ultimate
6END-C1	1C1(B)	ESR	Pushover	0.45	1.14	1.40
			Dynamic	-	-	1.55
		ICDR	Pushover	-	1.72	14.88
			Dynamic	-	-	16.72
Model	Member	Evaluation	Analysis	Measuring Points (Base Shear)		
6END-C1	1C2(B)	ESR	Pushover	0.68	1.31	1.63
			Dynamic	-	-	1.71
		ICDR	Pushover	-	2.76	18.32
			Dynamic	-	-	19.67
Model	Member	Evaluation	Analysis	Measuring Points (Base Shear)		
6END-C1	1C3(B)	ESR	Pushover	0.68	1.31	1.62
			Dynamic	-	-	1.67
		ICDR	Pushover	-	2.76	18.26
			Dynamic	-	-	19.39

Model	Member	Evaluation	Analysis	Measuring Points (Base Shear)		
				Design	Yield	Ultimate
6END-C1	1C4(B)	ESR	Pushover	0.68	1.31	1.62
			Dynamic	-	-	1.67
		ICDR	Pushover	-	2.76	18.29
			Dynamic	-	-	19.32
Model	Member	Evaluation	Analysis	Measuring Points (Base Shear)		
6END-C1	1C5(B)	ESR	Pushover	0.68	1.29	1.60
			Dynamic	-	-	1.65
		ICDR	Pushover	-	2.78	18.34
			Dynamic	-	-	19.21
Model	Member	Evaluation	Analysis	Measuring Points (Base Shear)		
6END-C1	1C6(B)	ESR	Pushover	0.49	1.23	1.54
			Dynamic	-	-	1.60
		ICDR	Pushover	-	1.99	17.78
			Dynamic	-	-	18.2

LA21 ground motion was used in case of dynamic analysis

B: The bottom of CFT column members

Table 9.4 Damage evaluations for RCFT columns (HSS 16X16X500) for the 6END-C7 model case

Model	Member	Evaluation	Analysis	Measuring Points (Base Shear)		
				Design	Yield	Ultimate
6END-C1	1C1(B)	ESR	Pushover	0.33	1.08	1.46
			Dynamic	-	-	1.28
		ICDR	Pushover	-	1.77	15.92
			Dynamic	-	-	11.29
Model	Member	Evaluation	Analysis	Measuring Points (Base Shear)		
6END-C1	1C2(B)	ESR	Pushover	0.50	1.21	1.65
			Dynamic	-	-	1.43
		ICDR	Pushover	-	2.61	19.62
			Dynamic	-	-	15.03
Model	Member	Evaluation	Analysis	Measuring Points (Base Shear)		
6END-C1	1C3(B)	ESR	Pushover	0.50	1.20	1.65
			Dynamic	-	-	1.43
		ICDR	Pushover	-	2.47	19.85
			Dynamic	-	-	14.97

Model	Member	Evaluation	Analysis	Measuring Points (Base Shear)		
				Design	Yield	Ultimate
6END-C1	1C4(B)	ESR	Pushover	0.49	1.21	1.65
			Dynamic	-	-	1.43
		ICDR	Pushover	-	2.43	19.85
			Dynamic	-	-	14.96
Model	Member	Evaluation	Analysis	Measuring Points (Base Shear)		
6END-C1	1C5(B)	ESR	Pushover	0.49	1.20	1.64
			Dynamic	-	-	1.41
		ICDR	Pushover	-	2.45	20.01
			Dynamic	-	-	14.87
Model	Member	Evaluation	Analysis	Measuring Points (Base Shear)		
6END-C1	1C6(B)	ESR	Pushover	0.32	1.17	1.58
			Dynamic	-	-	1.36
		ICDR	Pushover	-	1.94	18.56
			Dynamic	-	-	13.78

LA21 ground motion was used in case of dynamic analysis

B: The bottom of CFT column members

Table 9.5 Damage evaluations for CCFT columns (HSS 18X500)
for the 6END-C8 model case

Model	Member	Evaluation	Analysis	Measuring Points (Base Shear)		
				Design	Yield	Ultimate
6END-C1	1C1(B)	ESR	Pushover	0.38	1.12	1.56
			Dynamic	-	-	1.56
		ICDR	Pushover	-	1.64	18.02
			Dynamic	-	-	16.54
Model	Member	Evaluation	Analysis	Measuring Points (Base Shear)		
6END-C1	1C2(B)	ESR	Pushover	0.60	1.29	1.80
			Dynamic	-	-	1.67
		ICDR	Pushover	-	2.55	21.98
			Dynamic	-	-	17.82
Model	Member	Evaluation	Analysis	Measuring Points (Base Shear)		
6END-C1	1C3(B)	ESR	Pushover	0.60	1.30	1.80
			Dynamic	-	-	1.67
		ICDR	Pushover	-	2.60	21.98
			Dynamic	-	-	17.83

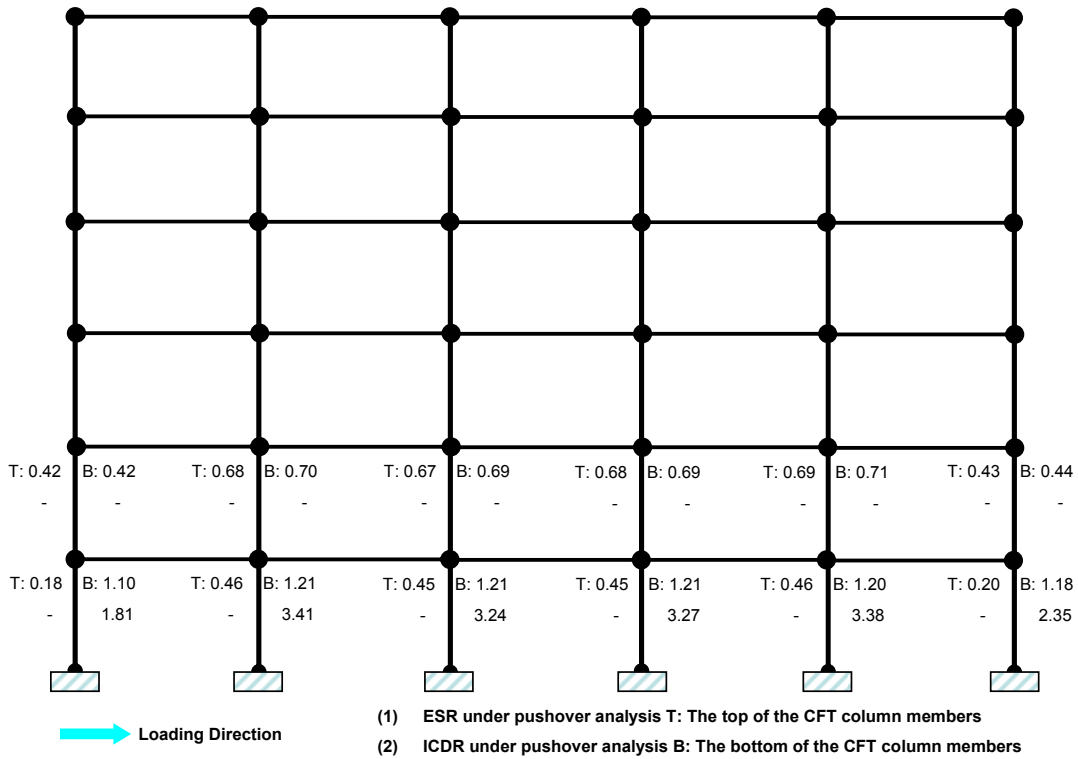
Model	Member	Evaluation	Analysis	Measuring Points (Base Shear)		
				Design	Yield	Ultimate
6END-C1	1C4(B)	ESR	Pushover	0.60	1.30	1.80
			Dynamic	-	-	1.67
		ICDR	Pushover	-	2.60	21.96
			Dynamic	-	-	17.82
Model	Member	Evaluation	Analysis	Measuring Points (Base Shear)		
6END-C1	1C5(B)	ESR	Pushover	0.60	1.29	1.80
			Dynamic	-	-	1.65
		ICDR	Pushover	-	2.58	21.88
			Dynamic	-	-	17.82
Model	Member	Evaluation	Analysis	Measuring Points (Base Shear)		
6END-C1	1C6(B)	ESR	Pushover	0.40	1.20	1.62
			Dynamic	-	-	1.60
		ICDR	Pushover	-	2.05	18.43
			Dynamic	-	-	17.24

LA21 ground motion was used in case of dynamic analysis

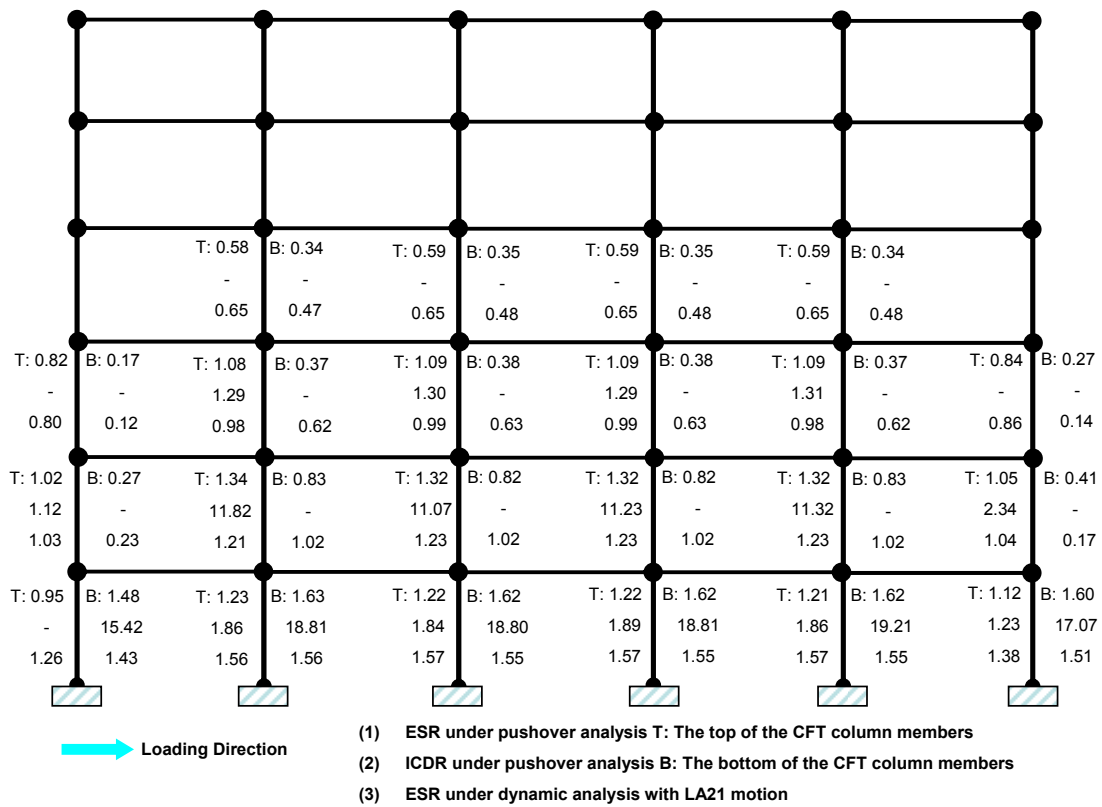
B: The bottom of CFT column members

The damage evaluations for the whole buildings subjected to either pushover loads or the earthquake ground motions are shown in Figures 9.7 to 9.10. Two performance levels, the yield point and the ultimate point, were used. The letter T on the figures indicates the top and B the bottom of the column element. According to the performance levels - design (1), yield (2), and ultimate (3) - indicate the available damage evaluations expressed as the numbers on the frames (See Figure 9.7 to Figure 9.10). At the yield point level, damage ratios which exceed the limit state are limited to the first floor. The most severe damage occurs at the interior column bases of the first floor, whose ESR ranged from 1.20 to 1.30 under this performance level. As the pushover continues, damage ratios over 1.0 spread to the higher stories. Simultaneously, the amount of plastic deformation is also increasing. Therefore, structural damage associated with member yielding and ultimate failures moves gradually from the first to the third floor as the loads approach ultimate. The values of ICDR rise very rapidly because of material hardening, which is associated with a small tangent slope of the stress-strain curve. The ratios for structures with symmetric configurations show a symmetric distribution. For example, the damage ratios on the selected interior column line (from 1C3 to 6C3 columns) show a similar distribution with those on the neighbor interior column line (from 1C2 to 6C2). The same trend for the damage ratios is clear for the exterior column lines.

Hinges were detected by investigating the stresses at the fiber sections in the column elements. Consistent with the description in Figure 9.5, the composite columns with large ESR also show the largest damage. Relationships between damage evaluations by ESR and mechanisms are shown in Figure 9.11. The distributions of ESR and ICDR shown in Figures 9.7 to 9.10 correspond to those of failure hinges presented in Figures 8.21 to 8.24.

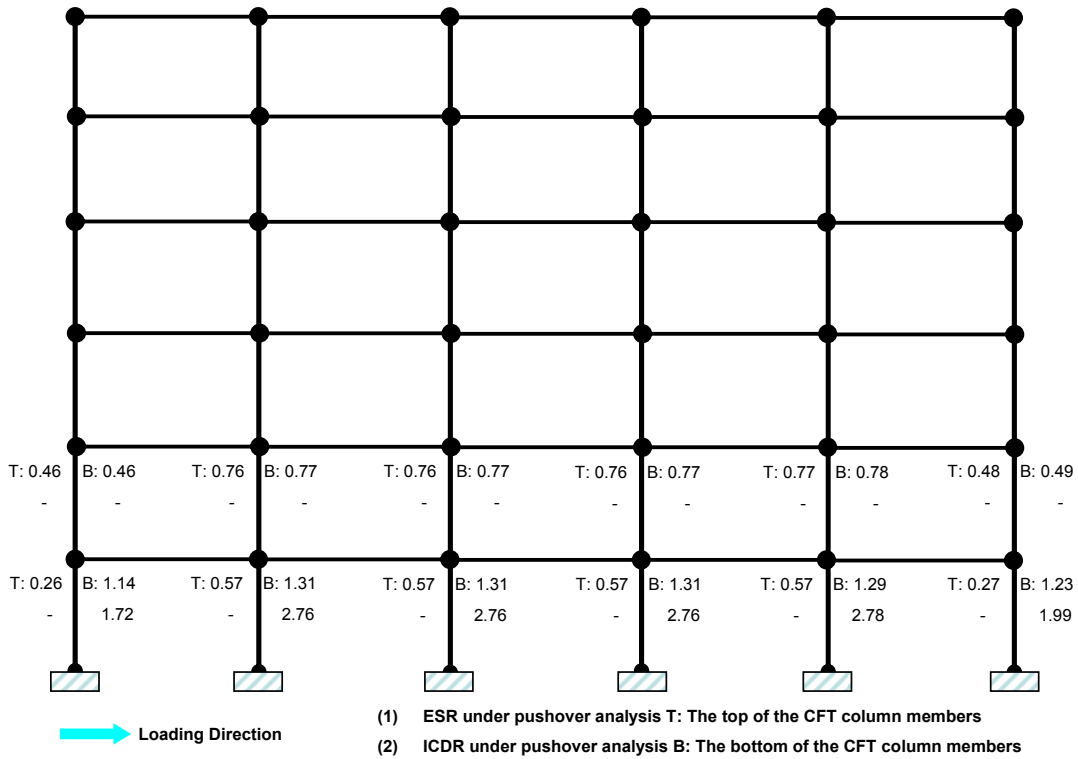


(a) Damage Evaluations for RCFT Columns under Yield Base Shear Force ($V=634$ kip)

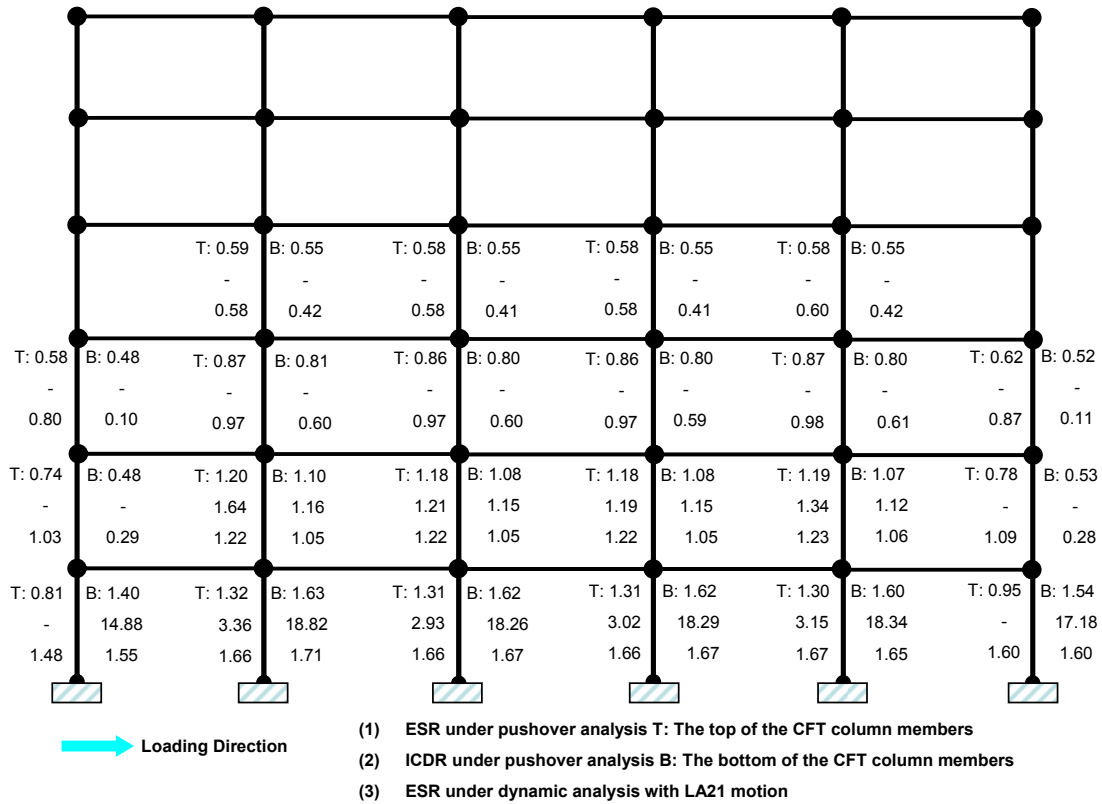


(b) Damage Evaluations for RCFT Columns under Ultimate Base Shear Force

Figure 9.7 Damage Evaluations of the 6END-C1 model

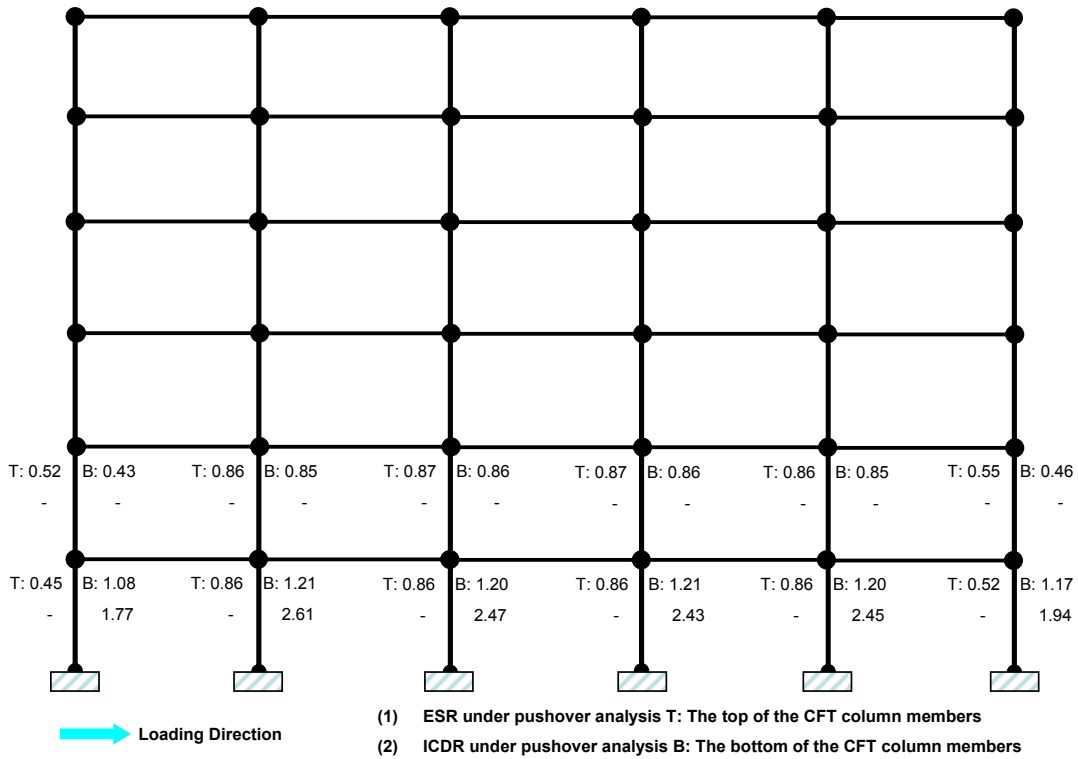


(a) Damage Evaluations CCFT Columns under Yield Base Shear Force ($V=564$ kip)

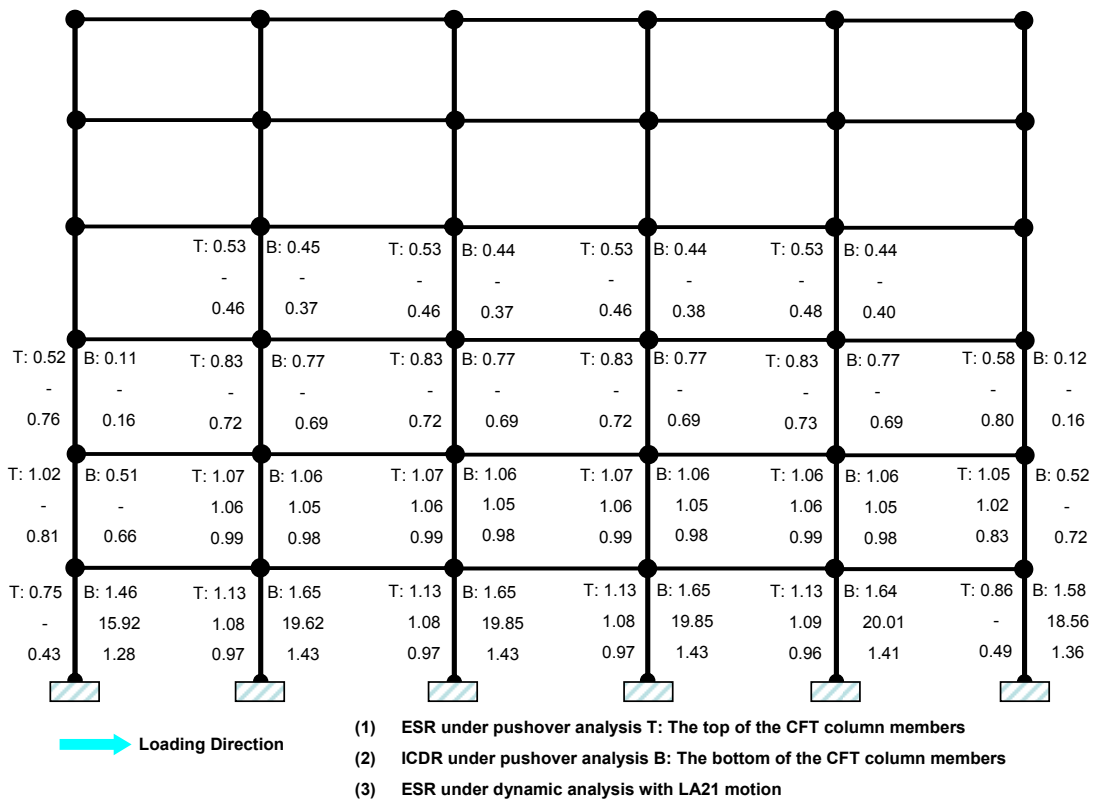


(b) Damage Evaluations for CCFT Columns under Ultimate Base Shear Force

Figure 9.8 Damage Evaluations of the 6END-C2 model

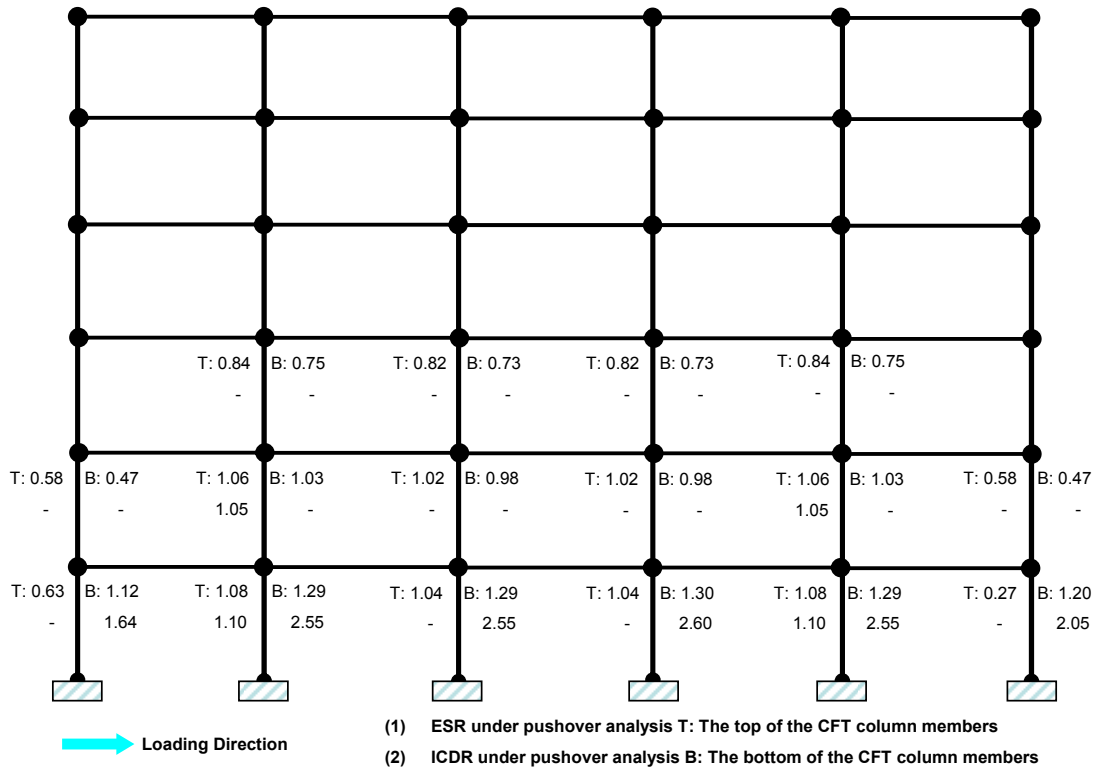


(a) Damage Evaluations for RCFT Columns under Yield Base Shear Force (V=772 kip)

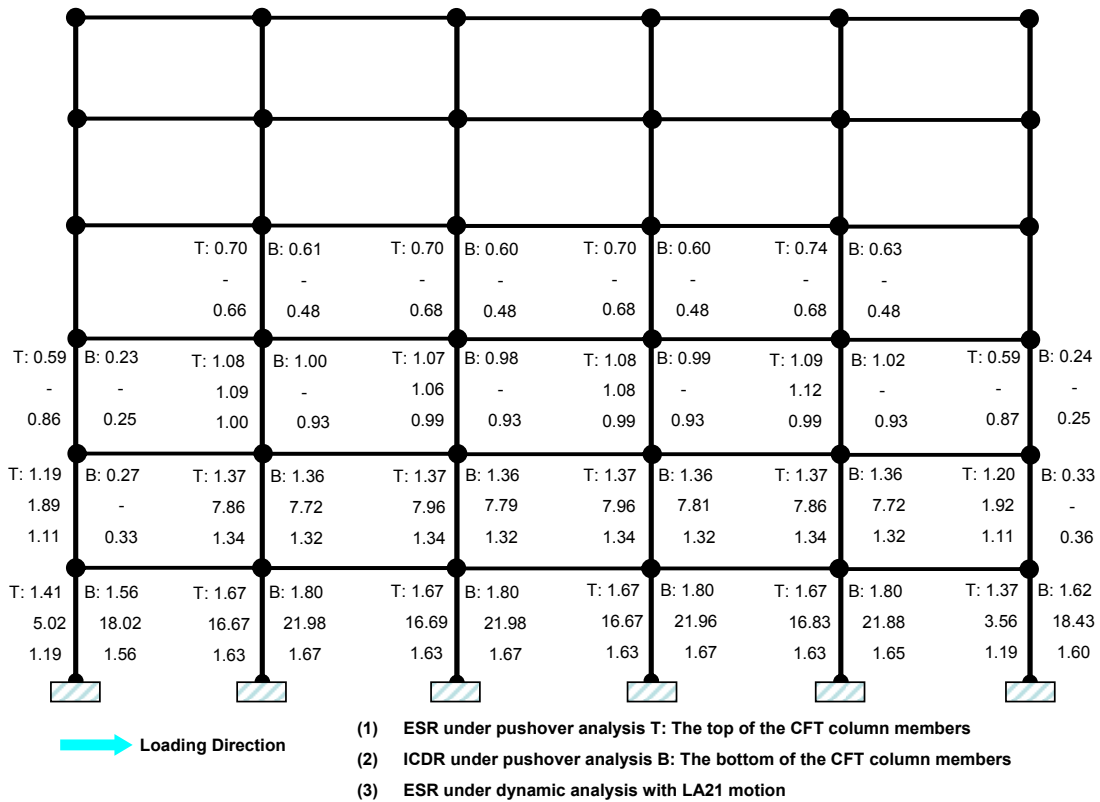


(b) Damage Evaluations for RCFT Columns under Ultimate Base Shear Force

Figure 9.9 Damage Evaluations of the 6END-C7 model



(a) Damage Evaluations for CCFT Columns under Yield Base Shear Force (V=692kip)



(b) Damage Evaluations for CCFT Columns under Ultimate Base Shear Force

Figure 9.10 Damage Evaluations of the 6END-C8 model

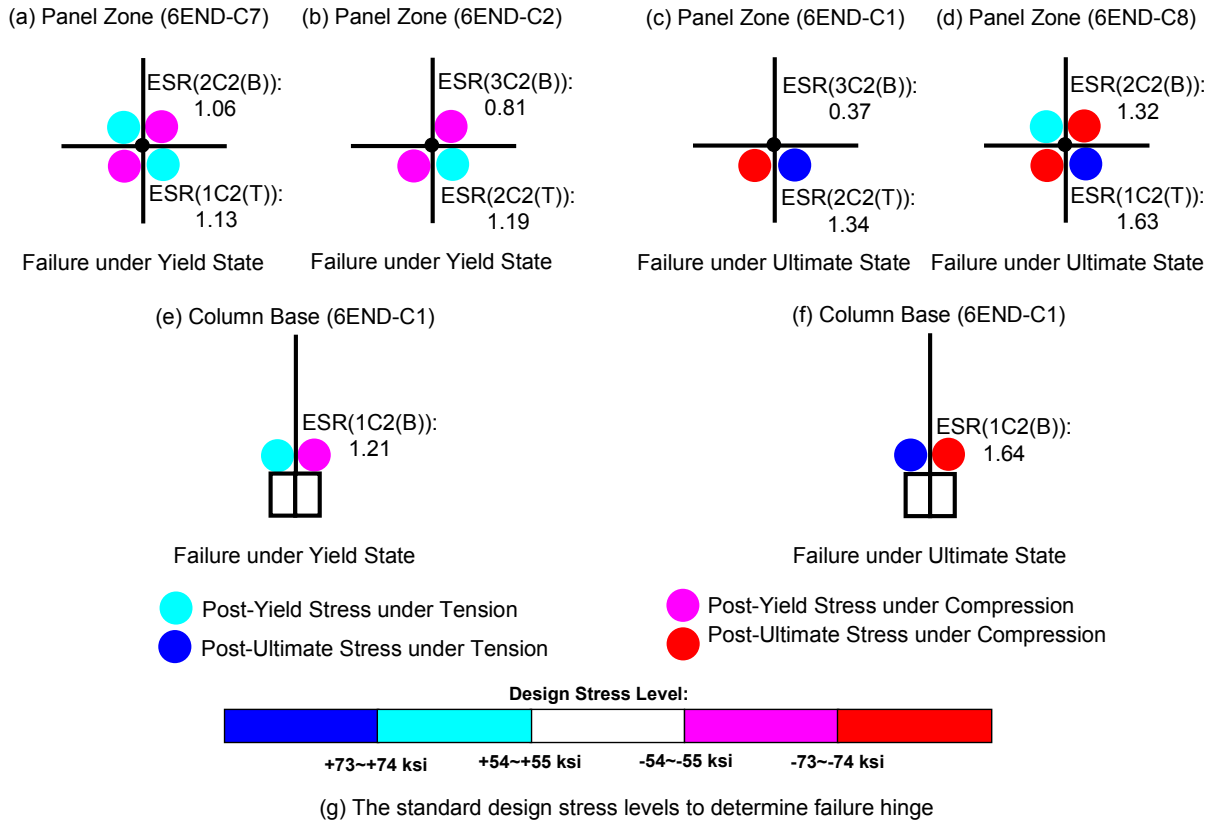


Figure 9.11 Relationship between ESR and failure hinges during the pushover analyses

9.3 Comparisons for Damage Evaluation

One of the objectives in this study is to verify that composite PR frames show structural advantages over welded FR frames. To this end, interstory drift ratios (ISDR) for PR frames will be compared with those of corresponding welded frames. ISDR at the interior column line next to the centerline of the frame and at one exterior column line were selected as representative of typical ISDR ratios observed.

ISDR are generally accepted as a significant parameter related to structural and non-structural damage as well as overall building stability. For steel frames, the ISDR are matched to global performance levels in accordance with the FEMA 273/356 criteria: Operational (OP), Immediate Occupancy (IO), Life Safety (LS), and Collapse Prevention (CP). The levels are discrete points on a continuous scale reflecting the expected performance, economic loss, damage and disruption for the building structure due to a series of progressively more damaging events. However, the performance levels for composite frames based on ISDR are not specified in any design guide. Therefore, the performance levels used in this section were determined by results of the pushover tests shown in Figure 8.4 to Figure 8.7 (See also Figure 8.13).

In order to compare the seismic performance of the PR frames with that of the welded frames, performance levels with identical ISDR regardless of the frame model case should be used. Two ISDR limits were selected as the performance levels after examination of the monotonic pushover curves for the welded frames. A 1.5 percent and a 3.0 percent ISDR limit were applied to the 6 story moment frames, while a 2.5 percent and 5.0 percent ISDR limits were applied to the 4 story moment frames. These ISDR limits correspond roughly to the middle of the hardening range and the ultimate point, respectively, for the monotonic pushover curves. These pushover curves were measured at the roof level of the welded frames. After they reach at 3.0 or 5.0 percentile inter-story drift ratio (ISDR) at the 6 or 4 story frame building respectively, the welded frames show a rapid strength deterioration and become unstable. The performance levels on the pushover curves are shown in Figure 9.12.

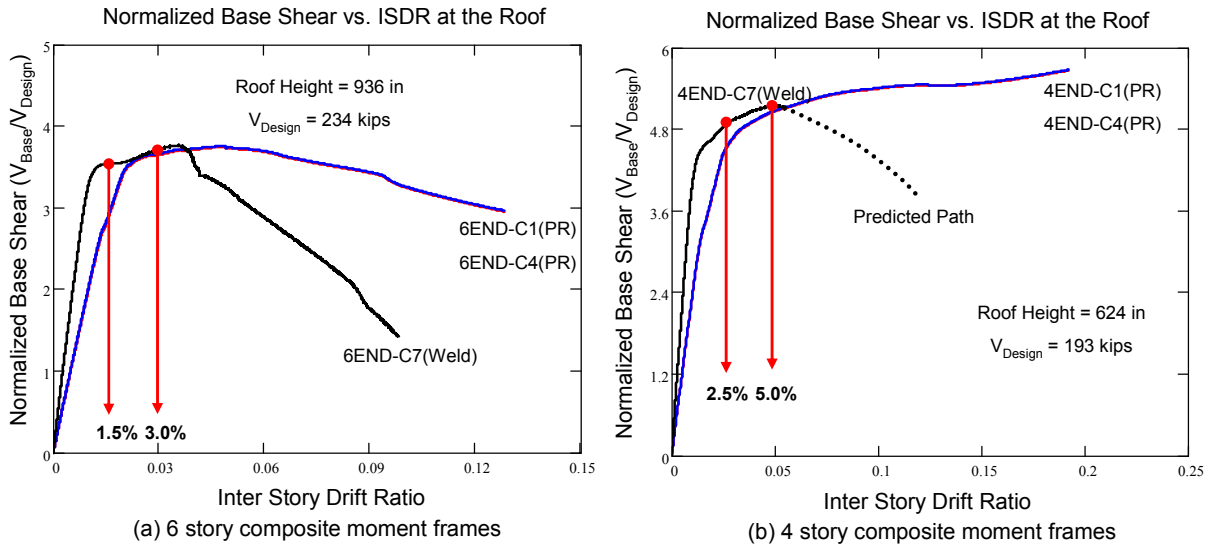


Figure 9.12 The performance levels on the pushover curves

PR frames are compared with welded frames in terms of ESR for the same performance level in Figures 9.13 to 9.20. In each of these figures, the two frames shown for comparison share the same member sizes but differ on the connection type. Overall, welded frames show larger ESR throughout the height than PR frames at the same inter-story drift level. The larger bending moments acting on the welded connections cause more severe damage to the composite columns and cause the sudden failure at the connections. Severe damage is indicated by the larger ESR concentrated on the lower story of the building. The red dashed lines in these figures indicate the unit value of ESR. ESR at the column bases exceed the red lines even at the first performance level (1.5 or 2.5 percent ISDR). Welded frames show more severe damage than PR frames at this first performance level.

The difference in ESR between any two frame models in these comparisons decreases at the second performance level (3.0 or 5.0 percent ISDR for the 4 and 6 story frames, respectively), with larger ESR along the story height still found for the welded frames. It can be concluded that welded frames are more susceptible to severe damage than PR frames under a reasonable range of story drifts.

The smaller P-M interaction capacities for CCFT columns used contribute to the larger damage ratios, so composite moment frames with CCFT columns show larger ESR than those with RCFT columns (i.e. 6END-C1 vs. 6END-C2, see Figure 9.13 and Figure

9.14). ESR distributions for interior columns are closer to the red limit lines than those for exterior columns. The larger gravity loads assigned to interior columns is the cause of these increased damage ratios. It is also shown that ESR for end-plate connection frames are generally larger than those for T-stub connection frames (i.e. 6END-C2 vs. 6TSU-C2) due to the larger mass converted from dead loads and partial live loads. This is true in spite of smaller capacities of composite columns used in T-stub connection frames.

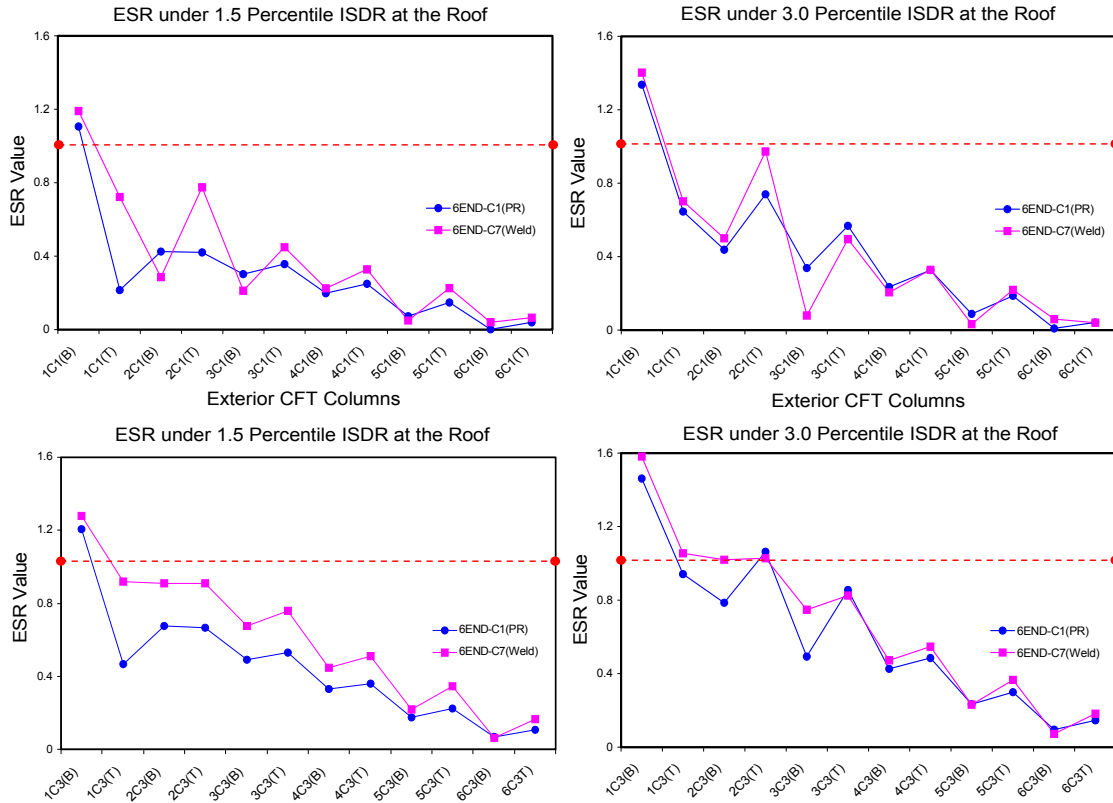


Figure 9.13 Comparisons of ESR under pushover loads (6END-C1 vs. 6END-C7)

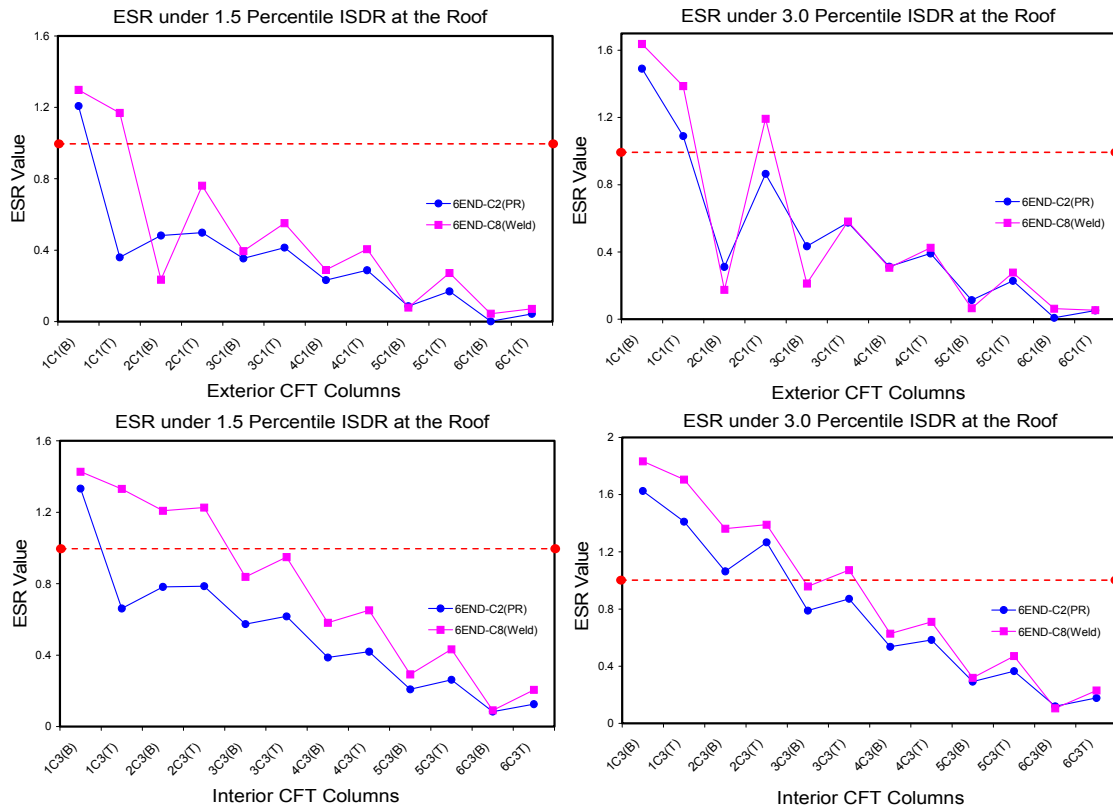


Figure 9.14 Comparisons of ESR under pushover loads (6END-C2 vs. 6END-C8)

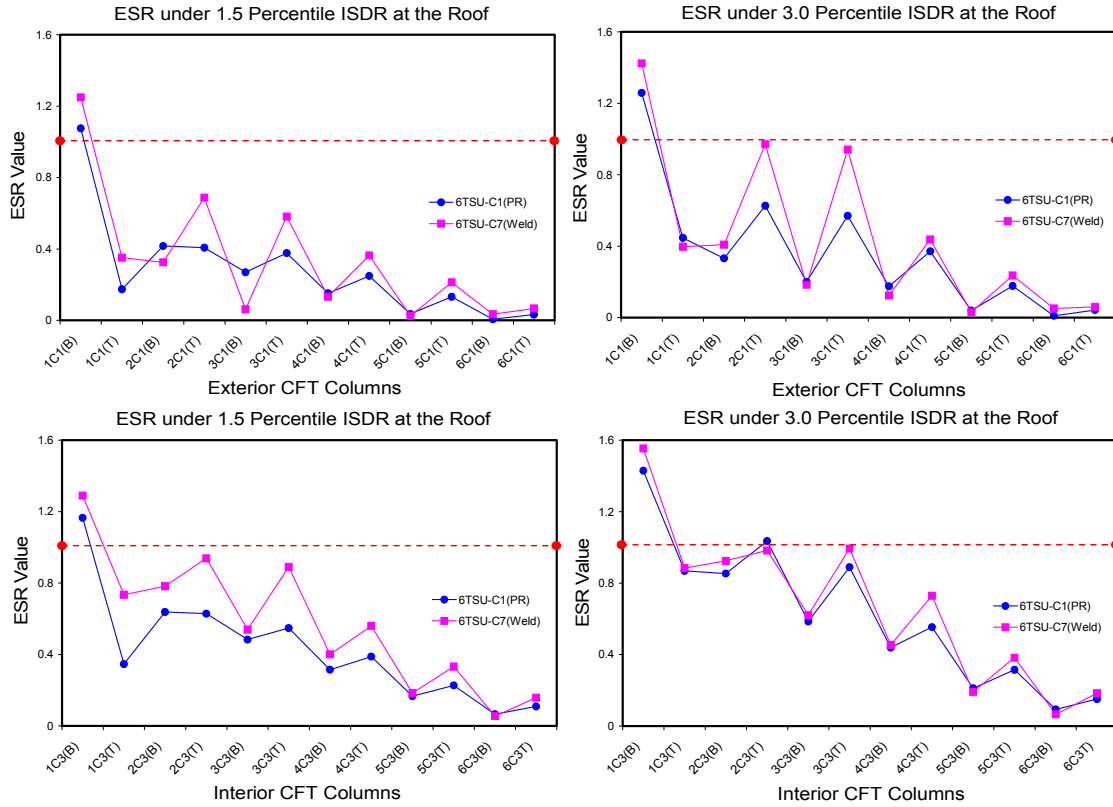


Figure 9.15 Comparisons of ESR under pushover loads (6TSU-C1 vs. 6TSU-C7)

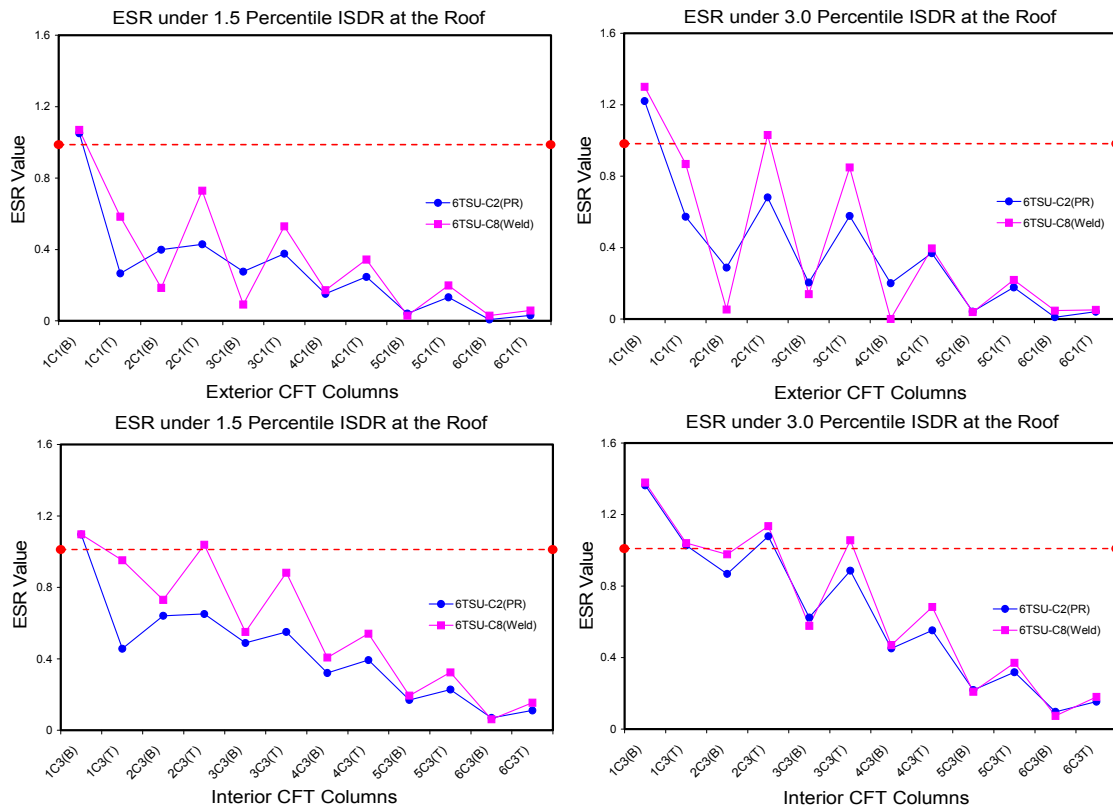


Figure 9.16 Comparisons of ESR under pushover loads (6TSU-C2 vs. 6TSU-C8)

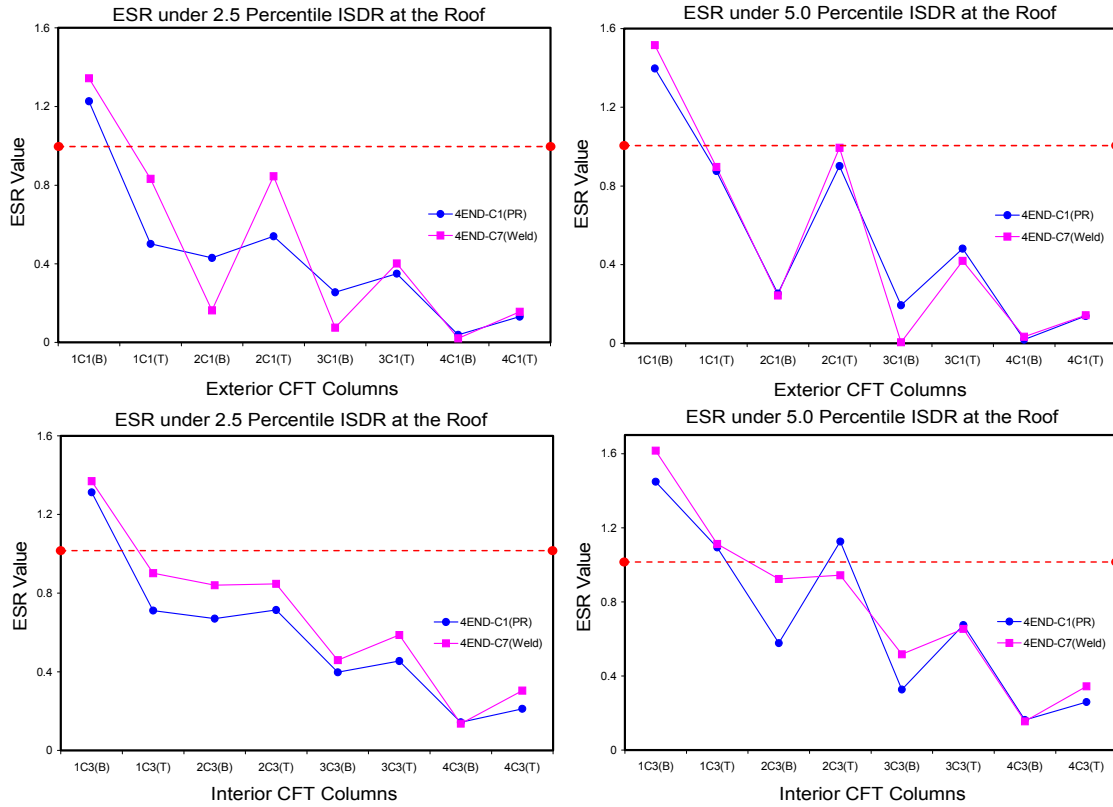


Figure 9.17 Comparisons of ESR under pushover loads (4END-C1 vs. 4END-C7)

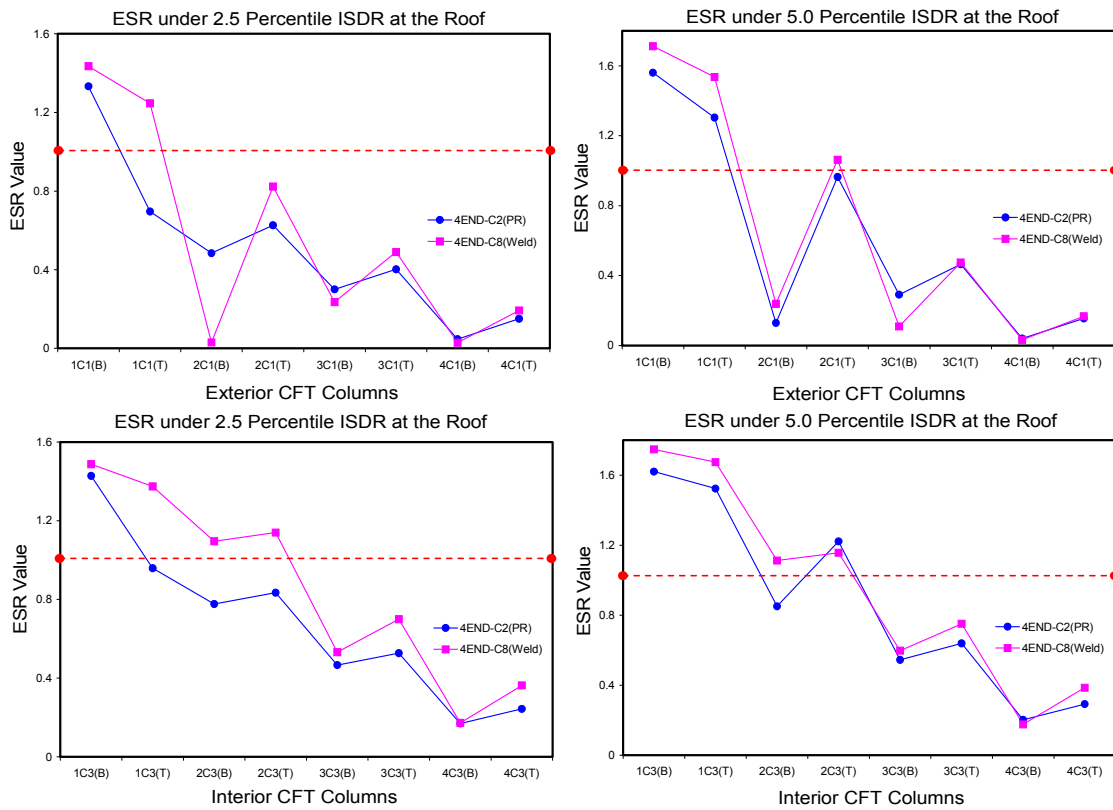


Figure 9.18 Comparisons of ESR under pushover loads (4END-C2 vs. 4END-C8)

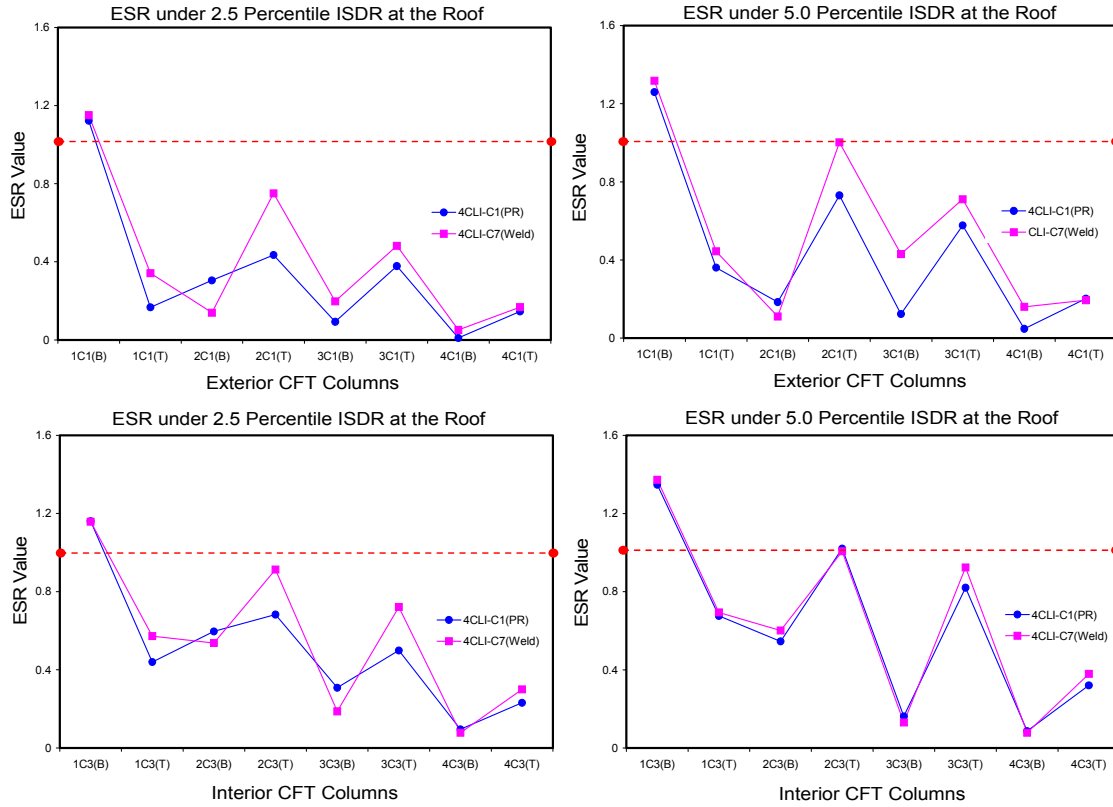


Figure 9.19 Comparisons of ESR under pushover loads (4CLI-C1 vs. 4CLI-C7)

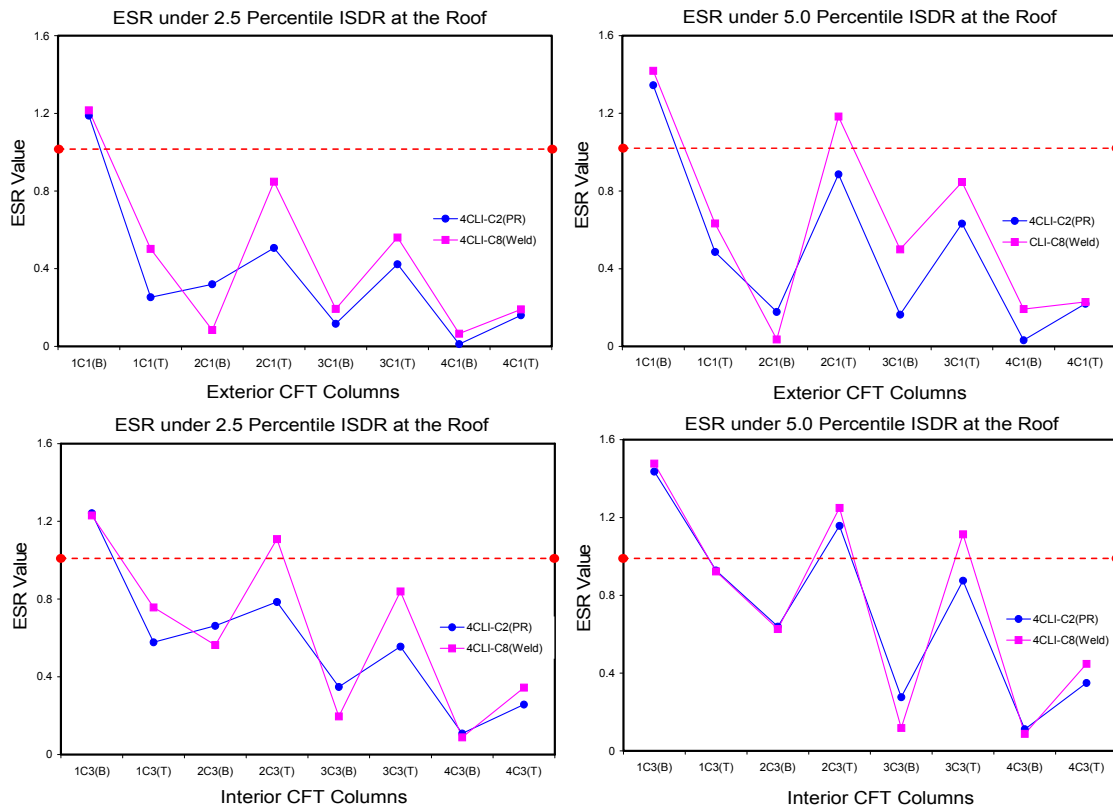


Figure 9.20 Comparisons of ESR under pushover loads (4CLI-C2 vs. 4CLI-C8)

Finally, the nonlinear dynamic analyses performed using 20 ground motions were evaluated with respect to their damage potential. ESR along the column lines were evaluated as shown in Figures 9.21 to 9.23. Rather than using the concept of performance levels as done for the pushover cases, ESR were calculated at the time when the maximum base shear force occurred. The most severe damage for the composite columns appears to correspond to this time step for the vast majority of cases.

Similarly to the results for the ESR evaluations performed for the pushover analyses, the most severe damage concentrated on the lower story levels. The column bases fail as their ESR exceeds 1.50. As expected, the frames with larger masses show larger ESR. From the damage evaluation for the interior columns, it can be seen that the ESR exceeded its limit values even at the third story level (Figure 9.21 and Figure 9.23). As for the pushover case, the weaker capacities of the CCFT columns as compared to the RCFT ones enabled the 6END-C2 model to have larger ESR than the 6END-C1 model.

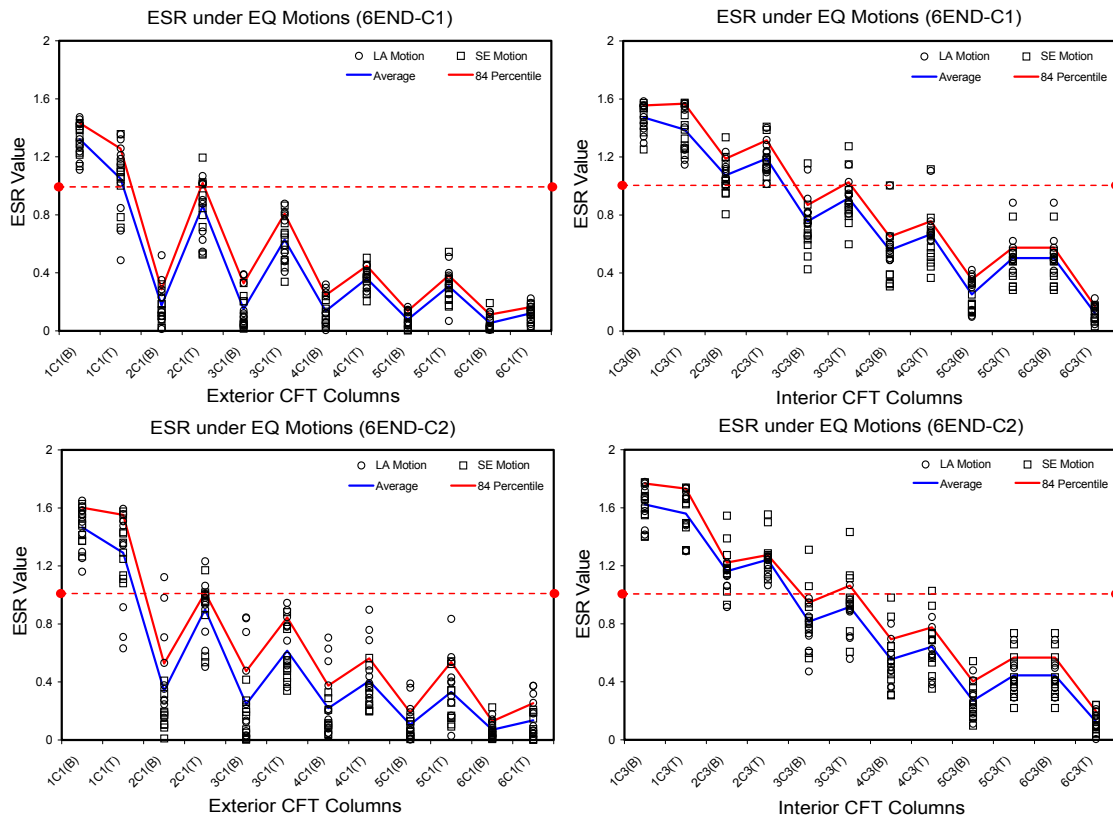


Figure 9.21 ESR under various ground motions (6END-C1 & 6END-C2)

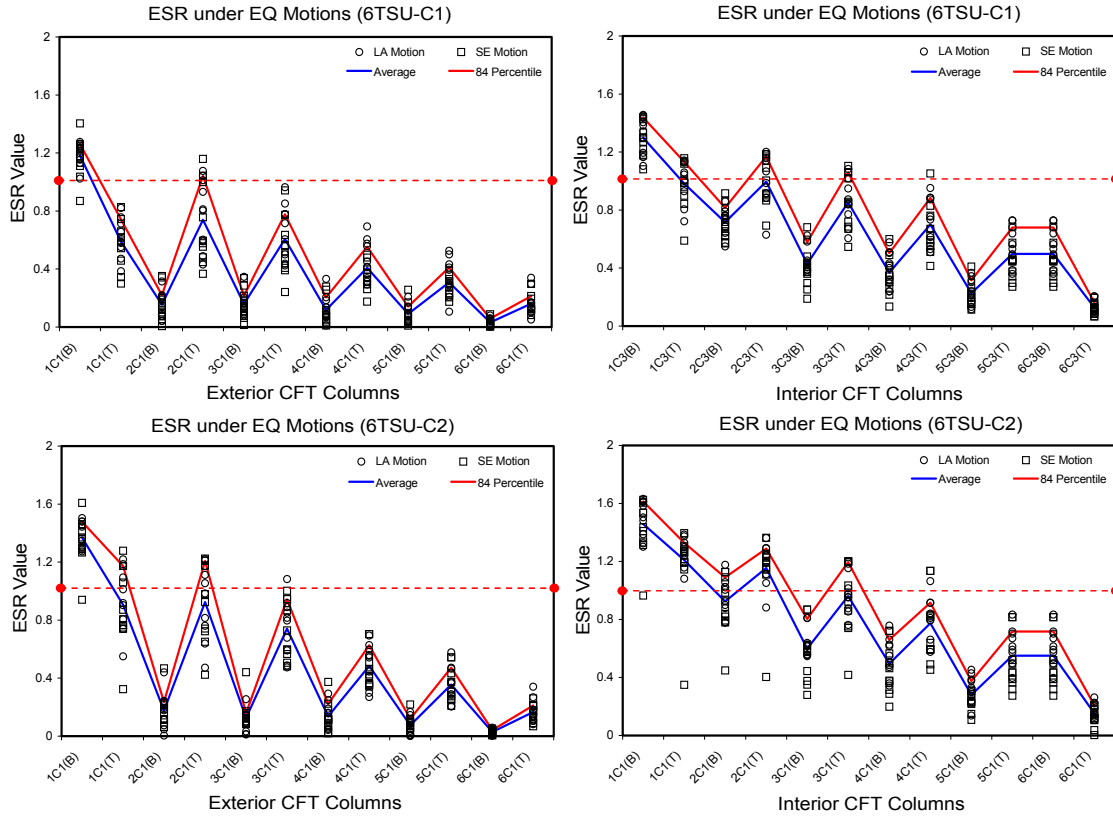


Figure 9.22 ESR under various ground motions (6TSU-C1 & 6TSU-C2)

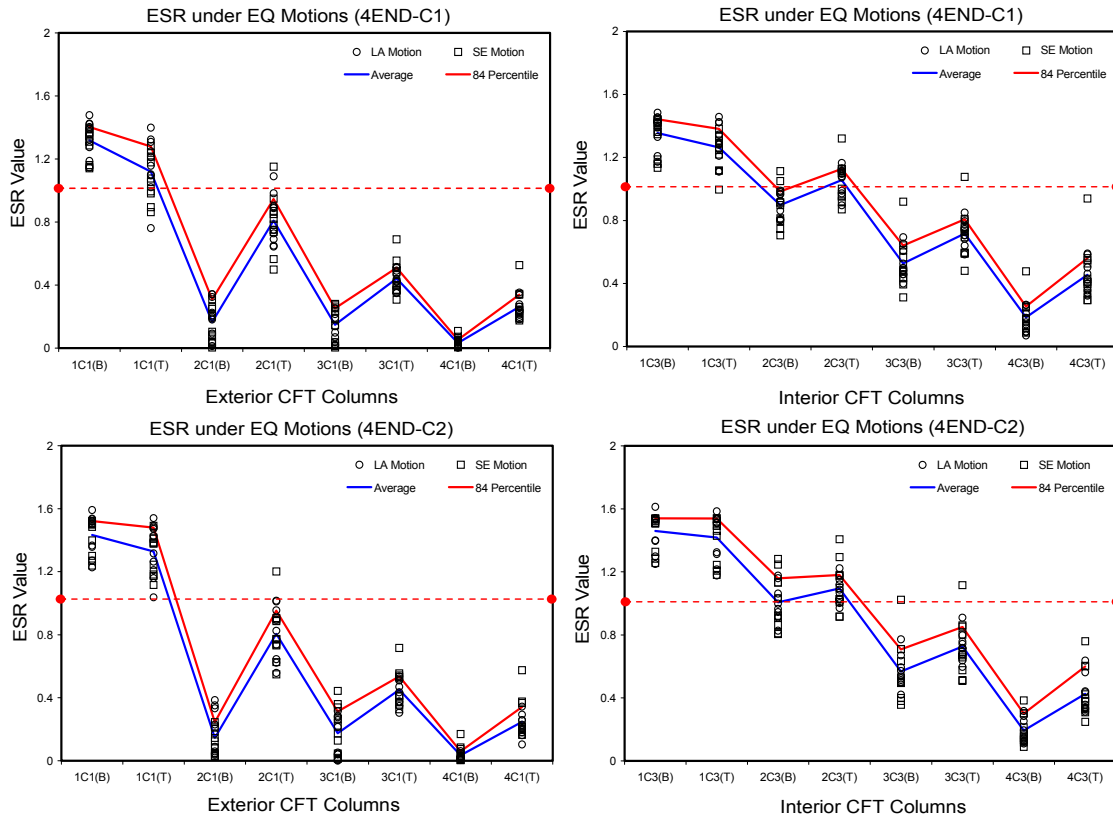


Figure 9.23 ESR under various ground motions (4END-C1 & 4END-C2)

9.4 Summary and Discussion

The damage evaluations for the composite moment frames were conducted by investigation of either strength or deformation capacity of the composite cross sections. The degree of structural damage in composite moment frames subjected to seismic loading was expressed as the ratios of the required member response to the member capacity. The required member response was obtained by the computational simulations for a series of composite moment frames. Damage ratios presented in this research were divided into elastic strength ratios (ESR) and inelastic curvature ductility ratios (ICDR). The basic member capacity to determine damage evaluations are defined as the limit state based on CFT cross sectional strength or ductility. The P-M interaction strength capacity for the composite section was utilized for ESR as the limit state, while the ductility capacity for the section deformation was utilized for ICDR.

Chapter 10

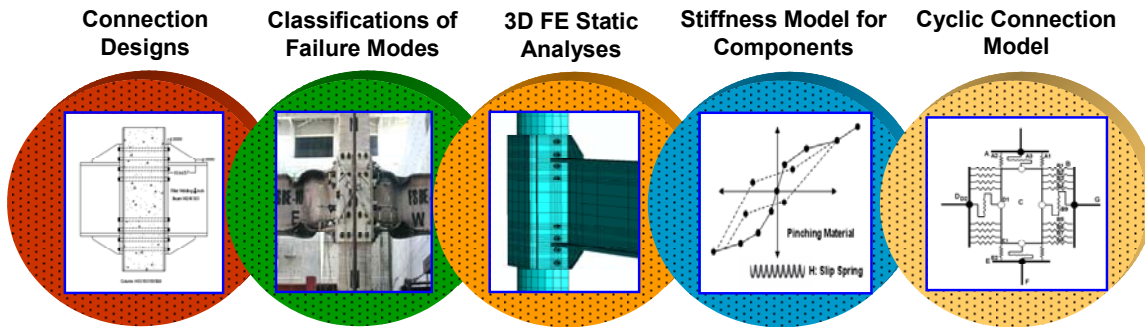
Summary and Conclusions

10.1 Summary

The two primary purposes of this dissertation were to develop new types of composite bolted connections utilizing smart materials and to assess the performance of these connections in low-rise composite moment frames. These objectives were achieved first through the development of moment-rotation curves for these PR connections utilizing refined 3D finite element analyses. These refined models led to simplified 2D joint elements capable of capturing the main components of response for these new connections. In the second step, the system performance was assessed through pushover and non-linear time history analyses of a series of low-rise frames.

The flowchart summarizing the research is shown as Figure 10.1. This approach was intended to provide an integrated approach that combined connection designs, failure modes, numerical models, frame design checks, computational nonlinear analyses, and performance evaluations. In order to illustrate these approaches systematically, the dissertation can be divided into two parts. Smart SMA PR-CFT connections were described in Chapters 3 to 6, while composite moment frames were described in Chapters 7 to 9. The first part includes design procedures, design strength models, failure modes, connection types, FE model analyses, and simplified 2D joint models related to smart SMA PR-CFT connections. The second part includes frame designs, nonlinear analyses, and damage evaluations for composite moment frames. A summary of the overall approach is given in Figure 10.1.

Part 1: Smart PR-CFT Connections



Part 2: Composite Moment Frames

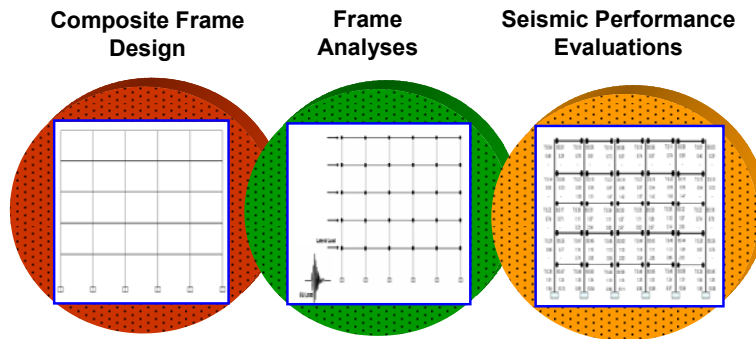


Figure 10.1 Summary of the overall procedures in the dissertation

In the first step in Part I (Fig. 10.1), end-plate, T-stub, and clip angle connections were designed using the 2001 AISC LRFD and 2005 AISC Seismic Provisions (ANSI/AISC 358-05, ANSI/AISC 341-05). These designs followed state-of-the-art design procedures based on assessing the strength of the different components and their governing failure modes. For example, the rectangular (RCFT) and circular concrete filled tube columns (CCFT) were designed following the P-M interaction diagrams generated based on the full plastic strength of the composite cross section (Chapter 3 and Appendix A).

In the second step, all possible failure modes for the proposed connections were studied and addressed based on their deformation and stiffness properties. This included the governing modes for connections with SMA tension bars running through the composite column (Chapter 4).

In the third step, 3D finite element (FE) analyses were performed in order to generate the monotonic behavior curves for smart SMA PR-CFT connections. These FE connection models incorporated material plasticity, surface interactions, contact elements,

bolt pretension, equation constraints, and symmetric boundary condition to provide as accurate and robust models as possible. The responses obtained were used to develop stiffness models for simple spring elements to be used in developing a 2D joint element suitable for full frame analyses (Chapter 5).

Numerical tests with the 2D simplified joint elements were performed using OpenSEES to simulate the cyclic behavior of smart SMA PR-CFT connections. Connection components were modeled as spring elements (Step 4) and the model extended to cyclic behavior (Step 5). One equivalent spring element including behavior from all connection components was formulated by assembling spring elements in either parallel or series. Different parametric effects were investigated with numerical simulations using this 2D joint element model (Chapter 6).

In the first step of Part 2, composite moment frames were designed in accordance with the *AISC 2005 Seismic Provisions* (AISC 2005 Seismic Provisions) and the *IBC 2003* (IBC 2003) for gravity loads and lateral loads respectively, for the loads prescribed by ASCE 7-05 (ASCE 2005). Perimeter moment resisting frame systems were used in the prototype 4 and 6 story buildings with either PR or welded connections. A total of 36 frames were studied with models that included the behavior of the panel zones by 2D simplified joint elements (Chapter 7).

In the second step of Part 2, nonlinear pushover analyses and nonlinear dynamic analyses were performed using the current version of the OPENSEES program. From the nonlinear pushover analyses, either monotonic behavior or cyclic behavior for all composite models subjected to the lateral loads was investigated (Chapter 8).

In the last step of Part 2, the structural damage was evaluated in accordance with the ratio of the required response to the member capacity. These structural damage evaluations were established through the elastic strength ratios (ESR) and the inelastic curvature ductility ratios (ICDR) in this research (Chapter 9).

10.2 Conclusions

The main conclusions of this research will be summarized in five subsections.

10.2.1 Smart SMA PR-CFT Connection Design

From the design results for the smart SMA PR-CFT connections (Chapters 3 and 4), the following conclusions were reached:

- All composite filled columns designed in this research satisfied the limits listed in the *2005 AISC Specification*. These designs showed that this approach is conservative and that linear interpolation based on obtaining a few points on the P-M interaction curve provides excellent match to the results generated by the a more complex fiber analysis with hardening materials.
- The strength models for PR connection components were capable of assessing the influence of slip and prying action of the bolts with more than sufficient accuracy for design.
- A refined composite panel zone models was developed. The strength of the composite panel zone was based on the superposition of the shear strengths of the steel and concrete materials, including the strength loss due to bolt holes in the column flanges. A similar approach was used to generate the stiffness of the panel zone.
- Careful identification and quantification of individual yielding/failure modes led to design governed by yielding of the girder, the intended governing mechanism for strong column-weak beam framing systems.
- The combination of steel and SMA bars should provide a good balance between energy dissipation and recentering capabilities. This requires careful consideration of the deformation characteristics of the two materials so that their size and placement within the connection maximizes their synergistic properties.

10.2.2 Numerical Analyses for Smart SMA PR-CFT Connections

Numerical analyses were performed using the ABAQUS and OPENSEES programs. From the results of the numerical analyses for smart SMA PR-CFT connections, the following conclusions were reached (Chapters 5 and 6):

- 3D finite element (FE) models that include nonlinear material properties, surface interactions and bolt pretension can be used to accurately simulate the monotonic behavior for PR-CFT connections if sufficient development time and computational resources are available. These types of analyses are required for the development of new systems but cannot be required for design.
- As expected, end-plate connections showed the largest strength and stiffness capacity as the lack of slip benefited their performance in these categories. T-stub and clip angle connections showed slip, which was extremely sensitive to the shear bolt alignment and clearance.
- The force distributions from the stem/angle leg into the flange were approximately uniform across the width of the T-stub/clip angle. Deformation models for the components were sensitive to bar pretension. Tension bars in the T-stub connections were not sufficient to fully develop an adequate plastic mechanism due to the large deformation in the thin stem. Inadvertent bending of the tension bars as the result of prying action in the clip angle reduced their capacity.
- Stress distributions indicated stress concentrations and severe deformations underneath the tension bar heads. Nevertheless, all PR-CFT connections showed ductile beam failure modes as the confining action of the CFT prevented brittle concrete failures.
- The cyclic behavior of smart SMA PR-CFT connections was generated using 2D joint element models on the OPENSEES program. Based on the results of 3D FE analyses, the stiffness models for the component behavior, including slippage, prying response, and force-deformation response were generated and assigned to spring elements. These spring elements were used to build a 2D joint element whose properties were extended to cover cyclic behavior, including the recentering effect from the SMA bars. These analytical predictions showed good agreement with cyclic test data for a variety of failure modes.

- It was concluded that both 2D and 3D numerical analyses could model sufficiently well the behavior of smart SMA PR-CFT connections so that the number of experimental tests needed to pre-qualify these connections could be minimized.

10.2.3 Composite Frame Design

From the results of the composite moment frame designs, the following conclusions were reached (Chapter 7):

- Composite moment frames were designed as either PR frames (C-PRMF) or special moment frames (C-SMF). C-PRMF were detailed for three types of smart SMA PR-CFT connection systems: end-plate, T-stub, or clip angle connections. The composite moment frames with end-plate connections provide the largest strength capacity, allow for the use of larger beam, and column sizes with a resulting increase in bay length.
- The design of the prototype buildings should be accompanied with advanced FE frame analyses in order to select adequate column and beam sections and check/satisfy all design limits.
- 2D numerical frame models were used for the nonlinear analyses. The exact behavior for the composite panel zone was simulated using 2D joint elements with a tri-linear backbone curve. The required information for this model such as initial slope, yield shear force, and ultimate shear force at the panel zone was provided by the strength model proposed by Wu et al. (2007).

10.2.4 Nonlinear Analyses for Frame Models

Pushover analyses and dynamic analyses with 20 ground motions were performed with OPENSEES. From the results of these analyses, the following conclusions were reached (Chapter 8):

- Both monotonic and cyclic pushover analyses utilizing the equivalent lateral load pattern used for design were carried out. Pushover curves plotted as the normalized shear force versus inter story drift ratio (ISDR) showed significant transition points: elastic range or proportional limit, full yielding of the cross-section, strength

hardening, ultimate strength, and strength degradation or stability limit. These limits were affected by member slenderness ratios and level of the gravity loads.

- Overall, the initial stiffness of the frames with welded connections was larger than that of those of the frames with PR connections. However, strength after reaching its maximum value deteriorated very rapidly because the welded connections were susceptible to brittle failure and P-Delta effects. In contrast, the use of flexible tension bars provided extra deformation capacity, so composite frames with PR connections showed more gradual strength degradation. The strength of the taller frames deteriorated more rapidly than that of the shorter frame because of the large P-Delta effect due to the heavier gravity loads.
- Composite moment frames with PR connections showed smaller residual displacements than those with welded connections due to the recentering effect. In addition, composite frames with PR connections showed a more gradual strength degradation. Overall, the envelope of the monotonic curves corresponded to that of the cyclic curves when the same models were compared.
- Based on the transition points in the monotonic pushover curves, three performance levels were defined: Design Point, Yield Point, and Ultimate Point. All frames were stable up to the yield point level. After reaching the Ultimate Point, plastic rotation increased significantly and concentrated on the lower levels. This led to severe deformations at the column bases eventually resulting in the complete plastification of the columns at these locations.
- The nonlinear dynamic analyses consisted of two suites of 20 earthquake ground motions with 2% probability of exceedence in 50 years for the western USA. Composite moment frames with welded connections showed the largest roof displacements. The outstanding energy dissipation properties of the PR connections resulted in lower drifts. The base shear forces were affected by lumped masses converted from the gravity loads, so the 6 story frames showed higher maximum base shears than the 4 story frames.
- Overall, maximum displacement, velocity, and pseudo-acceleration occurred at the roof. The occurrence time for each peak value subjected to the same ground motion

was slightly different and trailed the occurrence of the peak ground acceleration (PGA).

- Statistical distributions of the peak ISDR were obtained from the dynamic analyses. The peak ISDR showed the largest values at the first story level. They ISDR decreased as one moved up the structure. The position of the failure hinge points was symmetric with the center of the frames.

10.2.5 Seismic Performance and Damage Evaluation

Damage evaluations were conducted by comparing elastic strength ratios (ESR) and inelastic curvature ductility ratios (ICDR). From these results, the following conclusions were reached (Chapter 9):

- The specific levels to evaluate the building damage were determined from the ratios of the required member response to the corresponding member capacity. The value of the ESR was determined by the position of the required strength on the P-M domain with a simplified bilinear interpolation. ICDR levels were selected arbitrarily and changed according to the nominal yield curvature and the type of loading.
- All frame models were designed with a symmetric configuration and uniform gravity loads along all bays and stories. As a result, a regular distribution of the damage ratios was found along both the interior and the exterior column lines. The ESR for the interior columns were generally larger than those for the exterior columns. The high ESR were accompanied by high ICDR, so the members which underwent significant deformations showed larger values of both ESR and ICDR. The most severe damage occurred at the column bases.
- Welded frames are more susceptible to severe damage than PR frames at a reasonable range of the story drift because higher bending moments acting on the welded connections cause an increase of the damage ratios.
- Failure hinge mechanisms are related to the damage ratios. Yield failure hinges were generated at the ends of the column elements where ESR were more than unit value.
- Statistical approaches with 20 ground motion data were derived from the nonlinear dynamic analyses. ESR were calculated at the time when the peak base shear force occurs at the column bases. Similarly to ESR evaluations performed by the pushover

analyses. The most severe damage, which was expressed by a distribution with large ESR, were concentrated on the lower story levels.

10.3 Recommendations for Future Work

From the research conclusion presented in this dissertation, four original contributions to create innovative designs and integrated approaches for composite frame structures were suggested as summarized in Figure 10.2. Besides, some additional interesting items should be investigated in the future:

- In order to generalize the results described herein, the numerical analysis results should be compared with corresponding experimental test results. Limited comparisons between numerical models for T-stubs and angle connections developed based on experimental data (Swanson 1999) showed good results. However, more comparison work is necessary to generalize modeling methods suggested in this research.
- In spite of lots of structural advantages, more practical applications and experimental programs for composite PR connections are absolutely necessary.
- There is little work on probabilistic evaluation of composite moment frames. Performance levels based on the probabilistic approaches are not clearly defined in any design codes. More research in this area is necessary.

Research Contributions



Figure 10.2 Original contributions for this research

Appendix

The List of Appendix

Appendix A: Detailed Design Examples for CFT Columns

Appendix B: Design Examples and Failure Modes

Appendix C: Instrumentation

Appendix D: The Equivalent Lateral Force Procedures

Appendix E: Detail Design Examples for Panel Zones

Appendix F: Earthquake Ground Motions

Appendix A

Detailed Design Examples for CFT Columns

A-1: Introduction

Detailed calculation procedures for the P-M interaction diagram of CFT beam-columns in accordance with the *AISC 2005 Specifications* are presented in this Appendix. The basic background, including the necessary notation and basic calculations, were described in Chapter 3. Examples for CFT columns used in this research are summarized in Section A-2 section with four case-by-case procedures. The CFT column details are summarized in Table A.1. In addition, the P-M interaction diagram using a straight line interpolations between five points are described in Section A-3. The necessary equations to calculate these points are summarized in Tables A-2 and Table A-3.

Table A.1 The Summarization of the CFT columns

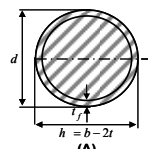
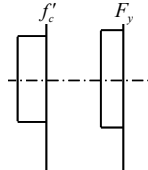
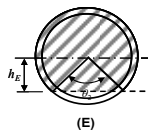
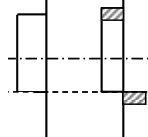
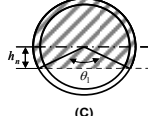
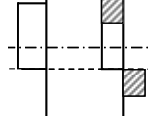
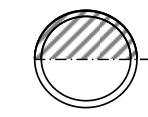
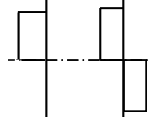
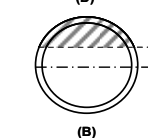
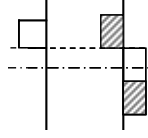
Column ID	Steel Section	d	t	F_y	f'_c
RCFT 16X16X500	HSS16X16X500	16	0.500	55	4
CCFT 18X500	HSS 18X500	18	0.500	55	4
RCFT 12X12X500	HSS 12X12X500	12	0.500	55	4
CCFT 14X500	HSS 14X500	14	0.500	55	4
RCFT 16X16X375	HSS 16X16X375	16	0.375	55	4
CCFT 18X375	HSS 18X375	18	0.375	55	4
RCFT 14X14X500	HSS 14X14X500	14	0.500	55	4
CCFT 16X500	HSS 16X500	16	0.500	55	4

Unit: kip and inch

Table A.2 Equations for the specific 5 points in the P-M interaction diagram
(RCFT columns)

Section		Stress Distribution	Point	Defining Equations
<p>(A)</p>			A	$P_A = A_s F_y + 0.85 f'_c A_c \quad M_A = 0$ $A_s = \text{Area of steel shape} \quad A_c = h_1 h_2 - 0.858 r_i^2$
<p>(E)</p>			E	$P_E = \frac{1}{2}(0.85 f'_c A_c) + 0.85 f'_c h_1 h_E + 4 F_y t_w h_E$ $M_E = M_{\max} - \Delta M_E \quad \Delta M_E = Z_{sE} F_y + \frac{1}{2} Z_{cE} (0.85 f'_c)$ $Z_{sE} = b h_E^2 - Z_{cE} \quad Z_{cE} = h_1 h_E^2 \quad h_E = \frac{h_n}{2} + \frac{d}{4}$
<p>(C)</p>			C	$P_C = 0.85 f'_c A_c \quad M_C = M_B$
<p>(D)</p>			D	$P_D = \frac{(0.85 f'_c A_c)}{2} \quad M_D = Z_s F_y + \frac{1}{2} Z_c (0.85 f'_c)$ $Z_s = b d^2 / 4 \quad Z_c = h_1 h_2^2 / 4 - 0.192 r_i^3$
<p>(B)</p>			B	$P_B = 0 \quad M_B = M_D - Z_{sn} F_y - \frac{1}{2} Z_{cn} (0.85 f'_c)$ $Z_{sB} = 2 t_w h_n^2 \quad Z_{cB} = h_1 h_n^2$ $h_n = \frac{(0.85 f'_c A_c)}{2(0.85 f'_c h_1 + 4 t_w F_y)} \leq \frac{h_2}{2}$

Table A.3 Equations for the specific 5 points in the P-M interaction diagram
(CCFT columns)

Section		Stress Distribution	Point	Defining Equations
 (A)			A	$P_A = A_s F_y + 0.85 f'_c A_c$ * $M_A = 0$ $A_c = (\pi h^2)/4$ $A_s = \pi r_m t$ $r_m = (d-t)/2$ $P_A = A_s F_y + 0.95 f'_c A_c$ (Loaded in only axial compression)
 (E)			E	$P_E = (0.85 f'_c A_c + F_y A_s) - \frac{1}{2} [F_y (d^2 - h^2) + \frac{1}{2} (0.85 f'_c) h^2] \left[\frac{\theta_2}{2} - \sin \frac{\theta_2}{2} \right]$ $M_E = Z_{sE} F_y + \frac{1}{2} Z_{cE} (0.85 f'_c)$ $h_E = \frac{h_n}{2} + \frac{d}{4}$ $Z_{sE} = \left(d^3 \sin^3 \left(\frac{\theta_2}{2} \right) \right) / 6 - Z_{cE}$ $Z_{cE} = \left(h^3 \sin^3 \left(\frac{\theta_2}{2} \right) \right) / 6$ $\theta_2 = \pi - 2 \arcsin \left(\frac{2h_E}{h} \right)$
 (C)			C	$P_C = 0.85 f'_c A_c$ $M_C = M_B$
 (D)			D	$P_D = (0.85 f'_c A_c) / 2$ $M_D = Z_s F_y + \frac{1}{2} Z_c (0.85 f'_c)$ $Z_s = d^3 / 6 - Z_c$ $Z_c = h^3 / 6$
 (B)			B	$P_B = 0$ $M_B = Z_{sB} F_y + \frac{1}{2} Z_{cB} (0.85 f'_c)$ $Z_{sB} = \left(d^3 \sin \left(\frac{\theta_1}{2} \right) \right) / 6 - Z_{cB}$ $Z_{cB} = \left(h^3 \sin \left(\frac{\theta_1}{2} \right) \right) / 6$ $\theta_1 = (0.026 K_c - 2 K_s) / (0.0848 K_c) + \sqrt{(0.026 K_c + 2 K_s)^2 + 0.857 K_c K_s} / (0.0848 K_c)$ $K_c = f'_c h^2$ $K_s = F_y r_m t$ $h_n = \frac{h}{2} \sin \left(\frac{\pi - \theta_1}{2} \right) \leq \frac{h}{2}$

A-2: Calculation Examples

Case 1: RCFT 16 X 16 X 500 Column

Develop an axial load-moment (P-M) envelope for a HSS 16X16X500 concrete filled with $f'_c = 4$ ksi strength. The effective length of the member is 12.5 ft. Assume A572 steel (Swanson 2002, Use the nominal stress value shown in Table 5.1: $F_y = 55$ ksi and $F_u = 73$ ksi). The units are kips and inches. Use the dimensions shown in Table A.1.

Limitation:

- 1) The cross-sectional area of the steel core shall comprise at least one percent of the total composite cross section.

$$A_s = 31.0 \text{ in.}^2 > (0.01) (16^2) = 2.56 \text{ in.}^2, \text{ (O.K.)}$$

Note that $\rho = \frac{31}{256} = 0.121$, or 12.1 % which is high ratio.

- 2) The slenderness of the tube wall is:

$$\left(\frac{t}{b}\right) = \frac{16 - 0.5}{0.5} = 31.0 \leq 2.26 \sqrt{\frac{E}{F_y}} = 2.26 \sqrt{\frac{29000}{55}} = 51.90 \text{ (O.K.)}$$

C1.1 Point A ($M_A=0$)

Determine the available compressive strength

$$P_o = A_s F_y + A_{sr} F_{yr} + 0.85 A_c f'_c$$

$$A_c = (b - 2 \cdot t)^2 = (16 - 2 \cdot 0.5)^2 = 225 \text{ in.}^2$$

$$P_o = A_s F_y + A_{sr} F_{yr} + 0.85 A_c f'_c = 31 \cdot 55 + 0 + 0.85 \cdot 225 \cdot 4 = 2,470 \text{ kips}$$

$$P_o = 2,470 \text{ kips}$$

$$C_3 = 0.6 + 2 \left(\frac{A_s}{A_c + A_s} \right) = 0.6 + 2 \left(\frac{35}{225 + 35} \right) = 0.87$$

$$I_s = \frac{d^4}{12} - \frac{(d - 2 \cdot t)^4}{12} = 1242 \text{ in}^4$$

$$I_c = \frac{(d - 2 \cdot t)^4}{12} = 4219 \text{ in}^4$$

$$E_c = 57000 \sqrt{f'_c} = 57000 \sqrt{4000} / 1000 = 3605 \text{ ksi}$$

$$EI_{eff} = E_s I_s + 0.5 E_s I_{sr} + C_3 E_c I_c$$

$$EI_{eff} = 29000 \cdot 1242 + 0.87 \cdot 3605 \cdot 4212 = 49.23 \cdot 10^6 \text{ kip-in}^2$$

$$P_e = \frac{\pi EI_{eff}}{(kL)^2} = \frac{(3.14159)^2 (49.23 \cdot 10^6)}{(1 \cdot 12.5 \cdot 12)^2} = 21593 \text{ kips}$$

$$\frac{P_o}{P_e} = \frac{2470}{21593} = 0.114 \leq 2.25 \quad \text{or} \quad \frac{P_e}{P_o} = \frac{21593}{2470} = 8.74 \geq 0.44$$

∴ Use EQ 3-1

$$P_n = P_o \left(0.658^{\left(\frac{P_o}{P_e} \right)} \right) = 2470 (0.658^{0.114}) = 2355 \text{ kips}$$

$$\phi_c P_n = 0.75 (2355) = 1766 \text{ kips}$$

C1.2 Point B ($P_B=0$)

Determine location of h_n

$$h_n = \frac{0.85 f'_c A_c}{2(0.85 f'_c h_1 + 4 t_w F_y)} \leq \frac{h_2}{2}$$

$$h_n = \frac{0.85 \cdot 4 \cdot 225}{2(0.85 \cdot 4 \cdot (16 - 2 \cdot 0.5) + 4 \cdot 0.5 \cdot 55)} = 2.37 \text{ in} \leq \frac{16}{2} = 8 \text{ in (O.K.)}$$

$$Z_s = 181 \text{ in}^3$$

$$Z_c = \frac{h_1 h_2^2}{4} - 0.192 r_i^3 = \frac{(16 - 2 \cdot 0.5)^3}{4} - 0 = 843.75 \text{ in}^3$$

$$M_D = Z_s F_y + \frac{1}{2} Z_c (0.85 f'_c) = 181 \cdot 55 + \frac{1}{2} \cdot 843.75 (0.85 \cdot 4) = 11,389.40 \text{ kip-in}$$

$$Z_{sB} = 2t_w h_n^2 = 2 \cdot 0.5 \cdot 2.37^2 = 5.65 \text{ in}^3$$

$$Z_{cB} = h_1 h_n^2 = (16 - 2 \cdot 0.5)(2.37)^2 = 84.67 \text{ in}^3$$

$$M_B = M_D - Z_{sB} F_y - \frac{1}{2} Z_{cB} (0.85 f'_c)$$

$$M_B = 11,389.40 - 5.65 \cdot 55 - \frac{1}{2} 84.67 (0.85 \cdot 4) = 10,935 \text{ kip-in}$$

$$\phi_B M_B = 0.9 \cdot 10,935 = 9,841.51 \text{ kip-in}$$

C1.3 Point C ($M_C = M_B$; $P_C = 0.85 f'_c A_c$)

$$P_C = (0.85 f'_c) A_c = 225(0.85 \cdot 4) = 765 \text{ kips}$$

$$M_C = M_B = 10,935 \text{ kip-in}$$

C1.4 Point D

$$P_C = \frac{(0.85 f'_c) A_c}{2} = \frac{225(0.85 \cdot 4)}{2} = 382.5 \text{ kips}$$

$$M_D = 11,389.40 \text{ kip-in (See computations for Point B)}$$

C1.5 Point E

$$h_E = \frac{h_n}{2} + \frac{d}{4} = \frac{2.37}{2} + \frac{16}{4} = 5.19 \text{ in}$$

$$P_E = \frac{1}{2} (0.85 f'_c) A_c + 0.85 f'_c h_1 h_E + 4 F_y t_w h_E$$

$$P_E = \frac{1}{2} (0.85 \cdot 4) \cdot 225 + 0.85 \cdot 4 \cdot 15 \cdot 5.19 + 4 \cdot 55 \cdot 0.5 \cdot 5.19 = 1,217.75 \text{ kips}$$

$$Z_{cE} = h_1 h_E^2 = (15)(5.19)^2 = 404.05 \text{ in}^3$$

$$Z_{sE} = b h_E^2 - Z_{cE} = (16)(5.19)^2 - 404.05 = 26.90 \text{ in}^3$$

$$\Delta M_E = Z_{sE} F_y + \frac{1}{2} Z_{cE} (0.85 f'_c) = 26.90 \cdot 55 + \frac{1}{2} \cdot 404.05 \cdot 0.85 \cdot 4 = 2,166 \text{ kip-in}$$

$$M_E = M_D - \Delta M_E = 9,222.78 \text{ kip-in}$$

The results are summarized in Section A-3.

Case 2: CCFT 18 X 500 Column

Develop an axial load-moment (P-M) envelope for a round HSS 18X500 concrete filled with $f'_c = 4$ ksi strength. The effective length of the member is 12.5 ft. Assume A572 steel (Design Strength: $F_y = 55$ ksi and $F_u = 73$ ksi). The units are kips and inches. Use the dimensions shown in Table A.1.

Basic Geometrical Property:

$$d = 18 \text{ in}$$

$$t = 0.5 \text{ in}$$

$$h = d - 2t = 17 \text{ in}$$

$$r_m = \frac{(d-t)}{2} = 8.75 \text{ in}$$

$$A_s = 2\pi \cdot r_m \cdot t = 27.49 \text{ in}^2$$

$$A_c = \frac{\pi h^2}{4} = 226.98 \text{ in}^2$$

$$A_g = A_s + A_c = 254.47 \text{ in}^2$$

$$E_c = 57000\sqrt{f'_c} = 57000\sqrt{4000}/1000 = 3605 \text{ ksi}$$

$$I_s = \frac{\pi}{64} [d^4 - (d-2t)^4] = 1053 \text{ in}^4$$

$$I_c = \frac{\pi}{64} (d-2t)^4 = 4100 \text{ in}^4$$

$$I_g = I_s + I_c = 5153 \text{ in}^4$$

Limits:

- 3) The cross-sectional area of the steel core shall comprise at least one percent of the total composite cross section.

$$\frac{A_s}{A_s + A_c} = \frac{27.49}{27.49 + 226.98} = 0.108 \geq 0.01 \text{ (O.K.)}$$

4) The slenderness of the tube wall is:

$$\left(\frac{t}{b}\right) = \frac{18 - 0.5}{0.5} = 35.0 \leq 0.15 \left(\frac{E_s}{F_y}\right) = 0.15 \left(\frac{29000}{55}\right) = 79.10 \text{ (O.K.)}$$

C2.1 Point A ($M_A=0$)

Determine the available compressive strength

$$C_2 = 0.95$$

$$C_3 = \min \left[0.9, 0.6 + 2 \cdot \left(\frac{A_s}{A_c + A_s} \right) \right] = 0.826$$

$$P_o = A_s F_y + A_{sr} F_{yr} + C_2 A_c f'_c$$

$$EI_{eff} = E_s I_s + 0.5 E_s I_{sr} + C_3 E_c I_c$$

$$P_o = A_s F_y + A_{sr} F_{yr} + C_2 A_c f'_c = 27.49 \cdot 55 + 0 + 0.95 \cdot 226.98 \cdot 4 = 2374.41 \text{ kips}$$

$$P_o = 2374.41 \text{ kips}$$

$$EI_{eff} = E_s I_s + 0.5 E_s I_{sr} + C_3 E_c I_c$$

$$EI_{eff} = 29000 \cdot 1053 + 0.826 \cdot 3605 \cdot 4100 = 42.75 \cdot 10^6 \text{ kip-in}^2$$

$$P_e = \frac{\pi EI_{eff}}{(kL)^2} = \frac{(3.14159)^2 (42.75 \cdot 10^6)}{(1 \cdot 12.5 \cdot 12)^2} = 18750 \text{ kips}$$

$$\frac{P_o}{P_e} = \frac{2374.41}{18750} = 0.127 \leq 2.25 \text{ or } \frac{P_e}{P_o} = \frac{18750}{2374.41} = 7.90 \geq 0.44, \lambda = \sqrt{\frac{P_o}{P_e}} = 0.356$$

∴ Use EQ 3-1

$$P_n = P_o \left(0.658 \left(\frac{P_o}{P_e} \right) \right) = 2374.41 (0.658^{0.127}) = 2251.50 \text{ kips}$$

$$\phi_c P_n = 0.75 (2251.50) = 1688.66 \text{ kips}$$

C2.2 Point B ($P_B=0$)

From definitions of Point C in Table A-3:

$$K_c = f'_c h^2 = 4 \cdot 17^2 = 1156 \text{ kips}$$

$$K_s = F_y r_m t = 55 \cdot 8.75 \cdot 0.5 = 240.625 \text{ kips}$$

$$\theta = \frac{0.0260 \cdot K_c - 2 \cdot K_s}{0.0848 \cdot K_c} + \sqrt{\frac{(0.0260 \cdot K_c + 2 \cdot K_s)^2 + 0.857 \cdot K_c \cdot K_s}{0.0848 \cdot K_c}}$$

$$\theta = \theta_1 = 2.61 \text{ rad} = 149.62 \text{ deg}$$

$$Z_{cB} = \left(h^3 \sin\left(\frac{\theta_1}{2}\right) \right) / 6 = 735.35 \text{ in}^3$$

$$Z_{sB} = \left(d^3 \sin\left(\frac{\theta_1}{2}\right) \right) / 6 - Z_{cB} = 137.55 \text{ in}^3$$

$$M_B = Z_{sB} F_y + \frac{1}{2} Z_{cB} (0.85 f'_c) = 8815.36 \text{ kip-in}$$

$$\phi_b M_B = 7933.83 \text{ kip-in}$$

C2.3 Point C

From calculations for Point B (above):

$$P_C = (0.85 f'_c) A_c = 771.73 \text{ kips}$$

$$M_C = M_B = 8815.36 \text{ kip-in}$$

C2.4 Point D

$$P_D = \frac{(0.85 f'_c A_c)}{2} = 385.87 \text{ kips}$$

$$Z_c = \frac{h^3}{6} = 818.83 \text{ in}^3$$

$$Z_s = \frac{d^3}{6} - Z_c = 153.17 \text{ in}^3$$

$$M_D = Z_s F_y + \frac{1}{2} Z_c (0.85 f'_c) = 9816.18 \text{ kip-in}$$

C2.5 Point E

$$h_E = \frac{h_n}{2} + \frac{d}{4} = 5.37 \text{ in}$$

$$\theta = \theta_2 = \pi - 2 \arcsin\left(\frac{2h_E}{h}\right) = 1.77 \text{ rad} = 101.41 \text{ deg}$$

$$Z_{cE} = \left(h^3 \sin^3\left(\frac{\theta_2}{2}\right) \right) / 6 = 381.69 \text{ in}^3$$

$$Z_{sE} = \left(d^3 \sin^3\left(\frac{\theta_2}{2}\right) \right) / 6 - Z_{cE} = 71.40 \text{ in}^3$$

$$P_E = (0.85 f'_c A_c + F_y A_s) - \frac{1}{2} \left[F_y (d^2 - h^2) + \frac{1}{2} (0.85 f'_c) h^2 \right] \left[\frac{\theta_2}{2} - \sin \frac{\theta_2}{2} \right] = 1803.21 \text{ kips}$$

$$M_E = Z_{sE} F_y + \frac{1}{2} Z_{cE} (0.85 f'_c) = 4575.75 \text{ kip-in}$$

Case 3: RCFT 12 X 12 X 500 Column

Develop an axial load-moment (P-M) envelope for a HSS 12X12X500 concrete filled with $f'_c = 4$ ksi strength. The effective length of the member is 12.5 ft. Assume A572 steel (Design Strength: $F_y = 55$ ksi and $F_u = 73$ ksi). The units are kips and inches. Use the dimensions shown in Table A.1.

Limitation:

- 5) The cross-sectional area of the steel core shall comprise at least one percent of the total composite cross section.

$$A_s = 23.0 \text{ in.}^2 > (0.01) (12^2) = 1.44 \text{ in.}^2, \text{ (O.K.)}$$

Note that $\rho = \frac{23}{144} = 0.160$, or 16.0 % which is high ratio.

- 6) The slenderness of the tube wall is:

$$\left(\frac{t}{b}\right) = \frac{12 - 0.5}{0.5} = 23.0 \leq 2.26 \sqrt{\frac{E}{F_y}} = 2.26 \sqrt{\frac{29000}{55}} = 51.90 \text{ (O.K.)}$$

C3.1 Point A ($M_A=0$)

Determine the available compressive strength

$$P_o = A_s F_y + A_{sr} F_{yr} + 0.85 A_c f'_c$$

$$A_c = (b - 2 \cdot t)^2 = (12 - 2 \cdot 0.5)^2 = 121 \text{ in}^2$$

$$P_o = A_s F_y + A_{sr} F_{yr} + 0.85 A_c f'_c = 23 \cdot 55 + 0 + 0.85 \cdot 121 \cdot 4 = 1676.40 \text{ kips}$$

$$P_o = 1676.40 \text{ kips}$$

$$C_3 = 0.6 + 2 \left(\frac{A_s}{A_c + A_s} \right) = 0.6 + 2 \left(\frac{23}{121 + 23} \right) = 0.920$$

$$I_s = \frac{d^4}{12} - \frac{(d - 2 \cdot t)^4}{12} = \frac{12^4}{12} - \frac{(12 - 2 \cdot 0.5)^4}{12} = 508 \text{ in}^4$$

$$I_c = \frac{(d - 2 \cdot t)^4}{12} = \frac{(12 - 2 \cdot 0.5)^4}{12} = 1220 \text{ in}^4$$

$$E_c = 57000 \sqrt{f'_c} = 57000 \sqrt{4000} / 1000 = 3605 \text{ ksi}$$

$$EI_{eff} = E_s I_s + 0.5 E_s I_{sr} + C_3 E_c I_c$$

$$EI_{eff} = 29000 \cdot 508 + 0.92 \cdot 3605 \cdot 1220 = 18.78 \cdot 10^6 \text{ kip-in}^2$$

$$P_e = \frac{\pi EI_{eff}}{(kL)^2} = \frac{(3.14159)^2 (18.78 \cdot 10^6)}{(1 \cdot 12.5 \cdot 12)^2} = 8237 \text{ kips}$$

$$\frac{P_o}{P_e} = \frac{1676.40}{8237} = 0.203 \leq 2.25 \quad \text{or} \quad \frac{P_e}{P_o} = \frac{21593}{2470} = 4. \geq 0.44$$

∴ Use EQ 3-1

$$P_n = P_o \left(0.658 \left(\frac{P_o}{P_e} \right) \right) = 1676.40 (0.658^{0.203}) = 1539.60 \text{ kips}$$

$$\phi_c P_n = 0.75 (1539.60) = 1154.69 \text{ kips}$$

C3.2 Point B ($P_B=0$)

Determine location of h_n

$$h_n = \frac{0.85 f'_c A_c}{2(0.85 f'_c h_1 + 4 t_w F_y)} \leq \frac{h_2}{2}$$

$$h_n = \frac{0.85 \cdot 4 \cdot 121}{2(0.85 \cdot 4 \cdot (12 - 2 \cdot 0.5) + 4 \cdot 0.5 \cdot 55)} = 1.40 \text{ in} \leq \frac{12}{2} = 6 \text{ in (O.K.)}$$

$$Z_s = 99.30 \text{ in}^3$$

$$Z_c = \frac{h_1 h_2^2}{4} - 0.192 r_i^3 = \frac{(16 - 2 \cdot 0.5)^3}{4} - 0 = 332.75 \text{ in}^3$$

$$M_D = Z_s F_y + \frac{1}{2} Z_c (0.85 f'_c) = 99.30 \cdot 55 + \frac{1}{2} \cdot 332.75 (0.85 \cdot 4) = 6027.38 \text{ kip-in}$$

$$Z_{sB} = 2 t_w h_n^2 = 2 \cdot 0.5 \cdot 1.40^2 = 1.96 \text{ in}^3$$

$$Z_{cB} = h_1 h_n^2 = (12 - 2 \cdot 0.5)(1.40)^2 = 42.21 \text{ in}^3$$

$$M_B = M_D - Z_{sB} F_y - \frac{1}{2} Z_{cB} (0.85 f'_c)$$

$$M_B = 6027.38 - 1.96 \cdot 55 - \frac{1}{2} 42.21 (0.85 \cdot 4) = 5848.30 \text{ kip-in}$$

$$\phi_B M_B = 0.9 \cdot 5838.30 = 5263.47 \text{ kip-in}$$

C3.3 Point C ($M_C = M_B$; $P_C = 0.85 f'_c A_c$)

$$P_C = (0.85 f'_c) A_c = 121(0.85 \cdot 4) = 411.40 \text{ kips}$$

$$M_C = M_B = 5848.30 \text{ kip-in}$$

C3.4 Point D

$$P_C = \frac{(0.85 f'_c) A_c}{2} = \frac{121(0.85 \cdot 4)}{2} = 205.70 \text{ kips}$$

$$M_D = 6027.28 \text{ kip-in (See computations for Point B)}$$

C3.5 Point E

$$h_E = \frac{h_n}{2} + \frac{d}{4} = \frac{1.40}{2} + \frac{12}{4} = 3.70 \text{ in}$$

$$P_E = \frac{1}{2} (0.85 f'_c) A_c + 0.85 f'_c h_1 h_E + 4 F_y t_w h_E$$

$$P_E = \frac{1}{2} (0.85 \cdot 4) \cdot 121 + 0.85 \cdot 4 \cdot 11 \cdot 3.70 + 4 \cdot 55 \cdot 0.5 \cdot 3.70 = 750.75 \text{ kips}$$

$$Z_{cE} = h_1 h_E^2 = (11)(3.70)^2 = 150.41 \text{ in}^3$$

$$Z_{sE} = b h_E^2 - Z_{cE} = (11)(3.70)^2 - 150.41 = 13.67 \text{ in}^3$$

$$\Delta M_E = Z_{sE} F_y + \frac{1}{2} Z_{cE} (0.85 f'_c) = 13.67 \cdot 55 + \frac{1}{2} \cdot 150.47 \cdot 0.85 \cdot 4 = 1007.32 \text{ kip-in}$$

$$M_E = M_D - \Delta M_E = 5019.44 \text{ kip-in}$$

The results are summarized in Section A-3.

Case 4: CCFT 14 X 500 Column

Develop an axial load-moment (P-M) envelope for a round HSS 14X500 concrete filled with $f'_c = 4$ ksi strength. The effective length of the member is 12.5 ft. Assume A572 steel (Design Strength: $F_y = 55$ ksi and $F_u = 73$ ksi). The units are kips and inches. Use the dimensions shown in Table A.1.

Basic Geometrical Property:

$$d = 14 \text{ in}$$

$$t = 0.5 \text{ in}$$

$$h = d - 2t = 13 \text{ in}$$

$$r_m = \frac{(d-t)}{2} = 6.75 \text{ in}$$

$$A_s = 2\pi \cdot r_m \cdot t = 21.21 \text{ in}^2$$

$$A_c = \frac{\pi h^2}{4} = 132.73 \text{ in}^2$$

$$A_g = A_s + A_c = 153.94 \text{ in}^2$$

$$E_c = 57000\sqrt{f'_c} = 57000\sqrt{4000}/1000 = 3605 \text{ ksi}$$

$$I_s = \frac{\pi}{64} [d^4 - (d-2t)^4] = 483.76 \text{ in}^4$$

$$I_c = \frac{\pi}{64} (d-2t)^4 = 1401.98 \text{ in}^4$$

$$I_g = I_s + I_c = 1885.74 \text{ in}^4$$

Limits:

- 7) The cross-sectional area of the steel core shall comprise at least one percent of the total composite cross section.

$$\frac{A_s}{A_s + A_c} = \frac{21.21}{21.21 + 132.73} = 0.138 \geq 0.01 \text{ (O.K.)}$$

8) The slenderness of the tube wall is:

$$\left(\frac{t}{b}\right) = \frac{14 - 0.5}{0.5} = 27.0 \leq 0.15 \left(\frac{E_s}{F_y}\right) = 0.15 \left(\frac{29000}{55}\right) = 79.10 \text{ (O.K.)}$$

C4.1 Point A ($M_A=0$)

Determine the available compressive strength

$$C_2 = 0.95$$

$$C_3 = \min \left[0.9, 0.6 + 2 \cdot \left(\frac{A_s}{A_c + A_s} \right) \right] = 0.876$$

$$P_o = A_s F_y + A_{sr} F_{yr} + C_2 A_c f'_c$$

$$EI_{eff} = E_s I_s + 0.5 E_s I_{sr} + C_3 E_c I_c$$

$$P_o = A_s F_y + A_{sr} F_{yr} + C_2 A_c f'_c = 21.21 \cdot 55 + 0 + 0.95 \cdot 132.73 \cdot 4 = 1617.60 \text{ kips}$$

$$P_o = 1617.60 \text{ kips}$$

$$EI_{eff} = E_s I_s + 0.5 E_s I_{sr} + C_3 E_c I_c$$

$$EI_{eff} = 29000 \cdot 483.76 + 0.876 \cdot 3605 \cdot 1401.98 = 18.46 \cdot 10^6 \text{ kip-in}^2$$

$$P_e = \frac{\pi EI_{eff}}{(kL)^2} = \frac{(3.14159)^2 (18.46 \cdot 10^6)}{(1 \cdot 12.5 \cdot 12)^2} = 8096 \text{ kips}$$

$$\frac{P_o}{P_e} = \frac{1617.60}{8096} = 0.200 \leq 2.25 \text{ or } \frac{P_e}{P_o} = \frac{8096}{1617.60} = 5.00 \geq 0.44, \lambda = \sqrt{\frac{P_o}{P_e}} = 0.447$$

∴ Use EQ 3-1

$$P_n = P_o \left(0.658 \left(\frac{P_o}{P_e} \right) \right) = 1617.60 (0.658^{0.2}) = 1487.52 \text{ kips}$$

$$\phi_c P_n = 0.75(1487.52) = 1115.64 \text{ kips}$$

C4.2 Point B ($P_B=0$)

From definitions of Point C in Table A-3:

$$K_c = f'_c h^2 = 4 \cdot 13^2 = 676 \text{ kips}$$

$$K_s = F_y r_m t = 55 \cdot 6.75 \cdot 0.5 = 185.625 \text{ kips}$$

$$\theta = \frac{0.0260 \cdot K_c - 2 \cdot K_s}{0.0848 \cdot K_c} + \sqrt{\frac{(0.0260 \cdot K_c + 2 \cdot K_s)^2 + 0.857 \cdot K_c \cdot K_s}{0.0848 \cdot K_c}}$$

$$\theta = \theta_1 = 2.70 \text{ rad} = 154.78 \text{ deg}$$

$$Z_{cB} = \left(h^3 \sin\left(\frac{\theta_1}{2}\right) \right) / 6 = 340.54 \text{ in}^3$$

$$Z_{sB} = \left(d^3 \sin\left(\frac{\theta_1}{2}\right) \right) / 6 - Z_{cB} = 84.79 \text{ in}^3$$

$$M_B = Z_{sB} F_y + \frac{1}{2} Z_{cB} (0.85 f'_c) = 5242.10 \text{ kip-in}$$

$$\phi_b M_B = 0.9 \cdot 5242.10 = 4717.80 \text{ kip-in}$$

C4.3 Point C

From calculations for Point B (above):

$$P_C = (0.85 f'_c) A_c = 451.28 \text{ kips}$$

$$M_C = M_B = 5242.10 \text{ kip-in}$$

C4.4 Point D

$$P_D = \frac{(0.85 f'_c A_c)}{2} = 225.64 \text{ kips}$$

$$Z_c = \frac{h^3}{6} = 366.17 \text{ in}^3$$

$$Z_s = \frac{d^3}{6} - Z_c = 84.79 \text{ in}^3$$

$$M_D = Z_s F_y + \frac{1}{2} Z_c (0.85 f'_c) = 5636.65 \text{ kip-in}$$

C4.5 Point E

$$h_E = \frac{h_n}{2} + \frac{d}{4} = 3.96 \text{ in}$$

$$\theta = \theta_2 = \pi - 2 \arcsin\left(\frac{2h_E}{h}\right) = 1.83 \text{ rad} = 104.90 \text{ deg}$$

$$Z_{cE} = \left(h^3 \sin^3\left(\frac{\theta_2}{2}\right) \right) / 6 = 182.90 \text{ in}^3$$

$$Z_{sE} = \left(d^3 \sin^3\left(\frac{\theta_2}{2}\right) \right) / 6 - Z_{cE} = 45.54 \text{ in}^3$$

$$P_E = (0.85 f'_c A_c + F_y A_s) - \frac{1}{2} [F_y (d^2 - h^2) + \frac{1}{2} (0.85 f'_c) h^2] \left[\frac{\theta_2}{2} - \sin \frac{\theta_2}{2} \right] = 1233.46 \text{ kips}$$

$$M_E = Z_{sE} F_y + \frac{1}{2} Z_{cE} (0.85 f'_c) = 2815.46 \text{ kip-in}$$

The calculations for other four cases were repeated with the same procedures mentioned above, so the procedures to calculate five points for other composite column cases were omitted. Instead, all results for five points in P-M interaction diagrams are summarized in Table A-4.

Table A.4 All calculation results for five points in P-M interaction diagram

Point	HSS 16X16X500		HSS 18X500		HSS 12X12X500		HSS 14X500		HSS 16X16X375		HSS 18X375		HSS 14X14X500		HSS 16X500	
	P	M	P	M	P	M	P	M	P	M	P	M	P	M	P	M
(A)	2470	0	2374	0	1676	0	1618	0	2079	0	1936	0	2060	0	1940	0
(B)	0	10935	0	8815	0	5848	0	5242	0	8413	0	6688	0	8130	0	6915
(C)	765	10935	771	8815	411	5848	451	5242	791	8413	795	6688	575	8130	601	6915
(D)	383	11389	386	9816	206	6027	226	5636	395	9062	397	7862	287	8455	300	7565
(E)	1218	2166	1803	4576	751	5019	1233	2815	1130	7051	1589	3335	971	6941	1507	3648

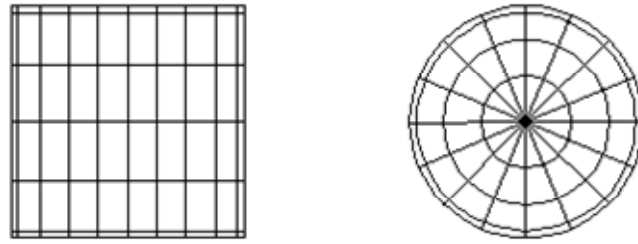
A-3: P-M Interaction Diagram

The *2005 AISC Specification* endorses the use of the full plastic stress distribution to calculate cross-sectional strength. The P-M interaction diagram for estimating the composite sectional strength based on this full plastic stress distribution can be generated as a conservative linear interpolation between five points summarized in Table A.4. The P-M interaction diagrams for all composite columns presented here are plotted in this section.

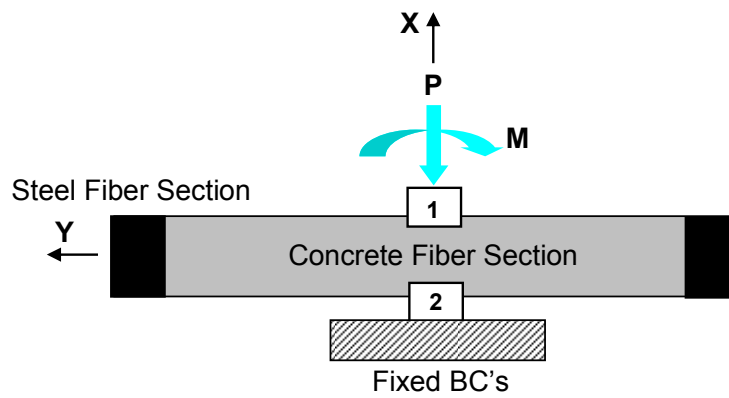
The cross-sectional strength for a composite column can be also estimated by performing a fiber analysis using the OPENSEES program. Relatively stocky cross sections for the CFT columns were modeled as numerical fiber sections (i.e. quadrilateral, circular and triangular shapes) as shown in Figure A.1 (a). The numerical CFT beam-column specimen was made up of the zero-length section elements with a nonlinear stress-strain material response with discrete fiber sections. This section element is defined by the two nodes at the same position and the discrete fiber based section shown in Figure A.1 (b).

P-M interaction points were also obtained from these fiber analyses. The model was subjected to various levels of axial force, roughly corresponding to the axial load levels of the five interpolation points given by the code provisions. The axial load was applied first and then the moment was increased. Both element forces and deformations ($P-\varepsilon$ and $M-\phi$) for the zero-length elements were recorded by using the Element Recorder. Therefore, corresponding moment-curvature diagrams for each axial force level were obtained as shown in Figures A.2 to A.9.

The monotonic analyses were carried out utilizing a (a) uniaxial bilinear stress-strain behavior with small kinematic hardening for the steel tube and (b) uniaxial compressive Kent-Scott-Park stress-strain behavior model for the confined concrete. The latter includes a degrading linear unloading/reloading stiffness. For the cyclic simulations, the stress-strain behavior of the steel fibers includes the effects of isotropic strain hardening, local buckling and biaxial stress. The cyclic stress-strain model for the concrete fibers includes the effects of stress degradation and crack opening and closing. The summary of P-M interaction diagrams for all CFT column cases are given to Figure A.2 to Figure A.9.



(a) Fiber based beam column elements



(b) Geometry of zero-length section element

Figure A.1 Numerical models and test setup for the fiber analyses

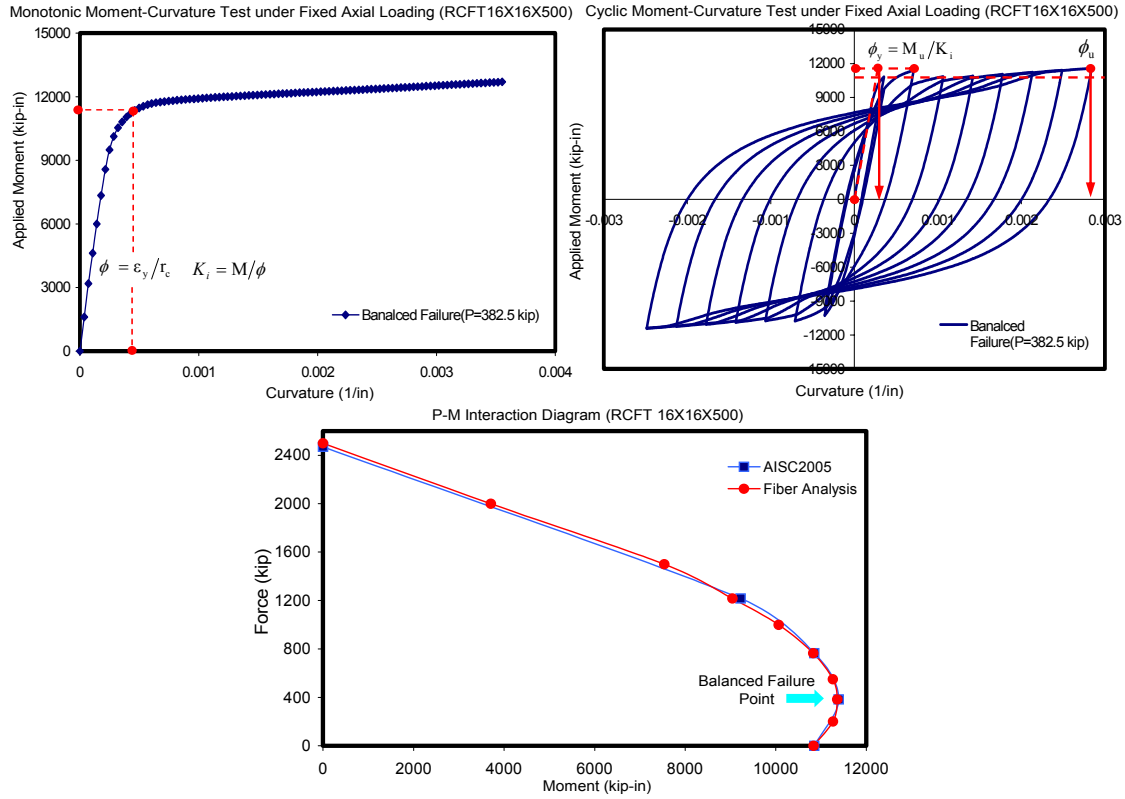


Figure A.2 Fiber analyses results and P-M interaction diagrams (RCFT 16X16X500)

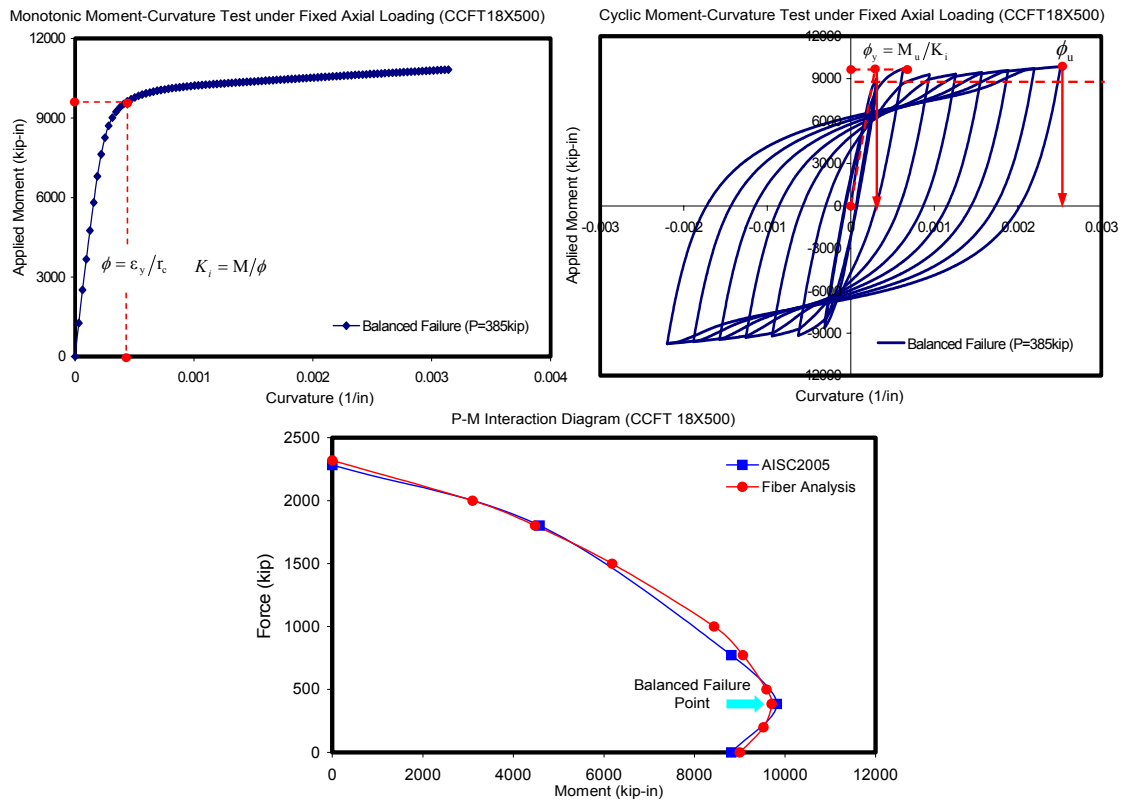


Figure A.3 Fiber analyses results and P-M interaction diagrams (CCFT 18X500)

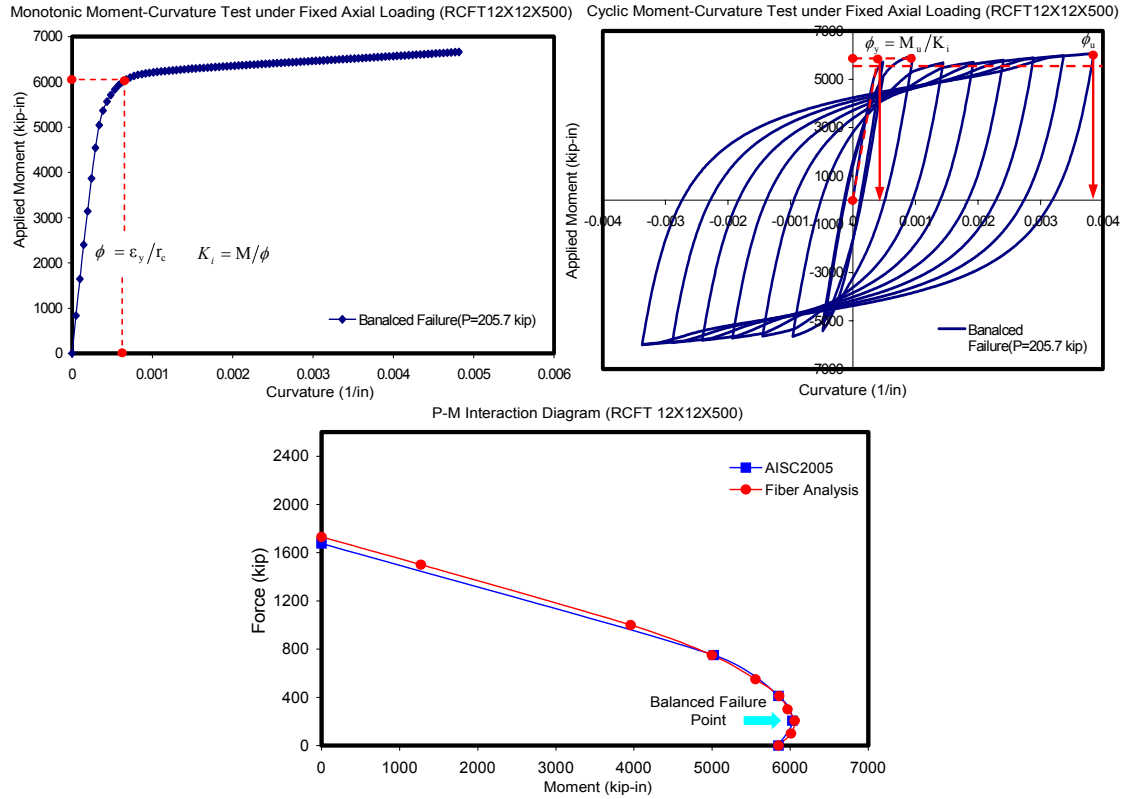


Figure A.4 Fiber analyses results and P-M interaction diagrams (RCFT 12X12X500)

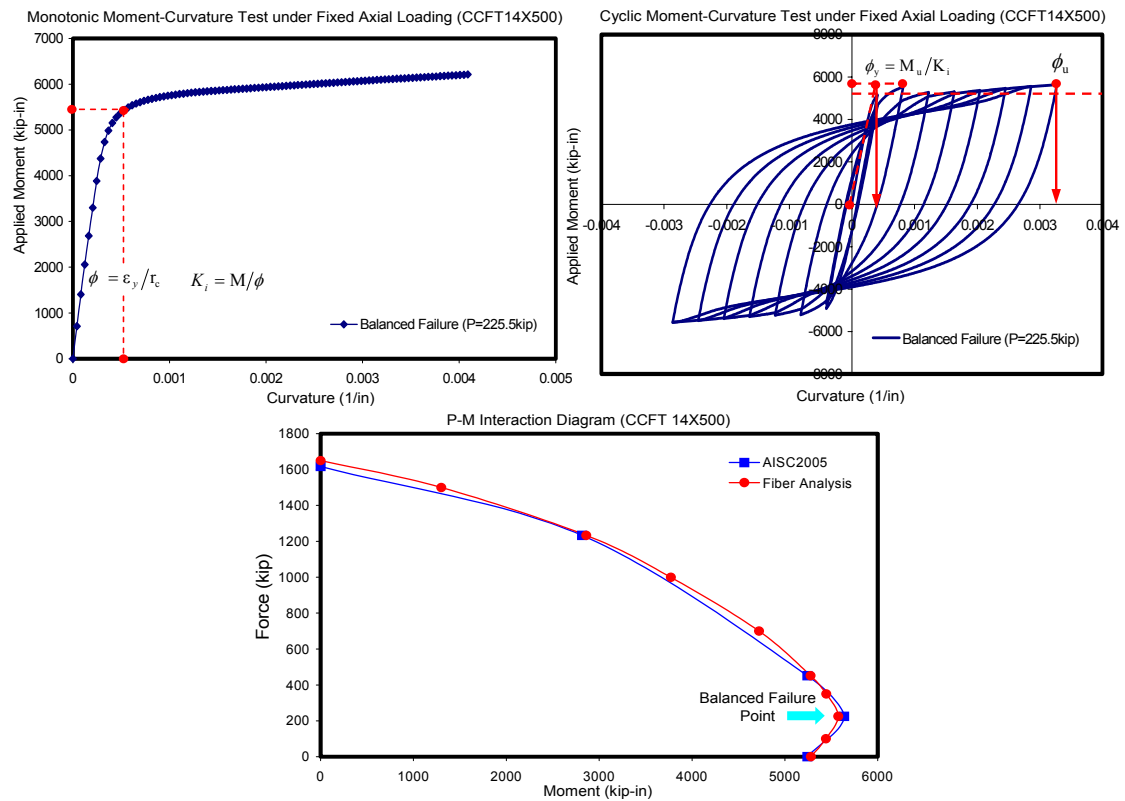


Figure A.5 Fiber analyses results and P-M interaction diagrams (CCFT 14X500)

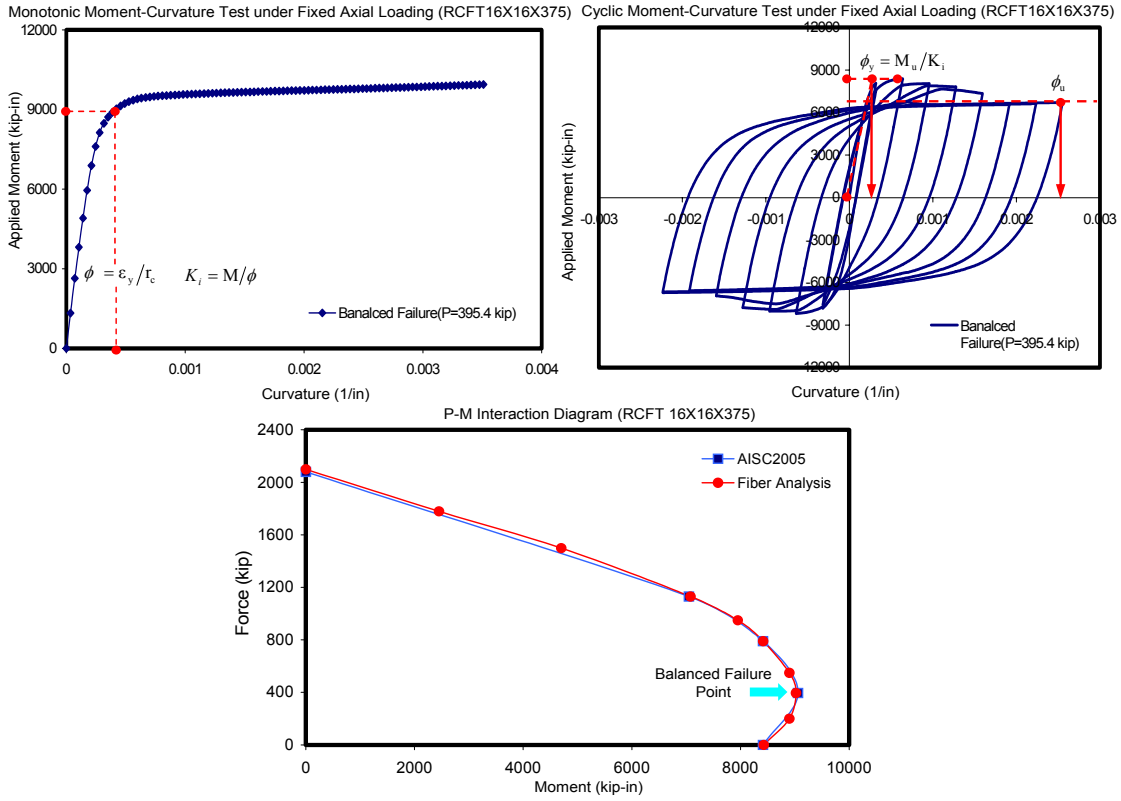


Figure A.6 Fiber analyses results and P-M interaction diagrams (RCFT 16X16X375)

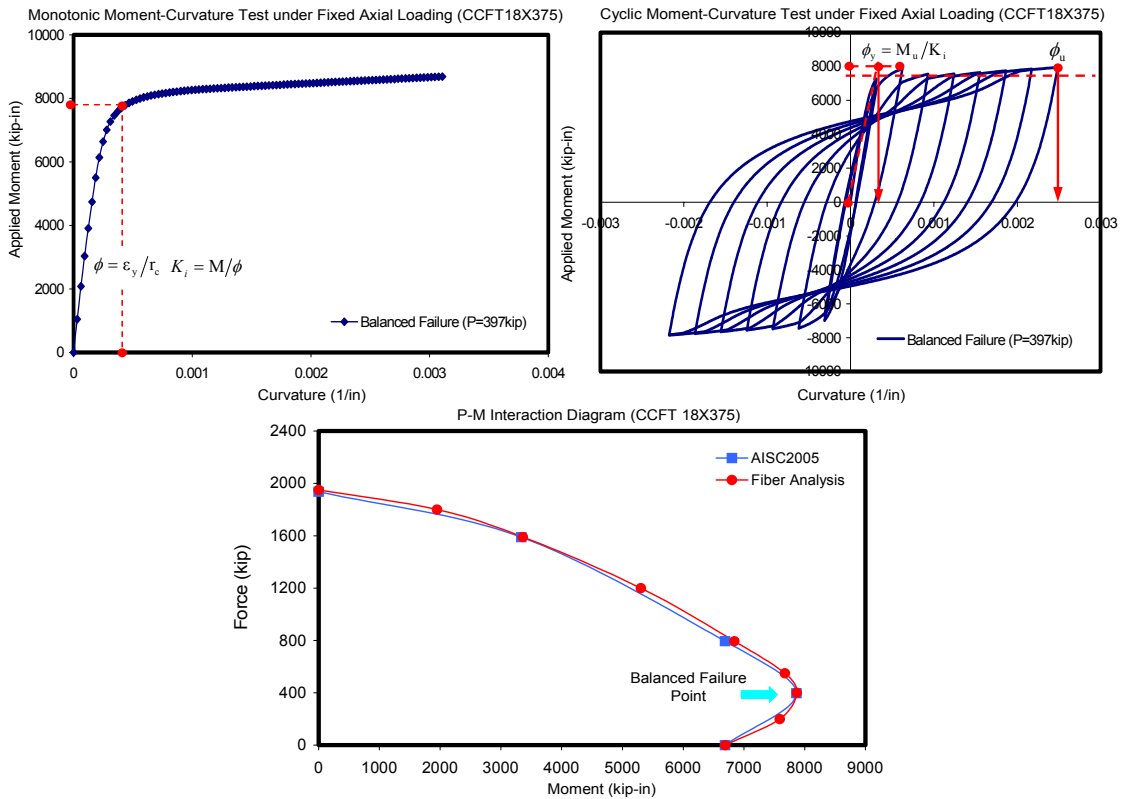


Figure A.7 Fiber analyses results and P-M interaction diagrams (CCFT 18X375)

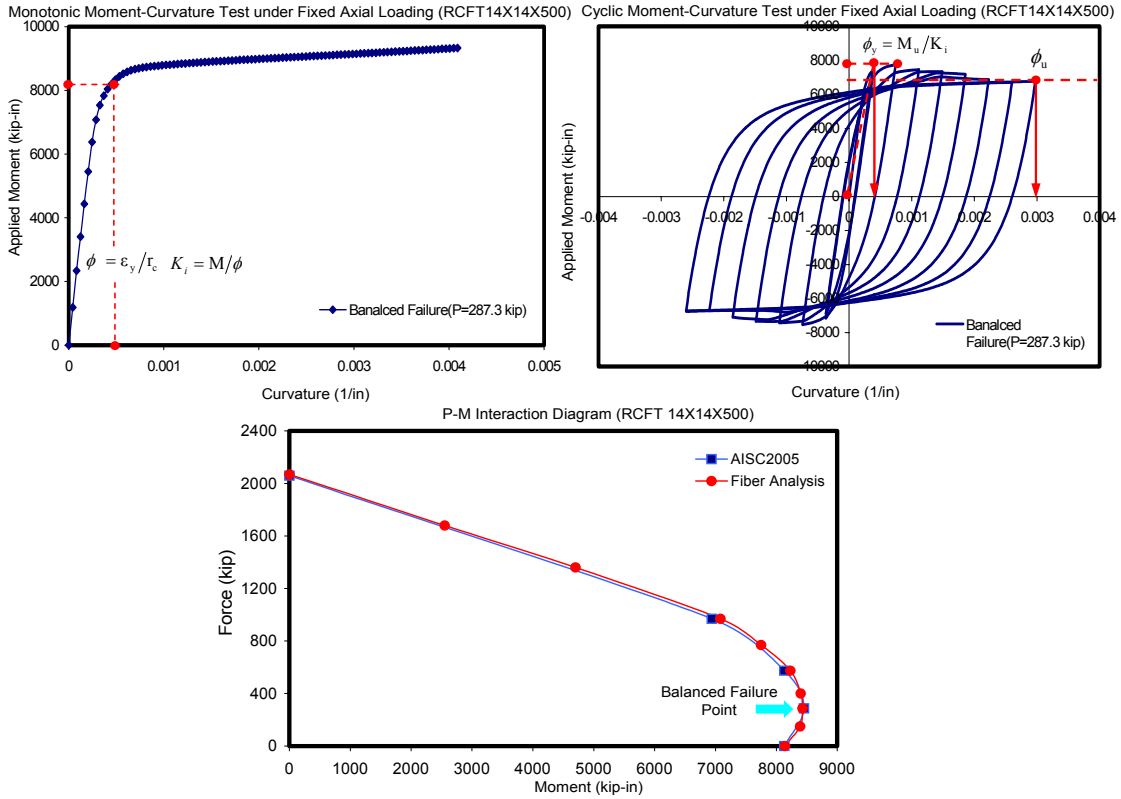


Figure A.8 Fiber analyses results and P-M interaction diagrams (RCFT 14X14X500)

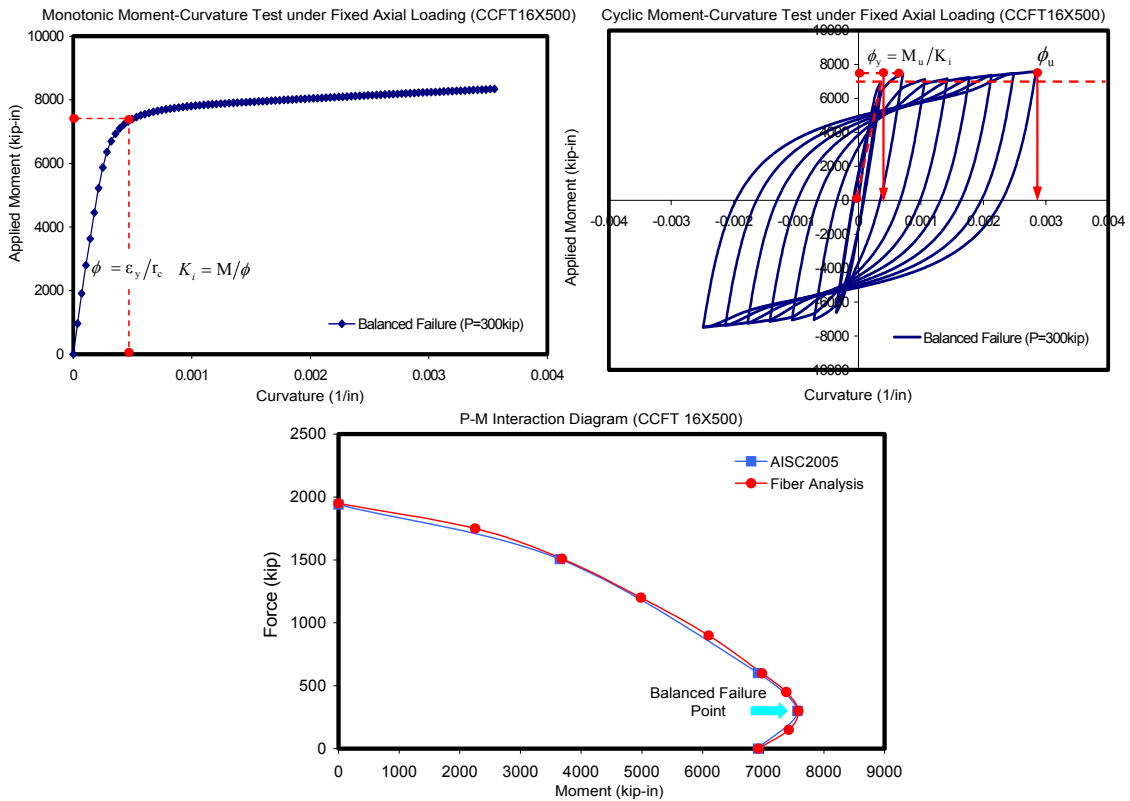


Figure A.9 Fiber analyses results and P-M interaction diagrams (CCFT 16X500)

Appendix B

Design Examples and Failure Modes

B-1: General Introduction

Idealized strength models for each connection component provide the basic background for connection design. The strength models and design procedures were described in Chapter 3, but specific design examples for them were omitted because of the limited space. Therefore, design procedures for the smart PR-CFT connections specified in Figures 4.2 to 4.7 are described in Section B-2.

In design, brittle failure modes such as bolt fracture, weld failure, and plate fracture should be avoided in order to prevent a potential collapse of the structure. The criteria for the design strength were determined by relatively ideal failure strength models based on achieving full yielding of the beam. The available failure modes for the connection components were described in Section 4.3. The necessary design checks, including strength models and different reduction factors, are shown in Section B-3.

B-2: Design Examples

Strength models and design procedures for connection components were described in Section 3.2 and Section 3.3, respectively. The detailed design procedures are described in this section.

Case 1: End-Plate Connection

The geometric details for end-plate connections were described in Figures 4.2 and 4.3. The connection components were designed in accordance with AISC-LRFD 2001 and AISC/ANSI 358-05. The design procedures for the end-plate connection are described in this section, with the design criteria based on ideal limit states. The US unit system (kip and inch) was used in this case.

Step 1: Check the basic information

(1) Determine prequalified limits and geometric dimensions

Table B.1 represents a summary of the range of the geometric parameters that have satisfactorily tested. The geometric parameters are given in Figure B.1.

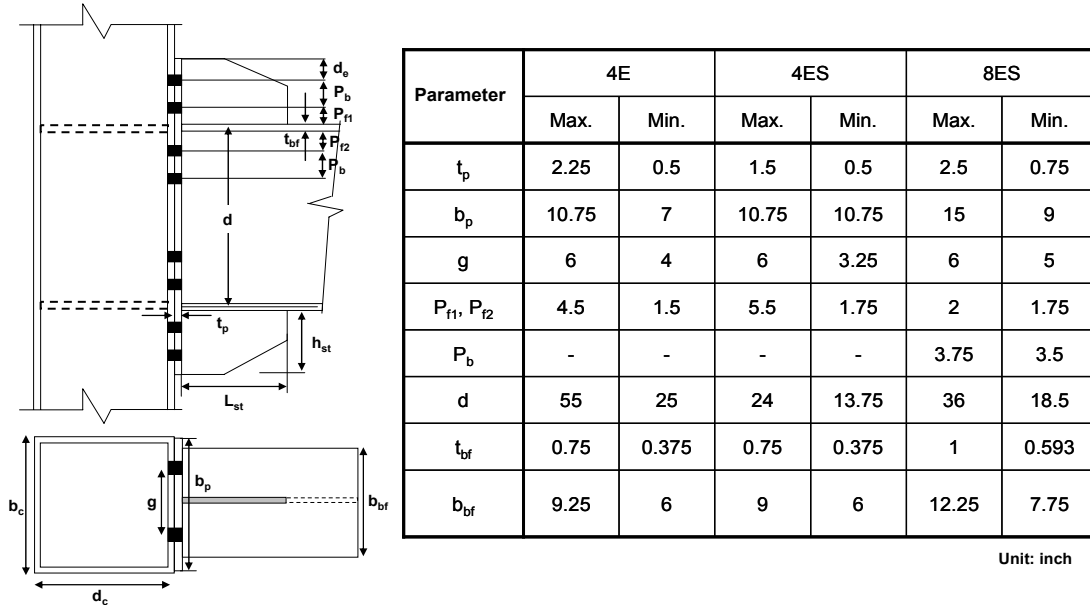


Figure B.1 8 bolt stiffened extended end-plate connection geometry (8ES)

Table B.1 Prequalification dimension limits

(2) Determine dimensions (Refer to Table B.1 and Figure B.1)

Choose 8 bolt stiffened extended end-plate connection system (8ES)

$t_p = 1.0$	The thickness of the end-plate (in)
$b_p = 15.0$	The width of the end-plate (in)
$g = 6.0$	The horizontal distance between bars (in)
$P_{f1} = P_{f2} = 1.75$	The vertical distance between beam flange and the center of bar holes (in)
$P_b = 3.5$	The distance between the centerline of bar holes (in)
$d = 24.5$	The depth of the beam (in)
$t_{bf} = 0.98$	The thickness of the beam flange (in)
$b_{bf} = 9.0$	The width of the beam flange (in)
$t_{bw} = 0.56$	The thickness of the beam web (in)
$d_e = 1.75$	The edge distance (in)
$Z_x = 280$	The plastic section modulus for the steel beam (in ³)

Figure B.2 The limit check for the geometric parameters

Eight Bolt Stiffened (8ES)				
Parameter	Max.	Min.	Design	Decision
t_p	2.5	0.75	1	OK
b_p	15	9	15	OK
g	6	5	6	OK
P_{f1}, P_{f2}	2	1.75	1.75	OK
P_b	3.75	3.5	3.5	OK
d	36	18.5	24.5	OK
t_{bf}	1	0.59	0.98	OK
b_{bf}	12.25	7.75	9	OK

Determine the position of the tension bars

$$h_1 = 29.75$$

$$h_2 = 26.25$$

$$h_3 = 24.5$$

$$h_4 = 21.0$$

where, h_i : the distance from the centerline of the beam compression flange to the centerline of the i^{th} tension bar row (in)

(3) Determine material properties

Use A572 Steel and A490M Bolt Materials (Swanson 2002, See Table 5.1)

$F_y = 55$ The design yield stress (ksi)

$F_{yp} = 55$ The design yield stress for the end plate (ksi)

$F_u = 73$ The design ultimate stress (ksi)

Step 2: Calculate the design strength

(4) Determine the factor to consider the peak connection strength

$$C_{pr} = \frac{F_y + F_u}{2F_y} = 1.164 \leq 1.20 \text{ (OK.) Generally taken as } C_{pr} = 1.1$$

(5) Determine the design strength based on the full plastic strength of the beam

$$M_{\text{design}} = C_{pr} R_y F_y Z_x = 16960 \text{ kip-in (} R_y = 1.1 \text{ for the material over strength factor)}$$

Step 3: Determine the required bar diameter

(6) Determine the average tensile strength for bars (Refer to Figure 3.20)

$$\sum_{i=1}^4 h_i = 101.5 \text{ in}$$

$F_{nt,SMA} = 80 \text{ ksi}$ The nominal strength of the SMA bar

$F_{nt,Steel} = 160 \text{ ksi}$ The nominal strength of the high tension steel bar

$$F_{nt} = \frac{\sum_i F_{nt,i} h_i}{\sum_i h_i} = 115.86 \text{ ksi}$$

(7) Choose the required bar diameter ($d_{b,req}$)

$$d_{b,req} = \sqrt{\frac{4M_{\text{design}}}{2\pi\phi_n F_{nt} (h_1 + h_2 + h_3 + h_4)}} = 0.985 \text{ in (} \phi_n = 0.9 \text{ for non-ductile limit state)}$$

Take $d_b = 1.0 \text{ in (OK.)}$

Step 4: Determine the thickness of the end-plate

(8) Calculate the yield line mechanism for the end-plate (Y_p See Figure B.5)

$$s = \frac{1}{2} \sqrt{b_p g} = 4.74 \text{ in}$$

Use case 1 ($d_e = 1.75 \leq s = 4.74$)

$$Y_p = \frac{b_p}{2} \left[h_1 \left(\frac{1}{2d_e} \right) + h_2 \left(\frac{1}{pf_1} \right) + h_3 \left(\frac{1}{pf_2} \right) + h_4 \left(\frac{1}{s} \right) \right] \\ + \frac{2}{g} \left[h_1 \left(d_e + \frac{p_b}{4} \right) + h_2 \left(pf_1 + \frac{3p_b}{4} \right) + h_3 \left(pf_2 + \frac{p_b}{4} \right) + h_4 \left(s + \frac{3p_b}{4} \right) + p_b^2 \right] + g$$

$$Y_p = 462.86 \text{ in}$$

(9) Choose the required thickness of the end-plate

$$t_{p, \text{req}} = \sqrt{\frac{1.11M_{pr}}{\phi_b F_{yp} Y_p}} = 0.932 \text{ in } (\phi_b = 1.0 \text{ for ductile limit state})$$

Take $t_p = 1.0$ in (OK.)

Step 5: Check the shear resistance

(10) Compute the tensile axial force (F_{fu})

$$F_{fu} = \frac{M_{\text{design}}}{d - t_{bf}} = 685.72 \text{ kip}$$

(11) Check the shear resistance for the end-plate

$$\phi_n R_{n, \text{shear}} = \phi_n 0.6 F_{yp} b_p t_p = 445.5 \text{ kip}$$

$$A_n = \left[b_p - 2 \left(d_b + \frac{1}{16} \right) \right] t_p = 12.75 \text{ in}^2$$

$$\phi_n R_{n, \text{shear}} = \phi_n 0.6 F_{up} A_n = 502.605 \text{ kip}$$

$$\frac{F_{fu}}{2} = 342.9 \leq \phi_n R_{n, \text{shear}} \text{ (OK.)}$$

This connection type did not require the shear bolt system. The design check for the shear bolt is not necessary.

Figure B.3 Geometry summary and yield line failure mechanism (4 Bolt Unstiffened, 4E)

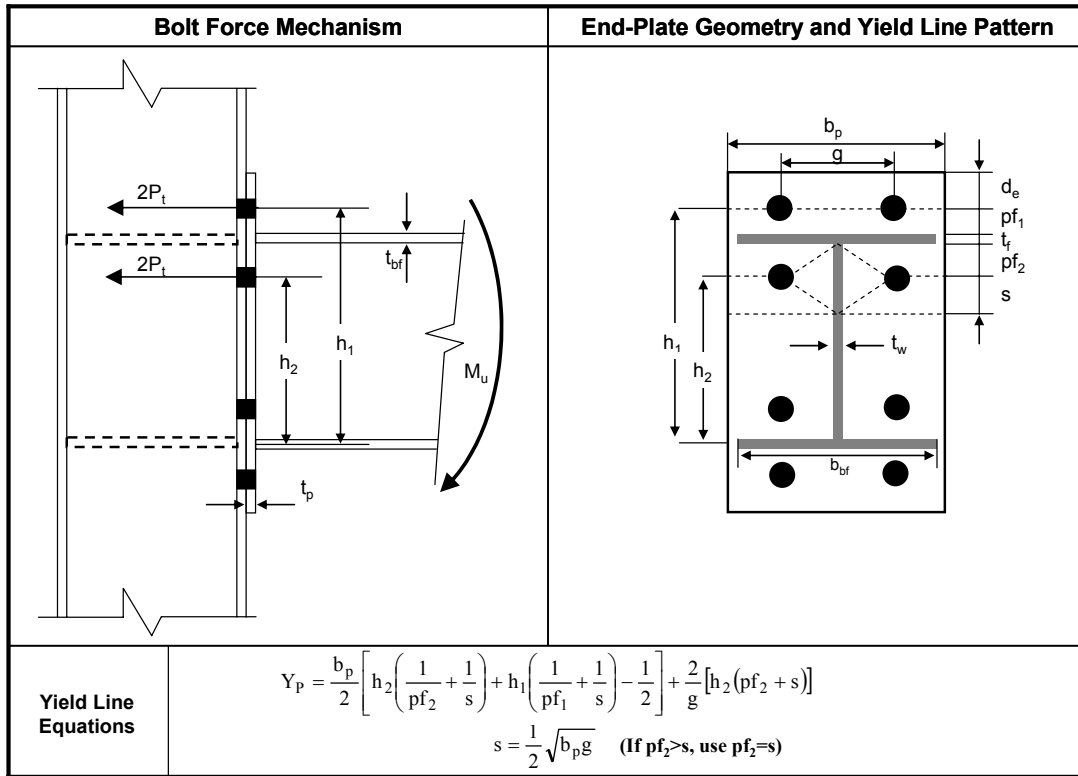


Figure B.4 Geometry summary and yield line failure mechanism (4 Bolt Stiffened, 4ES)

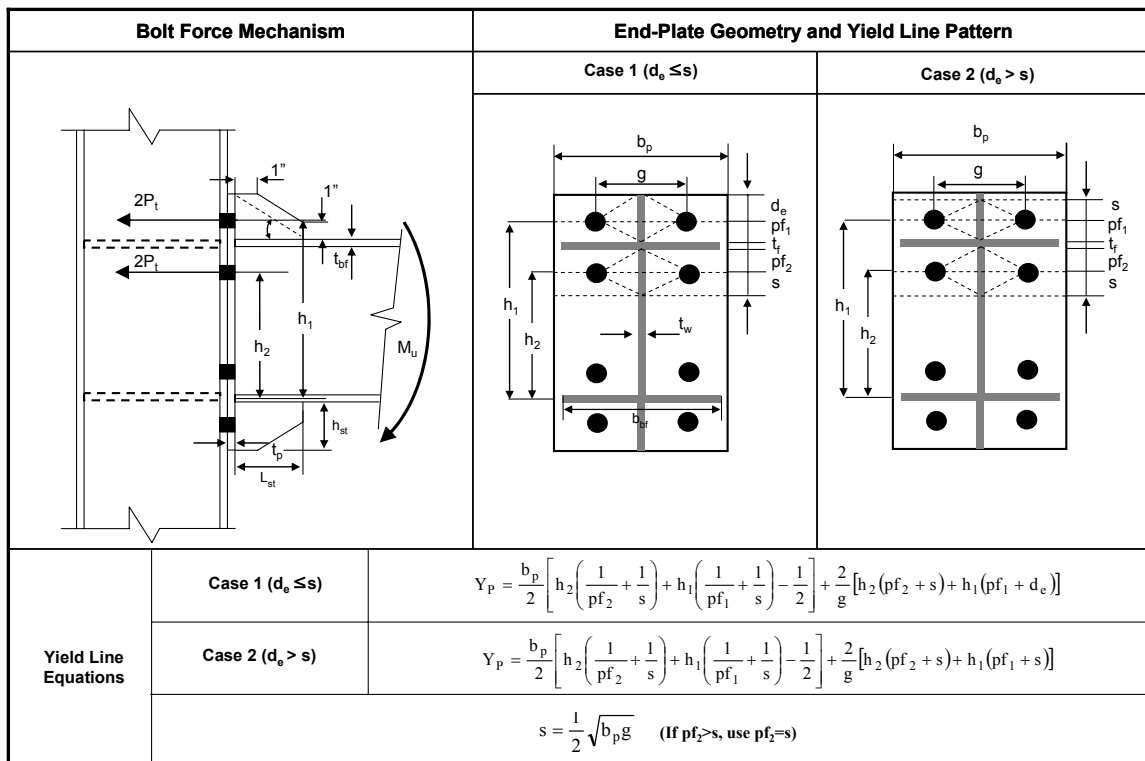
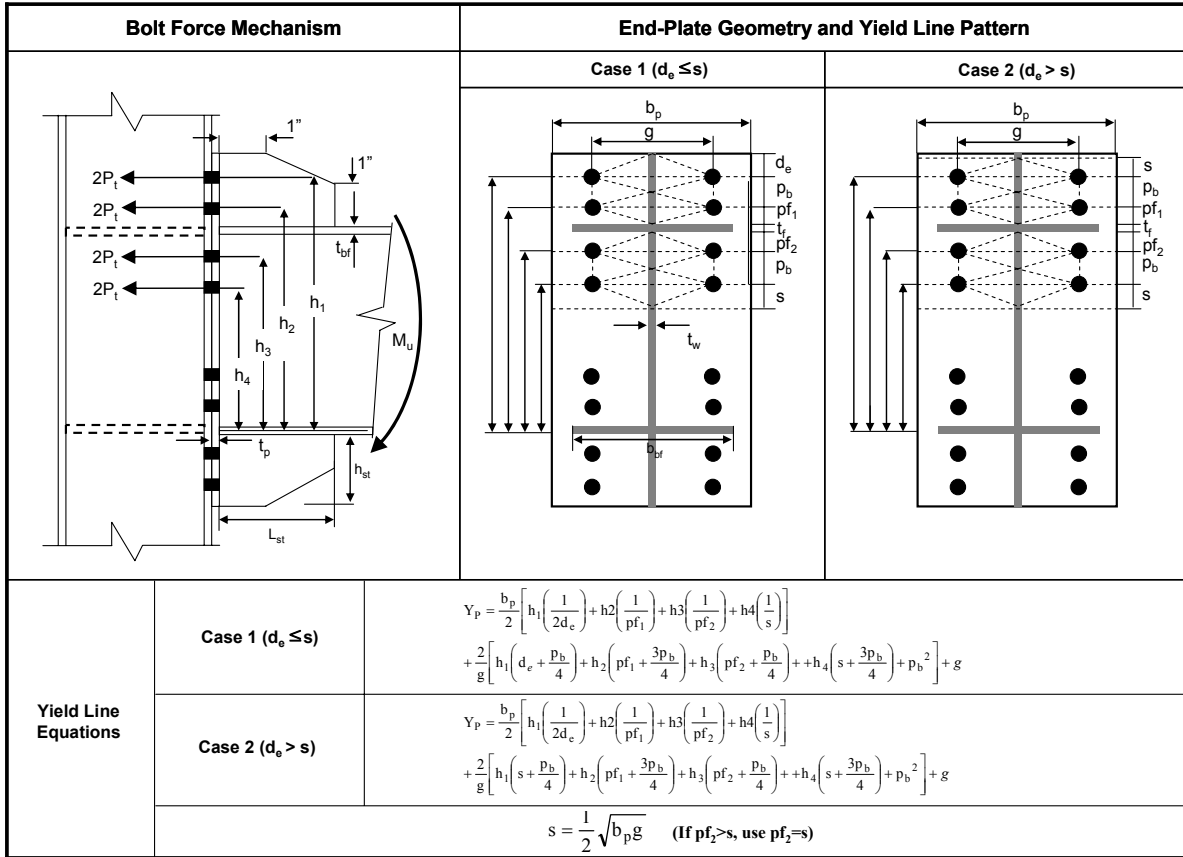


Figure B.5 Geometry summary and yield line failure mechanism (8 Bolt Stiffened, 8ES)



Step 6: Determine the size of the end-plate stiffener

(12) Determine the thickness of the stiffener (t_s)

$$t_{s, \min} = t_{bw} \left(\frac{F_{yb}}{F_{ys}} \right) = 0.56 \text{ in}$$

Take $t_s = 0.56 \text{ in}$

(13) Check the length of the stiffener (L_{st})

$$h_{st} = \left(7 - \frac{t_{bf}}{2} \right) = 6.51 \text{ in} \quad \text{The height of the stiffener}$$

$$L_{st} = \frac{h_{st}}{\tan 30^\circ} = 11.27 \text{ in}$$

$$\frac{h_{st}}{t_s} = 20.13 \geq 0.56 \sqrt{\frac{E}{F_{ys}}} = 12.86 \text{ Prevent the local buckling (OK.)}$$

Step 7: Check the rupture and bearing failure at the bars

(14) Check the tearing out failure at the end-plate

$$L_c = d_e - \left(\frac{d_b}{2} + \frac{1}{16} \right) = 1.20 \text{ in}$$

$$R_{ni} = 1.2L_c t_p F_u = 104.5 \leq 2.4d_b t_p F_u = 175.2 \text{ kip (OK.)}$$

$$R_{no} = 1.2L_c t_p F_u = 104.5 \leq 2.4d_b t_p F_u = 175.2 \text{ kip (OK.)}$$

$$L = 174 \text{ in} \quad \text{The length of the beam}$$

$$V_u = \frac{2M_{\text{design}}}{L} = 185.4 \text{ kip}$$

$$V_u \leq \phi_n R_{n,\text{bearing}} = \phi_n (N_i) R_{ni} + \phi_n (N_o) R_{no} = 1261 \text{ kip (OK.)}$$

Step 8: Check the steel column strength

I-shape steel columns require other design strength checks such as flexural yielding of the column flange, stiffener forces, local yielding of the column web, unstiffened column web buckling strength, and unstiffened column web crippling strength. CFT column systems were used in this connection system. These columns satisfied these design strength checks and these design checks are omitted in the design procedure.

Case2: T-Stub Connection

The geometric details for T-stub connections were described in Figures 4.4 and 4.5. The connection components were designed in accordance with AISC-LRFD 2001 and AISC 2005 Seismic Provisions. The design procedures for the T-stub connection are described in the next section based on ideal limit states. The US unit system (kip and inch) was used in this case.

Step 1: Determine the required design strength

(1) Determine the design strength (M_{design}) based on the full plastic strength of the steel beam in accordance with 2005 AISC Seismic Provisions.

$R_y = 1.1$ (For the types of rolled shapes and bars made by A572-Gr.50 steel)

$F_y = 55 \text{ kis}$ The design yield stress of the beam

$C_{pr} = 1.1$ Factor for the design strength

$Z_x = 134 \text{ in}^3$ The plastic section modulus for the steel beam

$M_{\text{design}} = C_{pr} R_y F_y Z_x = 8918 \text{ kip-in}$

(2) Calculate the required axial force (P_{req}) acting on the beam flange

$d = 23.57 \text{ in}$ The depth of the beam

$P_{\text{req}} = \frac{M_{\text{design}}}{d} = 378 \text{ kip}$

Step 2: Select the diameter of tension bars

(6) Determine the average tensile strength for bars (Refer to Figure 3.20)

$h_1 = 26.57 \text{ in}$

$h_2 = 20.57 \text{ in}$

$\sum_{i=1}^2 h_i = 47.14 \text{ in}$

$F_{nt,\text{SMA}} = 80 \text{ ksi}$ The nominal strength of the SMA bar

$$F_{nt,Steel} = 160 \text{ ksi}$$

The nominal strength of the high tension steel bar

$$F_{nt} = \frac{\sum F_{nt,i} h_i}{\sum h_i} = 97.45 \text{ ksi}$$

(7) Choose the required bar diameter ($d_{b,req}$)

$$d_{b,req} = \sqrt{\frac{4M_{design}}{4\pi\phi_n F_{nt} (h_1 + h_2)}} = 0.83 \text{ in}$$

($\phi_n = 0.9$ for non-ductile limit state, 4 bars arrangement in each row)

For easy of the construction, the same size of the tension bars should be used.

Take $d_b = 1.0 \text{ in}$ (OK.)

Step 3: Layout the shear bolts and tension bars

(8) Determine the gage length and bolt spacing for the shear bolts

For the easy construction, the same grade and size of bolts should be used for the shear bolts. Ten high strength bolts (A490) were used. Use lesser maximum gage that is permitted by the beam flange. The enough edge distance more than the required distance for 1" diameter bolts was used. The details for the shear bolt arrangement are given to below.

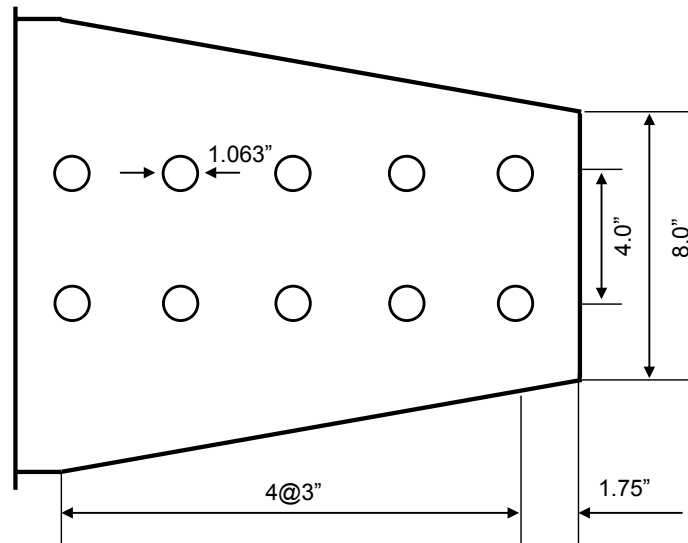


Figure B.6 The arrangement of the shear bolts on the T-stub

$g_s = 4.0 \leq b_f - 2 \cdot L_e = 4.0$ in (OK.) The gage length

$s = 3d_b = 3$ in (OK.) The bolt spacing

(9) Determine the arrangement for the tension bars

Use 6 inch center spacing to allow extra clearance: $W_{eff} = 15.50$ in

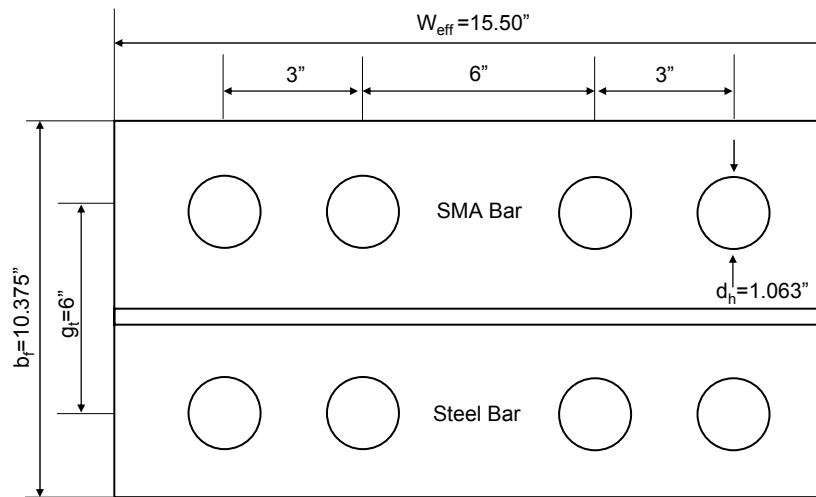


Figure B.7 The arrangement of the tension on the T-stub flange

Step 4: Determine the thickness of the T-stem

(10) Check the design strength model for the net section

$$\phi_f R_{n,net} = \phi_f F_u A_{net,stem} \quad (\phi_f = 0.75 \text{ for the fracture failure})$$

(11) Determine the thickness of the T-stem based on the design strength model

$n_{sb} = 2$ The number of shear bolts along the T-stem width

$$d_h = d_b + 1/16 = 1.063 \text{ in}$$

$$t_{stem,min} = \frac{M_{design}}{\phi_f F_u (W_{eff} - n_{sb} d_h) d} = 0.516 \text{ in} \quad (F_u = F_{us} = 166 \text{ ksi, ASTM A490 Bolts})$$

Check for $t_{stem,min}$ based on the bearing failure

$$t_{stem,min} = \frac{M_{design}}{\phi_f 2.4m \cdot n_{sb} F_u d_b d} = 0.288 \text{ in} \quad (m = 5 \text{ m} \cdot n_{sb} : \text{Total number of shear bolts})$$

$t_{stem} = 0.56$ in (T-stub: Cut from W16X100, OK.)

Step 5: Determine the b_f and t_f for the T-stub flange

(12) Determine the thickness of the T-stub flange

$$n_{tb} = 8 \quad \text{The total number of tension bars}$$

$$p = \frac{2W_{eff}}{n_{tb}} = 3.875 \text{ in} \quad \text{The effective flange width per tension bar}$$

$$\delta = 1 - \frac{d_h}{p} = 0.726 \quad \text{The ratio of the net section area to the flange area}$$

(See Figure 3.10)

The average bolt force should be used to estimate the bolt capacity. It causes to make design calculation easy.

$$T_{req} = \frac{P_{req}}{n_{tb}} = 47.25 \text{ kip} \quad \text{The required force at each tension bar}$$

Compare the required factored bar strength assuming a 40 percent prying and 8 tension bars.

$$\phi B_{req} = \frac{1.40P_{req}}{n_{tb}} = 66.15 \leq F_{nt} = 97.45 \text{ kip (OK.)}$$

$$b'_{f,req} = \left(\frac{\phi_f B_{req}}{T_{req}} \right) \cdot \left(\frac{1+\delta}{\delta} \right) \cdot 2d_b = 1.91 \text{ in}$$

$$g_{t,req} = 2b'_{f,req} + 2t_{stem} = 4.94 \text{ in}$$

Take $g_t = 6 \text{ in (OK.)}$

$$L_{e,min} = 1.25 \text{ in} \quad \text{The minimum distance between the center of the bar hole and the edge}$$

$$b_{f,req} = g_t + 2L_{e,min} = 8.5 \text{ in}$$

$$b_{f,req} = g_t + 4d_b = 10.0 \text{ in}$$

Take $b_f = 10.375 \text{ in (OK.)}$

(13) Determine the with of the T-stub flange

Use adjusted geometric parameters (a' and b' , See Figure 3.10)

$$a' = a + \frac{d_b}{2} = 2.69 \text{ in}$$

$$b' = b - \frac{d_b}{2} = 2.22 \text{ in}$$

Find the range for t_f

$$t_{f,\max} = \sqrt{\frac{4T_{\text{req}} b'}{\phi_b p F_y}} = 2.31 \text{ in } (\phi_b = 0.75 \text{ for bolt bearing or fracture})$$

$$t_{f,\min} = \sqrt{\frac{T_{\text{req}} (8d_b b' - d_b (2d_b + b'))}{3.75 \phi_b d_b p F_y}} = 1.03 \text{ in}$$

Take $t_f = 1.0 \approx t_{f,\min}$ in (OK.)

Step 6 & Step 7: Check the T-stub section and failure modes

After the T-stub section has been determined, the capacity of the T-stub section should be checked by looking at failure modes in either the flange or the stem. The failure mode checks in order to avoid brittle failure modes (net section failure at the T-stem, block shear failure, and shear bolt failure) are shown in Section B-3. The failure strength due to the brittle failures should be larger than the design strength based on the yielding of the beam.

Step 8: Determine the shear connection

(14) Calculate the required shear force at the connection

$$V_u = \frac{2M_{\text{design}}}{L} = 102.5 \text{ kips}$$

$$L_{\text{plate,max}} = d - b_f = 13.2 \geq L_{\text{plate}} = 9.0 \text{ in (OK.)}$$

(15) Design the shear plate

Use four 1" diameter A-490N bolts and two 0.56 inch thick plate would be sufficient with a capacity, $2\phi R_n = 176 \text{ kip}$. The connection detail is given to Figure D.8.

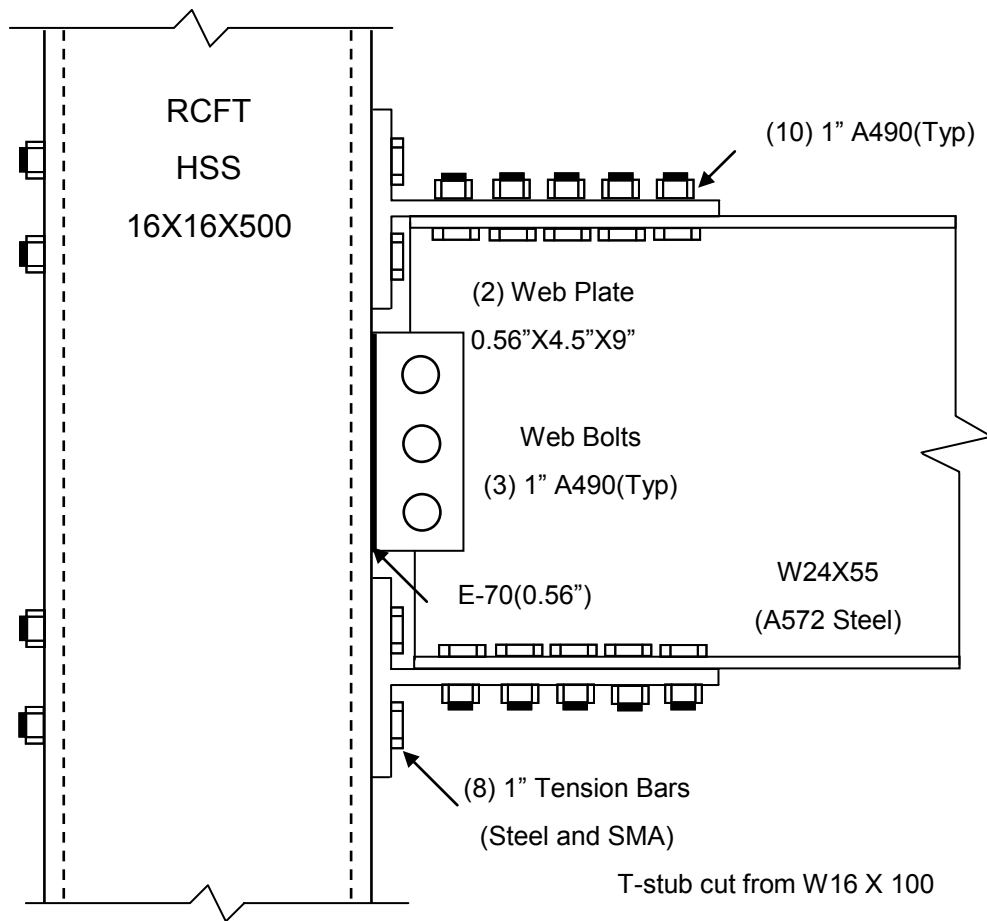


Figure B.8 The connection details (T-stub connection)

Case3: Clip Angle Connection

The geometric details for clip angle connections were described in Figures 4.6 and 4.7. The connection components were designed in accordance with AISC-LRFD 2001 and AISC 2005 Seismic Provisions. The design procedures for the clip angle connections are described based on ideal limit states. The US unit system (kip and inch) was used in this case.

Step 1: Determine the required design strength

(1) Determine the design strength (M_{design}) based on the full plastic strength of the steel beam in accordance with 2005 AISC Seismic Provisions.

$$R_y = 1.1 \text{ (For the types of rolled shapes and bars made by A572-Gr.50 steel)}$$

$$F_y = 55 \text{ ksi} \quad \text{The design yield stress of the beam}$$

$$C_{pr} = 1.1 \quad \text{Factor for the design strength}$$

$$Z_x = 101 \text{ in}^3 \quad \text{The plastic section modulus for the steel beam}$$

$$M_{\text{design}} = C_{pr} R_y F_y Z_x = 6722 \text{ kip-in}$$

(2) Calculate the required axial force (P_{req}) acting on the beam flange

$$d = 18.0 \text{ in} \quad \text{The depth of the beam}$$

$$P_{\text{req}} = \frac{M_{\text{design}}}{d} = 373 \text{ kip}$$

Step 2: Select the diameter of tension bars

(6) Determine the average tensile strength for bars (Refer to Figure 3.20)

$$h_1 = 25.40 \text{ in}$$

$$\sum_{i=1}^1 h_i = 25.40 \text{ in}$$

Tension bars are aligned on one row.

$$F_{nt,SMA} = 80 \text{ ksi} \quad \text{The nominal strength of the SMA bar}$$

$$F_{nt,Steel} = 160 \text{ ksi}$$

The nominal strength of the high tension steel bar

$$F_{nt} = \frac{\sum_i F_{nt,i} h_i}{\sum_i h_i} = 107 \text{ ksi}$$

(7) Choose the required bar diameter ($d_{b,req}$)

$$d_{b,req} = \sqrt{\frac{4M_{design}}{3\pi\phi_n F_{nt}(h_1)}} = 1.07 \text{ in (More than 1.0 inch diameter)}$$

($\phi_n = 0.9$ for non-ductile limit state, 4 bars arrangement in each row)

For increasing the bar strength, it is effective to use the steel bars with larger diameters than those of the SMA bars.

Take $d_{b,SMA} = 1.0$ in and $d_{b,Steel} = 1.07$ in (OK.)

Step 3: Layout the shear bolts and tension bars

(8) Determine the gage length and bolt spacing for the shear bolts

For the easy construction, the same grade and size of bolts should be used for the shear bolts. Four high strength bolts (A490) were used. Use lesser maximum gage that is permitted by the beam flange. The enough edge distance more than the required distance for 1" diameter bolts was used. The details for the shear bolt arrangement are given to below. The arrangement was satisfied with the limits.

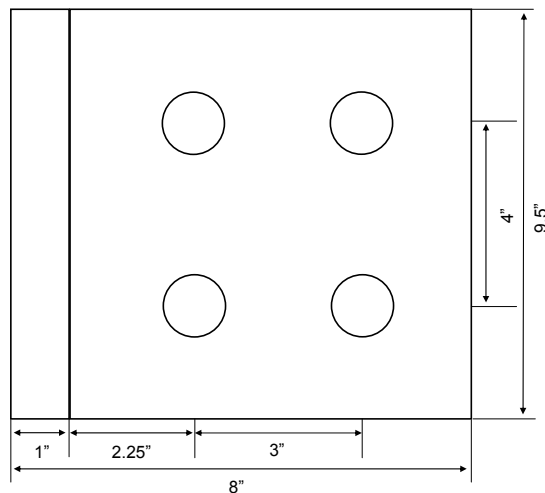


Figure B.9 The arrangement of the shear bolts on the clip angle

$g_s = 4.0 \leq b_f - 2 \cdot L_e = 4.0$ in (OK.) The gage length

$s = 3d_b = 3$ in (OK.) The bolt spacing

(9) Determine the arrangement for the tension bars

Use 6 inch center spacing to allow extra clearance: $W_{eff} = 9.0$ in

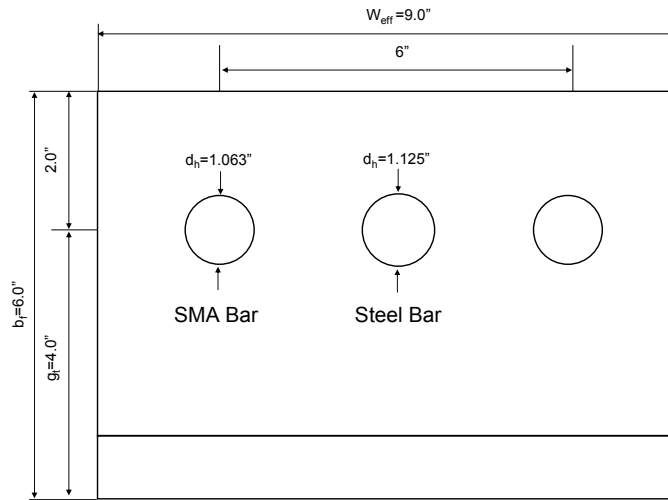


Figure B.10 The arrangement of the tension on the T-stub flange

Step 4: Determine the clip angle leg thickness

(10) Check the design strength model for the net section

$$\phi_f R_{n,net} = \phi_f F_u A_{net,stem} \quad (\phi_f = 0.75 \text{ for the fracture failure})$$

(11) Determine the thickness of the clip angle leg based on the design strength model

$n_{sb} = 2$ The number of shear bolts along the T-stem width

$d_h = d_b + 1/16 = 1.063$ in (Include the bolt clearance)

$$t_{leg,min} = \frac{M_{design}}{\phi_f F_u (W_{eff} - n_{sb} d_h) d} = 0.44 \text{ in } (F_u = F_{us} = 166 \text{ ksi, ASTM A490 Bolts})$$

Check for $t_{stem,min}$ based on the bearing failure

$$t_{leg,min} = \frac{M_{design}}{\phi_f 2.4 m \cdot n_{sb} F_u d_b d} = 0.312 \text{ in } (m = 2 \text{ m} \cdot n_{sb} : \text{Total number of shear bolts})$$

$t_{leg} = 1.00$ in (Clip Angle: L6X9X1 angle, Use thick clip angle)

Step 5: Determine the b_f and t_f for the clip angle flange

(12) Determine the thickness of the T-stub flange

$$n_{tb} = 3 \quad \text{The total number of tension bars}$$

$$p = \frac{W_{eff}}{n_{tb}} = 3.0 \text{ in} \quad \text{The effective clip angle width per tension bar}$$

$$\delta = 1 - \frac{d_h}{p} = 0.646 \quad \text{The ratio of the net section area to the flange area}$$

(See Figure 3.10)

The average bolt force should be used to estimate the bolt capacity. It causes to make design calculation easy. In order to estimate the bar prying action, the required force at each tension bar (T_{req}) should be assumed as below.

$$T_{req} = \frac{P_{req}}{n_{tb}} = 124.3 \text{ kip}$$

Compare the required factored bar strength assuming zero percent prying ($Q=0$) with three tension bars due to the heavy thickness of the clip angle.

$$\phi B_{req} = T_{req} = 124.3 \text{ kip}$$

Using moment equilibrium between T_{req} and ϕB_{req}

$$T_{req} \frac{d}{h_1} = 88.253 \leq F_{nt} \text{ (OK.)}$$

$$b'_{f,req} = \left(\frac{\phi_f B_{req}}{T_{req}} \right) \cdot \left(\frac{1+\delta}{\delta} \right) \cdot d_b = 2.548 \text{ in}$$

$$g_{t,req} = b'_{f,req} + t_{leg} = 3.548 \text{ in}$$

Take $g_t = 4 \text{ in}$ (OK.)

$$L_{e,min} = 1.25 \text{ in} \quad \text{The minimum distance between the center of the bar hole and the edge}$$

$$b_{t,req} = g_t + L_{e,min} = 5.25 \text{ in}$$

$$b_{t,req} = g_t + 2d_b = 6.0 \text{ in}$$

Take $b_t = 6.0$ in (OK.)

(13) Determine the width of the T-stub flange

Use adjusted geometric parameters (a' and b' , See Figure 3.10)

$$a' = a + \frac{d_b}{2} = 2.5 \text{ in}$$

$$b' = b - \frac{d_b}{2} = 2.5 \text{ in}$$

$$t_{f,\max} = \sqrt{\frac{4T_{\text{req}} b'}{\phi_b p F_y}} = 3.20 \text{ in } (\phi_b = 0.75 \text{ for bolt bearing or fracture})$$

Take $t_f = 1.0$ in (OK.)

Step 6 & Step 7: Check the clip angle section and failure modes

After the size of the clip angle has been determined, the capacity of the clip angle section should be checked against failure modes which can occur either in the flange or in the clip angle leg. The checks should verify that brittle failure modes (net section failure, block shear failure, and shear bolt failure) will not govern. These checks will be performed in Section B-3. The failure strength due to the brittle failures should be larger than the design strength based on the yielding of the beam.

Step 8: Determine the shear connection

(14) Calculate the required shear force at the connection

$$V_u = \frac{2M_{\text{design}}}{L} = 77.26 \text{ kips}$$

$$L_{\text{plate,max}} = d = 18.0 \geq L_{\text{plate}} = 9.0 \text{ in (OK.)}$$

(15) Design the shear plate

Use four 1" diameter A-490N bolts and two 0.56 inch thick plate would be sufficient with a capacity, $2\phi R_n = 176$ kip. The connection detail is given to Figure D.8.

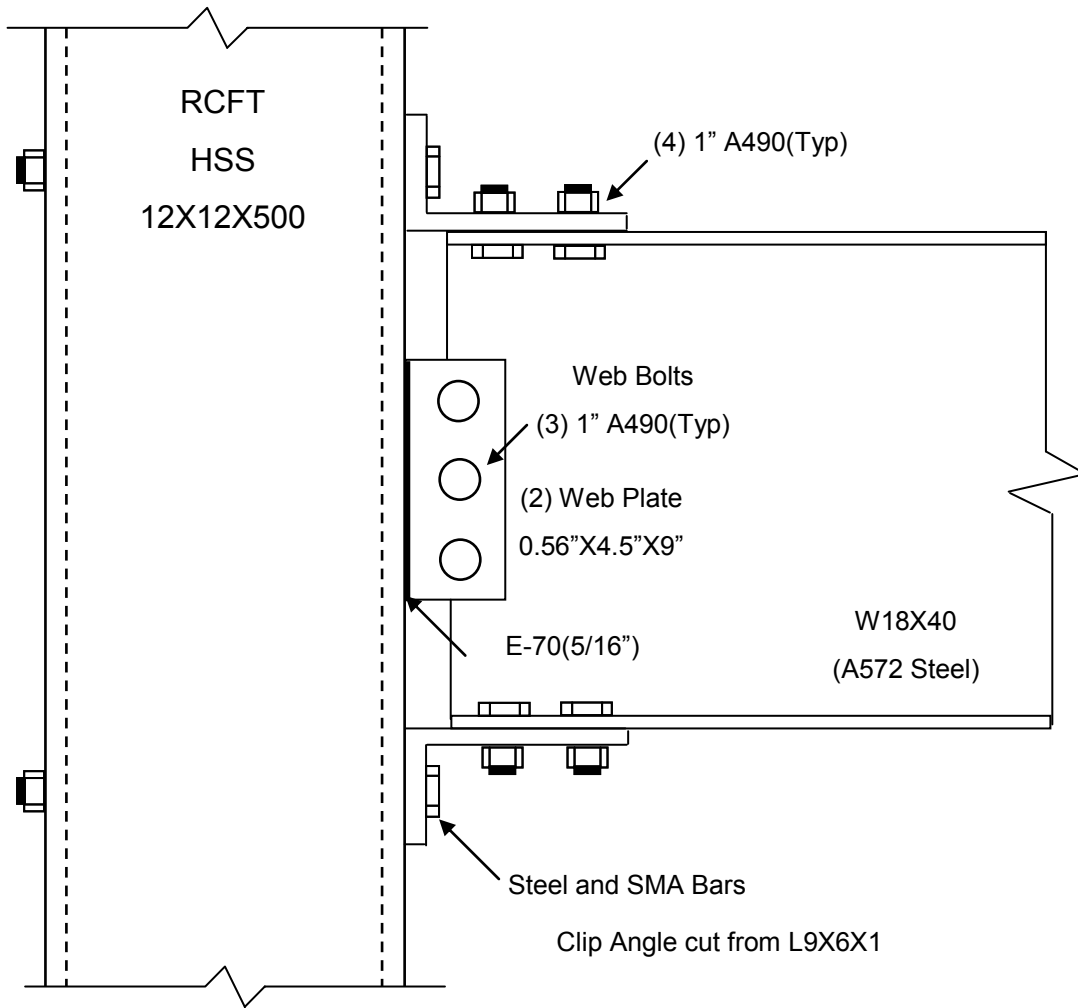


Figure B.11 The connection details (Clip angle connection)

B-3: Failure Mode Checks

The behavior of PR connections can be controlled by a number of different limit states including flexural yielding of the beam section, flexural yielding of the end-plates, yielding of the column panel zone, tension failure of the endplate bolts, shear failure of the end-plate bolts, or failure of various welds (See Figure 4.9). The intent of the design criteria presented here is to provide sufficient strength in the components of the connections to ensure that the inelastic deformation of the connection is achieved by beam yielding.

Case 1: End-Plate Connection with RCFT Columns

End-plate connection design check

Refer to AISC/ANSI 358-05 Manual

Refer to AISC-LRFD 2001

Refer to Eurocode 4 (Composite Column Design)

Refer to Steel Tip Manual (Astaneh-Asl, 1995)

Satisfy the prequalification limits: Table 6.1 in ANSI 358-05 (See Table B.1)

Use material properties for A.572 steel and A490 bolt based on the material test performed on SAC test models (Swanson, 2002).

Given Values

Table B.2 Material properties for the end-plate connection (Case 1)

Materials	F_y	F_u
Beam	55 ksi	73 ksi
Column	55 ksi	73 ksi
Plate	55 ksi	73 ksi
Concrete	3.2 ksi	4 ksi
Steel Bar	85 ksi	162 ksi
SMA Bar	60 ksi	80 ksi

Beam: W24X103

Column: HSS16X16X500

(From the standard shape in the AISC-LRFD 2001 specification)

$E = 29000$ ksi	The elastic modulus for the steel material
$F_y = 55$ ksi	The yield stress for the steel material
$F_u = 73$ ksi	The ultimate stress for the steel material
$F_{u,steel} = 162$ ksi	The ultimate strength for the steel bar
$F_{u,SMA} = 80$ ksi	The ultimate strength for the SMA bar
$d = 24.5$ in	The depth of the beam
$t_f = 0.98$ in	The thickness of the beam flange
$b_f = 9.0$ in	The width of the beam flange
$t_w = 0.56$ in	The thickness of the beam web
$S_{gy} = 245$ in ³	The section modulus of the beam
$Z_{gy} = 285$ in ³	The plastic section modulus of the beam
$h = 16.0$ in	The height or width of the column
$t_c = 0.5$ in	The thickness of the column
$b_p = 15.0$ in	The width of the end-plate
$d_p = 38.5$ in	The depth of the end-plate
$t_p = 1.0$ in	The thickness of the end-plate
$Z_{py} = \frac{b_p d_p^2}{4} = 5558$ in ³	The plastic section modulus of the end-plate
$d_b = 1.0$ in	The diameter of the tension bar
$d_h = 1.06$ in	The diameter of the bar hole

Geometric parameters were illustrated in Figure B.1

$\tau_{cu} = 6.5$ ksi	The ultimate strength of the confined concrete in PZ
$m = 2$	The number of tension bars per row
$n = 8$	The number of rows for the bar arrangement

A. Determine the Design Strength

The design strength (M_p) should be based on the full plastic strength of the beam.

$$M_p = Z_{gy} F_y = 15400 \text{ kip-in}$$

The design capacity for other component with the reduction factor (ϕ) should be larger than the factored design strength in order to achieve the ideal failure at the connection. An overstrength factor, taken as 1.25, was suggested in Astaneh-Asl (1995) in order to ensure that a ductile mode of behavior was reached.

B. Ductile Failure Modes

B.1 Slippage at the Shear Faying Surface

The check for the slippage strength is not available for the end-plate connections due to the lack of the shear faying surface.

B.2 Bearing yielding around the Shear Bolt Holes

The check for bearing strength around the shear bolt holes is not available for the end-plate connections due to absence of the shear bolt.

B.3 Yielding Failure of the Gross Section of the End-Plate ($M_{P, \text{end-plate}}$)

$\phi = 0.9$ Design reduction factor for the yielding failure

$$M_{P, \text{end-plate}} = Z_{py} F_y = 3.057 \cdot 10^5 \text{ kip-in}$$

$$\phi \cdot M_{P, \text{end-plate}} \geq 1.25 \cdot M_p \text{ (OK.)}$$

Satisfy the limit to occupy the ductile failure due to yielding of the beam

C. Mixed Failure Modes

C.1 Local Buckling at the beam flange

$$\frac{b_f}{2 \cdot t_f} = 4.592$$

$$\lambda_p = 0.38 \sqrt{\frac{E}{F_y}} = 8.726 \quad \text{The compact slenderness ratio}$$

$$\frac{b_f}{2 \cdot t_f} \leq \lambda_p \text{ (OK.)}$$

C.2 Local Buckling at the Composite Column

$$\frac{h}{t_c} = 32$$

$$42 \cdot \varepsilon = 42 \sqrt{\frac{34.08}{F_y}} = 33.061 \quad \text{Local buckling check (Eurocode 4, 2004)}$$

$$\frac{h}{t_c} \leq 42 \cdot \varepsilon \text{ (OK.)} \quad \text{Compact column case}$$

C.3 Shear Yielding of the Panel Zone (PZ)

Check shear yielding of the rectangular shaped panel zone (Wu et al., 2005)

$$K_f = \frac{2Eh \cdot (t_c + t_p)^3}{(d - t_f)^2} \quad \text{The stiffness of the generalized column flange}$$

$$K_f = 5.662 \cdot 10^3 \text{ kip/in}$$

$$r_A = 1 - m \frac{d_h}{h - 2t_c} = 0.858 \quad \text{The area reduction factor due to bar holes}$$

$$r_C = \left(1 - 2 \frac{nd_h}{d_b} + 2 \frac{nd_h}{d_b r_A} \right)^{-1} = 0.897 \quad \text{The reduction factor}$$

$$r_w = \left(1 - \frac{nd_h}{d_b} + \frac{nd_h}{d_b r_A} \right)^{-1} = 0.946 \quad \text{The reduction factor for bar holes}$$

$$K_w = 2(h - 2t_c) t_c \frac{3E}{7} \quad \text{The stiffness of the column web}$$

$$K_w = 1.864 \cdot 10^5 \text{ kip/in}$$

$$A_c = (h - 2t_c)^2 = 225 \quad \text{The area of the inside concrete}$$

Compute the yield shear strength (V_y) and ultimate shear strength (V_u) at the panel zone

$$V_y = \frac{2(h - 2t_c - md_h) t_c F_y}{\sqrt{3}} \left(1 + \frac{K_f}{r_w K_w} \right) + r_c \tau_{cu} A_c = 1734 \text{ kip}$$

$$V_u = \frac{2(h - 2t_c - md_h) t_c F_y}{\sqrt{3}} + r_c \tau_{cu} A_c + \frac{2h(t_c + t_p)^2 F_y}{3(d - t_f)} = 1777 \text{ kip}$$

$$1.25V_p = 1.25 \frac{M_p}{d} = 786 \text{ kip}$$

$\phi = 0.8$ The design reduction factor

$$1.25V_p \leq \phi V_y \text{ (OK.)}$$

Satisfy the limit to occupy the ductile failure due to yielding of the beam

D. Brittle (Fracture) Failure Modes

D.1 Block Shear Failure at the Shear Component

The check for block shear failure is not applicable to the end-plate connection due to absence of a plate under direct shear force.

D.2 Net Section Failure

The check for the net section failure is not applicable to the end-plate connection due to absence of a plate under direct tension force.

D.3 Fracture of the Tension Bars

Apply the AISC/ANSI 358-05 specifications

$$A_b = \frac{\pi d_b^2}{4} = 0.785 \text{ in}^2 \quad \text{The section area of the tension bar}$$

$$h_1 = 29.75 \text{ in}$$

$$h_2 = 26.25 \text{ in}$$

$$h_3 = 24.5 \text{ in}$$

$$h_4 = 21.0 \text{ in}$$

Here, h_i ($i = 1$ to 4) is the distance from the maximum bearing to each center of the bar hole (See Table B.5).

$$B_{n,steel} = F_{u,steel} A_b = 266 \text{ kip} \quad \text{The ultimate capacity for the steel tension bar}$$

$$B_{n,SMA} = F_{u,SMA} A_b = 128 \text{ kip} \quad \text{The ultimate capacity for the SMA tension bar}$$

Calculate the ultimate moment capacity due to the tension bars ($M_{p,bar}$)

$$M_{p,bar} = 2B_{n,SMA}(h_1 + h_2) + 2B_{n,steel}(h_3 + h_4) = 19280 \text{ kip-in}$$

$$1.25M_p \leq M_{p,bar} \text{ (OK.)}$$

For the non-ductile design for the tension bars, the design factor which is 1.25 occupies the enough safety against the bolt fracture failure (Check the $d_{b,req}$, Section B.2).

D.4 Shear Rupture Failure at the Tension Bar

$$B_s = n_b F_v A_b \quad \text{The capacity of the tension bar under shearing}$$

The nominal shear capacity of the SMA bar ($F_{v,SMA}$) is not provided on the specification. The check for the shear rupture failure shall be performed only at the steel tension bars with that of the steel bar ($F_{v,steel}$).

$$\phi = 0.75$$

$$\phi F_{v,steel} = 44.2 \text{ ksi} \quad \text{Single shear plane case (AISC 2001, Table 7-10)}$$

$$n_b = 8 \quad \text{The number of steel tension bars}$$

$$\phi B_s = \phi n_b F_{v,steel} A_b = 278 \text{ kips}$$

$$L_b = 175 \text{ in} \quad \text{The distance from the tip of the beam to the center of the column}$$

$$\frac{1.25M_p}{L_b} = 118 \leq \phi B_s \text{ (OK.)}$$

D.5 End-Plate Rupture Failure

$$L_c = d_c - \frac{d_h}{2} = 1.22 \text{ in}$$

$$1.2L_c t_p F_u = 107 \text{ kip}$$

$$r_f = 2.4d_h t_p F_u = 186 \text{ kip}$$

$$1.2L_c t_p F_u \leq 2.4d_h t_p F_u \text{ (OK.)}$$

$$R_{n, \text{tear}} = 8r_1 = 1489 \text{ kip}$$

$$\phi = 0.75$$

$$\frac{1.25M_p}{L_b} \leq \phi R_{n, \text{tear}} \quad (\text{OK.})$$

D.6 Fracture at the Welding Area

Refer to the AISC 2001 specification (Section 16-J2)

Use submerged arc welding

$$F_{\text{exx}} = 100 \text{ ksi} \quad \text{Electrode Strength (E100)}$$

$$\phi R_{n, w1} = 0.75 F_{\text{exx}} 0.6 t_f b_f = 396 \text{ kip} \quad \text{The welding capacity of the flange section}$$

$$\phi R_{n, w2} = 0.75 F_{\text{exx}} 0.6 t_w (d - 2t_f) = 994 \text{ kip} \quad \text{The welding capacity of the flange section}$$

$$\phi M_{p, \text{weld}} = \phi R_{n, w1} (d - t_f) + \phi R_{n, w2} \frac{d - 2t_f}{2} = 20540 \text{ kip-in} \quad \text{Moment Capacity at the welding}$$

$$1.25M_p \leq \phi M_{p, \text{weld}} \quad (\text{OK.})$$

Satisfy the limit to occupy the ductile failure due to yielding of the beam

E. Comparisons with FE Analysis

The Von-Mises stress at the column surface, the middle of the steel tension and SMA bars, and the beam were monitored as the applied static moment increased, are shown in Figure B.12. Based on the behavior modes of the components, safe and unsafe behavior zones can be established and the performance of the individual components checked. The stress paths should avoid entering the unsafe zone. This implies that the connections behaved in a ductile manner and exceeded the full plastic strength of the beam (M_p).

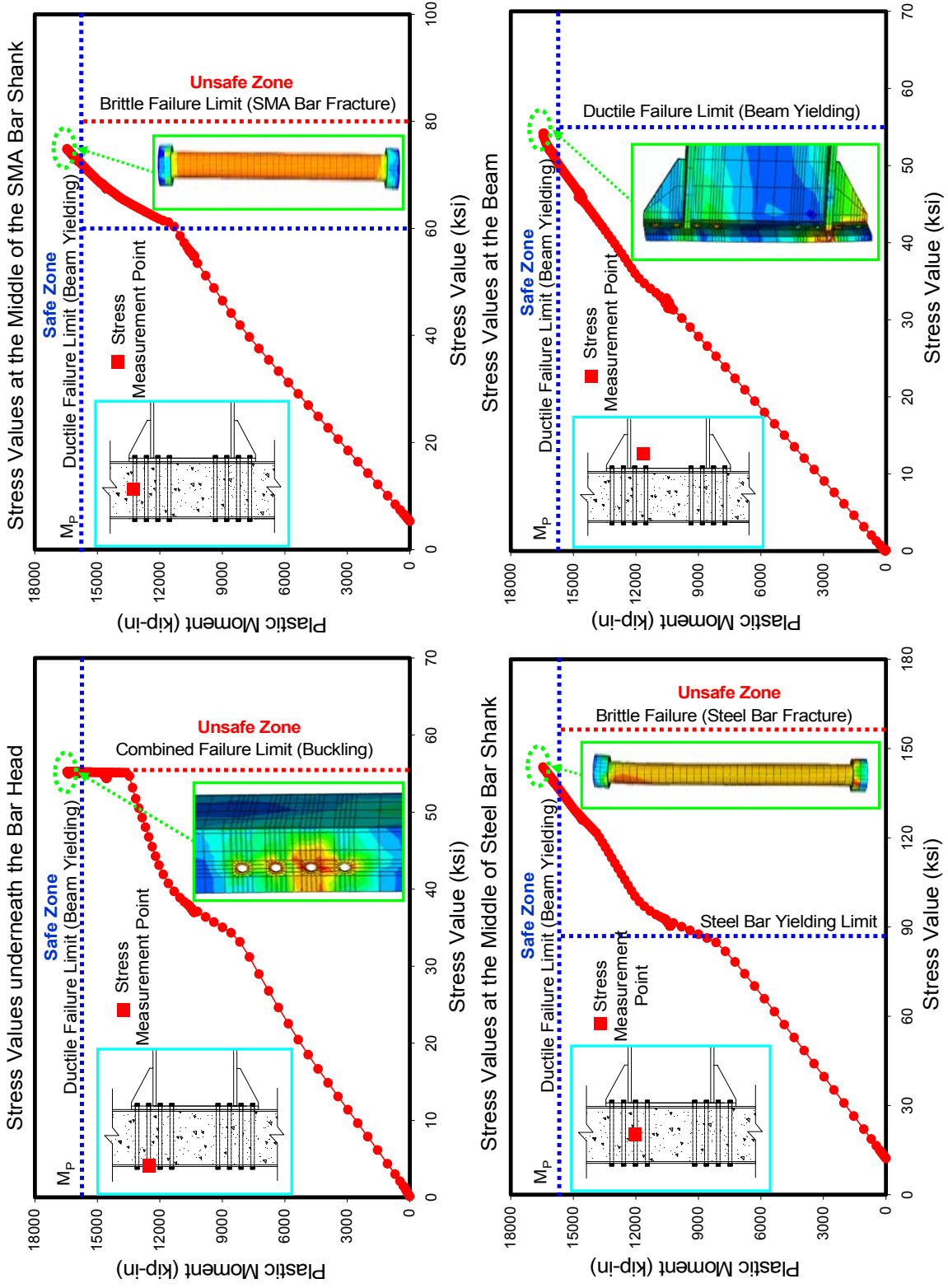


Figure B.12 Structural failure types based on the stress measurement (End-plate connection with RCFT Columns)

Case2: End-Plate Connection with CCFT Columns

End-plate connection design check

Refer to AISC/ANSI 358-05 Manual

Refer to AISC-LRFD 2001

Refer to Eurocode 4 (Composite Column Design)

Refer to Steel Tip Manual (Astaneh-Asl, 1995)

Satisfy the prequalification limits: Table 6.1 in ANSI 358-05 (See Table B.1)

Use material properties for A.572 steel and A490 bolt based on the material test performed on SAC test models (Swanson, 2002).

Given Values

Table B.3 Material properties for the end-plate connection (Case 2)

Materials	F_y	F_u
Beam	55 ksi	73 ksi
Column	55 ksi	73 ksi
Plate	55 ksi	73 ksi
Concrete	3.2 ksi	4 ksi
Steel Bar	85 ksi	162 ksi
SMA Bar	60 ksi	80 ksi

Beam: W24X103

Column: HSS18X500

(From the standard shape in the AISC-LRFD 2001 specification)

$E = 29000$ ksi

The elastic modulus for the steel material

$F_y = 55$ ksi

The yield stress for the steel material

$F_u = 73$ ksi

The ultimate stress for the steel material

$F_{u,steel} = 162$ ksi

The ultimate strength for the steel bar

$F_{u,SMA} = 80$ ksi

The ultimate strength for the SMA bar

$d = 24.5$ in	The depth of the beam
$t_f = 0.98$ in	The thickness of the beam flange
$b_f = 9.0$ in	The width of the beam flange
$t_w = 0.56$ in	The thickness of the beam web
$S_{gy} = 245$ in ³	The section modulus of the beam
$Z_{gy} = 285$ in ³	The plastic section modulus of the beam
$h = 18.0$ in	The height or width of the column
$t_c = 0.5$ in	The thickness of the column
$b_p = 15.0$ in	The width of the end-plate
$d_p = 38.5$ in	The depth of the end-plate
$t_p = 1.0$ in	The thickness of the end-plate
$Z_{py} = \frac{b_p d_p^2}{4} = 5558$ in ³	The plastic section modulus of the end-plate
$d_b = 1.0$ in	The diameter of the tension bar
$d_h = 1.06$ in	The diameter of the bar hole

Geometric parameters were illustrated in Figure B.1

$\tau_{cu} = 6.5$ ksi	The ultimate strength of the confined concrete in PZ
$m = 2$	The number of tension bars per row
$n = 8$	The number of rows for the bar arrangement

A. Determine the Design Strength

The design strength (M_p) should be based on the full plastic strength of the beam.

$$M_p = Z_{gy} F_y = 15400 \text{ kip-in}$$

B. Ductile Failure Modes

B.1 Slippage at the Shear Faying Surface

The check for the slippage strength is not available for the end-plate connections due to the lack of the shear faying surface.

B.2 Bearing yielding around the Shear Bolt Holes

The check for bearing strength around the shear bolt holes is not available for the end-plate connections due to absence of the shear bolt.

B.3 Yielding Failure of the Gross Section of the End-Plate ($M_{P,end-plate}$)

$\phi = 0.9$ Design reduction factor for the yielding failure

$$M_{P,end-plate} = Z_{py} F_y = 3.057 \cdot 10^5 \text{ kip-in}$$

$$\phi \cdot M_{P,end-plate} \geq 1.25 \cdot M_p \text{ (OK.)}$$

Satisfy the limit to occupy the ductile failure due to yielding of the beam

C. Mixed Failure Modes

C.1 Local Buckling at the beam flange

$$\frac{b_f}{2 \cdot t_f} = 4.592$$

$$\lambda_p = 0.38 \sqrt{\frac{E}{F_y}} = 8.726 \quad \text{The compact slenderness ratio}$$

$$\frac{b_f}{2 \cdot t_f} \leq \lambda_p \text{ (OK.)}$$

C.2 Local Buckling at the Composite Column

$$\frac{h}{t_c} = 36$$

$$60 \cdot \varepsilon^2 = 60 \left(\frac{34.08}{F_Y} \right) = 37.16 \quad \text{Local buckling check (Eurocode 4, 2004)}$$

$$\frac{h}{t_c} \leq 60 \cdot \varepsilon^2 \text{ (OK.)} \quad \text{Compact column case}$$

C.3 Shear Yielding of the Panel Zone (PZ)

Check shear yielding of the rectangular shaped panel zone (Wu et al., 2005)

$$K_f = \frac{2Eh \cdot (t_c + t_p)^3}{(d - t_f)^2} \quad \text{The stiffness of the generalized column flange}$$

$$K_f = 6.369 \cdot 10^3 \text{ kip/in}$$

$$r_A = 1 - m \frac{d_h}{h - 2t_c} = 0.875 \quad \text{The area reduction factor due to bar holes}$$

$$r_C = \left(1 - 2 \frac{nd_h}{d_b} + 2 \frac{nd_h}{d_b r_A} \right)^{-1} = 0.910 \quad \text{The reduction factor}$$

$$r_w = \left(1 - \frac{nd_h}{d_b} + \frac{nd_h}{d_b r_A} \right)^{-1} = 0.953 \quad \text{The reduction factor for bar holes}$$

$$K_w = 2(h - 2t_c) t_c \frac{3E}{7} \quad \text{The stiffness of the column web}$$

$$K_w = 2.113 \cdot 10^5 \text{ kip/in}$$

$$A_c = (h - 2t_c)^2 = 227 \quad \text{The area of the inside concrete}$$

Compute the yield shear strength (V_y) and ultimate shear strength (V_u) at the panel

zone

$$V_y = \frac{2(h - 2t_c - md_h) t_c F_y}{\sqrt{3}} \left(1 + \frac{K_f}{r_w K_w} \right) + r_C \tau_{cu} A_c = 1830 \text{ kip}$$

$$V_u = \frac{2(h - 2t_c - md_h) t_c F_y}{\sqrt{3}} + r_C \tau_{cu} A_c + \frac{2h(t_c + t_p)^2 F_y}{3(d - t_f)} = 1878 \text{ kip}$$

$$1.25V_p = 1.25 \frac{M_p}{d} = 786 \text{ kip}$$

$$\phi = 0.8 \quad \text{The design reduction factor}$$

$$1.25V_p \leq \phi V_y \text{ (OK.)}$$

Satisfy the limit to occupy the ductile failure due to yielding of the beam

D. Brittle (Fracture) Failure Modes

D.1 Block Shear Failure at the Shear Component

The check for the block shear failure is not available for the end-plate connection due to absence of the plate under the direct shear force.

D.2 Net Section Failure

The check for the net section failure is not available for the end-plate connection due to absence of the plate under the direct shear force.

D.3 Fracture of the Tension Bars

Apply the AISC/ANSI 358-05 specifications

$$A_b = \frac{\pi d_b^2}{4} = 0.785 \text{ in}^2 \quad \text{The section area of the tension bar}$$

$$h_1 = 29.75 \text{ in}$$

$$h_2 = 26.25 \text{ in}$$

$$h_3 = 24.5 \text{ in}$$

$$h_4 = 21.0 \text{ in}$$

Here, h_i ($i = 1$ to 4) is the distance from the maximum bearing to each center of the bar hole (See Table B.5).

$$B_{n,steel} = F_{u,steel} A_b = 266 \text{ kip} \quad \text{The ultimate capacity for the steel tension bar}$$

$$B_{n,SMA} = F_{u,SMA} A_b = 128 \text{ kip} \quad \text{The ultimate capacity for the SMA tension bar}$$

Calculate the ultimate moment capacity due to the tension bars ($M_{p,bar}$)

$$M_{p,bar} = 2B_{n,SMA} (h_1 + h_2) + 2B_{n,steel} (h_3 + h_4) = 19280 \text{ kip-in}$$

$$1.25M_p \leq M_{p,bar} \text{ (OK.)}$$

For the non-ductile design for the tension bars, the design factor which is 1.25 occupies the enough safety against the bolt fracture failure (Check the $d_{b,req}$, Section B.2).

D.4 Shear Rupture Failure at the Tension Bar

$$B_s = n_b F_v A_b$$

The capacity of the tension bar under shearing

The nominal shear capacity of the SMA bar ($F_{v,SMA}$) is not provided on the specification. The check for the shear rupture failure shall be performed only at the steel tension bars with that of the steel bar ($F_{v,steel}$).

$$\phi = 0.75$$

$$\phi F_{v,steel} = 44.2 \text{ ksi}$$

Single shear plane case (AISC 2001, Table 7-10)

$$n_b = 8$$

The number of steel tension bars

$$\phi B_s = \phi n_b F_{v,steel} A_b = 278 \text{ kips}$$

$$L_b = 175 \text{ in}$$

The distance from the tip of the beam to the center of the column

$$\frac{1.25M_p}{L_b} = 118 \leq \phi B_s \text{ (OK.)}$$

D.5 End-Plate Rupture Failure

$$L_c = d_c - \frac{d_h}{2} = 1.22 \text{ in}$$

$$1.2L_c t_p F_u = 107 \text{ kip}$$

$$r_i = 2.4d_h t_p F_u = 186 \text{ kip}$$

$$1.2L_c t_p F_u \leq 2.4d_h t_p F_u \text{ (OK.)}$$

$$R_{n,tear} = 8r_i = 1489 \text{ kip}$$

$$\phi = 0.75$$

$$\frac{1.25M_p}{L_b} \leq \phi R_{n,tear} \text{ (OK.)}$$

D.6 Fracture at the Welding Area

Refer to the AISC 2001 specification (Section 16-J2)

Use submerged arc welding

$$F_{exx} = 100 \text{ ksi}$$

Electrode Strength (E100)

$$\phi R_{n,w1} = 0.75F_{\text{cexx}} 0.6t_f b_f = 396 \text{ kip} \quad \text{The welding capacity of the flange section}$$

$$\phi R_{n,w2} = 0.75F_{\text{cexx}} 0.6t_w (d - 2t_f) = 994 \text{ kip} \quad \text{The welding capacity of the flange section}$$

$$\phi M_{p,\text{weld}} = \phi R_{n,w1} (d - t_f) + \phi R_{n,w2} \frac{d - 2t_f}{2} = 20540 \text{ kip-in} \quad \text{Moment Capacity at the welding}$$

$$1.25M_p \leq \phi M_{p,\text{weld}} \quad (\text{OK.})$$

Satisfy the limit to occupy the ductile failure due to yielding of the beam

E. Comparisons with FE Analysis

The Von-Mises stress at the column surface, the middle of the steel tension and SMA bars, and the beam were monitored as the applied static moment increased, are shown in Figure B.13.

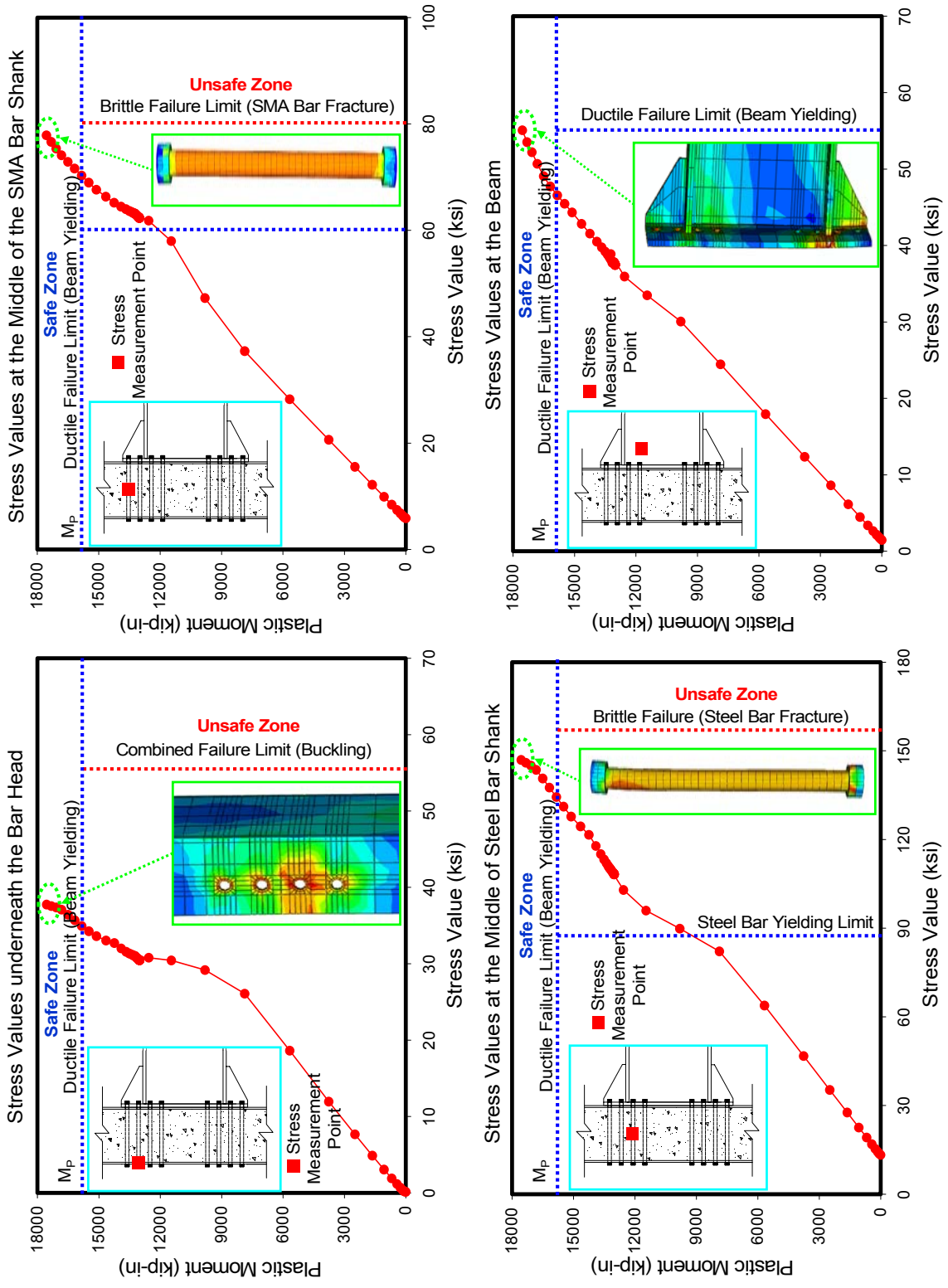


Figure B.13 Structural failure types based on the stress measurement (End-plate connection with CCFT Columns)

Case3: T-Stub Connection with RCFT Columns

T-stub connection design check

Refer to AISC-LRFD 2001

Refer to Eurocode 4 (Composite Column Design)

Refer to Steel Tip Manual (Astaneh-Asl, 1995)

Use material properties for A.572 steel and A490 bolt based on the material test performed on SAC test models (Swanson, 2001).

Given Values

Table B.4 Material properties for the T-stub connection (Case 3)

Materials	F_y	F_u
Beam	55 ksi	73 ksi
Column	55 ksi	73 ksi
T-Stub	55 ksi	73 ksi
Concrete	3.2 ksi	4 ksi
Steel Bar	85 ksi	162 ksi
SMA Bar	60 ksi	80 ksi
Shear Bolt	85 ksi	162 ksi
Web Bolts	85 ksi	162 ksi

Beam: W24X55

Column: HSS16X16X500

T-stub: Cut from W16X100

(From the standard shape in the AISC-LRFD 2001 specification)

$E = 29000$ ksi The elastic modulus for the steel material

$F_y = 55$ ksi The yield stress for the steel material

$F_u = 73$ ksi The ultimate stress for the steel material

$F_{u,steel} = 162$ ksi The ultimate strength for the steel bar

$F_{u,SMA} = 80$ ksi The ultimate strength for the SMA bar

$d = 23.6$ in	The depth of the beam
$t_f = 0.505$ in	The thickness of the beam flange
$b_f = 7.04$ in	The width of the beam flange
$t_w = 0.395$ in	The thickness of the beam web
$S_{gy} = 115$ in ³	The section modulus of the beam
$Z_{gy} = 135$ in ³	The plastic section modulus of the beam
$h = 16.0$ in	The height or width of the column
$t_c = 0.5$ in	The thickness of the column
$W_{eff} = 15.5$ in	The effective width of the T-stub
$g_t = 6.0$ in	The gage length
$b_f = 10.375$ in	The height of the T-stub
$t_{tf} = 1.0$ in	The thickness of the T-stub flange
$t_{stem} = 0.56$ in	The thickness of the T-stem
$d_b = 1.0$ in	The diameter of the tension bar
$d_h = 1.06$ in	The diameter of the bar hole
$d_s = 1.0$ in	The diameter of the shear bolt

Geometric parameters were illustrated in Figure B.7

$\tau_{cu} = 6.5$ ksi	The ultimate strength of the confined concrete in PZ
$m = 4$	The number of tension bars per row
$n = 4$	The number of rows for the bar arrangement
$T_m = 64$	The initial pretension force for the shear bolt (AISC-LRFD 2001, Table 8.1)
$A_b = 0.785$ in ²	The cross section area of shear bolt

A. Determine the Design Strength

The design strength (M_p) should be based on the full plastic strength of the beam.

$$M_p = Z_{gy} F_y = 7425 \text{ kip-in}$$

B. Ductile Failure Modes

B.1 Slippage at the Shear Faying Surface

$u = 0.33$ The mean slip coefficient (Class A coating)

$D_u = 1.13$ The multiplier

$T_m = 64$ kip The specified minimum pretension
(AISC Table 7.15)

$T_u = F_{u,steel} A_b = 129$ kip The required strength in tension

$N_b = 10$ The number of shear bolts

$\phi = 1.0$ The reduction factor for the standard hole

The nominal strength for the slip resistance ($R_{n,slip}$) can be calculated.

$$R_{n,slip} = u D_u T_m N_b \left(1 - \frac{T_u}{D_u T_m N_b} \right) = 196 \text{ kip}$$

$$M_{p,slip} = R_{n,slip} d = 4630 \text{ kip-in}$$

$$\phi M_{p,slip} \leq 0.8 M_p = 5940 \text{ kip-in (OK.)}$$

B.2 Bearing Yielding around the Shear Bolt Hole

$\phi = 0.9$ Design reduction factor for the yielding failure

$$R_{n,bearing} = 2.4 F_y d_h N_b t_{stem} = 786 \text{ kips}$$

$$M_{p,bearing} = R_{n,bearing} d = 18540 \text{ kip-in}$$

$$\phi M_{p,bearing} \geq 1.25 M_p = 9281 \text{ kip-in (OK.)}$$

B.3 Yielding Failure of the Gross Section of the T-stem ($M_{p,stem}$)

$\phi = 0.9$ Design reduction factor for the yielding failure

$$A_{stem} = W_{eff} t_{stem} = 8.68 \text{ in}^2 \quad \text{The gross section area of the T-stem}$$

$$R_{n,stem} = F_y A_{stem} = 478 \text{ kip}$$

$$M_{p,stem} = R_{n,stem} d = 11270 \text{ kip-in}$$

$$\phi \cdot M_{p,stem} \geq 1.25 \cdot M_p \text{ (OK.)}$$

Satisfy the limit to occupy the ductile failure due to yielding of the beam

C. Mixed Failure Modes

C.1 Local Buckling at the beam flange

$$\frac{b_f}{2 \cdot t_f} = 6.97$$

$$\lambda_p = 0.38 \sqrt{\frac{E}{F_y}} = 8.726 \quad \text{The compact slenderness ratio}$$

$$\frac{b_f}{2 \cdot t_f} \leq \lambda_p \text{ (OK.)}$$

C.2 Local Buckling at the Composite Column

$$\frac{h}{t_c} = 32$$

$$42 \cdot \varepsilon = 42 \sqrt{\frac{34.08}{F_y}} = 33.061 \quad \text{Local buckling check (Eurocode 4, 2004)}$$

$$\frac{h}{t_c} \leq 42 \cdot \varepsilon \text{ (OK.)} \quad \text{Compact column case}$$

C.3 Shear Yielding of the Panel Zone (PZ)

Check shear yielding of the rectangular shaped panel zone (Wu et al., 2005)

$$K_f = \frac{2Eh \cdot (t_c + t_{ff})^3}{(d - t_f)^2} \quad \text{The stiffness of the generalized column flange}$$

$$K_f = 5.872 \cdot 10^3 \text{ kip/in}$$

$$r_A = 1 - m \frac{d_h}{h - 2t_c} = 0.717 \quad \text{The area reduction factor due to bar holes}$$

$$r_C = \left(1 - 2 \frac{nd_h}{d_b} + 2 \frac{nd_h}{d_b r_A} \right)^{-1} = 0.875 \quad \text{The reduction factor}$$

$$r_w = \left(1 - \frac{nd_h}{d_b} + \frac{nd_h}{d_b r_A} \right)^{-1} = 0.934 \quad \text{The reduction factor for bar holes}$$

$$K_w = 2(h - 2t_c) t_c \frac{3E}{7} \quad \text{The stiffness of the column web}$$

$$K_w = 1.864 \cdot 10^5 \text{ kip/in}$$

$$A_c = (h - 2t_c)^2 = 225 \quad \text{The area of the inside concrete}$$

Compute the yield shear strength (V_y) and ultimate shear strength (V_u) at the panel zone

$$V_y = \frac{2(h - 2t_c - md_h) t_c F_y}{\sqrt{3}} \left(1 + \frac{K_f}{r_w K_w} \right) + r_c \tau_{cu} A_c = 1633 \text{ kip}$$

$$V_u = \frac{2(h - 2t_c - md_h) t_c F_y}{\sqrt{3}} + r_c \tau_{cu} A_c + \frac{2h(t_c + t_p)^2 F_y}{3(d - t_f)} = 1723 \text{ kip}$$

$$1.25V_p = 1.25 \frac{M_p}{d} = 393 \text{ kip}$$

$$\phi = 0.8 \quad \text{The design reduction factor}$$

$$1.25V_p \leq \phi V_y \text{ (OK.)}$$

Satisfy the limit to occupy the ductile failure due to yielding of the beam

D. Brittle (Fracture) Failure Modes

D.1 Block Shear Failure at the Shear Component

Check the block shear failure at the T-stub

$$s = 4 \text{ in} \quad \text{The shear bolt spacing}$$

$$A_{gt} = s \cdot t_{stem} = 2.24 \text{ in}^2 \quad \text{The gross area subjected to tension}$$

$$A_{nt} = (s - d_h) \cdot t_{stem} = 1.645 \text{ in}^2 \quad \text{The net section area subjected to tension}$$

$$d_e = 1.75 \text{ in} \quad \text{The edge distance}$$

$$A_{gv} = 2(d_e + 3 \cdot 4) \cdot t_{stem} = 15.4 \text{ in}^2 \quad \text{The gross area subjected to shear}$$

$$A_{nv} = 2(d_e + 3 \cdot 4 - 4.5d_h) \cdot t_{stem} = 10.05 \text{ in}^2 \quad \text{The net section area subjected to shear}$$

Check the failure condition

$$F_u A_{nt} = 120.1 \leq 0.6 F_u A_{nv} = 440 \text{ kip (OK.)}$$

$$R_{n,block} = 0.6 F_u A_{nv} + F_y A_{gt} = 563.2 \text{ kip}$$

Check the design reduction factors

$\phi_f = 0.75$ The design reduction factor for the fracture

$\phi_y = 0.90$ The design reduction factor for the yielding

$$\phi_f R_{n,block} = 422.4 \text{ kip}$$

$$1.25\phi_y \frac{M_p}{d} = 353.95 \leq \phi_f R_{n,block} \text{ (OK.)}$$

D.2 Net Section Failure

$$R_{n,net} = F_u A_{stem} = 633.6 \text{ kip}$$

$$\phi_f R_{n,net} = 570.26$$

$$1.25\phi_y \frac{M_p}{d} = 353.95 \leq \phi_f R_{n,net} \text{ (OK.)}$$

D.3 Fracture of the Tension Bars

Apply the AISC/ANSI 358-05 specifications

$$A_b = \frac{\pi d_b^2}{4} = 0.785 \text{ in}^2 \quad \text{The section area of the tension bar}$$

$$B_{n,steel} = F_{u,steel} A_b = 133 \text{ kip} \quad \text{The ultimate capacity for the steel tension bar}$$

$$B_{n,SMA} = F_{u,SMA} A_b = 64 \text{ kip} \quad \text{The ultimate capacity for the SMA tension bar}$$

Calculate the ultimate moment capacity due to the tension bars ($M_{p,bar}$)

$$M_{p,bar} = 4B_{n,SMA} \left(d + \frac{g_t}{2} - \frac{t_f}{2} \right) + 4B_{n,steel} \left(d - \frac{g_t}{2} - \frac{t_f}{2} \right) = 17230 \text{ kip-in}$$

$$\phi_f M_{p,bar} = 12920 \text{ kip-in}$$

$$1.25\phi_y M_p = 8353 \leq \phi_f M_{p,bar} \text{ (OK.)}$$

D.4 Shear Rupture Failure at the Tension Bar

$$B_s = n_b F_v A_b \quad \text{The capacity of the tension bar under shearing}$$

The nominal shear capacity of the SMA bar ($F_{v,SMA}$) is not provided on the specification. The check for the shear rupture failure shall be performed only at the steel tension bars with that of the steel bar ($F_{v,steel}$).

$$\phi = 0.75$$

$$\phi F_{v, \text{steel}} = 44.2 \text{ ksi}$$

Single shear plane case (AISC 2001, Table 7-10)

$$n_b = 8$$

The number of steel tension bars

$$\phi B_s = \phi n_b F_{v, \text{steel}} A_b = 278 \text{ kips}$$

$$L_b = 175 \text{ in}$$

The distance from the tip of the beam to the center of the column

$$\frac{1.25 M_p}{L_b} = 53.05 \leq \phi B_s \text{ (OK.)}$$

D.5 Shear Rupture Failure at the Shear Bolts

$$\phi = 0.75$$

$$\phi F_v = 44.2 \text{ ksi}$$

Single shear plane case (AISC 2001, Table 7-10)

$$n_s = 10$$

The number of shear bolts

$$A_s = \frac{\pi d_s^2}{4} = 0.785 \text{ in}^2$$

The cross section area of the shear bolts

$$\phi R_{n, \text{shear}} = \phi n_s F_v A_s = 350 \text{ kips}$$

$$\frac{1.25 \phi_y M_p}{d} = 353.95 \approx \phi B_s \text{ (OK.)}$$

D.6 T-Stub Rupture Failure

$$d_e = 1.75$$

The edge distance (Refer to Figure B.6)

$$L_c = d_e - \frac{d_h}{2} = 1.22 \text{ in}$$

$$1.2 L_c t_{\text{stem}} F_u = 59.85 \text{ kip}$$

$$r_i = 2.4 d_h t_{\text{stem}} F_u = 104.29 \text{ kip}$$

$$1.2 L_c t_p F_u \leq 2.4 d_h t_p F_u \text{ (OK.)}$$

$$R_{n, \text{tear}} = 10 r_i = 834.34 \text{ kip}$$

$$\phi = 0.75$$

$$\frac{1.25M_p}{d} \leq \phi R_{n, \text{tear}} \quad (\text{OK.})$$

D.7 Shear Tab Failure

Refer to AISC-LRFD 2001 (Table 10.1)

Use 4.5X9.5X0.56 double plate for shear tab.

Shear tab has enough strength to resist the applied shear force ($1.25M_p/L_b = 53.05$ kip).

Satisfy the limit to occupy the ductile failure due to yielding of the beam

D.8 Fracture at the Weld Area

There are no welds used in this connection. Thus, the weld failure checks are not available for this connection system.

E. Comparisons with FE Analysis

The Von-Mises stress at the column surface, the middle of the steel tension and SMA bars, the beam and the T-stem were monitored as the applied static moment increased, are shown in Figure B.14.

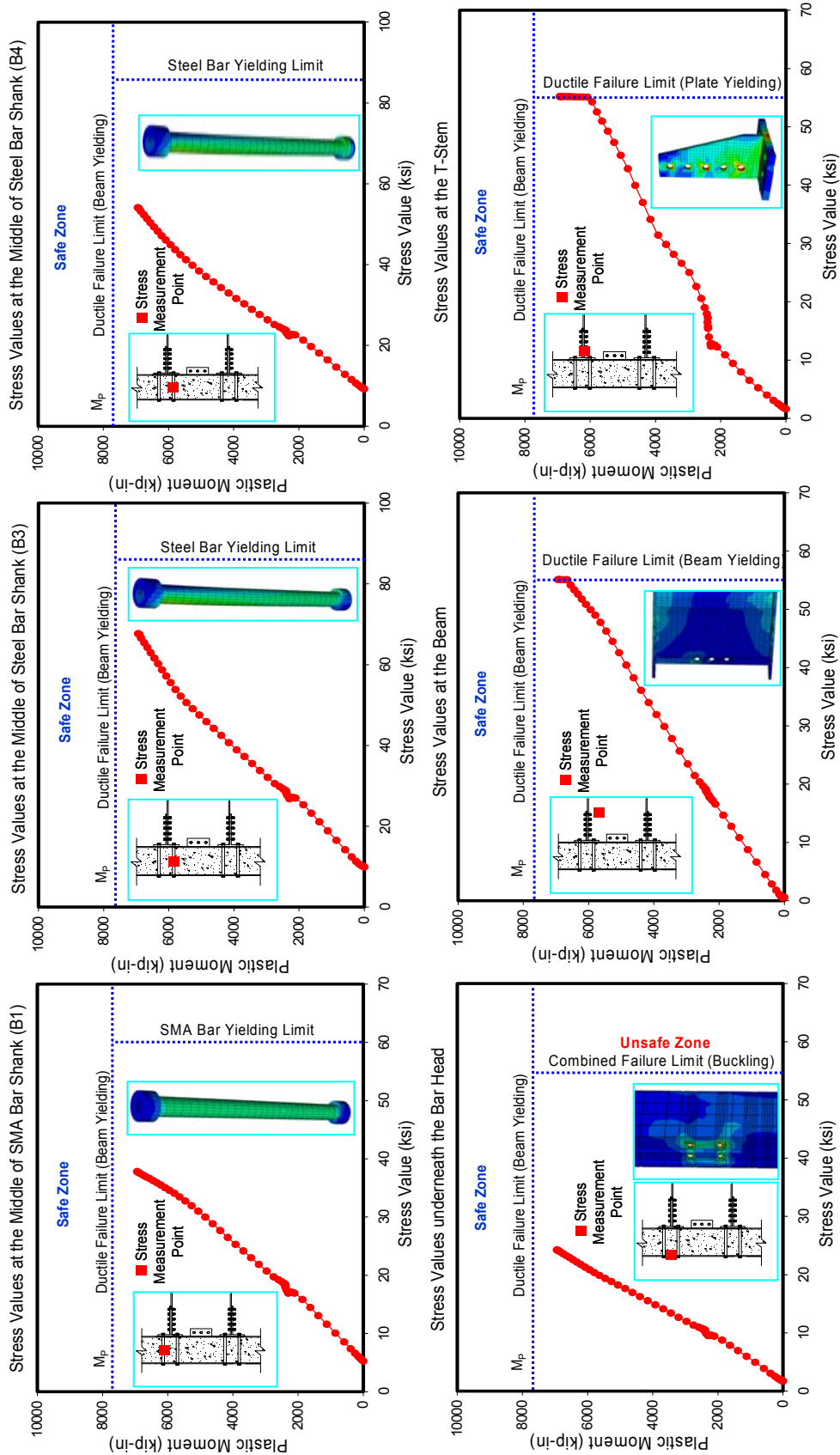


Figure B.14 Structural failure types based on the stress measurement (T-stub connection with RCFT Columns)

Case4: T-Stub Connection with CCFT Columns

T-stub connection with CCFT columns were designed with the same component as that with RCFT columns except for the panel zone and composite columns. Both cases show the same capacity against the failure modes. Thus, the procedures to estimate the identical failure strength with Case 3 are omitted in this section. Only mixed failure modes for the panel zone and composite columns will be investigated.

C. Mixed Failure Modes

C.1 Local Buckling at the beam flange

$$\frac{b_f}{2 \cdot t_f} = 6.97$$

$$\lambda_p = 0.38 \sqrt{\frac{E}{F_y}} = 8.726 \quad \text{The compact slenderness ratio}$$

$$\frac{b_f}{2 \cdot t_f} \leq \lambda_p \text{ (OK.)}$$

C.2 Local Buckling at the Composite Column

Use HSS 18X500 size columns

$$\frac{h}{t_c} = 36$$

$$60 \cdot \varepsilon^2 = 60 \left(\frac{34.08}{F_y} \right) = 37.16 \quad \text{Local buckling check (Eurocode 4, 2004)}$$

$$\frac{h}{t_c} \leq 60 \cdot \varepsilon^2 \text{ (OK.)} \quad \text{Compact column case}$$

C.3 Shear Yielding of the Panel Zone (PZ)

Check shear yielding of the rectangular shaped panel zone (Wu et al., 2005)

$$K_f = \frac{2Eh \cdot (t_c + t_p)^3}{(d - t_f)^2} \quad \text{The stiffness of the generalized column flange}$$

$$K_f = 6.369 \cdot 10^3 \text{ kip/in}$$

$$r_A = 1 - m \frac{d_h}{h - 2t_c} = 0.875 \quad \text{The area reduction factor due to bar holes}$$

$$r_C = \left(1 - 2 \frac{nd_h}{d_b} + 2 \frac{nd_h}{d_b r_A} \right)^{-1} = 0.910 \quad \text{The reduction factor}$$

$$r_w = \left(1 - \frac{nd_h}{d_b} + \frac{nd_h}{d_b r_A} \right)^{-1} = 0.953 \quad \text{The reduction factor for bar holes}$$

$$K_w = 2(h - 2t_c) t_c \frac{3E}{7} \quad \text{The stiffness of the column web}$$

$$K_w = 2.113 \cdot 10^5 \text{ kip/in}$$

$$A_c = (h - 2t_c)^2 = 227 \quad \text{The area of the inside concrete}$$

Compute the yield shear strength (V_y) and ultimate shear strength (V_u) at the panel zone

$$V_y = \frac{2(h - 2t_c - md_h) t_c F_y}{\sqrt{3}} \left(1 + \frac{K_f}{r_w K_w} \right) + r_C \tau_{cu} A_c = 1830 \text{ kip}$$

$$V_u = \frac{2(h - 2t_c - md_h) t_c F_y}{\sqrt{3}} + r_C \tau_{cu} A_c + \frac{2h(t_c + t_p)^2 F_y}{3(d - t_f)} = 1878 \text{ kip}$$

$$1.25V_p = 1.25 \frac{M_p}{d} = 786 \text{ kip}$$

$$\phi = 0.8 \quad \text{The design reduction factor}$$

$$1.25V_p \leq \phi V_y \text{ (OK.)}$$

Satisfy the limit to occupy the ductile failure due to yielding of the beam

E. Comparisons with FE Analysis

The Von-Mises stress at the column surface, the middle of the steel tension and SMA bars, the beam and the T-stem were monitored as the applied static moment increased, are shown in Figure B.15.

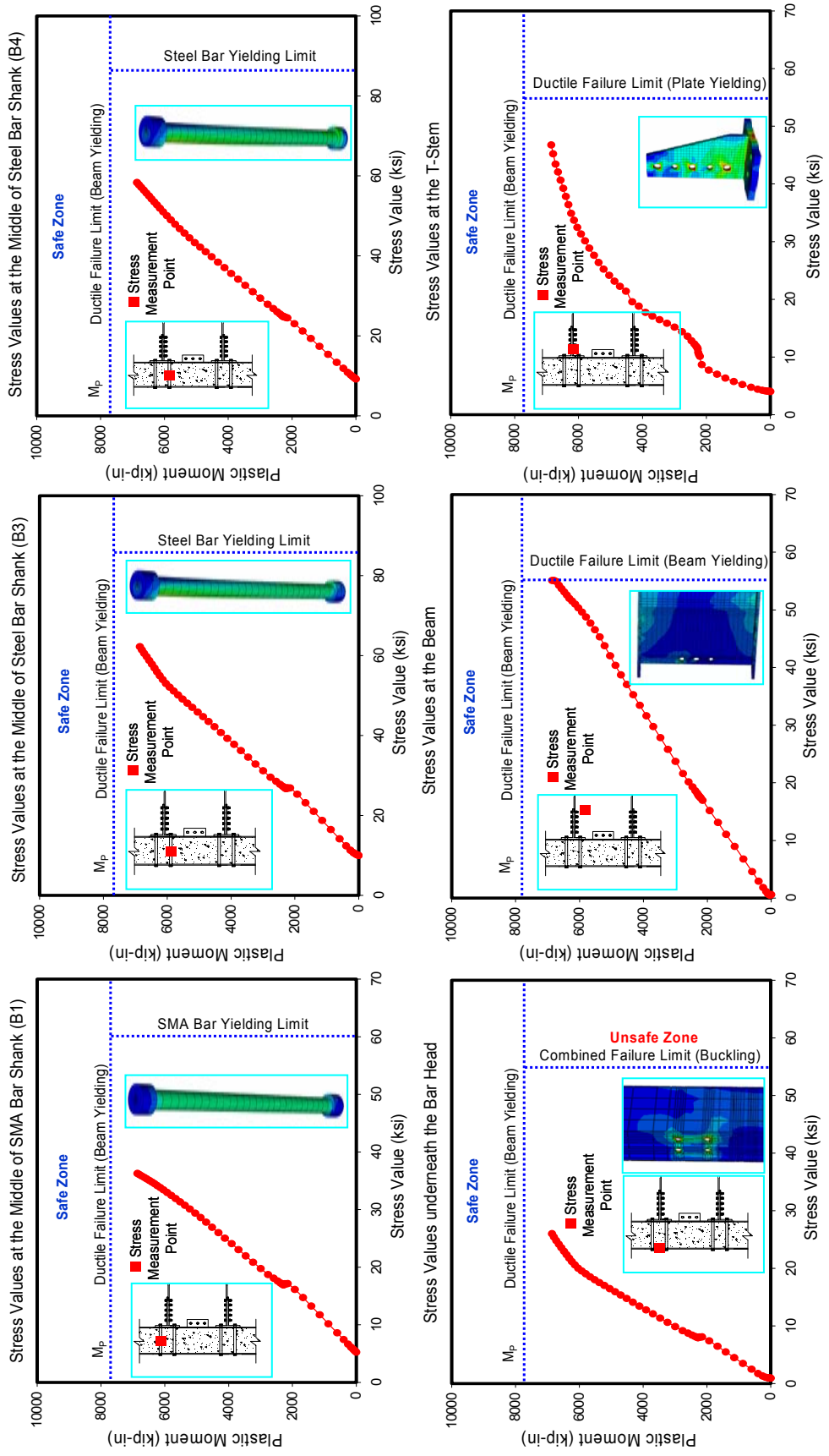


Figure B.15 Structural failure types based on the stress measurement (T-stub connection with CCFT Columns)

Case5: Clip Angle Connection with RCFT Columns

Clip angle connection design check

Refer to AISC/ANSI 358-05 Manual

Refer to AISC-LRFD 2001

Refer to Eurocode 4 (Composite Column Design)

Refer to Steel Tip Manual (Astaneh-Asl, 1995)

Use material properties for A.572 steel and A490 bolt based on the material test performed on SAC test models (Swanson, 2001).

Given Values

Table B.5 Material properties for the T-stub connection (Case 5)

Materials	F_y	F_u
Beam	55 ksi	73 ksi
Column	55 ksi	73 ksi
Clip Angle	55 ksi	73 ksi
Concrete	3.2 ksi	4 ksi
Steel Bar	85 ksi	162 ksi
SMA Bar	60 ksi	80 ksi
Shear Bolt	85 ksi	162 ksi
Web Bolts	85 ksi	162 ksi

Beam: W18X50

Column: HSS12X12X500

Clip Angle: L6X8X1

(From the standard shape in the AISC-LRFD 2001 specification)

$E = 29000$ ksi

The elastic modulus for the steel material

$F_y = 55$ ksi

The yield stress for the steel material

$F_u = 73$ ksi

The ultimate stress for the steel material

$F_{u,steel} = 162$ ksi

The ultimate strength for the steel bar

$F_{u,SMA} = 80 \text{ ksi}$	The ultimate strength for the SMA bar
$d = 18.0 \text{ in}$	The depth of the beam
$t_f = 0.57 \text{ in}$	The thickness of the beam flange
$b_f = 7.50 \text{ in}$	The width of the beam flange
$S_{gy} = 88.89 \text{ in}^3$	The section modulus of the beam
$Z_{gy} = 101 \text{ in}^3$	The plastic section modulus of the beam
$h = 12.0 \text{ in}$	The height or width of the column
$t_c = 0.5 \text{ in}$	The thickness of the column
$W_{eff} = 9.0 \text{ in}$	The effective width of the clip angle
$g_t = 6.0 \text{ in}$	The gage length
$b_f = 6.0 \text{ in}$	The height of the clip angle
$t_{tf} = 1.0 \text{ in}$	The thickness of the clip angle flange
$t_{leg} = 1.0 \text{ in}$	The thickness of the clip angle leg
$d_{b,steel} = 1.07 \text{ in}$	The diameter of the steel tension bar
$d_{b,SMA} = 1.0 \text{ in}$	The diameter of the SMA tension bar
$d_{h,steel} = 1.13 \text{ in}$	The diameter of the steel bar hole
$d_{h,SMA} = 1.06 \text{ in}$	The diameter of the SMA bar hole
$d_s = 1.0 \text{ in}$	The diameter of the shear bolt
$d_h = 1.06 \text{ in}$	The diameter of the shear bolt hole

Geometric parameters were illustrated in Figure B.7

$\tau_{cu} = 6.5 \text{ ksi}$	The ultimate strength of the confined concrete in PZ
$m = 3$	The number of tension bars per row
$n = 2$	The number of rows for the bar arrangement
$T_m = 64$	The initial pretension force for the shear bolt (AISC-LRFD 2001, Table 8.1)
$A_b = 0.785 \text{ in}^2$	The cross section area of shear bolt

A. Determine the Design Strength

The design strength (M_p) should be based on the full plastic strength of the beam.

$$M_p = Z_{gy} F_y = 5555 \text{ kip-in}$$

B. Ductile Failure Modes

B.1 Slippage at the Shear Faying Surface

$u = 0.33$ The mean slip coefficient (Class A coating)

$D_u = 1.13$ The multiplier

$T_m = 64 \text{ kip}$ The specified minimum pretension
(AISC Table 7.15)

$T_u = F_{u,steel} A_b = 129 \text{ kip}$ The required strength in tension

$N_b = 4$ The number of shear bolts

$\phi = 1.0$ The reduction factor for the standard hole

The nominal strength for the slip resistance ($R_{n,slip}$) can be calculated.

$$R_{n,slip} = u D_u T_m N_b \left(1 - \frac{T_u}{D_u T_m N_b} \right) = 52.98 \text{ kip}$$

$$M_{p,slip} = R_{n,slip} d = 954 \text{ kip-in}$$

$$\phi M_{p,slip} \leq 0.8 M_p = 4444 \text{ kip-in (OK.)}$$

B.2 Bearing Yielding around the Shear Bolt Hole

$\phi = 0.9$ Design reduction factor for the yielding failure

$$R_{n,bearing} = 2.4 F_y d_h N_b t_{leg} = 561 \text{ kips}$$

$$M_{p,bearing} = R_{n,bearing} d = 10100 \text{ kip-in}$$

$$\phi M_{p,bearing} \geq 1.25 M_p = 6944 \text{ kip-in (OK.)}$$

B.3 Yielding Failure of the Gross Section of the T-stem ($M_{p,stem}$)

$\phi = 0.9$ Design reduction factor for the yielding failure

$$A_{leg} = W_{eff} t_{leg} = 9.0 \text{ in}^2 \quad \text{The gross section area of the T-stem}$$

$$R_{n,leg} = F_y A_{leg} = 495 \text{ kip}$$

$$M_{p,leg} = R_{n,leg} d = 8910 \text{ kip-in}$$

$$\phi \cdot M_{p,leg} \geq 1.25 \cdot M_p \quad (\text{OK.})$$

Satisfy the limit to occupy the ductile failure due to yielding of the beam

C. Mixed Failure Modes

C.1 Local Buckling at the beam flange

$$\frac{b_f}{2 \cdot t_f} = 6.58$$

$$\lambda_p = 0.38 \sqrt{\frac{E}{F_y}} = 8.73 \quad \text{The compact slenderness ratio}$$

$$\frac{b_f}{2 \cdot t_f} \leq \lambda_p \quad (\text{OK.})$$

C.2 Local Buckling at the Composite Column

$$\frac{h}{t_c} = 24$$

$$42 \cdot \varepsilon = 42 \sqrt{\frac{34.08}{F_y}} = 33.061 \quad \text{Local buckling check (Eurocode 4, 2004)}$$

$$\frac{h}{t_c} \leq 42 \cdot \varepsilon \quad (\text{OK.}) \quad \text{Compact column case}$$

C.3 Shear Yielding of the Panel Zone (PZ)

Check shear yielding of the rectangular shaped panel zone (Wu et al., 2005)

$$K_f = \frac{2Eh \cdot (t_c + t_{tf})^3}{(d - t_f)^2} \quad \text{The stiffness of the generalized column flange}$$

$$K_f = 7.732 \cdot 10^3 \text{ kip/in}$$

$$r_A = 1 - m \frac{d_h}{h - 2t_c} = 0.710 \quad \text{The area reduction factor due to bar holes}$$

$$r_c = \left(1 - 2 \frac{nd_h}{d_b} + 2 \frac{nd_h}{d_b r_A} \right)^{-1} = 0.912 \quad \text{The reduction factor}$$

$$r_w = \left(1 - \frac{nd_h}{d_b} + \frac{nd_h}{d_b r_A} \right)^{-1} = 0.954 \quad \text{The reduction factor for bar holes}$$

$$K_w = 2(h - 2t_c) t_c \frac{3E}{7} \quad \text{The stiffness of the column web}$$

$$K_w = 1.367 \cdot 10^5 \text{ kip/in}$$

$$A_c = (h - 2t_c)^2 = 121 \quad \text{The area of the inside concrete}$$

Compute the yield shear strength (V_y) and ultimate shear strength (V_u) at the panel zone

$$V_y = \frac{2(h - 2t_c - md_h) t_c F_y}{\sqrt{3}} \left(1 + \frac{K_f}{r_w K_w} \right) + r_c \tau_{cu} A_c = 980 \text{ kip}$$

$$V_u = \frac{2(h - 2t_c - md_h) t_c F_y}{\sqrt{3}} + r_c \tau_{cu} A_c + \frac{2h(t_c + t_p)^2 F_y}{3(d - t_f)} = 1022 \text{ kip}$$

$$1.25V_p = 1.25 \frac{M_p}{d} = 385 \text{ kip}$$

$$\phi = 0.8 \quad \text{The design reduction factor}$$

$$1.25V_p \leq \phi V_y \text{ (OK.)}$$

Satisfy the limit to occupy the ductile failure due to yielding of the beam

D. Brittle (Fracture) Failure Modes

D.1 Block Shear Failure at the Shear Component

Check the block shear failure at the T-stub

$$s = 4.24 \text{ in} \quad \text{The shear bolt spacing}$$

$$A_{gt} = s \cdot t_{leg} = 4.24 \text{ in}^2 \quad \text{The gross area subjected to tension}$$

$$A_{nt} = (s - d_h) \cdot t_{leg} = 3.188 \text{ in}^2 \quad \text{The net section area subjected to tension}$$

$$d_e = 1.75 \text{ in} \quad \text{The edge distance}$$

$$A_{gv} = 2(d_e + 3 \cdot 1) \cdot t_{leg} = 9.5 \text{ in}^2 \quad \text{The gross area subjected to shear}$$

$$A_{nv} = 2(d_e + 3 \cdot 1 - 1.5d_h) \cdot t_{leg} = 6.313 \text{ in}^2 \quad \text{The net section area subjected to shear}$$

Check the failure condition

$$F_u A_{nt} = 232.7 \leq 0.6F_u A_{nv} = 276.5 \text{ kip (OK.)}$$

$$R_{n,\text{block}} = 0.6F_u A_{nv} + F_y A_{gt} = 510.3 \text{ kip}$$

Check the design reduction factors

$$\phi_f = 0.75 \quad \text{The design reduction factor for the fracture}$$

$$\phi_y = 0.90 \quad \text{The design reduction factor for the yielding}$$

$$\phi_f R_{n,\text{block}} = 382.7 \text{ kip}$$

$$1.25\phi_y \frac{M_p}{d} = 347.2 \leq \phi_f R_{n,\text{block}} \text{ (OK.)}$$

D.2 Net Section Failure

$$R_{n,\text{net}} = F_u A_{\text{leg}} = 657 \text{ kip}$$

$$\phi_f R_{n,\text{net}} = 492$$

$$1.25\phi_y \frac{M_p}{d} = 353.95 \leq \phi_f R_{n,\text{net}} \text{ (OK.)}$$

D.3 Fracture of the Tension Bars

Apply the AISC/ANSI 358-05 specifications

$$A_{b,\text{SMA}} = \frac{\pi d_{b,\text{SMA}}^2}{4} = 0.785 \text{ in}^2 \quad \text{The section area of the SMA tension bar}$$

$$A_{b,\text{steel}} = \frac{\pi d_{b,\text{steel}}^2}{4} = 0.899 \text{ in}^2 \quad \text{The section area of the steel tension bar}$$

$$B_{n,\text{SMA}} = F_{u,\text{SMA}} A_b = 64 \text{ kip} \quad \text{The ultimate capacity for the SMA tension bar}$$

$$B_{n,\text{steel}} = F_{u,\text{steel}} A_b = 148 \text{ kip} \quad \text{The ultimate capacity for the steel tension bar}$$

Calculate the ultimate moment capacity due to the tension bars ($M_{p,\text{bar}}$)

$$M_{p,\text{bar}} = 2B_{n,\text{SMA}} \left(d + \frac{g_t}{2} - \frac{t_f}{2} \right) + B_{n,\text{steel}} \left(d + \frac{g_t}{2} - \frac{t_f}{2} \right) = 6072 \text{ kip-in}$$

$$\phi_f M_{p,\text{bar}} = 4454 \text{ kip-in}$$

$$M_p = 5555 \leq M_{p,\text{bar}} = 6072 \text{ kip-in}$$

The diameter of the tension bar was designed in accordance with AISC/ANSI 358-05. For the non-ductile design for the tension bars, the diameters were determined by including the enough safety factor (Check the $d_{b,req}$, Section B.2).

D.4 Shear Rupture Failure at the Tension Bar

$$B_s = n_b F_v A_b$$

The capacity of the tension bar under shearing

The nominal shear capacity of the SMA bar ($F_{v,SMA}$) is not provided on the specification. The check for the shear rupture failure shall be performed only at the steel tension bars with that of the steel bar ($F_{v,steel}$).

$$\phi = 0.75$$

$$\phi F_{v,steel} = 44.2 \text{ ksi}$$

Single shear plane case (AISC 2001, Table 7-10)

$$n_b = 2$$

The number of steel tension bars

$$\phi B_s = \phi n_b F_{v,steel} A_{b,steel} = 59.58 \text{ kips}$$

$$L_b = 175 \text{ in}$$

The distance from the tip of the beam to the center of the column

$$\frac{1.25M_p}{L_b} = 39.69 \leq \phi B_s \text{ (OK.)}$$

D.5 T-Stub Rupture Failure

$$d_e = 1.75$$

The edge distance (Refer to Figure B.6)

$$L_c = d_e - \frac{d_h}{2} = 1.22 \text{ in}$$

$$1.2L_c t_{leg} F_u = 89.06 \text{ kip}$$

$$r_i = 2.4d_h t_{leg} F_u = 185.71 \text{ kip}$$

$$1.2L_c t_p F_u \leq 2.4d_h t_p F_u \text{ (OK.)}$$

$$R_{n,tear} = 4r_i = 742.85 \text{ kip}$$

$$\phi = 0.75$$

$$\frac{1.25M_p}{d} \leq \phi R_{n,tear} \text{ (OK.)}$$

D.6 Shear Tab Failure

Refer to AISC-LRFD 2001 (Table 10.1)

Use 4.5X9.5X0.56 double plate for shear tab.

Shear tab has enough strength to resist the applied shear force ($1.25M_p/L_b = 39.69$ kip).

Satisfy the limit to occupy the ductile failure due to yielding of the beam

D.7 Fracture at the Welding Area

There are no welds used in this connection. Thus, the weld failure checks are not available for this connection system.

E. Comparisons with FE Analysis

The Von-Mises stress at the column surface, the middle of the steel tension and SMA bars, the beam and the clip angle were monitored as the applied static moment increased, are shown in Figure B.16.

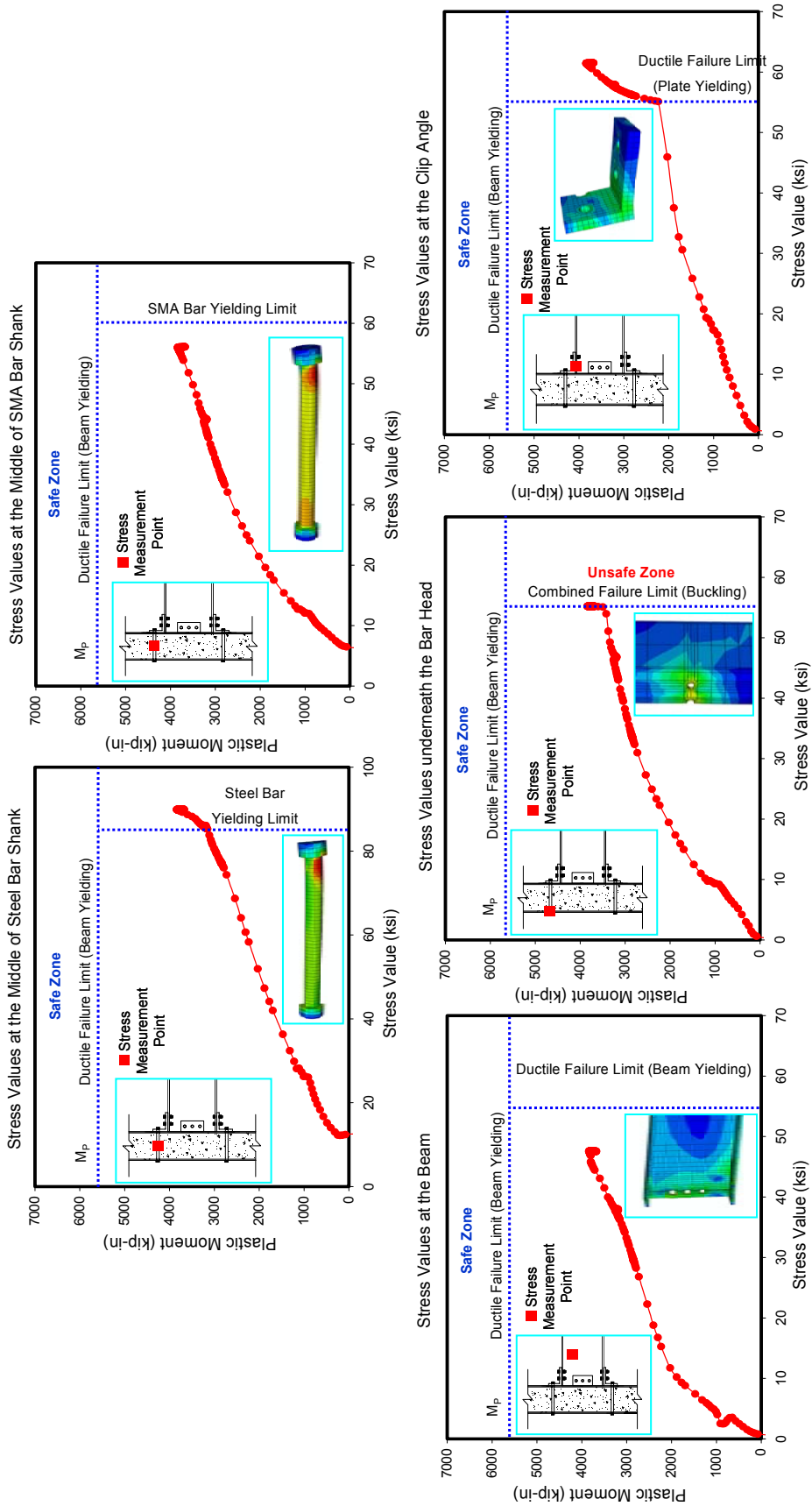


Figure B.16 Structural failure types based on the stress measurement (Clip angle connection with RCFT Columns)

Case6: Clip Angle Connection with CCFT Columns

Clip angle connections with CCFT columns were designed with the same components as those with RCFT columns except for the panel zone and composite columns. Both cases show the same capacity against the failure modes. Thus, the procedures to estimate the identical failure strength with Case 5 are omitted in this section. Only mixed failure modes shown at the panel zone and composite columns will be investigated.

D. Mixed Failure Modes

C.1 Local Buckling at the beam flange

$$\frac{b_f}{2 \cdot t_f} = 6.58$$

$$\lambda_p = 0.38 \sqrt{\frac{E}{F_y}} = 8.73 \quad \text{The compact slenderness ratio}$$

$$\frac{b_f}{2 \cdot t_f} \leq \lambda_p \text{ (OK.)}$$

C.2 Local Buckling at the Composite Column

Use HSS 14X500 size columns

$$\frac{h}{t_c} = 28$$

$$60 \cdot \varepsilon^2 = 60 \left(\frac{34.08}{F_y} \right) = 37.16 \quad \text{Local buckling check (Eurocode 4, 2004)}$$

$$\frac{h}{t_c} \leq 60 \cdot \varepsilon^2 \text{ (OK.)} \quad \text{Compact column case}$$

C.3 Shear Yielding of the Panel Zone (PZ)

Check shear yielding of the rectangular shaped panel zone (Wu et al., 2005)

$$K_f = \frac{2Eh \cdot (t_c + t_p)^3}{(d - t_f)^2} \quad \text{The stiffness of the generalized column flange}$$

$$K_f = 9.021 \cdot 10^3 \text{ kip/in}$$

$$r_A = 1 - m \frac{d_h}{h - 2t_c} = 0.755 \quad \text{The area reduction factor due to bar holes}$$

$$r_C = \left(1 - 2 \frac{nd_h}{d_b} + 2 \frac{nd_h}{d_b r_A} \right)^{-1} = 0.929 \quad \text{The reduction factor}$$

$$r_w = \left(1 - \frac{nd_h}{d_b} + \frac{nd_h}{d_b r_A} \right)^{-1} = 0.963 \quad \text{The reduction factor for bar holes}$$

$$K_w = 2(h - 2t_c) t_c \frac{3E}{7} \quad \text{The stiffness of the column web}$$

$$K_w = 1.616 \cdot 10^5 \text{ kip/in}$$

$$A_c = (h - 2t_c)^2 = 169 \quad \text{The area of the inside concrete}$$

Compute the yield shear strength (V_y) and ultimate shear strength (V_u) at the panel zone

$$V_y = \frac{2(h - 2t_c - md_h) t_c F_y}{\sqrt{3}} \left(1 + \frac{K_f}{r_w K_w} \right) + r_C \tau_{cu} A_c = 1350 \text{ kip}$$

$$V_u = \frac{2(h - 2t_c - md_h) t_c F_y}{\sqrt{3}} + r_C \tau_{cu} A_c + \frac{2h(t_c + t_p)^2 F_y}{3(d - t_f)} = 1398 \text{ kip}$$

$$1.25V_p = 1.25 \frac{M_p}{d} = 385 \text{ kip}$$

$$\phi = 0.8 \quad \text{The design reduction factor}$$

$$1.25V_p \leq \phi V_y \text{ (OK.)}$$

Satisfy the limit to occupy the ductile failure due to yielding of the beam

E. Comparisons with FE Analysis

The Von-Mises stress at the column surface, the middle of the steel tension and SMA bars, the beam and the clip angle were monitored as the applied static moment increased, are shown in Figure B.17.

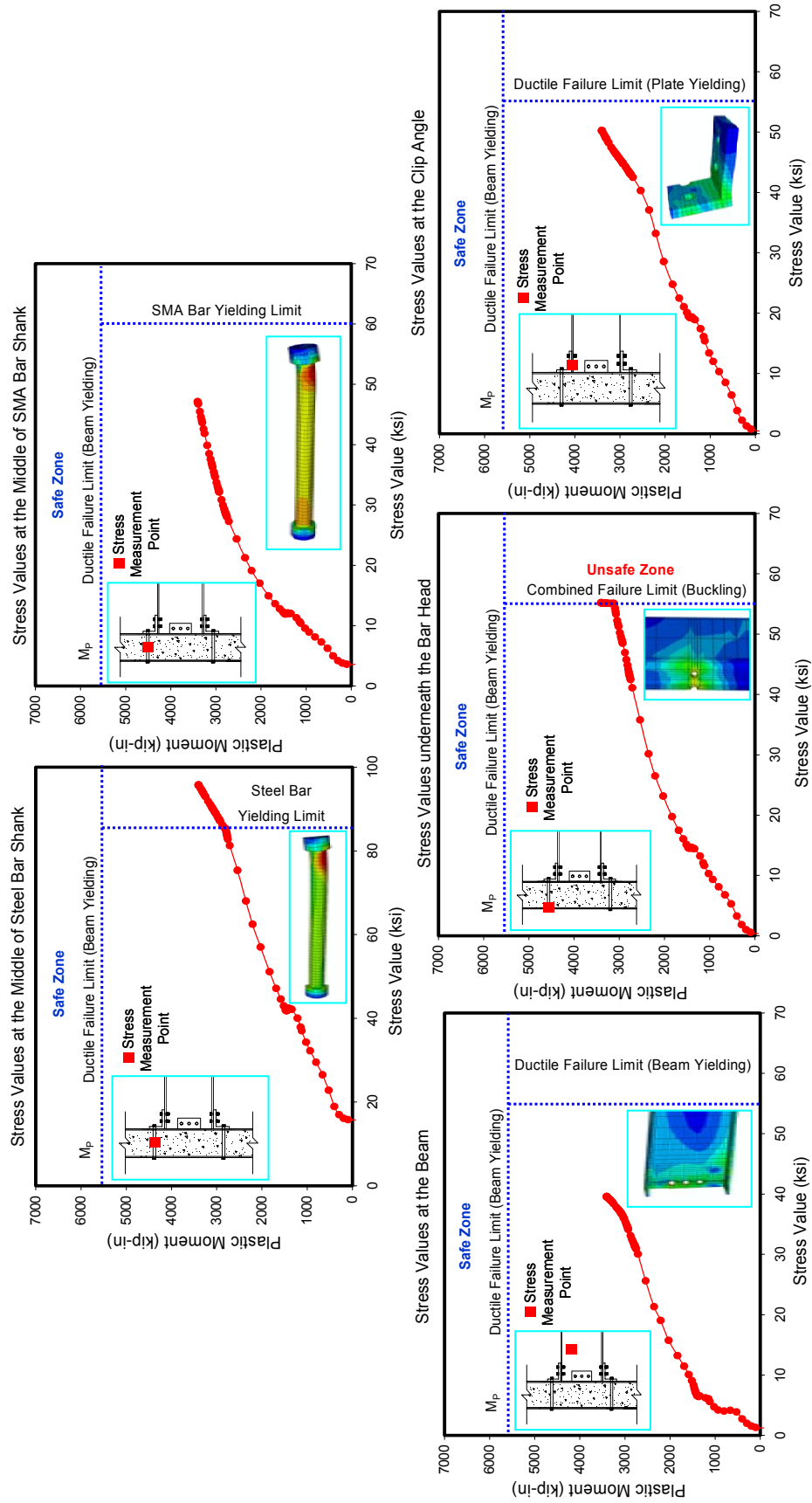


Figure B.17 Structural failure types based on the stress measurement (Clip angle connection with CCFT Columns)

Appendix C

Instrumentation

An important issue in comparing results from different analytical programs is to ensure that the measurement locations, type of measurement and equations used to process the raw data are consistent. As mentioned in Section 4.4, more details of how that was achieved in this research are given in this appendix. In this discussion, the measurements will be collected by “instrumentation” as if this were an actual physical test.

C-1: Data Collection Points

There are many contributions to the displacement and rotation of beam-to-column connections. The deformations corresponding to the applied force can be measured at the data collection points shown in Figures C.1 and C.2. The main “instrumentation” discussed in the following sections is related to: (1) overall moment and rotation of the connection (Point G), (2) applied force and displacement of the beam (Point G), (3) the axial forces and relative deformations between connection components (Point B and T), and (4) shear deformation of the panel zone (Point P). Each connection component was instrumented in order to measure the stiffness and deformation capacity as the loads increased. Measurement points were installed on the corresponding positions of FE models by using the “Set” tool in ABAQUS. The detailed procedures on how data points on the FE models were selected are described in Section C-2.

Stresses inside the confined concrete and tension bars, which are difficult to access in a physical test, can be easily measured on FE models. Failure modes can be determined by tracking strains and stresses in the connection components under static load increments (See Section 5.4). The points selected for strain and stress measurements are shown in Figures C.3 and C.4. Von-Mises stresses at the location of the integration points were used to quantify stresses in this research.

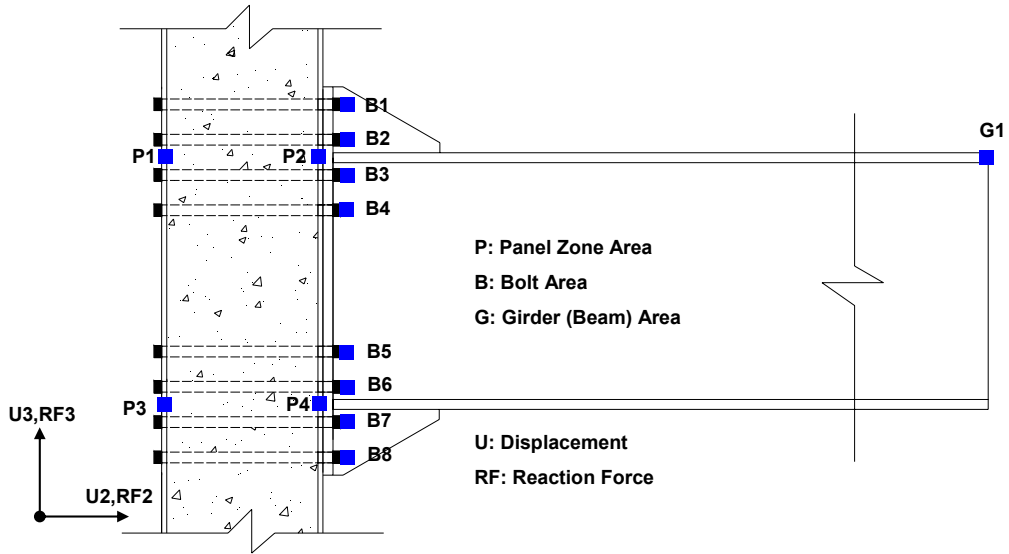


Figure C.1 The measurement points for displacements and reaction forces in the end-plate connection (without slippage)

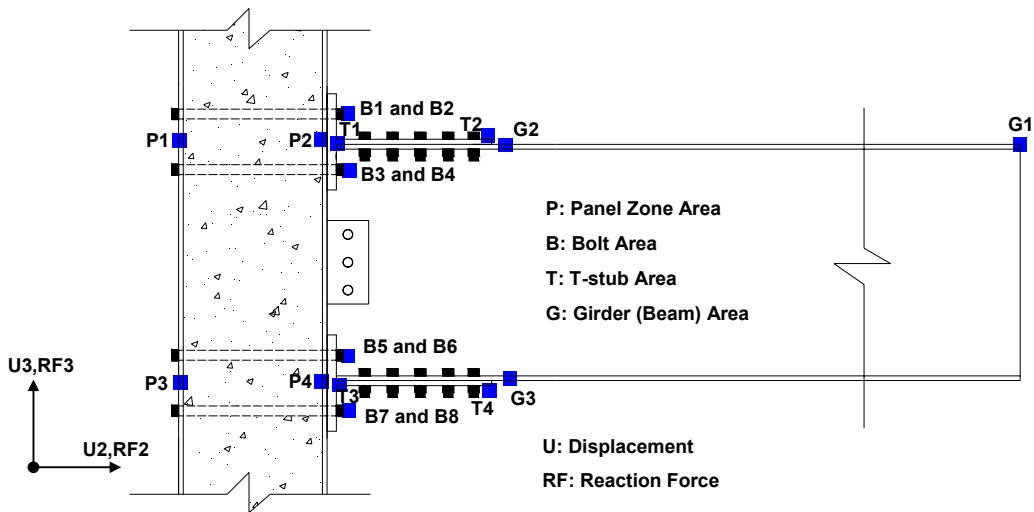


Figure C.2 The measurement points for displacements and reaction forces in the T-stub connection (with slippage)

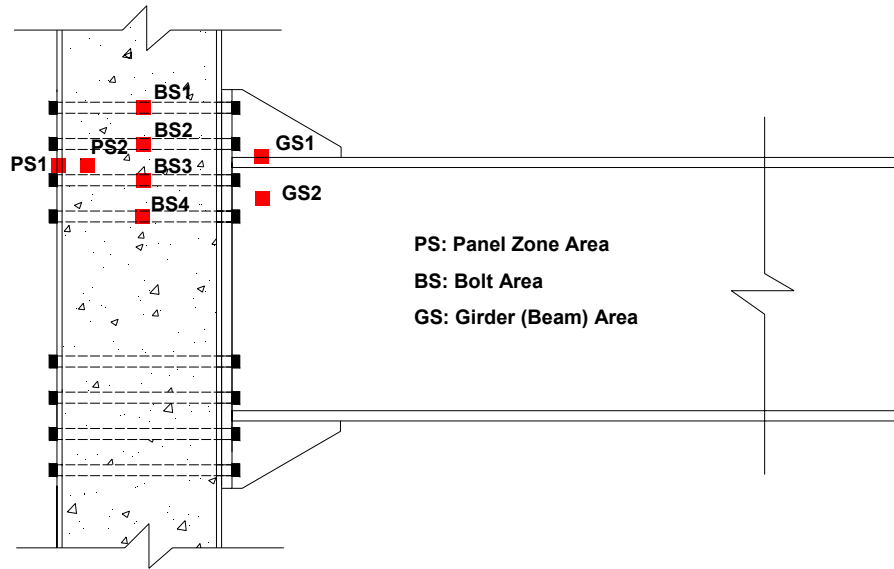


Figure C.3 The measurement points for strains and stresses in the end-plate connection

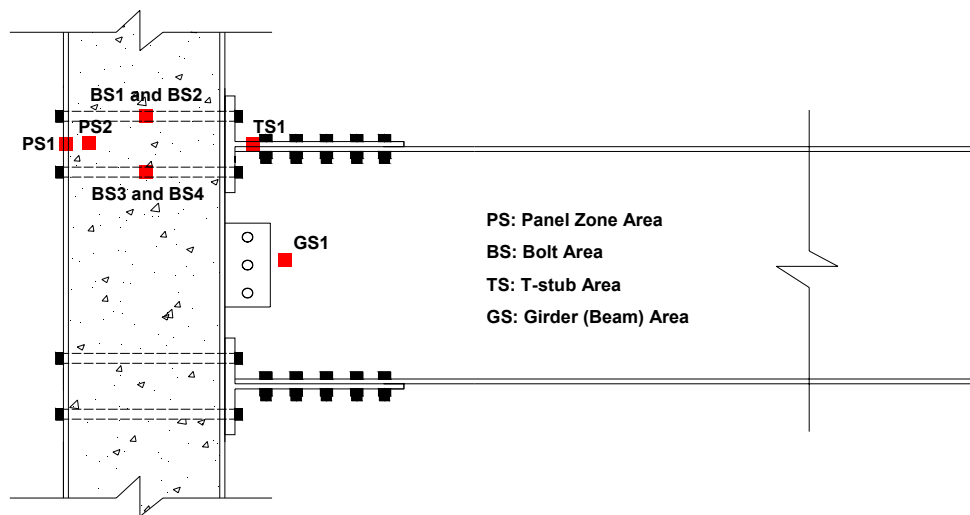


Figure C.4 The measurement points for strains and stresses in the T-stub connection

C-2: Instrumentation Install

The modeling procedures on the ABAQUS/CAE program follow a series of modules to define the geometry of the model and other physical properties. This data is then ported and submitted for analysis. The step by step module procedures are given in Figure C.5. ABAQUS computes the value of many variables at every increment of the given time step. The only a small subset of this data was collected by using output requests. Output requests were defined in the “Step” module. These output requests generally consist of history output request and filed output request. History output was generated to obtain the data at specific points in the FE models, while filed output was generated to obtain the data that are the spatially distributed over the entire model or over an element portion.

In order to measure reaction forces and relative deformations at specific points in the components under every loading increment step, the corresponding measurement points on the FE models should be selected as shown in Figure C.5. The red point on the head of the FE bar model shown in Figure C.5 corresponds to the “B3” measurement point shown in Figure C.2. The filed output does not require the definition of the set points. This definition was conducted in the “Step” module.

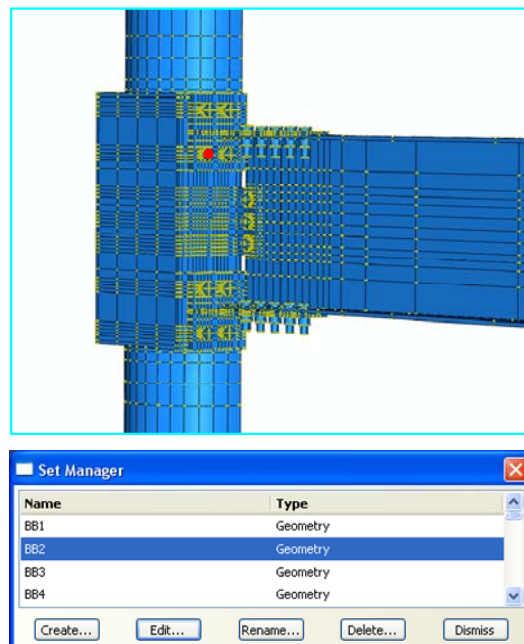


Figure C.5 The definition of the set points

Lists of all of the output requests that are desired are defined by the output request manager. The history and field output managers are shown in Figure C.6. Edit buttons allow the user to edit lists of output requests. The displacement (U) and reaction force (RF) variables were requested using the history output request to a specific measurement point. On the other hand, the stress variables were requested using the field output request for the whole model. The definition of the output requests is given to Figure C.7.

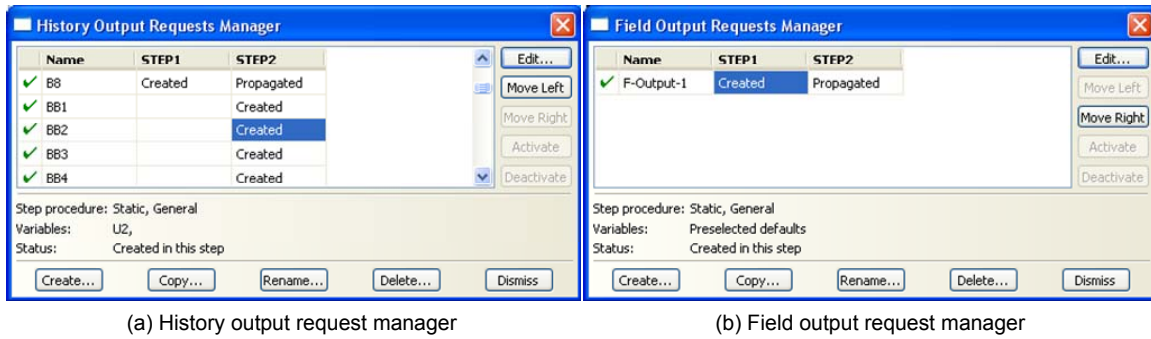


Figure C.6 The output request manager

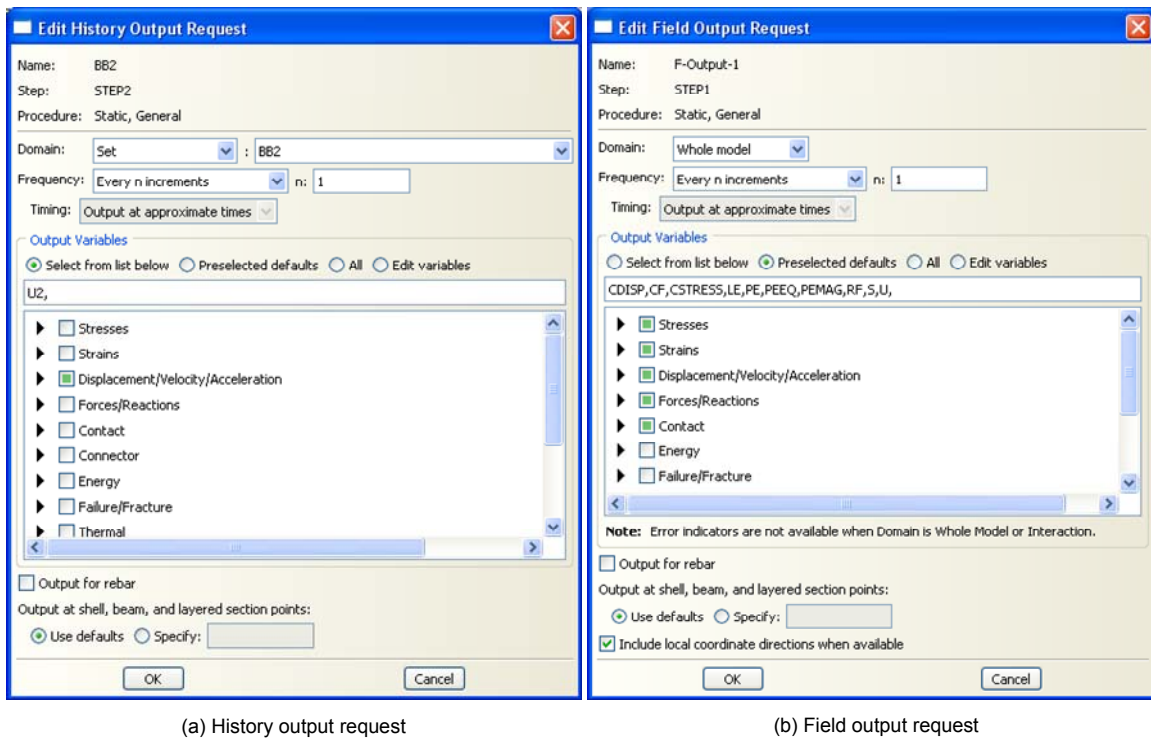


Figure C.7 The definition of the output request

The results of the analyses can be checked in the “Visualization” module which is the post-processor in the ABAQUS program. The creation of the results for the output request is shown in Figure C. 8. Using the ODB history output, the reaction forces and displacements on the special set points were plotted with the loading time increments. The stress distributions over the whole models or over the element portions were displayed by using OBD filed output. The creation of the stress at every time increment is shown in Figure C.9. The highlighted element in red on the T-stem of the FE model corresponds to the “TS1” measurement point shown in Figure C.4. All stress components at the numerical integration points on the highlighted element were measured.

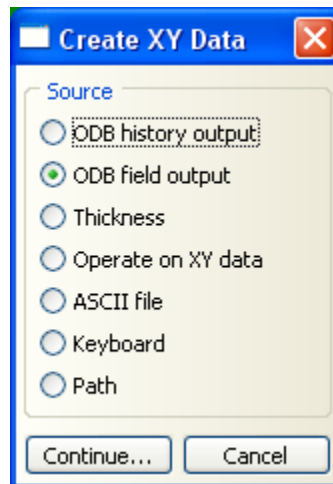
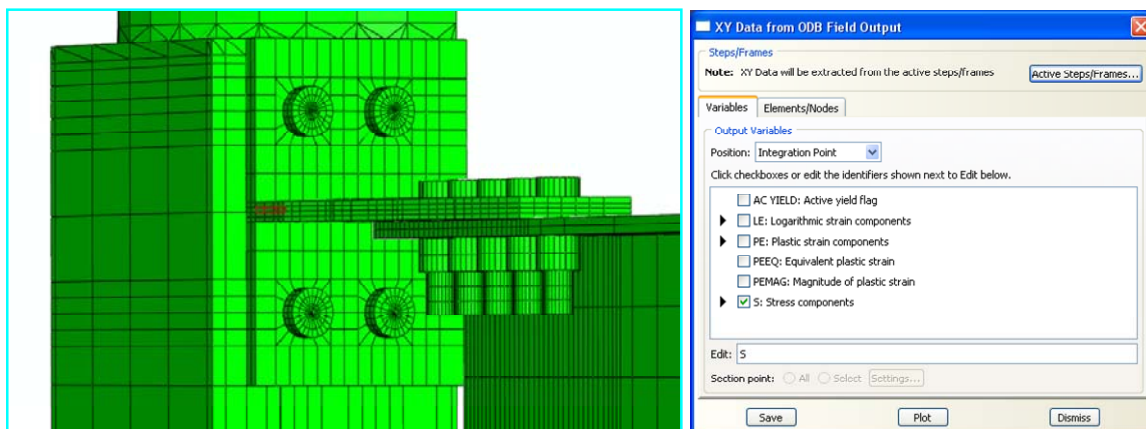


Figure C.8 The creation of the results for the output requests



(a) The corresponding point on the FE T-stem to the TS1 point

(b) The creation of the stress output request

Figure C.9 The stress measurement at the T-stem

C-3: Data Reduction Equations

The following equations were used in reducing the force and displacement data measured by the OBD history output results in order to simulate the (a) stiffness properties for the connection components and (b) moment and rotation characteristics for the whole connection.

C-3.1 Moment and Rotation

The moment generated at the connection of the FE model was calculated by:

$$M = T \cdot L_b \quad (\text{EQ C-1})$$

where, T is the total applied force obtained by using the history output request and L_b is the beam length measured from the tip of the beam to the centerline of the column.

The total rotation of the connection was calculated by:

$$\theta_c = \frac{U_{3_{G1}}}{L_b} \quad (\text{EQ C-2})$$

where, $U_{3_{G1}}$ is the relative displacement at the tip of the beam corresponding to the point “G1”. It was also obtained by using the history output request.

The elastic rotation of the connection was calculated by:

$$\theta_{el} = \frac{M}{K_e} \quad (\text{EQ C-3})$$

where, K_e is the elastic stiffness.

The plastic rotation of the connection was calculated by:

$$\theta_{pl} = \theta_c - \theta_{el} \quad (\text{EQ C-4})$$

C-3.2 Force and Deformation

The converted axial forces of the connection components were calculated by:

$$P = \frac{M}{d_b} = \frac{TL_b}{d_b} \quad (\text{EQ C-5})$$

where, d_b is the depth of the beam.

The converted axial forces are almost equal to the summation of the bar reaction forces with the prying effect negligible.

$$P = \sum B \quad (\text{EQ C-6})$$

The relative deformation of the tension bar due to the converted axial force was calculated by:

$$\Delta_{Bi} = U2_{Bi} - U2_{p1} \quad (\text{EQ C-7})$$

where, $i = 1, 2, \dots, 6$. Subscript “i” represents the bar number at the end-plate connection. These equations were available for the bars under the tensile axial force instead of the bearing force. As shown in Figure C.1, $U2_{Bi}$ and $U2_{p1}$ are the displacements at the tension bars (B1 to B6 points) and the panel zone (P1 point), respectively. There were obtained by using the history output request.

The displacement at the bottom flange under the bearing force was calculated by:

$$\Delta_{\text{Bearing}} = U2_{P4} \quad (\text{EQ C-8})$$

where, $U2_{P4}$ is the displacement at the steel tube surface corresponding to the point “P4”.

The relative deformation of T-stem due to the converted axial force was calculated by:

$$\Delta_{\text{T-stem}} = U2_{T2} - U2_{T1} \quad (\text{EQ C-9})$$

where, $U_{2_{T1}}$ and $U_{2_{T2}}$ are the displacements at the T-stem corresponding to the points “T1” and “T2”, respectively.

The relative slip distance of the T-stub component due to the converted axial force was calculated by:

$$\Delta_{\text{Slip}} = U_{2_{G2}} - U_{2_{T2}} \quad (\text{Top}) \quad (\text{EQ C-10})$$

$$\Delta_{\text{Slip}} = U_{2_{G3}} - U_{2_{T4}} \quad (\text{Bottom}) \quad (\text{EQ C-11})$$

where, $U_{2_{G2}}$ and $U_{2_{G3}}$ are the displacements at the beam corresponding to the points “G2” and “G3”, respectively. Slippage occurred due to the tensile axial force or the bearing axial force.

C-3.3 Panel Zone Deformation

The panel zone deformation expressed as the average shear strain was calculated by:

$$\gamma = \frac{(U_{2_{p2}} - U_{2_{p4}}) + (U_{2_{p1}} - U_{2_{p3}})}{2d_b} \quad (\text{EQ C-12})$$

Displacements along the 3 direction (U_3) were negligible in comparison with those along the 2 direction (U_2). Therefore, the simplified equation was used for calculating the shear deformation.

Appendix D

The Equivalent Lateral Force Procedures

The design base shear forces were selected based on the equivalent lateral load procedures outlined in ASCE 7-05 and IBC 2003. Based on these codes, calculation procedures and examples for the seismic design of composite frames are described in this appendix.

D-1: Calculation Procedures in accordance with IBC 2003

Both codes share the same formulation procedures to calculate the equivalent lateral loads, so only the IBC 2003 code procedures are described in here.

D-1.1 Design Response Spectrum

According to Section 1615 and Section 1616 of the IBC 2003, ground motion accelerations which are represented by design response spectra shall be determined in accordance with these following procedures.

- The mapped maximums considered earthquake spectral response accelerations for the short period (S_S) and at the 1-second period (S_1) are determined from either a seismic hazard map or the USGS web site. S_S and S_1 for Los Angeles area (Zip code 90045 L.A area 33.96 Lat. / -118.4 Long.) were obtained from the web site (<http://eqint.cr.usgs.gov>) in this study. IBC 2003 provides the hazard map in Section 1615.1.
- L.A areas have larger values of the short period spectral acceleration and those of the 1 second period spectral response acceleration in comparison with other areas. Next, the site shall be classified as one of the site classes shown in Table 1615.1.1 in IBC 2003. For this study, good site conditions, corresponding to site classes A and C were chosen because of strong ground motion accelerations in L.A areas.
- The maximum considered earthquake spectral accelerations for the short periods (S_{MS}) and the 1-second period (S_{M1}) adjusted for site class effect shall be determined by Equation (D-1) and Equation (D-2), respectively:

$$S_{MS} = F_a S_s \quad (\text{EQ D-1})$$

$$S_{M1} = F_v S_1 \quad (\text{EQ D-2})$$

where, F_a : the site coefficient defined in Table 1615.1.2(1) in IBC 2003

F_v : the site coefficient defined in Table 1615.1.2(2) in IBC 2003

S_s : the mapped spectral accelerations for the short period as defined in Section 1615.1.2 in IBC 2003.

S_1 : the mapped spectral accelerations for 1-second period as defined in Section 1615.1.2 in IBC 2003

The site coefficient for the site class A and C can be determined by the tables. Good site class conditions have smaller values for both coefficients.

- Five percent damped design spectral acceleration at the short period (S_{DS}) and 1-second period (S_{D1}) shall be determined by Equation (D-3) and Equation (D-4), respectively:

$$S_{DS} = \frac{2}{3} S_{MS} \quad (\text{EQ D-3})$$

$$S_{D1} = \frac{2}{3} S_{M1} \quad (\text{EQ D-4})$$

where, S_{MS} : the maximum considered earthquake spectral response accelerations for the short period as determined in Section 1615.1.2 in IBC 2003

S_{M1} : the maximum considered earthquake spectral response accelerations for 1-second period as determined in Section 1615.1.2 in IBC 2003

- The general design response spectrum curves shall be developed as indicated in Figure B.1 and as following equations:

$$S_a = 0.6 \frac{S_{DS}}{T_o} T + 0.4 S_{DS} \quad (\text{EQ D-5})$$

$$S_a = \frac{S_{D1}}{T} \quad (\text{EQ D-6})$$

where, S_a : the design spectral response acceleration at the short period as determined in Section 1615.1.3 in IBC 2003

S_a : the design spectral response acceleration at 1-second period as determined in Section 1615.1.3 in IBC 2003

For periods less than or equal to T_o , the design spectral response acceleration (S_a) shall be determined by Equation D-5. For periods greater than or equal to T_o , and less than or equal to T_s , the design spectral response acceleration (S_a) shall be taken equal to S_{DS} . For periods greater than T_s , the design spectral response acceleration (S_a) shall be determined by Equation D-6. The period limits are given to following equations.

$$T_o = 0.2 \frac{S_{D1}}{S_{DS}} \quad (\text{EQ D-7})$$

$$T_s = \frac{S_{D1}}{S_{DS}} \quad (\text{EQ D-8})$$

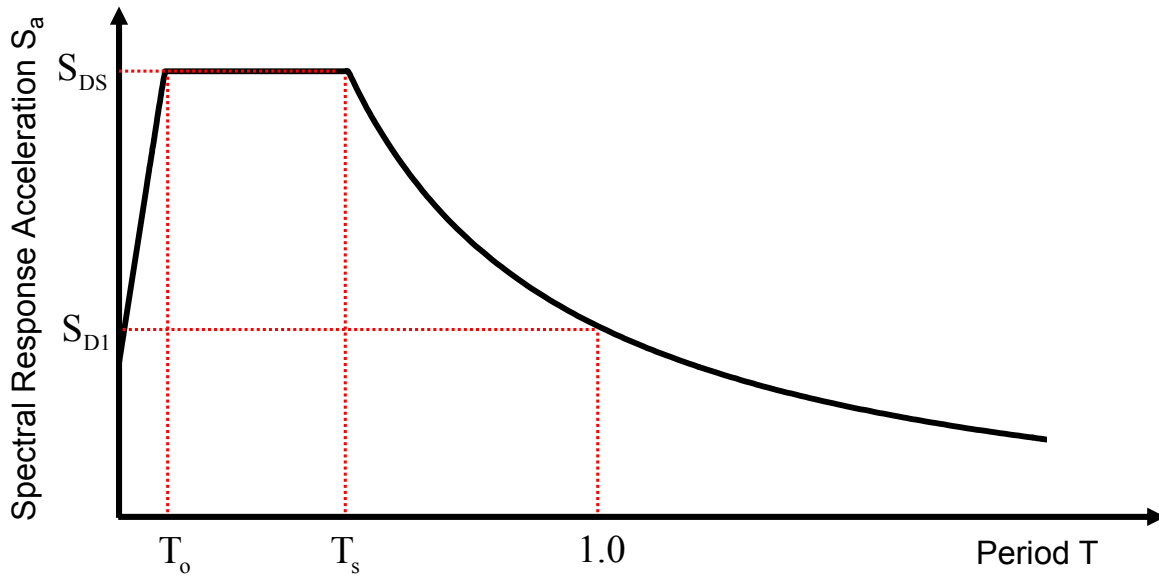


Figure D.1 Design Response Spectrum

D-1.2 Seismic Design Category

All structures shall be assigned to a seismic design category (SDC) based on their seismic use group and the design spectral acceleration coefficients, S_{DS} and S_{D1} , determined in accordance with Section 1615.1.3 or 1615.2.5 in IBC 2003. Seismic design categories are adopted in this design code in order to determine permissible structural systems, limitations on height and irregularity, those components designed with seismic resistance, and the types of the lateral force analysis. Each group structure shall be assigned to the most severe seismic design category in accordance with Tables 1616.3 (1) and (2) in IBC 2003, irrespective of the fundamental period of vibration of the structure, T. Seismic Use Group I for the ordinary building was assumed for this study. According to the tables 1616.3(1) and (2) in IBC 2003, SDC D was selected for this study.

D-1.3 Minimum Design Lateral Force and Related Effects

The seismic load effect, E and E_m , for use in the load combinations includes the components from both vertical and horizontal accelerations shall be determined as following equations:

$$E = \rho Q_E \pm 0.2S_{DS}D \quad (\text{EQ D-9})$$

$$E_m = \Omega_o Q_E \pm 0.2S_{DS}D \quad (\text{EQ D-10})$$

where, D: the effect of the dead load

E: the combined effect of horizontal and vertical induced forces

E_m : the maximum seismic load effect

ρ : the reliability factor based on the system redundancy

Ω_o : the system over-strength factor as given in Table 1617.6 in IBC 2003

Q_E : the effect of horizontal seismic forces

A reliability factor (ρ) all be assigned to all structures based on the extent of structural redundancy inherent in the lateral force-resisting system. A redundancy factor results in 1.0 for structures assigned to SDC A, B, or C. In case of structures in SDC D, E, or F, the reliability factor shall be taken as the largest value of ρ_i calculated at each story “i” of the structure in accordance with Equation D-11 as follows.

$$\rho_i = 2 - \frac{20}{r_{\max i} \sqrt{A_i}} \quad (\text{EQ D-11})$$

for SI unit system:

$$\rho_i = 2 - \frac{20}{(r_{\max})_i \sqrt{A_i}} \quad (\text{EQ D-11})$$

where, $(r_{\max})_i$: the ratio of the design story shear resisted by the most heavily loaded single element in the story to the total story shear

A_i : the floor area in square feet immediately above the story

For moment frames, $(r_{\max})_i$ shall be taken as the maximum of the summation of the shears in any two adjacent columns in the plane of a moment frame divided by the story shear. For columns common to two bays with moment resisting connections on opposite sides at the level under consideration, 70 percent of the shear in that column may be permitted in the column shear summation. The value of ρ shall not be less than 1.0 and need not exceed 1.5.

D-1.4 Equivalent Lateral Force Procedures for Seismic Design

Section 1617.4 and Section 1617.5 in IBC 2003 provide required standards for the equivalent lateral force procedure to perform seismic analysis of structures. An equivalent lateral force analysis shall consist of the application of equivalent static lateral forces to a linear mathematical model of the structure. For purposes of this analysis procedure, the building structures are considered to be fixed at the base. The seismic base shear (V) in a given direction shall be determined in accordance with the following equation.

$$V = C_s W \quad (\text{EQ D-12})$$

where, C_s : the seismic response coefficient

W : the effective seismic weight of the structure including total dead loads plus 20 percents of total live loads

The seismic base shear (V) obtained by the simplified analysis procedure for seismic design is given to the following equation.

$$V = \frac{1.2S_{DS}}{R} W \quad (\text{EQ D-13})$$

where, R: the response modification factor

The seismic response coefficient (C_s) is determined using equations shown below:

$$C_s = \frac{S_{DS}I_E}{R} \quad (\text{EQ D-14})$$

It must satisfy

$$C_s = \frac{S_{D1}I_E}{RT} \text{ and } C_s = 0.044S_{DS}I_E \quad (\text{EQ D-15})$$

where, I_E : the occupancy important factor

T: the fundamental period of the building

The fundamental period of the building (T) in direction under consideration shall be established using the structural properties and deformational characteristics of the resisting element in a properly substantiated analysis or shall be determined as the approximate fundamental period (T_a) using following equations:

$$T_a = C_T(h_n)^{0.8} \quad (\text{EQ D-16})$$

or

$$T_a = 0.1N \quad (\text{EQ D-17})$$

where, C_T : building period coefficient

h_n : the height above the base to the highest level of the building

N: the number of stories

The calculated fundamental period (T) shall not exceed the product of the coefficient for upper limit on calculated period (C_u) and the approximate fundamental period (T_a).

After the seismic base shear force is calculated, the distribution of the forces to all the floors is determined from the following equations:

$$F_x = C_{vx} V \quad (\text{EQ D-18})$$

$$C_{vx} = \frac{w_x h_x^k}{\sum_{i=1}^n w_i h_i^k} \quad (\text{EQ D-19})$$

where, C_{vx} : the vertical distribution factor

k: a distribution exponent related to the building period (k=1 for $T \leq 0.5$, k=2 for $T \geq 2.5$, $k=0.5T+0.75$ for $0.5 < T < 2.5$)

h_x : the height from the base to level i or x

V: Total design lateral force or design base shear force calculated by Equation D-12 or Equation D-13

w_x : the portion of the total gravity load of the building (W) located or assigned to level i or x

The seismic design story shear in a story (V_x) shall be determined from the following equation:

$$V_x = \sum_{i=1}^n F_i \quad (\text{EQ D-20})$$

where, F_i : the portion of the seismic base shear (V) induced at level i or x

D-2: Calculation Examples

Case 1: 4END Frames

The equivalent lateral loads acting on the 4 story composite moment resisting frames with end plate connections were calculated in accordance with the IBC 2003 code. The US unit system was used in this section. Four-13 feet story heights and five-36 feet bay lengths were used in the moment resisting frames. In case of the gravity loads, 100 psf (pound per square feet) and 80 psf applied as uniform loads at all story levels were used for dead loads and live loads, respectively. The detailed geometric configurations for the frames were given in Figure 7.4. The step-by-step calculation procedures are given below:

Step 1: Calculation for the Gravity Loads

Table 1607.1 in the IBC 2003 handles the minimum distributed live load and the minimum concentrated live load limits. General case demands more than 80 psf.

DL=100 psf	The uniform dead load
LL=80 psf	The uniform live load
h=13'	Each story height
a= 30'	One bay length at the NS direction on the plan view
b=36'	One bay length at the EW direction on the plan view

Total gravity weight including dead and live loads

$$A_{\text{plan}} = (0.5 \cdot a) \cdot (n \cdot b) = (0.5 \cdot 30) \cdot (5 \cdot 36) = 2700 \text{ feet}^2$$

$$\text{Dead} = \frac{\text{DL}}{1000} A_{\text{plan}} = 270 \text{ kips} \quad \text{Total dead load at each story}$$

$$\text{Live} = \frac{\text{LL}}{1000} A_{\text{plan}} = 216 \text{ kips} \quad \text{Total live load at each story}$$

$$\text{WT}_i = \text{Dead} + 0.2 \cdot \text{Live} = 313.2 \text{ kips} \quad \text{Total weight including some portion of LL}$$

Total mass at each story including some portion of live loads

$$\text{Mass} = \frac{\text{Dead} + 0.2\text{Live}}{386.4} = 0.811 \text{ kip} \cdot \text{sec}/\text{in}^2$$

Summation of weight and mass for all stories

$$\text{WT} = \begin{pmatrix} 4 \cdot \text{WT} \\ 3 \cdot \text{WT} \\ 2 \cdot \text{WT} \\ 1 \cdot \text{WT} \end{pmatrix} = \begin{pmatrix} 1252.8 \\ 939.6 \\ 626.4 \\ 313.2 \end{pmatrix} \text{ kips} \quad \text{MT} = \begin{pmatrix} 4 \cdot \text{Mass} \\ 3 \cdot \text{Mass} \\ 2 \cdot \text{Mass} \\ 1 \cdot \text{Mass} \end{pmatrix} = \begin{pmatrix} 3.244 \\ 2.433 \\ 1.622 \\ 0.811 \end{pmatrix} \text{ kips} \cdot \text{sec}/\text{in}^2$$

Step 2: Calculate the Seismic Shear

$I_E = 8$	The important occupancy factor (Table 1604.5)
$S_S = 1.5491 \text{ g}$	USGS zip code (90045 L.A Area)
$S_1 = 0.5897 \text{ g}$	USGS zip code (90045 L.A Area)
$F_a = 1.0$	Soft rock area (Site Class C)
$F_v = 1.3$	Soft rock area (Site Class C)
	Use the stable site class to satisfy SDS D class

Compute the design response spectrum

$$S_{MS} = F_a \cdot S_S = 1.5491$$

$$S_{M1} = F_a \cdot S_1 = 0.7666$$

$$S_{DS} = \frac{2}{3} \cdot S_{MS} = 1.033$$

$$S_{D1} = \frac{2}{3} \cdot S_{M1} = 0.5110$$

$$T_o = 0.2 \frac{S_{DS}}{S_{D1}} = 0.0989 \text{ sec}$$

$$T_o = \frac{S_{DS}}{S_{D1}} = 0.4947 \text{ sec}$$

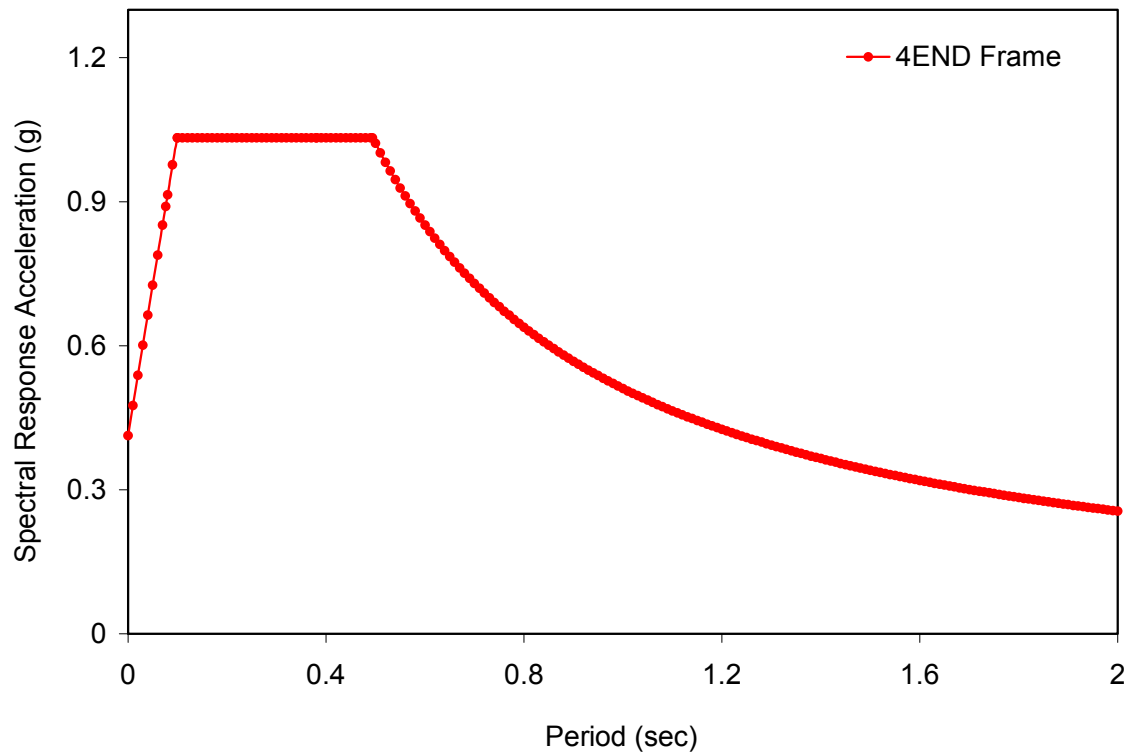


Figure D.2 Design Response Spectrum (4END Case)

Calculate seismic response coefficient by using simplified analysis

$$R = 8.0 \quad \text{Response modification factor (S-CMF case)}$$

$$C_s = \frac{1.2S_{DS}}{R} = 0.15495$$

$$W = \sum W T_i = 1252.8 \text{ kips}$$

$$V = C_s W = 194.054 \text{ kips} \quad \text{Total design base shear force}$$

Step 3: Calculate the Fundamental Period

$$C_T = 0.028 \quad \text{Building period coefficient}$$

$$H = 13 \cdot 4 = 52' \quad \text{Total height of the building}$$

$$T_a = C_T (H)^{0.8} = 0.661 \text{ sec}$$

$$T_n = T_a$$

Step 4: Calculate the Lateral Forces

$$K = 1 + \frac{T_n - 0.5}{2} = 1.08 \quad (\text{If } 0.5 < T_n < 2.5)$$

$$C_{vx,i} = \frac{WT_x h_x^k}{\sum_{i=1}^n WT_i h_i^k} \quad \text{The vertical distribution factor}$$

$$C_{vx,i} = \begin{pmatrix} 0.187 \\ 0.297 \\ 0.307 \\ 0.209 \end{pmatrix} \quad \sum C_{vx} = 1.0 \quad (\text{OK.})$$

Calculate the equivalent lateral force

$$F = F_i = C_{vx,i} V = \begin{pmatrix} 36.326 \\ 57.609 \\ 59.515 \\ 40.604 \end{pmatrix} \text{ kips} \quad \sum F_i = V = 194.054 \text{ kips (OK.)}$$

The equivalent lateral loads for 4END frames based on these calculation procedures are summarized in Table 7.4 (a).

Case 2: 6END Frames

The equivalent lateral loads acting on the 6 story composite moment resisting frames with end plate connections were calculated in accordance with the IBC 2003 code. The US unit system was used in this section. Six-13 feet story heights and five-36 feet bay lengths were used in the moment resisting frames. In case of the gravity loads, 100 psf (pound per square feet) and 80 psf applied uniformly loads at all story levels were used for dead loads and live loads, respectively. The detailed geometric configurations for these frames were shown in Figure 7.4. The step-by-step calculation procedures are given below:

Step 1: Calculation for the Gravity Loads

Table 1607.1 in the IBC 2003 handles the minimum distributed live load and the minimum concentrated live load limits. General case demands more than 80 psf.

DL=100 psf	The uniform dead load
LL=80 psf	The uniform live load
h=13'	Each story height
a= 30'	One bay length at the NS direction on the plan view
b=36'	One bay length at the EW direction on the plan view

Total gravity weight including dead and live loads

$$A_{\text{plan}} = (0.5 \cdot a) \cdot (n \cdot b) = (0.5 \cdot 30) \cdot (5 \cdot 36) = 2700 \text{ feet}^2$$

$$\text{Dead} = \frac{\text{DL}}{1000} A_{\text{plan}} = 270 \text{ kips} \quad \text{Total dead load at each story}$$

$$\text{Live} = \frac{\text{LL}}{1000} A_{\text{plan}} = 216 \text{ kips} \quad \text{Total live load at each story}$$

$$\text{WT}_i = \text{Dead} + 0.2 \cdot \text{Live} = 313.2 \text{ kips} \quad \text{Total weight including some portion of LL}$$

Total mass at each story including some portion of live loads

$$\text{Mass} = \frac{\text{Dead} + 0.2\text{Live}}{386.4} = 0.811 \text{ kip} \cdot \text{sec}/\text{in}^2$$

Summation of weight and mass for all stories

$$\text{WT} = \begin{pmatrix} 6 \cdot \text{WT} \\ 5 \cdot \text{WT} \\ 4 \cdot \text{WT} \\ 3 \cdot \text{WT} \\ 2 \cdot \text{WT} \\ 1 \cdot \text{WT} \end{pmatrix} = \begin{pmatrix} 1879.2 \\ 1566.0 \\ 1252.8 \\ 939.6 \\ 626.4 \\ 313.2 \end{pmatrix} \text{ kips}$$

$$\text{MT} = \begin{pmatrix} 6 \cdot \text{Mass} \\ 5 \cdot \text{Mass} \\ 4 \cdot \text{Mass} \\ 3 \cdot \text{Mass} \\ 2 \cdot \text{Mass} \\ 1 \cdot \text{Mass} \end{pmatrix} = \begin{pmatrix} 4.866 \\ 4.055 \\ 3.244 \\ 2.433 \\ 1.622 \\ 0.811 \end{pmatrix} \text{ kips} \cdot \text{sec}/\text{in}^2$$

Step 2: Calculate the Seismic Shear

$I_E = 8$	The important occupancy factor (Table 1604.5)
$S_S = 1.5491 \text{ g}$	USGS zip code (90045 L.A Area)
$S_1 = 0.5897 \text{ g}$	USGS zip code (90045 L.A Area)
$F_a = 0.8$	Hard rock area (Site Class A)
$F_v = 0.8$	Hard rock area (Site Class A)
	Use the very stable site class to satisfy SDS D class

Compute the design response spectrum

$$S_{MS} = F_a \cdot S_S = 1.2393$$

$$S_{M1} = F_a \cdot S_S = 0.4718$$

$$S_{DS} = \frac{2}{3} \cdot S_{MS} = 0.8262$$

$$S_{D1} = \frac{2}{3} \cdot S_{M1} = 0.3146$$

$$T_o = 0.2 \frac{S_{DS}}{S_{D1}} = 0.076 \text{ sec}$$

$$T_o = \frac{S_{DS}}{S_{D1}} = 0.381 \text{ sec}$$

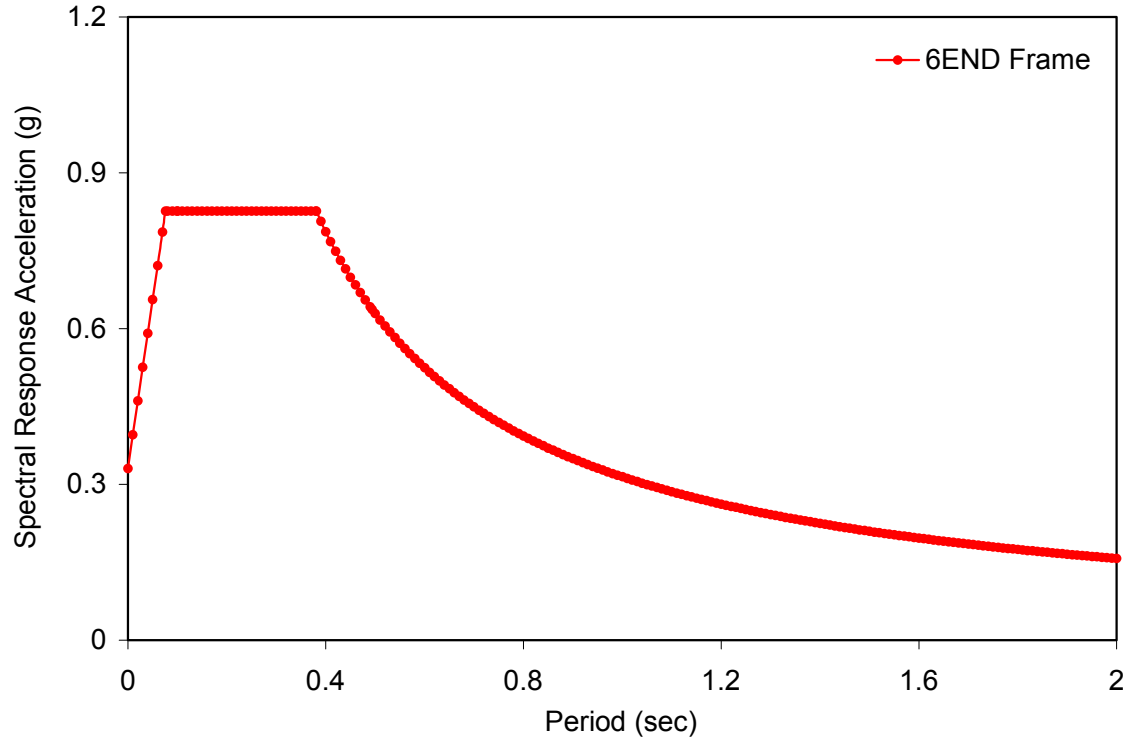


Figure D.3 Design Response Spectrum (6END Case)

Calculate seismic response coefficient by using simplified analysis

$R = 8.0$ Response modification factor (S-CMF case)

$$C_s = \frac{1.2S_{DS}}{R} = 0.1240$$

$$W = \sum WT_i = 1879.2 \text{ kips}$$

$V = C_s W = 232.87 \text{ kips}$ Total design base shear force

Step 3: Calculate the Fundamental Period

$C_T = 0.028$ Building period coefficient

$H = 13 \cdot 6 = 78'$ Total height of the building

$$T_a = C_T(H)^{0.8} = 0.914 \text{ sec}$$

$T_n = T_a$

Step 4: Calculate the Lateral Forces

$$K = 1 + \frac{T_n - 0.5}{2} = 1.207 \quad (\text{If } 0.5 < T_n < 2.5)$$

$$C_{vx,i} = \frac{WT_x h_x^k}{\sum_{i=1}^n WT_i h_i^k} \quad \text{The vertical distribution factor}$$

$$C_{vx,i} = \begin{pmatrix} 0.084 \\ 0.162 \\ 0.211 \\ 0.224 \\ 0.196 \\ 0.122 \end{pmatrix} \quad \sum C_{vx} = 1.0 \quad (\text{OK.})$$

Calculate the equivalent lateral force

$$F = F_i = C_{vx,i} V = \begin{pmatrix} 19.614 \\ 37.731 \\ 49.239 \\ 52.259 \\ 45.606 \\ 28.416 \end{pmatrix} \text{ kips} \quad \sum F_i = V = 232.865 \text{ kips} \quad (\text{OK.})$$

The equivalent lateral loads for 6END frames based on these calculation procedures are summarized in Table 7.4 (c).

D-3: Load Application

The nonlinear pushover analyses for the composite moment frames were performed on 2D numerical models with load combinations including the equivalent lateral loads calculated in Section D-2. The loads, based on the dominant load combination (Sec. 2.3.3 in the ASCE 7-05), are given in Figures D.4 and D.5.

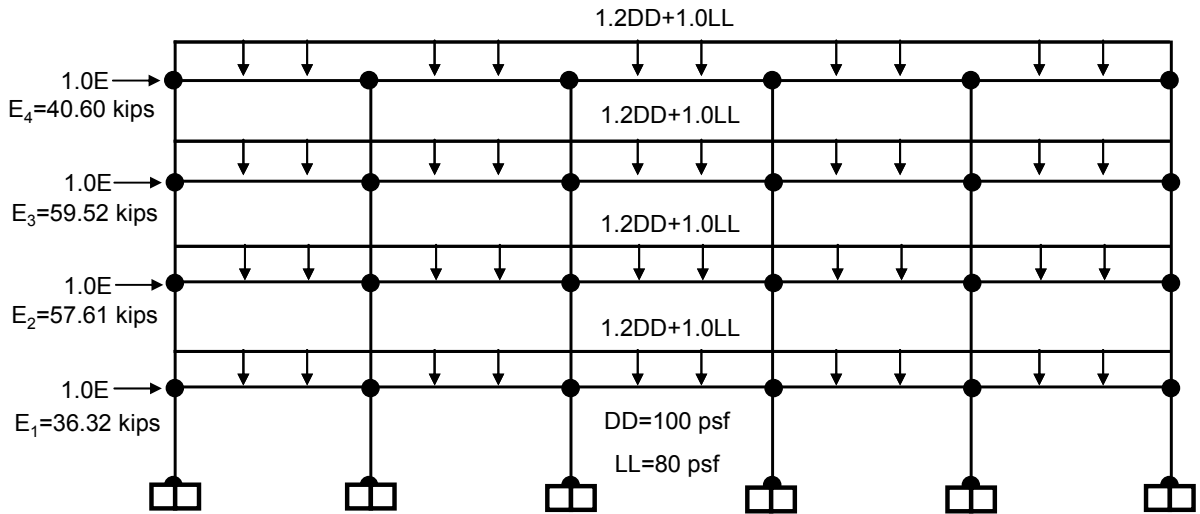


Figure D.4 Dominant load combination (LC5) and load application in the 4END frame model

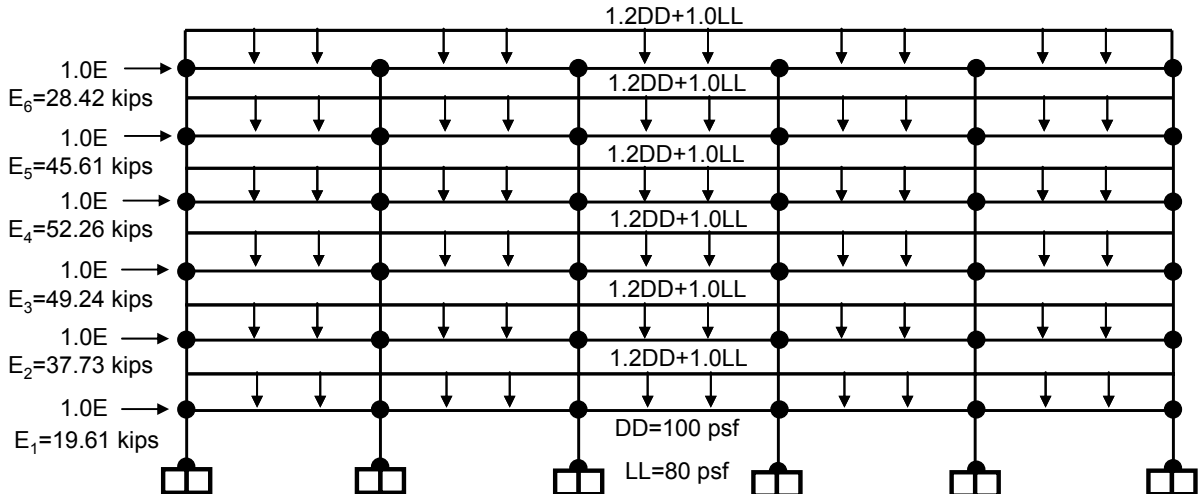


Figure D.5 Dominant load combination (LC5) and load application in the 6END frame model

Appendix E

Detail Design Examples for Panel Zones

E-1: Introduction

The strength models for the composite panel zone were described in Chapter 3. Based on these strength models, the calculations using the theoretical equations for the stiffness, yield shear strength, and ultimate shear strength in the panel zone are illustrated in detail in this appendix. The geometric configuration and notation are given in Figure E.1. A rectangular concrete filled-tube panel zone was made up of steel and concrete, with both materials contributing to the stiffness and strength mechanism. The two materials can be assumed to behave independently, and strength superposition may be applied to the theoretical equations (Wu et al. 2007).

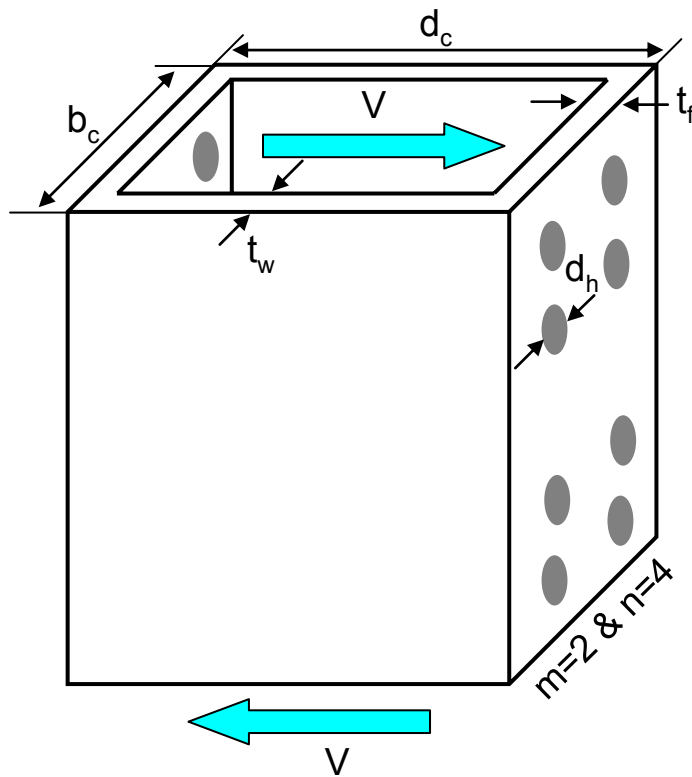


Figure E.1 The geometric dimensions of the panel zone

The moment acting on the connection can be converted into equivalent axial forces at the beam flanges, which in turn result in the shear forces in the panel zone. These shear forces cause shear deformations in the panel zone webs and flexural deformation in the panel zone flanges. Bolt holes which exist in the panel zone flanges reduce the flexural strength of the panel zone flanges. The identifications and geometric dimensions for the panel zone models are summarized in Table E.1. The strength models obtained from these calculations will be assigned to the numerical joint element models in order to simulate the exact behavior of the composite panel zone.

Table E.1 Summary of the geometric dimensions for panel zone models

ID	Connection Type	Beam Size	Column Size	$b_c=d_c$	$t_f=t_w$	d_h
PZ Case1	End-Plate	W24X103	HSS16X16X500	16"	0.500"	1.063"
PZ Case2	End-Plate	W24X103	HSS18X500	18"	0.500"	1.063"
PZ Case3	End-Plate	W24X84	HSS16X16X500	16"	0.500"	1.063"
PZ Case4	End-Plate	W24X84	HSS18X500	16"	0.500"	1.063"
PZ Case5	Clip Angle	W18X50	HSS14X14X500	14"	0.500"	1.063"
PZ Case6	Clip Angle	W18X50	HSS16X500	16"	0.500"	1.063"
PZ Case7	T-Stub	W24X62	HSS16X16X375	16"	0.375"	1.063"
PZ Case8	T-Stub	W24X62	HSS18X375	18"	0.375"	1.063"
PZ Case9	T-Stub	W24X55	HSS16X16X375	16"	0.375"	1.063"
PZ Case10	T-Stub	W24X55	HSS18X375	18"	0.375"	1.063"

Unit: kips, rad and in

E-2: Calculation Examples

PZ Case 1: End Plate Connection with RCFT

This panel zone model (PZ Case 1) was designed for the 6END frame model in the lower story levels. The steel beams were made up of A.572-Gr.50 steel with a 24X103 cross section. The RCFT columns, with a HSS16X16X500 cross section, were selected for these panel zone models. The computational procedures for the yield shear strength ($V_{y,pro}$), shear stiffness (K_{pro}), and ultimate strength ($V_{u,pro}$) for the panel zone model are illustrated in the step-by step process shown in the next section. The US unit system (kip and inch) was used in this appendix.

Step 1: Check the basic information

(1) Determine dimensions (See Figure E.1 and Table E.1):

$b_c = 16$	The width of the column (in)
$d_c = 16$	The depth of the column (in)
$t_f = 0.5$	The thickness of the column flange (in)
$t_w = 0.5$	The thickness of the column web (in)
$d_b = 24.6$	The depth of the H-beam (in)
$t_{bf} = 0.98$	The thickness of the H-beam flange (in)
$t_{bw} = 0.56$	The thickness of the H-beam web (in)
$t_{ep} = 1$	The thickness of the end-plate (in)
$d_h = 1.063$	The diameter of the bolt hole (in)
$n = 4$	The number of rows of bolt holes in the PZ
$m = 2$	The number of bolt holes in one row

(2) Determine material properties:

$E_s = 29000$	Elastic modulus of the steel (ksi)
---------------	------------------------------------

$F_y = 55$	The yield stress of the A.572-Gr. 50 steel (ksi)
$\nu_s = 0.333$	Poisson's ratio of the steel
$u = 0.3$	The friction coefficient at the interface
$\beta = 1.5$	The strain hardening factor of the steel
$f'_c = 7.0$	The confined compressive concrete stress including the strengthened diaphragms (ksi)
$E_c = 57\sqrt{1000 \cdot f'_c} = 4769$	The elastic modulus of the concrete (ksi)

(3) Preloading:

$t = 10$	The average pre-stress of each bar (kips)
$P = 400$	The axial compression acting on the CFT columns (Interior columns at the 1 st story level, kips)

Step 2: Calculation Procedures

(4) Calculate the shear stiffness for two generalized column flanges (K_f):

$$I_f = \frac{b_c \cdot (t_f + t_{ep})^3}{12} = \frac{16 \cdot (0.5 + 1)^3}{12} = 4.5 \text{ in}^4$$

$$K_f = 2 \frac{12E_s I_f}{(d_b - t_{bf})^2} = 2 \frac{12 \cdot 29000 \cdot 4.5}{(16 - 0.98)^2} = 5614 \text{ kip/rad}$$

(5) Calculate the shear stiffness for two column webs without the bolt hole (K_w):

$$G_s = \frac{E_s}{2(1 + \nu_s)} = \frac{29000}{2(1 + 0.333)} = 1.09 \cdot 10^4 \text{ ksi/rad}$$

$$K_w = 2(d_c - 2 \cdot t_f) t_w G_s = 2(16 - 2 \cdot 0.5) \cdot 0.5 \cdot 10878 = 1.63 \cdot 10^5 \text{ kip/rad}$$

(6) Calculate the shear stiffness of the steel column including the stiffness loss due to bar holes (K_{wh}):

$$K_{wh} = 2(d_c - 2 \cdot t_f - m \cdot d_h) t_w G_s$$

$$= 2(16 - 2 \cdot 0.5 - 2 \cdot 1.063) \cdot 0.5 \cdot 10878 = 1.40 \cdot 10^5 \text{ kip/rad}$$

(7) Use the superposition and calculate the shear stiffness of two column webs (K_{w1}):

$$\begin{aligned}
K_{w1} &= \left[\left(1 - \frac{nd_h}{d_b} \right) \cdot \left(\frac{1}{K_w} \right) + \left(\frac{nd_h}{d_b} \right) \cdot \left(\frac{1}{K_{wh}} \right) \right]^{-1} \\
&= \left[\left(1 - \frac{4 \cdot 1.063}{24.6} \right) \cdot \left(\frac{1}{163166} \right) + \left(\frac{4 \cdot 1.063}{24.6} \right) \cdot \left(\frac{1}{140040} \right) \right]^{-1} = 1.59 \cdot 10^5 \text{ kip/rad}
\end{aligned}$$

(8) Calculate the pre-stress of all tension bars (T) and friction force between end-plate and steel tube (F):

$$T = 2mnt = 2 \cdot 2 \cdot 4 \cdot 10 = 160 \text{ kips (Pre-stress is elastic state)}$$

$$F = 2Tu = 2 \cdot 160 \cdot 0.3 = 96 \text{ kips}$$

(9) Calculate the yield strength of two column webs including the loss due to the bolt holes (V_{why}):

$$V_{why} = \frac{2(d_c - 2t_f - m \cdot d_h) t_w F_y}{\sqrt{3}} = \frac{2(16 - 2 \cdot 0.5 - 2 \cdot 1.063) \cdot 0.5 \cdot 55}{\sqrt{3}} = 409 \text{ kips}$$

(10) Calculate the corresponding shear strain of the steel tube (γ_2):

$$\gamma_2 = \frac{V_{why}}{K_{w1}} = \frac{409}{158638} = 0.00258 \text{ rad}$$

(11) Calculate the yield strength of two column webs without bolt holes (V_{wy}):

$$V_{wy} = \frac{2(d_c - 2t_f) t_w F_y}{\sqrt{3}} = \frac{2(16 - 2 \cdot 0.5) \cdot 0.5 \cdot 55}{\sqrt{3}} = 476 \text{ kips}$$

(12) Calculate the yield strength of the generalized column flanges (V_{fy}):

$$V_{fy} = \frac{2(t_f + t_{ep}) b_c F_y}{3(d_b - t_{bf})} = \frac{2(0.5 + 1) \cdot 16 \cdot 55}{3(24.6 - 0.98)} = 56 \text{ kips}$$

(13) Calculate the axial compressive stress (σ_x) and the lateral pre-stress acted on the concrete (σ_y) in the panel zone:

$$A_c = (b_c - 2t_f) (d_b - 2t_w) = 225 \text{ in}^2$$

$$A_s = b_c d_c - A_c = 31 \text{ in}^2$$

$$\sigma_x = f_{cp} = \frac{-PE_c}{E_s A_s + E_c A_c} = \frac{-400 \cdot 4769}{(29000 \cdot 31 + 4769 \cdot 225)} = -0.98 \text{ ksi}$$

$$\sigma_y = f_{ct} = \frac{-T}{b_c d_b} = \frac{-160}{16 \cdot 24.6} = -0.45 \text{ ksi}$$

(14) Calculate the ultimate shear stress of the inside confined concrete (τ_{cu}):

$$f_t = \frac{7.5\sqrt{1000f'_c}}{1000} = 0.627 \text{ ksi}$$

$$m_r = \frac{f_t}{f'_c} = 0.09$$

$$\tau_{cu} = \frac{1}{1+m_r} \sqrt{(f'_c + \sigma_x - m_r\sigma_y)(f'_c + \sigma_y - m_r\sigma_x)} = 5.80 \text{ ksi}$$

(15) Calculate the reduction factor for the shear stiffness of the confined concrete (r_c):

$$r_A = 1 - \frac{md_h}{(d_c - 2t_f)} = 1 - \frac{2 \cdot 1.063}{(16 - 2 \cdot 0.5)} = 0.858$$

$$r_c = \left(1 - \frac{2nd_h}{d_b} + \frac{2nd_h}{d_b r_A}\right)^{-1} = \left(1 - \frac{2 \cdot 4 \cdot 1.063}{24.6} + \frac{2 \cdot 4 \cdot 1.063}{24.6 \cdot 0.858}\right)^{-1} = 0.946$$

(16) Calculate the ultimate shear stress of the inside confined concrete (\bar{V}_{cu}):

$$\bar{V}_{cu} = r_c \tau_{cu} A_c = 0.946 \cdot 5.8 \cdot 225 = 1240 \text{ kips}$$

Step 3: Panel Zone Strength

(17) Calculate the yield strength, shear stiffness, and the ultimate shear strength for the composite panel zone using the superposition theory

$$V_{y,pro} = (K_f + K_{w1})\gamma_2 + F + \bar{V}_{cu} = 1758 \text{ kips}$$

$$K_{y,pro} = K_f + K_{w1} + \frac{(F + \bar{V}_{cu})}{\gamma_2} = 6.82 \cdot 10^5 \text{ kip/rad}$$

$$V_{y,pro} = V_{fy} + V_{wy} + F + \bar{V}_{cu} = 1866 \text{ kips}$$

PZ Case 2: End Plate Connection with CCFE

This panel zone model (PZ Case 2) was designed for the 6END frame model in the lower story levels. The steel beams were made up of A.572-Gr.50 steel with a 24X103 cross section. The RCFT columns, with a HSS18X500 cross section, were selected for these panel zone models. The computational procedures for the yield shear strength ($V_{y,pro}$), shear stiffness (K_{pro}), and ultimate strength ($V_{u,pro}$) for the panel zone model are illustrated in the step-by step process shown in the next section. The US unit system (kip and inch) was used in this appendix.

Step 1: Check the basic information

(1) Determine dimensions (See Figure E.1 and Table E.1):

$b_c = 18$	The width of the column (in)
$d_c = 18$	The depth of the column (in)
$t_f = 0.5$	The thickness of the column flange (in)
$t_w = 0.5$	The thickness of the column web (in)
$d_b = 24.6$	The depth of the H-beam (in)
$t_{bf} = 0.98$	The thickness of the H-beam flange (in)
$t_{bw} = 0.56$	The thickness of the H-beam web (in)
$t_{ep} = 1$	The thickness of the end-plate (in)
$d_h = 1.063$	The diameter of the bolt hole (in)
$n = 4$	The number of rows of bolt holes in the PZ
$m = 2$	The number of bolt holes in one row

(2) Determine material properties:

$E_s = 29000$	Elastic modulus of the steel (ksi)
$F_y = 55$	The yield stress of the A.572-Gr. 50 steel (ksi)
$\nu_s = 0.333$	Poisson's ratio of the steel
$u = 0.3$	The friction coefficient at the interface

$\beta = 1.5$	The strain hardening factor of the steel
$f'_c = 6.6$	The confined compressive concrete stress including the strengthened diaphragms (ksi)
$E_c = 57\sqrt{1000 \cdot f'_c} = 4769$	The elastic modulus of the concrete (ksi)

(3) Preloading:

$t = 10$	The average pre-stress of each bar (kips)
$P = 400$	The axial compression acting on the CFT columns (Interior columns at the 1 st story level, kips)

Step 2: Calculation Procedures

(4) Calculate the shear stiffness for two generalized column flanges (K_f):

$$I_f = \frac{b_c \cdot (t_f + t_{ep})^3}{12} = \frac{18 \cdot (0.5 + 1)^3}{12} = 5.06 \text{ in}^4$$

$$K_f = 2 \frac{12E_s I_f}{(d_b - t_{bf})^2} = 2 \frac{12 \cdot 29000 \cdot 5.06}{(18 - 0.98)^2} = 6315 \text{ kip/rad}$$

(5) Calculate the shear stiffness for two column webs without the bolt hole (K_w):

$$G_s = \frac{E_s}{2(1 + \nu_s)} = \frac{29000}{2(1 + 0.333)} = 1.09 \cdot 10^4 \text{ ksi/rad}$$

$$K_w = 2(d_c - 2 \cdot t_f) t_w G_s = 2(18 - 2 \cdot 0.5) \cdot 0.5 \cdot 10878 = 1.85 \cdot 10^5 \text{ kip/rad}$$

(6) Calculate the shear stiffness of the steel column including the stiffness loss due to bar holes (K_{wh}):

$$K_{wh} = 2(d_c - 2 \cdot t_f - m \cdot d_h) t_w G_s$$

$$= 2(18 - 2 \cdot 0.5 - 2 \cdot 1.063) \cdot 0.5 \cdot 10878 = 1.62 \cdot 10^5 \text{ kip/rad}$$

(7) Use the superposition and calculate the shear stiffness of two column webs (K_{w1}):

$$\begin{aligned}
K_{w1} &= \left[\left(1 - \frac{nd_h}{d_b} \right) \cdot \left(\frac{1}{K_w} \right) + \left(\frac{nd_h}{d_b} \right) \cdot \left(\frac{1}{K_{wh}} \right) \right]^{-1} \\
&= \left[\left(1 - \frac{4 \cdot 1.063}{24.6} \right) \cdot \left(\frac{1}{184921} \right) + \left(\frac{4 \cdot 1.063}{24.6} \right) \cdot \left(\frac{1}{167195} \right) \right]^{-1} = 1.80 \cdot 10^5 \text{ kip/rad}
\end{aligned}$$

(8) Calculate the pre-stress of all tension bars (T) and friction force between end-plate and steel tube (F):

$$T = 2mnt = 2 \cdot 2 \cdot 4 \cdot 10 = 160 \text{ kips (Pre-stress is elastic state)}$$

$$F = 2Tu = 2 \cdot 160 \cdot 0.3 = 96 \text{ kips}$$

(9) Calculate the yield strength of two column webs including the loss due to the bolt holes (V_{why}):

$$V_{why} = \frac{2(d_c - 2t_f - m \cdot d_h) t_w F_y}{\sqrt{3}} = \frac{2(18 - 2 \cdot 0.5 - 2 \cdot 1.063) \cdot 0.5 \cdot 55}{\sqrt{3}} = 472 \text{ kips}$$

(10) Calculate the corresponding shear strain of the steel tube (γ_2):

$$\gamma_2 = \frac{V_{why}}{K_{w1}} = \frac{472}{180462} = 0.00262 \text{ rad}$$

(11) Calculate the yield strength of two column webs without bolt holes (V_{wy}):

$$V_{wy} = \frac{2(d_c - 2t_f) t_w F_y}{\sqrt{3}} = \frac{2(18 - 2 \cdot 0.5) \cdot 0.5 \cdot 55}{\sqrt{3}} = 540 \text{ kips}$$

(12) Calculate the yield strength of the generalized column flanges (V_{fy}):

$$V_{fy} = \frac{2(t_f + t_{ep}) b_c F_y}{3(d_b - t_{bf})} = \frac{2(0.5 + 1) \cdot 18 \cdot 55}{3(24.6 - 0.98)} = 63 \text{ kips}$$

(13) Calculate the axial compressive stress (σ_x) and the lateral pre-stress acted on the concrete (σ_y) in the panel zone:

$$A_c = (b_c - 2t_f) (d_b - 2t_w) = 289 \text{ in}^2$$

$$A_s = b_c d_c - A_c = 35 \text{ in}^2$$

$$\sigma_x = f_{cp} = \frac{-PE_c}{E_s A_s + E_c A_c} = \frac{-400 \cdot 4769}{(29000 \cdot 35 + 4625 \cdot 289)} = -0.79 \text{ ksi}$$

$$\sigma_y = f_{ct} = \frac{-T}{b_c d_b} = \frac{-160}{18 \cdot 24.6} = -0.40 \text{ ksi}$$

(14) Calculate the ultimate shear stress of the inside confined concrete (τ_{cu}):

$$f_t = \frac{7.5\sqrt{1000f'_c}}{1000} = 0.608 \text{ ksi}$$

$$m_r = \frac{f_t}{f'_c} = 0.092$$

$$\tau_{cu} = \frac{1}{1+m_r} \sqrt{(f'_c + \sigma_x - m_r\sigma_y)(f'_c + \sigma_y - m_r\sigma_x)} = 5.53 \text{ ksi}$$

(15) Calculate the reduction factor for the shear stiffness of the confined concrete (r_c):

$$r_A = 1 - \frac{md_h}{(d_c - 2t_f)} = 1 - \frac{2 \cdot 1.063}{(18 - 2 \cdot 0.5)} = 0.87$$

$$r_c = \left(1 - \frac{2nd_h}{d_b} + \frac{2nd_h}{d_b r_A}\right)^{-1} = \left(1 - \frac{2 \cdot 4 \cdot 1.063}{24.6} + \frac{2 \cdot 4 \cdot 1.063}{24.6 \cdot 0.87}\right)^{-1} = 0.95$$

(16) Calculate the ultimate shear stress of the inside confined concrete (\bar{V}_{cu}):

$$\bar{V}_{cu} = r_c \tau_{cu} A_c = 0.95 \cdot 5.53 \cdot 289 = 1523 \text{ kips}$$

Step 3: Panel Zone Strength

(17) Calculate the yield strength, shear stiffness, and the ultimate shear strength for the composite panel zone using the superposition theory

$$V_{y,pro} = (K_f + K_{w1})\gamma_2 + F + \bar{V}_{cu} = 2108 \text{ kips}$$

$$K_{y,pro} = K_f + K_{w1} + \frac{(F + \bar{V}_{cu})}{\gamma_2} = 8.06 \cdot 10^5 \text{ kip/rad}$$

$$V_{y,pro} = V_{fy} + V_{wy} + F + \bar{V}_{cu} = 2222 \text{ kips}$$

PZ Case 5: Clip Angle Connection with RCFT

This panel zone model (PZ Case 5) was designed for the 4CLI frame model in the lower story levels. The steel beams were made up of A.572-Gr.50 steel with a W18X50 cross section. The RCFT columns, with a HSS14X14X500 cross section, were selected for these panel zone models. The computational procedures for the yield shear strength ($V_{y,pro}$), shear stiffness (K_{pro}), and ultimate strength ($V_{u,pro}$) for the panel zone model are illustrated in the step-by step process shown in the next section. The US unit system (kip and inch) was used in this appendix.

Step 1: Check the basic information

(1) Determine dimensions (See Figure E.1 and Table E.1):

$b_c = 14$	The width of the column (in)
$d_c = 14$	The depth of the column (in)
$t_f = 0.5$	The thickness of the column flange (in)
$t_w = 0.5$	The thickness of the column web (in)
$d_b = 24.0$	The distance between top and bottom bar hole (in)
$t_{bf} = 0.57$	The thickness of the H-beam flange (in)
$t_{bw} = 0.36$	The thickness of the H-beam web (in)
$t_{an} = 1$	The thickness of the clip angle (in)
$d_h = 1.063$	The diameter of the bolt hole (in)
$n = 2$	The number of rows of bolt holes in the PZ
$m = 3$	The number of bolt holes in one row

(2) Determine material properties:

$E_s = 29000$	Elastic modulus of the steel (ksi)
$F_y = 55$	The yield stress of the A.572-Gr. 50 steel (ksi)
$\nu_s = 0.333$	Poisson's ratio of the steel
$u = 0.3$	The friction coefficient at the interface

$\beta = 1.5$	The strain hardening factor of the steel
$f'_c = 6.4$	The confined compressive concrete stress including the strengthened diaphragms (ksi)
$E_c = 57\sqrt{1000 \cdot f'_c} = 4542$	The elastic modulus of the concrete (ksi)

(3) Preloading:

$t = 10$	The average pre-stress of each bar (kips)
$P = 300$	The axial compression acting on the CFT columns (Interior columns at the 1 st story level, kips)

Step 2: Calculation Procedures

(4) Calculate the shear stiffness for two generalized column flanges (K_f):

$$I_f = \frac{b_c \cdot (t_f + t_{an})^3}{12} = \frac{14 \cdot (0.5 + 1)^3}{12} = 3.94 \text{ in}^4$$

$$K_f = 2 \frac{12E_s I_f}{(d_b - t_{bf})^2} = 2 \frac{12 \cdot 29000 \cdot 3.94}{(14 - 0.57)^2} = 4992 \text{ kip/rad}$$

(5) Calculate the shear stiffness for two column webs without the bolt hole (K_w):

$$G_s = \frac{E_s}{2(1 + \nu_s)} = \frac{29000}{2(1 + 0.333)} = 1.09 \cdot 10^4 \text{ ksi/rad}$$

$$K_w = 2(d_c - 2 \cdot t_f) t_w G_s = 2(14 - 2 \cdot 0.5) \cdot 0.5 \cdot 10878 = 1.41 \cdot 10^5 \text{ kip/rad}$$

(6) Calculate the shear stiffness of the steel column including the stiffness loss due to bar holes (K_{wh}):

$$K_{wh} = 2(d_c - 2 \cdot t_f - m \cdot d_h) t_w G_s$$

$$= 2(14 - 2 \cdot 0.5 - 3 \cdot 1.063) \cdot 0.5 \cdot 10878 = 1.07 \cdot 10^5 \text{ kip/rad}$$

(7) Use the superposition and calculate the shear stiffness of two column webs (K_{w1}):

$$\begin{aligned}
K_{w1} &= \left[\left(1 - \frac{nd_h}{d_b} \right) \cdot \left(\frac{1}{K_w} \right) + \left(\frac{nd_h}{d_b} \right) \cdot \left(\frac{1}{K_{wh}} \right) \right]^{-1} \\
&= \left[\left(1 - \frac{2 \cdot 1.063}{24.0} \right) \cdot \left(\frac{1}{141410} \right) + \left(\frac{2 \cdot 1.063}{24.0} \right) \cdot \left(\frac{1}{106721} \right) \right]^{-1} = 1.37 \cdot 10^5 \text{ kip/rad}
\end{aligned}$$

(8) Calculate the pre-stress of all tension bars (T) and friction force between end-plate and steel tube (F):

$$T = 2mnt = 2 \cdot 2 \cdot 4 \cdot 10 = 120 \text{ kips (Pre-stress is elastic state)}$$

$$F = 2Tu = 2 \cdot 160 \cdot 0.3 = 72 \text{ kips}$$

(9) Calculate the yield strength of two column webs including the loss due to the bolt holes (V_{why}):

$$V_{why} = \frac{2(d_c - 2t_f - m \cdot d_h) t_w F_y}{\sqrt{3}} = \frac{2(14 - 2 \cdot 0.5 - 3 \cdot 1.063) \cdot 0.5 \cdot 55}{\sqrt{3}} = 311 \text{ kips}$$

(10) Calculate the corresponding shear strain of the steel tube (γ_2):

$$\gamma_2 = \frac{V_{why}}{K_{w1}} = \frac{311}{137452} = 0.00227 \text{ rad}$$

(11) Calculate the yield strength of two column webs without bolt holes (V_{wy}):

$$V_{wy} = \frac{2(d_c - 2t_f) t_w F_y}{\sqrt{3}} = \frac{2(14 - 2 \cdot 0.5) \cdot 0.5 \cdot 55}{\sqrt{3}} = 412 \text{ kips}$$

(12) Calculate the yield strength of the generalized column flanges (V_{fy}):

$$V_{fy} = \frac{2(t_f + t_{an}) b_c F_y}{3(d_b - t_{bf})} = \frac{2(0.5 + 1) \cdot 14 \cdot 55}{3(24.0 - 0.57)} = 49 \text{ kips}$$

(13) Calculate the axial compressive stress (σ_x) and the lateral pre-stress acted on the concrete (σ_y) in the panel zone:

$$A_c = (b_c - 2t_f) (d_b - 2t_w) = 169 \text{ in}^2$$

$$A_s = b_c d_c - A_c = 27 \text{ in}^2$$

$$\sigma_x = f_{cp} = \frac{-PE_c}{E_s A_s + E_c A_c} = \frac{-300 \cdot 4542}{(29000 \cdot 27 + 4542 \cdot 169)} = -0.878 \text{ ksi}$$

$$\sigma_y = f_{ct} = \frac{-T}{b_c d_b} = \frac{-120}{14 \cdot 24.0} = -0.40 \text{ ksi}$$

(14) Calculate the ultimate shear stress of the inside confined concrete (τ_{cu}):

$$f_t = \frac{7.5\sqrt{1000f'_c}}{1000} = 0.597 \text{ ksi}$$

$$m_r = \frac{f_t}{f'_c} = 0.094$$

$$\tau_{cu} = \frac{1}{1+m_r} \sqrt{(f'_c + \sigma_x - m_r\sigma_y)(f'_c + \sigma_y - m_r\sigma_x)} = 5.21 \text{ ksi}$$

(15) Calculate the reduction factor for the shear stiffness of the confined concrete (r_c):

$$r_A = 1 - \frac{md_h}{(d_c - 2t_f)} = 1 - \frac{3 \cdot 1.063}{(14 - 2 \cdot 0.5)} = 0.75$$

$$r_c = \left(1 - \frac{2nd_h}{d_b} + \frac{2nd_h}{d_b r_A}\right)^{-1} = \left(1 - \frac{2 \cdot 2 \cdot 1.063}{24.0} + \frac{2 \cdot 2 \cdot 1.063}{24.0 \cdot 0.75}\right)^{-1} = 0.94$$

(16) Calculate the ultimate shear stress of the inside confined concrete (\bar{V}_{cu}):

$$\bar{V}_{cu} = r_c \tau_{cu} A_c = 0.94 \cdot 5.21 \cdot 169 = 832 \text{ kips}$$

Step 3: Panel Zone Strength

(17) Calculate the yield strength, shear stiffness, and the ultimate shear strength for the composite panel zone using the superposition theory

$$V_{y,pro} = (K_f + K_{w1})\gamma_2 + F + \bar{V}_{cu} = 1220 \text{ kips}$$

$$K_{y,pro} = K_f + K_{w1} + \frac{(F + \bar{V}_{cu})}{\gamma_2} = 5.43 \cdot 10^5 \text{ kip/rad}$$

$$V_{y,pro} = V_{fy} + V_{wy} + F + \bar{V}_{cu} = 1366 \text{ kips}$$

PZ Case 6: Clip Angle Connection with CCFT

This panel zone model (PZ Case 6) was designed for the 4CLI frame model in the lower story levels. The steel beams were made up of A.572-Gr.50 steel with a 24X55 cross section. The RCFT columns, with a HSS14X14X500 cross section, were selected for these panel zone models. The computational procedures for the yield shear strength ($V_{y,pro}$), shear stiffness (K_{pro}), and ultimate strength ($V_{u,pro}$) for the panel zone model are illustrated in the step-by-step process shown in the next section. The US unit system (kip and inch) was used in this appendix.

Step 1: Check the basic information

(1) Determine dimensions (See Figure E.1 and Table E.1):

$b_c = 16$	The width of the column (in)
$d_c = 16$	The depth of the column (in)
$t_f = 0.5$	The thickness of the column flange (in)
$t_w = 0.5$	The thickness of the column web (in)
$d_b = 24.0$	The distance between top and bottom bar hole (in)
$t_{bf} = 0.57$	The thickness of the H-beam flange (in)
$t_{bw} = 0.36$	The thickness of the H-beam web (in)
$t_{an} = 1$	The thickness of the clip angle (in)
$d_h = 1.063$	The diameter of the bolt hole (in)
$n = 2$	The number of rows of bolt holes in the PZ
$m = 3$	The number of bolt holes in one row

(2) Determine material properties:

$E_s = 29000$	Elastic modulus of the steel (ksi)
$F_y = 55$	The yield stress of the A.572-Gr. 50 steel (ksi)
$\nu_s = 0.333$	Poisson's ratio of the steel
$u = 0.3$	The friction coefficient at the interface

$\beta = 1.5$	The strain hardening factor of the steel
$f'_c = 6.5$	The confined compressive concrete stress including the strengthened diaphragms (ksi)
$E_c = 57\sqrt{1000 \cdot f'_c} = 4595$	The elastic modulus of the concrete (ksi)

(3) Preloading:

$t = 10$	The average pre-stress of each bar (kips)
$P = 300$	The axial compression acting on the CFT columns (Interior columns at the 1 st story level, kips)

Step 2: Calculation Procedures

(4) Calculate the shear stiffness for two generalized column flanges (K_f):

$$I_f = \frac{b_c \cdot (t_f + t_{an})^3}{12} = \frac{16 \cdot (0.5 + 1)^3}{12} = 4.5 \text{ in}^4$$

$$K_f = 2 \frac{12E_s I_f}{(d_b - t_{bf})^2} = 2 \frac{12 \cdot 29000 \cdot 4.50}{(16 - 0.57)^2} = 5705 \text{ kip/rad}$$

(5) Calculate the shear stiffness for two column webs without the bolt hole (K_w):

$$G_s = \frac{E_s}{2(1 + \nu_s)} = \frac{29000}{2(1 + 0.333)} = 1.09 \cdot 10^4 \text{ ksi/rad}$$

$$K_w = 2(d_c - 2 \cdot t_f) t_w G_s = 2(16 - 2 \cdot 0.5) \cdot 0.5 \cdot 10878 = 1.63 \cdot 10^5 \text{ kip/rad}$$

(6) Calculate the shear stiffness of the steel column including the stiffness loss due to bar holes (K_{wh}):

$$K_{wh} = 2(d_c - 2 \cdot t_f - m \cdot d_h) t_w G_s$$

$$= 2(16 - 2 \cdot 0.5 - 3 \cdot 1.063) \cdot 0.5 \cdot 10878 = 1.28 \cdot 10^5 \text{ kip/rad}$$

(7) Use the superposition and calculate the shear stiffness of two column webs (K_{w1}):

$$\begin{aligned}
K_{w1} &= \left[\left(1 - \frac{nd_h}{d_b} \right) \cdot \left(\frac{1}{K_w} \right) + \left(\frac{nd_h}{d_b} \right) \cdot \left(\frac{1}{K_{wh}} \right) \right]^{-1} \\
&= \left[\left(1 - \frac{2 \cdot 1.063}{24.0} \right) \cdot \left(\frac{1}{163165} \right) + \left(\frac{2 \cdot 1.063}{24.0} \right) \cdot \left(\frac{1}{128476} \right) \right]^{-1} = 1.59 \cdot 10^5 \text{ kip/rad}
\end{aligned}$$

(8) Calculate the pre-stress of all tension bars (T) and friction force between end-plate and steel tube (F):

$$T = 2mnt = 2 \cdot 2 \cdot 4 \cdot 10 = 120 \text{ kips (Pre-stress is elastic state)}$$

$$F = 2Tu = 2 \cdot 160 \cdot 0.3 = 72 \text{ kips}$$

(9) Calculate the yield strength of two column webs including the loss due to the bolt holes (V_{why}):

$$V_{why} = \frac{2(d_c - 2t_f - m \cdot d_h) t_w F_y}{\sqrt{3}} = \frac{2(16 - 2 \cdot 0.5 - 3 \cdot 1.063) \cdot 0.5 \cdot 55}{\sqrt{3}} = 375 \text{ kips}$$

(10) Calculate the corresponding shear strain of the steel tube (γ_2):

$$\gamma_2 = \frac{V_{why}}{K_{w1}} = \frac{375}{159354} = 0.00235 \text{ rad}$$

(11) Calculate the yield strength of two column webs without bolt holes (V_{wy}):

$$V_{wy} = \frac{2(d_c - 2t_f) t_w F_y}{\sqrt{3}} = \frac{2(16 - 2 \cdot 0.5) \cdot 0.5 \cdot 55}{\sqrt{3}} = 476 \text{ kips}$$

(12) Calculate the yield strength of the generalized column flanges (V_{fy}):

$$V_{fy} = \frac{2(t_f + t_{an}) b_c F_y}{3(d_b - t_{bf})} = \frac{2(0.5 + 1) \cdot 16 \cdot 55}{3(24.0 - 0.57)} = 56 \text{ kips}$$

(13) Calculate the axial compressive stress (σ_x) and the lateral pre-stress acted on the concrete (σ_y) in the panel zone:

$$A_c = (b_c - 2t_f) (d_b - 2t_w) = 225 \text{ in}^2$$

$$A_s = b_c d_c - A_c = 31 \text{ in}^2$$

$$\sigma_x = f_{cp} = \frac{-PE_c}{E_s A_s + E_c A_c} = \frac{-300 \cdot 4595}{(29000 \cdot 31 + 4595 \cdot 225)} = -0.713 \text{ ksi}$$

$$\sigma_y = f_{ct} = \frac{-T}{b_c d_b} = \frac{-120}{16 \cdot 24.0} = -0.34 \text{ ksi}$$

(14) Calculate the ultimate shear stress of the inside confined concrete (τ_{cu}):

$$f_t = \frac{7.5\sqrt{1000f'_c}}{1000} = 0.600 \text{ ksi}$$

$$m_r = \frac{f_t}{f'_c} = 0.093$$

$$\tau_{cu} = \frac{1}{1+m_r} \sqrt{(f'_c + \sigma_x - m_r\sigma_y)(f'_c + \sigma_y - m_r\sigma_x)} = 5.50 \text{ ksi}$$

(15) Calculate the reduction factor for the shear stiffness of the confined concrete (r_c):

$$r_A = 1 - \frac{md_h}{(d_c - 2t_f)} = 1 - \frac{3 \cdot 1.063}{(16 - 2 \cdot 0.5)} = 0.79$$

$$r_c = \left(1 - \frac{2nd_h}{d_b} + \frac{2nd_h}{d_b r_A}\right)^{-1} = \left(1 - \frac{2 \cdot 2 \cdot 1.063}{24.0} + \frac{2 \cdot 2 \cdot 1.063}{24.0 \cdot 0.79}\right) = 0.95$$

(16) Calculate the ultimate shear stress of the inside confined concrete (\bar{V}_{cu}):

$$\bar{V}_{cu} = r_c \tau_{cu} A_c = 0.95 \cdot 5.50 \cdot 225 = 1182 \text{ kips}$$

Step 3: Panel Zone Strength

(17) Calculate the yield strength, shear stiffness, and the ultimate shear strength for the composite panel zone using the superposition theory

$$V_{y,pro} = (K_f + K_{w1}) \gamma_2 + F + \bar{V}_{cu} = 1642 \text{ kips}$$

$$K_{y,pro} = K_f + K_{w1} + \frac{(F + \bar{V}_{cu})}{\gamma_2} = 6.98 \cdot 10^5 \text{ kip/rad}$$

$$V_{y,pro} = V_{fy} + V_{wy} + F + \bar{V}_{cu} = 1787 \text{ kips}$$

PZ Case 9: T-Stub Connection with RCFT

This panel zone model (PZ Case 9) was designed for the 6TSU frame model in the lower story levels. The steel beams were made up of A.572-Gr.50 steel with a 24X55 cross section. The RCFT columns, with a HSS16X16X375 cross section, were selected for these panel zone models. The computational procedures for the yield shear strength ($V_{y,pro}$), shear stiffness (K_{pro}), and ultimate strength ($V_{u,pro}$) for the panel zone model are illustrated in the step-by-step process shown in the next section. The US unit system (kip and inch) was used in this appendix.

Step 1: Check the basic information

(1) Determine dimensions (See Figure E.1 and Table E.1):

$b_c = 16$	The width of the column (in)
$d_c = 16$	The depth of the column (in)
$t_f = 0.375$	The thickness of the column flange (in)
$t_w = 0.375$	The thickness of the column web (in)
$d_b = 23.6$	The depth of the beam (in)
$t_{bf} = 0.505$	The thickness of the H-beam flange (in)
$t_{bw} = 0.395$	The thickness of the H-beam web (in)
$t_{\bar{n}} = 1$	The thickness of the clip angle (in)
$d_h = 1.063$	The diameter of the bolt hole (in)
$n = 2$	The number of rows of bolt holes in the PZ
$m = 4$	The number of bolt holes in one row

(2) Determine material properties:

$E_s = 29000$	Elastic modulus of the steel (ksi)
$F_y = 55$	The yield stress of the A.572-Gr. 50 steel (ksi)
$\nu_s = 0.333$	Poisson's ratio of the steel
$u = 0.3$	The friction coefficient at the interface

$\beta = 1.5$	The strain hardening factor of the steel
$f'_c = 7.0$	The confined compressive concrete stress including the strengthened diaphragms (ksi)
$E_c = 57\sqrt{1000 \cdot f'_c} = 4769$	The elastic modulus of the concrete (ksi)

(3) Preloading:

$t = 10$	The average pre-stress of each bar (kips)
$P = 200$	The axial compression acting on the CFT columns (Interior columns at the 4 th story level, kips)

Step 2: Calculation Procedures

(4) Calculate the shear stiffness for two generalized column flanges (K_f):

$$I_f = \frac{b_c \cdot (t_f + t_n)^3}{12} = \frac{16 \cdot (0.375 + 1)^3}{12} = 3.50 \text{ in}^4$$

$$K_f = 2 \frac{12E_s I_f}{(d_b - t_{bf})^2} = 2 \frac{12 \cdot 29000 \cdot 3.50}{(16 - 0.505)^2} = 4572 \text{ kip/rad}$$

(5) Calculate the shear stiffness for two column webs without the bolt hole (K_w):

$$G_s = \frac{E_s}{2(1 + \nu_s)} = \frac{29000}{2(1 + 0.333)} = 1.09 \cdot 10^4 \text{ ksi/rad}$$

$$K_w = 2(d_c - 2 \cdot t_f) t_w G_s = 2(16 - 2 \cdot 0.375) \cdot 0.375 \cdot 10878 = 1.26 \cdot 10^5 \text{ kip/rad}$$

(6) Calculate the shear stiffness of the steel column including the stiffness loss due to bar holes (K_{wh}):

$$K_{wh} = 2(d_c - 2 \cdot t_f - m \cdot d_h) t_w G_s$$

$$= 2(16 - 2 \cdot 0.375 - 4 \cdot 1.063) \cdot 0.375 \cdot 10878 = 0.91 \cdot 10^5 \text{ kip/rad}$$

(7) Use the superposition and calculate the shear stiffness of two column webs (K_{w1}):

$$\begin{aligned}
K_{w1} &= \left[\left(1 - \frac{nd_h}{d_b} \right) \cdot \left(\frac{1}{K_w} \right) + \left(\frac{nd_h}{d_b} \right) \cdot \left(\frac{1}{K_{wh}} \right) \right]^{-1} \\
&= \left[\left(1 - \frac{2 \cdot 1.063}{23.6} \right) \cdot \left(\frac{1}{125990} \right) + \left(\frac{2 \cdot 1.063}{23.6} \right) \cdot \left(\frac{1}{90838} \right) \right]^{-1} = 1.21 \cdot 10^5 \text{ kip/rad}
\end{aligned}$$

(8) Calculate the pre-stress of all tension bars (T) and friction force between end-plate and steel tube (F):

$$T = 2mnt = 2 \cdot 2 \cdot 4 \cdot 10 = 160 \text{ kips (Pre-stress is elastic state)}$$

$$F = 2Tu = 2 \cdot 160 \cdot 0.3 = 96 \text{ kips}$$

(9) Calculate the yield strength of two column webs including the loss due to the bolt holes (V_{why}):

$$V_{why} = \frac{2(d_c - 2t_f - m \cdot d_h) t_w F_y}{\sqrt{3}} = \frac{2(16 - 2 \cdot 0.375 - 4 \cdot 1.063) \cdot 0.375 \cdot 55}{\sqrt{3}} = 265 \text{ kips}$$

(10) Calculate the corresponding shear strain of the steel tube (γ_2):

$$\gamma_2 = \frac{V_{why}}{K_{w1}} = \frac{265}{121746} = 0.00218 \text{ rad}$$

(11) Calculate the yield strength of two column webs without bolt holes (V_{wy}):

$$V_{wy} = \frac{2(d_c - 2t_f) t_w F_y}{\sqrt{3}} = \frac{2(16 - 2 \cdot 0.375) \cdot 0.375 \cdot 55}{\sqrt{3}} = 367 \text{ kips}$$

(12) Calculate the yield strength of the generalized column flanges (V_{fy}):

$$V_{fy} = \frac{2(t_f + t_{fl}) b_c F_y}{3(d_b - t_{bf})} = \frac{2(0.375 + 1) \cdot 16 \cdot 55}{3(23.6 - 0.505)} = 48 \text{ kips}$$

(13) Calculate the axial compressive stress (σ_x) and the lateral pre-stress acted on the concrete (σ_y) in the panel zone:

$$A_c = (b_c - 2t_f) (d_b - 2t_w) = 232 \text{ in}^2$$

$$A_s = b_c d_c - A_c = 24 \text{ in}^2$$

$$\sigma_x = f_{cp} = \frac{-PE_c}{E_s A_s + E_c A_c} = \frac{-200 \cdot 4768}{(29000 \cdot 24 + 4768 \cdot 232)} = -0.531 \text{ ksi}$$

$$\sigma_y = f_{ct} = \frac{-T}{b_c d_b} = \frac{-160}{16 \cdot 23.6} = -0.454 \text{ ksi}$$

(14) Calculate the ultimate shear stress of the inside confined concrete (τ_{cu}):

$$f_t = \frac{7.5\sqrt{1000f'_c}}{1000} = 0.627 \text{ ksi}$$

$$m_r = \frac{f_t}{f'_c} = 0.0996$$

$$\tau_{cu} = \frac{1}{1+m_r} \sqrt{(f'_c + \sigma_x - m_r\sigma_y)(f'_c + \sigma_y - m_r\sigma_x)} = 6.01 \text{ ksi}$$

(15) Calculate the reduction factor for the shear stiffness of the confined concrete (r_c):

$$r_A = 1 - \frac{md_h}{(d_c - 2t_f)} = 1 - \frac{3 \cdot 1.063}{(16 - 2 \cdot 0.375)} = 0.721$$

$$r_c = \left(1 - \frac{2nd_h}{d_b} + \frac{2nd_h}{d_b r_A}\right)^{-1} = \left(1 - \frac{2 \cdot 2 \cdot 1.063}{23.6} + \frac{2 \cdot 2 \cdot 1.063}{23.6 \cdot 0.721}\right) = 0.93$$

(16) Calculate the ultimate shear stress of the inside confined concrete (\bar{V}_{cu}):

$$\bar{V}_{cu} = r_c \tau_{cu} A_c = 0.93 \cdot 6.01 \cdot 232 = 1305 \text{ kips}$$

Step 3: Panel Zone Strength

(17) Calculate the yield strength, shear stiffness, and the ultimate shear strength for the composite panel zone using the superposition theory

$$V_{y,pro} = (K_f + K_{w1}) \gamma_2 + F + \bar{V}_{cu} = 1680 \text{ kips}$$

$$K_{y,pro} = K_f + K_{w1} + \frac{(F + \bar{V}_{cu})}{\gamma_2} = 7.68 \cdot 10^5 \text{ kip/rad}$$

$$V_{y,pro} = V_{fy} + V_{wy} + F + \bar{V}_{cu} = 1820 \text{ kips}$$

PZ Case 10: T-Stub Connection with CCFT

This panel zone model (PZ Case 10) was designed for the 6TSU frame model in the lower story levels. The steel beams were made up of A.572-Gr.50 steel with a 24X55 cross section. The RCFT columns, with a HSS18X375 cross section, were selected for these panel zone models. The computational procedures for the yield shear strength ($V_{y,pro}$), shear stiffness (K_{pro}), and ultimate strength ($V_{u,pro}$) for the panel zone model are illustrated in the step-by-step process shown in the next section. The US unit system (kip and inch) was used in this appendix.

Step 1: Check the basic information

(1) Determine dimensions (See Figure E.1 and Table E.1):

$b_c = 18$	The width of the column (in)
$d_c = 18$	The depth of the column (in)
$t_f = 0.375$	The thickness of the column flange (in)
$t_w = 0.375$	The thickness of the column web (in)
$d_b = 23.6$	The depth of the beam (in)
$t_{bf} = 0.505$	The thickness of the H-beam flange (in)
$t_{bw} = 0.395$	The thickness of the H-beam web (in)
$t_{\bar{n}} = 1$	The thickness of the clip angle (in)
$d_h = 1.063$	The diameter of the bolt hole (in)
$n = 2$	The number of rows of bolt holes in the PZ
$m = 4$	The number of bolt holes in one row

(2) Determine material properties:

$E_s = 29000$	Elastic modulus of the steel (ksi)
$F_y = 55$	The yield stress of the A.572-Gr. 50 steel (ksi)
$\nu_s = 0.333$	Poisson's ratio of the steel
$u = 0.3$	The friction coefficient at the interface

$\beta = 1.5$	The strain hardening factor of the steel
$f'_c = 6.3$	The confined compressive concrete stress including the strengthened diaphragms (ksi)
$E_c = 57\sqrt{1000 \cdot f'_c} = 4506$	The elastic modulus of the concrete (ksi)

(3) Preloading:

$t = 10$	The average pre-stress of each bar (kips)
$P = 200$	The axial compression acting on the CFT columns (Interior columns at the 4 th story level, kips)

Step 2: Calculation Procedures

(4) Calculate the shear stiffness for two generalized column flanges (K_f):

$$I_f = \frac{b_c \cdot (t_f + t_n)^3}{12} = \frac{18 \cdot (0.375 + 1)^3}{12} = 3.94 \text{ in}^4$$

$$K_f = 2 \frac{12E_s I_f}{(d_b - t_{bf})^2} = 2 \frac{12 \cdot 29000 \cdot 3.94}{(18 - 0.505)^2} = 5144 \text{ kip/rad}$$

(5) Calculate the shear stiffness for two column webs without the bolt hole (K_w):

$$G_s = \frac{E_s}{2(1 + \nu_s)} = \frac{29000}{2(1 + 0.333)} = 1.09 \cdot 10^4 \text{ ksi/rad}$$

$$K_w = 2(d_c - 2 \cdot t_f) t_w G_s = 2(18 - 2 \cdot 0.375) \cdot 0.375 \cdot 10878 = 1.42 \cdot 10^5 \text{ kip/rad}$$

(6) Calculate the shear stiffness of the steel column including the stiffness loss due to bar holes (K_{wh}):

$$K_{wh} = 2(d_c - 2 \cdot t_f - m \cdot d_h) t_w G_s$$

$$= 2(18 - 2 \cdot 0.375 - 4 \cdot 1.063) \cdot 0.375 \cdot 10878 = 1.07 \cdot 10^5 \text{ kip/rad}$$

(7) Use the superposition and calculate the shear stiffness of two column webs (K_{w1}):

$$\begin{aligned}
K_{w1} &= \left[\left(1 - \frac{nd_h}{d_b} \right) \cdot \left(\frac{1}{K_w} \right) + \left(\frac{nd_h}{d_b} \right) \cdot \left(\frac{1}{K_{wh}} \right) \right]^{-1} \\
&= \left[\left(1 - \frac{2 \cdot 1.063}{23.6} \right) \cdot \left(\frac{1}{142524} \right) + \left(\frac{2 \cdot 1.063}{23.6} \right) \cdot \left(\frac{1}{107372} \right) \right]^{-1} = 1.38 \cdot 10^5 \text{ kip/rad}
\end{aligned}$$

(8) Calculate the pre-stress of all tension bars (T) and friction force between end-plate and steel tube (F):

$$T = 2mnt = 2 \cdot 2 \cdot 4 \cdot 10 = 160 \text{ kips (Pre-stress is elastic state)}$$

$$F = 2Tu = 2 \cdot 160 \cdot 0.3 = 96 \text{ kips}$$

(9) Calculate the yield strength of two column webs including the loss due to the bolt holes (V_{why}):

$$V_{why} = \frac{2(d_c - 2t_f - m \cdot d_h) t_w F_y}{\sqrt{3}} = \frac{2(18 - 2 \cdot 0.375 - 4 \cdot 1.063) \cdot 0.375 \cdot 55}{\sqrt{3}} = 313 \text{ kips}$$

(10) Calculate the corresponding shear strain of the steel tube (γ_2):

$$\gamma_2 = \frac{V_{why}}{K_{w1}} = \frac{313}{138441} = 0.00226 \text{ rad}$$

(11) Calculate the yield strength of two column webs without bolt holes (V_{wy}):

$$V_{wy} = \frac{2(d_c - 2t_f) t_w F_y}{\sqrt{3}} = \frac{2(18 - 2 \cdot 0.375) \cdot 0.375 \cdot 55}{\sqrt{3}} = 416 \text{ kips}$$

(12) Calculate the yield strength of the generalized column flanges (V_{fy}):

$$V_{fy} = \frac{2(t_f + t_{fl}) b_c F_y}{3(d_b - t_{bf})} = \frac{2(0.375 + 1) \cdot 18 \cdot 55}{3(23.6 - 0.505)} = 54 \text{ kips}$$

(13) Calculate the axial compressive stress (σ_x) and the lateral pre-stress acted on the concrete (σ_y) in the panel zone:

$$A_c = (b_c - 2t_f) (d_b - 2t_w) = 297 \text{ in}^2$$

$$A_s = b_c d_c - A_c = 27 \text{ in}^2$$

$$\sigma_x = f_{cp} = \frac{-PE_c}{E_s A_s + E_c A_c} = \frac{-200 \cdot 4506}{(29000 \cdot 27 + 4506 \cdot 297)} = -0.427 \text{ ksi}$$

$$\sigma_y = f_{ct} = \frac{-T}{b_c d_b} = \frac{-160}{18 \cdot 23.6} = -0.402 \text{ ksi}$$

(14) Calculate the ultimate shear stress of the inside confined concrete (τ_{cu}):

$$f_t = \frac{7.5\sqrt{1000f'_c}}{1000} = 0.593 \text{ ksi}$$

$$m_r = \frac{f_t}{f'_c} = 0.0949$$

$$\tau_{cu} = \frac{1}{1+m_r} \sqrt{(f'_c + \sigma_x - m_r\sigma_y)(f'_c + \sigma_y - m_r\sigma_x)} = 5.36 \text{ ksi}$$

(15) Calculate the reduction factor for the shear stiffness of the confined concrete (r_c):

$$r_A = 1 - \frac{md_h}{(d_c - 2t_f)} = 1 - \frac{3 \cdot 1.063}{(18 - 2 \cdot 0.375)} = 0.753$$

$$r_c = \left(1 - \frac{2nd_h}{d_b} + \frac{2nd_h}{d_b r_A}\right)^{-1} = \left(1 - \frac{2 \cdot 2 \cdot 1.063}{23.6} + \frac{2 \cdot 2 \cdot 1.063}{23.6 \cdot 0.721}\right) = 0.944$$

(16) Calculate the ultimate shear stress of the inside confined concrete (\bar{V}_{cu}):

$$\bar{V}_{cu} = r_c \tau_{cu} A_c = 0.944 \cdot 5.36 \cdot 297 = 1506 \text{ kips}$$

Step 3: Panel Zone Strength

(17) Calculate the yield strength, shear stiffness, and the ultimate shear strength for the composite panel zone using the superposition theory

$$V_{y,pro} = (K_f + K_{w1}) \gamma_2 + F + \bar{V}_{cu} = 1927 \text{ kips}$$

$$K_{y,pro} = K_f + K_{w1} + \frac{(F + \bar{V}_{cu})}{\gamma_2} = 8.51 \cdot 10^5 \text{ kip/rad}$$

$$V_{y,pro} = V_{fy} + V_{wy} + F + \bar{V}_{cu} = 2070 \text{ kips}$$

The yield shear strength, shear stiffness, and ultimate shear strength for all panel zone models are summarized in Table E.2.

Table E.2 Theoretical results for the panel zone strength

Unit: kips, rad and in

ID	PZ Size*	V_{ypro}	K_{ypro}	V_u	K_t
PZ Case1	16X16" (0.5")	1.758×10^3	6.820×10^5	1.866×10^3	$0.01 K_{ypro}$
PZ Case2	18X18" (0.5")	2.108×10^3	8.055×10^5	2.222×10^3	$0.01 K_{ypro}$
PZ Case3	16X16" (0.5")	1.742×10^3	6.755×10^5	1.851×10^3	$0.01 K_{ypro}$
PZ Case4	18X18" (0.5")	2.139×10^3	8.068×10^5	2.253×10^3	$0.01 K_{ypro}$
PZ Case5	14X14" (0.5")	1.219×10^3	5.429×10^5	1.366×10^3	$0.01 K_{ypro}$
PZ Case6	16X16" (0.5")	1.642×10^3	6.981×10^5	1.787×10^3	$0.01 K_{ypro}$
PZ Case7	16X16" (0.375")	1.693×10^3	7.773×10^5	1.833×10^3	$0.01 K_{ypro}$
PZ Case8	18X18" (0.375")	1.932×10^3	8.531×10^5	2.075×10^3	$0.01 K_{ypro}$
PZ Case9	16X16" (0.375")	1.687×10^3	7.443×10^5	1.827×10^3	$0.01 K_{ypro}$
PZ Case10	18X18" (0.375")	1.925×10^3	8.499×10^5	2.068×10^3	$0.01 K_{ypro}$

*() indicate the thickness of steel tube section

These results will be used for the panel zone models in the numerical joint element models. The behavior of the panel zone in the joint element models can be simulated as shown in Figure E.2.

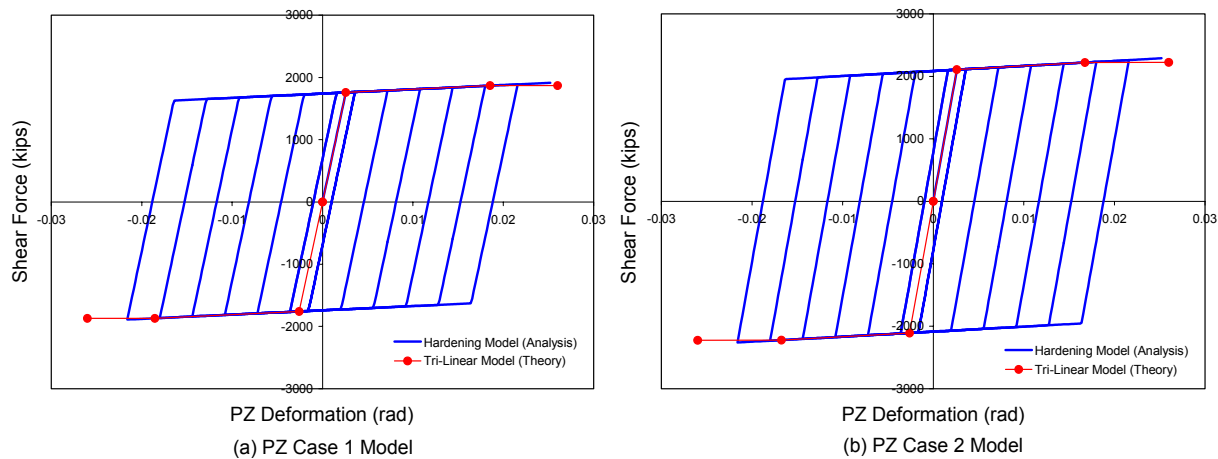


Figure E.2 The behavioral models for composite panel zones

Appendix F

Earthquake Ground Motions

Table 8.2 provides detailed information on the records generated for Los Angeles (LA) and Seattle (SE) with probabilities of exceedence of 2 % in 50 years. Ten historical ground motion pairs (a total 20 ground motions) used in this research have been derived from historical records. The detailed acceleration time history for all of the ground motions listed in the table below are shown in Fig. F1 through F.10.

Table F.1 Earthquake ground motions with 2% probability of exceedence in 50 years

SAC Name	Record	Earthquake Magnitude	Distance (km)	Scale Factor	Number of Points	DT (sec)	Duration (sec)	PGA (g)
LA21	1995 Kobe	6.9	3.4	1.15	3000	0.02	59.98	1.283
LA22	1995 Kobe	6.9	3.4	1.15	3000	0.02	59.98	0.92069
LA23	1989 Loma Prieta	7	3.5	0.82	2500	0.01	24.99	0.418097
LA24	1989 Loma Prieta	7	3.5	0.82	2500	0.01	24.99	0.472976
LA25	1994 Northridge	6.7	7.5	1.29	2990	0.005	14.945	0.868544
LA26	1994 Northridge	6.7	7.5	1.29	2990	0.005	14.945	0.943678
LA27	1994 Northridge	6.7	6.4	1.61	3000	0.02	59.98	0.926758
LA28	1994 Northridge	6.7	6.4	1.61	3000	0.02	59.98	1.330016
LA29	1974 Tabas	7.4	1.2	1.08	2500	0.02	49.98	0.809218
LA30	1974 Tabas	7.4	1.2	1.08	2500	0.02	49.98	0.991908
SE21	1992 Mendocino	7.1	8.5	0.98	3000	0.02	59.98	0.7551332
SE22	1992 Mendocino	7.1	8.5	0.98	3000	0.02	59.98	0.4852179
SE23	1992 Erzincan	6.7	2	1.27	4156	0.005	20.775	0.6048157
SE24	1992 Erzincan	6.7	2	1.27	4156	0.005	20.775	0.5390563
SE25	1949 Olympia	6.5	56	4.35	4000	0.02	79.98	0.8948236
SE26	1949 Olympia	6.5	56	4.35	4000	0.02	79.98	0.8209028
SE27	1965 Seattle	7.1	80	10.04	4092	0.02	81.82	1.7549437
SE28	1965 Seattle	7.1	80	10.04	4092	0.02	81.82	1.3904852
SE29	1985 Valpariso	8	42	2.9	4000	0.025	99.975	1.6358349
SE30	1985 Valpariso	8	42	2.9	4000	0.025	99.975	1.5726635

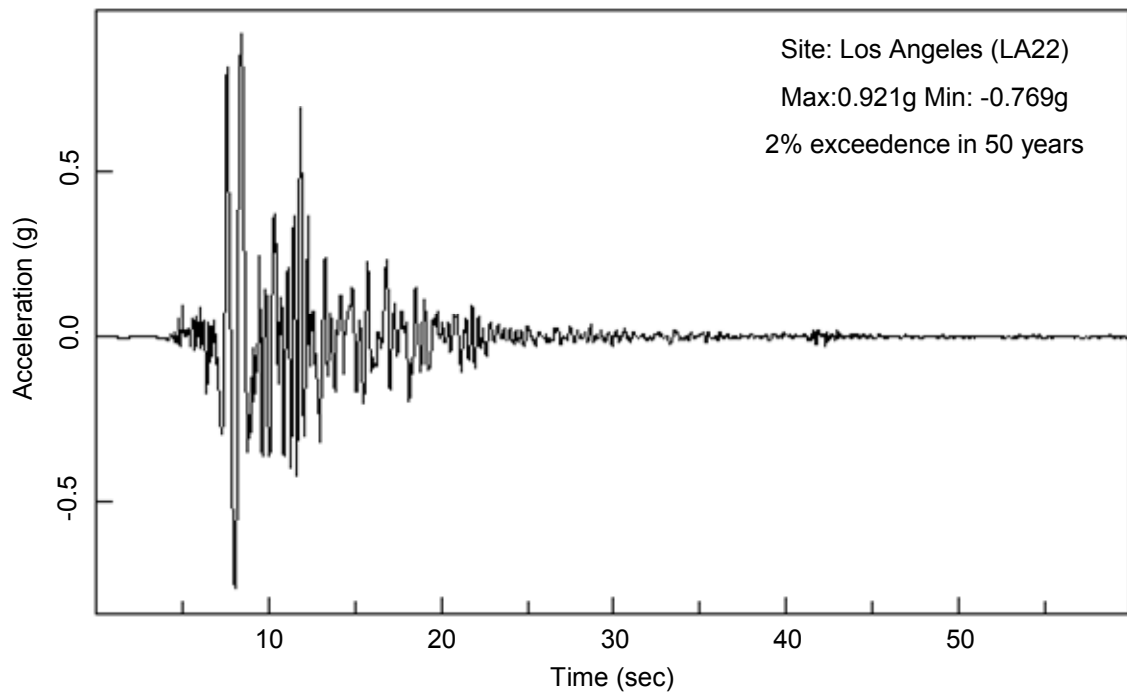
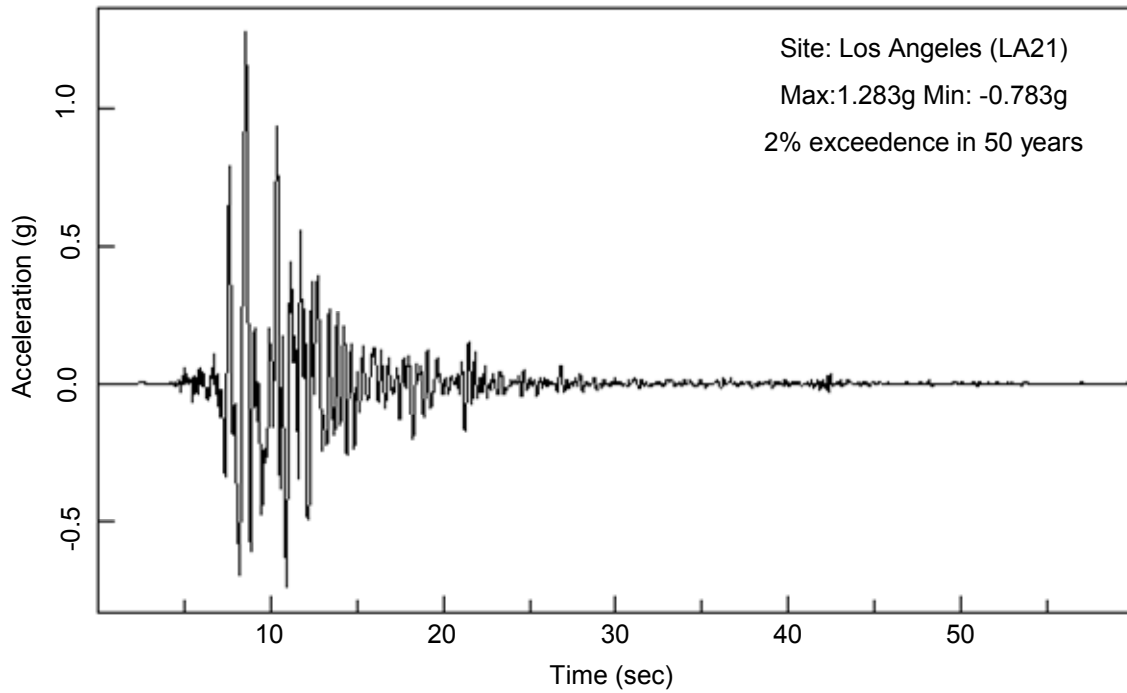


Figure F.1 Earthquake ground motions in 1995 Kobe

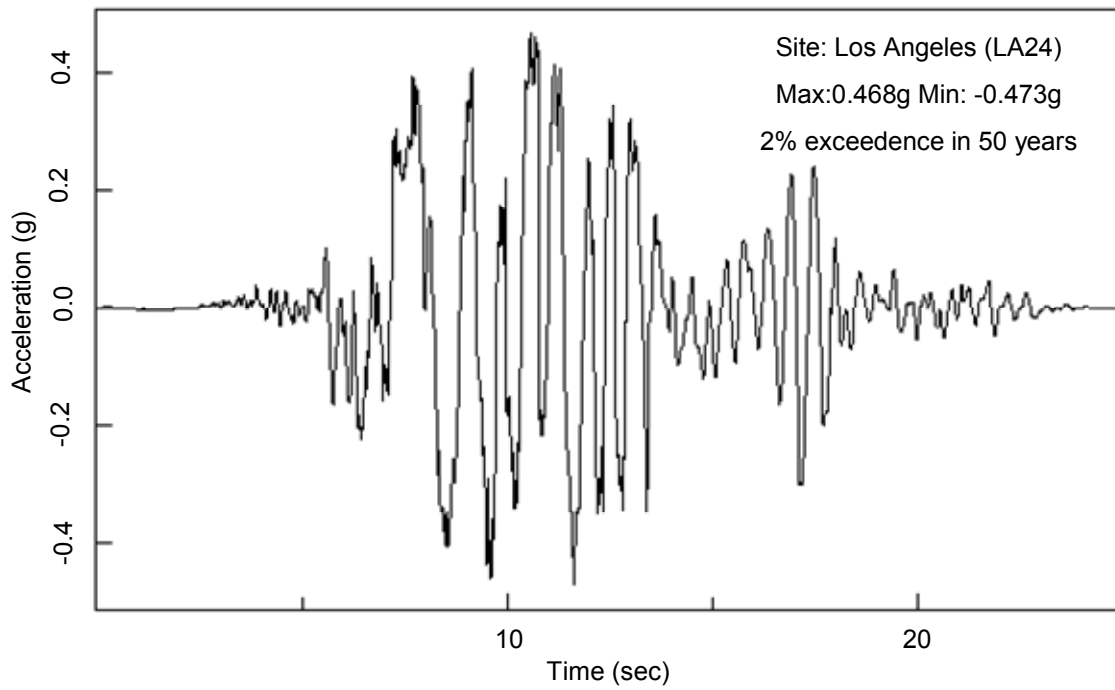
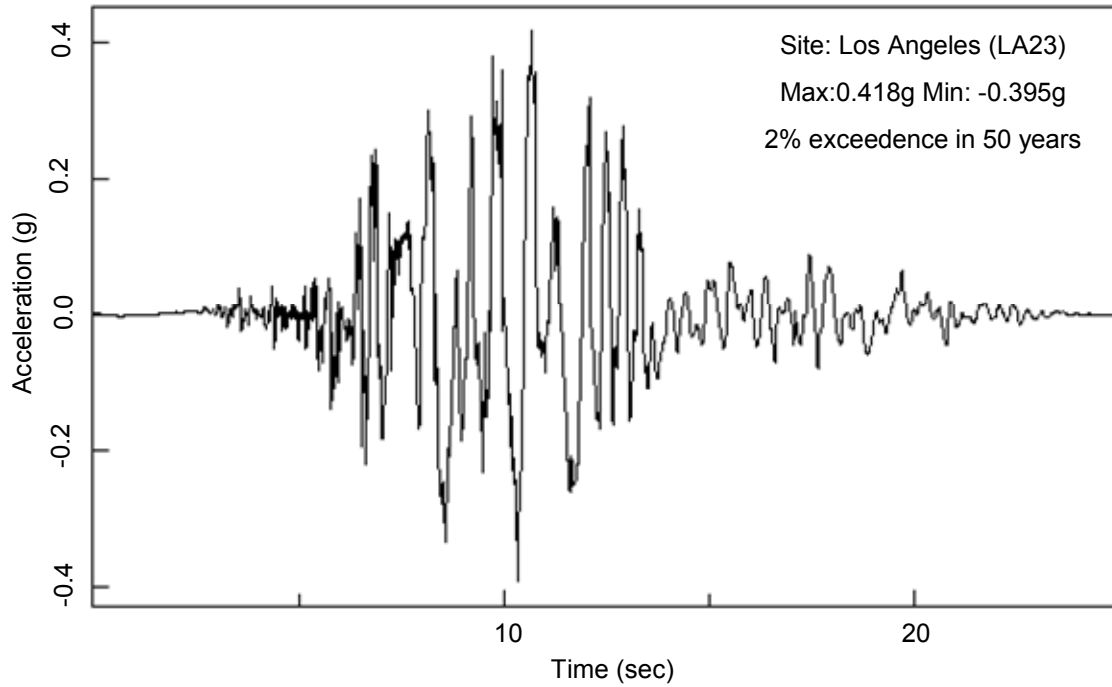


Figure F.2 Earthquake ground motions in 1989 Loma Prieta

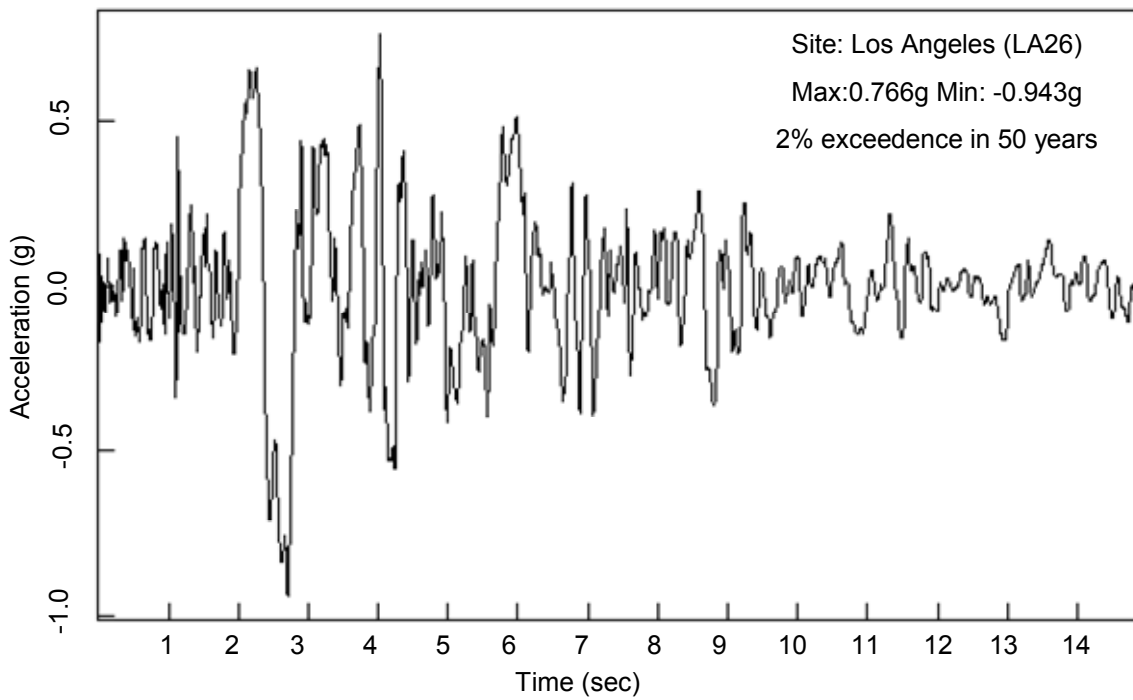
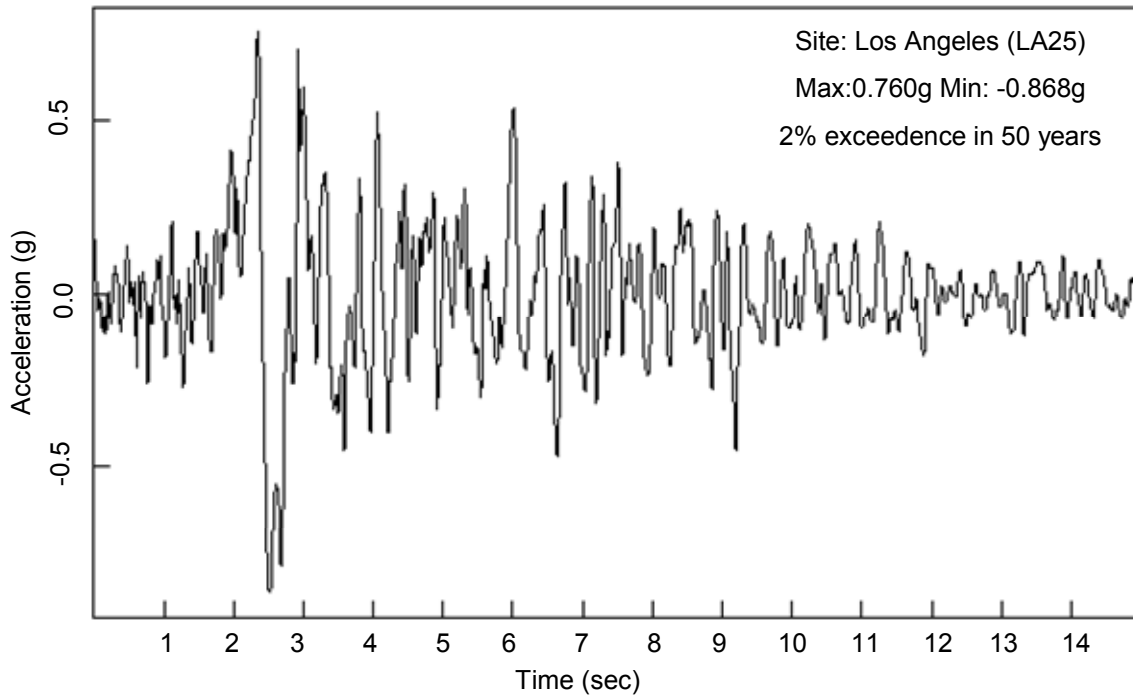


Figure F.3 Earthquake ground motions in 1994 Northridge

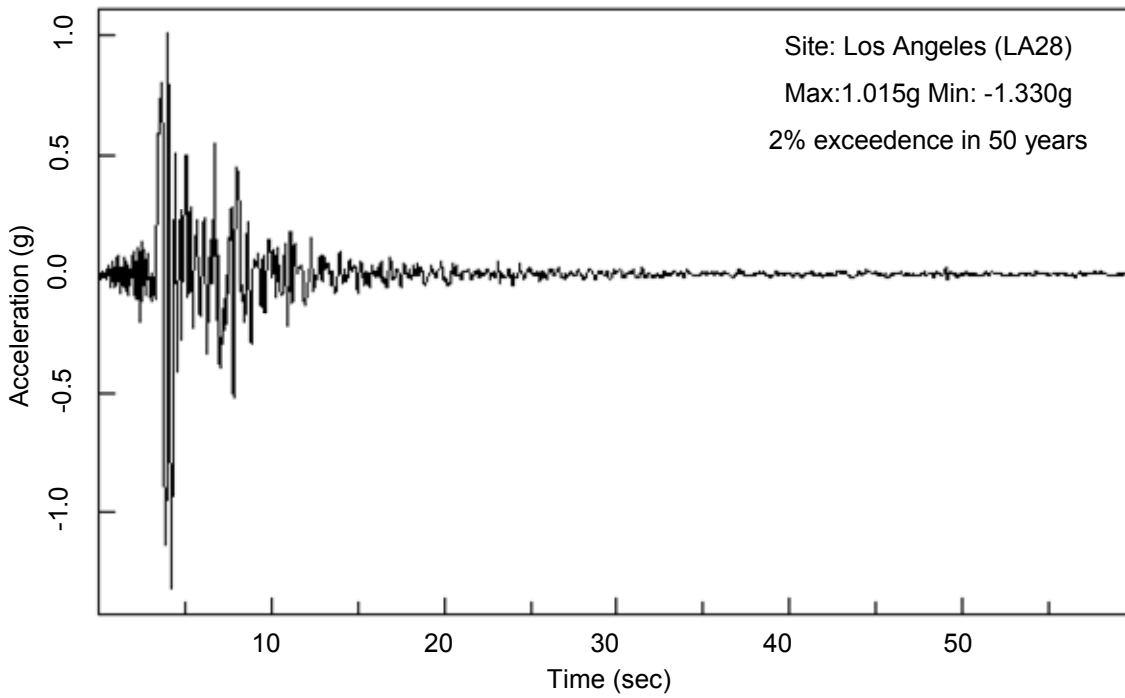
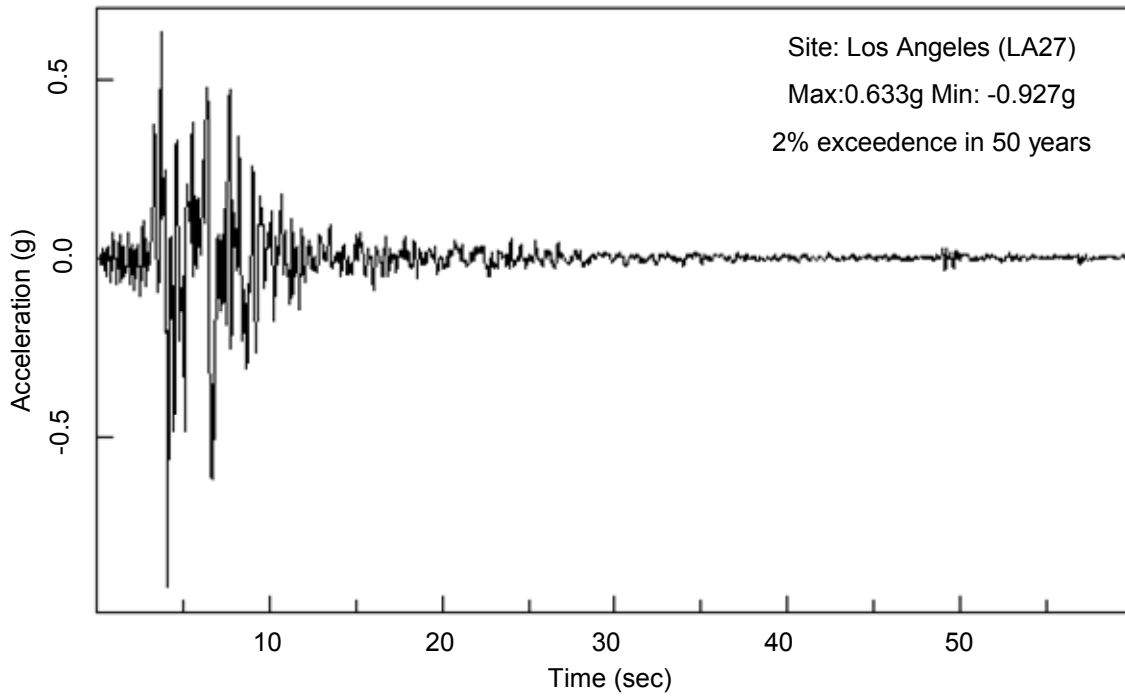


Figure F.4 Earthquake ground motions in 1994 Northridge

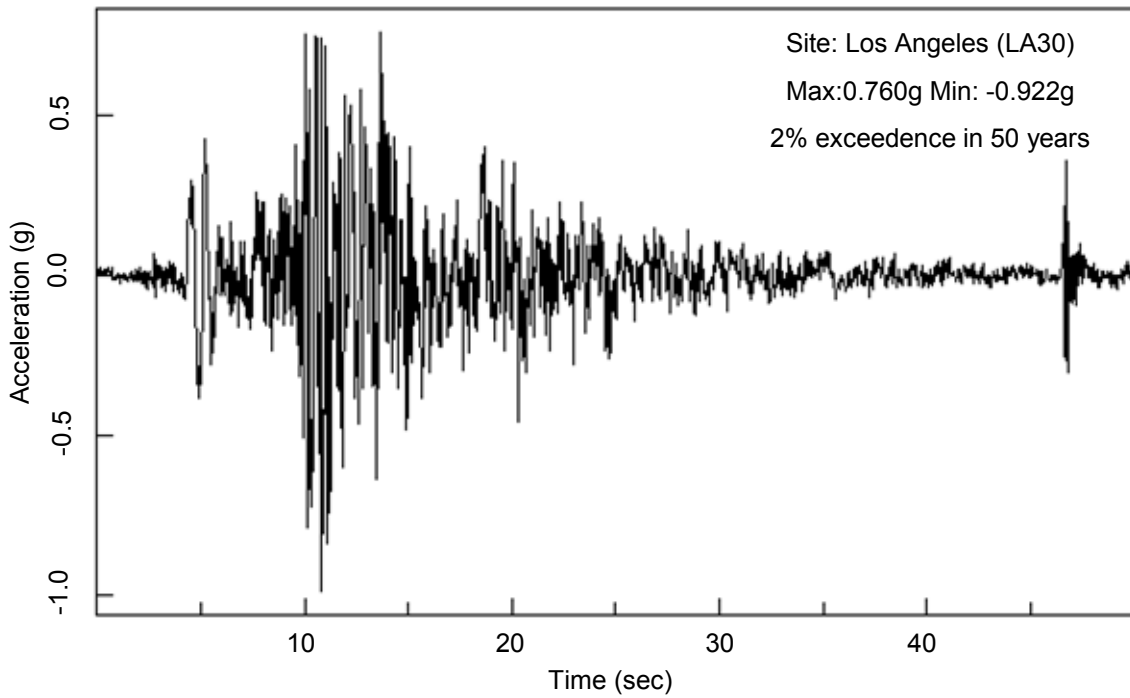
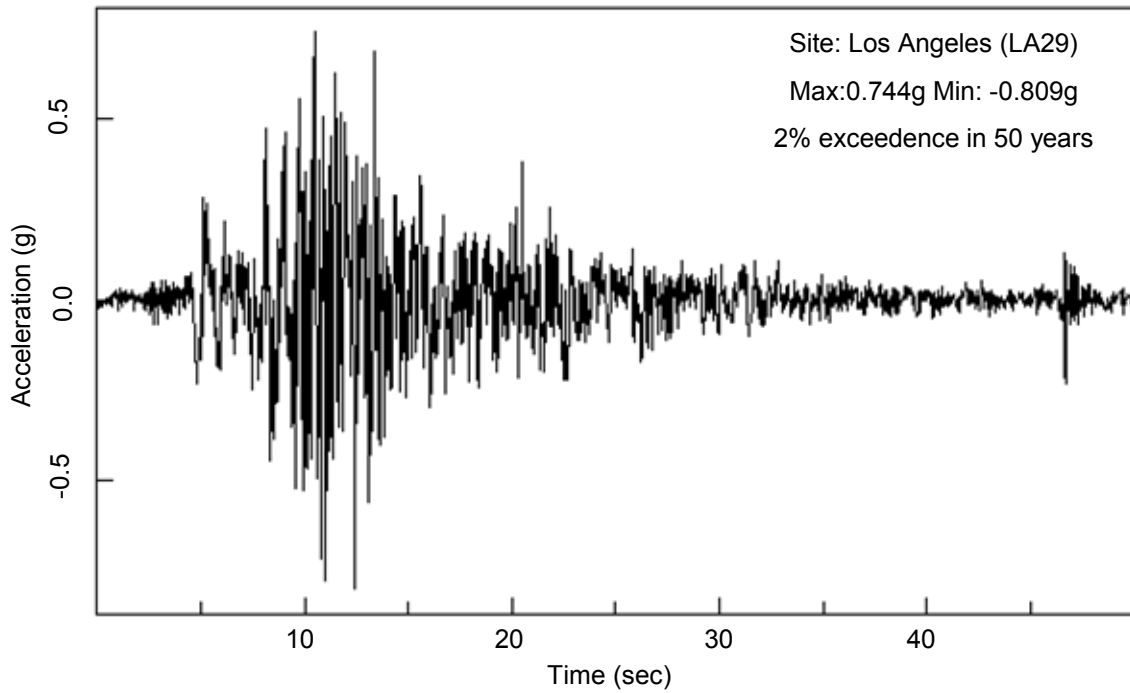


Figure F.5 Earthquake ground motions in 1974 Tabas

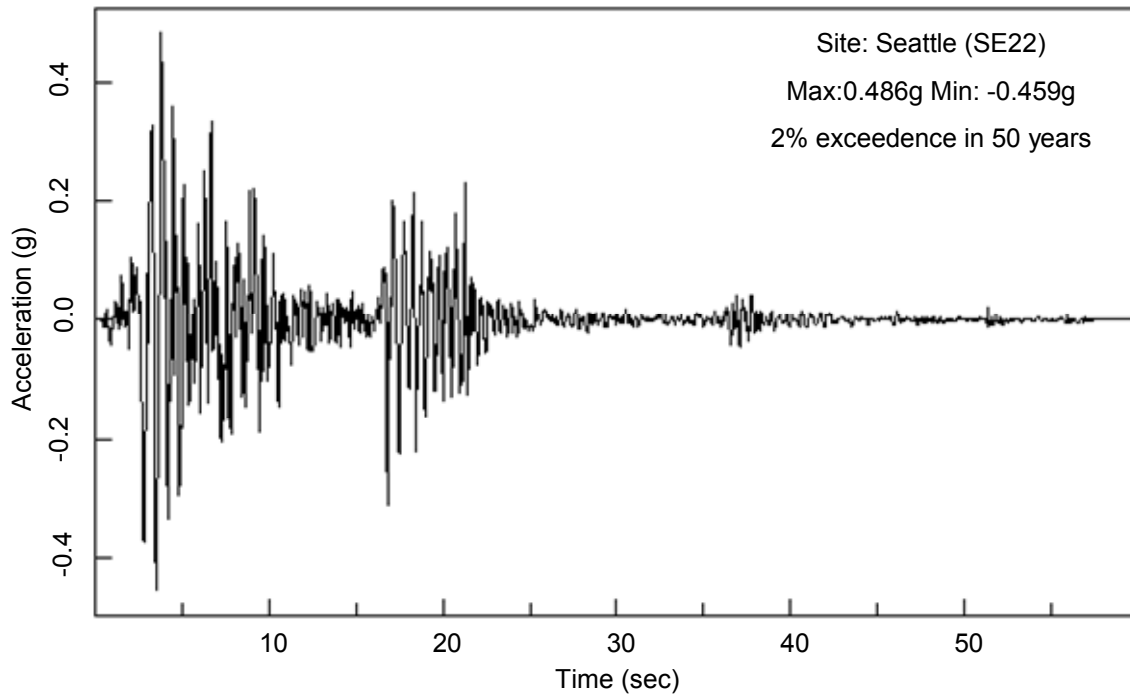
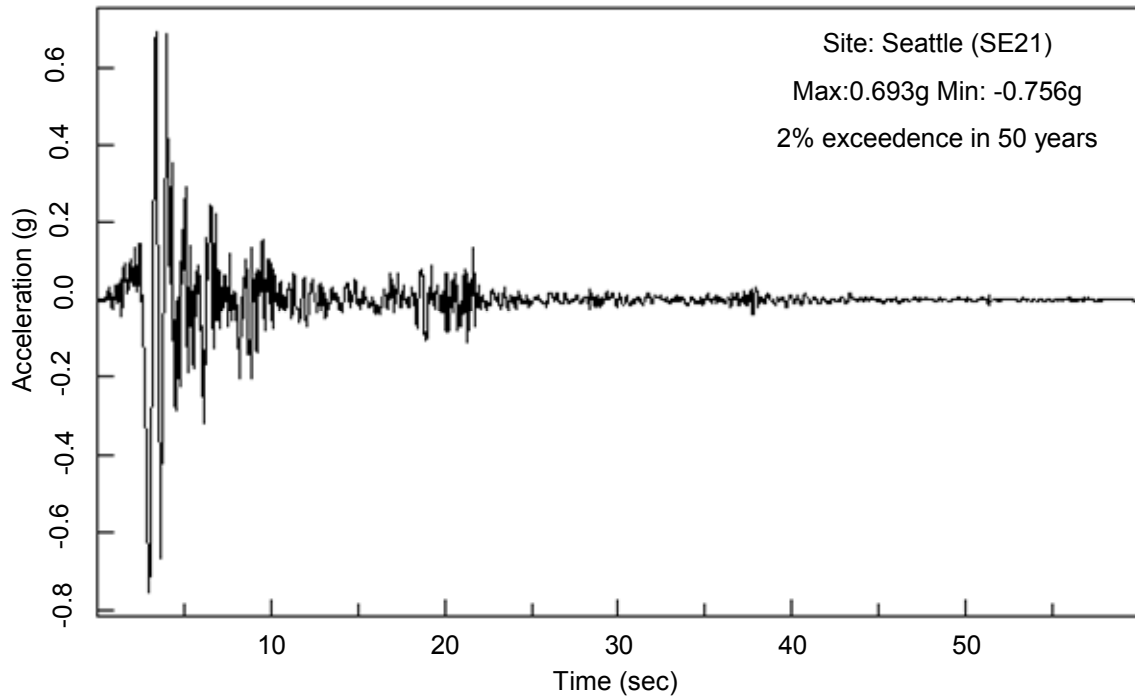


Figure F.6 Earthquake ground motions in 1992 Mendocino

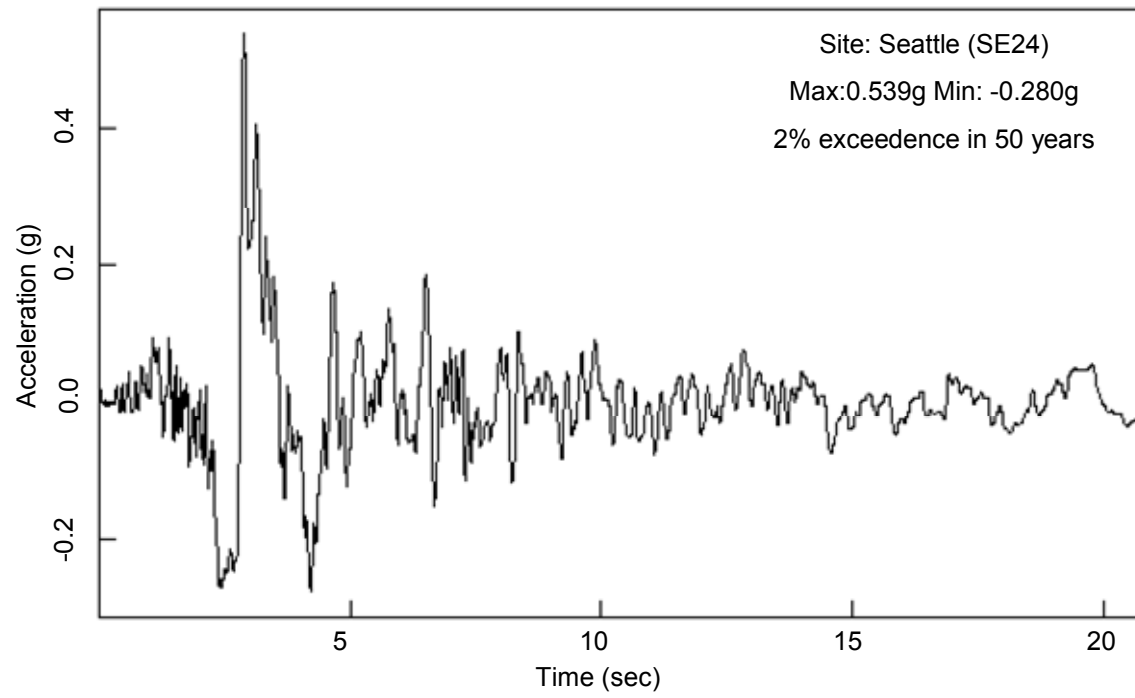
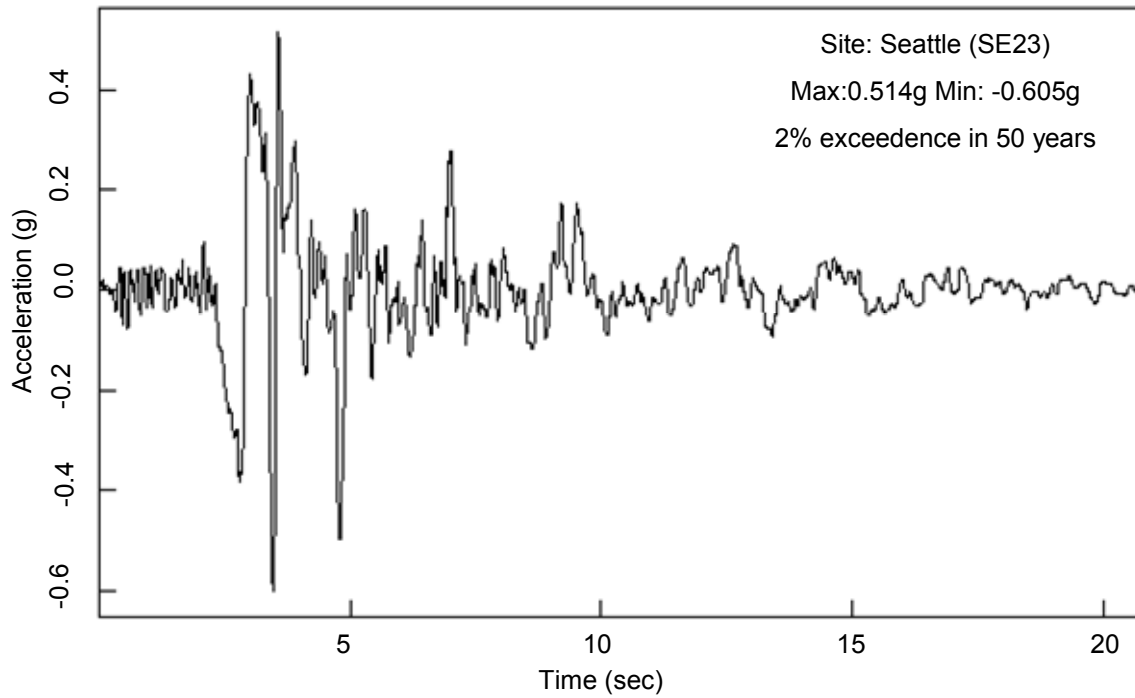


Figure F.7 Earthquake ground motions in 1992 Erzincan

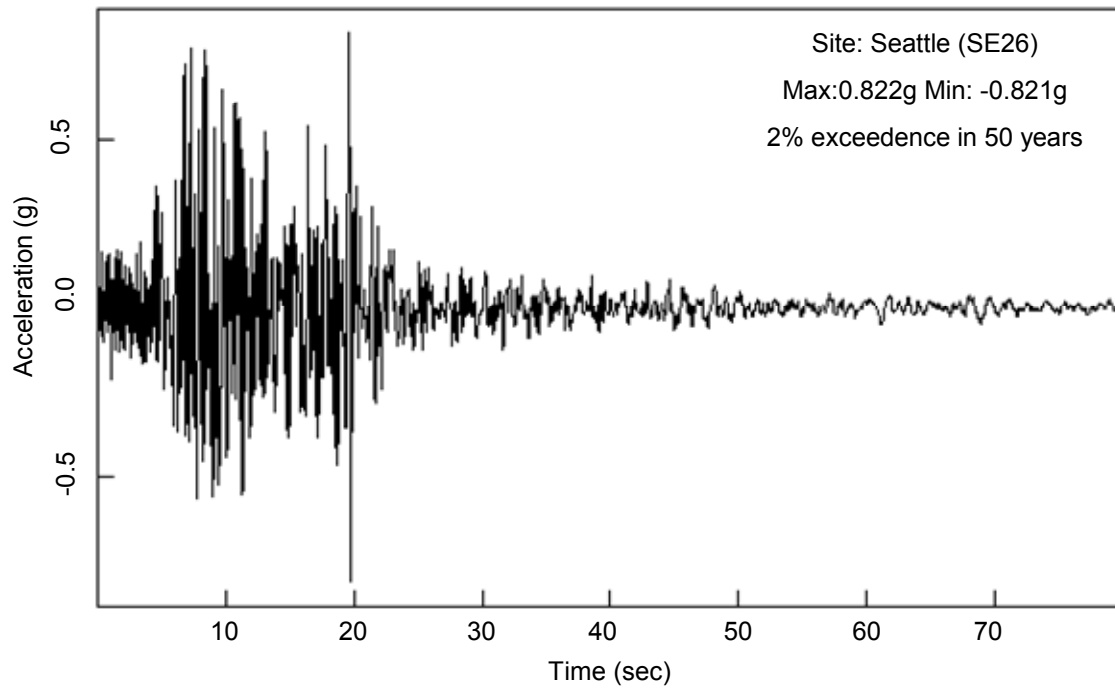
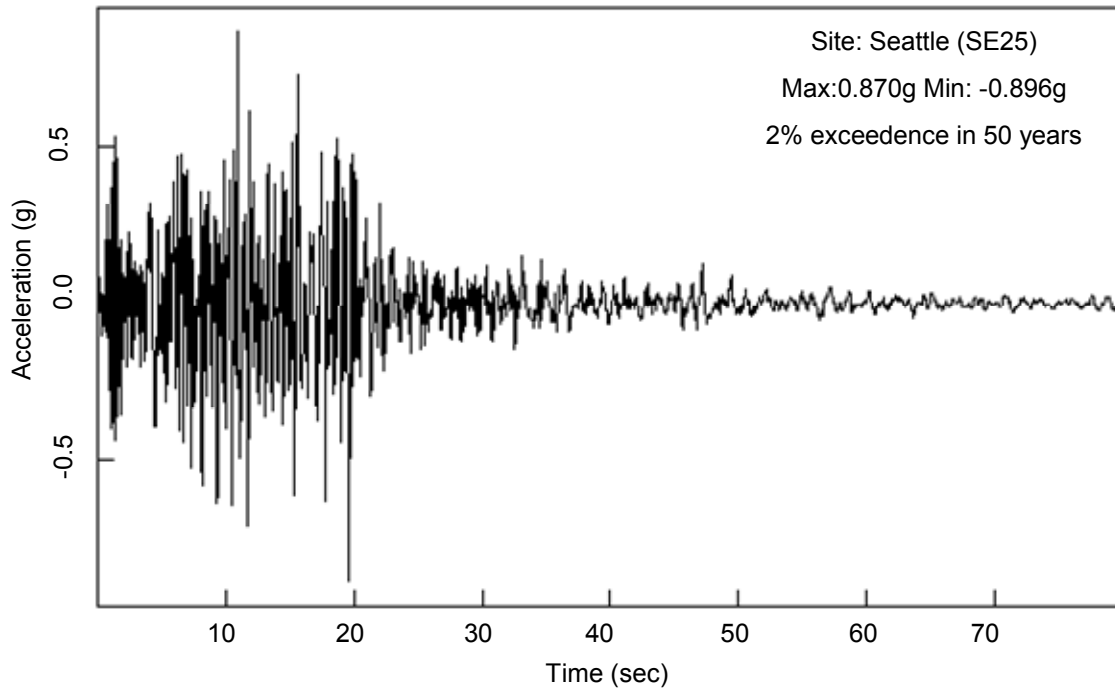


Figure F.8 Earthquake ground motions in 1949 Olympia

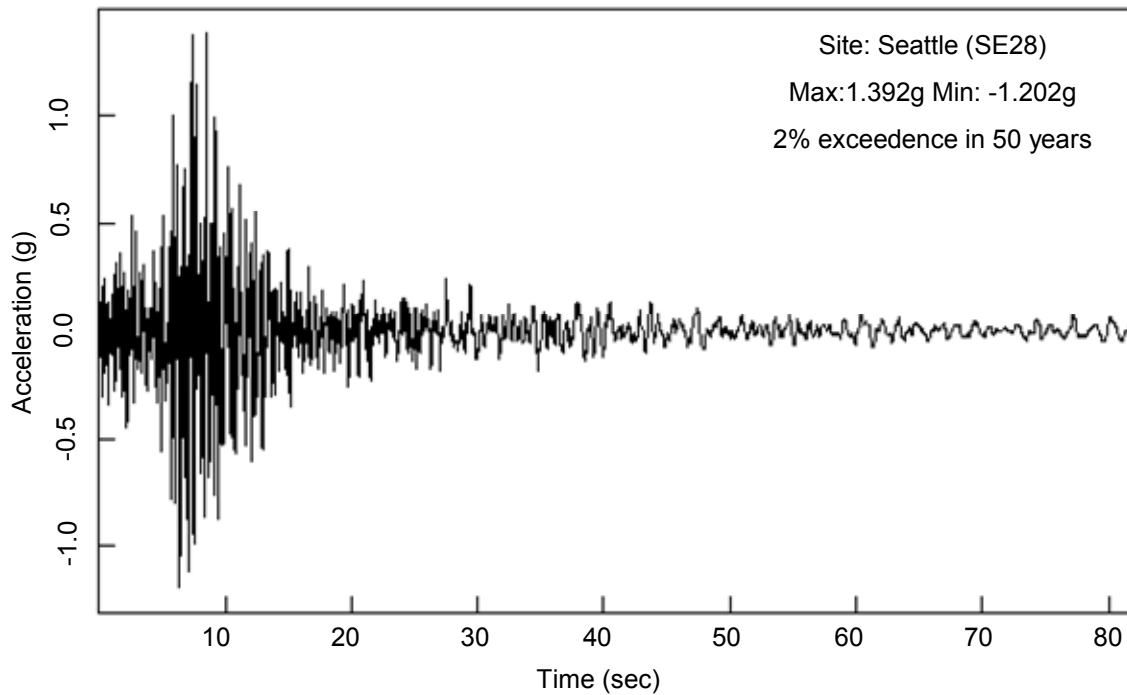
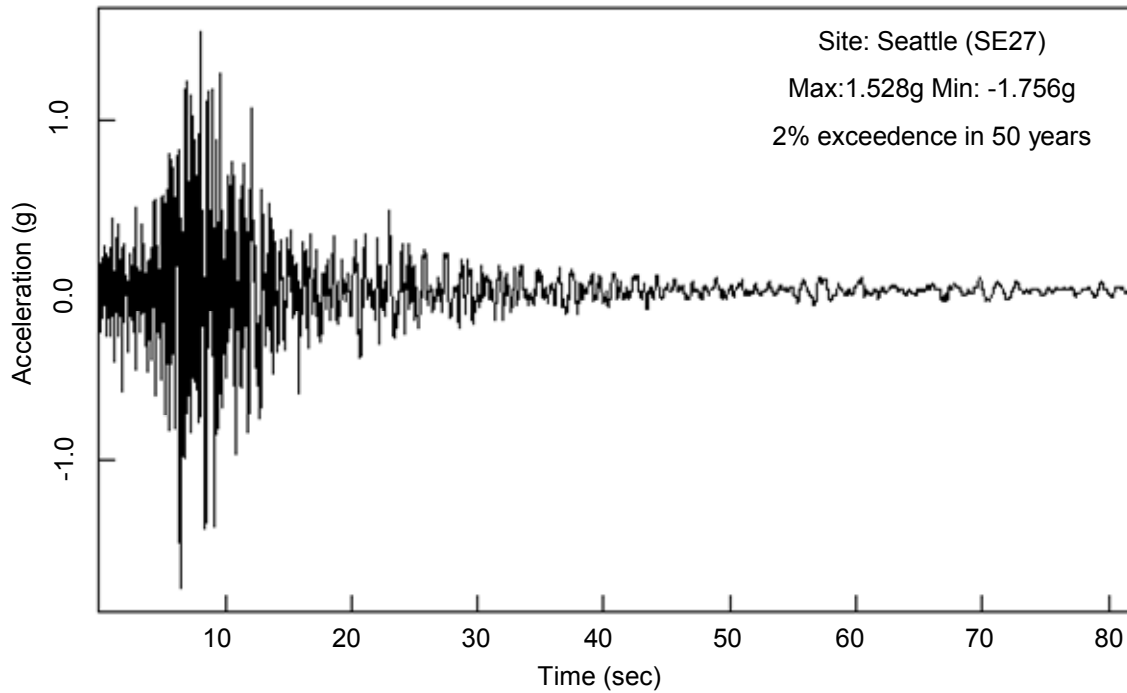


Figure F.9 Earthquake ground motions in 1965 Seattle

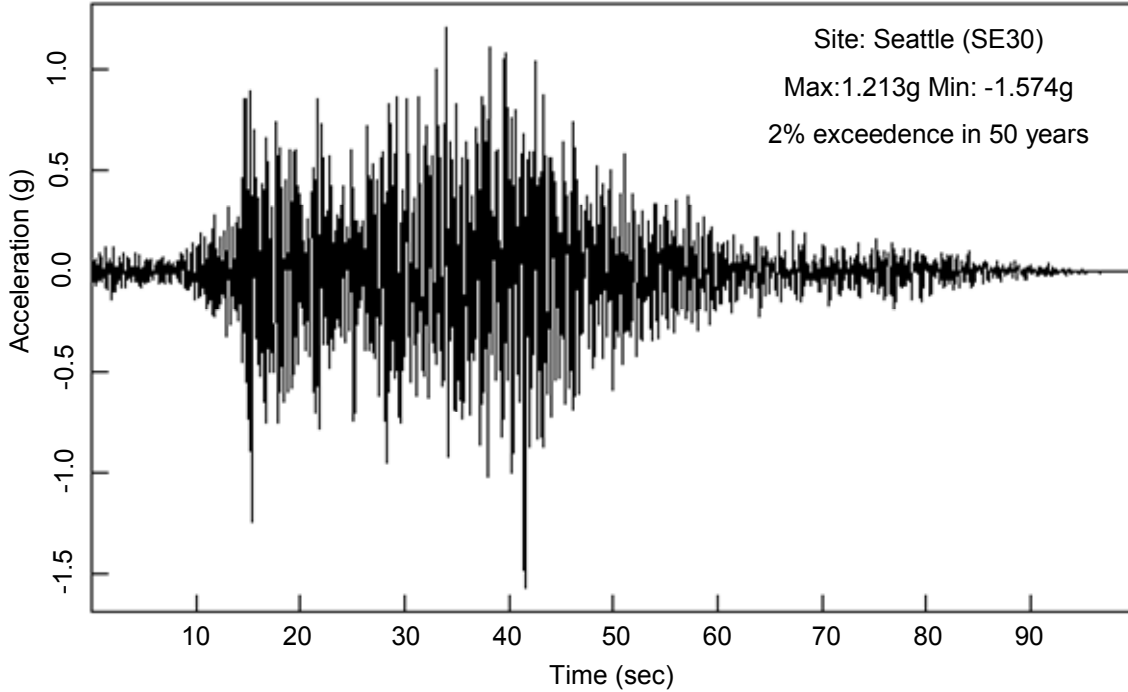
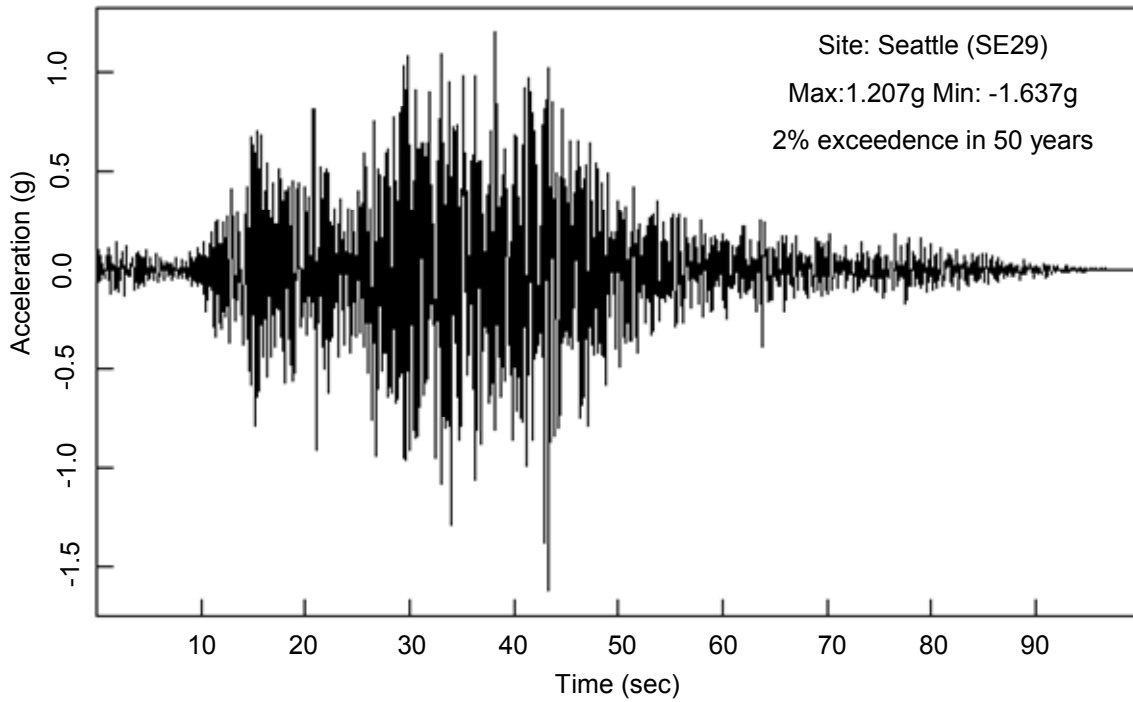


Figure F.10 Earthquake ground motions in 1985 Valpariso

References

ABAQUS ver. 6.6-1 (2006), Theory and User's Manual, Hibbit, Karlsson & Sorensen, Inc., Pawtucket, RI.

Adey, B. T., Grondin, G. Y. and Cheng J.J.R. (2000), Cyclic Loading of End-Plate Moment Connection, *Canadian Journal of Civil Engineering*, v. 27, n. 4, pp 683-701

Alostaz, Y. M. and Schneider, S. P. (1997), Analytical Behavior of Connections to Concrete Filled Steel Tubes, *Journal of Constructional Steel Research*, v. 40, n.2 pp 95-127

Altman, W. G. , Azizinamini, A., Bradbrun, J. H. And Radziminski, J .B. (1982), Moment-Rotation Characteristics of Semi-Rigid Steel Beam-Column Connections, Earthquake Hazard Mitigation Program, NSF, Final Report, University of South Carolina, Columbia, SC.

American Institute of Steel Construction (AISC). (1994), *Manual of Steel Construction, Load and Resistance Factor Design (LRFD)*, 2nd Ed., Chicago, IL.

American Institute of Steel Construction (AISC). (2001), *Manual of Steel Construction, Load and Resistance Factor Design (LRFD)*, 3rd Ed., Chicago, IL.

American Institute of Steel Construction (AISC). (2005), *Prequalified Connections for Special and Intermediate Steel Moment Frames for Seismic Applications (ANSI/AISC 358-05)*, Chicago, IL.

American Institute of Steel Construction (AISC). (2005), *Seismic Provisions for Structural Steel Buildings (ANSI/AISC 341-05)*, Chicago, IL.

American Institute of Steel Construction (AISC). (2005), *Specification for Structural Steel Buildings (ANSI/AISC 360-05)*, Chicago, IL.

American Society of Civil Engineers (ASCE). (2005), *Minimum Design Loads for Buildings and Other Structures*, ASCE 7-05

Astaneh-Asl, A. (1995), Seismic Design of Bolted Steel Moment-Resisting Frames, Steel Tips published by Structural Steel Educational Council, Technical Informational &Product Service, July

Astaneh-Asl, A. (1997), Seismic Design of Steel Column-Tree Moment-Resisting Frames, Steel Tips published by Structural Steel Educational Council, Technical Informational &Product Service, April

Azizinamini, A. and Prakash, B. (1993), A Tentative Design Guideline for a New Steel Beam Connection Detail to Composite Tube Columns, *AISC Engineering Journal*, 3rd quarter, pp 103-115

Azizinamini, A. and Schneider, S. P. (2001), Moment Connections to Circular Concrete-Filled Steel Tube Columns, *J. of Structural Engineering*, ASCE, v. 130, n. 2, pp 213-222

Azizinamini, A., Bradbrun, J. H. And Radzimirski, J .B. (1985), Static and Cyclic Behavior of Semi-Rigid Steel Beam-Column Connections, Technical Report, Department of Civil Engineering, University of South Carolina, Columbia, SC.

Bailey, J. R. (1970), Strength and Rigidity of Bolted Beam-to-Column Connections, Conference on Joints in Structures, Univ. of Sheffield

Batho, C. and Rowan, H.C. (1934), Investigation on Beam and Stanchion Connections, 2nd Report, Steel Structures Research Committee, Department of Scientific and Industrial Research, His Majesty's Stationary Office, London, v. 1-2 pp. 61-137

Bell, W. G., Chesson, E. J. and Munse, W. H. (1958), Static Tests of Standard Riveted and Bolted Beam to Column Connections, University of Illinois Engineering Experiment Station, Urbana, IL.

Bjorhovde, R. (1984), Effect of End-Restraint on Column Strength-Practical Applications. *AISC Eng. J.* 20(1)

Casciati, F., Faravelli, L. and Petrini, L. (1998), Energy Dissipation in Shape Memory Alloy Devices, *Computed-Aided Civil and Infrastructure Engineering*, v. 13, pp 433-442

Chan, S. L. and Chui, P.P.T. (2000), Non-Linear Static and Cyclic Analysis of Steel Frame with Semi-Rigid Connections, Elsevier Press

Chen W. F. and Lui, E. M. (1991), Stability Design of Steel Frames, CRC Press Inc.

Choi, E.S., Nam, T. H. and Cho, B.S.(2005), A New Concept of Isolation Bearings for Highway Steel Bridges using Shape Memory Alloys, *Canadian Journal of Civil Engineering*, v. 32, pp 957-067

Chopra, A.K. (1995), *Dynamics of Structures: Theory and Applications to Earthquake Engineering*, Prentice-Hall, Upper Saddle River, NJ.

Christopoulos, C., Filiatrault, A., Uang, C. M. and Folz, B. (2002), Posttensioned Energy Dissipating Connections for Moment-Resisting Steel Frames, *J. of Structural Engineering*, ASCE, v. 129, n. 9, pp 1111-1120

Citipitioglu, A.M., Haj-Ali, R.M., and White, D.W. (2002), Refined 3D Finite Element Modeling of Partially-Restrained Connections Including Slip, *J of Constructional Steel Research*, v 58,995-1013

Computer and Structures, Inc (CSI), (1984-2004), SAP2000 Nonlinear Version 10.02: Structural Analysis Program, Berkeley, CA.

Corbi, O. (2003), Shape Memory Alloys and their Application in Structural Oscillations Attenuation, *Simulation Modeling Practice and Theory*, v.11, pp 387-402

Corey S. S. (1999), Behavior of Full-Scale Bolted Beam-to-Column T-Stub and Clip Angle Connections Under Cyclic Loading, Master's Thesis, Georgia Institute of Technology, Atlanta, GA.

Davison, J. B., Kirby, P. A. and Nethercot, D. A. (1987), Rotational Stiffness Characteristics of Steel Beam to Column Connections, *J of Constructional Steel Research*, v. 8, pp 17-54

Deierlein, G. G. (1998), Summary of SAC Case Study Building Analysis, *J. of Performance of Constructed Facilities*, ASCE, v. 12, n. 4, pp 202-212

DesRoches, R. and Dlelamont, M. (2002), Seismic Retrofit of Simply Supported Bridges using Shape Memory Alloys, *Engineering Structures*, v.24, pp 325-332

DesRoches, R., McCormick, J., and Delemont, M. (2004), Cyclic Properties of superelastic shape memory alloy wires and bars, *J. of Structural Engineering*, ASCE, v. 130, n. 1, pp 38-46

Dolce, M., Cardone, D., Marnetto, R. (2000), Implementation and Testing of Passive Control Devices based on Shape Memory Alloys, *Earthquake Engineering and Structural Dynamics*, v. 29, pp 945-968

Dolce, M., Cardone, D., Marnetto, R. (2001), SMA Re-centering Devices for Seismic Isolation of Civil Structures, *Proceedings of SPIE*, 4330, pp 238-249

Douty, R. T. (1964), Strength Characteristics of High Strength Bolted Connections with Particular Application to the Plastic Design of Steel Structures, Ph.D. Thesis, Cornell University, Ithaca, NY.

Elremaily, A. and Azizinamini, A. (2001), Experimental Behavior of Steel Beam to CFT Column Connections, *Journal of Constructional Steel Research*, v. 57, pp 1099-1119

El-Tawil, S. and Deierlein, G. G. (2001), Nonlinear Analyses of Mixed Steel-Concrete Moment Frames. Part I - Beam-Column Element Formulation, *Journal of Structural Engineering*, ASCE, Vol. 127, No. 6, pp. 647-655

El-Tawil, S. and Deierlein, G. G. (2001), Nonlinear Analyses of Mixed Steel-Concrete Moment Frames. Part II - Implementation and Verification, *Journal of Structural Engineering*, ASCE, Vol. 127, No. 6, pp. 656-665

El-Tawil, S., Kanno, R., and Deierlein, G. G. (1996), Inelastic Models for Composite Moment Connections in RCS Frames, *Composite Construction in Steel and Concrete III*, ASCE Special Publication, Edited by Buckner, C. D and Shahrooz, B., SEI, American Society of Civil Engineers, pp. 197-210

Eurocode4 (2004), CEN: Design of Composite Steel and Concrete Structures, European Committee for Standardization, Brussels

Federal Emergency Management Agency (FEMA). (1995), *NEHRP Recommended Provisions for Seismic Regulations for New Buildings and Other Structures*, Part 1 and 2, 1994 ed., Report FEMA 222A and 223A, Federal Emergency Management Agency, Washington, D.C., July

Federal Emergency Management Agency (FEMA). (2000), Recommended Seismic Design Criteria for New Steel Moment-Frame Buildings, *Ref. No. FEMA-350, SAC Joint Venture, Washington, D.C.*

Federal Emergency Management Agency (FEMA). (2000), State of the Art Report on Systems Performance of Steel Moment Frames Subjected to Earthquake Ground Shaking, *Ref. No. FEMA-355C, SAC Joint Venture, Washington, D.C.*

Galambos, T. V. (ed.) (1998), Guide to Stability Design Criteria for Steel Structures, Structural Stability Research Council, 5th edition, John Wiley and Sons, New York, NY.

Gardener, A. P. and Goldsworthy, H.M. (2005), Experimental Investigation of the Stiffness of Critical Components in a Moment-Resisting Composite Connection, *Journal of Constructional Steel Research*, v. 61, pp 709-726

Green, T. P., Leon, R. T., and Rassati, G. A. (2004), Bidirectional Tests on Partially Restrained, Composite Beam-Column Connections, *Journal of Structural Engineering*, v. 130, n. 2, pp 320-327

Hajjar, J. F. (2002), Composite steel and concrete structural systems for seismic engineering, *J of Constructional Steel Research*, v. 58, pp 703-723

Hajjar, J. F., Gourley, B. C., O'Sullivan, B. P., and Leon, R. T. (1998), Analysis of Mid-Rise Steel Frame Damaged in Northridge Earthquake, *J. of Performance of Constructed Facilities*, ASCE, v. 12, n. 4, pp 221-231

Hechtman, R. A. and Johnston, B. G. (1947), Riveted Semi-Rigid Beam-to-Column Building Connections, Committee of Steel Structures Research, AISC, Progress Report No. 1, November

Hetchman, R. A. and Johnston, B. G. (1947), Riveted Semi-Rigid Beam to Column

Building Connections, *Committee of Steel Structures Research*, AISC, Progress Rept No. 1, November

Hu, T., Huang, C. S. and Chen, Z. L. (2005), Finite Element Analysis of CFT columns subjected to an axial compressive force and bending moment in combination, *J of Constructional Steel Research*, v. 62, pp 1692-1712

Indirli, M. et al. (2001), Demo Application of Shape Memory Alloy Devices: the Rehabilitation of S. Georgio Church Bell Tower, *Proceedings of SPIE*, 4330, pp 262-272

International Code Council, (2003), International Building Codes (IBC)

Johnson, N.D. and Walpole, W. R. (1981), Bolted End-Plate Beam-to-Column Connections under Earthquake Type Loading, *Research Report 81-7*, Department of Civil Engineering, University of Canterbury, Christchurch, New Zealand.

Kahn, M. M. and Lagoudas, D. (2002), Modeling of Shape Memory Alloy Pseudoelastic Spring Elements using Preisach Model for Passive Vibration Isolation. *Proceeding of SPIE*, 4693, pp336-347

Kanatani, H., Tabuchi, M., Kamba, T. Hsiaolien, J. and Ishikawa, M. (1987), A Study on Concrete Filled RHS Columns to H-Beam Connections Fabricated with HT-Bolts in Rigid Frames, *ASCE Proceedings Composite Construction of Steel and Concrete*, pp. 614-635

Kennedy, D. J. L. and Hafez, M. A. (1986), A Study of End-Plate Connections for Steel Beams, *Can. J. Civil Eng.*

Kim, D. H. (2003), Seismic Performance of PR Frames in Areas of Infrequent Seismicity, Ph.D Dissertation, Georgia Institute of Technology, Atlanta, GA.

Kim, D. K. (2005), A Database for Composite Columns, Master Thesis in School of Civil and Environmental Engineering, Georgia Institute of Technology, GA.

Kulak, G. L. , Fisher, J. W. and Struik, J. H. A. (1987), Guide to Design Criteria for

Bolted and Riveted Joint, 2nd Ed., Johns Wiley & Sons.

Leon, R. T. (1990), Semi-Rigid Composite Connection, *Journal of Constructional Steel Research*, v. 15, n.2, pp 99-120

Leon, R. T. (1997), Seismic Performance of Bolted and Riveted Connections, Background Reports: Metallurgy, Fracture Mechanics, Welding, Moment Connections, and Frame System Behavior, FEMA Publication No.288, Federal Emergency Management Association, Washington D.C., March.

Leon, R. T. and Kim, D. H. (2004), Seismic Performance of PR Frames in Zones in Infrequency Seismicity, *Proceeding of the 13th World Conference of Earthquake Engineering*, Paper 2696, IAEE, Vancouver, BC, Canada.

Leon, R. T., DesRoches, R., Ocel, J. Hess, G. (2001), Innovative Beam Column using Shape Memory Alloys, *Proceedings of SPIE*, 4330, pp227-237

Leon, R.T., Hu, J.W., and Schrauben, C. (2005), Rotational Capacity and Demand in Top-and-Seat Angle Connections Subjected to Seismic Loading, in Connections in Steel Structure 5, AISC/ECCS. (in print)

Lipson, S. L. (1977), Single-Angle Welded-Bolted Beam Connections, *J. Struct. Div.*, ASCE 103(ST3), pp. 559-571

Lipson, S. L. and Antonio, M. (1980), Single-Angle Welded-Bolted Connections, *Can. J. Civil Eng.* 7, pp. 315-324

Liu, J., and Astaneh-Asl, A. (2000), Cyclic Tests of Simple Connection Including the Effect of Slabs, *J. of Structural Engineering*, ASCE, v. 126, n. 1, pp 32-39

Lowes, L.N and Altoontash, A. (2003), Modeling Reinforced-Concrete Beam-Column Joints Subjected to Cyclic Loading, *J. of Structural Engineering*, ASCE, v. 129, n. 12, pp 1686-1697

McCormick, J.P. (2006), Cyclic Behavior of Shape Memory Alloys: Material Characterization and Optimization, Ph.D. Dissertation, Georgia Institute of Technology,

Atlanta, GA.

Mazzoni, S., McKenna, F., Fenves, G. L. (2006), Opensees Command Language Manual, Department of Civil Environmental Engineering, University of California, Berkeley.

Morino, S., Kawanguchi, J., Yasuzaki, C. and Kanazawa, S. (1992), Behavior of Concrete Filled Steel Tubular Three Dimensional Subassemblages, *ASCE Proceedings Composite Construction of Steel and Concrete*, pp. 726-741

Nethercot, D. A. (1985), Steel Beam-to-Column Connections – A Review of Test Data, Construction Industry Research and Information Association, London, England

Newmark, N. M. (1959), A Method of Computation for Structural Dynamics, ASCE, Journal of the Engineering Mechanics Division, Vol. 85 No. EM3, (1959).

Ocel, J. M. (2002), Cyclic Behavior of Steel Beam-Column Connections with Shape Memory Alloy Connection Elements, Master's thesis, Georgia Institute of Technology.

Ocel, J. M., DesRoches, R., Leon, R. T., Hess, W. G., Krumme, R., Hayes, J. R., and Sweeney, S. (2004), Steel Beam-Column Connections using Shape Memory Alloys, *J. of Structural Engineering*, ASCE, v. 130, n. 5, pp 732-740

Ostrander, J. R. (1970), An Experimental Investigation of End-Plate Connections, MS Thesis, University of Saskatchewan, Saskatoon, SK, Canada.

Otani, S., Hiraishi, H. and Midorikawa, M. (2000), Development of Smart Systems for Building Structures, *Proceedings of SPIE*, 3988, pp2-9

Penar, B. W. (2005), Recentering Beam-Column Connections using Shape Memory Alloys, Master's thesis, Georgia Institute of Technology.

Prion, H.G. and McLellan, A. B. (1992), Connecting Steel Beam to Concrete-Filled Steel Columns, Proceeding of the ASCE Structures Congress on Composite Compression Members, San Antonio, TX, pp 918-921

Rassati, G. A., Leon, R. T., and Noe, S. (2004), Component Modeling of Partially Restrained Composite Joints under Cyclic and Dynamic Loading, *J. of Structural*

Engineering, ASCE, v. 130, n. 2, pp 343-351

Rathburn, J. C. (1936), Elastic Properties of Riveted Connections, *ASCE Trans.*, 101(1933), pp. 524-563

Roeder, C. W. (2000), Seismic Behavior of Steel Braced Frame Connections to Composite Columns, in Connections in Steel Structure 4 (R. Leon and S. Easterling, eds.), AISC, pp. 51-62

Saadat, S., Noori, M., Davoodi, H., Zhou, Z., Suzuki, Y. and Masuda, A. (2001), Using NiTi SMA Tendons for Vibration Control of Coastal Structures, *Smart Materials and Structures*, v. 10, pp695-704

Saadat, S., Salichs, J., Noori, M., Hou, Z., Davoodi, H., Bar-on, I., Suzuki, Y. and Masuda, A. (2002), An Overview of Vibration and Seismic Application of NiTi Shape Memory Alloy, *Smart Materials and Structures*, v. 11, pp218-229

Salmon, C. G. and Johnson, J. E. (1990), *Steel Structures: Design and Behavior, Emphasizing Load and Resistance Factor Design*, 3rd Ed., Harper and Row, New York, NY.

SAP 2000 ver. 11 (2007). SAP 2000 Steel Design Manual, Computer and Structures, Inc. Berkeley, California, USA

Schneider, S. P. and Alostaz, Y. F (1997), Experimental Behavior of Connections to Concrete-Filled Steel Tubes, *Journal of Constructional Steel Research*, v. 45, n.3, pp 321-351

Shakir-Khalil, H. (1992), Full Scale Test on Composite Connection, *ASCE Proceedings Composite Construction of Steel and Concrete*, pp. 539-554

Sherbourne, A. N. (1961), Bolted Beam-to-Column Connections, *Struct. Engineer* 39(6), pp. 203-210

Smallidge, J. M. (1999), Behavior of Bolted Beam-to-Column T-Stub Connections under Cyclic Loading, MS Thesis, Georgia Institute of Technology.

Somerville, P.G., Smith, N., Punyamurthula, S., & Sun, J. (1997), Development of Ground Motion Time Histories for Phase 2 of the FEMA/SAC Steel Project, SAC Background Document, Report No. SAC/BD 97/04.

Sommer, W. H. (1969), Behavior of Welded Header Plate Connections, Master's Thesis, Univ. of Toronto, ON. Canada

Sommer, W. H. (1969), Behaviour of Welded Header Plate Connections, MS Thesis, University of Toronto, ON. Canada.

Song, G., Ma, N., Li, N. H. (2006), Application of Shape Memory Alloys in Civil Structures, *Engineering Structures*, v.28, pp 1266-1274

Swanson, J. A. and Leon, R. T. (2000), Bolted Steel Connections: Tests on T-Stub Components, *J. of Structural Engineering*, ASCE, v. 126, n. 1, pp 50-56

Swanson, J. A. and Leon, R. T. (2001), Stiffness Modeling of Bolted T-Stub Connection Components, *J. of Structural Engineering*, ASCE, v. 127, n. 5, pp 498-505

Swanson, J.A. (1999), Characterization of the Strength, Stiffness, and Ductility Behavior of T-stun Connection. Ph.D Dissertation, Georgia Institute of Technology, Atlanta, GA.

Swanson, J.A., Kokan, D.K., and Leon, R.T. (2002), Advanced Finite Element Modeling of Bolted T-stub Connection Components, *J of Constructional Steel Research*, v. 58, pp 1015-1031

Tami, H. and Kitagawa, Y. (2002), Pseudoelastic behavior of Shape Memory Alloy Wires and its Application to Seismic Resistance Member for Building, *Computational Material Science*, v. 25, pp 218-227

Thermou, G. E., Elnashai, A. S., Plumier, A. and Doneaux, C. (2004), Seismic Design and Performance of Composite Frames, *Journal of Constructional Steel Research*, Vol. 60, pp.31-57

Thornton, W. A., (1985), Prying Action – A General Treatment, *Engineering Journal*, American Institute of Steel Construction (AISC), v. 22, n. 2

Tompson, L. E., Mckee, R. J., and Visintainer, D. A. (1970), An Investigation of Rotation Characteristics of Web Shear Framed Connections using A-36 and A-41 Steels, Dep. of Civil Engineers, Univ. of Missouri-Rolla, Rolla. MO.

Torres, LI. Lopez-Almansa, F. and Bozzo, L. M. (2004), Tension-Stiffening Model for Cracked Flexural Concrete Members, *J. of Structural Engineering*, ASCE, v. 130, n. 8, pp 1242-1251

Tsai K. C. et al. (2004), Pseudo Dynamic Tests of a Full-Scale CFT/BRB Composite Frame, *Proceeding of the 2004 Structure Congress*, ASCE

Viest, I. M. et al. (1997), Composite Construction Design for Building, Co-published by ASCE, McGraw-Hill, Chapter 5.3

Wilde, K., Gardoni, P. and Fujino, Y. (2000), Base Isolation System with Shape Memory Alloy Device for Elevated Highway Bridges, *Engineering Structures*, v. 22, pp 222-229

Wilson, W. M. and Moore, H. F. (1917), Tests to Determine the Rigidity of Riveted Joints of Steel Structures, University of Illinois Engineering Experiment Station, Bulletin No. 104, Urbana, IL.

Wu, L. Y., Chung, L. L, Tsai, S. F., Lu, C. F. and Huang, G. L. (2005), Seismic Behavior of Bolted Beam to Column Connections for Concrete Filled Steel Tube, *Journal of Constructional Steel Research*, v. 61, pp 1387-1410

Wu, L. Y., Chung, L. L, Tsai, S. F., Lu, C. F. and Huang, G. L. (2007), Seismic Behavior of Bidirectional Bolted Connections for CFT Columns and H-Beams, *Engineering Structures*, v.29, pp. 395-407

Young, C. R. and Jackson, K. B. (1934), The Relative Rigidity of Welded and Riveted Connections, *Canadian Journal of Research*, v. 11, n. 1, July, pp. 62-134

Zoetemeijer, P. and Kolstein, M. H. (1975), Flush End Plate Connections, Stevin

Laboratory Report No. 6-75-20, Delft Univ. of Technology, The Netherlands

Vita

Jong Wan Hu was born on June 2, 1974 in Incheon, Korea. Jong Wan Hu received his B.S. and M.S. degrees in 2000 and 2002, respectively, from the Department of Civil Engineering at Inha University, South-Korea. He worked as a post M.S. with the Steel Structure Laboratory at the Inha University from 2002 to 2003, where he performed several research projects for promoting the use of steel structures by introducing innovative new connection designs in construction. At Georgia Institute of Technology, he received his M.S. degree in Civil Engineering in 2005. He is currently a Ph.D. candidate in Civil Engineering, as well as an M.S. candidate in Mechanical Engineering at Georgia Institute of Technology. He is planning to receive both degrees in 2008. His primary research interests include applications of smart structures and materials, advanced computational technology for refined structural modeling and numerical simulations, self healing structures with smart material applications, seismic design and performance of composite structures and bridges, and earthquake engineering in the Civil Engineering field, as well as micro-mechanics and lattice materials in Mechanical Engineering field. He is a member of American Society of Civil Engineers (ASCE), American Institute of Steel Construction (AISC), Earthquake Engineering Research Institute (EERI) and American Society of Mechanical Engineers (ASME). He is a registered professional engineer (PE) in Ohio. He graduated Inha University as Best Honor Students and received Best Award for Abroad Study Scholarship from Korean Science Foundation (KSF) and Korean Ministry of Science & Technology. At Georgia Institute of Technology, he received NEESR/NSF Fellowship for Graduate Student.